C. L. Tien
Professor.
Fellow ASME

L. S. Yao
Graduate Student.

Department of Mechanical Engineering,
University of California,
Berkeley, Calif.

Analysis of Conduction-Controlled Rewetting of a Vertical Surface

The present paper presents a two-dimensional analysis of conduction-controlled rewetting of a vertical surface, whose initial temperature is greater than the rewetting temperature. The physical model consists of an infinitely extended vertical slab with the surface of the dry region adiabatic and the surface of the wet region associated with a constant heat transfer coefficient. The physical problem is characterized by three parameters: the Peclet number or the dimensionless wetting velocity, the Biot number, and a dimensionless temperature. Limiting solutions for large and small Peclet numbers obtained by utilizing the Wiener-Hopf technique and the kernel-substitution method exhibit simple functional relationships among the three dimensionless parameters. A semi- empirical relation has been established for the whole range of Peclet numbers. The solution for large Peclet numbers possesses a functional form different from existing approximate two-dimensional solutions, while the solution for small Peclet numbers reduces to existing one-dimensional solution for small Biot numbers. Discussion of the present findings has been made with respect to previous analyses and experimental observations.

Introduction

Surface rewetting refers to the phenomenon of establishing liquid contact with a solid surface whose initial temperature is greater than the rewetting temperature, the temperature up to which the surface may wet. Rewetting phenomena exist in many industrial processes involving very hot solid objects to be cooled in liquids such as in metallurgical quenching or very cold liquids to be in contact with solid surfaces such as in filling a cryogenic liquid into a container. Recently, considerable interest in this problem has been generated as a result of emergency core cooling considerations in the postulated loss-of-coolant accidents in water reactors. Numerous experimental and analytical studies have been made on surface rewetting by a falling water film as in the case of BWR (boiling water reactor) spray cooling and by bottom water flooding in the case of BWR and PWR (pressurized water reactor) core reflooding. It is now generally recognized that falling-film rewetting is conduction-controlled, while bottom-flooding rewetting is conduction-controlled in the initial period, then followed by an almost instantaneous rewetting phase, the controlling mechanism of which is not yet entirely known.

For the conduction-controlled case, the one-dimensional (axial) conduction model has been quite successful in correlating rewetting phenomena at low coolant flow rates [1, 2, 3].[1] Recent investigations [4, 5, 6], however, suggest that at high coolant-flow rates two-dimensional conduction should be considered for predicting rewetting characteristics. Several two-dimensional analyses and numerical calculations have appeared very recently [4, 5, 7–9]. The validity as well as limitations of these analytical and numerical solutions are not at all clear, particularly in view of the fact that the basic functional forms of these solutions differ among one another.

The present paper presents an analysis of conduction-controlled surface rewetting based on the conventional model [5–9] of two-region two-dimensional conduction with a constant wet-region heat transfer coefficient. The approach follows closely the Wiener-Hopf technique [10, 11], coupled with the kernel-substitution method [10]. The solution for large Peclet numbers agrees well with the numerical results [8, 9] and reveals the limitations of other approximate analytical solutions. The solution for small Peclet numbers contains explicitly the influence of the Biot number, and reduces to the one-dimensional solution [1–3] for small Biot numbers as expected. A similar mathematical model for the case of small Peclet numbers has been suggested by Horvay [12] for the dip-forming process. He applied also the Wiener-Hopf technique, but due to approximation of the resulting kernel in terms of the infinite product of its roots, his solution is expressed in an infinite series convergent for small Peclet numbers. In the present prob-

Contributed by the Heat Transfer Division and presented at the Winter Annual Meeting, New York, New York, November 17–22 1974, of THE AMERICAN SOCIETY OF MECHANICAL ENGINEERS. Journal Manuscript received by the Heat Transfer Division July 31, 1974. Paper No. 74-WA/HT-49.

[1] Numbers in brackets designate References at end of paper.

lem, however, the wetting-front velocity is unknown a priori and the infinite-series solution would not give a clear physical picture of the rewetting mechanism.

Analysis

The physical model under consideration is an infinitely extended vertical slab with liquid coolant supplied from above as shown in Fig. 1. As the liquid film progresses downward, the surface which is initially at a temperature, T_w, higher than the rewetting temperature, T_0, is first cooled down to the rewetting temperature at which the surface begins to wet. Behind the wet front, the surface temperature drops sharply and approaches the liquid saturation temperature, T_s. The heat transfer characteristics outside the slab are simplified by assuming a uniform surface heat transfer coefficient, h, over the wet surface and the dry surface to be adiabatic [1, 2, 5–9]. This common assumption allows the decoupling of the heat transfer phenomena inside the slab from outside.

The present model simulates primarily surface rewetting due to falling liquid films. For the bottom-flooding rewetting case, the existence of a vapor-film boundary layer would require that an appropriate heat transfer coefficient be incorporated into the model as in the one-dimensional case [13]. With some modification, the present model for a slab can also embrace the cylindrical-rod case. In fact, the results of these two cases are nearly the same, as to be indicated later.

Consider now the basic mathematical formulation. The transient two-dimensional conduction equation in a coordinate system moving with the wet front at a constant velocity u can be written as [4–9]

$$\rho c u \frac{\partial T}{\partial \tilde{x}} = k\left(\frac{\partial^2 T}{\partial \tilde{x}^2} + \frac{\partial^2 T}{\partial \tilde{y}^2}\right) \tag{1}$$

where ρ is the density, c the specific heat, and k the thermal conductivity. Equation (1) can be expressed in the following dimensionless form:

$$\theta_x - \frac{1}{\mathrm{P}}(\theta_{xx} + \theta_{yy}) = 0 \tag{2}$$

where

$$\theta \equiv \frac{T_w - T}{T_w - T_s}, \quad x = \frac{\tilde{x}}{\delta}, \quad y = \frac{\tilde{y}}{\delta} \tag{3}$$

$$\mathrm{P} \equiv \frac{\rho c u \delta}{k}, \text{ (Peclet number)} \tag{4}$$

and subscripts x and y denote derivatives with respect to x and y, respectively, and 2δ is the thickness of the slab. The associated boundary conditions are

$$\text{As } x \longrightarrow -\infty: \quad \theta = 0 \tag{5}$$

$$\text{As } x \longrightarrow \infty: \quad \theta = 1 \tag{6}$$

$$\text{At } y = 0, \ x \geq 0: \quad \theta_y = \mathrm{B}(\theta - 1) \tag{7}$$

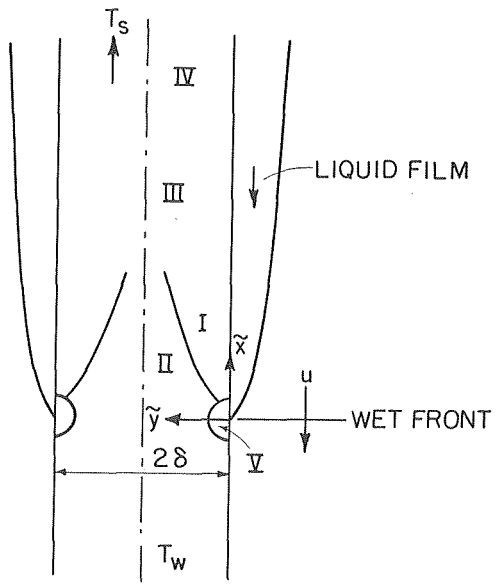

Fig. 1 Falling-film rewetting of a slab

$$\text{At } y = 0, \ x < 0: \quad \theta_y = 0 \tag{8}$$

$$\text{At } y = 1, \text{ for all } x: \quad \theta_y = 0 \tag{9}$$

$$\text{At } x = 0, \ y = 0: \quad \theta = \theta_0 \tag{10}$$

where

$$\mathrm{B} = \frac{h\delta}{k} \text{ (Biot number)} \tag{11}$$

Before attempting to solve the mathematical problem as prescribed in the foregoing, it is essential to understand various physical regions of differing nature. When the wet-front velocity is sufficiently large or $\mathrm{P} \gg 1$, thermal boundary layers are developed in the slab behind the moving wet front as illustrated by Region I in Fig. 1. Region II is the undisturbed thermal region. At a distance from the wet front, the two thermal boundary layers merge but the thermal field is still developing (i.e., T is still a function of x and y). This is Region III. Finally, the thermal field approaches asymptotically the fully developed state in Region IV. The phenomenon is very similar to the thermal entrance phenomenon in a fully developed flow channel. In the present problem, however, heat conduction in the axial direction is important in the neighborhood of the wet front (Region V), where the boundary-layer assumption is no longer valid. Thus the present problem, in contrast with the thermal entrance problem, requires an accurate description of the

Nomenclature

a = constants, equations (45)–(47)
A = constant, equation (22)
B = Biot number, equation (11)
c = specific heat of solid
d = constants, equations (23)–(25)
D = constant, equation (38)
i = $\sqrt{-1}$
h = heat transfer coefficient
k = thermal conductivity of solid
P = Peclet number, equation (4)
t = time
T = temperature
T_0 = rewetting temperature
T_s = saturation temperature
T_w = initial dry-wall temperature
u = wetting front velocity
$\tilde{x}$ = axial coordinate, Fig. 1
x = dimensionless axial coordinate, equation (3) or (33)
$\tilde{y}$ = transverse coordinate, Fig. 1
y = dimensionless transverse coordinate, equation (3) or (33)
α = transformation variable, equation (12) or (39)
δ = one half slab thickness, Fig. 1
θ = dimensionless temperature, equation (3)
θ_0 = dimensionless Leidenfrost temperature, $(T_w - T_0)/(T_w - T_s)$
Θ = $\Theta_+ + \Theta_-$
Θ_+ = Fourier transform of θ for $x \geq 0$, equation (12) or (39)
Θ_- = Fourier transform of θ for $x \leq 0$, equation (13) or (40)
λ = constant, equation (19)
ρ = density of solid

Subscripts

x, y = derivatives with respect to x and y, respectively

temperature field in Region V. Since this region is very small, it can be expected that the solution for $P \gg 1$ does not contain the parameter δ. Also, solutions for slabs and rods should be identical in this limit. Region V becomes larger with decreasing P and covers eventually the whole slab for $P \ll 1$. In the latter case, other regions do not exist. If, in addition, the Biot number is very small ($B \ll 1$), temperature variations in y are negligible and the one-dimensional solution in x should be a good approximation. Again, in the one-dimensional limit, solutions for slabs and rods are nearly the same. It should be noted that for $P \gg 1$, one-dimensional solution does not hold regardless of the values of B.

To obtain a general analytical solution to equation (2) with its associated boundary conditions as given in equations (5)–(10) does not seem to be practical. A numerical solution is possible but would not reveal any functional relationship among various system parameters. Moreover, the numerical solution for $P \gg 1$ may contain substantial errors if proper care is not exercised, since the smallness of Region V for $P \gg 1$ requires the use of an extremely fine grid for computation. At the present state of knowledge on surface rewetting, it appears much more logical to seek approximate analytical solutions that would reveal simple functional forms. This is achieved here by applying the Wiener-Hopf method coupled with the kernel-substitution method [10, 11], both being standard techniques in mathematical physics, to the individual cases of $P \ll 1$ and $P \gg 1$ and then matching the limiting solutions for the whole range in a semiempirical manner. The adopted techniques are particularly attractive for the present problem in the sense that solutions for the wet-front velocity can be readily obtained without solving first the complex temperature field everywhere.

Solution for $P \ll 1$. Following the Wiener-Hopf method, the Fourier transform used to reduce equation (2) to an ordinary equation is defined as

$$\Theta_+(\alpha, y) = \int_0^\infty e^{i\alpha x}\theta(x, y)dx \tag{12}$$

$$\Theta_-(\alpha, y) = \int_{-\infty}^0 e^{i\alpha x}\theta(x, y)dx \tag{13}$$

and the inverse transform is

$$\theta(x, y) = \frac{1}{2\pi}\int_{-\infty+i\tau}^{\infty+i\tau}\Theta(\alpha, y)e^{-i\alpha x}d\alpha \quad (\tau = \text{real, positive}) \tag{14}$$

where

$$\Theta(\alpha, y) = \Theta_+(\alpha, y) + \Theta_-(\alpha, y)$$

Equation (2) becomes

$$iP\alpha\Theta + \left(-\alpha^2\Theta + \frac{d^2\Theta}{dy^2}\right) = 0 \tag{15}$$

The associated boundary conditions given in equations (5)–(9) become

$$\frac{d\Theta_+(\alpha, 0)}{dy} = B\left(\Theta_+(\alpha, 0) + \frac{1}{i\alpha}\right) \tag{16}$$

$$\frac{d\Theta_-(\alpha, 1)}{dy} = \frac{d\Theta_-(\alpha, 0)}{dy} = 0 \tag{17}$$

Solving equations (15)–(17) gives

$$\Theta_+(\alpha, 0) + \Theta_-(\alpha, 0) = \left(\frac{-B\coth\lambda}{\lambda}\right)\left(\Theta_+(\alpha, 0) + \frac{1}{i\alpha}\right) \tag{18}$$

where

$$\lambda = (\alpha(\alpha - iP))^{1/2} \tag{19}$$

Equation (18) is equivalent to an integral equation and the term in parenthesis, $(-B \coth \lambda/\lambda)$, is the kernel function whose transform must be decomposed in accordance with the Wiener-Hopf method. Exact decomposition of the above kernel in terms of simple functions seems unlikely to exist. Since the major contribution of the kernel is in the neighborhood of singular points corresponding to $\lambda \approx 0$, it should be a good approximation to represent $\coth \lambda$ by the first two terms in the asymptotic series expansion near $\lambda = 0$:

$$\coth\lambda = \frac{1}{\lambda} + \frac{\lambda}{3} + O(\lambda^3) \tag{20}$$

Substitution of equation (20) into equation (18) yields

$$\left\{\left(\frac{B+3}{3}\right)\left[\frac{\alpha - i((P/2) - \sqrt{(P/2)^2 + A})}{\alpha}\right]\Theta_+(\alpha, 0) - \left(\frac{iB}{3}\right)\left[\frac{d_1}{\alpha} + \frac{d_2}{\alpha^2}\right]\right\}_+ = \left\{\left[\frac{\alpha - iP}{\alpha - i((P/2) + \sqrt{(P/2)^2 + A})}\right] \times \Theta_-(\alpha, 0) + \left(\frac{iB}{3}\right)\frac{d_3}{\alpha - i[(P/2) + \sqrt{(P/2)^2 + A}]}\right\}_- \tag{21}$$

where

$$A = \frac{3B}{3 + B} \tag{22}$$

$$d_1 = \frac{3 + P[(P/2) + \sqrt{(P/2)^2 + A}]}{[(P/2) + \sqrt{(P/2)^2 + A}]^2} \tag{23}$$

$$d_2 = \frac{3i}{[(P/2) + \sqrt{(P/2)^2 + A}]} \tag{24}$$

$$d_3 = \frac{-9}{(B + 3)[(P/2) + \sqrt{(P/2)^2 + A}]} \tag{25}$$

The key step in the Wiener-Hopf method is the established requirement that both sides as in equation (21) are identically zero. Thus, there follows

$$\Theta_+(\alpha, 0) = \frac{iA}{3}\left\{\left(\frac{3 + P[(P/2) + \sqrt{(P/2)^2 + A}]}{[(P/2) + \sqrt{(P/2)^2 + A}]^2} - \frac{3}{A}\right) \times \frac{1}{\alpha - i[(P/2) - \sqrt{(P/2)^2 + A}]} + \frac{3}{A\alpha}\right\} \tag{26}$$

$$\Theta_-(\alpha, 0) = \frac{-iA}{[(P/2) + \sqrt{(P/2)^2 + A}](\alpha - iP)} \tag{27}$$

The temperature distribution on the surface can be obtained by applying the inverse Fourier transform of equations (26) and (27) as

$$\theta(x, 0) = \left\{\frac{A + [AP((P/2) + \sqrt{(P/2)^2 + A})/3]}{[(P/2) + \sqrt{(P/2)^2 + A}]^2} - 1\right\} \times \exp\{[(P/2) - \sqrt{(P/2)^2 + A}]x\} + 1, \quad (x \geq 0) \tag{28}$$

$$\theta(x, 0) = \frac{A}{[(P/2) + \sqrt{(P/2)^2 + A}]^2}\exp(Px), \quad (x \leq 0) \tag{29}$$

At the wet front, the temperature is

$$\theta_0 = \theta(0, 0) = \frac{A + O(P)}{[(P/2) + \sqrt{(P/2)^2 + A}]^2} \tag{30}$$

The discrepancy in higher-order terms between $\lim_{x \to -0}\theta(x,0)$ and $\lim_{x \to +0}\theta(x,0)$ results from the asymptotic approximation of the kernel, which is valid for $P \ll 1$.

Thus for $P \ll 1$ equation (30) yields

$$\frac{\sqrt{A}}{P} = \theta_0^{1/2}(1 - \theta_0)^{-1} \tag{31}$$

For $B \ll 1$, $A \cong B$, and equation (31) reduces to

$$\frac{\sqrt{B}}{P} = \theta_0^{1/2}(1 - \theta_0)^{-1} \tag{32}$$

which is, as expected, the one-dimensional solution [1–3]. This verifies that the one-dimensional assumption is indeed valid for the case when both the Peclet number and the Biot number are small.

Solution for P ≫ 1. The thermal region that exerts the greatest influence on the speed of the advancing wet front is Region V, a very small region normally neglected in thermal entrance considerations. Since the major concern in surface rewetting is to correlate the wetting velocity, Region V is in fact the only region of interest here. Due to the smallness of the region, the parameter δ does not play any role in the problem and the independent variables $\tilde{x}$ and $\tilde{y}$ are nondimensionalized by

$$x = \frac{\tilde{x}}{(2\delta/\mathrm{P})} = \frac{\tilde{x}}{(2k/\rho cu)}, \quad y = \frac{\tilde{y}}{(2\delta/\mathrm{P})} = \frac{\tilde{y}}{(2k/\rho cu)} \tag{33}$$

Equation (1) becomes

$$2\theta_x - (\theta_{xx} + \theta_{yy}) = 0 \tag{34}$$

For the associated boundary conditions, equations (5), (8), and (10) remain unchanged but equations (6), (7), and (9) are replaced, respectively, by

$$\text{As } x \longrightarrow \infty, \quad \theta \text{ is bounded} \tag{35}$$

$$\text{At } y = 0, \begin{cases} x \geq 0, & \theta_y = 2D(\theta - 1) \\ x \leq 0, & \theta_y = 0 \end{cases} \tag{36}$$

$$\text{As } y \longrightarrow \infty, \quad \theta \longrightarrow 0 \tag{37}$$

where

$$D = \frac{\mathrm{B}}{\mathrm{P}} = \frac{h}{\rho cu} \tag{38}$$

For the convenience of simplifying subsequent algebraic developments the Fourier transform employed here is defined as

$$\Theta_+(\alpha, y) = \int_0^\infty e^{(i\alpha-1)x}\theta(x, y)dx \tag{39}$$

$$\Theta_-(\alpha, y) = \int_{-\infty}^0 e^{(i\alpha-1)x}\theta(x, y)dx \tag{40}$$

and the inverse transform is

$$\theta(x, y) = \frac{1}{2\pi}\int_{-\infty}^{\infty} e^{-(i\alpha-1)x}\Theta(\alpha, y)d\alpha \tag{41}$$

Following a similar procedure as in the case for P ≪ 1, equation (34) and the associated boundary conditions give

$$\Theta_+(\alpha, 0) + \Theta_-(\alpha, 0) = \frac{-2D}{\sqrt{\alpha^2 + 1}}\left[\Theta_+(\alpha, 0) - \frac{i}{\alpha + i}\right] \tag{42}$$

As in the previous case, exact decomposition of the kernel does not appear to be fruitful. In the present case, the standard approximate method of kernel substitution [10] is used. Replacing $(1/\sqrt{\alpha^2 + 1})$ in equation (42) by $(2/(\alpha^2 + 2))$, the Fourier transforms of which have the identical area and first moment, gives

$$\Theta_+(\alpha, 0) = \frac{i4D(\alpha + i\sqrt{2})}{\alpha + i\sqrt{4D + 2}}\left[\frac{a_1}{\alpha + i} + \frac{a_2}{\alpha + i\sqrt{2}}\right] \tag{43}$$

$$\Theta_-(\alpha, 0) = \frac{-i4a_3D}{\alpha - i\sqrt{2}} \tag{44}$$

where

$$a_1 = \frac{1}{(\sqrt{2} - 1)[1 + \sqrt{4D + 2}]} \tag{45}$$

$$a_2 = \frac{-1}{(\sqrt{2} - 1)\sqrt{2}(1 + \sqrt{2D + 1})} \tag{46}$$

$$a_3 = \frac{1}{\sqrt{2}(1 + \sqrt{2D + 1})[1 + \sqrt{4D + 2}]} \tag{47}$$

By the inverse transform of equations (43) and (44), the surface temperature distribution near the wet front is obtained as

$$\theta(x, 0) = \frac{4D}{4D + 1} - \frac{2(2 + \sqrt{2})D\exp[-(\sqrt{4D + 2} - 1)x]}{[4D + 1](1 + \sqrt{D + 1})}, \quad (x \geq 0) \tag{48}$$

$$\theta(x, 0) = \frac{2\sqrt{2}D\exp[(\sqrt{2} + 1)x]}{(1 + \sqrt{2D + 1})[1 + \sqrt{4D + 2}]}, \quad (x \leq 0) \tag{49}$$

Applying the condition that $\theta = \theta_0$ at $x = 0$ to equation (48) or (49) gives

$$\frac{\mathrm{B}}{\mathrm{P}} = \frac{1 + \sqrt{2}}{\sqrt{2}}\left[\frac{\theta_0}{1 - \theta_0}\right] + \frac{(1 + \sqrt{2})^2}{4}\left[\frac{\theta_0}{1 - \theta_0}\right]^2 \tag{50}$$

or, in the explicit form,

$$u^{-1} = \left(\frac{\rho c}{h}\right)\left[\frac{1 + \sqrt{2}}{\sqrt{2}}\left(\frac{T_w - T_0}{T_0 - T_s}\right) + \frac{(1 + \sqrt{2})^2}{4}\left(\frac{T_w - T_0}{T_0 - T_s}\right)^2\right] \tag{51}$$

The first term of equation (51) confirms the functional form of Blair's asymptotic solution [6, 7] but the numerical constants involved are slightly different: 1.707 (i.e., $[1 + \sqrt{2}]/\sqrt{2}$) as compared to Blair's 1.571 (i.e., $\pi/2$). It should be noted, however, that for most cases the second term in equation (51) must be included. The present solution agrees well with the numerical results [8, 9], which have already demonstrated the inadequacy of the Duffey-Porthouse solution [5]. The difference between the present analytical solution and the numerical results for P ≫ 1 is less 20 percent and, as expected, is increasingly small with the increase of P and the decrease of B. The absence of δ and k in equation (51) has already been suggested previously as a result of smallness of Region V for P ≫ 1. This is further confirmed by Thompson's numerical solution [6].

Semiempirical Matching. Equations (32) and (51) contain the limiting relations for P ≪ 1 and P ≫ 1, respectively. For engineering applications, it is advantageous to establish a continuous expression for the whole range of P. Rearranging equations (32) and (51) gives

$$\frac{\mathrm{B}(1 - \theta_0)}{\mathrm{P}\theta_0} = \left(\frac{\mathrm{P}}{1 - \theta_0}\right)\left[1 + \frac{\mathrm{P}^2}{3\theta_0}\left(\frac{\theta_0}{1 - \theta_0}\right)^2\right], \ (\mathrm{P} \ll 1)$$

$$\frac{\mathrm{B}(1 - \theta_0)}{\mathrm{P}\theta_0} = \frac{1}{(1 - \theta_0)}[1.707 - 0.25\theta_0], \ (\mathrm{P} \gg 1) \tag{52}$$

and the expression

$$\frac{\mathrm{B}(1 - \theta_0)}{\mathrm{P}\theta_0} = \frac{\mathrm{P}}{(1 - \theta_0)} \cdot \frac{(1.707 - 0.25\theta_0)[3(1 - \theta_0)^2 + \mathrm{P}^2\theta_0]}{\{[3(1 - \theta_0)^2(1.707 - 0.25\theta_0)] + \mathrm{P}[3(1 - \theta_0)^2 + \mathrm{P}^2\theta_0]\}} \tag{53}$$

satisfies both limits in equation (52) and provides a smooth continuous relation for all values of P. In Fig. 2, equation (53) is used to show the variation of P with respect to B at different values of θ_0. Also shown in the figure are the one-dimensional solution valid for P ≪ 1 as given in equation (32) and the solution for P ≫ 1, equation (50). Compared with the numerical solution [8], the semiempirical formula overpredicts the value of (B/P) by a factor of 10 to 30 percent.

Discussion

The present two-dimensional analysis not only generalizes the widely quoted one-dimensional solution [1–3], but also provides for the first time a clear physical picture of the roles played by the Peclet number and the Biot number in the general problem. It further clarifies the various existing analytical and numerical two-dimensional solutions reported in the recent literature [5–9], which deal, in essence, only the limiting case of P ≫ 1.

In the framework of the adopted simple physical model, the present analysis depicts a rather complete analytical picture of the falling-film rewetting problem. It should be emphasized, however, that the present model represents an idealization of the actual processes involved. Many complex factors have been omitted in this

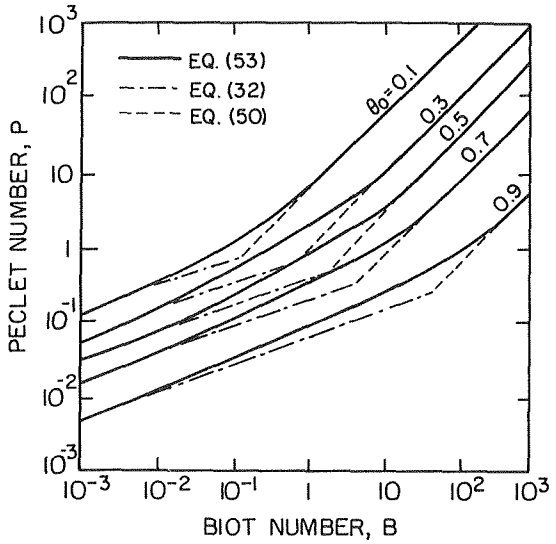

Fig. 2 Variations of Peclet number in falling-film rewetting

idealization, such as the variable heat transfer coefficient in the sputtering as well as the film region, the true nature of the rewetting temperature, the subcooling of the coolant, the coupling of the liquid-film convection and the solid conductions, and the precursory cooling in the dry region ahead of the wetting front. Some of these factors which have been assessed individually include the numerical study with a variable heat transfer coefficient [4], the experimental study of the subcooling effect [14], and the one-dimensional analysis with precursory cooling [3]. For further improvement of the present analysis, instead of seeking more general and exact solutions, the logical direction appears to generalize the physical model by incorporating some of these effects presently neglected.

No comparison between the present analysis and the existing experimental data is presented here, since it will merely duplicate what has already been available in the literature. At low wetting rates or small Peclet numbers, the one-dimensional solution which is valid for small Biot numbers has been correlated successfully with experimental data [1–3]. Existing measurements for small Peclet numbers do not provide a wide range of Biot numbers so that a definitive comparison of data with the two-dimensional and the one-dimensional solutions as given in equations (31) and (32) can be made.

For high wetting rates or large Peclet numbers, experimental data have been correlated in similar analytical forms by Duffey and Porthouse [5] for the atmospheric-pressure case and by Thompson [6] for the high-pressure case. In accordance with Duffey and Porthouse's correlation of experimental data at large Peclet numbers, the wet-side heat transfer coefficient in the present physical model would be a linear function of the coolant flow rate, and is of the order of $10^5 - 10^6$ W/m^{2}K for the mass flow per unit wetting perimeter of the range from 0.04 to 0.4 Kg/m-s. At large coolant flow rates, in fact, there exists a large scatter among Duffey-Porthouse [15] and Yoshioka-Hasegawa's data [14]. This scatter, however, was not shown in Fig. 6 of the Duffey-Porthouse paper [5]. The scattering of data as well as the uncommonly large heat transfer coefficient is probably due to the fact that at large coolant flow rates the precursory cooling effect and the subcooling effect are more likely to exert considerable influence. Since both effects are not taken into account in the present physical model and both tend to increase the wetting velocity in the actual situation [13, 14], the use of the present solution to correlate data would logically result in a large scatter of data and a large heat transfer coefficient. Probably due to the same reason, the heat transfer coefficient obtained by Thompson [6] from correlating high-pressure data is also quite high, in the order of 10^5 W/m^{2}k. Despite all these shortcomings, however, experimental data at large coolant flow rates show a definite quantitative trend as predicted, and this has been successfully demonstrated by Duffey and Porthouse [5] and by Thompson [6].

Acknowledgment

The authors wish to acknowledge the support of the Nuclear Energy Division, General Electric Company in this research.

References

1 Semeria, R., and Martinet, B., "Calefaction Spots on a Heating Wall; Temperature Distribution and Resorption," *Symposium on Boiling Heat Transfer in Steam-Generating Units and Heat Exchangers,* Manchester, England, Sept. 1965.

2 Yamanouchi, A., "Effect of Core Spray Cooling in Transient State After Loss-of-Coolant Accident," *Journal of Nuclear Science and Technology,* Vol. 5, 1968, pp. 547–558.

3 Sun, K. H., Dix, G. E., and Tien, C. L., "Cooling of a Very Hot Vertical Surface by a Falling Liquid Film," JOURNAL OF HEAT TRANSFER, TRANS. ASME, Series C, Vol. 96, 1974, pp. 126–131.

4 Thompson, T. S., "An Analysis of the Wet-Side Heat Transfer Coefficient During Rewetting of a Hot Dry Patch," *Nuclear Engineering and Design,* Vol. 22, 1972, pp. 212–224.

5 Duffey, R. B., and Porthouse, D. T. C., "The Physics of Rewetting in Water Reactor Emergency Core Cooling," *Nuclear Engineering and Design,* Vol. 25, 1973, pp. 379–394.

6 Thompson, T. S., "Rewetting of a Hot Surface," *Proceedings of the Fifth International Heat Transfer Conference,* Vol. 4, 1974, pp. 139–143.

7 Blair, J. M., "An Analytical Solution to a Two-Dimensional Model of the Rewetting of a Very Hot Dry Rod," Chalk River Nuclear Laboratories, Ontario, Canada, Personal Communication, June 1974.

8 Andersen, J. G. M., and Hansen, P., "Two-Dimensional Heat Conduction in Rewetting Phenomena," Report No. NORHAV-D-6, Danish Atomic Energy Comission Research Establishment Risø, Denmark, June, 1974.

9 Coney, M. W. E., "The Calculation of the Rate of Rewetting of Hot Fuel Rods by Emergency Cooling Systems in Water Reactors," to appear in *Nuclear Engineering and Design.*

10 Carrier, G. F., Krook, M., and Pearson, C. E., *Functions of a Complex Variable,* McGraw-Hill, New York, 1966.

11 Noble, B., *Methods Based on the Wiener-Hopf Technique,* Pergamon Press, New York, 1958.

12 Horvay, G., "The Dip-Forming Process," JOURNAL OF HEAT TRANSFER, TRANS. ASME, Series C, Vol. 87, No. 1, 1965, pp. 1–16.

13 Sun, K. H., Dix, G. E., and Tien, C. L., "Effect of Precursory Cooling on Falling-Film Rewetting," ASME Paper No. 74-WA/HT-52; to appear in the JOURNAL OF HEAT TRANSFER.

14 Yoshioka, K., and Hasegawa, S., "A Correlation in Displement Velocity of Liquid Film Boundary Formed on a Heated Vertical Surface in Emergency Cooling," *Journal of Nuclear Science and Technology,* Vol. 7, 1970, pp. 418–425.

15 Duffey, R. B., and Porthouse, D. T. C., "Experiments on the Cooling of High Temperature Surfaces by Water Jets and Drops," Report No. RD/B/N2386, Berkeley Nuclear Laboratories, England, Aug. 1972.

O. C. Iloeje
D. N. Plummer
W. M. Rohsenow
P. Griffith

Department of Mechanical Engineering,
Massachusetts Institute of Technology,
Cambridge, Mass.

An Investigation of the Collapse and Surface Rewet in Film Boiling in Forced Vertical Flow

A transient boiling experiment has been run in such a way that one can acquire data in forced convection film, transition, and nucleate boiling regions for a specified pressure, quality, and mass flux. Transient boiling experiments were conducted at the Nuclear Energy Division of the General Electric Company for water in a 0.492 in. ID inconel X-750 tube at mass fluxes of 50,000, 100,000, and 250,000 lbm/hr-ft^2, quality range of 30–100 percent and a pressure of 1000 psia. The reduced boiling curves for these data indicated temperature differences at burnout on the order of 100–200°F and temperature differences at the minimum ranging from 700 to 1100°F. These results (higher than in other experiments) are felt to be caused by scale deposit, axial conduction, and roughnesses on the test surface. Physical evidence indicates that the test surface became coated with an appreciable scale deposit when subjected to the initial temperatures in excess of 1500 °F in a steam atmosphere. It has been found (reference [1][1]) that BWR fuel will normally have scale deposit on the heat transfer surface and thus the qualitative effects of scale deposits in this report are expected to apply in BWR Loss-of-Coolant accident evaluation. An empirical correlation was developed for the data for minimum film boiling temperature differences. The correlation was based on Berenson's minimum pool film boiling temperature difference correlation in order to provide a technique for extrapolating to different pressures.

Introduction

Considerable difficulty exists in isolating and characterizing the many factors which control the transition from film to nucleate boiling in forced convection. Even the problem of a generally accepted classification of the phenomenon remains unresolved. It is argued, for instance, that since the heating surface must be cooled to a certain temperature before contact between it and the liquid will be possible, that the limiting surface temperature must be a thermodynamic property of the fluid. Others take the view that the transition temperature is completely determined by the ratio of the group of properties controlling conduction in both liquid and solid, i.e., the $k\rho c$ ratio. In some previous treatments of the subject in pool or Leidenfrost boiling, e.g., [12, 13], the effect of depositions of oxide film or other foreign matter on the surface, and of roughness, have been noted. In forced convection, however, these surface effects have not been considered. In particular, the effects of mass flux and flow quality have been ignored. Surface effects are particularly important to designers of reactor cores where water metal reactions at elevated temperatures leave considerable oxide deposits on the heat transfer surfaces [1]. Similarly, the effects of mass flux and quality are held very relevant to the rewet process. This report takes the view that the wall superheat at the transition is controlled by the total heat transfer process leading to transition. The existing forced convection transition models, [5, 6] may only be used as approximate representations for particular flow regimes. The analysis of the experimental results showed a substantial increase, over expected range, which we could only attribute to surface effects.

Experimental Apparatus

The entire experimental program was conducted at the General Electric Laboratories in San Jose, California. The test loop was constructed to allow for both steady-state and transient test runs, but the results analyzed here were obtained in the transient section. For details of the test loop reference may be made to [2].

Details of the transient test piece are shown in Fig. 1. The 4 in. long × 0.492 in. ID × 1.0 in. OD test section was made of inconel

[1] Numbers in brackets designate References at end of paper.

Contributed by the Heat Transfer Division and presented at the Winter Annual Meeting, Detroit, Mich., November 1973. Journal manuscript received by the Heat Transfer Division February 17, 1975. Paper No. 73-WA/HT-20.

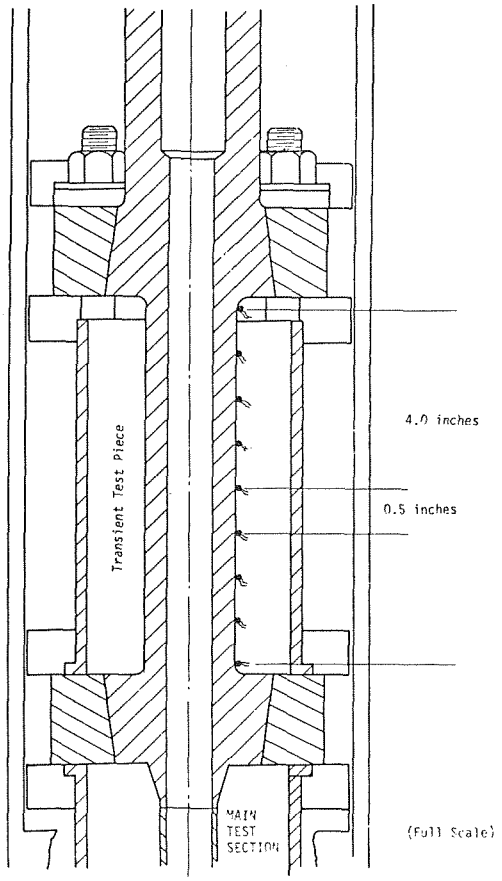

Fig. 1 Transient test section

X-750 with a very low dependence on temperature of its resistivity. Both the steady-state and transient test sections were electrically heated, but the electrical supplies were independent of each other. A 1.5 in. unheated section of the flow tube between the two test sections were inevitable because of bus bar connections. However, the whole flow channel from inlet to exit was of the same internal diameter. Thermocouples were positioned at ½ in. intervals on the transient piece and the test system was instrumented to measure the mass flux, heat flux, quality, and pressure.

Experimental Method. All the test runs were made at 1000 psia. By using either the preheater, or the steady-state test section, the required quality at the entrance to the transient test piece, for a given mass flux, was set at a steady value. Power was then applied to the transient section until steady film boiling was established in it. Power to the transient test piece was then cut off and the temperature transient recorded on a Sanborn recorder. One of the eight thermocouple outputs was fed to DYMEC which digitized the continuous output at a preset rate. Since the output of the DYMEC was that chosen as the data for the particular run, the thermocouple chosen had to satisfy certain criteria:

1 The Sanborn trace must have clearly shown film boiling.
2 The thermocouple must be close to the midplane of the test piece to avoid end effects.
3 The trace must be relatively free of noise.

Because of the nature of the test, all regimes of boiling existed on the test piece at one time or the other during the transient. A run was terminated when nucleate boiling was re-established. In determining the quality at inlet to the transient test piece, allowance was made for heat losses in the steady-state test section, irrespective of whether the preheater or the long test section was used to develop the required quality. Since the test piece was short, it was possible to assume that the quality variation with distance and time was negligible.

Data Reduction. As opposed to using the lengthy finite difference or integral technique, an exact solution of the inverse heat transfer problem was used to obtain the temperatures and heat fluxes at the inside tube wall from the temperature-time data of the thermocouple welded to the outside of the test piece. Such a solution, developed by O. R. Burggraf [3], needs only the boundary conditions at one point as a function of time in order to obtain conditions at another point in the homogeneous medium. The temperature-time history at an interior point could then be obtained in terms of the conditions at an outside boundary, as shown in equation (1).

$$T(r_i, t) = T_{0(t)} + \left(\frac{r_0^2}{4\alpha}\left(\left(\frac{r_i}{r_0}\right)^2 - 1 - 2\ln\frac{r_i}{r_0}\right)\right)\frac{dT_0}{dt} + \left(\frac{1}{64\alpha^2}(r_i^4 - 5r_0^4) - \frac{r_0^2 r_i^2}{8\alpha^2}\ln\frac{r_i}{r_0} - \frac{r_0^4}{16\alpha^2}\ln\frac{r_i}{r_0} + \frac{r_0^2 r_i^2}{16\alpha^2}\right)\frac{d^2T_0}{dt^2} + \ldots \quad (1)$$

To obtain the inside wall heat flux, the foregoing equation is differentiated with respect to r_i, and the result multiplied by the thermal conductivity of the solid. The resulting expression was extended to three terms by including the next term in the series of equation (1).

Nomenclature

A, B, n, m = correlation constants
c = specific heat at constant pressure (Btu/lb-° F)
G = mass flux (lbm/hr-ft²)
g_c = gravitational constant (32.2 lbm-ft/lbf-s²)
h_{fg} = enthalpy of evaporation (Btu/lbm)
k = thermal conductivity (Btu/hr-ft-° F)
p = pressure (psia)
q/A = heat flux (Btu/hr-ft²)
r = radial distance from origin (ft)
T = temperature (° F)
t = time (hr)
V = velocity (ft/hr)
We_{crit} = critical Weber number
X = flow quality
α = thermal diffusivity (ft²/hr)
δ = droplet diameter (ft)
ΔT = wall superheat ($T_w - T_{sat}$) (° F)
ΔV = $V_v - V_L$ (ft/hr)
ρ = density (lbm/ft³)
σ = surface tension (lbf/ft)
μ = dynamic viscosity (lbf/hr-ft)

Subscripts

BER = Berenson's
c = thermodynamic critical state
cr2 = value at film boiling minimum heat flux
E = for equilibrium quality
f = property calculated at film temperature ($T_w + T_{sat}$)/2
i = inside boundary (radius)
L = liquid
min = minimum
0 = outside boundary (radius)
sat = saturation
v = vapor
w = wall
wet = wetting

$$q/A(r_i, t) = \rho c\left(\frac{r_i^2 - r_0^2}{2r_i}\right)\frac{dT_0}{dt} + \left(\frac{(\rho c)^2}{k}\right)\left(\frac{r_i^3}{16} - \frac{r_0^4}{16r_i} - \frac{r_0^2 r_i}{4}\ln\frac{r_i}{r_0}\right)\frac{d^2T_0}{dt^2} + \frac{(\rho c)^3}{k^2}\left(\frac{r_i^5}{384} - \frac{3r_0^4 r_i}{128} + \frac{3r_0^2 r_i^3}{128} - \frac{r_0^6}{384r_i} - \frac{r_0^2 r_i^3}{32}\ln\frac{r_i}{r_0} - \frac{r_0^4 r_i}{32}\ln\frac{r_i}{r_0}\right)\frac{d^3T_0}{dt^3}$$

For a detailed solution of the problem using the Burggraf method, reference may be made to [2] and Appendix A of the same report.

Equations (1) and (2) show that derivatives of the temperature-time plot were needed. Because of some fluctuations in the measured temperatures the resulting derivatives would behave badly if a finite difference technique was used to obtain them. The method chosen was to use a least square technique to obtain a smooth profile. To increase accuracy, the data were divided into segments and the order of the curve fit used for each segment made as high as possible (but less than 6) without reintroducing the irregularities inherent in the pure data. Fig. 2 shows a typical result obtained with the foregoing procedure. Fig. 3 represents a typical boiling curve. The various boiling regimes are easily identifiable from this graph. For the complete output reference may be made to [2]. The minimum ΔT's in film boiling were then visually selected from these plots.

The Rewet Phenomenon

In an earlier work by the authors [4] three different controlling mechanisms for forced convection rewet were isolated. These are impulse cooling collapse, axial conduction controlled rewet, and dispersed flow rewet. The distinguishing factor between all three modes are the hydrodynamics of the fluid flow and the geometry of the fluid in the heat transfer process leading into transition.

Impulse Cooling Collapse. In the annular vapor film boiling regime (rod flow) the liquid/vapor interface is wavy and fluctuates about a mean position. If the wall superheat or heat flux is lowered, the vapor thickness falls until the liquid contacts the surface. Depending on the temperature level and the rate of heat supply to the cooled region of material beneath the liquid, either permanent liquid/solid contact will be maintained, or the liquid will be pushed away from the surface with the formation of vapor. In the second alternative each contact is equivalent to an impulsive cooling of the surface. In a quenching process repeated contacts will eventually lower the surface temperature enough to permit rewet. This in fact is the basis of Kalinin's model [5]. His experimental results, however, were correlated in terms of $(k\rho c)_L/(k\rho c)_w$. Hydrodynamic parameters of the flow were completely absent (equation (3)).

$$\frac{T_{cr2} - T_{sat}}{T_c - T_L} = 1.65(0.16 + 2.4[(k\rho c)_L/(k\rho c)_w]^{0.25}) \quad (3)$$

Axial Conduction Controlled Rewet. In a system with an already wetted upstream surface, the liquid/vapor/solid interface, assumed to be at a wetting temperature, is propagated downstream via axial conduction, as successive points downstream are brought to that temperature. Simon and Simoneau [6] have assumed this interface temperature to be a thermodynamic property of the fluid, and to be determined by the equation of Spiegler, et al. [7].

$$\frac{T_{wet}}{T_c} = 0.13\frac{p}{p_c} + 0.84 \quad (4)$$

They also assumed that this temperature was equivalent to the wall temperature at the minimum in film boiling.

Dispersed Flow Reset. *In the dispersed flow regime, the authors postulate that transition is controlled by the limiting effects of two processes, namely, heat transfer to the vapor, and heat transfer due to the presence of the droplets, some of which may be touching the surface, and some of which may not. At high wall superheats fewer droplets are able to touch the surface as a result of*

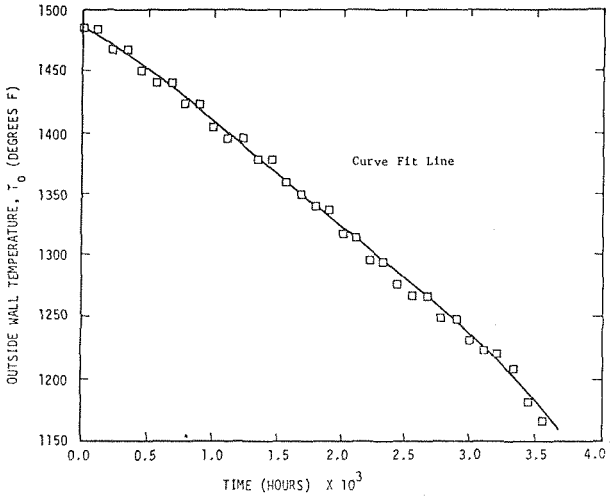

Fig. 2 Sample of accuracy of curve fitting technique

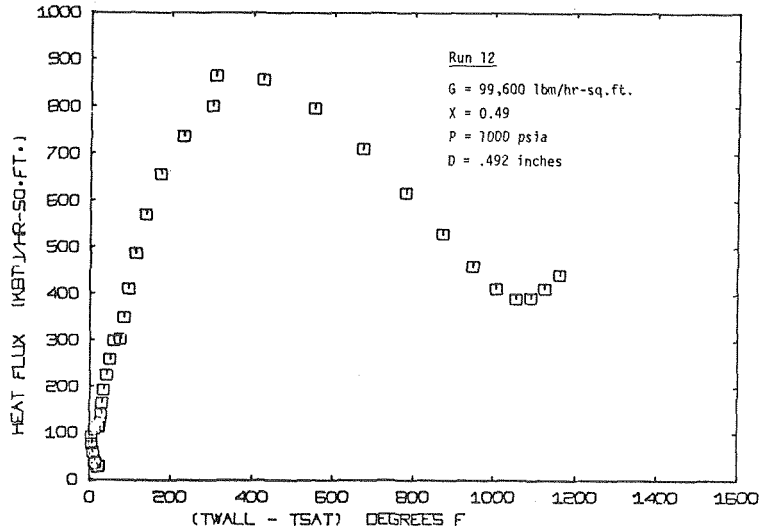

Fig. 3 Reduced data from G. E. transient test section

the repulsive force of the vapor generated as the wall is approached. Subsequently, the enhancement of the total heat transfer due to the droplets touching the wall is smaller. This component of the total heat transfer changes with wall superheat as shown in Fig. 4. On the other hand, heat transfer to the vapor assuming no effect of the presence of droplets, as well as to the droplets not touching the wall, increases with wall superheat. The sum of all these components gives the total heat flux and indicates the location of the minimum (q/A) and ΔT in film boiling. The transition in the experiments presented here is controlled by this phenomenon. Hydrodynamically, such factors as the size of the droplets and the general nearness of the droplets from the wall are important. These in turn are related to the system pressure, mass flux, quality, and flow history prior to the collapse point.

Results and Parametric Effects

Effect of Mass Flux. Figure 5 shows a plot of the transition superheat versus quality at two mass flux levels. Clearly ΔT_{min} increases with mass flux. At higher mass fluxes for a given quality there is greater mixing of the flow, reduced superheating of the vapor and greater momentum of the randomly moving droplets. There is also, physically, more liquid present per unit elemental volume. Subsequently, liquid drop deposition on the surface is higher. All factors help to increase the heat transfer to drops contacting the surface. Heat transfer to the other components also increase but the former seems predominant, leading to an increase in ΔT_{min} with mass flux.

Effect of Quality. Fig. 4 shows a sketch of heat transfer due to the liquid droplets and the vapor for the same mass flux at two quality levels. The variations of the heat transfer components with wall superheat are as described earlier. At a higher quality the heat transferred to the vapor increases while that to the droplets falls. When the summing effect is applied to obtain the total heat flux and locate the ΔT_{min}, the value of ΔT_{min} is seen to fall with increasing qualities. This trend is borne out by the data in Fig. 5. The results were extrapolated to much lower qualities and the variation of ΔT_{min} with quality was seen to become very small. The previously described effect could be further exemplified with Fig. 6. In the run giving this output, the equilibrium quality at inlet to the test piece was approximately 1.0. Thus the droplet sizes and population that there might have been would have found it difficult to penetrate the thermal boundary layer toward the wall. Heat transfer would have approximated that to pure vapor. No rewet could have been expected and none occurred.

History and Flow Regime. Fig. 7 shows results for the same mass flux but different means of developing the quality. The curve with higher ΔT's corresponds to data for which quality was generated in the preheater with the steady-state test section power off. For the lower curve, the preheater was off and the long test section power was on. This latter data series represented higher superheat levels. With higher superheat, droplets are further removed from the wall, leading to reduced droplet heat transfer and lower ΔT_{min}. On the other hand, lower superheat implies less liquid for the same equilibrium quality. This should also lead to lower ΔT_{min}. However, Fig. 7 shows that the former process was controlling. Data with steady-state test section power on, approximated conditions in an actual reactor, and were used in the analysis.

Surface Effects.

Conductivity. While it is not absolutely necessary that the liquid remain permanently in contact with the surface prior to collapse, yet Stock [8] and Berenson [9] for pool boiling transition and Kalinin [5] for low quality forced convection quenching observed such contacts. In the event that it occurs, the sustenance of the depression in wall temperature at point of contact will depend on the rate at which heat is supplied from the surrounding heater material to the contact region. A very highly conducting material will therefore supply heat at such a high rate as to delay collapse to a lower temperature, and inversely for a poor conductor.

$k\rho c$ Effect. Transient one-dimensional conduction analysis of a slab of liquid in contact with solid shows that the ratio $(k\rho c)_L/(k\rho c)_w$ is the property group that appears in the expression for the temperature distribution and transient in the system. It determines the amount of local wall temperature depression on contact with liquid. Kalinin [5] used this parameter to correlate his results. It is obvious, however, that the temperature measured at the back of the tube will reflect an averaging effect of axial conduction from the dry to the wet sections of the wall. This in turn will be influenced by the heat transfer coefficients on the inside wall surface. Thus one would not expect a correlation in terms of the $k\rho c$ ratio to tell the whole story.

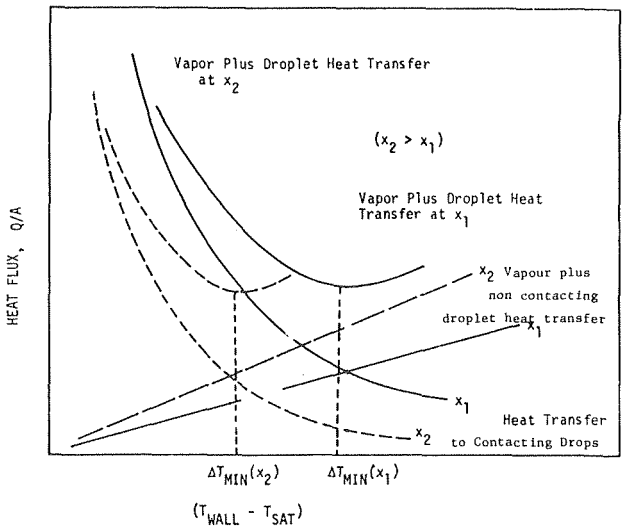

Fig. 4 Film boiling minimum ΔT sketch showing effect of quality

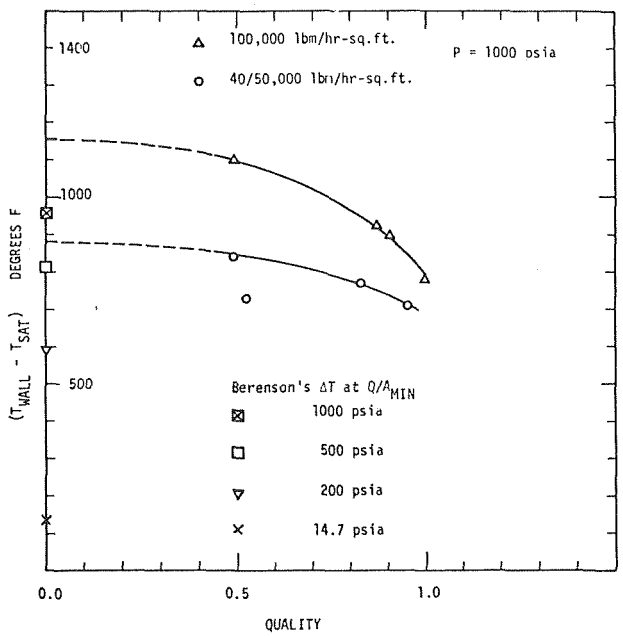

Fig. 5 Film boiling minimum ΔT versus equilibrium quality, effect of mass flux

Oxidation Roughness, or Foreign Matter Deposits on Surface. Examination of Fig. 5 shows that the wall superheats were of the order of 900°F for the low mass flux data. L. S. Tong [10] reported a transition wall superheat of the order of 350°F at 1000 psia and $G = 0.28 - 3.86 \times 10^6$ lb/hr-ft^2, for water. In particular, quench data obtained from General Electric report NEDE 13204 [11] gave an average transition wall superheat of 385°F for apparently similar conditions. Differences in results of this order of mag-

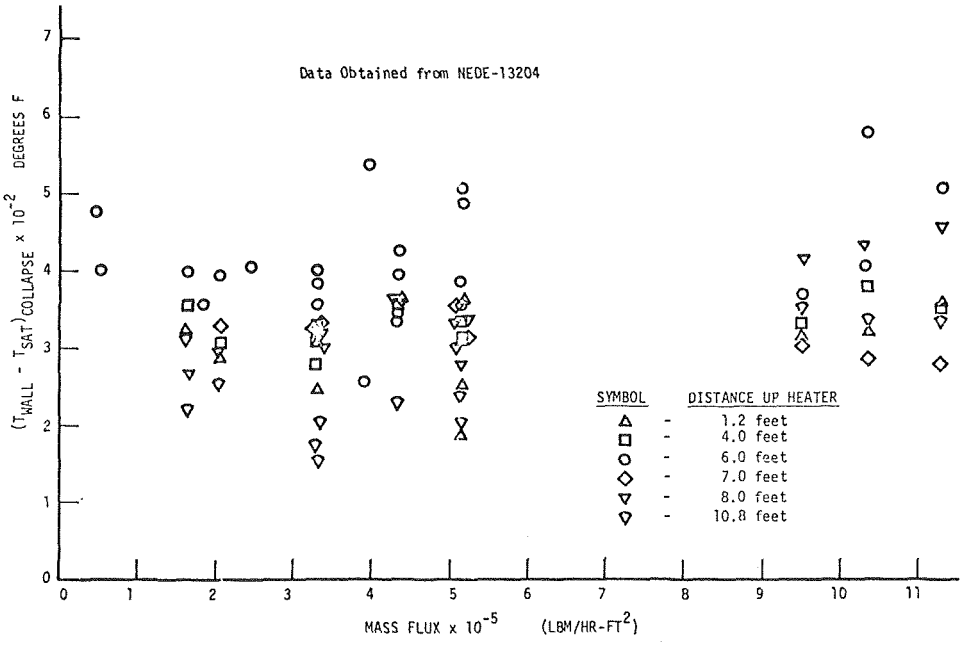

Fig. 6 Reduced data from G.E. transient test section

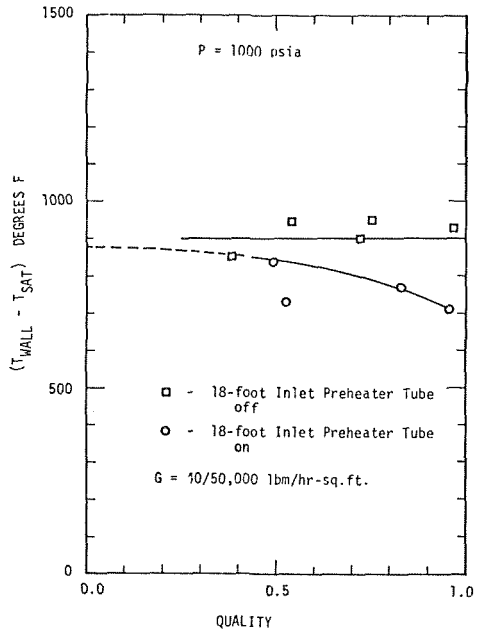

Fig. 7 Film boiling minimum ΔT versus equilibrium quality effect of history of flow regime

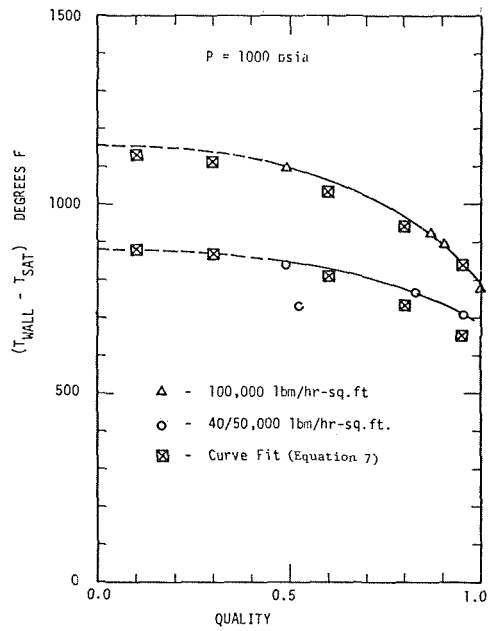

Fig. 8 Film boiling minimum ΔT versus equilibrium quality effect of mass flux

nitude (~500°F) would be very difficult to explain if indeed the conditions were the same.

In NEDE 13204, the experimental procedure involved switching the power, heating the tube up to a safe high temperature, before switching on the flow to quench the tube. Examination of the results (see Fig. 8) revealed some relation between the transition temperature level at a given point and the possible wall temperature level at that point. The heat flux was a chopped cosine distribution, with the peak over the 5 ft–7 ft levels. Transition wall superheats ranged from 150°F to 600°F. The low values corresponded to the extremes of the tube while the highest values were found at the 6 ft position, where wall temperatures, and hence surface oxidation, were expected to be highest. The oxide is of a much lower conductivity than the material of the tube. Thus it acts as an insulator to the inner surface of the tube whose temperature is estimated. It is then possible for this surface to be at a higher temperature than the surface of the oxide film, when the latter is at a low enough temperature to allow transition.

The maximum wall temperature in NEDE 13204 was 1500°F. For the current report it was 1900°F. Thus the transition wall superheat levels appear, at least qualitatively, to follow the expected crud deposition levels. The roughness of the surface may also influence the transition ΔT. Roughnesses projecting into the flow boundary layer can get in contact with liquid droplets, become cooled, and by conduction, propagate the cooling to the rest of the surface. Additionally the rough projections can physically trap droplets from the flow. These two effects can cause premature wetting.

Oxidation can influence the transition wall superheat in three different ways. The conductivity is poor and the oxidized surface tends to be rougher. The effects of these two factors are as explained in the foregoing. Thirdly, the oxide surface may reduce the liquid/solid contact angle, thereby increasing the contact surface area. Also, as can be seen from Plate 1, the oxide is spongy, a factor that facilitates the spreading of the liquid in contact, and also increases the effective heat transfer area. Subsequently, heat transfer to drops in contact is increased, and hence ΔT_{min} is also increased.

Plate 1 is a photo, with polaroid 52 film, of an electron-microscope display of a cross section of a piece of the heat transfer material. The oxidized surface was first protected by electrolytically depositing Nickel on it. The piece was then embedded in a bakelite mould and the cross section polished. The final grain size of the polishing cloth was 0.3 μ in. A spectroscopic analysis of the oxide film revealed it to vary in constitution from 50 to 80 percent Nickel-Oxide, the rest being mostly Chromium-Oxide. The section displayed in Plate 1 was mostly Nickel-Oxide. The Thermal Conductivity of Nickel-Oxide, at around 1500°F varies from 2–4 Btu/hr-ft°F at 11.5 percent porosity to 1.7 Btul/hr-ft°F at 25.7 percent porosity, [14]. Inspection of the plate would indicate a porosity of about 30–40 percent. A thermal conductivity of about 1 Btu/hr-ft °F was therefore assumed. Fig. 3 would suggest a minimum heat flux of the order of 300,000 Btu/hr-ft^2. The oxide film thickness was about 3.5×10^{-5} ft. On a steady-state basis, the oxide film would be able to support a temperature differential of about 10°F. Since this does not account for the 500°F difference in ΔT_{min} as reported here, over what is normally assumed, it is suggested that roughness, contact angle, and spongy effects, as described above, must have been very significant.

Finally, though this is not a surface effect, the high value of ΔT_{min} may have been contributed to by axial conduction. Axial conduction will cause the first point of inflexion on the temperature-time plot and hence the recorded ΔT_{min} to occur at a higher wall temperature.

Correlation of Results

It is observed from Fig. 5 that the plots asymptote to certain values, or different mass fluxes, as one would intuitively expect that this asymptote would be close to or equal to a pool boiling value. This does not imply that the equivalent quality for pool boiling is zero, but at least the expectation is that it would be low. Superimposed on Fig. 5 are data for pool boiling transition, for various pressures, and calculated from Berenson's [1] correlation, equation (5). The data point for 1000 psia is very close to the asymptote for 40–50,000 lbm/hr-ft^2. Moreover, the transition wall temperatures (for water) have been shown to vary considerably, at the same pressure, for various experiments. These values are mostly higher than the thermodynamic critical temperature for water. For these reasons, it is argued that the transition wall temperature cannot be a thermodynamic property of the fluid. Berenson's pool boiling correlation reflects this argument. An equation of the form

$$\Delta T_{min} = \Delta T_{BER}(1 - AX^n)(1 + BG^m) \quad (5)$$

where

$$\Delta T_{BER} = 0.217 \frac{\rho_v}{k_v f} h_{fg} \left[\frac{g(\rho_L - \rho_v)}{\rho_L + \rho_v}\right]^{2/3} \left[\frac{g_c \sigma}{g(\rho_L - \rho_v)}\right]^{1/2} \times \left[\frac{\mu_f}{g_c(\rho_L - \rho_v)}\right]^{1/3}$$

was used with data at 40–50,000 lbm/hr-ft^2 and 100,000 lbm/hr-ft^2 at qualities of 0.3, 0.6, and 0.8. The resulting equation is

$$\Delta T_{min} = 0.29 \Delta T_{BER}(1 - 0.295 X_E^{2.45})(1 + (G \times 10^{-4})^{0.49}) \quad (6)$$

Fig. 9 shows a superposition of this correlation on the experimental data. Confidence in using this equation outside the range $40{,}000 \leq G \leq 100{,}000$ lbm/hr-ft^2 is very doubtful.

Sources of Error. The source of error that is expected to be of greatest significance is that due to axial conduction in the test piece. Equations (1) and (2) had been obtained on the basis of one-dimensional heat flow. From the output temperature-time plots, the percentage errors in heat flux due to axial conduction and in the vicinity of transition were estimated to range from 0 to 10 percent (see reference [2]). As explained earlier, axial conduction has the effect of causing the first inflexion point in the temperature-time plot, and hence the recorded ΔT_{min}, to occur at higher wall superheats. The error due to this factor, on ΔT_{min}, will depend on the propagation rate of the wetted region.

Errors could also have arisen via the thermocouples. Since the process was transient, the heat capacity of the thermocouple junction would cause a lag in measured temperatures relative to actual temperatures. However, the thermocouples junctions were not of the beaded type. Instead, each of the two wires had been individually welded to the tube outside diameter, thus forming an intrinsic thermocouple. The response of this type is by far superior to the beaded type.

It may also be mentioned that the solution of the conduction equation within the test piece material leading to equations (1) and (2) had been done assuming no heat flux at the 4-in. test piece outside boundary.

Conclusion

1 No complete answer yet exists for the problem of predicting the collapse of forced convection film boiling. An attempt has been made to isolate and describe some of the more important influencing factors.

2 Use of the dual mode heat transfer model appears to conceptually describe many of the observed effects on ΔT_{min}, and has not been found to be in contradiction with any other effect. The problem that will be encountered in applying it to theoretically predict ΔT_{min} will lie in being able to theoretically represent the droplet component of heat transfer.

3 The considerable variations in ΔT_{min}, for the same fluid and system pressure, as well as the fact that Tw_{min} is in some cases much greater that T_c lead one to conclude that Tw_{min} is not a thermodynamic property of the fluid.

4 While a pure conduction one-dimensional model between wall and liquid masses may be an approximate model for the impulse cooling collapse, the possibilities of axial conduction effects make such a model seem poor, even if the effects of mass flux and quality are negligible. Thus $k\rho c$ ratio alone would not adequately describe the collapse process.

5 The higher levels of ΔT_{min} recorded in this report have been attributed, phenomenologically, to surface effects, namely—oxide film resistance, wettability and sponginess of oxide film, and sur-

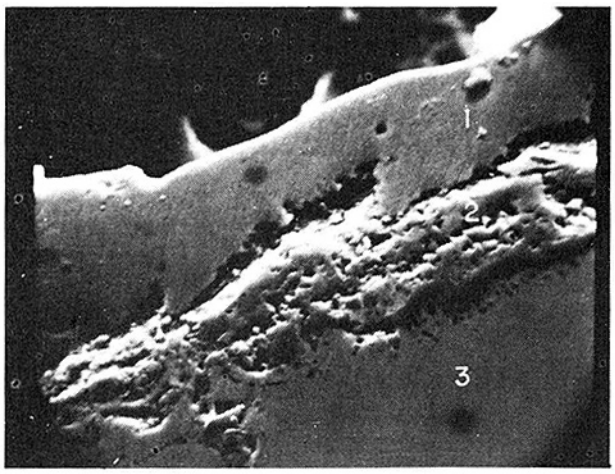

Plate 1 Oxide film magnification 2200: (1) protective nickel layer, (2) oxide film, (3) inconel X-750

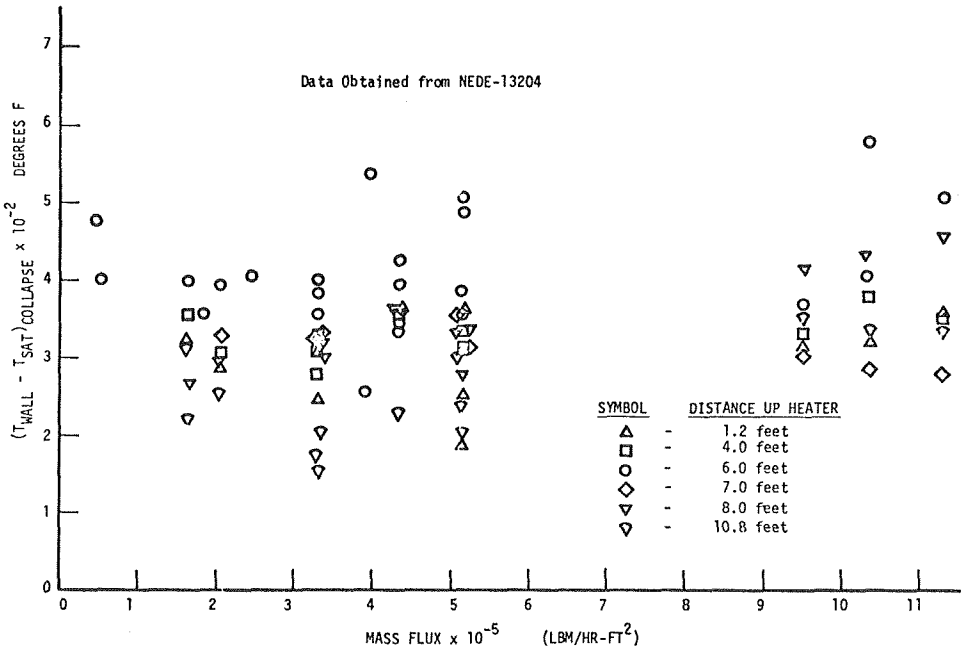

Fig. 9 Collapse temperature difference versus mass flux

face roughness. Axial conduction effects are assumed to have contributed to the higher levels, also.

The oxide film thickness and thermal conductivity were estimated, and using a steady-state model, the effect of oxide film resistance was calculated. This did not account predominantly for the observed surface effects. Thus, axial conduction, surface roughness, and increased wettability were assumed to have been primarily responsible for the increase.

6 Mass flux and flow quality have been shown to be very important parameters in forced convection collapse of dispersed film boiling, contrary to what has been hitherto assumed. Mass flux increases ΔT_{min} and quality decreases it.

7 A correlation for ΔT_{min} of the form shown in equation (6) appears to be quite appropriate. Berenson's pool boiling expression has been used as a base, though this is not mandatory. The correlation is designed to have a pool boiling limit as mass flux and quality tend to zero.

References

1 Blok, J., Sawochka, S. G., and Snyder, D. T., "Corrosion Products on Fuel at the None Mile Point Boiling Water Reactor," To be published at the 19th Annual Meeting of ANS, Chicago, Ill., June 10–15, 1975.

2 Plummer, D. N., Iloeje, O. C., Griffith, P., and Rohsenow, W. M., "A Study of Post Critical Heat Flux Heat Transfer in a Forced Convection System," DSR-73645-80, March 1973, Massachusetts Institute of Technology, Cambridge, Mass.

3 Burggraf, O. R., "An Exact Solution of Inverse Problem in Heat Conduction Theory and Applications," JOURNAL OF HEAT TRANSFER, TRANS. ASME, Series C, Vol. 86, Aug. 1964, pp. 373–382.

4 Iloeje, O. C., Plummer, D. N., and Rohsenow, W. M., "Transition From Film Boiling to Nucleate Boiling in Forced Convection Vertical Flow," DSR-72718-78, Massachusetts Institute of Technology, Cambridge, Mass., Mar. 1972.

5 Kalinin, E. K., Yarko, S. A., Yskochelaev, V., and Berlin, I. I., "Investigation of the Crisis in Film Boiling in Channels," *Proceedings of Two Phase Flow and Heat Transfer in Rod Bundles*, ASME Winter Annual Meeting, Los Angeles, Calif., 1969.

6 Simon, F. F., and Simoneau, R. J., "Transition From Film to Nucleate Boiling in Vertical Forced Flow," TMX-52597, 1967, NASA.

7 Spiegler, P., et al., "Onset of Stabel Film Boiling and the Foam Limit," *International Journal of Heat and Mass Transfer*, Vol. 6, 1963.

8 Stock, B. J., "Observations on Transition Boiling Heat Transfer Phenomenon," ANL-6175, June 1960.

9 Berenson, P. J., "On Transition Boiling Heat Transfer From a Horizontal Surface," PhD thesis in Mechanical Engineering, M.I.T., Cambridge, Mass., Feb. 1960.

10 Tong, L. S., "Heat Transfer in Water Cooled Nuclear Reactors," *Nuclear Engineering and Design*, Vol. 6, 1967, p. 301.

11 General Electric Company, San Jose, Calif; Company Private Report, NEDE 13204, June 1971.

12 Baumeister, K. J., and Simon, F. F., "Leidenfrost Temperature—Its Correlation for Liquid Metals, Cryogens, Hydrocarbons and Water," JOURNAL OF HEAT TRANSFER, TRANS. ASME, Series C, Vol. 95, May 1973.

13 Bergles, A. E., and Thompson, W. G., "The Relationship of Quench Data to Steady State Pool Boiling Data," *International Journal of Heat and Mass Transfer*, Vol. 13, 1970, pp. 55–68.

14 "Thermophysical Properties of High Temperature Solid Materials," Y. S. Touloukian, ed., Vol. 4, Thermophysical Properties Research Centre, Purdue University, Purdue.

U. Magrini
Professor.

E. Nannei
Asst. Professor.

Istituto di Fisica Tecnica e Impianti Termotecnici,
Facoltà di Ingegneria,
Università degli Studi di Genova,
Genova, Italy

On the Influence of the Thickness and Thermal Properties of Heating Walls on the Heat Transfer Coefficients in Nucleate Pool Boiling[1]

An experimental investigation was conducted under conditions of saturated pool boiling of water at atmospheric pressure on thin, horizontal, cylindrical walls of different metals and thicknesses, electrically heated. The heating walls, ranging in thickness from 5 to 250 μm, were obtained by plating copper, silver, zinc, nickel, and tin on nonmetallic rods. Experiments showed that the heat transfer coefficient can be affected, in particular conditions, by the heating wall thickness. In particular, it resulted that the smaller the thermal conductivity of the metal layer, the higher the influence of the thickness. A semiempirical correlation of the form $\Delta T = (q/A)^n f(\kappa d, \sqrt{\kappa \rho c})$ *suitable to correlate the experimental data within ±15 percent in the whole range of variables here investigated is proposed.*

1 Introduction

The study of the mechanism of nucleate boiling requires that many factors which affect the heat transfer process be taken into account. Besides the fluid dynamics aspects of the problem, roughness, surface conditions, thermal properties, and thickness must be considered.

As it is shown in Section 2, the strong effect of the heating surface material on the heat transfer coefficient during nucleate boiling has already been observed by several investigators [1–17].[2] Though some authors have hypothesized that the thickness of the heating surface has a strong influence on nucleate boiling heat transfer, [4, 15, 17], only a few works are available dealing with the effect of surface thickness on the boiling process, [4, 14, 15, 16, 17].

This work was aimed, therefore, at investigating the combined effects of the thermal properties and thickness of the heating wall on the heat transfer coefficient during nucleate boiling. In particular, the experiments were performed on heating walls of different materials (silver, copper, zinc, nickel, and tin) and thicknesses (5–250 μm) in saturated pool boiling of water at atmospheric pressure.

The test specimens consisted of thin metal layers electroplated on epoxy-resin rods.

2 Summary of Previous Work

The influence of the thermal properties of the heating wall on the boiling process was pointed out by Bonilla and Perry [1] who reported boiling data of ethanol with copper, gold, and chromium electroplated surfaces. Farber and Scorah [2] observed different values for the heat transfer coefficient when boiling occurred on wires of different materials. Berenson [3] obtained boiling curves with *n*-pentane as a function of the wall material. Sharp discussed in reference [4] the influence on the boiling curve of both the thermal properties and the thickness of the heating wall. Bliss, et al. [5] used horizontal stainless-steel tubes plated with copper, zinc, tin, nickel cadmium, and chromium as heaters. Horizontal wires of different materials were tested by Fontana [6] in boiling water. Kovalev, et al. [7] found a marked influence on the boiling curves by coating a heating wall with a layer of a low-heat conductivity material. In reference [8] Grigoriev and Dudkevich proposed a correlation of experimental data taking into account the wall thermal conductivity of several heat-transfer surfaces in boiling nitrogen. The influence of the thermal properties of the heating wall was made clearly evident by the results of certain experiments carried out by König [9] under particular pool-boiling conditions causing bubble growth to develop without the presence of an evaporating microlayer. Finally, Nagarajan, et al. [10] observed that boiling on electroplated heating surfaces is affected by the grain size of the coating, which is known to depend upon the electroplating process.

It is worth noting that the thermal properties and thickness of the heating wall affect the following: the frequency and magnitude of the surface temperature fluctuations during the boiling process, as shown by Hsu and Schmidt [11], R. Morin [12], C. Bonnet, et al.

[1] The research reported here has been sponsored in part by the United States Government.

[2] Numbers in brackets designate References at end of paper.

Contributed by the Heat Transfer Division for publication in the JOURNAL OF HEAT TRANSFER. Manuscript received by the Heat Transfer Division August 8, 1974. Paper No. 75-HT-TT.

[13], and Guglielmini and Nannei [14]; and the density of active sites, frequency, growth rate, and break-off diameter of the bubbles, as reported by Kotake [15], Fantini and Bartolini [16], and Dzakovich and Frost in reference [17]. The effects of thickness and thermal properties of the heating wall were also observed in burnout and incipient boiling phenomena as demonstrated in references [18–29].

3 Test Specimens and Their Preparations

The specimens tested were CW 211 CIBA ARALDIT (thermal conductivity = 0.7 W/m°C, softening temperature = 160°C) molded epoxy resin rods of 10 mm OD and 190 mm in length plated with silver, copper, zinc, nickel, and tin. The plating thicknesses ranged from 5 to sometimes 250 μm.

Surface temperatures were measured with eight 28 AWG chromel-alumel thermocouples located as follows: four hot junctions lay on two perpendicular diameters of one cross section of the rod, the others being placed identically in another cross section, 4 cm apart. The bundle of the thermocouple wires with the hot junctions already positioned as above described was immersed in the polymerizing resin, so that the joints became embedded in the outside surface of the molded rod (Fig. 1). The thermal contact resistance between the hot junctions and the metal-plated layer was found negligible for all the specimens as well as for all the temperatures tested. The quality of the contact was controlled by electrical measurements.

It should be noted that the temperature indicated by the thermocouples, located as shown previously, may differ from the actual temperature of the surface when boiling occurs. By solving the steady-state source problem with Fourier's equation such temperature difference can be approximately evaluated as $\Delta T_e = (q/A)(d/2\kappa)$.

Only in the case of the thickest nickel surface (250 μm) with the highest specific heat flux here experimented (10^6 W/m^2) does the error reach the value of 10.6 percent. With the other heating walls of higher thermal conductivity the error was only 1–2 percent.

4 Experimental Setup and Procedure

The test specimens electrically heated were placed horizontally in a Pyrex tank (500 mm × 200 mm × 300 mm) containing demineralized water and equipped with auxiliary resistance heaters to maintain water at saturation temperature (Fig. 1).

Power was supplied to the 120 mm long test section from a 1800 A − 10 V/900 A − 20 V d-c solid-state power unit through clamp connectors; an interposed nickel-plated copper braid insured good electrical contact. Heat flux was evaluated from voltage drop measurements with a known current flowing through the test section. Voltage measurements made at the ends of the section and measurements made at the ends of the clamp connection differed less than 1–2 percent. In order to remove absorbed gases from the surface of the specimen and to de-gas the water, boiling was allowed to proceed for about an hour at 40 percent peak heat flux.

Each run included measurements of specific heat flux q/A, gradually increasing from 5×10^4 to approximately 8×10^5 W/m^2, and temperature difference ΔT. The waiting period to attain steady-state conditions between each test was 15 min.

The specimens were prepared as follows:

The resin rods with embedded thermocouples were first metal-coated by chemical reduction of silver from silver nitrate to obtain an electroconductive surface 0.1 μm in thickness. Electrodeposition of silver, copper, zinc, nickel, and tin on this surface, up to the required thickness, was then performed in suitable electroplating baths.

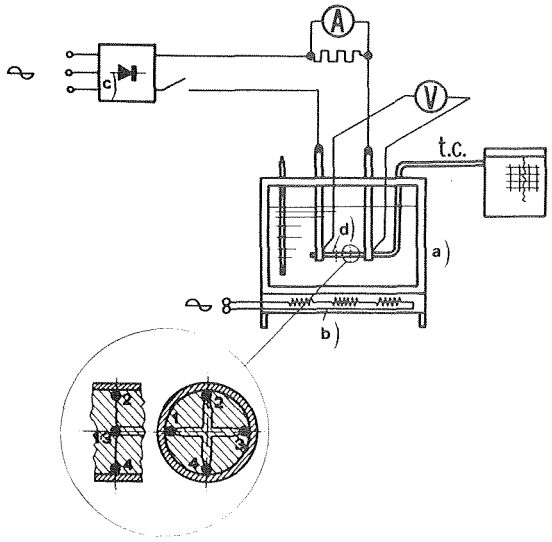

Fig. 1 Experimental apparatus and schemating diagram showing the thermocouples installed: *(a)* Pyrex tank; *(b)* auxiliary resistors; *(c)* d-c power supply; *(d)* test section

In order to obtain test specimens of the same metals with about the same surface characteristics, the outside layer 5 μm thick was processed under the same plating conditions (current density, bath temperature, and time of processing). Therefore, the processing of the thicker specimens was stopped when about 5 μm were still required to reach the prescribed thickness. The specimens were then taken out of the bath, polished with emery paper and reintroduced into the bath to plate the outside layer 5 μm thick.

Four test methods were used for measuring the thickness of the electroplated layer:

(a) a method based on weighing a piece of metal coating of known area;

(b) a method based on the anodic solution of the coating at controlled current; the tests were performed with a KOCOUR Electronic Thickness Tester, mod. S77;

(c) a method based on measuring the electrical resistance of the whole coating from its volt-ampere characteristic;

(d) coating thicknesses higher than 50 μm were measured with a precision thickness gauge on pieces of coating.

The thickness values obtained with the first three methods agreed within 10 percent. Surface roughness was determined with a TALYSURF METER, mod. 3. Average surface roughness values of 0.7–1.0 μm were found for the five kinds of metals here tested. An example of the records obtained from the Talysurf Meter is reported in Fig. 2.

5 Experimental Results

Nucleate boiling heat transfer experiments were performed on several specimens (about 60) of different thicknesses (in the range 5–250 μm) for each of the five metals tested. Each boiling run was performed by measuring the average heat flux q/A and the difference ΔT between the average surface temperature of the heater

Nomenclature

a = thermal diffusivity (m^2/s)
c = specific heat (J/kg°C)
d = thickness of the heating element (m)
q/A = specific heat flux (W/m^2)
ΔT = excess of surface temperature over the saturation temperature (°C)
ΔT_e = temperature difference in the thickness of the heating wall (°C)
κ = thermal conductivity (W/m°C)
ρ = density (kg/m^3)

Superscript

n = index of specific heat flux

(evaluated by averaging the readings of the eight thermocouples of the sample) and the saturation temperature of the fluid.

Some typical experimental curves are shown in Figs. 3 and 4. A satisfying reproducibility of the experimental data was obtained, as seen in Fig. 5, for some nickel test specimens. Referring to Figs. 3 and 4, it may be observed that, for some of the metals tested, (nickel, tin, and zinc) the heat transfer coefficient increases with the decreasing of the heater thickness. In particular, the effect of thickness results in a change in the heat transfer coefficient by as much as 500–700 percent, in the case of nickel or tin, and 100 percent for zinc.

However, when the heater thickness exceeds a certain value, which can be defined as "limiting value," the influence of the wall thickness on the heat transfer coefficient becomes negligible. This limiting value is approximately 70 μm for zinc, 15 μm for both tin and nickel. No appreciable effect of thickness was observed for the copper and silver specimens tested.

Finally, the boiling curves obtained for each of the metals used along with test specimens of thicknesses above the "limiting value" are collected in Fig 6.

6 Analysis and Correlation of Data

Some of the thermophysical properties of the five metal platings tested are reported in Table 1 and taken from references [30, 31].

From Fig. 6 we see that in the range of thicknesses above the limiting value, the heat transfer coefficient decreases from copper to tin. This effect seems to be comparable with the decrease in the parameter $\sqrt{\kappa\rho c}$ for the five metals tested (see Table 1), and agrees with that observed by other experimenters [4, 8].

In the thickness range below the limiting value, Figs. 3 and 4 show that the smaller the heat conductivity of the heating material (as in the case of nickel or tin), the higher the effect of thickness on the heat transfer coefficient. No appreciable influence can be observed in the case of the highest thermal conductivity metals (i.e., copper and silver), while a less-pronounced effect is shown by zinc, whose thermal conductivity has an intermediate value.

Finally, the two metals here tested with approximately the same value of thermal conductivity (tin and nickel) show the same increasing of heat transfer coefficient with the decreasing of wall thickness.

It seems reasonable to assume that in a very thin metal layer transverse heat conduction along the heating material should be one of the dominant factors. Therefore in accordance with Fourier's law, both variables κ and d should be involved.

Taking into consideration both of the factors here affecting the process (i.e., the product of thermal conductivity per thickness $\kappa \cdot d$ and thermal diffusivity $\sqrt{\kappa\rho c}$), as well as the specific heat flux q/A, the ΔT can be expressed by the following relationship:

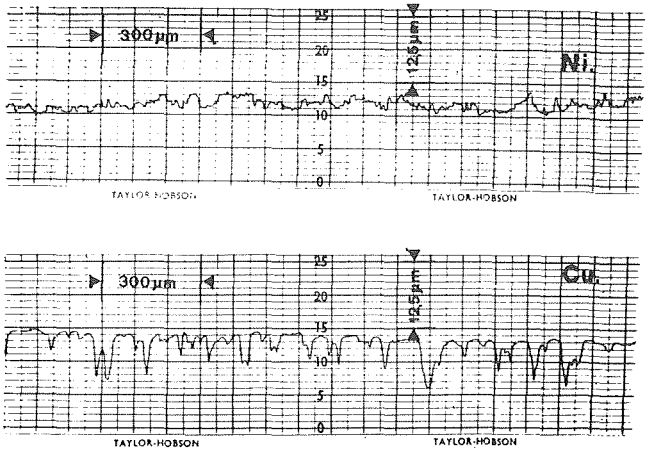

Fig. 2 Talysurf trace showing roughness of nickel and copper plated surfaces

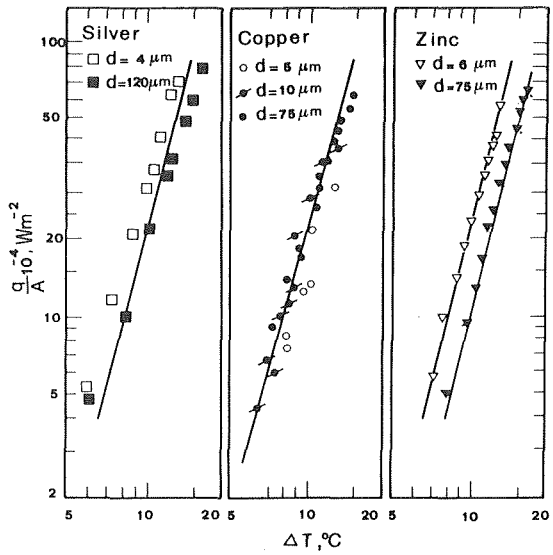

Fig. 3 Heat transfer curves for different thickness of silver, copper, and zinc heaters in pool boiling of water

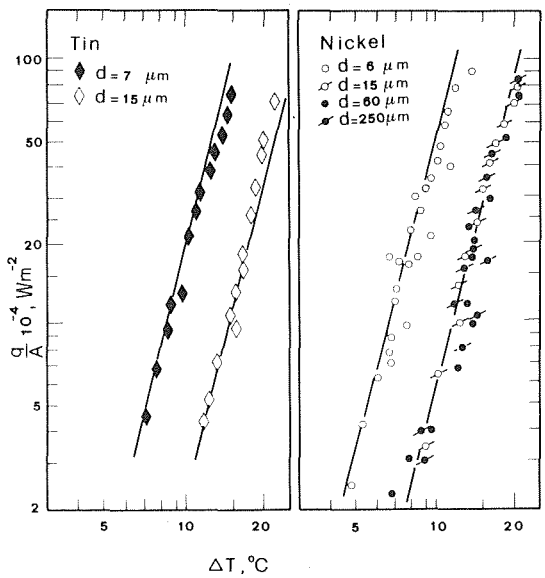

Fig. 4 Heat transfer curves for different thickness of tin and nickel heaters in pool boiling of water

$$\Delta T = f_0\{\frac{q}{A},\ \kappa d,\ \sqrt{\kappa\rho c}\} \tag{1}$$

or in a more suitable form:

$$\Delta T = (\frac{q}{A})^n \cdot f\{\kappa d,\ \sqrt{\kappa\rho c}\} \tag{2}$$

where the power n does not depend on the thermal properties of the wall material. The value of the power n was obtained by plotting the observed heat flux q/A against ΔT using the logarithmic scale. From the slope of the curves, the values of the power n resulted in approximately 0.25 (the same value of n was proposed by Fritz in reference [32]).

The most convenient form of the relation (2) obtained in order to correlate the experimental data resulted in the following (deviation ±15 percent):

$$\Delta T = 0.27\,(\frac{q}{A})^{0.25}\{1 + \frac{4\cdot 10^4}{\sqrt{\kappa\rho c}}\,[1 - e^{-4.5\cdot 10^9(\kappa d)^3}]\}^{0.75} \tag{3}$$

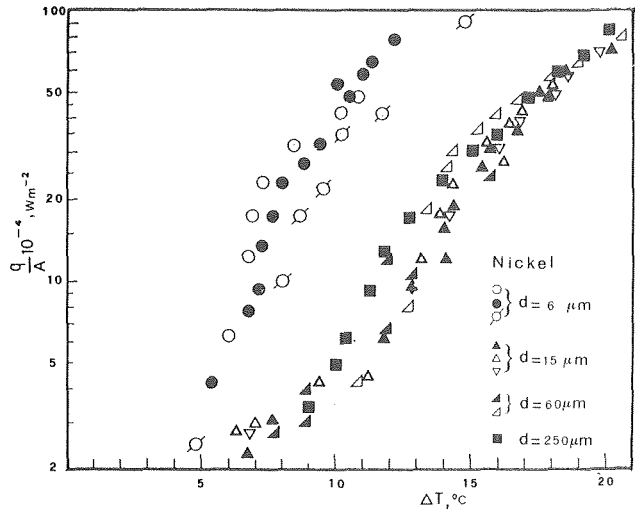

Fig. 5 Reproducibility of data for nickel heaters

In Figs. 3 and 4 unbroken lines have been obtained by plotting the correlation (3); in Fig. 7 all experimental data are correlated with the relation (3).

In the same figure, the data obtained by Bliss, et al. [5], using stainless-steel cylinders of 2.5 mm OD, 0.8 mm wall thickness, and surface roughness (0.08–0.15 μm) somewhat different from our own, are included within the dotted lines. The uncertainty in the location of the representative points is due to the lack of knowledge of the thermophysical properties of the metal used. We performed tests of verification using steel test-tubes AISI 316, of 10 mm OD, a thickness of 1 mm, and a roughness of about 0.7 μm, and the experimental data obtained is reported in Fig. 7. Taking into account the differing surface characteristics, it seems to us that relation (3) approximates sufficiently both our data and that obtained by Hsu, et al.

7 Discussion

(a) **Influence of the Heater Material.** It was previously pointed out that, above the limiting value of thickness, the heat transfer coefficient seems to be dependent mainly upon the parameter $\sqrt{\kappa\rho c}$. This behavior is consistent with that observed by König, under different experimental conditions [9], and by Sharp [4].

In a recent work [33], Grigoriev, et al., using helium at saturation temperature, have observed an increase in the heat transfer coefficient with an increase in the thermal effusivity of the metal layer tested. If one agrees with Sharp's [4] suggestion that the evaporation of the microlayer of liquid is checked by transient conduction, then the heat transfer coefficient can be qualitatively interpreted as being dependent upon the parameter $\sqrt{\kappa\rho c}$. For the highest values of the thickness of the metal layer (above the limiting thickness) this condition is approximated by a temperature pulse on a semi-infinite solid body. In such a case, therefore, the resulting heat transfer flux is a growing function of the thermal effusivity.

Table 1

Metal	$c\rho$ $\left[\frac{J}{m^3°C}\right]$	a $\left[\frac{m^2}{s}\right]$	κ $\left[\frac{W}{m°C}\right]$	$\sqrt{\kappa\rho c}$ $\left[\frac{J}{m^2°Cs^{1/2}}\right]$
Copper	$32.9\cdot10^5$	$1.19\cdot10^{-4}$	393	$3.595\cdot10^4$
Silver	$25.4\cdot10^5$	$1.63\cdot10^{-4}$	414	$3.242\cdot10^4$
Zinc	$28.8\cdot10^5$	$0.38\cdot10^{-4}$	110	$1.778\cdot10^4$
Nickel	$42.8\cdot10^5$	$0.15\cdot10^{-4}$	60.7	$1.639\cdot10^4$
Tin	$17.6\cdot10^5$	$0.34\cdot10^{-4}$	60.6	$1.032\cdot10^4$

(b) **Influence of the Heater Thickness.** Sharp [4] hypothesized that a decreasing value of the heat transfer coefficient together with the decreasing of the heating wall thickness below 250 μm was a consequence of the decreasing of the heater thermal capacity.

On the contrary, in the present investigation a higher heat transfer coefficient was obtained upon decreasing the heater thickness. In fact, the lower the metal layer thermal capacity, the more appreciable was this effect. Moreover, Figs. 3 and 4 show that for nickel heaters of decreasing thicknesses the heat transfer coefficient increased at about 500–600 percent, whereas no appreciable increase was found for copper heaters, although the two metals have about the same specific capacity value ρc (Table 1).

This leads one to suppose that in the case of a low conductivity metal layer, the transient heat conduction along the heater material, rather than the heater thermal capacity, might be the most im-

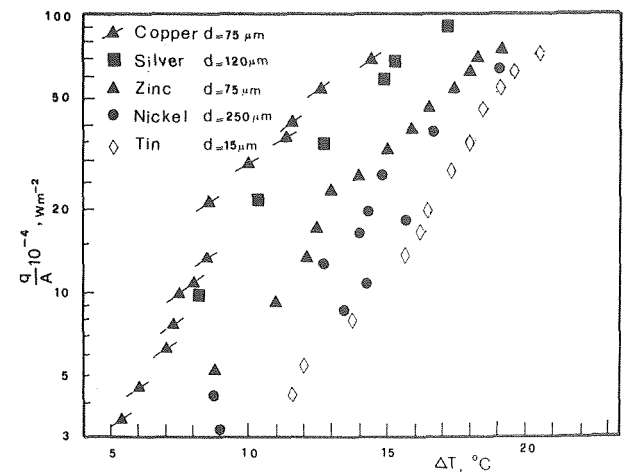

Fig. 6 Heat transfer curves for heaters of different metals above the "limiting value"

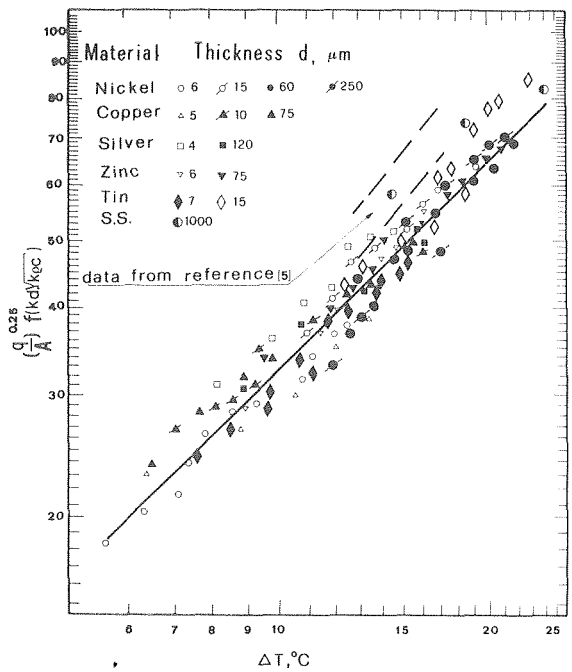

Fig. 7 Correlation of experimental data

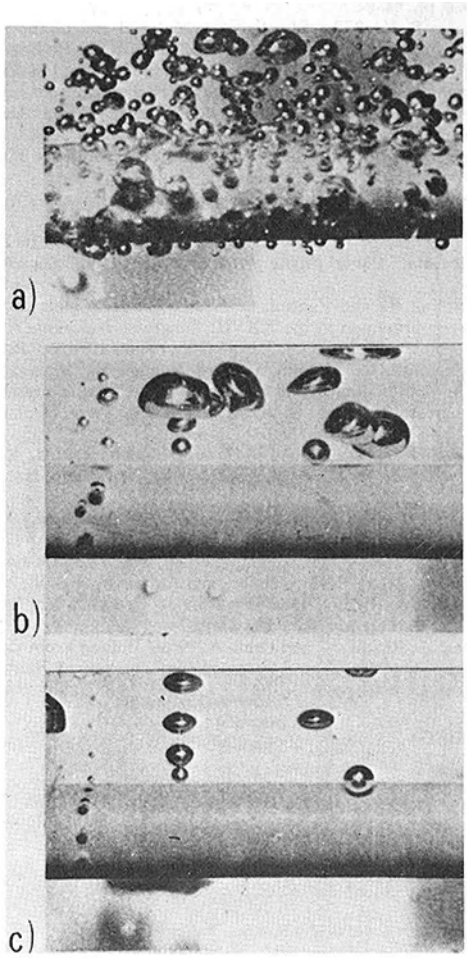

Fig. 8 Influence of nickel thickness on bubble population:

(a) $d = 5\ \mu m$ $q/A = 2.4 \cdot 10^4\ W/m^2$ $\Delta T = 4°C$
(b) $d = 50\ \mu m$ $q/A = 2.4 \cdot 10^4\ W/m^2$ $\Delta T = 8°C$
(c) $d = 50\ \mu m$ $q/A = 10^4\ W/m^2$ $\Delta T = 4°C$

portant parameter affecting the value of the heat transfer coefficient in nucleate pool boiling. A possible explanation of the basic mechanism for very thin heaters of low thermal conductivity could be the following.

The higher resistance to the transverse heat flux which results in the case of a thin wall of low-conductivity under the limiting thickness can cause a strong decrease in the heat flux directed to the base of the bubble by the surrounding area. This is valid no matter what the mechanism of the bubble formation may be. In such a case each bubble extracts heat from a more restricted portion of the heating surface. Thus, at the same heat flux and heating surface, a higher density of active sites must results, each operating in a more restricted zone of influence from that which was established on a thicker metal layer or one which was of higher conductivity. A greater bubble population may produce a greater stirring of the liquid near the wall, and therefore, at the same heat flux, a lower surface temperature. The following experimental results, obtained by various authors, lend some support to the hypothesis of the foregoing advanced mechanism.

Bartolini and Fantini [28], in their photographic study using a nickel heating surface in pool boiling of water at atmospheric pressure, demonstrated the strong increase in bubble population with decreasing thickness in the thickness range of 5–50 μm. The photographs in Fig. 8, reported from reference [28], show the difference in bubble population obtained on the surface of 5 μm thickness and on the surface of 50 μm at the same surface temperature and at the same specific heat flux. Guglielmini and Nannei [14], in their measurements of the temperature fluctuations on thin nickel layers during nucleate boiling, observed that on the thinner walls used (5 μm), a higher frequency of temperature fluctuations resulted. This effect may be connected with the temperature fluctuations inside the fluid near the heating surface as a consequence of the increased bubble population. The test specimens used in references [14, 16, 28] were performed following the same procedure described in the present work.

Finally, data reported by Heled, et al. [34] show a stronger cooling effect of the surface and a higher film coefficient when the bubble population was increased. (Active sites were produced artificially.) On the contrary, even when the thinnest layers (5 μm) of higher thermal conductivity metals (copper, silver) were tested, the transverse thermal resistance was so weak that no influence on the heat transfer process was observed.

Few experimental data regarding the behavior of thin copper and silver surfaces in nucleate boiling are available. Unfortunately, the data of Bartolini and Fantini reported in [16] are obtained only at very low heat flux. Nevertheless, they seem to show a less increasing bubble population with decreasing thickness on copper surfaces as compared to nickel ones. Guglielmini and Nannei [14] also observed a lessening increase of the surface temperature fluctuations with a decreasing of the thickness for copper with respect to nickel surfaces. This leads one to assume that the stirring effect could be lower in the case of higher thermal conductivity metal layers in the range of thickness here experimented with. Consequently, the influence of the heating wall thickness on the film coefficient is not here remarkable. The limiting value of thickness for copper and silver surfaces would be lower than the thickness of the thinnest walls here tested.

8 Conclusions

From the present investigation it is concluded that:

(a) Low-conductivity-metal heaters of thicknesses less than the limiting value showed an increase in the heat transfer coefficient up to 600 percent with decreasing thickness.

(b) When the heater thickness is greater than the limiting value, the heat transfer coefficient for the tested metals is affected by the parameter $\sqrt{\kappa \rho c}$.

(c) A semiempirical correlation is proposed accounting for both the thickness and thermo-physical properties of the heating wall.

References

1 Bonilla, C. F., and Perry, C. W., "Heat Transmission to Boiling Binary Liquid Mixtures," *Trans. AIChE*, Vol. 37, 1941, pp. 685–705.

2 Farber, E. A., and Scorah, R. L., "Heat Transfer to Water Boiling Under Pressure," TRANS. ASME, Vol. 70, 1968, pp. 369–384.

3 Berenson, P. J., "Experiments on Pool-Boiling Heat Transfer," *International Journal of Heat and Mass Transfer*, Vol. 5, 1962, pp. 985–999.

4 Sharp, R. R., "The Nature of Liquid Film Evaporation During Nucleate Boiling," NASA TN D-1997, 1964.

5 Bliss, F. E., Jr., Hsu, S. T., and Crawford, M., "An Investigation Into the Effects of Various Platings on the Film Coefficient During Nucleate Boiling From Horizontal Tubes," *International Journal of Heat and Mass Transfer*, Vol. 12, 1969, pp. 1061–1072.

6 Fontana, D. M., "Ebollizione su fili metallici; studio sperimentale sulla influenza delle proprietà del metallo nella ebollizione satura in convezione naturale," *Ricerche di Termotecnica*, Vol. 19, 1969, pp. 18–27—(*Supplemento* al Vol. XXIII, No. 5, de la Termotecnica, 1969).

7 Kovalev, S. A., Zhukov, V. M., Kazakov, G. M., and Kuzmakichta, Y. A., "Effect of Coating With Low Thermal Conductivity Upon Boiling Heat Transfer of Liquid on Isothermal and Non-Isothermal Surfaces," 4th International Heat Transfer Conference, Paris-Versailles, B.1.4, 1970.

8 Grigoriev, V. A., and Dudkevich, A. S., Some peculiarities of boiling of cryogenic liquids, 4th Int. Heat Transfer Conf., Paris-Versailles, B 8–13, 1970.

9 König, A., "Der einfluss der thermischen Heirwandeigenschaften auf den Wärmaübergang bei der blasenverdampfung," *Wärme und Stoffübertragung*, Vol. 6, 1973, pp. 38–44.

10 Nagarajan and Adelman, "An Experimental Investigation of the Influence of the Grain Size of the Metal Surface on Pool Boiling Heat Transfer," *Can. J. Chem. Engng.*, Vol. 48, 1970, p. 39.

11 Hsu, S. T., and Schmidt, F. W., "Measured Variations in Local Surface Temperature in Pool Boiling of Water," JOURNAL OF HEAT

TRANSFER, Series C, Vol. 83, 1961, pp. 254–260.

12 Morin, R., "Wall Temperature Fluctuation During Bubble Generation in Boiling," Symposium on Two-Phase Flow; Proc.s, Vol. 1, Exeter 21–23 June 1965.

13 Bonnet, C., Macke, E., and Morin, R., "Visualization of Bubble Formation at Atmospheric and Related Measurement of the Wall Temperature Variation," *EUR*, 1962e, 1965.

14 Guglielmini, G., and Nannei, E., "Sulle oscillazioni di temperatura superficiale in ebollizione nucleata: influenza delle caratteristiche fisiche della superficie termotrasmettente," Paper presented to XXVIII Congresso Nazionale A.T.I. (Associazione Termotecnica Italiana), Torino (Italy) Sept. 1973, pp. 12–15.

15 Kotake, S., "On the Liquid Film of Nucleate Boiling," *International Journal of Heat and Mass Transfer*, Vol. 14, 1970, pp. 1595–1609.

16 Bartolini, R., and Fantini, L., "Photographic Study of Bubble Population in Nucleate Boiling on Thin Heating Walls," in Supplement to the Bulletin of the International Institute of Refrigeration, Commission B-1, B-2 and E-1, Freudenstadt 1972, Annex 1972-1.

17 Dzacovich, G. S., and Frost, W., "Vapor Bubble Growth in Saturated Pool-Boiling by Microlayer Evaporation of Liquid at the Heated Surface," 4th International Heat Transfer Conference, Paris-Versailles, B.2-2, 1970.

18 Tachibana, F., Akiwama, M., and Kawamura, H., "Non-Hydrodynamic Aspects of Pool-Boiling Burnout," *Journal of Nuclear Science and Technology*, Vol. 4, No. 3, 1967, pp. 121–130.

19 Ivey, H. J., and Morris, O. J., "The Effect of Test Section Parameters on Saturation Pool Boiling Burnout at Atmospheric Pressure," Rep. A.E.E.W., 160 (1967).

20 Ivey, H. I., and Morris, O. J., "Burnout in Subcooled Pool Boiling at Atmospheric Pressure," U.K.A.E.A. Rep., A.E.E.W., 1967, p. 157.

21 Carne, M., "Some Effect of Test Section Geometry in Saturated Pool Boiling on the Critical Heat Flux for Some Organic Liquids and Liquid Mixtures," *Chemical Engng. Prog. Symp. Ser.*, Vol. 61, 1965, pp. 281–289.

22 Carne, M., and Charlesworth, D. H., "Thermal Conduction Effects on the Critical Heat Flux in Pool Boiling," *Chemical Engng. Prog. Symp. Ser.*, Vol. 62, 1966, pp. 24–34.

23 Averin, E. K., "The Effect of the Material and of the Mechanical Treatment of the Surface on the Heat Exchange in the Boiling of Water," *IzvAkad, Nauk*, SSSR Otdel Tekh. Nauk, Vol. 3, 1954, pp. 166–172.

24 Houchin, W. R., and Lienhard, J. H., "Boiling Burnout in Low Thermal Capacity Heaters," ASME Paper presented at the Winter Annual Meeting and Energy System Exposition, New York, Nov.–Dec. 1966.

25 Magrini, U., "Boiling Burnout on Thin Wall: Influence of Wall Properties," Report No. 11, *(FTR-11)*, Genova, May 1972.

26 Bernath, L., "Prediction of Heat Transfer Burnout," *Chem. Engng. Prog. Symp. Ser.*, Vol. 52, 1956, pp. 1–6.

27 Bernath, L., "A Theory of Local-Boiling Burnout and Its Application to Existing Data," *Chem. Engng. Prog. Symp. Ser.*, Vol. 56, 1960, pp. 95–116.

28 Bartolini, R., and Fantini, L., "Sull'ebollizione incipiente su pareti sottili," Paper presented at the XXVIII Congresso Nazionale A.T.I. (Associazione Termotecnica Italiana), Torino (Italy) Sept. 1973, pp. 12–15.

29 Guglielmini, G., Magrini, U., and Nannei, E., "Flusso termico di 'burnout' in 'pool boiling' su tubi a parete sottile," Paper presented at the XXIX Congresso Nazionale A.T.I. (Associazione Termotecnica Italiana), Torino (Italy) Sept. 1974.

30 Goldsmith, A., Waterman, T. E., and Hirschhorn, H. J., *Handbook of Thermophysical Properties of Solid Materials*, Macmillan, New York, Revised ed., Vol. 1, 1959.

31 Fowle, F. E., *Smithsonian Physical Tables*, Eighth ed., Smithsonian Institution, Washington, D. C., 1934.

32 Jacob, M., *Heat Transfer*, Vol. 1, Wiley, New York, 1964, p. 642.

33 Grigoriev, V. A., Pavlov, Yu. M., and Ametistov, YE. V., "An Investigation of Nucleate Boiling Heat Transfer of Helium," 5th International Heat Transfer Conference, Tokyo, B 2.4, 1974.

34 Heled, J., Ricklis, J., and Orell, A., "Pool Boiling From Large Arrays of Artificial Nucleation Sites," *International Journal of Heat and Mass Transfer* Vol. 13, 1970, pp. 503–516.

M. S. Bhatti
PhD Candidate.
Student Mem. ASME

C. W. Savery
Assoc. Professor.
Mem. ASME

Mechanical Engineering and
Mechanics Department,
Drexel University,
Philadelphia, Pa.

Augmentation of Heat Transfer in a Laminar External Gas Boundary Layer by the Vaporization of Suspended Droplets

A theory is developed for the restricted regime of two-phase flow wherein droplets suspended in a gas stream penetrate the boundary layer and vaporize without deposition. The equations of motion of the droplets are derived taking into account Stokes' drag, buoyancy, and gravity forces. Superimposed free stream turbulence propels a fraction of the droplets into the boundary layer. Using these results a two-region model is developed for determining the heat transfer rate. The application of the theory is illustrated by calculating several quantities of practical interest for the finned surface of a dry cooling tower.

Introduction

It is apparent that in the next several decades the growing demand for electrical power in the United States will be met by the addition of large thermal power plants. Generally these plants are not able to meet the thermal discharge standards for rivers and lakes and hence most new thermal power plants include the provision of cooling towers to reject heat. The current generation power plants are equipped with evaporative cooling towers. These consume large quantities of water, develop insufficient draft in certain geographic locations and produce undesirable plumes and drift. This general consideration and in particular the concept of utilizing a fogging approach to enhance dry cooling performance only during temporary periods of high ambient dry bulb temperatures and power demand prompted the present investigation. In fogging, water droplets are sprayed into the inlet air stream thereby lowering the dry bulb temperature of the inlet air and in addition enhancing air side heat transfer due to vaporization without wetting the heat transfer surfaces. The second effect is the focus of this study.

In recent years there have been several investigations of two-phase, two-component flow. Most of these concerned themselves with injection of liquid droplets into the gas stream and obtaining a liquid film which displaces the gas boundary layer from the solid surface. This, of course, results in considerable enhancement in heat transfer rates due to sensible heating and evaporation of the liquid film. This possibility was first suggested by Elperin [1].[1] In this country the first investigation was reported by Acrivos, et al., who measured heat transfer from a single vertical cylinder exposed to an air-water spray [2]. This work was followed by the investigations of Hoelscher [3], Takahara [4], and Smith [5]. There is a conflict between the results of Takahara and Smith which was resolved by Hodgson, et al. [6]. The experimental results of these investigators agree with those of Smith but not with those of Takahara.

An analytical investigation of the two-phase flow over a circular cylinder was made by Goldstein, et al. [7]. Their theoretical predictions compare favorably with the experimental results of Acrivos, et al. Tifford [8] conducted an exploratory analytical study applicable to a flat plate. Goldstein [9] considered a flat plate oscillating harmonically in its own plane. Thomas and Sunderland [10] made an analytical and experimental study to determine heat transfer rate and liquid film thickness for a wedge-shaped body.

Farmer, et al. [11] made an attempt to investigate the mechanism of droplet deposition. Their analysis applies to adiabatic flow in vertical tubes without vaporization.

The physical model of the dynamics of the droplets postulated by us assumes that free stream turbulence propels the droplets toward the solid surface without contributing directly to the enhancement in heat transfer rate. Sugawara, et al. [12] reported

Contributed by the Heat Transfer Division for publication in the JOURNAL OF HEAT TRANSFER. Manuscript received by the Heat Transfer Division, September 13, 1974. Paper No. 75-HT-OO.

[1] Numbers in brackets designate References at end of paper.

large increases in heat transfer rates for modest free stream turbulence in single-phase flow over a flat plate. But their predictions are not borne out by the findings of the other investigators like Edwards and Furber [13] and Kestin, et al. [14]. Junkhan and Serovy [15] concluded from their experimental studies that the effect of free stream turbulence on heat transfer through a laminar boundary layer on a flat plate with zero pressure gradient is negligible but becomes significant when a pressure gradient is present.

A rigorous solution of laminar flow of a suspension over a semi-infinite flat plate is given by Soo [16] but his analysis is restricted to rigid particles whereas the present analysis applies to relatively fine droplets evaporating in the boundary layer with zero pressure gradient and a transverse temperature gradient.

Analysis

Equations of the motion of the droplets penetrating the hydrodynamic gas boundary layer on a flat surface and vaporizing therein are derived taking into account Stokes' drag, buoyancy, and the gravity forces. Small free stream turbulence superimposed on the boundary layer is assumed to cause the initial transverse velocity component which propels the droplets toward the solid surface. Solving the transverse and the flow direction equations of motion simultaneously, an expression for the exposure time of the droplets is obtained. This enables the determination of several quantities of practical interest.

The following simplifying assumptions enter into the analysis explicitly or implicitly.

1 Droplets obey Stokes' law and as such the analysis is applicable to droplets with Reynolds number less than unity.

2 Flow in the two-component, two-phase stream is laminar, steady, incompressible, and involves Newtonian fluids with constant properties.

3 In the free stream the velocity and temperature of the droplets are the same as those of the gas phase.

4 The tranverse velocity component of the laminar gas boundary layer is ignored.

5 The free stream turbulence is isotropic and the level of turbulence is small, so that the laminar boundary layer flow remains unaffected.

6 A linear velocity profile is assumed across the boundary layer.

7 In the boundary layer droplets move horizontally with the local gas velocity.

There is some slipping or relative motion in the horizontal direction, but this problem is relatively unimportant. The x-direction velocity of the droplet is of the order of v_t and the x-direction velocity of the gas boundary layer is of the order of u_∞. Therefore, x-momentum of the droplets ignoring slipping is of the order of mu_∞ and taking into account slipping is of the order of $m(u_\infty - v_t)$. Since v_t is a small fraction of u_∞, the horizontal slipping of the droplet is insignificant.

Transverse Direction Equation of Motion. As shown in Fig. 1, the various forces acting on the droplet in the boundary layer in the transverse direction are: the gravity force, mg downward, the buoyancy force, $mg\ (\rho/\rho_l)$ upward, and the drag force $6\pi\mu R\ (dp/dt)$ upward. According to Newton's second law of motion,

$$\frac{d}{dt}\left(m\frac{dp}{dt}\right) = mg - mg\left(\frac{\rho}{\rho_l}\right) - 6\pi\mu R\frac{dp}{dt}$$

Expressing m in terms of R, simplifying, differentiating, and rearranging,

$$\frac{d^2p}{dt^2} + \left(\frac{3}{R}\frac{dR}{dt} + \frac{9\mu}{2\rho_l R^2}\right)\frac{dp}{dt} = \left(1 - \frac{\rho}{\rho_l}\right)g \qquad (1)$$

The variation of droplet radius with time can be determined from the vaporization rate [17],

$$\frac{dm}{dt} = \frac{2\pi RM\rho D\mathrm{Sh}}{\bar{M}}\ln\left(\frac{1-\omega_\infty}{1-\omega_0}\right)$$

Nomenclature

A = integration constant, dimensionless
B = integration constant, m
b = flat surface width, m
C = parameter defined by equation (13), m
D = binary vapor diffusivity, m^2/s
g = acceleration due to gravity, m/s^2
h = heat transfer coefficient in the presence of droplets, W/m^2K
$\bar{h}$ = average heat transfer coefficient in the absence of droplets, W/m^2K
h_1 = heat transfer conductance of the outer boundary layer region, W/m^2K
h_2 = heat transfer conductance of the inner boundary layer region, W/m^2K
h_{fg} = enthalpy of evaporation, J/kg
k = thermal conductivity, W/mK
K = parameter defined by equation (24)
l = flat surface length, m
m = droplet mass, kg
Δm = decrease in droplet mass due to vaporization, kg
$\dot{m}''$ = mass flux of the droplets in the free stream, kg/m^2s
M = molecular weight of the droplet, kg/kg mole
$\bar{M}$ = average molecular weight of the boundary layer, kg/kg mole
Nu = Nusselt number, dimensionless
Pr = Prandtl number, dimensionless
p = depth of penetration of the droplets, m
$\dot{q}$ = heat transfer rate, W
$\dot{q}''$ = heat flux, W/m^2
R = droplet radius at any instant, m
R_0 = initial droplet radius, m
R_1 = convective resistance of the inner region of the boundary layer, K/W
R_2 = convective resistance of the outer region of the boundary layer, K/W
R_3 = conductive resistance of the outer region of the boundary layer, K/W
R_{eq} = equivalent resistance of the boundary layer, K/W
Re = Reynolds number, dimensionless
s = spacing between two flat surfaces, m
Sc = Schmidt number, dimensionless
Sh = Sherwood number, dimensionless
t = time, s
t_{exp} = exposure time of the droplet in the boundary layer, s
T = temperature, K
T_0 = flat surface temperature, K
T_∞ = free stream temperature, K
T_i = temperature between the two regions of the boundary layer, K
u_∞ = flow direction free stream velocity, m/s
v_t = transverse velocity due to turbulence superimposed at the boundary layer edge, m/s
x = flow direction distance coordinate, m
y = transverse direction distance coordinate, m
α = parameter defined by equation (7), m^2/s
β = parameter defined by equation (7), m/s^2
γ = parameter defined by equation (18)
δ = boundary layer thickness, m
δ_0 = boundary layer thickness at the point of entry of the droplet, m
μ = dynamic viscosity coefficient, kg/ms
ν = kinematic viscosity, m^2/s
ξ = point of entry of the droplet in the boundary layer, m
ρ = boundary layer density, kg/m^3
ρ_l = droplet density, kg/m^3
λ = parameter defined by equation (4), m^2/s
ω_0 = mole fraction of the vapor at the droplet surface temperature
ω_∞ = mole fraction of the vapor at the average boundary layer temperature

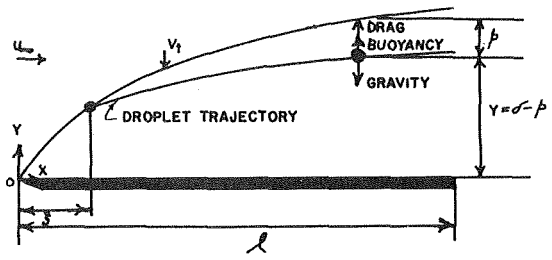

Fig. 1 Forces on a droplet in the boundary layer

Writing m in terms of R, we get

$$\frac{dR}{dt} = \frac{1}{2R}\left[\frac{M}{\bar{M}}\frac{\rho}{\rho_l} D\mathrm{Sh}\ \ln\left(\frac{1-\omega_\infty}{1-\omega_0}\right)\right] \tag{2}$$

Sh depends on droplet diameter which varies with time. The correlation between Sh and the diameter is given by the Ranz-Marshall relation [18]:

$$\mathrm{Sh} = 2 + 0.6\ \mathrm{Re}^{1/2}\ \mathrm{Sc}^{1/3} \tag{3}$$

Here Re is based on $2R_0$ and v_t.

Also, the mole fractions ω_0 and ω_∞ are functions of time. However, if we take a suitable average value for Sh, ω_0, and ω_∞, we can set the slightly varying bracketed quantity in equation (2) equal to a constant and obtain a simple expression for the variation of droplet radius with time. Thus, defining a parameter, λ,

$$\lambda = \frac{1}{2}\left[\frac{M}{\bar{M}}\frac{\rho}{\rho_l} D\mathrm{Sh}\ \ln\left(\frac{1-\omega_\infty}{1-\omega_0}\right)\right] \tag{4}$$

equation (2) assumes the form $dR/dt = \lambda/R$.

Integrating and evaluating the constant of integration through the initial condition at $t = 0$, $R = R_0$, we obtain

$$R^2 = R_0^2 + 2\lambda t \tag{5}$$

Substitution of equation (5) into equation (1) gives

$$\frac{d^2p}{dt^2} + \frac{1}{R^2}\left(3\lambda + \frac{9\mu}{2\rho_l}\right)\frac{dp}{dt} = \left(1 - \frac{\rho}{\rho_l}\right)g \tag{6}$$

The quantities in the parentheses are constants. Defining parameters α and β,

$$\alpha \equiv \left(3\lambda + \frac{9\mu}{2\rho_l}\right) \text{ and } \beta \equiv \left(1 - \frac{\rho}{\rho_l}\right)g \tag{7}$$

the foregoing assumes the form

$$\frac{d^2p}{dt^2} + \frac{\alpha}{R_0^2 + 2\lambda t}\frac{dp}{dt} = \beta \tag{8}$$

This is a second order linear differential equation with variable coefficients. Its solution is

$$p = A(R_0^2 + 2\lambda t)^{(1-\alpha/2\lambda)} + B + \frac{\beta(R_0^2 + 2\lambda t)^2}{4\lambda(\alpha + 2\lambda)} \tag{9}$$

To evaluate the integration constants A and B, we have the following two boundary conditions: at $t = 0$, $p = 0$ and $dp/dt = v_t$.

Using these boundary conditions with equation (9), we obtain

$$A = \left[\frac{\beta R_0^2}{\alpha + 2\lambda} - v_t\right]\frac{R_0^{\alpha/\lambda}}{(\alpha - 2\lambda)} \tag{10}$$

$$B = -R_0^2\left[\frac{\beta R_0^2 - 4\lambda v_t}{4\lambda(\alpha - 2\lambda)}\right] \tag{11}$$

Having evaluated the constants A and B it is now possible to determine the penetration p from equation (9). In the numerous calculations performed using equation (9), it was observed that the contribution of the first term on the right-hand side is negligible. This is because λ, being numerically small and negative quantity, renders A vanishingly small. Therefore ignoring this term,

$$p \simeq B + \frac{\beta(R_0^2 + 2\lambda t)^2}{4\lambda(\alpha + 2\lambda)} \tag{12}$$

Finally changing independent variable

$$y = \delta_0 - p \simeq \delta_0 - B - \frac{\beta(R_0^2 + 2\lambda t)^2}{4\lambda(\alpha + 2\lambda)}$$

Substituting for B from equation (11),

$$y = \delta_0 + R_0^2\left[\frac{\beta R_0^2 - 4\lambda v_t}{4\lambda(\alpha - 2\lambda)}\right] - \frac{\beta(R_0^2 + 2\lambda t)^2}{4\lambda(\alpha + 2\lambda)}$$

Letting

$$C = \delta_0 + R_0^2\left[\frac{\beta R_0^2 - 4\lambda v_t}{4\lambda(\alpha - 2\lambda)}\right] \tag{13}$$

the foregoing can be written as

$$y = C - \frac{\beta(R_0^2 + 2\lambda t)^2}{4\lambda(\alpha + 2\lambda)} \tag{14}$$

Equation (14) gives the transverse location of the droplet at any time t as a function of the boundary layer thickness (δ_0) at the point of entry. Note that C is a function of δ_0.

Flow Direction Equation of Motion. Assuming a linear velocity profile across the boundary layer, the flow direction equation of motion is

$$\frac{dx}{dt} = u_\infty\left(\frac{y}{\delta}\right) \tag{15}$$

The boundary layer thickness along a flat surface is given by Blasius [19]

$$\delta = 5\left(\frac{\nu x}{u_\infty}\right)^{1/2} \tag{16}$$

Substituting equations (14) and (16) into equation (15) and separating the variables,

$$x^{1/2}dx = -\frac{u_\infty^{3/2}}{20\nu^{1/2}\lambda(\alpha + 2\lambda)}\{4\lambda^2\beta t^2 + 4\lambda\beta R_0^2 t + [\beta R_0^4 - 4\lambda(\alpha + 2\lambda)C]\}\,dt$$

Integrating and using the boundary condition at $t = 0$, $x = \xi$ to evaluate the integration constant, we get

$$4\lambda^2\beta t^3 + 6\lambda\beta R_0^2 t^2 + 3[\beta R_0^4 - 4\lambda(\alpha + 2\lambda)C]t + \gamma(x^{3/2} - \xi^{3/2}) = 0 \tag{17}$$

where

$$\gamma \equiv \frac{40\nu^{1/2}\lambda(\alpha + 2\lambda)}{u_\infty^{3/2}} \tag{18}$$

Equation (17) is a cubic in t from which the exposure time of the droplet in the boundary layer can be determined. Since the length of the flat surface is l, the exposure time in the boundary layer will correspond to $x = l$. Thus, from equation (17),

$$4\lambda^2\beta t_{\mathrm{exp}}^3 + 6\lambda\beta R_0^2 t_{\mathrm{exp}}^2 + 3[\beta R_0^4 - 4\lambda(\alpha + 2\lambda)C]t_{\mathrm{exp}} + \gamma(l^{3/2} - \xi^{3/2}) = 0 \tag{19}$$

Heat Transfer Coefficient in the Presence of the Droplets. A simple two region model is developed for determining the heat transfer coefficient in the presence of droplets that penetrate and vaporize within the boundary layer. The boundary between the two regions is determined by the depth of penetration of the droplets during a given time. This depth of penetration (p) is given by equation (12). In the outer region the heat transfer occurs by convection as well as by the vaporization of the droplets. In the inner region which is free of droplets, the heat transfer occurs by convection only. This suggests that the total resistance of the boundary layer can be divided into three resistances as shown in Fig. 2.

R_1 and R_2 are convective resistances and by analogy with Ohm's law equations (20) and (21) are written

$$R_1 = \frac{1}{\bar{h}bl}\left(\frac{\delta - p}{\delta}\right) \tag{20}$$

$$R_2 = \frac{1}{\bar{h}bl}\left(\frac{p}{\delta}\right) \tag{21}$$

R_3 is a conductive resistance and is due to the vaporization of the droplets. Again by analogy with Ohm's law, equation (22) can be written

$$R_3 = \frac{p}{kbl} \tag{22}$$

Assuming the free stream turbulence to be isotropic, the mass of the droplets directed toward the flat surface per unit time is 1/6 $\dot{m}''bs$. But the decrease in the mass of the droplet due to vaporization is Δm. Therefore, the mass of the droplets actually abstracting heat from the boundary layer is $(1/6)(\Delta m/m)\dot{m}''bs$. Thus, the heat abstracted in vaporizing the droplet is $(1/6)(\Delta m/m)\dot{m}''bs\, h_{fg}$. Also from Fourier's law this quantity is given by $[kbl(T_i - T_\infty)/p]$. Equating the two expressions for the quantity of heat abstracted from the solid surface, we get

$$\frac{1}{k} = \frac{6m}{\Delta m}\frac{(T_i - T_\infty)l}{\dot{m}''sph_{fg}}$$

Substituting this into equation (22), we get an expression for the conductive resistance R_3 in terms of measurable quantities. Thus,

$$R_3 = K(T_i - T_\infty) \tag{23}$$

where

$$K = \frac{6m}{\dot{m}''\Delta m h_{fg} bs} \tag{24}$$

The resistances R_1, R_2, *and* R_3 being known from equations (20), (21), and (23), we can determine the total resistance of the boundary layer. R_2 and R_3 are in parallel and R_1 is in series with them, so that the equivalent resistance of the boundary layer is

$$R_{eq} = \frac{R_1R_2 + R_2R_3 + R_3R_1}{R_2 + R_3} \tag{25}$$

For the determination of R_3 we need to know the temperature T_i. This can be determined as follows:

From the steady-state condition in the boundary layer $\dot{q} = h_1(T_i - T_\infty) = h_2(T_0 - T_i)$, where the conductances h_1 and h_2 of the outer and inner region, respectively of the boundary layer are given by

$$h_1 = \frac{R_2 + R_3}{R_2R_3bl} \quad \text{and} \quad h_2 = \frac{1}{R_1bl}$$

Introducing these into the steady-state condition and solving for T_i, we get

$$T_i = \frac{K(R_1T_\infty + R_2T_0) - R_1R_2}{K(R_1 + R_2)} \tag{26}$$

Having determined the equivalent resistance, we are in a position to write down the expression for heat flow from the boundary layer. In analogy with Ohm's law

$$\dot{q} = \frac{T_0 - T_\infty}{R_{eq}} \tag{27}$$

The total area of the flat surface being bl, the expression for the heat flux from the solid surface is

$$\dot{q}'' = \frac{T_0 - T_\infty}{R_{eq}bl}$$

whence the heat transfer coefficient in the presence of droplets is

$$h = \frac{\dot{q}''}{T_0 - T_\infty} = \frac{1}{R_{eq}bl} \tag{28}$$

The average heat transfer coefficient $\bar{h}$ in the absence of droplets can be determined from the Pohlhausen relation [20]:

$$\mathrm{Nu} = \frac{\bar{h}l}{k} = 0.664\ \mathrm{Re}^{1/2}\ \mathrm{Pr}^{1/3} \tag{29}$$

Here Re is based on u_∞ and l.

Forming the ratio $h/\bar{h}$, the enhancement in heat transfer coefficient due to the vaporization of the droplets can be determined.

Results and Discussion

The use of the various equations derived in the preceding section is illustrated by applying them to the finned surface of a dry cooling tower. Typical bench test conditions existing in an experimental rig at the Franklin Institute Research Laboratories were used for performing the various calculations. These conditions were

$u_\infty = 1.524$ m/s, $v_t = 1.524 \times 10^{-2}$ m/s, $T_\infty = 308$ K, $T_0 = 323$ K, $\dot{m}'' = 1.492 \times 10^{-2}$ kg/m^{2}s, $b = 0.3048$m, $l = 5.715 \times 10^{-2}$m, $s = 6.350 \times 10^{-3}$m.

The average surface temperature of the water droplet injected into the air-stream was the wet bulb temperature corresponding to the average boundary layer temperature, $(1/2)(T_0 + T_\infty)$, and exact measured inlet air humidity. From the knowledge of the droplet surface temperature and the average boundary layer temperature, the partial pressures of water vapor at these temperatures can be found from the thermodynamic tables whence the mole fraction ω_0 and ω_∞ can be determined.

The diameter of the droplets used in calculation ranged from 10 to 120μ and for these droplets the average Sherwood number was computed to be 2.59.

The physical properties used in the various computations described in the following are

$M = 18$ kg/kg mole, $\bar{M} = 28$ kg/kg mole, $\rho = 0.125$ kg/m^3, $\rho_l = 101$ kg/m^3, $\mu = 2.530 \times 10^{-3}$ kg/ms, $\nu = 2.035 \times 10^{-5}$ m^2/s, $\mathfrak{D} = 2.942 \times 10^{-5}$ m^2/s, $k = 0.034$ W/mK, $h_{fg} = 2.400 \times 10^6$ J/kg.

Exposure Time. The effect of droplet diameter upon droplet exposure time is given by equation (19). In order to obtain a typical result an entry-point, $\xi = 2.539 \times 10^{-2}$ m, was selected. This point corresponds to the average momentum boundary layer thickness on the finned heat exchanger surface of the bench test. The calculated results are shown in Fig. 3 where the limits of no penetration and surface wetting are indicated. An increasing exposure time with an increasing initial droplet diameter trend is shown. This trend is due to the greater penetration and consequent slowing down of the larger-sized droplets. Droplets smaller than 10μ do not penetrate the boundary layer and travel with the free stream velocity u_∞. Consequently they all have the same exposure time of 20 milli-s corresponding to the free stream velocity.

Penetration of Droplets. Having calculated the exposure time, the penetration of the droplets was calculated using equation (12). The results of the various calculations are plotted on Fig. 4.

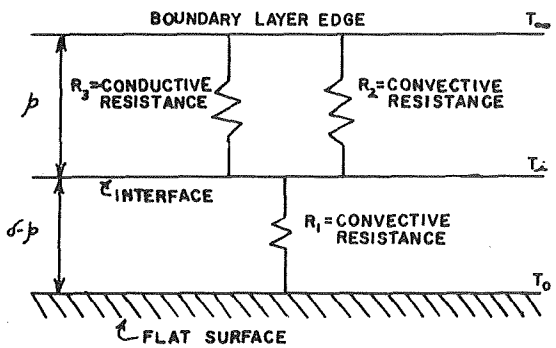

Fig. 2 Thermal resistance of the boundary layer

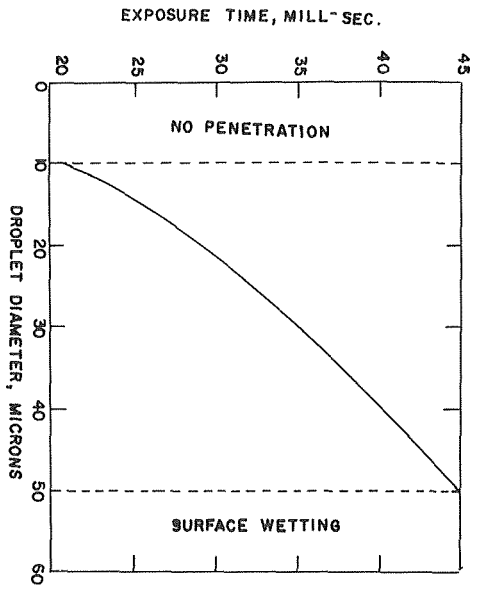

Fig. 3 Variation of exposure time with droplet diameter

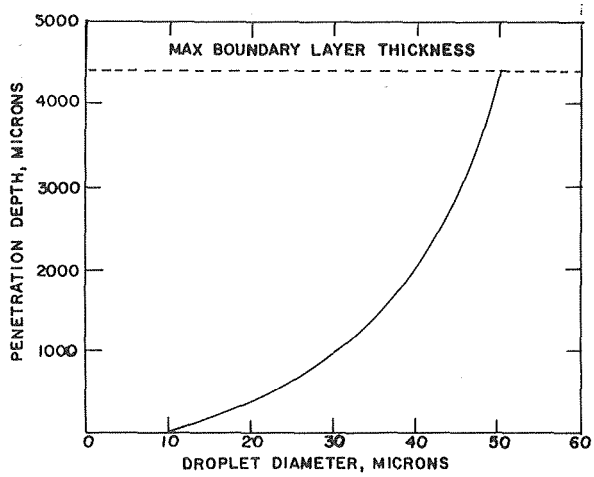

Fig. 4 Variation of penetration depth with droplet diameter

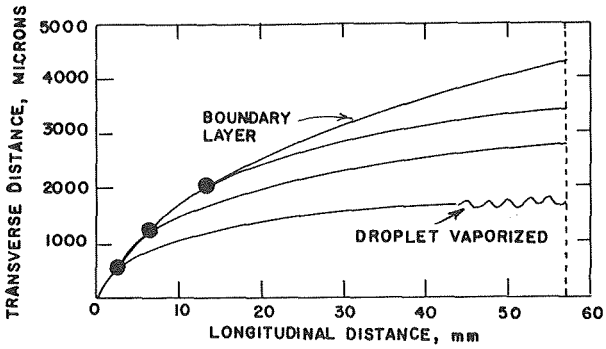

Fig. 5 Trajectories of droplets in the boundary layer

As expected, the larger the droplet diameter the greater is the penetration. Fig. 4 shows that under the specified bench test conditions the 10μ droplets will not penetrate the boundary layer whereas 50μ droplets will penetrate the boundary layer completely and cause wetting of the solid surface. The theory thus gives upper as well as the lower limits of the droplet diameter required to penetrate the boundary layer without causing surface wetting.

Trajectory of the Droplets. The time required by the droplets to transverse any distance downstream can be calculated from equation (17). Knowing this time the transverse location of the droplet in the boundary layer can be determined from equation (14) as a function of time. Thus, the trajectory of the droplets in the boundary layer can be readily predicted. The trajectories of 20μ droplets entering the boundary layer at different points are determined as explained in the foregoing and sketched on Fig. 5.

It is seen from the figure that as the droplets move downstream, their transverse distance from the flat surface increases. This can be explained as due to thickening of the boundary layer. Also, it is clear from the figure that a droplet entering the boundary layer near the leading edge of the flat surface follows a trajectory closer to the flat surface than the trajectory followed by a droplet entering the boundary layer at a point farther downstream. This is to be expected since the exposure time and hence the penetration of the former is greater than that of the latter.

Heat Transfer Calculations. Knowing the penetration and the boundary layer thickness at the trailing end of the fin, the resistances R_1 and R_2 can be readily calculated from equations (20) and (21). Knowing the exposure time, the final droplet diameter can be calculated from equation (5), and the mass defect due to vaporization can be determined. The temperature (T_i) of the interface between the two regions of the boundary layer can be calculated from equation (26). Finally knowing the flux of the droplets in the free stream, the resistance, R_3, can be calculated from equations (23) and (24).

The knowledge of R_1, R_2, and R_3 enables the determination of R_{eq} from equation (25) and h from equation (28). In the absence of droplets $\bar{h}$ can be calculated from equation (29). A comparison of h and $\bar{h}$ gives the enhancement.

The detailed calculations were carried out for different diameter droplets and different droplet fluxes. The results are plotted in Fig. 6 which shows that for constant droplet flux, the larger diameter droplets cause greater enhancement in the heat transfer coefficient. This greater enhancement is due to greater vaporization rates which result from increased exposure time and penetration of the larger-sized droplets. Fig. 6 also shows that as the droplet flux in the main stream increases, the enhancement for the same diameter droplet also increases. This is to be expected since the increase in droplet flux implies that a greater number of droplets are available for vaporization.

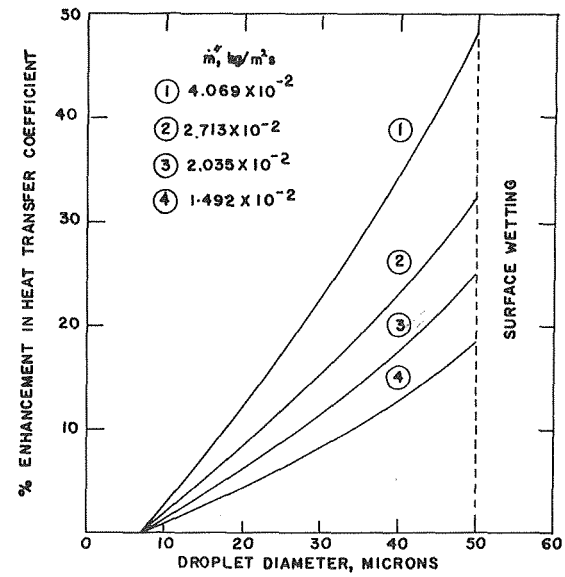

Fig. 6 Dependence of the heat transfer coefficient on the droplet diameter and mass flux

It may be pointed out that the enhancement in heat transfer rates plotted in Fig. 6 is for the upward facing surface of the fin only. According to this theory, droplets do not penetrate the boundary layer formed on the downward facing surface of the fin. This fact was confirmed by the observations made on the experimental rig referred to at the beginning of this section. The observations also confirmed the fact that when the droplets are within certain size range, there is no wetting of the upward facing surface of the fin even for a completely saturated air stream.

Acknowledgment

The authors are indebted to Franklin Institute Research Laboratories for support as a subcontractor under the U. S. Atomic Energy Commission Contract No. AT(11-1)2241.

References

1 Elperin, I. T., "Heat Transfer of Two-Phase Flow With a Bundle of Tubes," *Inzhererno Fizicheski Zhurnal,* Vol. 4, No. 8, 1961, pp. 30–35.

2 Acrivos A., Ahren, J. E., and Nagy, A. R., Jr., "Research Investigation of Two-Component Heat Transfer," The Marquardt Corp., ARL Report ARL 64-116, Wright-Patterson AFB, Ohio, 1964.

3 Hoelscher, F., "Study of Heat Transfer From a Heated Cylinder in Two-Phase Water-Air Flow," MS thesis, Air Force Institute of Technology, Wright-Patterson AFB., Ohio, 1965.

4 Takahara, E. W., "Experimental Study of Heat Transfer From a Heated Circular Cylinder in Two-Phase, Water-Air-Flow," MS thesis, Air Force Institute of Technology, Wright-Patterson AFB, Ohio, 1966.

5 Smith, J. E., "Heat Transfer Studies of Water-Spray Flows," Northern Research and Engineering Corp., ARL Report ARL 66-0091, Wright-Patterson AFB, Ohio, 1966.

6 Hodgson, J. W., Staterbak, R. T., and Sunderland, J. E., "An Experimental Investigation of Heat Transfer from a Spray Cooled Isothermal Cylinder," JOURNAL OF HEAT TRANSFER, TRANS. ASME, Series C, Vol. 90, Nov. 1968, pp. 457–463.

7 Goldstein, M. E., Wen-Jei Yang, and Clark, J. A., "Momentum and Heat Transfer in Laminar Flow of a Gas With Liquid Flow of a Gas With Liquid Droplet Suspension Over a Circular Cylinder," JOURNAL OF HEAT TRANSFER, TRANS. ASME, Series C, Vol. 89, May 1967, pp. 185–194.

8 Tifford, A. N., "Heat Transfer and Frictional Effects in Two Phase Laminar Boundary Layer of Gas-Liquid Spray Systems," U.S.A.F. Research Laboratory Report ARL-64-136, Wright-Patterson AFB, Ohio, Sept. 1964.

9 Goldstein, M. E., Wen-Jei Yang, and Clark, J. A., "Boundary Layer Analysis of Two-Phase Flow over an Oscillating Flat Plate," *AIAA Journal,* Vol. 5, No. 1, Jan. 1967, pp. 43–50.

10 Thomas, W. C., and Sunderland, J. E., "Heat-Transfer Between a Plane Surface and Air Containing Suspended Water Droplets," *Ind. Eng. Chem. Fundam.,* Vol. 9, No. 3, 1970, pp. 368–374.

11 Farmer, R., Griffith, P., and Rohsenow, W. M., "Liquid Droplet Deposition in Two-Phase Flow," JOURNAL OF HEAT TRANSFER, TRANS. ASME, Series C, Vol. 92, Nov. 1970, pp. 587–594.

12 Sugawara, S., Sato, T., Komatsu, H., and Osaka, H., "The Effect of Free Stream Turbulence on Heat Transfer From a Flat Plate," U. S. National Advisory Committee for Aeronautics, Technical Memorandum 1441, 1958.

13 Edwards, A., and Furber, B. N., "The Influence of Free Stream Turbulence on Heat Transfer by Convection From an Isolated Region on a Plane Surface in Parallel Air Flow," *The Institute of Mechanical Engineers Proceedings,* Vol. 170, 1956, pp. 951–954.

14 Kestin, J., Maeder, P. F., and Wang, H. E., "Influence on the Transfer of Heat from Plates With and Without Pressure Gradient," International Development in Heat Transfer Conference, University of Colorado and London, England, ASME, 1961, pp. 432–438.

15 Junkhan, G. H., and Serovy, G. K., "Effects of Free Stream Turbulence and Pressure Gradient on Flat Plate Boundary Layer Velocity Profiles and on Heat Transfer," JOURNAL OF HEAT TRANSFER, TRANS. ASME, Series C, Vol. 89, May 1967, pp. 169–176.

16 Soo, S. L., *Fluid Dynamics of Multiphase Systems,* Blaisdell Publishing Co., 1967, pp. 324–341.

17 Savery, C. W., Juedes, D. L., and Borman, G. L., "n-Heptane, Carbon Dioxide, and Chlorotrifluoromethane Droplet Vaporization Measurements at Supercritical Pressures," *Ind. Eng. Chem. Fundam.,* Vol. 10, No. 4, 1971, pp. 543–553.

18 Bird, R. B., Stewart, W. E., and Lightfoot, E. N., *Transport Phenomena,* Wiley, New York, 1960, p. 409.

19 Schlichting, H., *Boundary Layer Theory,* McGraw-Hill, New York, Sixth ed., 1968, p. 130.

20 Kays, W. M., *Convective Heat and Mass Transfer,* McGraw-Hill, New York, 1966, pp. 204–209, 109.

T. S. Chen
Mem. ASME

M. E. Lohman[1]
Department of Mechanical and Aerospace Engineering,
University of Missouri-Rolla,
Rolla, Mo.

Axial Heat Conduction Effects in Forced Convection Along a Cylinder

An analytical study is performed to determine the effects of axial heat conduction and transverse curvature on laminar forced convective heat transfer of liquid metals along a circular cylinder. The flow and thermal boundary layers for this problem are nonsimilar, the non-similarity arising both from the transverse curvature $\xi = (4/R)(\nu x/u_\infty)^{1/2}$ *of the cylindrical surface and from the axial heat conduction effect expressible as* $\Omega = 1/Pe_x$, *where* Pe_x *is the local Peclet number. The governing equations are solved by the local nonsimilarity method in which all the terms in the conservation equations are retained and only terms in the derived subsidiary equations are selectively deleted according to the levels of truncation. Numerical results are presented for liquid metals having representative Prandtl numbers of 0.03, 0.008, and 0.003 over a wide range of* ξ *values from 0 (i.e., a flat plate) to 4.0 and* Ω *values from 0 (i.e., without axial heat conduction effect) to 0.20. The results indicate that the local surface heat transfer rate increases with an increase in the transverse curvature of the cylindrical surface, an increase in Prandtl number, and an increase in the axial heat conduction parameter or a decrease in Peclet number.*

Introduction

In the study of convective heat transfer over a surface, it is usually assumed that the axial heat conduction inside the boundary layer is insignificant compared to heat conduction normal to the surface. However, for fluids with very low Prandtl numbers, such as liquid metals, the axial heat conduction becomes important and can no longer be neglected.

The problems of forced convection in duct flows, in which the axial heat conduction is included in the analysis, have been studied extensively (see, for example, references [1, 2][2]). To the best knowledge of the authors, studies on heat transfer for low Prandtl number fluids over external surfaces, on the other hand, have only been carried out for flow over a flat plate [3–5]. The present study is concerned with forced convective heat transfer of liquid metals over an isothermal circular cylinder in longitudinal flow, in which the effect of axial heat conduction is taken into account in the analysis. This problem does not admit similarity solutions, the nonsimilarity arising both from the transverse curvature of the cylinder and from the effect of axial heat conduction.

The present problem is of technical interest in connection with liquid metal heat transfer, for example, in the secondary heat exchanger of a liquid metal fast breeder reactor. In the entrance region of such a heat exchanger, the flow and heat transfer characteristics are essentially of the boundary layer type and the present analysis is expected to provide useful information on the heat transfer characteristics in this region.

In solving the nonsimilarity boundary layers, the method of truncated series, of local similarity, and of local nonsimilarity have been presented. The local similarity method of solution has been found to give more accurate results than the series solution by Lloyd and Sparrow [6], and by Sparrow, Heinisch, and Yu [3], among others. In this method, certain terms involving the axial derivatives are deleted from the transformed boundary layer equations, thereby simplifying these equations to those that resemble the equations for a similarity boundary layer. This results in a system of ordinary differential equations that can be solved by well-known techniques. Another attractive feature of the local similarity method is that the solution at any axial location is independent of the solutions at upstream locations. However, the numerical results of the local similarity method are of uncertain accuracy, because there is no direct way to determine whether or not the terms involving the axial derivative that are deleted, are significant as compared to the rest of the terms in the conservation equation.

In order to overcome the shortcomings of the local similarity method, Sparrow and co-workers [7, 8] have recently presented the local nonsimilarity method for solving nonsimilar boundary layer problems. This method retains the most attractive features of the

[1] Presently at Commonwealth Edison, Chicago, Ill.

[2] Numbers in brackets designate References at end of paper.

Contributed by the Heat Transfer Division for publication in the JOURNAL OF HEAT TRANSFER. Manuscript received by the Heat Transfer Division August 12, 1974. Paper No. 75-HT-GG.

local similarity method (i.e., quasi-ordinary differential equations and locally independent solutions) and at the same time retains all the nonsimilar terms that are deleted from the transformed conservation equations in the local similarity method. The only terms that are selectively deleted in the local nonsimilarity method are from the derived subsidiary equations. The manner in which these terms are deleted gives rise to the two-equation and three-equation models of the local nonsimilarity method. Furthermore, the accuracy of the local nonsimilarity method of solution can be ascertained by making a direct comparison among the results from the local similarity model and local nonsimilarity two-equation and three-equation models.

In the present study, the local nonsimilarity method of solution is employed to analyze the effects of transverse curvature and axial heat conduction on the heat transfer characteristics for external convective flow along an isothermal cylinder. The systems of equations for the flow and thermal fields are solved by using the Runge-Kutta integration schemes for the third and second order differential equations, respectively. An iterative scheme using the modified Newton-Raphson method is employed along with a least-squares approach to refine the initial values that need to be guessed in the numerical integration.

The local surface heat transfer results and respresentative temperature profiles are presented for liquid metals with Prandtl numbers of 0.03, 0.008, and 0.003 for a wide range of axial heat conduction parameter Ω ranging from 0 (i.e., without axial heat conduction effect) to 0.20 and for curvature parameter ξ from 0 to 4.0.

To assess the accuracy of the local nonsimilarity method, results from the local similarity model and local nonsimilarity two-equation and three-equation models are compared for representative values of Prandtl number and axial heat conduction parameter. This comparison lends strong support to the high accuracy of the numerical results provided by the local nonsimilarity method of solution.

Analysis

Description of the Problem. Consider a semi-infinite cylinder of radius R which is aligned longitudinally parallel to a uniform free stream with velocity u_∞ and temperature T_∞. Let x and r be the axial and radial coordinates, respectively, of the system. The surface of the cylinder is maintained at a constant temperature T_w. Consideration is given here to the situation in which the Reynolds number is sufficiently high so that the conventional boundary layer assumptions for the flow field apply, but where the Prandtl number of the fluid (and, therefore, the Peclet number) is low enough such that the axial heat conduction effect needs to be taken into account in the analysis. In addition, all properties of the fluid are assumed to be constant. The starting point of the analysis is the following conservation equations for laminar boundary-layer flow in cylindrical coordinates

$$\frac{\partial u}{\partial x} + \frac{1}{r}\frac{\partial}{\partial r}(rv) = 0 \tag{1}$$

$$u\frac{\partial u}{\partial x} + v\frac{\partial u}{\partial r} = \nu\frac{1}{r}\frac{\partial}{\partial r}(r\frac{\partial u}{\partial r}) \tag{2}$$

$$u\frac{\partial T}{\partial x} + v\frac{\partial T}{\partial r} = \alpha[\frac{\partial^2 T}{\partial x^2} + \frac{1}{r}\frac{\partial}{\partial r}(r\frac{\partial T}{\partial r})] \tag{3}$$

where u and v are the streamwise and radial velocity components, respectively, T is the temperature of the fluid, α is the thermal diffusivity, and ν is the kinematic viscosity. The system of equations (1)–(3) is subject to the following boundary conditions:

$$u = v = 0,\ T = T_w \text{ at } r = R \tag{4a}$$

$$u \longrightarrow u_\infty,\ T \longrightarrow T_\infty \text{ as } r \longrightarrow \infty \tag{4b}$$

$$u = u_\infty,\ T = T_\infty \text{ at } x = 0,\ r \geq R \tag{4c}$$

In writing boundary conditions (4c) it is postulated that the flow and thermal boundary layers begin with zero thickness at the leading edge of the cylinder ($x = 0$) and that the axial heat conduction upstream of the leading edge ($x \leq 0$) is neglected. These conditions are impossible to fulfill in practice. However, it has been demonstrated by Seban and Bond [9] that for forced convection along a cylinder without axial heat conduction effect, the applicability of the solution is not essentially restricted by the assumption of zero boundary layer thickness at $x = 0$. In addition, the work of Henneke [1] for liquid metal heat transfer in duct flows has shown that the axial heat conduction effect upstream can be neglected if the Peclet number is larger than 50 for the case of uniform wall temperature and larger than 10 for the case of uniform surface heat flux. For the boundary layer flow under consideration, the flow field, unlike that of a duct flow, is not bounded and as a result the overall axial heat conduction effect upstream will be smaller than that in a duct flow. For these reasons, it is expected that the present analysis, although based on somewhat unrealistic assumptions, will provide results that are believed to be valid except possibly in the region very near $x = 0$ when the Prandtl number is very small.

Transformation of the Governing Equations. To facilitate the analysis, the system of equations (1)–(4) needs to be transformed from the (x, r) coordinates to (ξ, η) coordinates. The coordinate η is a pseudo-similarity variable which contains both x and r, and is chosen such that it reduces to a similarity variable for boundary layers that are similar. The coordinate ξ, on the other hand, depends only on x and is so chosen that x does not appear explicitly in the transformed conservation equations and their boundary conditions. In this connection, it is convenient to use the variables

$$\xi = \frac{4}{R}(\frac{\nu x}{u_\infty})^{1/2},\ \eta = (\frac{r^2 - R^2}{4R})(\frac{u_\infty}{\nu x})^{1/2} \tag{5}$$

as suggested by Seben and Bond [9] in the transformation of the coordinates. It is noted here that the transformed axial coordinate ξ gives both a measure of the transverse curvature of the cylindrical surface and the boundary layer thickness relative to the cylinder radius R. In addition, a reduced stream function $f(\xi, \eta)$ and a dimensionless temperature $\theta(\xi, \eta)$ defined, respectively, as

$$f(\xi,\eta) = \frac{\psi(x,r)}{R(\nu u_\infty x)^{1/2}} \text{ and } \theta(\xi,\eta) = \frac{T - T_\infty}{T_w - T_\infty} \tag{6}$$

are introduced, wherein $\psi(x, r)$ is the stream function that satisfies the continuity equation (1) with

$$u = \frac{1}{r}\frac{\partial \psi}{\partial r} \text{ and } v = -\frac{1}{r}\frac{\partial \psi}{\partial x} \tag{7}$$

In terms of the new variables ξ and η, equations (1)–(4) become, after transformation,

$$(1 + \xi\eta)f''' + (f + \xi)f'' = \xi(f'g' - f''g) \tag{8}$$

$$f(\xi,0) + \xi g(\xi,0) = 0, f'(\xi,0) = 0, f'(\xi,\infty) = 2 \tag{9}$$

$$\frac{1}{\text{Pr}}(1 + \xi\eta)\theta'' + (f + \frac{\xi}{\text{Pr}})\theta' + \Omega[\eta^2\theta'' + 3\eta\theta' - 2\xi\eta\phi' - \xi\phi + \xi^2\chi] = \xi(f'\phi - g\theta') \tag{10}$$

$$\theta(\xi,0) = 1, \quad \theta(\xi,\infty) = 0 \tag{11}$$

In the foregoing equations, the primes denote partial differentiation with respect to η,

$$g = \frac{\partial f}{\partial \xi},\ \phi = \frac{\partial \theta}{\partial \xi},\ \chi = \frac{\partial \phi}{\partial \xi} = \frac{\partial^2 \theta}{\partial \xi^2} \tag{12}$$

and

$$\Omega = \frac{\alpha}{u_\infty x} = \frac{1}{\text{Pe}_x} \tag{13}$$

where the local Peclet number Pe_x is the product of Prandtl number Pr and local Reynolds number $\text{Re}_x = u_\infty x/\nu$.

The magnitude of the parameter Ω determines the importance

of the axial heat conduction effect. Since Ω is proportional to $1/x$, the effect of axial conduction, which is large when x is small, decreases as x increases.

Local Similarity Model. The first set of equations to be derived corresponds to the local similarity model and is obtained by deleting the terms $\xi\partial f/\partial\xi$, $\xi\partial f'/\partial\xi$, $\xi\partial\theta/\partial\xi$, $\xi\partial\theta'/\partial\xi$, and $\xi\partial^2\theta/\partial\xi^2$ in equations (8)–(11). The effect of this first level of truncation is to eliminate all terms containing the product of ξ and ξ derivatives from the transformed conservation equations. This can be done since these terms are small for small values of ξ. When ξ becomes large, it is assumed in the local similarity model that $\partial/\partial\xi$ becomes small. With these simplifications, one obtains the following governing equations for the local similarity model

$$(1 + \xi\eta)f''' + (f + \xi)f'' = 0 \tag{14}$$

$$f(\xi,0) = 0,\ f'(\xi,0) = 0,\ f'(\xi,\infty) = 2 \tag{15}$$

$$\frac{1}{\Pr}(1 + \xi\eta)\theta'' + (f + \frac{\xi}{\Pr})\theta' + \Omega(\eta^2\theta'' + 3\eta\theta') = 0 \tag{16}$$

$$\theta(\xi,0) = 1,\quad \theta(\xi,\infty) = 0 \tag{17}$$

The assumption that $\partial/\partial\xi$ becomes small when ξ becomes large is the weakness of the local similarity method, because in this model there is no direct way to assess the accuracy of this assumption.

Equations (14) and (16) can be treated as ordinary differential equations when the parametric values ξ and Ω are prescribed. Their solutions can be obtained by using the numerical techniques appropriate for similarity boundary layers. By assigning a succession of ξ values, the flow field can be determined by solving equation (14) subject to boundary conditions (15). Once the flow field is solved, the thermal field is obtained from equation (16) for a prescribed value of Ω. Thus, the solution at any axial position can be obtained independently of solutions at other axial positions.

Local Nonsimilarity Models. In deriving the equations for the local similarity model, the terms $\xi\partial f/\partial\xi$, $\xi\partial f'/\partial\xi$, $\xi\partial\theta/\partial\xi$, $\xi\partial\theta'/\partial\xi$, and $\xi\partial^2\theta/\partial\xi^2$ in equations (8)–(10) were deleted. In the local nonsimilarity method, however, it is desirable to retain as many of these terms in the transformed conservation equations as possible. To do this, auxiliary equations are obtained by taking the partial derivatives of the transformed momentum and energy equations and their boundary conditions with respect to ξ.

Differentiation of equations (8)–(11) with respect to ξ results in the first set of subsidiary equations.

$$(1 + \xi\eta)g''' + (f + \xi)g'' - f'g' + 2f''g + \eta f''' + f'' = \xi[(g')^2 + f'h' - gg'' - f''h] \tag{18}$$

$$2g(\xi,0) + \xi h(\xi,0) = 0, g'(\xi,0) = 0, g'(\xi,\infty) = 0 \tag{19}$$

$$\frac{1}{\Pr}(1 + \xi\eta)\phi'' + (f + \frac{\xi}{\Pr})\phi' - f'\phi + \frac{\eta}{\Pr}\theta'' + (2g + \frac{1}{\Pr})\theta' + \Omega[-2\xi\eta\chi' - \xi\chi + \xi^2\frac{\partial\chi}{\partial\xi} + \eta^2\phi'' + 5\eta\phi' + \phi - 2\frac{\eta^2}{\xi}\theta'' - 6\frac{\eta}{\xi}\theta'] = \xi[f'\chi + g'\phi - g\phi' - h\theta'] \tag{20}$$

$$\phi(\xi,0) = 0,\quad \phi(\xi,\infty) = 0 \tag{21}$$

where $\chi = \dfrac{\partial\phi}{\partial\xi} = \dfrac{\partial^2\theta}{\partial\xi^2}$ as before,

$$h = \frac{\partial g}{\partial\xi} = \frac{\partial^2 f}{\partial\xi^2}, \tag{22}$$

and the term Ω/ξ comes from $-\frac{1}{2}\partial\Omega/\partial\xi$.

When equations (18)–(21) are differentiated with respect to ξ, there emerges the second set of subsidiary equations

$$(1 + \xi\eta)h''' + (f + \xi)h'' - 2f'h' + 3f''h + 2\eta g''' + (4g + 2)g'' - 2(g')^2 = \xi[3g'h' + f'\frac{\partial h'}{\partial\xi} - gh'' - 2g''h - f''\frac{\partial h}{\partial\xi}] \tag{23}$$

$$3h(\xi,0) + \xi\frac{\partial h(\xi,0)}{\partial\xi} = 0, h'(\xi,0) = 0, h'(\xi,\infty) = 0 \tag{24}$$

$$\frac{1}{\Pr}(1 + \xi\eta)\chi'' + (f + \frac{\xi}{\Pr})\chi' - 2f'\chi + 2\frac{\eta}{\Pr}\phi'' + (4g + \frac{2}{\Pr})\phi' - 2g'\phi + 3h\theta' + \Omega[\eta^2\chi'' + 7\eta\chi' + 2\chi - \xi\frac{\partial\chi}{\partial\xi} - 2\xi\eta\frac{\partial\chi'}{\partial\xi} + \xi^2\frac{\partial^2\chi}{\partial\xi^2} - 4\frac{\eta^2}{\xi}\phi'' - 16\frac{\eta}{\xi}\phi' - \frac{2}{\xi}\phi + 6\frac{\eta^2}{\xi^2}\theta'' + 18\frac{\eta}{\xi^2}\theta'] = \xi[2g'\chi + f'\frac{\partial\chi}{\partial\xi} + h'\phi - g\chi' - 2h\phi' - \frac{\partial h}{\partial\xi}\theta'] \tag{25}$$

$$\chi(\xi,0) = 0,\quad \chi(\xi,\infty) = 0 \tag{26}$$

The higher order subsidiary equations can be derived by differentiating equations (23)–(26) with respect to ξ, and so on.

To obtain the equations for the two-equation model corresponding to the second level of truncation, all terms involving $\xi\partial^2/\partial\xi^2$ or $\xi\partial^3/\partial\xi^3$ of f and θ and their derivatives with respect to η, namely, the terms ξh, $\xi h'$, $\xi\chi$, $\xi\chi'$, and $\xi\partial\chi/\partial\xi$ in equations (8)–(11) and (18)–(21) are deleted. This is done since these terms are small when ξ is small and $\partial/\partial\xi$ is assumed to be small when ξ becomes large. Thus, the governing equations and the boundary conditions for the two-equation model are

$$(1 + \xi\eta)f''' + (f + \xi)f'' = \xi(f'g' - f''g) \tag{27}$$

$$(1 + \xi\eta)g''' + (f + \xi)g'' - f'g' + 2f''g + \eta f''' + f'' = \xi[(g')^2 - gg''] \tag{28}$$

$$\begin{aligned} f(\xi,0) &= 0, \quad f'(\xi,0) = 0, \quad f'(\xi,\infty) = 2 \\ g(\xi,0) &= 0, \quad g'(\xi,0) = 0, \quad g'(\xi,\infty) = 0 \end{aligned} \tag{29}$$

$$\frac{1}{\Pr}(1 + \xi\eta)\theta'' + (f + \frac{\xi}{\Pr})\theta' + \Omega[\eta^2\theta'' + 3\eta\theta' - 2\xi\eta\phi' - \xi\phi] = \xi[f'\phi - g\theta'] \tag{30}$$

$$\frac{1}{\Pr}(1 + \xi\eta)\phi'' + (f + \frac{\xi}{\Pr})\phi' - f'\phi + \frac{\eta}{\Pr}\theta'' + (2g + \frac{1}{\Pr})\theta' + \Omega[\eta^2\phi'' + 5\eta\phi' + \phi - 2\frac{\eta^2}{\xi}\theta'' - 6\frac{\eta}{\xi}\theta'] = \xi[g'\phi - g\phi'] \tag{31}$$

$$\begin{aligned} \theta(\xi,0) &= 1, \quad \theta(\xi,\infty) = 0; \\ \phi(\xi,0) &= 0, \quad \phi(\xi,\infty) = 0 \end{aligned} \tag{32}$$

It can be seen that in the two-equation model terms are selectively deleted in the subsidiary equations for g and ϕ. The transformed momentum conservation equation is left intact and only the term $\xi^2\partial^2\theta/\partial\xi^2$ is left out in the transformed energy conservation equation. Thus, the two-equation model should provide numerical results that are more accurate than those from the local similarity model. For a specified value of ξ, equations (27) and (28) can be treated as two coupled ordinary differential equations that must be solved simultaneously. The same is true of equations (30) and (31) when the values of ξ and Ω are prescribed.

The three-equation model corresponding to the third level of truncation is obtained by eliminating all terms that contain $\xi\partial^3/\partial\xi^3$ and $\xi\partial^4/\partial\xi^4$ of f and θ and their η derivatives in equations (8)–(11), (18)–(21), and (23)–(26). With the terms $\xi\partial h/\partial\xi$, $\xi\partial h'/\partial\xi$, $\xi\partial\chi/\partial\xi$, $\xi\partial\chi'/\partial\xi$, and $\xi\partial\chi^2/\partial\xi^2$ deleted, the governing equations for this model become

$$(1 + \xi\eta)f''' + (f + \xi)f'' = \xi[f'g' - f''g] \tag{33}$$

$$(1 + \xi\eta)g''' + (f + \xi)g'' - f'g' + 2f''g + \eta f''' + f'' = \xi[(g')^2 + f'h' - gg'' - f''h] \tag{34}$$

$$(1 + \xi\eta)h''' + (f + \xi)h'' - 2f'h' + 3f''h + 2\eta g''' + (4g + 2)g'' - 2(g')^2 = \xi[3g'h' - gh'' - 2g''h] \tag{35}$$

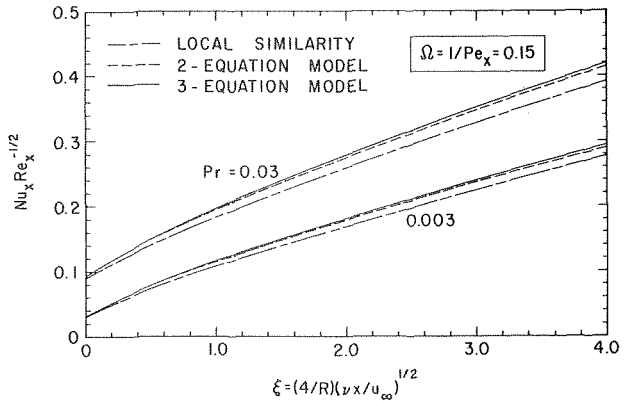

Fig. 1 A comparison of representative heat transfer results among the various models, $\Omega = 1/\mathrm{Pe}_x = 0.15$

$$f(\xi,0) = 0, \quad f'(\xi,0) = 0, \quad f'(\xi,\infty) = 2$$
$$g(\xi,0) = 0, \quad g'(\xi,0) = 0, \quad g'(\xi,\infty) = 0 \qquad (36)$$
$$h(\xi,0) = 0, \quad h'(\xi,0) = 0, \quad h'(\xi,\infty) = 0$$

$$\frac{1}{\mathrm{Pr}}(1+\xi\eta)\theta'' + (f + \frac{\xi}{\mathrm{Pr}})\theta' + \Omega[\eta^2\theta'' + 3\eta\theta' - 2\xi\eta\phi' - \xi\phi + \xi^2\chi] = \xi[f'\phi - g\theta'] \qquad (37)$$

$$\frac{1}{\mathrm{Pr}}(1+\xi\eta)\phi'' + (f + \frac{\xi}{\mathrm{Pr}})\phi' - f'\phi + \frac{\eta}{\mathrm{Pr}}\theta'' + (2g + \frac{1}{\mathrm{Pr}})\theta' + \Omega[-2\xi\eta\chi' - \xi\chi + \eta^2\phi'' + 5\eta\phi' + \phi - 2\frac{\eta^2}{\xi}\theta'' - 6\frac{\eta}{\xi}\theta'] = \xi[f'\chi + g'\phi - g\phi' - h\theta'] \qquad (38)$$

$$\frac{1}{\mathrm{Pr}}(1+\xi\eta)\chi'' + (f + \frac{\xi}{\mathrm{Pr}})\chi' - 2f'\chi + 2\frac{\eta}{\mathrm{Pr}}\phi'' + (4g + \frac{2}{\mathrm{Pr}})\phi' - 2g'\phi + 3h\theta' + \Omega[\eta^2\chi'' + 7\eta\chi' + 2\chi - 4\frac{\eta^2}{\xi}\phi'' - 16\frac{\eta}{\xi}\phi' - \frac{2}{\xi}\phi + 6\frac{\eta^2}{\xi^2}\theta'' + 18\frac{\eta}{\xi^2}\theta'] = \xi[2g'\chi + h'\phi - g\chi' - 2h\phi'] \qquad (39)$$

$$\theta(\xi,0) = 1, \quad \theta(\xi,\infty) = 0$$
$$\phi(\xi,0) = 0, \quad \phi(\xi,\infty) = 0 \qquad (40)$$
$$\chi(\xi,0) = 0, \quad \chi(\xi,\infty) = 0$$

In the three-equation model, no terms are deleted from the transformed momentum equation and its first subsidiary equation and from the transformed energy equation. Only one term $\xi\partial\chi/\partial\xi$ in the first subsidiary energy equation and a few terms each of the third level truncation for momentum and energy conservation are deleted. This is an improvement over the local nonsimilarity two-equation model. Thus, it is expected that the three-equation model should yield results that are better than those from the two-equation model; that is, it should give the best results among the three models. For a prescribed value of ξ, the momentum equation and its subsidiary equations, equations (33)–(36), can . be treated as a system of ordinary differential equations that must be solved simultaneously. With the solutions for f, g, and h and their η derivatives available for various ξ values, the energy equation and its subsididary equations, equations (37)–(40), are then solved simultaneously as a system of ordinary differential equations for a prescribed value of Ω.

From the discussion of the nonsimilarity models, it is obvious that the local nonsimilarity method of solution possesses, in addition to providing more accurate results, the two most attractive features of the local similarity method; namely, the governing equations can be treated as ordinary differential equations and their solution at a certain value of ξ can be obtained independently of the solutions from other ξ values.

As a note, it is pointed out that the local nonsimilarity method described in the present study differs somewhat from that outlined in references [7, 8]. In forming the two equation model, for example, one encounters the terms $\xi\partial/\partial\xi(f'g' - f''g) = \xi(g'g' - gg'' + f'\partial g'/\partial\xi - f''\partial g/\partial\xi)$ and $\xi\partial/\partial\xi(f'\phi - g\theta') = \xi(g'\phi - g\phi' + f'\partial\phi/\partial\xi - \theta'\partial g/\partial\xi)$ in the first subsidiary momentum and energy equations, respectively. In [7, 8], these terms are altogether deleted, while the present work retains, respectively, the terms $\xi(g'g' - gg'')$ and $\xi(g'\phi - g\phi')$ and deletes only those terms involving $\xi\partial/\partial\xi$ of g,g' and ϕ. This latter approach is consistent with the spirit of local similarity model in which the terms involving $\xi\partial/\partial\xi$ of f, f', and θ, etc., are deleted. A similar approach is taken in formulating the three-equation model. However, the numerical results from these two different approaches did not show any significant difference.

The governing equations for the local similarity model and local nonsimilarity two-equation and three-equation models were solved by employing Runge-Kutta integration scheme, starting at $\eta = 0$ and integrating toward $\eta = \eta_\infty$, a numerical approximation to $\eta = \infty$, with a proper step size $\Delta\eta$. The procedure used is similar to that outlined by Dewey and Gross [10] and by Hayday and co-workers [11] for the numerical solution of ordinary differential equations. As is well known, the initiation of Runge-Kutta integration for a system of differential equations of total order n requires n numerical values for the functions and their derivatives. Thus, for example, for the three-equation model, a total of nine function and derivative values for the flow field and a total of six function and derivative values for the thermal field are needed at $\eta = 0$, but only six and three are available from equations (36) and (40), respectively. Therefore, it was necessary to determine each of the three

Table 1 The $-\theta'(\xi, 0)$ results from the local nonsimilarity three-equation model**

ξ	$-\theta'(\xi,0)$				
	$\Omega = 0$	0.05	0.10	0.15	0.20
	Pr = 0.03				
0	0.1689*	0.1751	0.1816	0.1981	0.1989
1.0	0.3736	0.3804	0.3869	0.3932	0.3993
2.0	0.5350	0.5424	0.5496	0.5565	0.5633
3.0	0.6794	0.6874	0.6952	0.7028	0.7102
4.0	0.8136	0.8223	0.8309	0.8391	0.8470
	Pr = 0.08				
0	0.0931*	0.0963	0.0992	0.1032	0.1059
1.0	0.2754	0.2792	0.2889	0.2864	0.2898
2.0	0.4156	0.4201	0.4245	0.4286	0.4326
3.0	0.5415	0.5467	0.5516	0.5563	0.5609
4.0	0.6592	0.6649	0.6704	0.6756	0.6807
	Pr = 0.003				
0	0.0587*	0.0609	0.0625	0.0648	0.0680
1.0	0.2257	0.2282	0.2307	0.2331	0.2355
2.0	0.3528	0.3559	0.3589	0.3618	0.3647
3.0	0.4673	0.4709	0.4745	0.4779	0.4812
4.0	0.5747	0.5788	0.5828	0.5866	0.5904

*Similarity solution.

** The results for $\xi = 0$ and $\Omega \neq 0$ correspond to $-\theta'(\Omega,0)$ values.

missing starting values. They were successfully determined by the use of modified Newton-Raphson shooting method in conjunction with a least-squares technique [12]. The details of the numerical solution are given in Lohmann [13].

Results and Discussion

Numerical results were obtained for liquid metals with Prandtl numbers of 0.03, 0.008, and 0.003. They cover a wide range of ξ values from 0 (i.e., a flat plate) to 4.0 and Ω values from 0 (i.e., without axial heat conduction effect) to 0.20. It suffices to present only the results for local Nusselt number and temperature profiles. The wall shear results and velocity profiles have been previously given [7].

The local Nusselt number gives an indication of the surface heat transfer characteristics and is defined by

$$\mathrm{Nu}_x = \frac{hx}{k} \tag{41}$$

where k is the thermal conductivity and

$$h = q_w/(T_w - T_\infty) \tag{42}$$

is the heat transfer coefficient. By employing Fourier's law, $q_w = -k(\partial T/\partial r)_{r=R}$, one obtains

$$\mathrm{Nu}_x = -\frac{1}{2}\theta'(\xi,0)\mathrm{Re}_x^{1/2} \tag{43}$$

To illustrate the accuracy of the results from the various model, the local heat transfer results as given by $\mathrm{Nu}_x\mathrm{Re}_x^{-1/2} = -\theta'(\xi, 0)/2$ from the local similarity model and local nonsimilarity two-equation and three-equation models are compared, respectively, in Fig. 1 for a representative case of $\Omega = 1/\mathrm{Pe}_x = 0.15$, with Pr = 0.03 and 0.003. It can be seen from the figure that the heat transfer results exhibit the trend of increasing accuracy with increasing level of truncation. The two-equation and three-equation models provide results that are in good agreement over the entire range of ξ values and for the range of Prandtl numbers considered in the calculations. The local similarity model, on the other hand, is seen to give results of low accuracy. Although not shown, this similar trend is also observed for the cases of Ω = 0.05, 0.10, and 0.20 that were studied. In view of this and due to the fact that considerable scattering of experimental data usually exists in low Prandtl number fluids, the heat transfer results from the two-equation model probably would be more than adequate for practical purposes. However, for better accuracy, the final results of interest were obtained from solution of the three-equation model.

The results for $-\theta'(\xi, 0)$ from the local nonsimilarity three-equation model were obtained for Pr = 0.03, 0.008, and 0.003, $\Omega = 1/\mathrm{Pe}_x$ = 0, 0.05, 0.10, 0.15, and 0.20, and ξ = 0, 1, 2, 3, and 4. These results are listed in Table 1. For the case of a flat plate ($\xi = 0$), Ω is taken as the x-dependent transformation variable. Thus, the results for $\xi = 0$ correspond to $-\theta'(\Omega, 0)$.

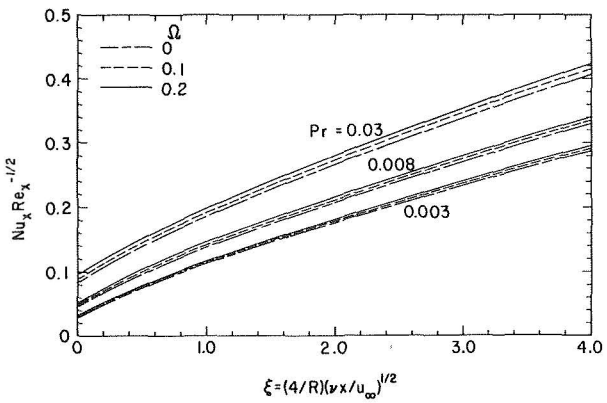

Fig. 2 Representative heat transfer results from the three-equation model

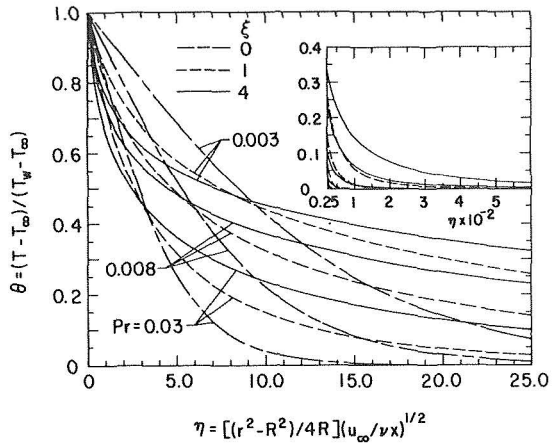

Fig. 3 Representative temperature profiles from the three-equation model for $\Omega = 1/\mathrm{Pe}_x = 0.20$

The heat transfer results $\mathrm{Nu}_x\mathrm{Re}_x^{-1/2} = -\theta'(\xi, 0)/2$ are collectively presented in Fig. 2 for all three Prandtl numbers. However, to preserve clarity of the figure, only the curves for Ω = 0, 0.10, and 0.20 are illustrated. All results are from the three-equation model except for the case of a flat plate (i.e., $\xi = 0$). For this particular case, the problem reduces to a similarity problem when $\Omega = 0$; for $\Omega > 0$, the results are from the two-equation model. It can be seen from the figure that the effect of increasing ξ is to increase the value of $\mathrm{Nu}_x\mathrm{Re}_x^{-1/2}$. In addition, the rate of heat transfer increases with increasing Prandtl number and increasing Ω for a given Prandtl number. Therefore, the effect of axial heat conduction is to increase the rate of surface heat transfer. That is, the heat transfer rate increases as the Peclet number decreases.

Fig. 3 shows the representative temperature profiles for the case of $\Omega = 1/\mathrm{Pe}_x = 0.2$. Curves are given for Pr = 0.03, 0.008, and 0.003 and axial locations ξ = 0, 1.0, and 4.0. To conserve space, the temperature profiles for the cases of Ω = 0, 0.05, 0.10, and 0.15 are not shown. It can be seen from the figure that the temperature gradient at the surface (i.e., $\eta = 0$) increases with increasing Prandtl number and increasing axial location. In addition, the thermal boundary layer thickness is seen to increase with increasing value of ξ for a given Prandtl number and with decreasing value of Prandtl number for a given ξ.

To show the effect of the axial heat conduction parameter or Peclet number on the temperature profiles for various Prandtl numbers, the curves for two axial locations ξ = 0 and 4.0 are compared in Fig. 4. An inspection of the figure reveals that for a given ξ an

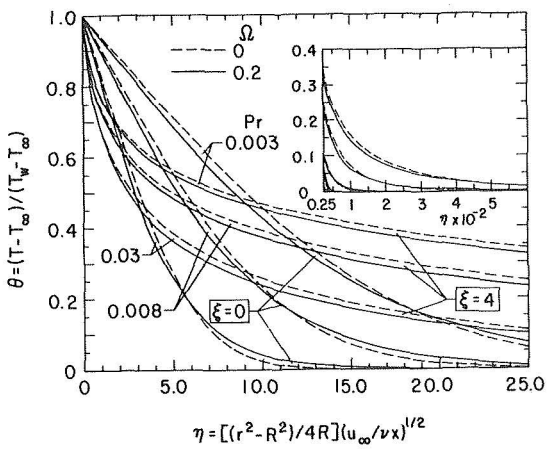

Fig. 4 A comparison of representative temperature profiles between Ω = 0 and 0.20, three-equation model

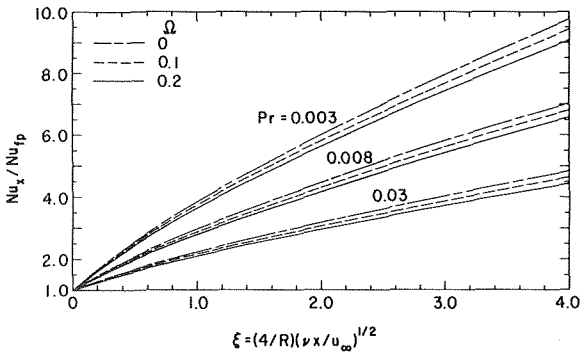

Fig. 5 The effect of curvature on the local Nusselt number

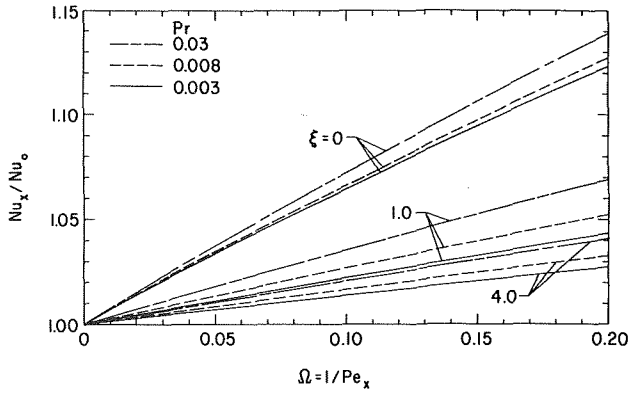

Fig. 6 The effect of axial heat conduction on the local Nusselt number

increase in the axial conduction parameter Ω or a decrease in the Peclet number causes an increase in the temperature gradient at the wall and an increase in the thermal boundary layer thickness. In general, the effect of axial heat conduction is to cause a more rapid decrease in temperature in the region near the wall, while an opposite behavior is observed in the region away from the wall.

The effect of ξ on the local Nusselt number can be seen more readily from Fig. 5 in which the ratio of the local Nusselt number Nu_x to the local Nusselt number for a flat plate Nu_{fp} is plotted against ξ. The ratio Nu_x/Nu_{fp} is found to increase with increasing values of ξ and Peclet number Pe_x and decreasing values of Prandtl number and axial heat conduction parameter Ω. Thus, the effect of curvature on the relative increase of local Nusselt number becomes increasingly important as the Prandtl number decreases.

In Fig. 6 the effect of axial heat conduction parameter Ω on the local Nusselt number is shown in a Nu_x/Nu_0 versus $1/Pe_x$ plot, where Nu_0 is the local Nusselt number without axial heat conduction (i.e., $\Omega = 0$ or $Pe_x = \infty$). From the figure, it can be seen that the ratio Nu_x/Nu_0 increases with increasing value of Ω or decreasing value of Pe_x. The relative increase in Nu_x/Nu_0 becomes more pronounced as ξ becomes smaller. For a given value of ξ, this ratio decreases with decreasing Prandtl number.

Conclusions

In this paper, the effects of axial heat conduction on laminar forced convective heat transfer along a circular cylinder are analyzed by the local nonsimilarity method of solution. In the analysis, both the flow and thermal boundary layers are assumed to develop at the leading edge of the cylinder and the axial heat conduction effect upstream of the leading edge is neglected. It is found that the rate of surface heat transfer increases as the axial heat conduction parameter increases or as the Peclet number decreases.

Within the framework of the assumptions in the analysis, the present study provides heat transfer results that are believed to be of high accuracy except in the region very near the leading edge of the cylinder.

Acknowledgments

The Department of Mechanical and Aerospace Engineering, University of Missouri-Rolla provided funds for the computations of the numerical results reported in this paper.

References

1 Hennecke, D. K., "Heat Transfer by Hagen-Poiseuille Flow in the Thermal Development Region with Axial Conduction," *Warme-und Stoffübertragung,* Vol. 1, 1968, pp. 177–184.

2 Hsu, Chia-Jung, "An Exact Analysis of Low Peclet Number Thermal Entry Region Heat Transfer in Transversely Nonuniform Velocity Fields," *AIChE Journal,* Vol. 17, 1971, pp. 732–740.

3 Sparrow, E. M., Heinisch, R. P., and Yu, H. S., "Streamwise Heat Conduction Effects in Forced-Convection Boundary Layers Without and With Superposed Free Convection," *Nuclear Science and Engineering,* Vol. 39, 1970, pp. 387–393.

4 Grosh, R. J., and Cess, R. D., "Heat Transfer to Fluids With Low Prandtl Numbers for Flow Across Plates and Cylinders of Various Cross Section," TRANS. ASME, Vol. 80, 1958, pp. 667–676.

5 Pozzi, A., and Contursi, F., "Energy Equation for Large Reynolds Numbers and Small Prandtl Numbers," *American Rocket Society Journal,* Vol. 32, 1962, pp. 1278–1280.

6 Lloyd, J. R., and Sparrow, E. M., "Combined Forced and Free Convection Flow on Vertical Surfaces," *International Journal of Heat and Mass Transfer,* Vol. 13, 1970, pp. 434–438.

7 Sparrow, E. M., Quack, H., and Boerner, C. J., "Local Nonsimilarity Boundary-Layer Solutions," *AIAA Journal,* Vol. 8, 1970, pp. 1936–1942.

8 Sparrow, E. M., and Yu, H. S., "Local Nonsimilarity Thermal Boundary-Layer Solutions," JOURNAL OF HEAT TRANSFER, TRANS. ASME, Series C, Vol. 93, 1971, pp. 328–334.

9 Seban, R. A., and Bond, R., "Skin Friction and Heat Transfer Characteristics of a Laminar Boundary Layer on a Cylinder in Axial Incompressible Flow," *Journal of the Aeronautical Sciences,* Vol. 18, 1951, pp. 671–675.

10 Dewey, C. F., Jr., and Gross, J. F., "Exact Similar Solutions of the Laminar Boundary Layer Equations," *Advances in Heat Transfer,* Academic Press, New York, Vol. 4, 1967, pp. 317–446.

11 Hayday, A. A., Bowlus, D. A., and McGraw, R. A., "Free Convection From a Vertical Flat Plate With Step Discontinuities in Surface Temperature," JOURNAL OF HEAT TRANSFER, TRANS. ASME, Series C, Vol. 89, 1967, pp. 244–250.

12 Nachtsheim, P. R., and Swigert, P., "Satisfaction of Asymptotic Boundary Conditions in Numerical Solution of Systems of Nonlinear Equations of Boundary-Layer Type," NASA Technical Note, NASA TN D-3004, 1965.

13 Lohmann, M. E., "Liquid Metal Heat Transfer in Longitudinal Flow Along a Cylinder and Flat Plate," MS thesis, University of Missouri-Rolla, 1974.

E. M. Sparrow
L. Lee[1]

Department of Mechanical Engineering, University of Minnesota, Minneapolis, Minn.

Analysis of Flow Field and Impingement Heat/Mass Transfer Due to a Nonuniform Slot Jet

An analysis is made of the fluid flow and heat transfer characteristics associated with the impingement of a slot jet which issues from a delivery duct with a nonuniform velocity profile. Consideration is given to velocity profiles similar to that for a fully developed laminar channel flow. The velocity field within the impinging jet is solved for within the framework of an inviscid flow model. Results from the inviscid solution are used as input for the analysis of the boundary layer heat or mass transfer on the impingement surface. The stagnation point heat (or mass) transfer coefficients corresponding to the initially nonuniform velocity profile are found to be almost twice as large as those for an initially flat velocity profile. Furthermore, the transfer coefficients are insensitive to the separation distance between the duct exit and the impingement surface, within the range investigated. The analytical results compared satisfactorily with experimentally determined mass transfer coefficients.

Introduction

Jet impingement is a frequently used technique to obtain localized and controlled surface heat transfer coefficients. In investigations of the heat transfer characteristics of impinging jets, a factor which has received relatively little attention is the shape of the velocity profile at the exit of the nozzle or duct from which the jet emerges. Flat exit velocity profiles are encountered when the jet issues from a short nozzle with a high contraction ratio. On the other hand, if the fluid stream is delivered by a tube or duct of sufficient length, the velocity profile at the exit cross section corresponds to fully developed flow.

Once the jet has emerged from the delivery nozzle or duct, the persistence of the exit profile depends, in part, on the degree of mixing between the jet fluid and that of the environment. When a liquid jet is introduced into a gaseous environment (e.g., a water jet into air), mixing processes play a minor role and the initial profile can persist for appreciable distances. If, on the other hand, both the jet and the surroundings are the same fluid (e.g., air into air or water into water), there is a substantial amount of mixing between the outer layers of the jet and surrounding fluid. The inner layers of the jet stream, the so-called core, are not directly involved in the mixing process, and in these layers the initial velocity profile continues to persist. The mixing zone progressively eats into the core, ultimately engulfing it. Even after the core has disappeared, there may still be residual influences of the shape of the initial velocity profile which tend to die away with increasing distance from the delivery nozzle or duct.

A circular jet emerging from a fully developed turbulent duct flow possesses an exit-plane maximum velocity that can be as much as 20 percent greater than the uniform velocity provided by a nozzle. More highly peaked profiles are encountered when a jet issues from a laminar duct flow. For instance, the velocity maxima in a circular tube and in a parallel-plate channel are, respectively, twice and 3/2 times the corresponding mean velocity.

Within the knowledge of the authors, the effect of exit profile shape on impingement heat transfer has not been investigated for jet flows that are turbulent at exit. Research on jet flows that are laminar at exit has been reported in [1, 2].[2] Those studies were concerned with impingement mass transfer, but the results are applicable to heat transfer via the heat-mass transfer analogy. In [1],

[1] On leave from Mechanical Engineering Department, University of Maine, Orono, Maine.

Contributed by the Heat Transfer Division for publication in the JOURNAL OF HEAT TRANSFER. Manuscript received by the Heat Transfer Division November 7, 1974. Paper No. 75-HT-UU.

[2] Numbers in brackets designate References at end of paper.

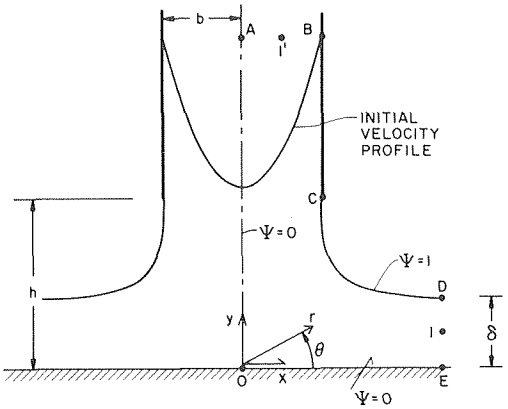

Fig. 1 Schematic diagram of the problem

a solution was obtained for the inviscid flow field in an impinging circular jet fed by a fully developed laminar pipe flow. The inviscid velocity solution was employed as input to a boundary layer analysis of the mass transfer on the impingement surface. The predictions of the analysis were supported by experimental results obtained using the naphthalene sublimation technique. Both the jet flow and the environment fluid were air. At the stagnation point on the impingement surface, the transfer coefficient was found to be more than twice as large as the analytically predicted value for a flow of equal Reynolds number but with an initially flat velocity profile. Experiments for the latter case are, apparently, unavailable for the laminar regime.

Measurements of mass transfer coefficients resulting from the impingement of an initially laminar slot jet are reported in [2]. Air flow was delivered by a 12:1 aspect ratio rectangular duct of sufficient length to ensure fully developed conditions at exit; the environment fluid was also air. The measured transfer coefficients were compared (after suitable conversion involving the Schmidt and Prandtl numbers) with the results of heat transfer experiments [3, 4] in which the initial velocity profile was partially developed. It was found that the transfer coefficients from the experiments with the initially fully developed velocity profile exceeded those for the case of initially partially developed flow by as much as about 40 percent. The outcome of the comparison has, however, to be regarded as qualitative because the extent of the velocity development in the experiments of [3, 4] is unknown.

The present investigation is concerned with the slot jet and was motivated by the objective of obtaining a quantitative assessment of the effect of an initially nonuniform laminar velocity profile on impingement transfer coefficients. As a first step in the fulfillment of this objective, the inviscid flow field associated with the impinging jet is determined for several values of the separation distance between the jet exit and the impingement surface. A presentation will be made of illustrative velocity field results obtained from this phase of the investigation. To verify the validity of the solution method, flow field results for a slot jet with an initially flat velocity profile are obtained and compared with an exact solution [5] based on conformal mapping and complex variable theory.

The velocity field solutions provide input information for the boundary layer analysis of the surface heat and mass transfer coefficients. The analysis is specifically applied to the stagnation region. The thus-determined transfer coefficients for impinging slot jets with a nonuniform initial velocity profile are compared with those for slot jets having a uniform initial profile. In addition, the analytical predictions for the transfer coefficients corresponding to an initially nonuniform slot jet are compared with the experimental results of [2].

Analysis

A schematic diagram which depicts the problem to be analyzed is presented in Fig. 1. A parallel-plate channel of half width b and of sufficient length to ensure complete hydrodynamic development conveys a laminar flow to its exit plane, which is situated at a distance h from a wall. The jet issuing from the channel impinges on the wall, turns, and then flows along the surface, ultimately forming a wall jet.

In this investigation, primary attention is focused on the stagnation region, that is, the region adjacent to point O in Fig. 1. The boundary layer flow in the stagnation region is driven by the adjacent inviscid flow. Therefore, the solution of the inviscid flow is a prerequisite for the boundary layer analysis. The inviscid flow model does not take account of mixing (i.e., entrainment) which may occur between the outer layers of the jet and the environment. The model thus presupposes the existence of a core that is unaffected by the mixing. Owing to the turning caused by the impingement, the outer layers are deflected away from the core. Consequently, there is good reason to expect that the core of an impinging jet will persist at least as long as that in a free jet.

The domain in which the problem has to be solved includes not only the region occupied by the jet itself, but also the portion of the delivery duct situated just upstream of the exit cross section. The reason that the latter region has to be considered is that the pressure gradients associated with the deflection and turning of the jet by the impingement surface can cause a precursive effect within the channel. In the analysis and solution of the problem, considerable insight was gained from reference [1].

For the heat transfer problem to be solved here, the impinging jet is assumed to be isothermal at a temperature T_∞, whereas the stagnation region on the impingement surface is maintained at a

Nomenclature

b = channel half width
c = concentration of transferred species
$\mathcal{D}$ = diffusion coefficient
h = separation distance between duct exit and wall
h_h = heat transfer coefficient
h_m = mass transfer coefficient
k = thermal conductivity
$\dot{m}$ = mass transfer rate per unit area
Pr = Prandtl number
q = heat transfer rate per unit area
r = radial coordinate
R = dimensionless radial coordinate, r/b
Re = Reynolds number, $(4b)\bar{v}/\nu$
Sc = Schmidt number
Sh = Sherwood number
T = temperature
U = velocity magnitude on free streamline, equation (19)
V_i = dimensionless velocity component, $v_i/\bar{v}$
v_i = velocity component
v_{max} = maximum velocity magnitude for initial profile
$\bar{v}$ = mean velocity magnitude for initial profile
X, Y = dimensionless coordinates, x/b, y/b
x, y = coordinates, Fig. 1
Δ = dimensionless length, δ/b
δ = length of segment DE
θ = angular coordinate
ν = kinematic viscosity
ϕ = dimensionless temperature or concentration, equation (31)
Ψ = dimensionless stream function, $\psi/\bar{v}b$
ψ = stream function
Ω = dimensionless vorticity, equation (2a)
ω = vorticity, equation (2)

Subscripts

0 = stagnation point, $x = 0$
w = impingement surface
∞ = free stream

different uniform temperature T_w. For the analogous mass transfer problem, the concentrations of the transferred species in the jet and in the stagnation region are c_∞ and c_w, respectively.

The Flow Model. Although it might be sufficient to begin the analysis by stating the inviscid flow equations without derivation, greater insights are obtained by deriving them from the complete Navier-Stokes equations. If one begins by writing the x- and y-momentum equations appropriate to two-dimensional constant property flow and then eliminates the pressure by subtracting $\partial/\partial y$ of the first equation from $\partial/\partial x$ of the second equation, there is obtained

$$v_x \frac{\partial \omega}{\partial x} + v_y \frac{\partial \omega}{\partial y} = \nu \nabla^2 \left(\frac{\partial v_y}{\partial x} - \frac{\partial v_x}{\partial y}\right) \tag{1}$$

where ω is the vorticity

$$\omega = \partial v_y/\partial x - \partial v_x/\partial y \tag{2}$$

and ∇^2 is the two-dimensional Laplace operator. The left- and right-hand sides of equation (1) can be identified as representing the convection and diffusion of vorticity.

If dimensionless variables are introduced (see Nomenclature), then the foregoing become

$$V_x \frac{\partial \Omega}{\partial X} + V_y \frac{\partial \Omega}{\partial Y} = \frac{4}{\mathrm{Re}} \nabla^2 \left(\frac{\partial V_y}{\partial X} - \frac{\partial V_x}{\partial Y}\right) \tag{1a}$$

$$\Omega = \partial V_y/\partial X - \partial V_x/\partial Y \tag{2a}$$

where Re is the Reynolds number based on the hydraulic diameter ($= 4b$) of the channel

$$\mathrm{Re} = (4b)\bar{v}/\nu \tag{3}$$

The quantity $\bar{v}$ is the magnitude of the mean velocity of the channel flow.

For a fully developed channel flow, the right-hand side of equation (1a) is identically zero for any Reynolds number. Owing to the fact that streamline deflection associated with the jet impingement is caused primarily by the action of pressure forces rather than viscous forces, it will be assumed that the right-hand side continues to be negligibly small within the channel in the present problem. The validity of this assumption is enhanced when the Reynolds number is not too small, e.g., for Re > 100–200, and its acceptance by knowledgeable investigators is witnessed by its use in prior analyses of related problems [1, 5].

In the jet itself, the flow is assumed inviscid. In support of this model, one may examine the conditions under which the viscous diffusion of vorticity is negligible. The time required for vorticity to diffuse across the half width of the jet is given by one-dimensional theory as

$$t_d \sim b^2/\nu \tag{4}$$

On the other hand, the time t_c for convective transport between the channel exit and the impingement surface can be estimated as

$$t_c \sim h/\bar{v} \tag{5}$$

If the diffusion time is much greater than the convection time, then the diffusion can be neglected. With the aid of equations (4), (5), and (3), the condition $t_d \gg t_c$ becomes

$$\mathrm{Re} >> 4(h/b) \tag{6}$$

For gas jets in a gas environment or liquid jets in a liquid environment, a core region of substantial breadth exists for $h/b < \sim 5$. Consequently, for such flows, the neglect of viscous diffusion appears reasonable for Re > ~200.

In light of the foregoing, the analysis will be performed using equation (1a) with zero right-hand side. If the dimensionless stream function Ψ ($\partial\Psi/\partial Y = V_x$, $\partial\Psi/\partial X = -V_y$) is introduced, then

$$\frac{\partial \Psi}{\partial Y}\frac{\partial \Omega}{\partial X} - \frac{\partial \Psi}{\partial X}\frac{\partial \Omega}{\partial Y} = 0 \tag{7}$$

It is easily verified that equation (7) is satisfied by

$$\Omega = -f(\Psi) \tag{8}$$

where f is any function of Ψ. When equations (8) and (2a) are combined, one has

$$\partial^2\Psi/\partial X^2 + \partial^2\Psi/\partial Y^2 = f(\Psi) \tag{9}$$

Equation (9) underscores the difference between the present case of an initial nonuniform velocity profile and the case of the initial uniform profile. For the latter, $\nabla^2\Psi = 0$, so that conformal mapping and complex variable theory can be used. In the present problem, $f(\Psi) \neq 0$ (the flow is not a potential flow) and, as a consequence, the task of finding a solution is much more formidable.

It remains to identify the function $f(\Psi)$. Inasmuch as equation (9) holds anywhere in the flow field, it can be applied at some distance into the channel where the velocity profile is fully developed and parabolic, that is

$$V_y = -(3/2)(1 - X^2);\ \Psi = (3/2)(X - X^3/3) \tag{10}$$

Upon introducing Ψ from equation (10) into (9), there follows

$$f(\Psi) = -3X \tag{11}$$

Furthermore, by solving the cubic in the Ψ,X equation of (10), one can find

$$X = g_i(\Psi),\ i = 1, 2, 3 \tag{12}$$

where the g_i are nonlinear functions of Ψ. Thus, from equations (12) and (11), it is seen that $f(\Psi)$ is nonlinear, which means that the differential equation (9) is also nonlinear.

It is interesting to note that the corresponding analysis for the circular jet [1] does not lead to a nonlinear governing differential equation for the stream function. This is a somewhat surprising outcome inasmuch as problems involving the parallel-plate channel are usually thought to be simpler than are problems involving the circular tube.

The nonlinear differential equation for Ψ that corresponds to the initial parabolic velocity profile makes for a solution task of monumental difficulty, which is compounded by the fact that the position of the free boundary of the jet is unknown. It is, therefore, reasonable to employ an initial velocity profile which closely approximates the parabola and yet leads to a linear differential equation for Ψ. These characteristics are possessed by the cosine profile[3]

$$V_y = -(\pi/2)\cos(\pi X/2),\ \Psi = \sin(\pi X/2) \tag{13}$$

Correspondingly, $f(\Psi) = -(\pi/2)^2\Psi$ and, from equation (9),

$$\partial^2\Psi/\partial X^2 + \partial^2\Psi/\partial Y^2 = -(\pi/2)^2\Psi \tag{14}$$

which is a linear partial differential equation.

Solution Method. Equation (14) can be solved by employing the separation of variables method. To facilitate subsequent operations related to fitting the boundary conditions, it is convenient to recast the Laplace operator in cylindrical coordinates and to write the solution with R,θ as independent variables. The outcome

[3] The replacement of the parabola by a cosine profile was also employed by Yih [6] in analyzing channel flow in the presence of a sink of mass situated at the center of a wall at the end of the channel.

of the separation of variables solution is

$$\Psi(R,\theta) = \sum_{n=1}^{\infty} A_{2n} J_{2n}(\pi R/2) \sin 2n\theta \tag{15}$$

As written, equation (15) already satisfies certain boundary conditions. In particular, $\Psi = 0$ on the impingement surface $\theta = 0$ and on the symmetry line $\theta = \pi/2$ (see Fig. 1). In addition, the finiteness condition at $R = 0$ has been employed to eliminate the Bessel function of the second kind.

In view of the fact that the shape of the free boundary (CD in Fig. 1) is both unknown and unlikely to coincide with a coordinate line, the coefficients A_{2n} that appear in equation (15) cannot be determined by conventional Fourier methods. Therefore, an alternative procedure must be sought. With a view to keeping the subsequent numerical work to a reasonable level, the boundary conditions are applied over a finite domain $ABCDEOA$ as shown in Fig. 1. The dimensions OA and OE have to be chosen large enough so that they do not affect the flow field in the stagnation region, which is the main interest of this study.

The conditions on the various boundaries will now be discussed. The $\Psi = O$ condition on OA and OE is already incorporated in equation (15). On AB, which corresponds to an axial station sufficiently distant from the channel exit so that streamline deflections due to the jet impingement are negligible,

$$\Psi = \sin(\pi R_A/2 \tan\theta) \tag{16}$$
$$R = R_A/\sin\theta,\ \theta_B \leq \theta \leq \pi/2$$

where equation (13) has been used. The segment BC lies along the channel wall and is, therefore, a streamline. Consequently,

$$\Psi = 1,\ R = 1/\cos\theta,\ \theta_C \leq \theta \leq \theta_B \tag{17}$$

Along the free streamline CD

$$\Psi = 1,\ R = R(\theta),\ \theta_D \leq \theta \leq \theta_C \tag{18}$$

The position of the free streamline, as represented by the function $R = R(\theta)$, is unknown. It must be determined as part of the solution. The condition for determining the positioning of the free streamline is that the pressure is constant in the environment adjacent to the streamline. From this and from Bernoulli's equation, it follows that the magnitude of the velocity is constant at all points along the streamline. If $U(\theta)$ represents the velocity magnitude at any point on the streamline, then the solution must satisfy

$$U(\theta) = (V_r^2(\theta) + V_\theta^2(\theta))^{1/2} = \text{constant} \tag{19}$$

The boundary DE is taken to be a cross section where the flow is essentially parallel to the wall and the pressure is equal to that of the environment. To derive the boundary condition for Ψ, consider a typical point 1 on DE and a related point 1′ on AB such that 1 and 1′ lie on the same streamline (Fig. 1). The pressures and velocities at the two points are related via Bernoulli's equation. Bernoulli's equation is also written between points B and D. By combining the two Bernoulli equations and noting the equality of pressure at 1 and D and at 1′ and B, the zero velocity at B, and the fact that $V_y^2 = (\pi/2)^2(1 - \Psi^2)$ at 1′, one obtains for the velocity of point 1

$$V_x^2(1) = V_x^2(Y) = (\pi/2)^2(1 - \Psi^2) + U^2 \tag{20}$$

where U is the velocity on the free streamline.

The variation of Ψ along DE is then obtained by integrating $d\Psi = V_x dY$ with equation (20) as input. The result is

$$\Psi = (1 + (2U/\pi)^2)^{1/2} \sin(\pi Y/2) \tag{21}$$

where

$$Y = R_E \tan\theta,\ 0 \leq \theta \leq \theta_D \tag{22}$$

Since $\Psi = 1$ at point D, equation (21) indicates the length of the segment DE (denoted by δ in Fig. 1) to be

$$\Delta = \delta/b = (2/\pi)\sin^{-1}(1 + (2U/\pi)^2)^{-1/2} \tag{23}$$

With the solution domain thus defined and the boundary conditions stated, attention may be turned to the determination of the coefficients A_{2n} of equation (15). The general approach is first to postulate the position of the free streamline CD and then to evaluate equation (15) at a discrete number of points on the boundaries AB, BC, CD, and DE, using the boundary conditions stated in equations (16), (17), (18), and (21). If a total of P points are employed, then P linear algebraic equations are generated in this way. The series on the right-hand side of equation (15) is truncated after M terms, so that there are M unknown A's. If $M < P$, the coefficients are determined by a least squares solution of the algebraic equations.

With these A values, the velocity components V_r and V_θ are evaluated at points along the free streamline, and the velocity magnitudes $U(\theta)$ are calculated in accordance with equation (19). If these magnitudes do not satisfy the condition $U(\theta)$ = constant, the free streamline is repositioned, and the procedure for determining the A's is repeated. These operations are continued until the free streamline condition U = constant is satisfied.

Although the conceptual scheme of the solution method is readily understood, its implementation requires a considerable amount of art, especially with regard to the initial positioning and subsequent repositioning of the free streamline. The initial positioning for a given separation distance h/b was based on experience gained with solutions for other h/b. With respect to the repositioning of the streamline to better fulfill the condition U = constant, it appeared reasonable to attempt to employ the procedure used in [1] in connection with the circular jet. If $(k + 1)$ denotes the next repositioning and k denotes the present position, then the correction equation of [1] for the radial coordinate on the free streamline is

$$R_{k+1}(\theta) = [1 + \Phi_1 \log_{10}[\frac{U(\theta)}{U_C}]][R_k(\theta) + \Phi_2(R_{D,k+1} - R_{D,k})] \tag{24}$$

where

$$\Phi_1 = [\frac{\theta - \theta_D}{\theta_C - \theta_D}]^{1/2},\ \Phi_2 = \frac{\theta - \theta_C}{\theta_D - \theta_C} \tag{24a}$$

The values of R_D needed for equation (24) were evaluated from $(R_E^2 + \Delta^2)^{1/2}$, where Δ is from equation (23).

It was found that convergence could not be attained by direct application of equation (24). Rather, satisfactory convergence was achieved by employing equation (24) in conjunction with a damping procedure. If R_{k+1}* denotes the radial coordinate actually used for the $k + 1$ repositioning and R_{k+1} is the value given by equation (24), the damping equation can be written as

$$R_{k+1}^* = R_k + \lambda(R_{k+1} - R_k) \tag{25}$$

where λ is the damping factor.

After an initial period of numerical experimentation, the following computational parameters were selected: *(a)* 20 points on each of segments AB, BC, CD, and DE, with the points situated at a uniform increment $\Delta\theta$ within each segment; *(b)* 8 terms in the series of equation (15); *(c)* a value of 0.2 for the damping factor λ. It was found that the stagnation region results were insensitive to modest departures from the U = constant condition as well as to the lengths of OA and OE beyond certain minimum values.

Stagnation Region Velocity. A major motivation for the inviscid flow solution is to furnish the free stream velocity for the boundary layer on the impingement surface, that is, to provide $V_r(R)$ at $\theta = 0$. Noting that $RV_r = \partial\Psi/\partial\theta$, one can obtain the de-

sired result from equation (15). If attention is focused on small values of R (i.e., the stagnation region) and suitable representations are used for the Bessel functions, there is obtained

$$V_r(R) = \sum_{n=1}^{M} \frac{A_{2n}\pi^{2n}}{2^{4n}(2n-1)!} R^{2n-1} \tag{26}$$

From the boundary layer standpoint, $V_r(R)$ is better denoted by $V_x(X)$ since $X = R$ on the impingement surface. For the boundary layer stagnation point solution, the needed input quantity is dV_x/dX at $X = 0$. From equation (26)

$$(dV_x/dX)_0 = (\pi^2/16)A_2 \tag{27}$$

Boundary Layer Equations. The governing equations for stagnation point flow and heat/mass transfer are well established and will be stated here without derivation. The similarity variable η and dimensionless stream function F are

$$\eta = y((dv_x/dx)_0/\nu)^{1/2}, \quad \psi = ((dv_x/dx)_0\nu)^{1/2} xF(\eta) \tag{28}$$

where $(dv_x/dx)_0$ is related to the dimensionless derivative expressed by equation (27) via

$$(dv_x/dx)_0 = (\bar{v}/b)(dV_x/dX)_0 \tag{29}$$

The governing differential equation for F is

$$F''' + FF'' - (F')^2 + 1 = 0 \tag{30}$$

with boundary conditions $F(0) = F'(0) = 0$, $F'(\infty) = 1$

For heat or mass transfer, one defines dimensionless variables as

$$\phi(\eta) = \frac{T - T_\infty}{T_w - T_\infty} \text{ or } \phi(\eta) = \frac{c - c_\infty}{c_w - c_\infty} \tag{31}$$

with which the energy or species equations take the form

$$\phi'' + \Lambda F\phi' = 0 \tag{32}$$

where Λ = Pr or Sc. The boundary conditions are $\phi(0) = 1$, $\phi(\infty) = 0$.

The surface fluxes of heat or mass, q and $\dot{m}$, respectively, are evaluated from

$$q = -(k\partial T/\partial y)_{y=0}, \quad \dot{m} = -(\mathfrak{D}\partial c/\partial y)_{y=0} \tag{33}$$

and the corresponding heat and mass transfer coefficients h_h and h_m are

$$h_h/k = h_m/\mathfrak{D} = -\phi'(0)((dv_x/dx)_0/\nu)^{1/2} \tag{34}$$

where $\phi'(0)$ is obtained from the solution of equation (32). Equation (34) explicitly indicates the role played by the inviscid solution in fixing the magnitudes of the heat and mass transfer coefficients. It is seen that h_h and h_m are proportional to the square root of the streamwise velocity gradient $(dv_x/dx)_0$. Numerical values of this quantity are provided by the inviscid solution as described in the preceding sections of the paper.

Flat Initial Velocity Profile. Before concluding the Analysis portion of the paper, brief mention will be made of some auxiliary studies that were undertaken to validate the application of the solution method that was used for the inviscid problem. Inasmuch as an exact solution, obtained via conformal mapping and complex variable theory, is available [5] for the case of a flat initial velocity profile, the present solution method was employed for that case. The modifications of the foregoing inviscid formulation to accommodate the flat velocity profile will now be outlined.

The differential equation (9) for the stream function simplifies appreciably because $f(\Psi) = 0$, and the solution, which replaces equation (15), is

$$\Psi(R,\theta) = \sum_{n=1}^{M} B_{2n}R^{2n} \sin 2n\theta \tag{35}$$

In lieu of equation (16), the boundary condition for Ψ along AB is $\Psi = X = R_A/\tan\theta$. The boundary conditions along BC and CD remain as before, but (21) and (23) for the segment DE are replaced by

$$\Psi = UY, \quad \Delta = 1/U \tag{36}$$

The velocity gradient $(dV_x/dX)_0$ is equal to $2B_2$.

These modifications were introduced into the computer program for the case of the nonuniform initial profile, and all subsequent aspects of the solution were carried out in an identical manner for the two problems. A comparison of the results for the flat profile case with those of [5] will be made in the Results section.

Results

The presentation of results will begin with a validation of the flow field solution method based on a comparison of results for the flat initial velocity profile. Next, velocity field results corresponding to the initially nonuniform velocity profile will be presented. The stagnation point heat and mass transfer results will be dealt with in the final section.

Validation of the Solution Method. As noted earlier, the availability of an exact solution [5] for the flow field corresponding to an initially flat velocity profile provides an opportunity for validating the present solution method. Inasmuch as the essential contribution of the flow field solution to the subsequent heat/mass transfer analysis is $(dV_x/dX)_0^{1/2}$, comparisons will be made of the numerical values of this quantity.

Numerical results for $(dV_x/dX)_0^{1/2}$ are not reported in [5], but they were deduced by explicit differentiation of equation (5) of [5] and subsequent application of the limit as $X \to 0$. Table 1 contains a comparison of the results from [5] and from the present solution method. Inspection of the table indicates very good agreement between the two sets of results. This outcome lends a strong measure of confidence to the present solution method. The result for $h/b = \infty$ from [5] is included as an asymptotic value.

Flow Field Results. From the solutions corresponding to the initially nonuniform velocity profile, three types of results will be presented. These include the velocity gradient $(dV_x/dX)_0^{1/2}$, the velocity distribution along the stagnation streamline and along the impingement surface, and the streamline pattern in general.

Velocity gradient results are listed in Table 2 as a function of the dimensionless separation distance h/b. It is seen from Table 2 that the velocity gradient is relatively insensitive to separation distance within the range investigated and that, furthermore, it

Table 1 $(dV_x/dX)_0^{1/2}$, **flat initial profile**

h/b	Present	[5]
1	0.975	0.982
2	0.758	0.755
3	0.676	0.667
∞		0.627

Table 2 $(dV_x/dX)_0^{1/2}$, **nonuniform initial profile**

h/b	$(dV_x/dX)_0^{1/2}$
0.5	1.32
0.75	1.27
1	1.23
2	1.23
3	1.23

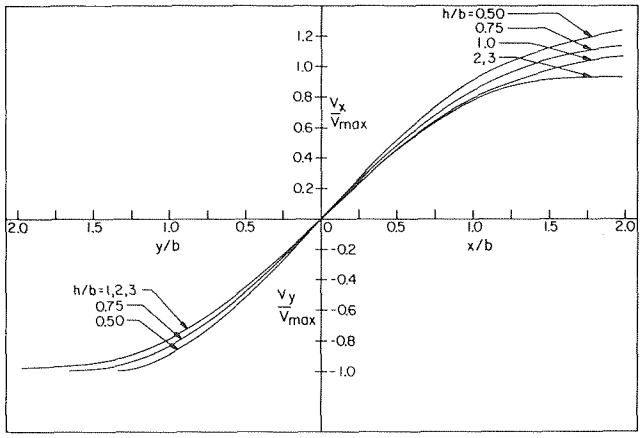

Fig. 2 Velocity distributions along the stagnation streamline and along the impingement surface

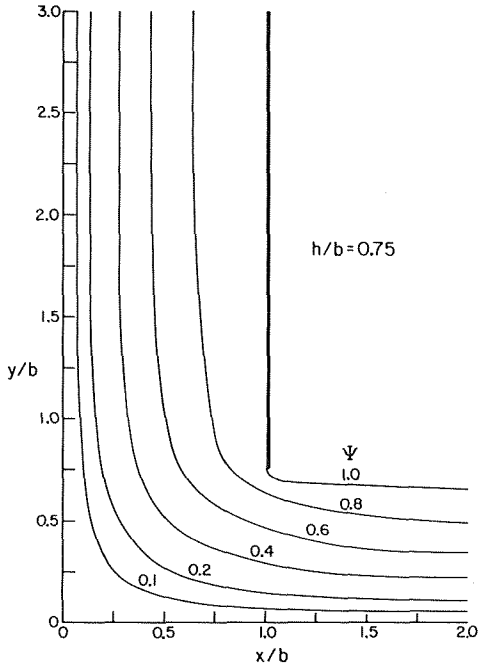

Fig. 3 Streamline map, $h/b = 0.75$

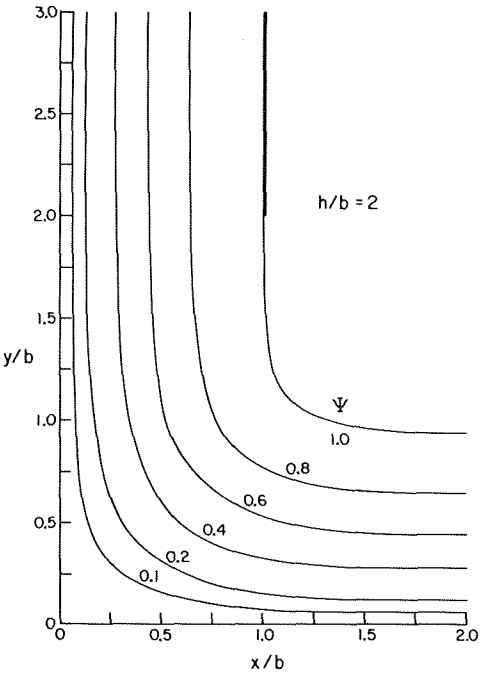

Fig. 4 Streamline map, $h/b = 2.0$

reaches its asymptotic value at a small separation distance. Similar trends were encountered in [1] for the circular jet. In contrast, the velocity gradient results for the case of a flat velocity profile (Table 1) are much more sensitive to separation distance and attain their asymptotic value at a larger separation distance. The relative insensitivity of the nonuniform jet results to h/b will be made plausible later, when the streamline maps are presented.

It is especially interesting to compare the magnitudes of the velocity gradients for the two cases. The asymptotic value of $(dV_x/dX)_0^{1/2}$ corresponding to the nonuniform profile is almost twice as large as that for the flat profile. At smaller separations, the ratio decreases (note that $(dV_x/dX)_0^{1/2} = 1.15$ for the flat profile when $h/b = 0.5$). However, within the range of h/b relevant to applications, which would normally be $h/b > 1$, the $(dV_x/dX)_0^{1/2}$ values for the nonuniform profile are substantially larger than those for the uniform profile. This finding has implications in the design of impinging jets for heating or cooling applications. Since, according to equation (34), the transfer coefficients are proportional to $(dV_x/dX)_0^{1/2}$, the use of jets having an initially nonuniform profile would maximize the transfer rate at a given jet Reynolds number.

Velocity distributions along the stagnation streamline and along the impingement surface (OA and OE in Fig. 1) are plotted in Fig. 2. The quadrant at the upper right of the figure contains the distribution curves for the impingement surface, whereas the lower left-hand quadrant is for the stagnation streamline. The velocities that are plotted on the ordinate are normalized by the maximum velocity magnitude v_{max} of the initial profile. The use of such an ordinate variable is motivated by the fact that $|v_y| \rightarrow v_{max}$ as y increases along the stagnation streamline.

The figure shows that higher impingement surface velocities are encountered when the jet exit is closer to the surface. Furthermore, as expected, the length along the stagnation streamline where $|v_y|$ changes from v_{max} to zero is greater at larger separation distances.

Representative streamline maps, respectively for $h/b = 0.75$ and 2.0, are presented in Figs. 3 and 4. It is seen from the figures that the streamlines which are relatively near the stagnation streamline do not deflect until they reach the immediate vicinity of the impingement surface. It is especially interesting to note from a comparison of Figs. 3 and 4 that the positions of these internal streamlines are essentially the same for the two separation distances depicted by the figures. The free streamline and those adjacent to it begin to deflect much sooner than do the internal streamlines. The greater the separation distance between the exit plane and the impingement surface, the more gradual is the deflection of the external streamlines.

The fact that the major differences in the flow pattern are evidenced by the external streamlines is consistent with the insensitivity of the $(dV_x/dX)_0^{1/2}$ values to h/b. For an initially nonuniform velocity profile, relatively little fluid is transported in the portion of the jet adjacent to the free streamline. Consequently, the early deflection of this fluid has very little effect on the main body of the flow which is concentrated adjacent to the stagnation streamline.

Heat/Mass Transfer Results. From the combination of equations (34) and (29), the stagnation point heat and mass transfer coefficients can be written as

$$\frac{h_h b/k}{(\bar{v}b/\nu)^{1/2}} = \frac{h_m b/\mathfrak{D}}{(\bar{v}b/\nu)^{1/2}} = -\phi'(0)\left[\frac{dV_x}{dX}\right]_0^{1/2} \tag{37}$$

The heat transfer grouping is essentially a Nusselt number—

Table 3 Results for $\phi'(0)$

Pr or Sc	0.7	1.0	2.5	5	10	20	50
$-\phi'(0)$	0.4959	0.5705	0.8086	1.043	1.339	1.710	2.353

square root of Reynolds number ratio, and the mass transfer group is similarly interpreted in terms of the Sherwood and Reynolds numbers. These groups are seen to be proportional to $-\phi'(0)$, which is a function of the Prandtl number, and to $(dV_x/dX)_0^{1/2}$, which is furnished by the flow field solutions and listed in Table 2.

As already indicated in the discussion of Table 2, $(dV_x/dX)_0^{1/2}$ is very nearly constant over the range of h/b that was investigated. Therefore, the transfer coefficients are similarly insensitive to h/b. It is also relevant to reiterate that the $(dV_x/dX)_0^{1/2}$ values corresponding to the nonuniform initial velocity profile are substantially higher than are those for the flat initial profile, as is evidenced by a comparison of Tables 1 and 2. For the larger values of h/b, which is the range that is expected to be encountered in practice, the transfer coefficients for the former exceed those for the latter by nearly a factor of two.

Numerical values of $\phi'(0)$ are scattered throughout the literature. New results were generated here in order to obtain a set of $\phi'(0)$ values of known and consistent accuracy. These results are listed in Table 3.

The predictions of the present analysis will now be compared to the stagnation point mass transfer coefficients measured in [2] by the naphthalene sublimation technique. The smallest h/b of the experiments was four, so that the asymptotic value of $(dV_x/dX)_0^{1/2}$ from Table 2 is appropriate for evaluating the transfer coefficients from equation (37). The $\phi'(0)$ value was taken from Table 3 at Sc = 2.5. The results of [2] were presented in terms of a Sherwood number and a Reynolds number based on the equivalent diameter $D = 3.7b$ of the 12:1 aspect ratio rectangular duct which was used to create the jet. When b is replaced by $D/3.7$ and constants are introduced as discussed above, equation (37) becomes

$$\mathrm{Sh}_D = 1.91\ \mathrm{Re}_D^{1/2} \tag{38}$$

Equation (38) is plotted in Fig. 5 along with experimental data from [2] for $h/b = 4$. The open symbols are the data points as they were reported in [2], with a Reynolds number based on a mean velocity $\bar{\bar{v}}$ evaluated by dividing the measured volume flow by the cross-sectional area of the duct. Inasmuch as there are end effects in a 12:1 aspect ratio duct, $\bar{\bar{v}}$ is not truly representative of the mean velocity in the center span region of the duct, where end effects are entirely negligible. The proper mean velocity $\bar{v}$ for the center span region of the 12:1 duct is 1.055 $\bar{\bar{v}}$, and the blackened symbols reflect the re-evaluation of the Reynolds number on the basis of $\bar{v}$.

In assessing the comparison of the analytical and experimental results, note should be taken of the fact that the $v_{max}/\bar{v}$ value for the analysis was 1.57, whereas that for the experiment was 1.50. Therefore, it is to be expected that the analytical predictions would lie about 10 percent above the experimental data. Inspection of Fig. 5 indicates that this is indeed the case at the higher Reynolds numbers. With decreasing Reynolds number, there is a trend toward increasing deviations. This trend was anticipated during the presentation and discussion of the analytical model. As indicated there, viscous diffusion of vorticity begins to become increasingly important at lower Reynolds numbers, and it is believed that this is responsible for the deviations in evidence in the figure.

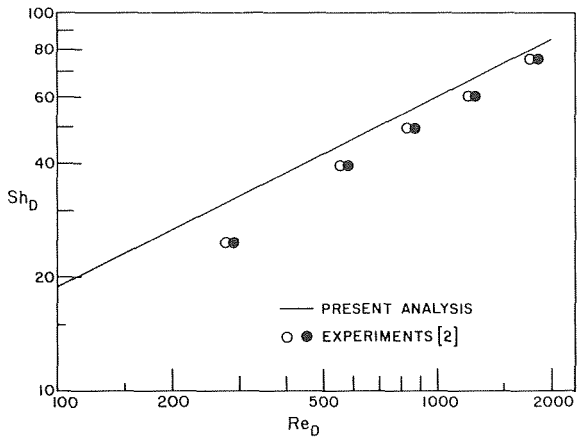

Fig. 5 Comparison of analytical and experimental stagnation point mass transfer coefficients, Sc = 2.5

It was observed in [2] that the transfer coefficients on the impingement surface were constant in a region adjacent to the stagnation point. For $h/b = 4$, the region of constancy extended from $x/b = 0$ to $x/b = 0.5$–0.6 [7]. According to boundary layer theory, the constancy of the transfer coefficient implies that the velocity gradient dV_x/dX should also be constant within this region. It is interesting to enquire whether the velocity distributions obtained from the present analysis yield a constant velocity gradient within a stagnation region whose size is consistent with that of the experiments. In this connection, attention may be turned to the impingement-surface velocity distributions shown in the upper right-hand quadrant of Fig. 2. From the curve for $h/b = 2$ or 3, which represents the asymptotic condition, it is shown that the slope is constant out to $x/b \simeq 0.5$, whereafter it begins to gradually drop off. This is in good agreement with the aforementioned experimental finding.

References

1 Scholtz, M. T., and Trass, O., "Mass Transfer in a Nonuniform Impinging Jet," *AIChE Journal*, Vol. 16, 1970, pp. 82–96.

2 Sparrow, E. M., and Wong, T. C., "Impingement Transfer Coefficients Due to Low Reynolds Number Slot Jets," *International Journal of Heat and Mass Transfer*, Vol. 18, 1975, pp. 597–606.

3 Gardon, R., and Akfirat, J C., "Heat Transfer Characteristics of Impinging Two-Dimensional Air Jets," JOURNAL OF HEAT TRANSFER, TRANS. ASME, Series C, Vol. 88, 1966, pp. 101–108.

4 Gardon, R., and Akfirat, J. C., "The Role of Turbulence in Determining the Heat Transfer Characteristics of Impinging Jets," *International Journal of Heat and Mass Transfer*, Vol. 8, 1965, pp. 1261–1272.

5 Miyazaki, H., and Silberman, E., "Flow and Heat Transfer on a Flat Plate Normal to a Two-Dimensional Laminar Jet Issuing From a Nozzle of Finite Height," *International Journal of Heat and Mass Transfer*," Vol. 15, 1972, pp. 2097–2107.

6 Yih, C. S., "Two Solutions for Inviscid Rotational Flow With Corner Eddies," *Journal of Fluid Mechanics*, Vol. 5, 1959, pp. 36–40.

7 Wong, T. C., "Mass Transfer in an Impinging Jet," MS thesis, Department of Mechanical Engineering, University of Minnesota, Minneapolis, Minn., 1974.

T. S. Chen
Mem. ASME

A. Mucoglu

Department of Mechanical and Aerospace Engineering, University of Missouri-Rolla, Rolla, Mo.

Bouyancy Effects on Forced Convection Along a Vertical Cylinder

The effects of buoyancy forces on the longitudinal forced convective flow and heat transfer along an isothermal vertical cylinder are studied analytically. This problem does not admit similarity solutions, the nonsimilarity arising both from the transverse curvature $\xi = (4/r_0)\,(\nu x/u_\infty)^{1/2}$ *of the cylindrical surface and from the buoyancy effect expressible as* $\Omega = Gr_x/Re_x^2$ *where* Gr_x *and* Re_x *are, respectively, the Grashof and Reynolds numbers. The governing equations are solved by the local nonsimilarity method in which all the nonsimilar terms are retained in the conservation equations and only in the derived subsidiary equations are terms selectively neglected according to the two-equation or three-equation model. Numerical results for the velocity and temperature profiles, wall shear stress, and surface heat transfer for the case of assisting flow are presented for gases having a Prandtl number of 0.7 over a wide range of values of* ξ *from 0 (i.e., a flat plate) to 4.0 and* Ω *from 0 (i.e., pure forced convection) to 2.0. It is found that the wall shear and surface heat transfer rate increase with increasing buoyancy force and increasing curvature of the surface.*

Introduction

In the study of fluid flow over heated surfaces, it is customary to neglect the effects of buoyancy force when the flow is horizontal. However, such a practice is not justified when the forced flow is along an inclined or a vertical surface, because under these conditions the buoyancy force modifies considerably the flow field and hence the heat transfer rate from the surface. Such a flow is termed combined forced and free convective flow. In studying the combined convective heat transfer, one considers either the buoyancy effects on forced convection or the forced-flow effects on free convection.

The problem of combined forced and free convection along a vertical flat plate has been treated by many investigators [1–6].[1] Convective heat transfer from a circular cylinder, on the other hand, has been analyzed from the standpoint of pure forced convective flow [7–10] or pure free convective flow [11–14]. The present study is concerned with the effects of buoyancy force on forced convection along an isothermal vertical cylinder. This problem does not admit similarity solutions. The nonsimilarity arises both from the transverse curvature of the cylinder and from the buoyancy effect. In addition, owing to the presence of the buoyancy force, the flow and thermal fields are coupled through the conservation equations.

Among the techniques available at present for treating the nonsimilarity problems, the method of local similarity has been widely employed (see, for example, Lloyd and Sparrow [5], Sparrow, Heinisch, and Yu [15], among others). In this method, certain terms involving the axial derivatives are discarded, and the transformed and simplified boundary layer equations resemble those for a similarity boundary layer. These equations can, therefore, be treated as ordinary differential equations and solved by well established techniques. Another attractive feature of the local similarity method is that the solution at any axial location can be found independently of the solutions at upstream locations. However, the local similarity method provides numerical results that are of uncertain accuracy. This is because there is no positive way to establish how the deleted terms involving the axial derivative affect the final results.

To correct the drawbacks of the local similarity method, Sparrow and coworkers [10, 16] have recently described a local nonsimilarity method for obtaining solutions of the nonsimilar boundary-layer equations. This method preserves the most attractive features of the local similarity model (i.e., quasi-ordinary differential equations and locally independent solutions), while retaining all of the nonsimilarity terms in the conservation equations. Only terms in the equations subsidiary to the conservation equations are selectively neglected. In their work, Sparrow and co-workers have restricted themselves to forced-flow boundary layers [16] and pure forced-convection thermal boundary layers [10]. Thus, the velocity and temperature fields were treated separately in their studies.

For the problem of vertical cylinders under consideration, the flow and thermal fields are coupled and the conservation equations must be solved simultaneously. In the present study, the effects of

[1] Numbers in brackets designate References at end of paper.

Contributed by the Heat Transfer Division for publication in the JOURNAL OF HEAT TRANSFER. Manuscript received by the Heat Transfer Division December 18, 1974.

buoyancy forces and transverse curvature on the flow and heat transfer characteristics are analyzed by employing the local nonsimilarity method of solution in conjunction with an integration scheme. The solutions are further classified as two-equation and three-equation models, depending on the levels of truncation in the subsidiary equations. The analysis is carried out for both assisting flow (in which the buoyancy force acts in the same direction as the forced flow) and opposing flow (in which the buoyancy force acts in the opposite direction of the forced flow).

Numerical results are presented for gases with a Prandtl number of 0.7 for the case of assisting flow. These include local wall shear and local surface heat transfer for buoyancy parameter Ω ranging from 0 (i.e., pure forced convection) to 2.0 and transverse curvature ξ from 0 (i.e., a flat plate) to 4.0. Representative velocity and temperature profiles are also presented to illustrate the effects of buoyancy forces on the flow and thermal fields. To provide a perspective on the accuracy of the local nonsimilarity solutions, the results from the two- and three-equation models are compared with those from the local similarity solutions. In addition, a comparison of the present results with those of Oosthuizen and Hart [6] from the finite-difference method of solution and those of Kliegel [17] from experiments for the special case of a vertical flat plate lends further support to the high accuracy of the local nonsimilarity method of solution.

Analysis

In this section, attention will be given to the formulation of the governing equations for the local similarity and local nonsimilarity models. In the analysis, it will be postulated that the uniform undisturbed free stream remains parallel to the surface of the cylinder along its entire length.

Description of the Problem. Consider now a vertical cylinder of radius r_0 which is aligned parallel to a uniform free stream with velocity u_∞ and temperature T_∞. The surface temperature of the cylinder is maintained at T_w. Let x and r denote, respectively, the streamwise and radial coordinates and let the gravitational force act in the direction opposite to the x coordinate. The buoyancy force then acts in the same direction as the forced flow when $T_w > T_\infty$ and in the opposite direction to the forced flow when $T_w < T_\infty$. The former situation is referred to as assisting flow and the latter as opposing flow.

The starting point of the analysis is the conservation equations for laminar boundary-layer over a vertical cylinder:

$$\frac{\partial u}{\partial x} + \frac{1}{r}\frac{\partial}{\partial r}(rv) = 0 \tag{1}$$

$$u\frac{\partial u}{\partial x} + v\frac{\partial u}{\partial r} = \nu\frac{1}{r}\frac{\partial}{\partial r}\left(r\frac{\partial u}{\partial r}\right) \pm g_x\beta(T - T_\infty) \tag{2}$$

$$u\frac{\partial T}{\partial x} + v\frac{\partial T}{\partial r} = \alpha\frac{1}{r}\frac{\partial}{\partial r}\left(r\frac{\partial T}{\partial r}\right) \tag{3}$$

where u and v are, respectively, the velocity components in the x- and r-directions, T is the temperature of the fluid, g_x is the gravitational acceleration, β is the volumetric coefficient of thermal expansion, ν is the kinematic viscosity, and α is the thermal diffusivity. In writing the foregoing equations, the conventional assumptions of laminar boundary-layer theory have been applied and all the fluid properties are assumed to be constant except for the density effect on the buoyancy term in equation (2). The positive sign on that term applies in the assisting flow, whereas the negative sign applies in the opposing flow. Equations (1)–(3) are subject to the following boundary conditions:

$$u = v = 0,\ T = T_w \text{ at } r = r_0 \tag{4a}$$

$$u \longrightarrow u_\infty,\ T \longrightarrow T_\infty \text{ as } r \longrightarrow \infty \tag{4b}$$

$$u = u_\infty,\ T = T_\infty \text{ at } x = 0,\ r \geq r_0 \tag{4c}$$

Boundary conditions (4c) stem from the parallel uniform flow assumption of the free stream velocity at $x = 0$. That is, it is assumed that both the flow and thermal boundary layers begin with zero thickness at the leading edge of the cylinder.

Transformation of the Governing Equations. The first step in the analysis is the transformation from (x, r) coordinates to (ξ, η) coordinates. The coordinate ξ depends only on x and is so chosen that x does not appear explicitly in the transformed conservation equations and their boundary conditions. The coordinate η, which contains both x and r, is a pseudosimilarity variable; it is chosen such that it reduces to a true similarity variable for boundary layers that are similar. In accordance with this, it is convenient to employ the (ξ, η) variables [7] along with a reduced stream function $f(\xi, \eta)$ and a dimensionless temperature $\theta(\xi, \eta)$ in the form:

$$\xi = \frac{4}{r_0}\left(\frac{\nu x}{u_\infty}\right)^{1/2},\ \eta = \frac{r^2 - r_0^2}{4r_0}\left(\frac{u_\infty}{\nu x}\right)^{1/2} \tag{5}$$

$$f(\xi, \eta) = \frac{\Psi(x, r)}{r_0(\nu u_\infty x)^{1/2}},\ \theta(\xi, \eta) = \frac{T(x, r) - T_\infty}{T_w - T_\infty} \tag{6}$$

where the stream function Ψ satisfies the continuity equation with $u = \partial\Psi/r\partial r$ and $v = -\partial\Psi/r\partial x$. It is to be noted that the transformed axial coordinate ξ is a measure of both the transverse curvature of the cylinder and the boundary layer thickness relative to the cylinder radius. By introducing equations (5) and (6) into equations (2)–(4), one obtains the following system of equations

$$(1 + \xi\eta)f''' + (f + \xi)f'' \pm 8\Omega\theta = \xi(f'g' - f''g) \tag{7}$$

$$\frac{1}{\mathrm{Pr}}(1 + \xi\eta)\theta'' + \left(f + \frac{\xi}{\mathrm{Pr}}\right)\theta' = \xi(f'\phi - g\theta') \tag{8}$$

$$f'(\xi, 0) = 0,\ \xi g(\xi, 0) + f(\xi, 0) = 0,\ \theta(\xi, 0) = 1 \tag{9}$$

$$f'(\xi, \infty) = 2,\ \theta(\xi, \infty) = 0 \tag{10}$$

Nomenclature

C_f = local friction factor
f = reduced stream function
g = ξ—derivative of f
g_x = gravitational acceleration
Gr_x = Grashof number, $g_x\beta|T_w - T_\infty|x^3/\nu^2$
h = ξ—derivative of g
h = local heat transfer coefficient, $q_w/(T_w - T_\infty)$
k = thermal conductivity
Nu_x = local Nusselt number, hx/k
Pr = Prandtl number, ν/α
q_w = local surface heat transfer rate per unit area
r = radial coordinate
r_0 = radius of cylinder
Re_x = Reynolds number, $u_\infty x/\nu$
T = fluid temperature
T_w = wall temperature
T_∞ = free stream temperature
u = axial velocity component
u_∞ = free stream velocity
v = radial velocity component
x = axial coordinate
α = thermal diffusivity
β = volumetric coefficient of thermal expansion
η = pseudo-similarity variable
θ = dimensionless temperature, $(T - T_\infty)/(T_w - T_\infty)$
μ = dynamic viscosity
ν = kinematic viscosity
ξ = transformed axial coordinate
ρ = density
τ_w = wall shear stress
ϕ = ξ—derivative of θ
ψ = ξ—derivative of ϕ
Ψ = stream function
Ω = buoyancy parameter, equation (12)

wherein the primes denote partial differentiation with respect to η,

$$g = \partial f/\partial \xi, \quad \phi = \partial \theta/\partial \xi, \tag{11}$$

and

$$\Omega = g_x\beta \left| T_w - T_\infty \right| x/{u_\infty}^2 = \mathrm{Gr}_x/\mathrm{Re}_x^{\,2} \tag{12}$$

The Grashof number and Reynolds number are defined, respectively, by $\mathrm{Gr}_x = g_x\beta|T_w - T_\infty|x^3/\nu^2$ and $\mathrm{Re}_x = u_\infty x/\nu$. The quantitative effects of free convection on the forced convective flow are governed by the magnitude of the parameter Ω. Since Ω is proportional to x, the effect of buoyancy force increases with increasing axial distance.

Local Similarity Model. To derive the governing equations for the local similarity model, one neglects the terms $\xi\partial f/\partial\xi$, $\xi\partial f'/\partial\xi$, and $\xi\partial\theta/\partial\xi$ (namely, the terms ξg, $\xi g'$, and $\xi\phi$) in equations (7)–(9). The end result is

$$(1 + \xi\eta)f''' + (f + \xi)f'' \pm 8\Omega\theta = 0 \tag{13}$$

$$\frac{1}{\mathrm{Pr}}(1 + \xi\eta)\theta'' + (f + \frac{\xi}{\mathrm{Pr}})\theta' = 0 \tag{14}$$

$$f(\xi, 0) = f'(\xi, 0) = 0\,, \; f'(\xi, \infty) = 2, \; \theta(\xi, 0) = 1, \; \theta(\xi, \infty) = 0 \tag{15}$$

The reduction of equations (7)–(10) to (13)–(15) is clearly justifiable for ξ values that are close to zero. On the other hand, when ξ is not small, local similarity is based on the assumption that derivatives involving $\partial/\partial\xi$ are very small. The uncertainty as to the validity of this assumption is a weakness of the local similarity method.

In solving the system of coupled equations (13) and (14), the quantities Ω and ξ may be regarded as constant parameters. Thus, although equations (13) and (14) are partial differential equations, they can be treated as ordinary differential equations and solved by well-established techniques appropriate to similarity boundary layers. For a given value of Ω (i.e., buoyancy force), for example, the solution corresponding to any ξ value can be obtained independently of the solutions at any other ξ values. Thus, by assigning a succession of ξ values, the axial dependence of velocity and temperature fields can be determined.

Local Nonsimilarity Models. The governing equations for the local nonsimilarity models will now be derived. To begin with, one differentiates equations (7)–(10) with respect to ξ and obtains the first set of subsidiary equations and their boundary conditions

$$(1 + \xi\eta)g''' + (f + \xi)g'' - f'g' + 2f''g + \eta f''' + f'' \pm 8\Omega\phi \pm 16(\Omega/\xi)\theta - \xi(g'g' - gg'') = \xi(f'h' - f''h) \tag{16}$$

$$\frac{1}{\mathrm{Pr}}(1 + \xi\eta)\phi'' + (f + \frac{\xi}{\mathrm{Pr}})\phi' - f'\phi + \frac{1}{\mathrm{Pr}}\eta\theta'' + (2g + \frac{1}{\mathrm{Pr}})\theta' - (g'\phi - g\phi') = \xi(f'\psi - h\theta') \tag{17}$$

$$g'(\xi, 0) = 0, \; 2g(\xi, 0) + \xi h(\xi, 0) = 0, \; \phi(\xi, 0) = 0 \tag{18}$$

$$g'(\xi, \infty) = 0, \; \phi(\xi, \infty) = 0 \tag{19}$$

wherein the term Ω/ξ results from $d\Omega/2d\xi$ and

$$h = \partial g/\partial\xi = \partial^2 f/\partial\xi^2, \; \psi = \partial\phi/\partial\xi = \partial^2\theta/\partial\xi^2 \tag{20}$$

To derive the governing equations for the two-equation model, one retains all terms in the transformed conservation equations (7) and (8). In the first subsidiary equations, equations (16) and (17), however, the terms $\xi\partial g/\partial\xi$, $\xi\partial g'/\partial\xi$, and $\xi\partial\phi/\partial\xi$ are neglected in a manner similar to that done for the case of local similarity model. Thus, the governing system of equations for the two-equation model consists of:

(a) equations (7) and (8),

(b) equations (16) and (17) with terms on their respective right-hand side deleted,

(c) boundary conditions (15), and

(d) the additional boundary conditions

$$g(\xi, 0) = g'(\xi, 0) = g'(\xi, \infty) = 0, \; \phi(\xi, 0) = \phi(\xi, \infty) = 0 \tag{21}$$

Since the set of equations described in the foregoing for the four functions f, g, θ, and ϕ are coupled, these equations must be solved simultaneously. For a given value of Ω, if ξ is regarded as a constant prescribable parameter at any axial location, these equations may be treated as a system of coupled ordinary equations and solved by the conventional techniques for similarity boundary layers.

Next, the governing equations for the three-equation model are formulated as follows. First, equation (16)–(19) are differentiated with respect to ξ and terms involving $\xi\partial h/\partial\xi$, $\xi\partial h'/\partial\xi$, and $\xi\partial\psi/\partial\xi$ are then deleted from the resulting equations. The transformed conservation equations and their first subsidiary equations are, however, left intact. Thus, the equations for the three-equation model can be summarized as:

(a) equations (7) and (8),

(b) equations (16) and (17),

(c) the truncated equations for h and ψ

$$(1 + \xi\eta)h''' + (f + \xi)h'' - 2f'h' + 3f''h \pm 8\Omega\psi + 2\eta g''' + (2 + 4g)g'' - 2g'g' \pm 32\Omega\phi/\xi \pm 16\Omega\theta/\xi^2 - \xi(3g'h' - gh'' - 2g''h) = 0 \tag{22}$$

$$\frac{1}{\mathrm{Pr}}(1 + \xi\eta)\psi'' + (f + \frac{\xi}{\mathrm{Pr}})\psi' - 2f'\psi + \frac{2}{\mathrm{Pr}}\eta\phi'' + (4g + \frac{2}{\mathrm{Pr}})\phi' - 2g'\phi + 3h\theta' - \xi(2g'\psi - g\psi' + h'\phi - 2h\phi') = 0 \tag{23}$$

(d) boundary conditions (15) and (21), and

(e) the additional boundary conditions

$$h'(\xi, 0) = h(\xi, 0) = h'(\xi, \infty) = 0, \; \psi(\xi, 0) = \psi(\xi, \infty) = 0 \tag{24}$$

It is noted here that in the three-equation model, equations (7), (8), (16), (17), (22), and (23) are coupled and they must be solved simultaneously for the six unknown functions f, g, h, θ, ϕ, and ψ. As in the two-equation model, ξ may be considered as a constant parameter and the system of equations can be treated, for a given Ω, as a set of coupled ordinary differential equations of the similar type.

The local nonsimilarity solution method just described above preserves the two most attractive features of the local similarity method (i.e., the system of equations can be treated as ordinary differential equations and the solutions are independent of ξ). In addition, in the local nonsimilarity method, all nonsimilarity terms in the conservation equations (7) and (8) are retained. Terms are deleted selectively only in the subsidiary equations—in the first set of subsidiary equations for the two-equation model and in the second set for the three-equation model. This is an improvement over the local similarity method, where terms are deleted from the conservation equations themselves. It is thus expected that the local nonsimilarity models should provide more accurate results for the velocity and temperature fields, wall shear, and surface heat transfer than the local similarity model. This point, as verified by Sparrow and co-workers [10, 16] in their studies of pure forced convective flow and heat transfer, will be discussed further when the results are presented.

It should be pointed out that, although the solutions of the flow and thermal fields provide information for the f, g, θ, and ϕ functions for the two-equation model and the f, g, h, θ, ϕ, and ψ functions for the three-equation model, it is only f and θ and their derivatives that are physically relevant for both models. For example, the streamwise component of the velocity distribution is given by

$$u = \frac{1}{2}u_\infty f'(\xi, \eta) \tag{25}$$

and the temperature distribution by $\theta(\xi, \eta)$.

It is noted here that for the special case of a flat plate (i.e., $\xi = 0$) it is more convenient to take Ω as the x-dependent variable in formulating the local nonsimilarity models. Thus, for this case, the corresponding conservation equations were transformed using the (Ω, η) variables. The details can be found in Mucoglu [20].

Local Friction Factor and Nusselt Number. The wall shear stress τ_w and the local friction factor C_f are defined, respectively, by

$$\tau_w = \mu(\partial u/\partial r)_{r_0}, \quad C_f = 2\tau_w/\rho u_\infty^2 \tag{26}$$

With the aid of equations (5) and (25), it can be readily shown that

$$C_f = \frac{1}{2} f''(\xi, 0) \mathrm{Re}_x^{-1/2} \tag{27}$$

The heat transfer characteristics can be expressed in terms of a local Nusselt number and local heat transfer coefficient

$$\mathrm{Nu}_x = hx/k, \quad h = q_w/(T_w - T_\infty) \tag{28}$$

From Fourier's law, $q_w = -k(\partial T/\partial r)_{r_0}$, in conjunction with equations (5) and (6), it follows that

$$\mathrm{Nu}_x = -\frac{1}{2} \theta'(\xi, 0) \mathrm{Re}_x^{1/2} \tag{29}$$

Numerical Solutions

Each of the systems of governing equations for the local similarity model, local nonsimilarity two-equation model, and local nonsimilarity three-equation model was solved simultaneously using Runge-Kutta integration scheme. The procedure employed here to solve the system of ordinary differential equations resembles that outlined by Dewey and Gross [18] and by Hayday and co-workers [19], with some modifications to account for the coupling of the governing equations. The details of the numerical solution are given in Mucoglu [20] and, to conserve space, are omitted here.

Results and Discussion

The sets of equations presented in the Analysis section for the local similarity and nonsimilarity models apply for both assisting flow and opposing flow. However, numerical computations were carried out only for the case of assisting flow (in which the sign in front of the terms containing Ω in the momentum equation and its subsidiary equations is positive) for gases having a Prandtl number of 0.7. They cover buoyancy parameter Ω ranging from 0 (i.e., pure forced convection) to 2.0 and transformed axial coordinate ξ from 0 (i.e., a flat plate) to 4.0. All computations were performed on an IBM 370/165 digital computer using double precision arithmetic.

To illustrate the accuracy of solutions of the various models, the local heat transfer results $\mathrm{Nu}_x \mathrm{Re}_x^{-1/2} = -\theta'(\xi, 0)/2$ from the local similarity model (i.e., one-equation model) and local nonsimilarity two-equation and three-equation models are compared in Fig. 1 for two parametric values of the buoyancy force $\mathrm{Gr}_x/\mathrm{Re}_x^2 = 0$ and 1.0. It is seen from the figure that the results from the two-equation and three-equation models are in very good agreement over the entire range of ξ values that are considered in the analysis. The largest deviation between the two models is less than 2 percent for $\Omega = 1.0$. The closeness of the curves between the two-equation and three-equation models is an indication of the high accuracy of local nonsimilarity solution. The local similarity model, on the other hand, is seen to predict results that are of low accuracy. A similar trend is observed in the accuracy of the local wall shear results $C_f \mathrm{Re}_x^{1/2} = f''(\xi, 0)/2$ among the three models. To conserve space, a comparison of these results is omitted in this paper.

The results for $\xi = 0$ in Fig. 1 correspond to the case of a vertical flat plate. It must be stressed here that $\xi = 0$ implies $r_0 \to \infty$ and not $x \to 0$, because the boundary layer solutions do not apply at $x = 0$. This same implication about $\xi = 0$ also pertains to all other figures to be presented later.

The conjecture that the three-equation model should provide results that are more accurate than the two-equation model was also verified from a comparison of the numerical values between $\xi \partial f/\partial \xi$ and $\xi \partial g/\partial \xi$, $\xi \partial f'/\partial \xi$ and $\xi \partial g'/\partial \xi$, and $\xi \partial \theta/\partial \xi$ and $\xi \partial \phi/\partial \xi$. This comparison clearly showed that the solution converges to the physical solution from one- to two- to three-equation model, with the three-equation model giving the most accurate results. Furthermore, since the values of $\partial f/\partial \xi$, $\partial f'/\partial \xi$, $\partial \theta/\partial \xi$ and $\partial g/\partial \xi$, $\partial g'/\partial \xi$, $\partial \phi/\partial \xi$ decrease with an increase in ξ, the local nonsimilarity three-equation model can be expected to yield accurate results for ξ values that are much larger than those considered in the present investigation. This is particularly true when the Ω values are not very large. The work of Sparrow and co-workers [16] for the special case of pure forced convective flow without buoyancy effect (i.e., $\Omega = 0$) has verified this point from a comparison of their local wall shear results with those obtained by Glauert and Lighthill [21] for very large ξ values.

The effect of buoyancy force on the local wall shear results $C_f \mathrm{Re}_x^{1/2}$ is shown for $\xi = (4/r_0)(\nu x/u_\infty)^{1/2} = 0$, 1, 2, 3, and 4 in Fig. 2. The results for $\Omega = 0$ (i.e., pure forced convection) are in excellent agreement with those of Sparrow and co-workers [16]. As Ω increases, the wall shear increases. Thus, the effect of the buoyancy force is to increase the wall shear. In addition, it is seen from the figure that the wall shear increases with increasing value of ξ. The curve for $\xi = 0$ corresponds to the case of a vertical flat plate.

The heat transfer results for various Ω values are brought together in Fig. 3. It is seen from the figure that the heat transfer rate increases with an increase in Ω and ξ. Thus, the effect of buoyancy is to increase the rate of heat transfer, which in turn augments itself with an increase in ξ. The present results for the special case of combined forced and free convection along a vertical flat plate (i.e., the case of $\xi = 0$) are in excellent agreement with

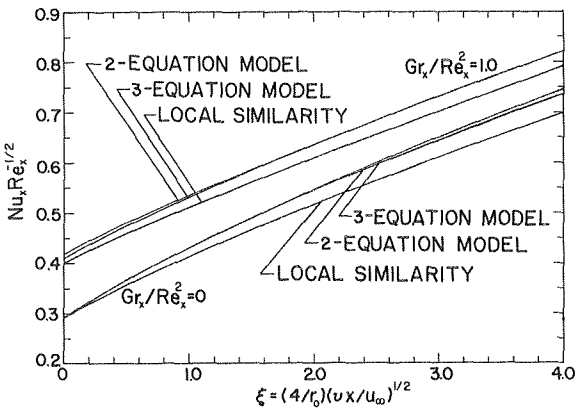

Fig. 1 A comparison of representative surface heat transfer results among various models

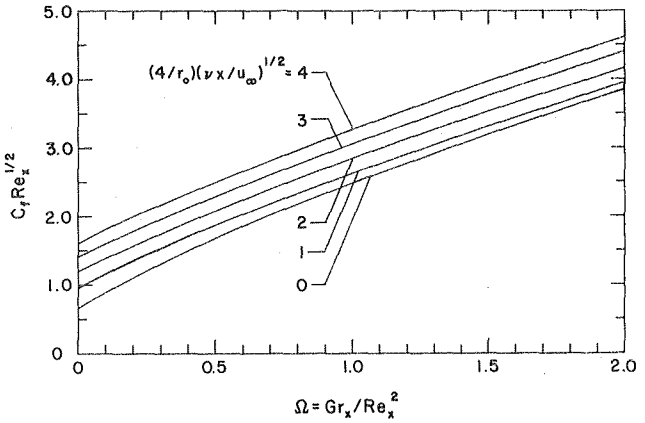

Fig. 2 Wall shear results from three-equation model

those reported by Oosthuizen and Hart [6] from the finite-difference method of solution. The experimental data of Kliegel [17] for a vertical flat plate, as shown with circles along the curve $\xi = 0$, are also in very good agreement with the results of the present analysis. These comparisons lend support to the present analytical method. Thus, it may be concluded that the local nonsimilarity solution method provides results of high accuracy.

For completeness, representative results of $f''(\xi, 0)$ and $-\theta'(\xi, 0)$ for parametric values of ξ and Ω that were investigated are listed in Table 1.

Representative velocity profiles at selected axial locations ξ for three parametric values $\Omega = 0$, 1.0, and 2.0 are illustrated in Fig. 4 in which u/u_∞ is plotted against η. It is seen from the figure that for a given Ω, the velocity profiles change as ξ increases, i.e., as one proceeds along the axial distance. The most evident changes are the increase of velocity gradient $\partial(u/u_\infty)/\partial\eta$ at the wall and the substantial growth in the flow boundary layer thickness. In general, as the buoyancy force Ω increases, the velocity gradient at the wall increases and the boundary layer thickness decreases. This is accompanied by a relatively sharp rise in the profile near the wall and an overshoot of the velocity beyond its free stream value, particularly at small ξ values. For example, for the case of a vertical plate ($\xi = 0$) with $\Omega = 2.0$, the overshoot is about 21 percent as compared to about 40 percent from the local similarity solution [5]. Thus, the local similarity model overpredicts the buoyancy effect on the velocity field.

In Fig. 5 are shown representative temperature profiles at axial locations $\xi = 0$, 1, and 4 for values of $\Omega = 0$, 1.0, and 2.0. An inspection of the figure reveals that for a given Ω, the most noteworthy trends with increasing axial distance ξ are the increase in temperature gradient $\partial\theta/\partial\eta$ at the wall and substantial growth in the thermal boundary layer thickness. As the buoyancy force Ω increases, the temperature gradient increases, while the thermal boundary thickness decreases.

To provide a better understanding of the effect of free convection on the flow and thermal fields, Figs. 6 and 7 have been prepared to show, respectively, the relative increase in the friction factor C_f/C_{f0} and in the Nusselt number Nu_x/Nu_0 with buoyancy

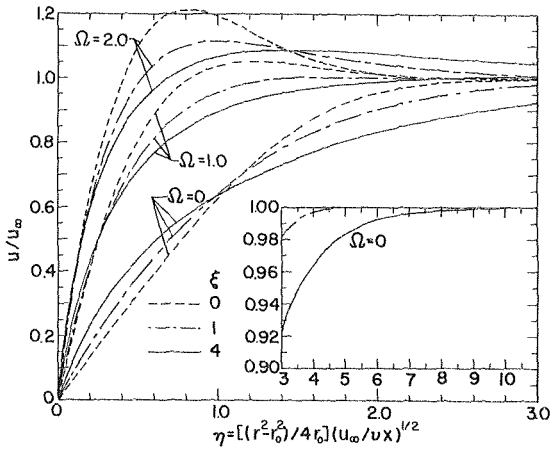

Fig. 4 Representative velocity profiles from three-equation model

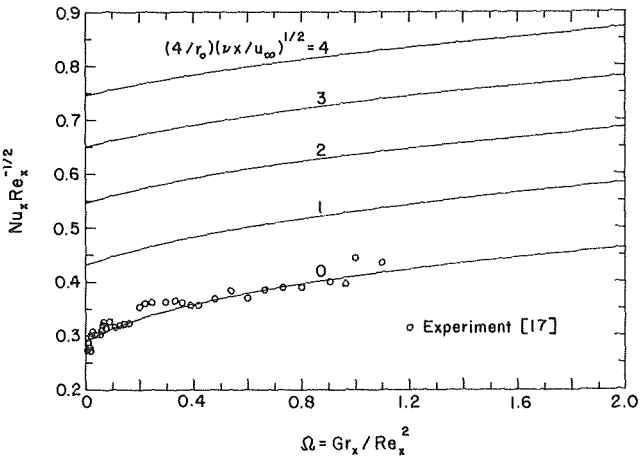

Fig. 3 Surface heat transfer results from three-equation model

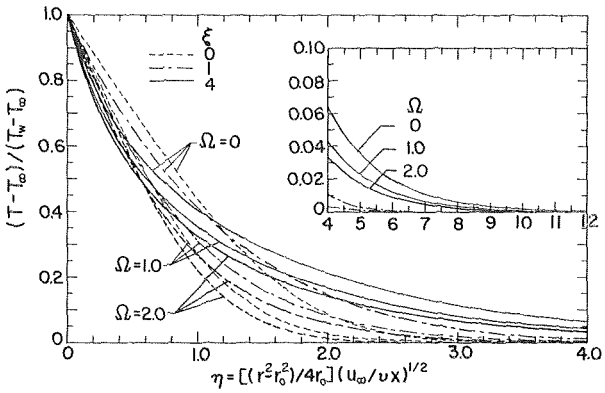

Fig. 5 Representative temperature profiles from three-equation model

Table 1 Representative results of $f''(\xi, 0)$ and $-\theta'(\xi, 0)$ from local nonsimilarity three-equation model for Pr = 0.7**

	f''(ξ,0)						-θ'(ξ,0)					
ξ	Ω=0	0.1	0.5	1.0	1.5	2.0	Ω=0	0.1	0.5	1.0	1.5	2.0
0	1.3282*	1.7866	3.3586	4.9668	6.3947	7.7126	0.5854*	0.6271	0.7393	0.8221	0.8822	0.9305
1.0	1.9172	2.3271	3.7396	5.2584	6.6230	7.8871	0.8669	0.8971	0.9852	1.0621	1.1208	1.1690
2.0	2.3981	2.7951	4.1821	5.7001	7.0765	8.3566	1.0968	1.1227	1.2004	1.2718	1.3279	1.3747
3.0	2.8270	3.2194	4.5990	6.1236	7.5147	8.8125	1.3021	1.3258	1.3979	1.4658	1.5203	1.5663
4.0	3.2235	3.6151	4.9963	6.5317	7.9393	9.2557	1.4921	1.5145	1.5830	1.6487	1.7022	1.7477

*Similarity solution
**The results for $\xi = 0$ and $\Omega \neq 0$ correspond to $f''(\Omega,0)$ and $-\theta'(\Omega,0)$.

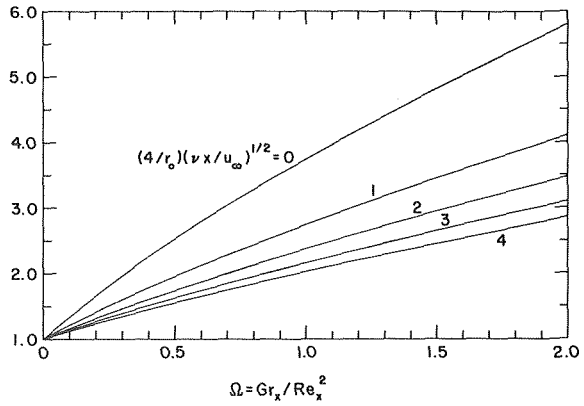

Fig. 6 The effect of buoyancy force on local fraction factor

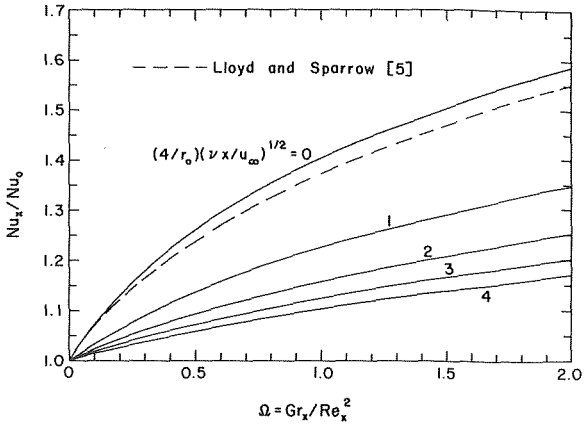

Fig. 7 The effect of buoyancy force on local Nusselt number

force Ω, where C_{f0} and Nu_0 are, respectively, the friction factor and Nusselt number without buoyancy effect (i.e., $\Omega = 0$). The results are from the three-equation model. It is seen from the figures that the relative increase in both friction factor and Nusselt number decreases with increasing value of ξ. The dotted line in Fig. 7 shows the results of Lloyd and Sparrow [5] from the local similarity model for a vertical flat plate ($\xi = 0$).

From the results presented in Fig. 7, the free convection effect on Nusselt number for forced convection is found to be less than 10 percent when

$$\Omega = \frac{Gr_x}{Re_x^2} \leq 0.15 + 0.2\xi \tag{30}$$

For the case of a vertical flat plate ($\xi = 0$), equation (30) reduces to $\Omega \leq 0.15$ which agrees well with the work of Lloyd and Sparrow [5] and Sparrow and Gregg [2].

Conclusions

In this paper, the problem of laminar combined forced and free convection along an isothermal vertical cylinder has been analyzed by employing the local nonsimilarity method of solution. In this method, the nonsimilarity terms in the conservation equations are retained without approximation, while only in the subsidiary equations are terms selectively deleted. The resulting system of governing equations can be treated as ordinary differential equations and their solutions at any axial location can be obtained without recourse to information from other axial locations. The wall shear and heat transfer information presented herein demonstrates that the present method of solution provides accurate results.

Acknowledgments

The computations of the numerical results were made possible through funds from the Department of Mechanical and Aerospace Engineering, University of Missouri—Rolla.

References

1 Acrivos, A., "Combined Laminar Free and Forced Convection Heat Transfer in External Flows," *AIChE Journal,* Vol. 4, 1958, pp. 285–289.

2 Sparrow, E. M., and Gregg, J. L., "Buoyancy Effects in Forced-Convection Flow and Heat Transfer," *Journal of Applied Mechanics,* Vol. 26, TRANS. ASME, Series E, Vol. 81, 1959, pp. 133–134.

3 Szewczyk, A. A., "Combined Forced and Free-Convection Laminar Flow," JOURNAL OF HEAT TRANSFER, TRANS. ASME, Series C, Vol. 86, 1964, pp. 501–507.

4 Merkin, J. H., "The Effect of Buoyancy Forces on the Boundary-Layer Flow Over a Semi-Infinite Vertical Flat Plate in a Uniform Free Stream," *Journal of Fluid Mechanics,* Vol. 35, 1969, pp. 439–450.

5 Lloyd, J. R., and Sparrow, E. M., "Combined Forced and Free Convection Flow on Vertical Surfaces," *International Journal of Heat and Mass Transfer,* Vol. 13, 1970, pp. 434–438.

6 Oosthuizen, P. H. and Hart, R., "A Numerical Study of Laminar Combined Convective Flow Over Flat Plates," JOURNAL OF HEAT TRANSFER, TRANS. ASME, Series C, Vol. 95, 1973, pp. 60–63.

7 Seban, R. A., and Bond, R., "Skin-Friction and Heat-Transfer Characteristics of a Laminar Boundary Layer on a Cylinder in Axial Incompressible Flow," *Journal of the Aeronautical Sciences,* Vol. 18, 1951, pp. 671–675.

8 Wanous, D. J., and Sparrow, E. M., "Heat Transfer for Flow Longitudinal to a Cylinder With Surface Mass Transfer," JOURNAL OF HEAT TRANSFER, TRANS. ASME, Series C, Vol. 87, 1965, pp. 317–319.

9 Eshghy, S. and Hornbeck, R. W., "Flow and Heat Transfer in the Axisymmetric Boundary Layer Over a Circular Cylinder," *International Journal of Heat and Mass Transfer,* Vol. 10, 1967, pp. 1757–1766.

10 Sparrow, E. M., and Yu, H. S., "Local Non-Similarity Thermal Boundary-Layer Solutions," JOURNAL OF HEAT TRANSFER, TRANS. ASME, Series C, Vol. 93, 1971, pp. 328–334.

11 Sparrow, E. M., and Gregg, J. L., "Laminar Free-Convection Heat Transfer From the Outer Surface of a Vertical Circular Cylinder," TRANS. ASME, Vol. 78, 1956, pp. 1823–1829.

12 Millsaps, K., and Pohlhausen, K., "The Laminar Free-Convective Heat Transfer From the Outer Surface of a Vertical Circular Cylinder," *Journal of the Aeronautical Sciences,* Vol. 25, 1958, pp. 357–360.

13 Fujii, T., and Uehara, H., "Laminar Natural-Convective Heat Transfer From the Outer Surface of a Vertical Cylinder," *International Journal of Heat and Mass Transfer,* Vol. 13, 1970, pp. 607–615.

14 Minkowycz, W. J., and Sparrow, E. M., "Local Nonsimilar Solutions for Natural Convection on a Vertical Cylinder," JOURNAL OF HEAT TRANSFER, TRANS. ASME, Series C, Vol. 96, 1974, pp. 178–183.

15 Sparrow, E. M., Heinisch, R. P., and Yu, H. S., "Streamwise Heat Conduction Effects in Forced-Convection Boundary Layers Without and With Superposed Free Convection," *Nuclear Sciences and Engineering,* Vol. 39, 1970, pp. 387–393.

16 Sparrow, E. M., Quack, H., and Boerner, C. J., "Local Nonsimilarity Boundary-Layer Solutions," *AIAA Journal,* Vol. 8, 1970, pp. 1936–1942.

17 Kliegel, J. R., "Laminar Free and Forced Convective Heat Transfer From a Vertical Flat Plate," PhD thesis, University of California, 1959.

18 Dewey, C. F., Jr., and Gross, J. F., "Exact Similar Solutions of the Laminar Boundary Layer Equations," *Advances in Heat Transfer,* Vol. 4, Academic Press, New York, 1967, pp. 317–446.

19 Hayday, A. A., Bowlus, D. A., and McGraw, R. A., "Free Convection From a Vertical Flat Plate With Step Discontinuities in Surface Temperature," JOURNAL OF HEAT TRANSFER, TRANS. ASME, Vol. 89, Series C, 1967, pp. 244–250.

20 Mucoglu, A., "Combined Forced and Free Convection on a Vertical Cylinder and Flat Plate," MS thesis, Univeristy of Missouri—Rolla, 1974.

21 Glauert, M. B., and Lighthill, M. J., "The Axisymmetric Boundary Layer on a Long Cylinder," *Proceedings of the Royal Society,* Series A. Vol. 230, 1966, pp. 188–203.

F. A. Kulacki
Assist. Professor.
Assoc. Mem. ASME

M. E. Nagle[1]
University Fellow.
Assoc. Mem. ASME

Mechanical Engineering Department,
The Ohio State University,
Columbus, Ohio

Natural Convection in a Horizontal Fluid Layer With Volumetric Energy Sources

Natural convection with volumetric heating in a horizontal fluid layer with a rigid, insulated lower boundary and a rigid, isothermal upper boundary is experimentally investigated for Rayleigh numbers from 114 to 1.8 × 10^6 times the critical value of linear stability theory. Joule heating by alternating current passing horizontally through the layer provides the volumetric energy source. Layer aspect ratios are kept small to minimize the effects of side walls. A correlation for mean Nusselt number is obtained for steady heat transfer, and data are presented on fluctuating temperatures at high Rayleigh numbers and on developing temperature distributions when the layer is subjected to a step change in power.

Introduction

Natural convection driven by energy release from distributed volumetric energy sources appears to play a fundamental role in energy transport problems in geophysics, astrophysics, and engineering. Convection with internal energy sources has been proposed for the earth's mantle [1, 2, 3][2] and for the outer region of star interiors [4]. Engineering processes in which a fluid supports an exothermic chemical or nuclear reaction are common today, and correct process design often requires accurate correlations for heat transfer coefficient at boundary surfaces. On this last point, it may be noted that assessment of and design for post-accident heat removal in LMFBR nuclear reactors hinges on prediction of natural convection heat transfer with volumetric heat release at high Rayleigh numbers.

Despite its relevance to a wide spectrum of technological and physical problems, natural convection with volumetric energy sources has received relatively slight treatment both analytically and experimentally. With the view that accurate heat transfer data are highly desirable in this area, even for systems of an idealized nature, our objective was to experimentally obtain a correlation for mean Nusselt number as a function of Rayleigh number in a horizontal fluid layer with a rigid, insulated lower boundary and a rigid, isothermal upper boundary. Rayleigh numbers greatly exceeding the critical linear stability theory value were investigated since in many instances, systems of large vertical scale and/or large values of specific volumetric energy release rate are of practical importance. Our experiments cover the range $114 \leq \mathrm{Ra}/\mathrm{Ra}_c \leq 1.8 \times 10^6$ where $\mathrm{Ra}_c = 1386$ [5]. This places our results within the transition and fully turbulent regimes flow. In addition, a limited investigation of developing temperature profiles was performed for the case of a step change in power input to the layer.

Several experimental studies of natural convection in horizontal fluid layers with volumetric heating have been reported in the literature. The works of Tritton and Zarraga [6] and Schwab and Schwiderski [7] were largely qualitative investigations of the nature of the plan-form of motion in the immediate post-stability regime of flow. In both studies, an electrolytically heated fluid layer was bounded from below by a rigid, insulated surface and from above by a rigid, constant temperature surface. Tritton and Zarraga reported locally turbulent motion for Rayleigh numbers greater than eighty times the critical value of linear stability theory.

In 1971, Fiedler and Wille [8] reported measurements of mean heat transfer in an internally heated fluid layer with an insulated lower boundary and an isothermal upper boundary. Their apparatus consisted of a long rectangular cell 25 mm × 25 cm with fluid layer depths varying from 2.4 mm to 41.25 mm. The upper and lower surfaces were constructed of copper and also served as electrodes for passage of lternating current vertically through the electrolyte solution comprising the fluid layer. Kulacki and Goldstein [9] reported interferometric measurements of mean temperature fields and average heat transfer in an electrolytically heated fluid layer with two rigid isothermal boundaries of equal temperature for Rayleigh numbers up to 675 times the critical values of linear

[1] Present address: Westinghouse Electric Corp., Tampa Division, Tampa, Fla.

[2] Numbers in brackets designate References at end of paper.

Contributed by the Heat Transfer Division of The American Society of Mechanical Engineers and presented at the Winter Annual Meeting, New York, N. Y., November 17–22, 1974. Journal manuscript received by the Heat Transfer Division August 9, 1974. Paper No. 74-WA/HT-28.

stability theory. Their measurements covered the laminar, transition, and turbulent regimes of convection and showed that for $Ra_{L/2} > 500\ Ra_{L/2,c}$, approximately two thirds of the energy generated in the layer was transferred through the upper boundary. Due to interferometric requirements and requirements of the Boussinesq approximation, maximum temperature differences in the layer were held to 0.5°C in their study.

Experimental Apparatus and Procedure

The apparatus constructed for this study was similar to that of Kulacki and Goldstein [9] with the following exception: the lower boundary comprised a 1.9 cm thick Plexiglas plate with thermocouples arranged over the central portion so that the surface temperature and the temperature gradient within the plate could be measured. A nickel-chrome resistance heater was cemented to the underside of this plate to ensure a zero temperature gradient in the lower boundary. The upper boundary of the layer was an aluminum plate with a double spiral channel machined in it for the continuous circulation of thermostatically controlled water. The temperature of the circulating water was controlled to within 0.1°C. The surface of the aluminum plate in contact with the fluid layer was machined flat to less than 0.00254 cm. Thermocouples were also provided in this plate over its central region for the measurement of the temperature at the upper surface of the fluid layer. A thin (0.5 mm) sheet of pressure sensitive Mylar protected the aluminum from chemical attack. The overall dimensions of the fluid layer were 50.8 cm × 50.8 cm, and layer depths were varied from 2.54 cm to 12.7 cm. Additional details of the apparatus design and construction are given by Nagle [10].

The fluid layer in this study was a dilute aqueous solution of silver nitrate of approximately 0.02 *M*. Due to the large volumes of water contained in the convection chamber, especially at the larger depths, silver nitrate crystals were dissolved directly in the fluid layer several hours prior to each run. Since Rayleigh numbers in this study were greatly in excess of the critical value of linear stability theory and most of the mean heat transfer measurements were well within the turbulent flow regime, any nonuniformities in the electrical conductivity of the fluid layer due to nonuniformities in electrolyte concentration would be minimized by convective mixing with the layer. In addition, the long time needed to ensure fully developed and steady convection would favor reduction of nonuniformities in silver nitrate concentration within the layer.

Alternating current (60 Hz) was passed through the layer horizontally from silver plated electrodes contained in two of the side walls of the convection chamber. Power was supplied from a line voltage regulator through a secondary voltage regulator. Power dissipation in the layer was measured with a wattmeter transducer in conjunction with a digital voltmeter. The accuracy of power measurements with this arrangement was ±0.25 percent of measured power.

A Leeds and Northrup Type K-3 potentiometer in conjunction with a d-c null detector were used to measure all steady thermocouple emf outputs. The accuracy of this arrangement was ±0.015 percent +0.5 μV or ±0.014 C.

For measurement of mean and fluctuating temperatures within the layer, a small glass coated thermocouple was inserted into the fluid layer through the upper boundary. The thermocouple junction was 0.01 cm in diameter, and the glass tube containing the thermocouple leads was 0.19 cm in diameter nominally. The glass tube was tapered to enclose the thermocouple junction and fire polished at the junction. Calibration test for the response of the thermocouple probe determined its time constant to be of the order of 1 s for sudden temperature changes of the order of 1°C. This response proved sufficient for recording the temperature fluctuations encountered in this study. The signal from the probe was amplified and recorded on a strip chart. Mean temperatures at various positions in the layer were obtained from the strip chart record by graphically averaging the temperature-history over a one-hr period.

Prior to each run, the fluid layer was allowed to reach an isothermal condition. Power was applied to the layer, and a flow development time was allowed much greater than that required for development of the conduction temperature profile at the given level of power consumption. Usually, flow development times from 3 to 12 hr were required to reach steady state. Upon reaching steady state, four readings of both upper and lower surface temperatures were taken and averaged. Another set of temperature readings was taken one-half hr later, and when good agreement was reached, data were recorded. During the period of flow development and after steady state had been reached, care was taken to insure a zero heat flux lower boundary. Normally, no more than 2 W (particularly at high Rayleigh number) were needed for the resistance heater in the lower boundary plate.

Results

The Nusselt number at the upper surface for steady convection was defined in terms of the layer depth, L, as:

$$Nu_1 = \frac{Q_p L}{kA\Delta T}$$

where Q_p, the power input to the fluid, was corrected for side wall heat losses [10]. The Rayleigh number was defined in terms of this

Nomenclature

A = area of bonding surface
C, m = constants of correlation
D = smallest horizontal dimension of layer
Fo = Fourier number, $\alpha t/L^2$
g = gravitational constant
H = volumetric rate of energy generation in the fluid
k = thermal conductivity of the fluid
L = layer depth
L^* = portion of layer corresponding to upward energy transport, equation (7)
Nu_1 = Nusselt number, $Q_pL/kA\Delta T$
Pr = Prandtl number of the fluid
Q_p = power input to fluid layer
Ra_L = Rayleigh number, $\frac{g\beta}{\alpha\nu} L^3 \left(\frac{HL^2}{2k}\right)$
t = time
T = temperature at any z-position in layer
ΔT = maximum temperature difference in layer, $T(0) - T(L)$
z = vertcal position in the layer, $0 < z < L$
Z = z/L
α = thermal diffusivity of fluid
β = isobaric coefficient of volumetric expansion of the fluid
δ_T = thermal boundary layer thickness, L/Nu
ν = kinematic viscosity of fluid

Subscripts

0 = value at $z = 0$
1 = value at $z = L$ or upper boundary
c = critical alue frm linear stability analysis or conduction value
L = based on layer depth for characteristic length
$L/2$ = based on layer half-thickness for characteristic length
L^* = based on L^* for characteristic length
T = referring to thermal boundary layer thickness

same length scale and the maximum temperature difference, $HL^2/2k$, which would exist in the layer for purely conductive heat transfer. Thus,

$$\mathrm{Ra}_L = \frac{g\beta}{\alpha\nu} L^3 \frac{HL^2}{2k}$$

Steady-state Nusselt numbers along with other important experimental data are presented in Table 1.

Mean Nusselt numbers correlated well with Rayleigh numbers assuming a relation of the form

$$\mathrm{Nu}_1 = C\ \mathrm{Ra}_L{}^m \tag{1}$$

The linear regression of $\ln(\mathrm{Nu}_1)$ on $\ln(\mathrm{Ra}_L)$ gave:

$$\begin{aligned} &\mathrm{Nu}_1 = 0.305\ \mathrm{Ra}_L{}^{0.239 \pm 0.005} \\ &1.5 \times 10^5 \leq \mathrm{Ra}_L \leq 2.5 \times 10^9 \\ &0.05 \leq L/D \leq 0.25 \\ &6.21 \leq \mathrm{Pr} \leq 6.64 \\ &r = 0.995,\ 36 \text{ observations.} \end{aligned} \tag{2}$$

where r is the coefficient of correlation. This correlation is presented in Fig. 1 with the experiment data.

The data are almost as well represented by a correlation of the form:

$$\mathrm{Nu}_1 = (0.254 \pm 0.004)\ \mathrm{Ra}_L{}^{0.25} \tag{3}$$

over the same range of Ra_L. In either (2) or (3) no significant reduction in the error sum of squares in the regression could be obtained by including either Prandtl number or layer aspect ratio, L/D, in the correlation.

The possibility of discrete transitions in the heat flux was tested by plotting $\mathrm{Ra}_L \cdot \mathrm{Nu}_1$ versus Ra_L on linear coordinates. Existence of such transitions appear on a linear plot as an abrupt change in the slope of the curve. Discrete transitions in heat flux have been reported in turbulent natural convection in horizontal fluid layers with heating from below and with heating with within [9, 11, 12, 13, 14]. Five transition Ra_L were found in this study. They are listed in Table 2 where a comparison is made with the transition Rayleigh numbers found by Kulacki and Goldstein [9] for heat flux at the upper boundary of their system. The transition Rayleigh numbers of this study were obtained using either a single plate spacing or data overlapping data from two plate spacings. Fig. 2 presents an example of a transition with overlapping data from two plate spacings.

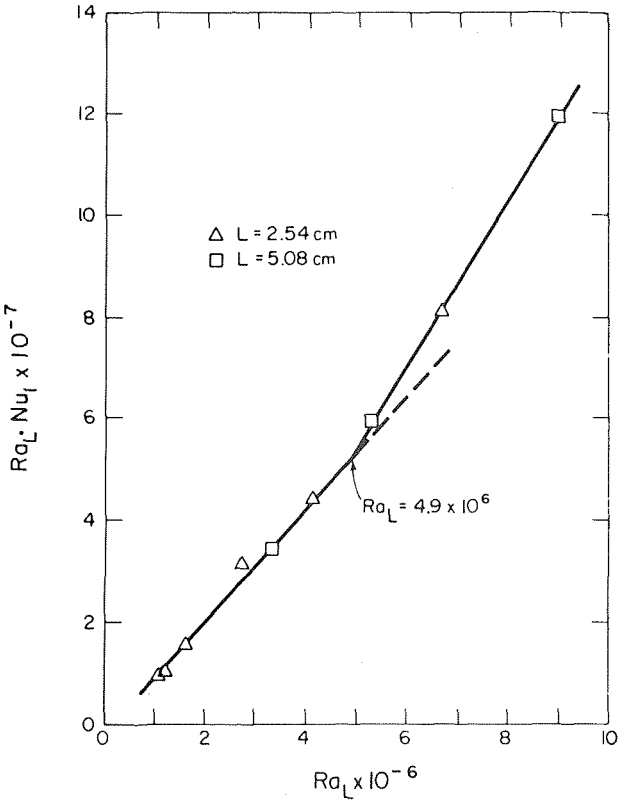

Fig. 2 A point of discrete transition in heat flux

The second phase of the study was concerned with investigation of some of the features of steady turbulent convection and developing convection when the layer was subjected to a step change in power input.

In steady turbulent convection at $\mathrm{Ra}_L = 9.3 \times 10^7 = 6.7 \times 10^4\ \mathrm{Ra}_{L,c}$, the thermocouple probe was positioned at various depths in

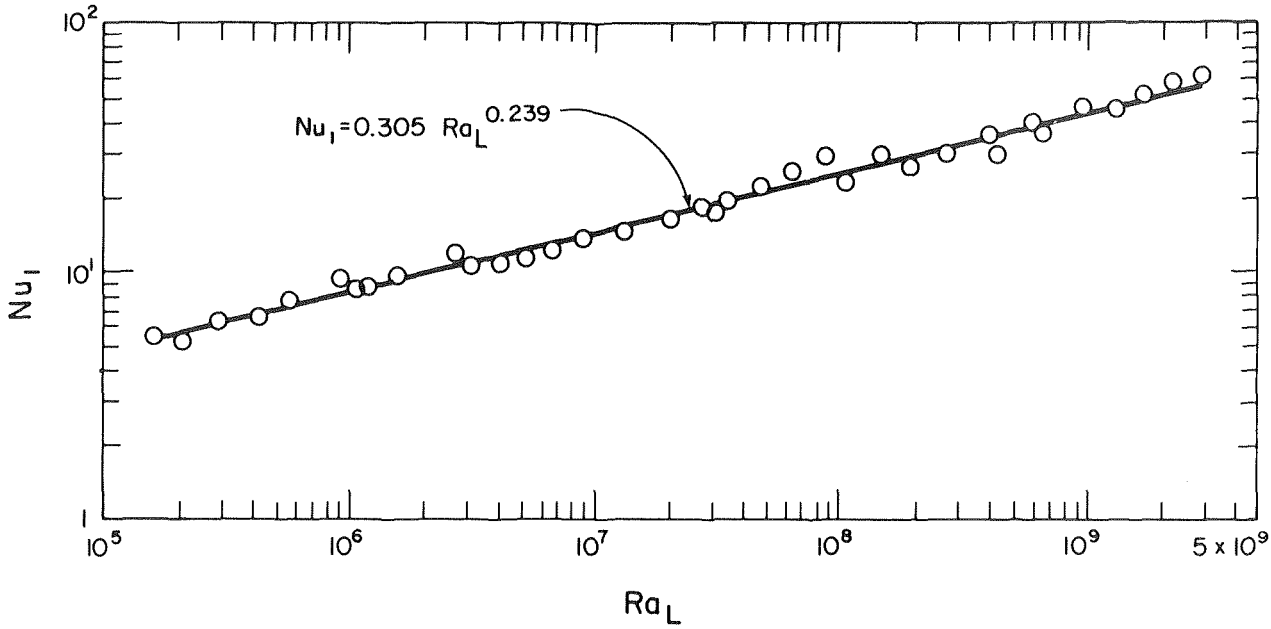

Fig. 1 Dimensionless heat transfer data and correlation of equation (2)

Table 1 Experimental data for steady-state transfer

L (cm)	Q_p (w)	$\Delta T/(HL^2/2k)$	Ra_L	Nu_1
12.70	175.29	0.032	2.595×10^9	62.16
12.70	148.36	0.034	2.187	57.72
12.70	118.73	0.039	1.719	51.25
12.70	90.18	0.044	1.306	45.25
12.70	66.82	0.043	9.532×10^8	45.61
12.70	45.20	0.055	6.448	36.18
10.16	103.40	0.050	5.940	39.75
12.70	30.38	0.067	4.301	29.85
10.16	73.54	0.056	4.195	35.83
10.16	48.73	0.068	2.767	29.67
10.16	34.44	0.078	1.944	26.04
7.62	69.51	0.065	1.432	30.51
10.16	17.94	0.089	1.048	22.95
7.62	49.27	0.071	8.846×10^7	28.14
7.62	35.78	0.075	6.461	26.28
5.08	131.63	0.090	4.881	21.93
5.08	92.80	0.102	3.406	19.59
7.62	17.27	0.118	3.074	17.04
5.08	76.00	0.109	2.773	18.22
5.08	56.36	0.122	2.037	16.12
5.08	38.02	0.135	1.382	14.76
5.08	24.76	0.150	8.971×10^6	13.39
3.81	57.24	0.164	6.670	12.18
5.08	14.56	0.180	5.272	11.23
3.81	35.25	0.184	4.089	10.98
5.08	9.11	0.195	3.332	10.29
3.81	23.51	0.171	2.696	11.63
3.81	13.60	0.197	1.561	9.87
3.81	10.36	0.219	1.190	8.82
3.81	9.09	0.277	1.054	8.63
2.54	39.76	0.211	9.078×10^5	9.37
2.54	25.32	0.250	5.752	7.87
2.54	18.67	0.293	4.237	6.75
2.54	13.14	0.318	2.977	6.21
2.54	9.18	0.368	2.079	5.34
2.54	7.20	0.350	1.582	5.71

Table 2 Transition Rayleigh numbers compared with those of Kulacki and Goldstein [9] at the upper boundary of an internally heated fluid layer with constant temperature surfaces

This Study		Kulacki and Goldstein	
Ra_L	$Ra_L/Ra_{L,c}$ ($Ra_{L,c}$ = 1386)	$Ra_{L/2}$	$Ra_{L/2}/Ra_{L/2,c}$ ($Ra_{L/2,c}$ = 560)
		1.2×10^4	0.21×10^2
		9.2×10^4	1.64×10^2
4.2×10^5	3.03×10^2	1.95×10^5	3.48×10^2
4.9×10^6	3.54×10^3		
3.05×10^7	2.20×10^4		
4.0×10^8	2.89×10^5		
1.4×10^9	1.01×10^6		

the layer. Its amplified signal was recorded over approximately a one-hr period. Although the frequency response of the probe was quite limited, the time scale of temperature fluctuations in the layer was sufficiently large so that a relatively clear, though qualitative, picture of the distribution of temperature fluctuations could be obtained. In Fig. 3 recorded temperature fluctuations are shown at positions in the layer from near the upper boundary (z/L = 0.934) to the lower boundary (z/L = 0). At z/L = 1, the mean temperature measured by the probe was the same as that of the upper boundary plate. Small fluctuations in the recorded temperature were observed at z/L = 1, but these were not considered a true indication of turbulent temperature fluctuations due to the possible existence of secondary flows in the probe well in the top plate.

From Fig. 3 it can be seen that the magnitude of temperature fluctuations decrease with distance from the upper boundary. At z/L = 0.934, the largest fluctuations were recorded. Although it is possible that even larger temperature fluctuations occurred closer to the upper boundary, it is worth noting that the region of most intense temperature fluctuations observed in this study, $0.869 \leq z/L \leq 0.934$, lies at the outer edge of the thermal boundary layer at the upper surface.[3] Temperature fluctuations in this region indicate the downward release of cooled fluid blobs (sometimes called thermals) from the thermal boundary layer on the upper surface. Relatively few of these fluid blobs are able to maintain their thermal identity in the central and lower regions of the layer as evidenced by the much lower magnitude of temperature fluctuations below $z/L < 0.6$. The interferometric data of Kulacki and Goldstein [9] indicate a similar behavior of eddy motion and temperature fluctuations in turbulent convection with energy sources and two isothermal boundaries.

After all steady-state measurements were completed, the nature of both developing and decaying convection was investigated by recording the temperature versus time at various vertical positions in the layer. The results for a step change in Ra_L from zero to 9.3×10^7 are shown in Fig. 4, and for a step change in Ra_L from 9.3×10^7 to zero in Fig. 5. The interesting feature of the temperature profiles was that for the first few minutes after power had been applied to the layer (i.e., a positive step change in Ra_L), a temperature bulge developed in the upper 25 percent of the layer. This behavior is believed to be caused by a dominating influence of conduction near the upper boundary of the layer in the early period of flow development. For the remainder of the layer, buoyant forces and mixing effects are apparently strong enough, even at the start of volume heating, to produce the well-mixed "isothermal core" characteristic of turbulent convection. After a period sufficient for development of strong mixing and eddying effects near the upper boundary, the local temperature excess is wiped out. For the data shown in Fig. 4, there is no evidence of a temperature bulge after a layer Fourier number of 0.045. It was found that for all values of z/L, steady state had effectively been reached when Fo = 0.27. When the power to the layer was suddenly turned off, temperature profiles (Fig. 5) appeared to decay without evidence of any temperature excess (or defect) as had occurred during heat-up. The decay process without the presence of internal energy sources apparently involves a gradual and uniform slowing down of mixing and eddy effects throughout the layer. By comparing Figs. 4 and 5, it can be seen that for the lower 75 percent of the layer, the development of the temperature profile with internal heating proceeds at about the same rate if the Fourier number is redefined as $Fo^+ = 0.268 - Fo$. This may indicate a dynamical similarity between turbulent natural convection with and without internal heating in regions sufficiently far removed from the influence of conductive boundaries.

Error Estimates

The combined uncertainties in the thermophysical properties of the silver nitrate solution (evaluated at T_1 in all cases), geometrical factors, and power measurements resulted in a maximum experimental uncertainty of 5–6 percent in Ra_L and 4–5 percent in Nu_1. The temperature variation of the electrical conductivity of the electrolyte solution was neglected since maximum temperature differences in the fluid were of the order of 2°C or less and for most of the steady-state heat transfer data, were of the order of 1°C.

[3] For $Ra_L = 9.3 \times 10^7$, (2) gives $Nu_1 = 24.5$. By defining the thermal boundary thickness as $\delta_T = L/Nu_1$, $\delta_T = 0.041$, or $(z/L)_T = (L - \delta_T)/L = 0.96$.

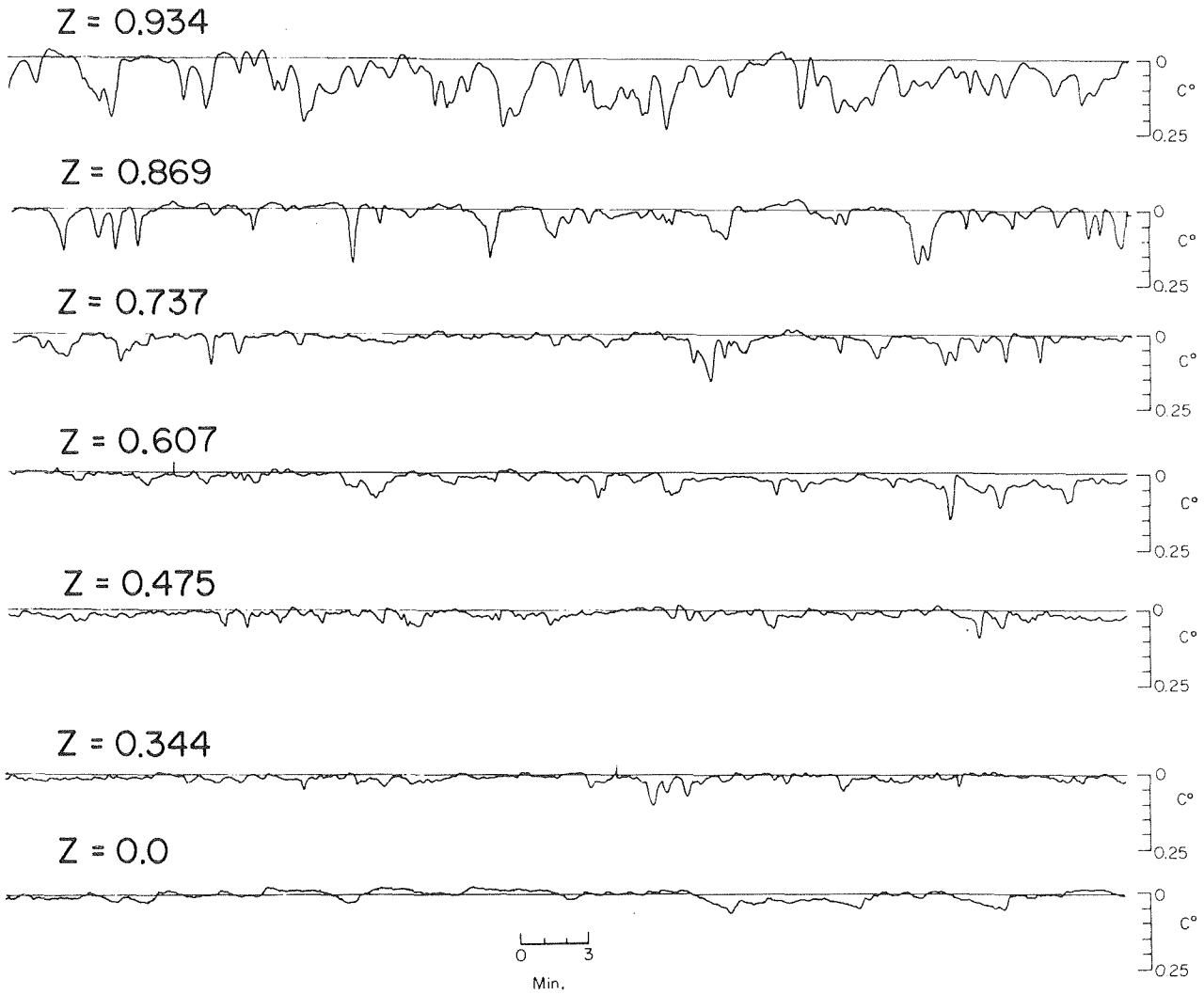

Fig. 3 Temperature fluctuation at various positions in the layer—Ra_L = 9.3×10^7, L = 7.62 cm, and ΔT = 1.10 C

Discussion

The correlation for mean heat transfer obtained in this study is at variance with that of Fiedler and Wille [8] but in good agreement with the correlation of Kulacki and Goldstein [9] for heat transfer at the upper boundary of an internally heated fluid layer with two constant temperature surfaces. Fiedler and Wille's results in terms of the definitions of Nu_1 and Ra_L are

$$\begin{aligned} &Nu_1 = 0.526\ Ra_L^{0.228} \\ &2 \times 10^5 < Ra_L < 6 \times 10^8 \\ &0.29 < L/D < 1.65 \end{aligned} \tag{5}$$

The correlation for Fiedler and Wille gives values of Nu_1 considerably greater than (2). In view of the fact that data in their experiment was for fluid layers with aspect ratios greater than 0.25 in a convection cell of 25 cm, it is entirely possible that the side walls of the cell had a marked effect on convection by aiding the development of a gross circulation pattern within the layer at high Rayleigh number. In the present study, however, the large horizontal extent of the layer would minimize effects of such secondary flow due to side walls on the vertical energy transport in the central region of the layer.

To compare the results of the present study to those of Kulacki and Goldstein [9], a redefinition of the Rayleigh and Nusselt numbers is necessary. First, we define a normalized Nusselt number such that:

$$Nu^* = Nu/Nu_c \tag{6}$$

where Nu_c = 2.0 for a layer with an insulated lower boundary and isothermal upper boundary, and Nu_c = 4.0 for a layer with two equal temperature boundaries. Second, we redefine the Rayleigh number in terms of the entire layer thickness in the correlations of [9]. Next, consider that when the layer has two isothermal boundaries, the upward heat flux corresponds to a certain percent of the energy generated in the layer. The fraction of the layer corresponding to the upward heat flux is given by:

$$\frac{L^*}{L} = \frac{Nu_1^*}{Nu_1^* + Nu_0^*} \tag{7}$$

From [9] and the redefinition of the Rayleigh number, (7) becomes:

$$\frac{L^*}{L} = \frac{0.0968\ Ra_L^{0.236}}{0.0968\ Ra_L^{0.236} + 0.381\ Ra_L^{0.094}} \tag{8}$$

The vertical position in the layer corresponding to a distance from the upper boundary equal to L^* is defined to be a plane of essentially zero heat flux. Thus, to compare the heat transfer rates given by (2) with the correlation of [9], both the Rayleigh and the Nusselt numbers in (2) are redefined in terms of L^*. Table 3 below lists values of Nusselt numbers computed with the two correlations for selected values of Rayleigh number.

From Table 3 it can be seen that (2) predicts Nusselt numbers

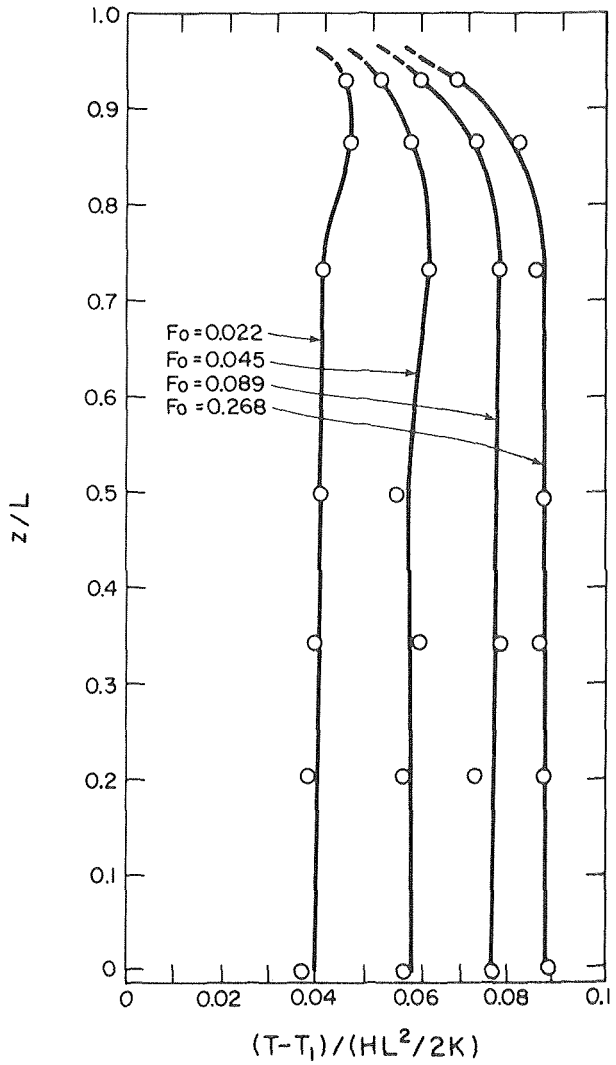

Fig. 4 Temperature profiles at various times after a step increase in Ra_L from zero to 9.3×10^7

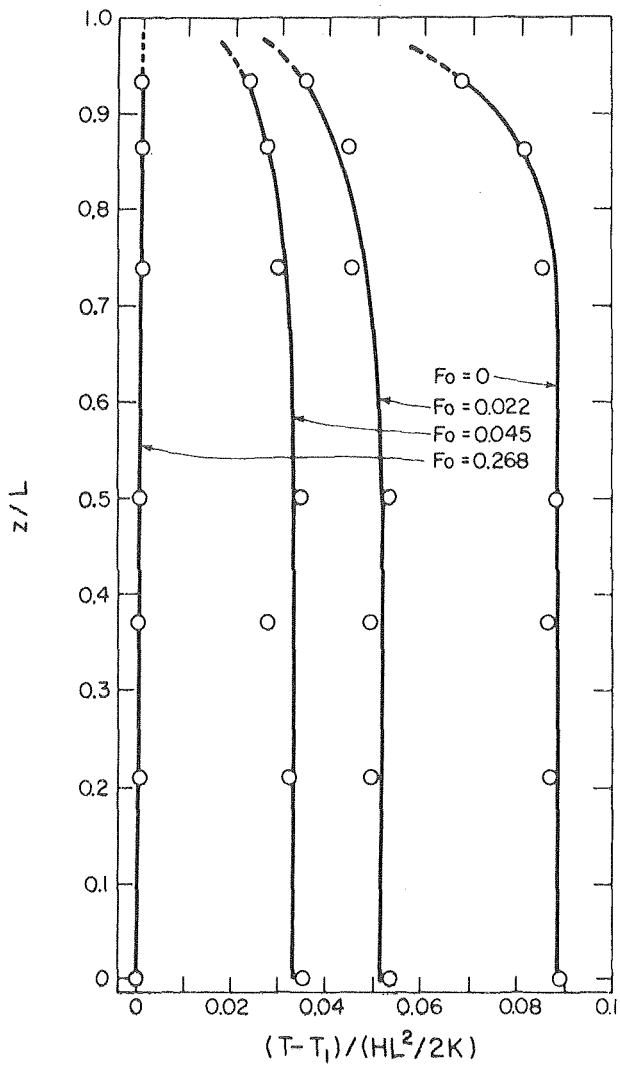

Fig. 5 Temperature profiles at various times after a step decrease in Ra_L from 9.3×10^7 to zero

Table 3 Comparison of Nusselt numbers for upward heat flux using (2) with the length scale L^* and the correlation for upward heat flux given by Kulacki and Goldstein [9]

Kulacki and Goldstein				This Study	
Ra_L	Nu_1^*	Nu_o^*	L^*/L	Ra_{L^*}	$Nu_{L^*,1}^*$
10^5	1.46	1.13	0.564	5.70×10^3	1.21
10^6	2.52	1.39	0.644	1.11×10^5	2.45
10^7	4.34	1.74	0.715	1.86×10^6	4.81
10^8	7.47	2.15	0.777	2.82×10^7	9.20
10^9	12.87	2.67	0.828	3.89×10^8	17.23

somewhat larger than those of the Kulacki-Goldstein correlation for $Ra_{L^*} > 10^6$. However, the agreement here is considered good since the $Ra_L/Ra_{L,c}$ range of present study extends considerably beyond that of [9].

It may be noted that prediction of both upward and downward heat fluxes in heat generating fluid layers with two isothermal boundaries may be made with fair accuracy with the results of the present study in conjunction with (7) and the definition of a plane of zero heat flux in the layer. The "half-layer" problem investigated here thus represents a convenient experimental technique for obtaining basic data for the more difficult problem of heat transfer in a layer with two equal temperature boundaries.

Aknowledgments

This investigation was supported by NASA Grant NGR-36-008-25, by a Sigma Xi Grant in Aid of Research to one of the authors (F.A.K.), and the Department of Mechanical Engineering.

References

1 *The Earth's Mantle,* Gaskell, T. F., ed., Academic Press, New York, 1967.

2 Runcorn, S. K., "Convection Currents in the Earth's Mantle," *Nature,* Vol. 195, 1962, p. 1248.

3 Tozer, D. C., "Heat Transfer and Convection Currents," *Proceedings Royal Society,* Vol. A258, London, 1966, p. 252.

4 Bethe, H. A., "Energy Production in Stars," *Science,* Vol. 161, 1968, p. 541.

5 Kulacki, F. A., "Thermal Convection in a Horizontal Fluid Layer With Uniform Volumetric Energy Sources," PhD thesis, University of Minnesota, 1971.

6 Tritton, D. J., and Zarraga, M. N., "Convection in Horizontal Fluid Layers With Heat Generation Experiments," *Journal of Fluid Mech.,* Vol. 30, 1967, p. 21.

7 Schwab, J. A., and Schwiderski, E. W., "Convection Experiments With Electrolytically Heated Fluid Layers," *Journal of Fluid Mech.,* Vol. 48, 1971, p. 703.

8 Fiedler, H. E. and Wille, R., "Turbulante Freie Konvektion in Einer Horizontalen Flussigkeitsschicht mit Volumen-Warmequelle," Paper NC 4.5, *Proceedings, Fourth International Heat Transfer Conference,* Paris, Versailles, 1970.

9 Kulacki, F. A., and Goldstein, R. J., "Thermal Convection in a Horizontal Fluid Layer With Uniform Volumetric Energy Sources," *Journal of Fluid Mech.,* Vol. 55, 1972, p. 271.

10 Nagle, M. E., *Natural Convection Energy Transport in a Horizontal Fluid Layer With Volumetric Heat Sources,* MSc thesis, The Ohio State University, 1974.

11 Malkus, V. W. R., "Discrete Transition in Turbulent Convection," *Proceedings Royal Society,* Vol. A255, London, 1954, p. 185.

12 Willis, G. E., and Deardorf, J. W., "Confirmation and Renumbering of Discrete Transitions of Malkus, "*Phys. Fluids,* Vol. 10, 1967, p. 1861.

13 Rossby, H. T., "An Experimental Study of Benard Connection With and Without Rotation," Dept. Geol. Geophys., M.I.T. Sci. Rept. HRF/SR27, 1966.

14 Chu, T. Y., and Goldstein, R. J., "Turbulent Connection in a Horizontal Layer of Water," *Journal of Fluid Mech.,* Vol. 60, 1973, p. 141.

S. M. Morcos[1]
Research Assistant.

A. E. Bergles
Professor and Chairman.
Mem. ASME

Department of Mechanical Engineering and Engineering Research Institute, Iowa State University, Ames, Iowa

Experimental Investigation of Combined Forced and Free Laminar Convection in Horizontal Tubes

The present study considers the effects of property variations on fully developed laminar flow heat transfer and pressure drop in horizontal tubes. A facility was developed to test electrically heated glass and stainless steel tubes, with distilled water and ethylene glycol as working fluids. The Nusselt number for fully developed flow depends primarily on Rayleigh number; however, the Prandtl number and a dimensionless tube wall parameter are also required to correlate the four sets of heat transfer data. This correlation agrees well with data of most previous investigations. The friction factor increases with increasing Rayleigh number; data are within the bounds of limiting analytical predictions.

Introduction

Laminar flow heat transfer in tubes is encountered in a wide variety of engineering situations, including heat exchangers designed for viscous liquids in chemical process and food industries, compact heat exchangers for gas flows, and heat exchangers for biomedical applications. Even though such heat exchangers are now being used widely, there is a lack of understanding of many details of laminar flow and heat transfer. In recent reviews, both Sabersky [1][2] and Porter [2] see a need to predict commonly occurring laminar heat transfer conditions with much greater accuracy. The difficulties with laminar flows are associated with the fact that fluids which in practice are in this flow regime usually have properties which are strongly dependent on temperature.

The present study is concerned with laminar flow in horizontal circular tubes which is the orientation of greatest industrial interest. During heating, the fluid near the wall is warmer and, therefore, lighter than the bulk fluid in the core. As a consequence, two upward currents flow along the side walls, and, by continuity, the heavier fluid near the center of the tube flows downward. This sets up two spiralling vortices which are symmetrical about a vertical meridional plane. As a result of this combined forced and free convection flow, the heat transfer coefficient and the friction factor are well above the constant property predictions.

The present experiments were performed with electrically heated tubes which approximate uniform wall heat flux. This boundary condition is representative of many engineering situations, for example, electric resistance (calrod) heating, nuclear heating, and counter-flow heat exchangers with equal thermal capacity rates. With uniform wall heat flux, a wall-minus-fluid temperature difference exists throughout the tube; therefore, the secondary motion continues along the tube axis. For a sufficiently long tube, a "fully developed" condition is reached such that the heat transfer coefficient is independent of the position (or reduced length, X). This is quite different from the uniform wall temperature boundary condition where the secondary motion develops to a maximum intensity and then diminishes to zero as the temperature difference decreases.

For the numerous analytical solutions which have been proposed for fully developed flow, the usual boundary conditions are: uniform heat flux axially and circumferentially (zero conductivity, ZC), and uniform average heat flux along the tube but uniform temperature at each axial location (infinite conductivity, IC). Most solutions utilize the IC boundary conditions [3–9]. The only study to consider the ZC boundary condition indicates that there are large differences between the IC and ZC solutions [10]; actual data would be expected to lie between these two limiting solutions.

Experimental data are rather abundant for various fluids: air [11–14], water [15–20], and ethylene glycol [8, 21]. A composite plot of available experimental data for fully developed conditions is presented in Fig. 1 in terms of the usual Nusselt number–Rayleigh number representation. The substantial disagreement among various investigations for a given fluid, as well as among results for each of the three different fluids, is quite clear.

Analytical results indicate that the friction factor for a fully developed laminar flow in a horizontal tube increases with increas-

[1] Currently with General Atomic Company, San Diego, Calif.

[2] Numbers in brackets designate References at end of paper.

Contributed by the Heat Transfer Division for publication in the JOURNAL OF HEAT TRANSFER. Manuscript received by the Heat Transfer Division August 2, 1974. Paper No. 75-HT-QQ.

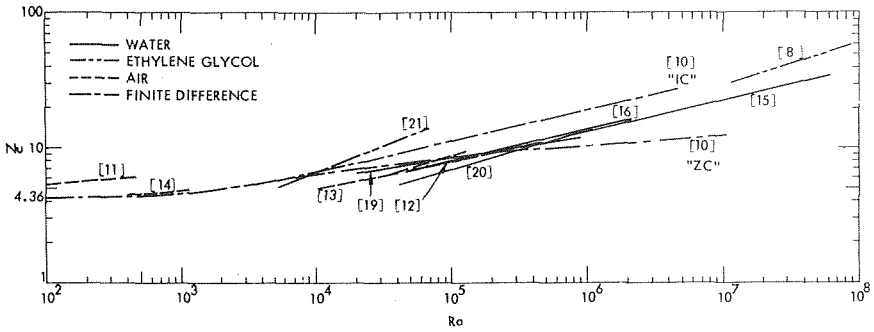

Fig. 1 Comparison of available experimental heat transfer data

ing intensity of the secondary flow. The analytical studies include perturbation analyses [3, 22, 23], a boundary layer approximation [7], a boundary vorticity analysis [9], and a finite-difference solution [10]. As in the case of the heat transfer solutions, the assumed boundary condition was *IC* except for the finite-difference study which considered both *IC* and *ZC* cases. A comparison of the available analytical predictions of the friction factor is presented in Fig. 2. The disagreement among the different investigations is, once more, quite clear.

The only experimental data for friction factor appear to be those of Hussain and McComas [13] for air. Their results were approximately 40 percent higher than the isothermal results over a Reynolds number range from 600 to 3000. No correlation of the experimental data was given. The shortage of experimental data makes it hard to judge the validity of the analytical predictions.

The foregoing review of analytical and experimental studies points out the need for a study of this important case of fully developed laminar flow in horizontal tubes with uniform wall heat flux. The present experiments are directed toward a better understanding of the different variables and dimensionless groups which affect the heat transfer coefficient so that a more accurate prediction can be achieved for different fluids and tube materials.

Experimental Apparatus

The test facility is shown in Fig. 3. The working fluid was circulated through the closed loop by a small centrifugal pump. An accumulator was installed at the pump outlet to dampen any pressure fluctuations. In the test-section line, fluid flowed through a filter, a flowmeter, and a preheater; it then flowed through the test section, merged with the fluid from the bypass line, passed through a heat exchanger, and returned to the pump. In order to minimize the dissolved gas in the system, a degassing tank, which also served as a surge tank, was provided. The loop was also equipped with a mixed-bed demineralizer to prevent fouling of the heated tubes when distilled water was used.

The inlet fluid temperature was measured by a thermocouple probe installed directly in the fluid stream just prior to the heated section. The bulk temperature of the exit fluid was measured by a thermocouple probe placed in the mixing chamber. Pressure taps were located 2.5 cm away from either side of the heated test sections. The pressure drop across the test section was measured with a precision inclined manometer.

One test section was constructed from a Pyrex, E-C coated glass tube (1.06 cm ID and 0.122 cm wall) manufactured by Corning Glass Company. The glass tube is externally coated with an optically transparent, electrically conductive, tin-oxide layer. This tubing represents the closest possible approximation to the *ZC* boundary condition. The length of the heated section was 1.13 m. A 1.90 m long stainless steel tube with a similar diameter was used as velocity approach length. The glass tube was powered by a 220 V a-c power supply controlled by an adjustable autotransformer. A wattmeter was used to measure the electrical power supplied.

Nomenclature

c_p = specific heat
d_1 = inside tube diameter
f = Fanning friction factor, $2g_c d_1 \Delta p/(L\rho u^2)$
Gr = Grashof number, $g\beta\rho^2 d_1^3 (\bar{T}_{w,i} - T_b)/\mu^2$
Gr* = modified Grashof number, Gr Nu $= g\beta\rho^2 d, {}^4q''/\mu^2 k$
g = gravitational acceleration
g_c = gravitational constant
h = circumferential average heat transfer coefficient, $\bar{q}_i''/(\bar{T}_{w,i} - T_b)$
$h(\theta)$ = local heat transfer coefficient, $q_i''/(T_{w,i} - T_b)$
k = fluid thermal conductivity
k_w = tube wall thermal conductivity
L_S = tube length from onset of heating to measuring section
Nu = circumferential average Nusselt number, hd_1/k
Pr = Prandtl number, $c_p\mu/k$
Pw = tube wall parameter, $hd_1^2/(k_w t)$
Pw^* = modified tube wall parameter, $Pw/\text{Nu} = kD/k_w t$
p = static pressure
Δp = pressure drop
q'' = local heat flux
$\bar{q}''$ = circumferential average heat flux
q''' = rate of volumetric heat generation
Ra = Rayleigh number, Gr Pr
Re = Reynolds number, $\rho u d_1/\mu$
r_1 = inside tube radius
r_2 = outside tube radius
s = coordinate along tube periphery
s^* = nondimensional coordinate along tube periphery, s/d_1
T = local fluid temperature
T_b = bulk or mixed-mean fluid temperature
T_w = local wall temperature
$\bar{T}_w$ = circumferential average wall temperature
t = tube wall thickness
u = average velocity
X = reduced length, $L_S/(d_1 \text{ Re Pr})$
β = isobaric thermal expansion coefficient, $-\frac{1}{\rho}\left(\frac{\partial\rho}{\partial T}\right)_p$
θ = angle measured clockwise from top of tube
μ = dynamic viscosity
ρ = density

Subscripts

b = evaluated at bulk fluid temperature
c = denotes circumferential heat flow
f = evaluated at fluid film temperature, $(\bar{T}_{w,i} + T_b)/2$
i = at inside wall of tube
o = at outside wall of tube; isothermal
w = evaluated at tube wall temperature

Fluid properties are evaluated at the bulk temperature unless otherwise indicated

The outside wall temperatures were measured at an axial location 1.05 m downstream from the onset of heating. Four thermocouples were placed 90 deg apart, circumferentially, at the measuring section to record the outer tube wall temperature profile. Vacuum couplings at both ends of the glass tube permitted the rotation of the tube during each run so that an accurate circumferential wall temperature profile could be obtained. Due to electrical pickup, it was necessary to electrically insulate the thermocouple beads from the wall with 0.008 cm thick strips of insulation paper.

In order to insure that the thermocouples were located in an adiabatic region, a guard shield surrounded the thermocouples at the measuring section. The guard shield was constructed from a 5 cm dia, 15 cm long aluminum tube which was slit nearly through, longitudinally, into four separate sections. Each section was wrapped with insulated heater wire connected to four separate variacs. Four thermocouples were then attached to the inside wall of the guard shield opposite the corresponding tube wall thermocouples. In this way, the inner wall temperatures of the guard shield segments could be independently adjusted to approximate the outer tube wall temperature profile. The remainder of the glass tube was insulated with a 2.5 cm thick glass fiber insulating tube.

The metal test section was constructed from a 304 stainless steel tube with an overall length of 3.26 m. Heat was applied to the last 1.22 m of the tube; the remainder of the tube was used to develop the flow hydrodynamically prior to its entering the heated section. The inside tube diameter and wall thickness were 1.02 cm and 0.05 cm, respectively. The circumferential conductance $(k_w t)$ of the metal tube was about seven times that of the glass tube, which was an adequate variation to test the influence of this parameter.

This test section was heated directly by a d-c current supplied by a motor-generator set. The power input to the test section was determined by measuring the current (calibrated shunt) and the total voltage (digital voltmeter) across the heated section. The outside wall temperature was measured at two axial locations, 0.28 m and 1.12 m from the onset of heating point, with four thermocouples at each axial location.

Experimental Procedure

Distilled water was the first working fluid to be used because of its availability and wide application. Several other fluids were considered, and ethylene glycol was found to be the most suitable for extending the Prandtl number range.

After filling the loop with distilled water, degassing was accomplished by bleeding a portion of the loop water into the top of the vigorously boiling degassing tank. The dissolved gas content was maintained at such a low level that no gas evolution was observed in the visual section during the course of the experiments. During preliminary experiments, it was found that gas bubbles significantly altered the heat transfer characteristics of the laminar flow.

After the water data for both the glass and metal test sections were collected, the loop was dried and filled with ethylene glycol. Since the gas content of the glycol in the loop was measured to be below 18 cc/l and no gas bubbles were observed during heating, there was no need for degassing.

The testing generally proceeded by increasing the power input to the test section while maintaining a constant flow rate and inlet temperature. After equilibrium was established, the outer wall temperatures were recorded with the heated section in two positions (0 and 45 deg). The eight temperature measurements and the condition of symmetry around a vertical meridional plane sufficed to accurately determine the circumferential wall temperature profile. The test-section flow rate, inlet and outlet fluid temperatures, and electric power input were also recorded.

Isothermal pressure drop data were obtained by varying the fluid inlet temperature for different flow rates. Due to the small pressure drop and the relatively large time constant of the measuring system, it was necessary to wait as much as one hour before recording the differential head of the indicating fluid. The procedure used for obtaining the nonisothermal pressure drop data was essentially the same as that followed in the heat transfer runs. The only difference was that the outer tube wall temperature was not recorded. Instead, the mean wall temperature was calculated from the heat transfer results, as described in the next section.

Data Reduction

The local bulk temperature at the measuring section was computed from inlet temperature, flow rate, and power input. Heat inputs based on fluid enthalpy rise could not be estimated accurately due to insufficient agitation of the fluid in the mixing chamber. The actual power input to the test section was, therefore, considered to be the measured electric power as corrected for heat loss through the insulation (about 1.5 percent).

The major task in the data reduction was to determine the circumferential variation of the heat flux and the inside wall temperature for both the glass and metal tubes. These quantities were deduced from the outside wall temperature measurements and the known total heat input. In order to determine the desired heat flux and temperature distributions, it was necessary to solve the two-dimensional conduction equation for the tube wall, taking into account both radial and tangential heat transfer. The glass and metal tubes were analyzed separately because, due to the nature of the heat generation, they have different boundary conditions at the outer surface of the tube. A periodic function was used to approximate the measured tube wall temperatures, and the heat conduction equations were solved by standard methods.

Typical derived inner tube wall parameters for the glass tube are

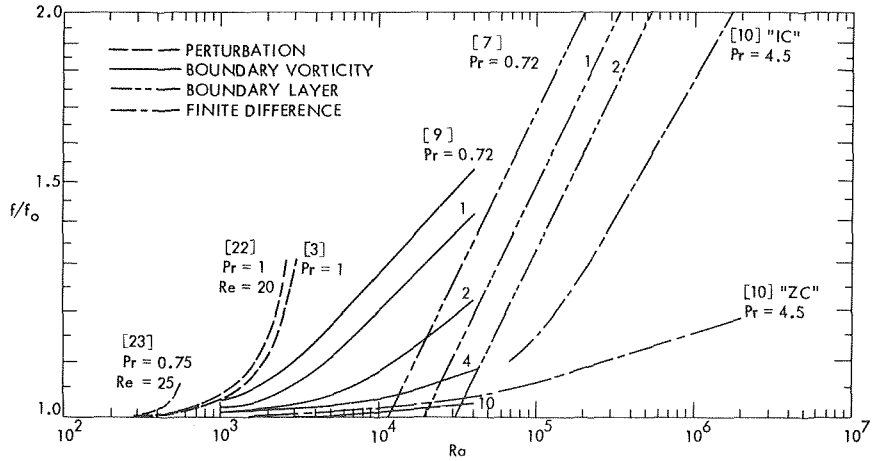

Fig. 2 Comparison of available analytical pressure drop predictions

shown in Fig. 4. It is evident that there is a significant deviation of the local heat flux from the average value. In accordance with the variation in inner wall temperature, there is a large variation in local Nusselt number. The two-dimensional solution for the inner wall temperature is compared with a one-dimensional solution obtained simply by subtracting a constant temperature drop from each measured value. This correction was obtained by solving the one-dimensional heat conduction equation using the average heat flux. Since the one-dimensional and two-dimensional solutions give essentially the same results, the simpler one-dimensional method was used for data reduction.

The tube wall temperature drop ranged from 1 to 22°C for the glass tube and was always less than 0.5°C for the metal tube. The circumferential average wall temperature was computed from the eight inner wall temperatures by numerical integration. The average heat transfer coefficient was then calculated by using the heat flux based on the inside tube surface area, average inner wall temperature, and calculated bulk fluid temperature at the measuring section. Reynolds and Nusselt numbers are based on the inside tube diameter. The Grashof number is defined in terms of the local average wall-to-bulk-fluid temperature difference and the inside tube diameter. Properties were evaluated at the local bulk fluid temperature or the film temperature, as described subsequently.

For isothermal pressure drop runs, inlet fluid temperature was used to evaluate all physical properties. The indicating fluid differential head was used to calculate the pressure drop across the test section. When taking data for the heating runs, only the inlet fluid temperature, flow rate, and power input were recorded. All conditions were evaluated at the midpoint of the test section. The average tube wall temperature was obtained through multiple iterations, using the correlation developed for the heat transfer data.

Further details of the apparatus, test procedure, and data reduction are given in [24].

Discussion of Results

Data Trends. The variation of Nu as a function of the reduced length, X, for various values of Ra is shown in Fig. 5 for ethylene glycol flow in the metal tube. Also shown, as limiting cases, are analytical predictions for pure forced convection with parabolic velocity distribution [25] and a composite of solutions for Pr = 5 [20]. The pronounced effect of free convection is quite clear from the present data which are as much as six times higher than the constant property predictions. The vertical spread in the data represents a range of heat fluxes, with the highest Nu corresponding to the highest heat flux. Since Ra was a dependent variable, lines of constant Ra could only be obtained by interpolating the data. Estimated lines of constant Ra in Fig. 5 are essentially horizontal for the range of the reduced length considered, which indicates that fully developed conditions were obtained prior to the measuring sections.

Since the data were taken under fully developed conditions, a more detailed comparison can be obtained by using Nu and Ra as correlation parameters in accordance with the examples given in [5, 20]. Such plots are shown in Fig. 6 for water and ethylene glycol; data from both tubes tested are included. The straight-line character of the four sets of data is quite clear in this figure. The ethylene glycol data lie above the water data for the same tube, and the metal tube data for both fluids are well above the glass tube data. These results suggest that the Nusselt number is affected not only by Ra and other variations in the physical properties of the working fluid, but also by the properties of the tube wall.

In view of the variable fluid properties and the pronounced effect of the tube wall circumferential conductance, it is not appropriate to make a direct comparison with other work reported in the literature except for glass tube water data given in [20] and the limiting IC and ZC boundary condition analyses presented in [10]. The metal tube water data are below the IC prediction, while the glass tube water data lie, in general, below the ZC prediction for $Ra < 2.5 \times 10^5$, and above the prediction for higher Rayleigh numbers. When compared with previous glass tube water data [20], the present data have less scatter and are in better agreement with the ZC prediction.

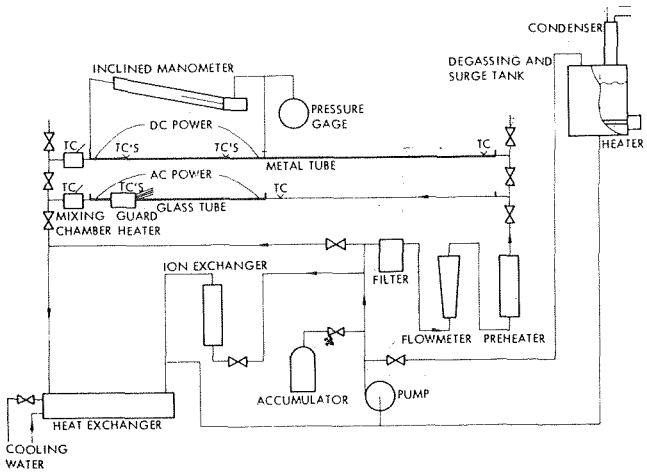

Fig. 3 Schematic layout of test loop

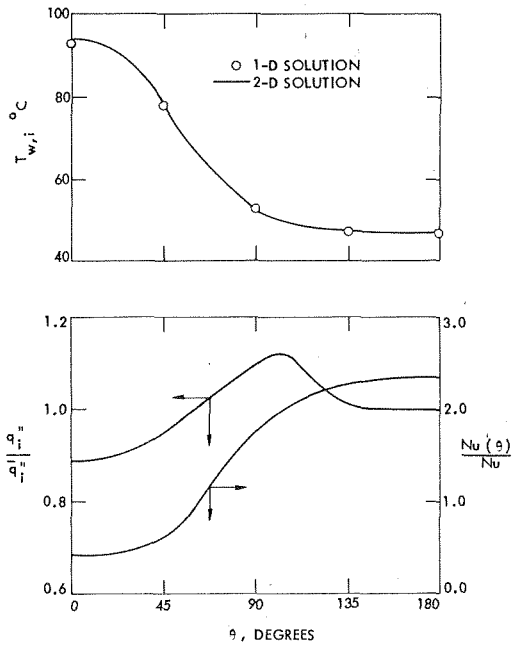

Fig. 4 Circumferential variation of inside wall temperature, heat flux, and Nusselt number for water with glass tube—run 31

Correlation of Heat Transfer Data. Different procedures were used to best correlate the four sets of heat transfer data. For the variable fluid properties, the traditional viscosity correction factor, $(\mu_w/\mu_b)^{0.14}$, was first employed. When applied to the two working fluids for each test section, this correction factor could not account for the variable property effect even when the exponent was varied. The inadequacy of this correction factor is due in part to the fact that no properties other than viscosity are considered. The recent proposal by Fand and Keswani [26] to include a more general property correction factor for each dimensionless parameter is somewhat impractical due to the difficulty of obtaining the many exponents.

Since the major velocity and thermal gradients occur in a thin layer near the wall, the mean film temperature is a reasonable choice for evaluation of all fluid properties. The Prandtl number was used as a correlating parameter in addition to Nu and Ra to reconcile data for the two fluids.

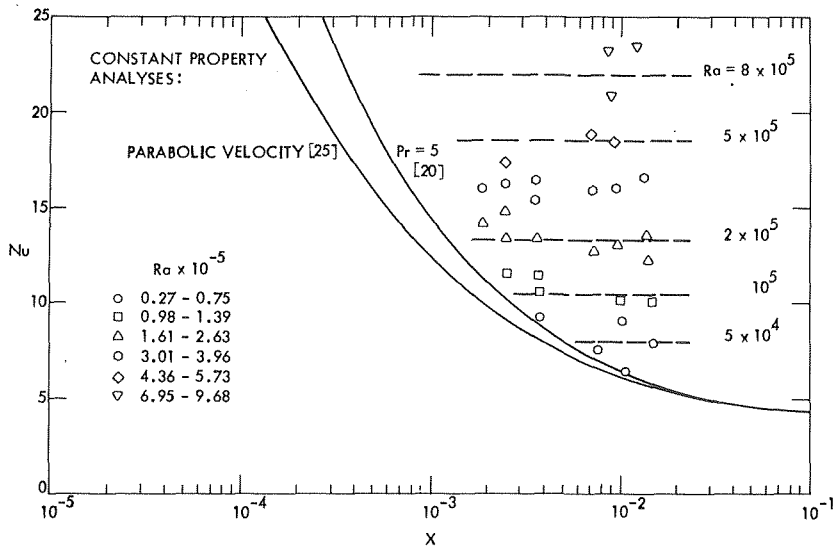

Fig. 5 Nusselt number as a function of reduced length for ethylene glycol with metal tube

Turning now to the tube wall effect, a steady-state energy balance for the tube element ds, shown in Fig. 7, yields

$$q_0'' + q'''t - h(\theta)(T_{w,i} - T_b) + k_w \frac{\partial^2}{\partial S^2} \int_{r_1}^{r_2} T_w dr = 0 \quad (1)$$

For the glass tube, $q''' = 0$, while for the metal tube $q_0'' = 0$. If the radial wall temperature variation across the thin tube wall is neglected compared to the circumferential variation, and the local heat transfer coefficient $h(\theta)$ is replaced by an average value h, equation (1) can be written as

$$\frac{q_0''}{h} + \frac{q'''t}{h} - (T_{w,i} - T_b) + \frac{1}{Pw} \frac{\partial T_{w,i}}{\partial S^{*2}} = 0 \quad (2)$$

where $Pw = (hd_1/k_w)(d_1/t)$. The tube wall parameter, Pw, represents the ratio between the peripheral and radial thermal resistances and can be regarded as an extension of the nondimensional group proposed by Iqbal, et al. [27] and Shah and London [28]. It can also be interpreted as the product of a Biot number and a two-dimensional geometry ratio. The two extreme theoretical values of Pw, zero and infinity, correspond to the IC and ZC tube boundary conditions, respectively.

The final correlation of fluid property and tube wall effects is presented in Fig. 8. Following the correlation scheme presented by Churchill and Usagi [29], the following equation was developed:

$$\mathrm{Nu}_f = \{(4.36)^2 + [0.055 (\frac{\mathrm{Gr}_f \mathrm{Pr}_f^{1.35}}{Pw^{0.25}})^{0.40}]^2\}^{1/2} \quad (3)$$

The Grashof number is utilized in this equation rather than Rayleigh number in order to avoid having two terms involving Prandtl number.

An alternate form of the correlation is given by equation (4) which incorporates redefined Grashof number and tube wall parameter:

$$\mathrm{Nu}_f = \{(4.36)^2 + [0.145(\frac{\mathrm{Gr}_f^* \mathrm{Pr}_f^{1.35}}{Pw_f^{*0.25}})^{0.265}]^2\}^{1/2}$$

This equation is more convenient for design as the Nusselt number is given explicitly, except for the iteration required to establish the film temperature. Based on the range of parameters tested, these correlation equations are expected to be valid for $3 \times 10^4 < \mathrm{Ra} < 10^6$, $4 < \mathrm{Pr} < 175$, and $2 < Pw < 66$.

Fig. 9 indicates that equation (3) is in good agreement with the data of a number of previous investigations. Included are a variety of metal test sections with air, water, and ethylene glycol as work-

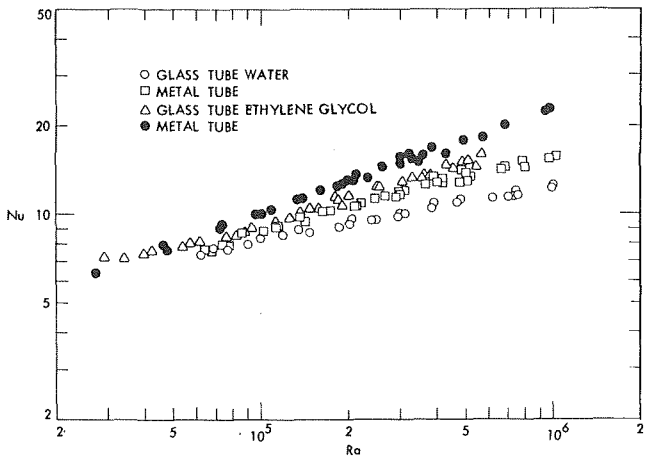

Fig. 6 Fully developed heat transfer data for water and ethylene glycol with different tubes

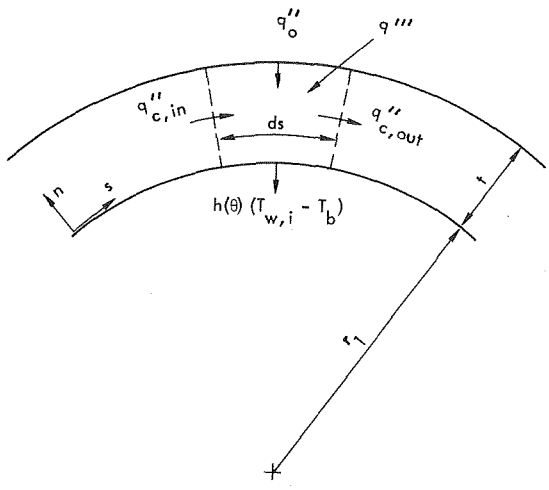

Fig. 7 Steady-state energy balance for a tube wall element

ing fluids. The data range is well outside the range of the present test data.

Two studies which would test the present correlation at the high end are not included in Fig. 9. The data of Ede [15] could not be interpreted in terms of the present coordinates as the data points were not identified according to Prandtl number or as to which of the several thick walled ($Pw_{max} \sim 2$) zinc tubes was used. The heat transfer data reported by Siegwarth, et al. [8] were taken with a 6.35 cm ID aluminum tube with 2.5 cm wall ($Pw_{max} \sim 0.25$). The estimated data of Ede and the data of Siegwarth, et al., extend several decades beyond the present data given in Fig. 9, and the Nusselt numbers are considerably lower.

Both of these tubes would be subject to axial conduction, which generally has the effect of making the calculated Nu too low and the calculated Gr too high; however, this does not appear to be a major factor. No satisfactory explanation for the discrepancy or alternate correlation technique was found to bring these data in line with the data shown in Fig. 9.

Correlation of Pressure Drop Data. Isothermal friction factor data for water flow in the glass tube, though not presented in the interests of space, are in good agreement with the Darcy friction factor prediction of 64/Re for laminar flow in tubes. Due to the very low values of pressure drop (20 to 50 N/m^2), it was very difficult to obtain an accurate indication of the changes in pressure drop due to heating. After considering various alternatives, the adiabatic pressure drop measurements were taken only for ethylene glycol, since the pressure drop level was more than ten times that for water.

The friction factor data for ethylene glycol, with and without heating, are presented in Fig. 10 for the glass and metal tubes. All fluid properties for the heating runs were evaluated at the mean film temperature, at an axial location halfway along the heated section. The pressure drop data were obtained for Re = 20–400 and Pr = 40–120. The isothermal friction factor data for both glass and metal tubes agree with Darcy's formula. The nonisothermal friction factor data, on the other hand, are as much as 50 percent higher than the corresponding isothermal values.

The nonisothermal factor data for ethylene glycol are presented in Fig. 11 as a ratio of f_f/f_0 versus Ra_f. The ratio f_f/f_0 increases with increasing Rayleigh number as a result of increasing secondary flow intensity. The type of tube wall does not seem to have a pronounced effect on the friction factor data. A correlation expression, which satisfies the lower limit value of the ratio f_f/f_0, is given by

$$\frac{f_f}{f_0} = \{1 + (0.195\ \mathrm{Ra}_f^{0.15})^{15}\}^{1/15} \tag{5}$$

Analytical predictions applicable to the ranges of Ra and Pr characterizing the experimental data are not available. Nevertheless, Fig. 11 shows that the present friction factor data are contained within the *IC* and *ZC* predictions of Newell and Bergles [10] for Pr = 4.5. The present data, however, do not reflect the

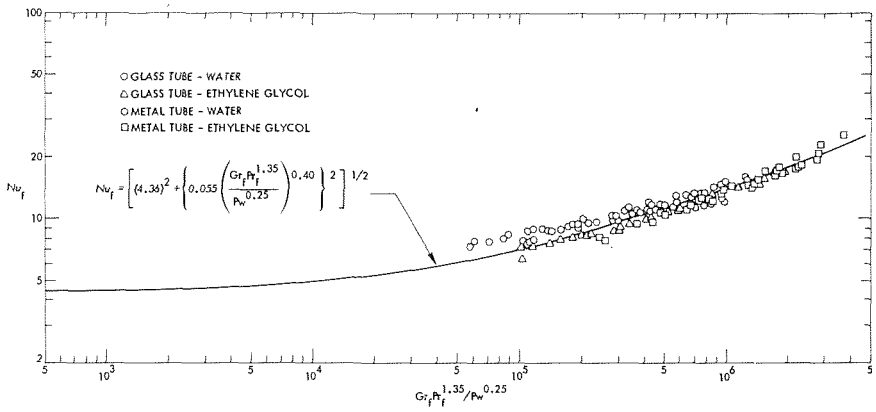

Fig. 8 Final correlation of data for forced and free convection

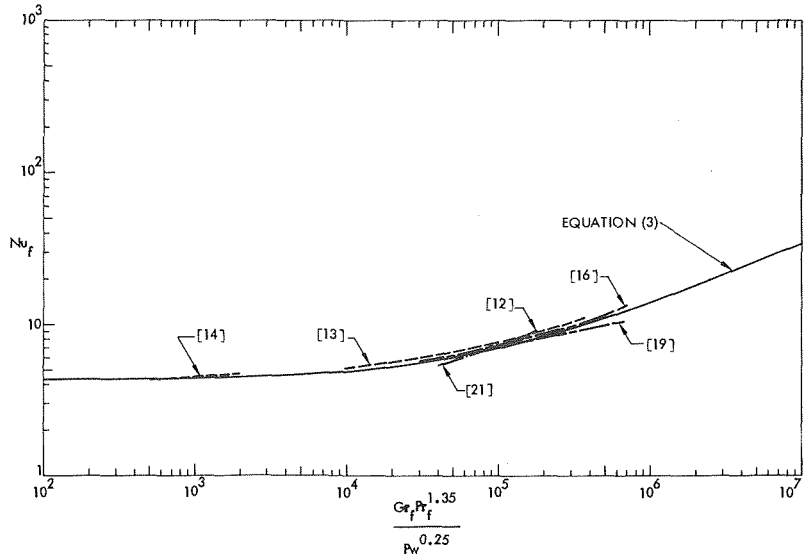

Fig. 9 Comparison of present correlation with available data

large difference in friction factor between the two boundary conditions of [10]. At low Ra, the present experimental results seem to approach the boundary vorticity prediction [9] for Pr = 10.

Conclusions

Experimental results for horizontal electrically heated tubes show that the heat transfer coefficients deviate by up to a factor of six from the traditional analytical predictions, mainly due to the inadequacy of the constant property assumptions. The data indicate that the Nusselt number is affected by the Rayleigh number, variations in the physical properties of the working fluid, and the circumferential conductance of the tube wall.

Fluid property effects are correlated by evaluating all fluid properties at the film temperature and by using Prandtl number as an additional correlation parameter. The tube wall parameter, $Pw = (hd_1/k_w)(d_1/t)$, successfully reconciles the data for glass and metal tubes. The final heat transfer correlation, which includes both Prandtl number and the tube wall correlation parameters, is in good agreement with most of the available data from previous investigations for various fluids and tube wall materials. Further tests should be conducted at large Rayleigh numbers where the correlation does not agree with reported data.

The pressure drop data indicate that the friction factor increases with increasing Rayleigh numbers. However, the type of tube wall has less effect on the friction factor than on the heat transfer coefficient. Within the range of Rayleigh and Prandtl numbers considered in this study, no data are available for comparison. However, the present data are within the lower and upper bounds established by analysis.

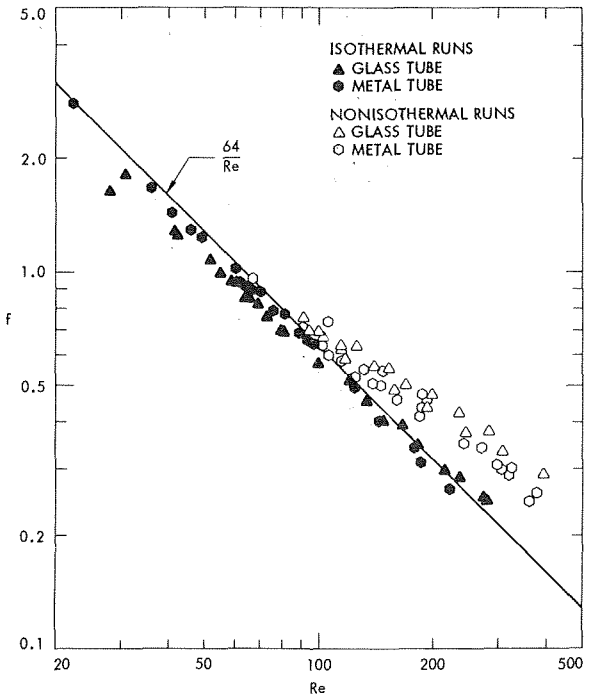

Fig. 10 Friction factor data for ethylene glycol with glass tube

Acknowledgments

This study was sponsored by the National Science Foundation, Heat Transfer Program, under Grant GK-36851, and received partial support from the Engineering Research Institute, Iowa State University. The work was performed in the Heat Laboratory of the Department of Mechanical Engineering at Iowa State University.

References

1 Sabersky, R. H., "Heat Transfer in the Seventies," *International Journal of Heat and Mass Transfer*, Vol. 14, 1971, pp. 1927–1949.

2 Porter, J. E., "Heat Transfer at Low Reynolds Number (Highly Viscous Liquids in Laminar Flow), Industrial Research Fellow Report," *Trans. IChE*, Vol. 49, 1971, pp. 1–29.

3 Morton, B. R., "Laminar Convection in Uniformly Heated Horizontal Pipes at Low Rayleigh Numbers," *Quarterly Journal of Mechanics and Applied Mathematics*, Vol. 12, 1959, pp. 410–420.

4 Iqbal, M., and Stachiewicz, J. W., "Influence of Tube Orientation on Combined Free and Forced Laminar Convection Heat Transfer," JOURNAL OF HEAT TRANSFER, TRANS. ASME, Series C, Vol. 88, 1966, pp. 410–420.

5 Iqbal, M., "Free Convection Effects Inside Tubes of Flat-Plate Solar Collectors," *Solar Energy*, Vol. 10, 1966, pp. 207–211.

6 Faris, G. N., and Viskanta, R., "An Analysis of Laminar Combined Forced and Free Convection Heat Transfer in a Horizontal Tube," *International Journal of Heat and Mass Transfer*, Vol. 12, 1969, pp. 1295–1309.

7 Mori, Y., and Futagami, K., "Forced Convection Heat Transfer in Uniformly Heated Horizontal Tubes, 2nd Report—Theoretical Study," *International Journal of Heat and Mass Transfer*, Vol. 10, 1967, pp. 1801–1813.

8 Siegwarth, D. P., Miksell R. D., Readal, T. C., and Hanratty, T. J., "Effect of Secondary Flow on the Temperature Field and Primary Flow in a Heated Horizontal Tube," *International Journal of Heat and Mass Transfer*, Vol. 12, 1969, pp. 1535–1552.

9 Hwang, G. J., and Cheng, K. C., "Boundary Vorticity Method for Convective Heat Transfer With Secondary Flow—Application to the Combined Free and Forced Convection in Horizontal Tubes," *Heat Transfer 1970*, Vol. 4, Paper No. NC 3.5, Elsevier Publishing Co., Amsterdam, 1970.

10 Newell, P. H., Jr., and Bergles, A. E., "Analysis of Combined Free and Forced Convection for Fully Developed Laminar Flow in Horizontal Tubes," JOURNAL OF HEAT TRANSFER, TRANS. ASME, Series C, Vol. 92, 1970, pp. 83–89.

11 McComas, S. T., and Eckert, E. R. G., "Combined Free and Forced Convection in a Horizontal Circular Tube," JOURNAL OF HEAT TRANSFER, TRANS. ASME, Series C, Vol. 88, 1966, pp. 147–153.

12 Mori, Y., Futagami, K., Tokuda, S., and Nakamura, M., "Forced

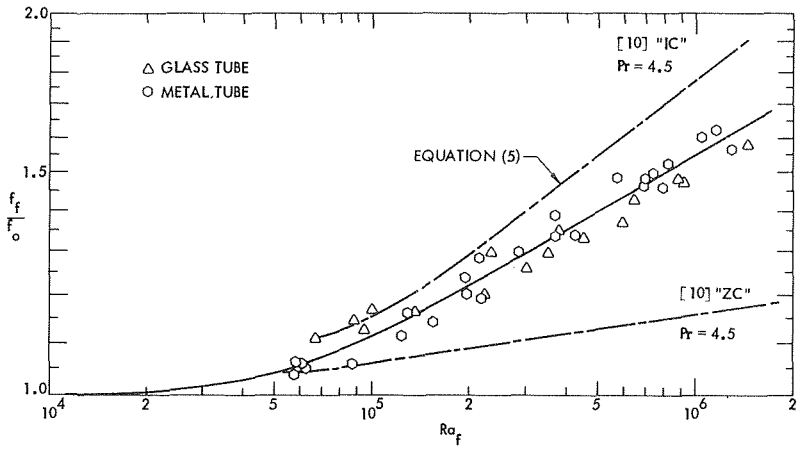

Fig. 11 Correlation of friction factor data and comparison with limiting analytical solutions

Convective Heat Transfer in Uniformly Heated Horizontal Tubes, 1st Report—Experimental Study on the Effect of Buoyancy," *International Journal of Heat and Mass Transfer,* Vol. 12, 1969, pp. 1535–1552.

13 Hussain, N. A., and McComas, S. T., "Experimental Investigation of Combined Convection in a Horizontal Circular Tube With Uniform Heat Flux," *Heat Transfer 1970,* Vol. 4, Paper No. NC 3.4, Elsevier Publishing Co., Amsterdam, 1970.

14 Lichtarowicz, A., "Combined Free and Forced Convection Effects in Fully Developed Laminar Flow in Horizontal Tubes," *Heat and Mass Transfer by Combined Forced and Free Convection,* Institute of Mechanical Engineers, London, 1972, pp. 13–16.

15 Ede, A. J., "The Heat Transfer Coefficient for Flow in a Pipe," *International Journal of Heat and Mass Transfer,* Vol. 4, 1961, pp. 105–110.

16 Petukhov, B. S., and Polyakov, A. F., "Experimental Investigation of Viscogravitational Fluid Flow in a Horizontal Tube," *High Temperature,* Vol. 5, 1967, pp. 75–81.

17 Petukhov, B. S., and Polyakov, A. F., "Effect of Free Convection on Heat Transfer During Forced Flow in Horizontal Pipe," *High Temperature,* Vol. 5, 1967, pp. 348–351.

18 Petukhov, B. S., Polyakov, A. F., and Strigin, B. K., "Heat Transfer in Tubes With Viscous-gravity Flow," *Heat Transfer—Soviet Research,* Vol. 1, 1969, pp. 24–31.

19 Shannon, R. L., and Depew, C. A., "Combined Free and Forced Laminar Convection in a Horizontal Tube With Uniform Heat Flux," JOURNAL OF HEAT TRANSFER, TRANS. ASME, Series C, Vol. 90, 1968, pp. 353–357.

20 Bergles, A. E., and Simonds, R. R., "Combined Forced and Free Convection for Laminar Flow in Horizontal Tubes with Uniform Heat Flux," *International Journal of Heat and Mass Transfer,* Vol. 14, 1971, pp. 1989–2000.

21 Shannon, R. L., and Depew, C. A., "Forced Laminar Flow Convection in a Horizontal Tube with Variable Viscosity and Free-Convection Effects," JOURNAL OF HEAT TRANSFER, TRANS. ASME, Series C, Vol. 91, 1969, pp. 251–258.

22 del Casal, E., and Gill, W. N., "A Note on Natural Convection Effects in Fully Developed Horizontal Tube Flow," *AIChE Journal,* Vol. 8, 1962, pp. 570–574.

23 Iqbal, M., and Stachiewicz, J. W., "Variable Density Effects in Combined Free and Forced Convection in Inclined Tubes," *International Journal of Heat and Mass Transfer,* Vol. 10, 1967, pp. 1625–1629.

24 Morcos, S. M., and Bergles, A. E., "Combined Forced and Free Laminar Convection in Horizontal Tubes," Technical Report HTL-1, ISU-ERI Ames 74008, Iowa State University, 1974.

25 Siegel, R., Sparrow, E. M., and Hallman, T. M., "Steady Laminar Heat Transfer in a Circular Tube With Prescribed Wall Heat Flux," *Applied Scientific Research,* Vol. 7, Section A, 1958, pp. 386–392.

26 Fand, R. M., and Keswani, K. K., "The Influence of Property Variation on Forced Convection Heat Transfer to Liquids," *International Journal of Heat and Mass Transfer,* Vol. 15, 1972, pp. 1515–1536.

27 Iqbal, M., Aggarwala, B. D., and Khatry, A. K., "On the Conjugate Problem of Laminar Combined Free and Forced Convection Through Vertical Non-Circular Ducts," JOURNAL OF HEAT TRANSFER, TRANS. ASME, Series C, Vol. 94, 1972, pp. 52–56.

28 Shah, R. K., and London, A. L., "Thermal Boundary Conditions and Some Solutions for Laminar Duct Flow Forced Convection," JOURNAL OF HEAT TRANSFER, TRANS. ASME, Series C, Vol. 96, 1974, pp. 159–165.

29 Churchill, S. W., and Usagi, R., "A General Expression for the Correlation of Rates of Transfer and Other Phenomena," *AIChE Journal,* Vol. 18, No. 6, 1972, pp. 1121–1128.

S. Ostrach
Professor. Mem. ASME

Y. Kamotani
Research Associate.

Department of Fluid, Thermal, and Aerospace Sciences,
Case Western Reserve University,
Cleveland, Ohio,

Heat Transfer Augmentation in Laminar Fully Developed Channel Flow by Means of Heating From Below

Results are reported of an experimental investigation of fully developed forced convection between two horizontal plates when the lower plate is heated and the upper one is cooled. The experiments covered a range of Rayleigh numbers between 100 and 13,500 and Reynolds numbers less than 100 using air. The heat transfer measurements show a sharp increase of heat transfer coefficient when longitudinal vortex rolls appear in the passage which indicates the considerable heat-transfer augmentation obtained in this way. Comparison of heat transfer coefficients for fully developed cases and those for confined cases indicates that there is no appreciable difference between them. Periodic spanwise temperature distributions created by vortex rolls are distorted by a second type of vortex rolls as the Rayleigh number increases. Because of the interaction the regular vortex structure disappears around Rayleigh number 8000.

1 Introduction

It is well known that a horizontal layer of fluid, when heated from below and cooled above, becomes unstable when the temperature difference is increased above a critical value. Above the critical value several forms of fluid motion have been observed [1].[1] In the case of a superposed fully developed flow between two horizontal flat plates where the lower plate is heated and the upper one is cooled, longitudinal vortex rolls appear in the passage when the temperature difference becomes larger than a critical value [2]. In either case, below the critical point heat is transported from the lower plate to the upper one by conduction through the fluid, and the temperature changes linearly in the fluid. Above the critical point the heat transfer rate is increased by the thermal instability and the temperature field is strongly influenced by the motion of vortex rolls.

There are several works available concerning the change of heat transfer rate due to the thermal instability for a confined horizontal layer of fluid. Mull and Reiher (reported by Jacob [3]) measured the heat transfer rate in the range of Ra = 1500–6.3 × 10^6 in air. Malkus [4] conducted experiments using distilled water and acetone in the range of Ra = 10–10^{10}. The work of Silveston [5] was done on several fluids and covered Ra = 350–3.8 × 10^5. Globe and Dropkin [6] used several fluids to investigate the effect of Prandtl number on heat transfer rate in the range of Ra between 1.51 × 10^5 and 6.76 × 10^8. Plows [7] studied the problem numerically, and calculated the change of heat transfer rate due to two-dimensional vortex rolls.

As for heat transfer with a superposed fully developed flow on a thermal instability between two horizontal plates only a few papers are available. Mori and Uchida [2] solved the governing nonlinear equations of the problem approximately using the energy integral method. They also reported experimental data taken mainly at Ra ≒ 8000, Re ≒ 520 to compare with their theoretical results. Ogura and Yagihashi [8] and Hwang and Cheng [9] solved the problem by numerical methods. As noted by Hwang and Cheng [9], the governing equations for the fully developed case are identical to those for the confined case with two-dimensional vortex rolls studied by Plows [7]. Nakayama, et al. [10] studied theoretically the onset of instability when both lower and upper plates were subjected to identical uniform axial temperature gradients, and Akiyama, et al. [11] verified the results experimentally.

In the present experiments the heat transfer rate was measured for a fully developed flow of air in the range Ra = 100–13,500. Temperature distributions were investigated more extensively and for a wider range of Rayleigh number in the present work than in Mori and Uchida's experiments in order to study the effects of vortex rolls on the temperature field in more detail.

[1] Number in brackets designate References at end of paper.

Contributed by the Heat Transfer Division for publication in the JOURNAL OF HEAT TRANSFER. Manuscript received by the Heat Transfer Division January 27, 1975. Paper No. 75-HT-SS.

2 Experimental Apparatus and Procedure

A sketch of the test apparatus is shown in Fig. 1. The test section was 26.7 cm wide and 26.7 cm long. The lower plate of the test section was made of a 6.35 mm thick aluminum plate whose surface was polished, and the flatness was carefully checked. Two electrical heating mats were bonded to the back of the aluminum plate to ensure uniform heating. One heater covered the entire upstream half of the plate, and the other covered the downstream half. The input to each heater was controlled individually by a voltage controller. The upper plate of the test section was made of a 6.35 mm thick plexiglas plate. The plate was reinforced by aluminum beams to keep it flat. The upper plate was cooled by water flowing above it. The cooling water was circulated by a constant temperature circulator which controlled the temperature of the water within ± 0.01 °C. The surface temperatures of the lower and upper plates were measured by several copper-constantan thermocouples embedded in both plates.

The side walls of the test section were made of 3.2 mm thick insulating boards to minimize heat conduction through them. The height of the test section was adjusted by the height of the side walls.

Air from a compressor passed through a channel diffuser and a 45.7 cm long rectangular channel before entering into the test section. The volume flow rate of air was measured by a flowmeter. The flow rate was controlled by a flowrate controller. The mean air speed at the test section was calculated from the total flow rate. To obtain fully developed velocity and temperature profiles over a large part of the test section, the Reynolds number (based on the mean speed and the height of the test section) was kept below 100.

The heat transfer rate was calculated from the net heat input to the air in the test section. The net heat input is given by

$$Q_{\text{NET}} = Q_{\text{TOTAL}} - Q_{L,C} - Q_{L,R} - Q_L$$

Q_{TOTAL} is the total input to the downstream heater. $Q_{L,C}$ is the heat loss to the back of the heater by conduction. $Q_{L,C}$ was calculated from the amount of heat passing through a 1.90 cm thick plexiglas plate which was placed underneath the heater. $Q_{L,C}$ was found to be about 14 percent of Q_{TOTAL}. $Q_{L,R}$ is the heat loss by radiation, and is calculated from the equation

$$Q_{L,R} = \epsilon\sigma(T_1^4 - T_2^4) \times (\text{Area})$$

$Q_{L,R}$ was about 5 percent of Q_{TOTAL}. Q_L is the heat loss not accounted for by the previous two, such as conduction loss through the side walls and the heat loss to the surrounding air. Q_L cannot be measured directly. When the flow is fully developed, and the temperature difference is below the critical value, heat is transfered from the lower plate to the upper one by conduction. Thus, since the thermal conductivity of air is known Q_{NET} can be calculated. Then Q_L was calculated using the measured values of Q_{TOTAL} $Q_{L,C}$, and $Q_{L,R}$. In this way the value of Q_L was checked under various experimental conditions. Q_L was found to be about 10 percent of Q_{TOTAL}.

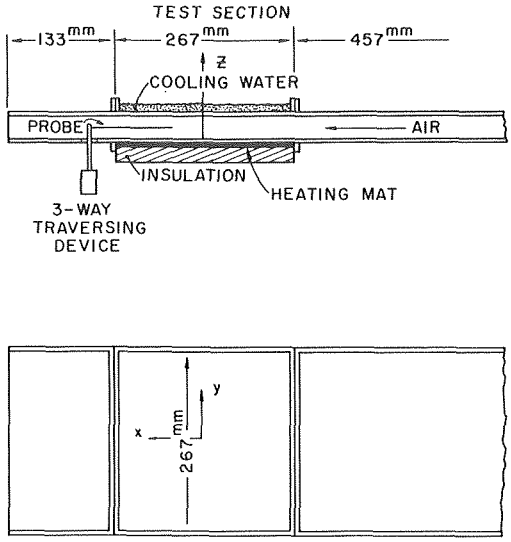

Fig. 1 Sketch of test apparatus

Since the surface temperature of the bottom plate was kept very uniform (the deviation was within the accuracy of thermocouples which was about ±1 percent) throughout the experiments, the edge effect was neglected.

The heat transfer coefficient and Nusselt number are defined as

$$\frac{Q_{\text{NET}}}{\text{Area}} = h(T_1 - T_2)$$

$$\text{Nu} = \frac{hD}{k}$$

The error due to all factors in the value of Nu was estimated to be ±10 percent.

To measure velocity and temperature distributions in the test section, a probe was inserted from the open end of the test section. The probe was supported by a three-way traversing device. Temperature was measured by a copper-constantan thermocouple probe. Velocity and temperature fluctuations were measured by a hot wire probe (5 micron dia platinum wire) which was operated by a constant current anemometer.

3 Experimental Results

3.1 Preliminary Investigation of Flow Field. The flow field was observed visually by slowly introducing cigarette smoke into the test section. Photographs were taken through the trans-

Nomenclature

D = height of the passage
Gr = Grashof number, $g\beta\Delta TD^3/\nu^2$
g = acceleration of gravity
h = heat transfer coefficient
Nu = Nusselt number, hD/k
Q_{TOTAL} = total input to the heater
Q_{NET} = net energy input
$Q_{L,C}$ = total energy lost to the back of the heater
$Q_{L,R}$ = total energy lost by radiation
Q_L = total energy loss minus $Q_{L,C}$ and $Q_{L,R}$
Ra = Rayleigh number, $g\beta\Delta TD^3/\nu\kappa$
Re = Reynolds number, $\bar{U}D/\nu$
T = temperature
T_1 = surface temperature of the heated plate
T_2 = surface temperature of the cooled plate
ΔT = temperature difference, $T_1 - T_2$
T_m = mean temperature in the passage, $\frac{1}{2}(T_1 + T_2)$
$\bar{T}$ = average temperature at a given z
T' = temperature fluctuation
$\bar{U}$ = volume averaged speed of the main flow
x = coordinate parallel to the main flow direction
y = coordinate in spanwise direction
z = coordinate normal to horizontal plates
β = coefficient of volumetric expansion
ϵ = emissivity
κ = thermal diffusivity of air at T_m
λ = wavelength (pitch) of vortex rolls
ν = kinematic viscosity of air at T_m
σ = Stefan-Boltzman constant

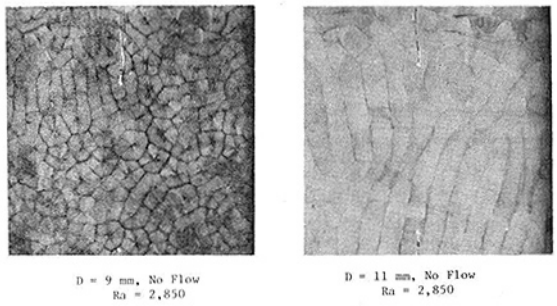

Fig. 2 Flow patterns

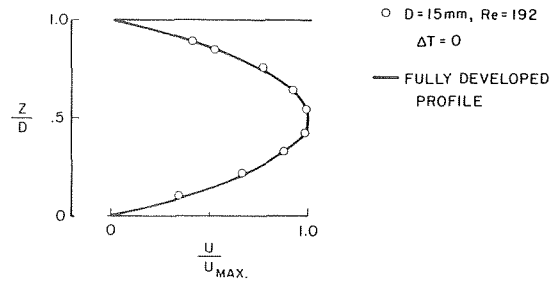

Fig. 3 Fully developed velocity distribution

parent upper wall for both the confined (no through flow) cases and the fully developed cases. For the confined cases both upstream and downstream ends of the test section were closed. Sample photographs are shown in Fig. 2.

For the confined cases the flow structure above the critical Rayleigh number changes with the gap between two plates as observed by Chandra [1]. At $D \doteqdot 9$ mm so-called Benard cells were clearly observed. For $D > 10$ mm hexagonal cells appeared only sporadically, and the flow field was dominated by longitudinal cells. Such variation of the flow structure with D is probably due to the variation of physical parameters (e.g., viscosity) with temperature (Schlüter, et al. [12], Segel and Stuart [13]). As D becomes smaller, the critical temperature difference rapidly increases (proportionally to D^{-3}) for a fixed Ra so that the nonuniformity of physical parameters in the flow field becomes important.

When the fluid in the test section is moving at a constant speed, longitudinal vortex rolls aligned to the flow direction are predominant. However, when the speed is very small, the flow structure resembles that of the enclosed cases. For $Re > 10$ (in all cases studied herein) we observed well defined longitudinal vortex rolls in the range of temperature difference and passage height studied herein.

Transverse (z-direction) velocity distributions were measured at the location halfway from the beginning of the test section when both walls were at equal temperature. The data are presented in

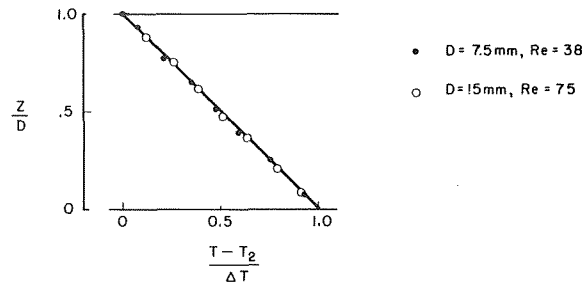

Fig. 4 Fully developed temperature distribution

Fig. 3 together with the parabolic profile for fully developed channel flow. Since hot wires cannot measure small speeds, the speed $\bar{U}$ was set higher (20cm/s) for this measurement than the value used for the present experiments. Fig. 3 confirms that the velocity profile is fully developed at the measuring location.

Similarly, transverse temperature distributions were measured at the same location with through flow when there was a temperature difference which did not exceed the critical value. The data given in Fig. 4 show that the temperature distribution is linear as in a fully developed flow.

Thus, in the range of Reynolds number studied here, both velocity and temperature distributions were found to be fully developed over the downstream half of the test section where the heat transfer measurements were made.

3.2 Heat Transfer Rate. In Fig. 5 Nusselt numbers versus Rayleigh numbers are plotted for both the fully developed case ($7.5 \text{ mm} < D < 15 \text{ mm}$, $10 < \text{Re} < 100$) and the confined case. The present data are compared with the empirical curve obtained by Silveston [5] for the confined case, and with the experimental data and the theoretical curve given by Mori and Uchida for the fully developed case which is written as

$$\text{Nu} = 1 + 1.413\left(1 - \frac{\text{Ra}_{cr}}{\text{Ra}}\right) \qquad (1)$$

The present results are also compared with the numerical results obtained by Hwang and Cheng [9].

As can be seen in Fig. 5 there is a sharp increase of Nusselt number across the critical Rayleigh number, and there is no appreciable difference in heat transfer rate between the fully developed case and the confined case. Both sets of the present data agree very well with Silveston's curve. Nu calculated from equation (1) is smaller than the present data, and the difference increases as Ra increases. Considering the approximation method adopted by Mori and Uchida, their results are expected to be good for Rayleigh number not very much larger than the critical value. In their experiments Mori and Uchida calculated the Nusselt number from the temperature gradient at the surface of the heated plate. Such a procedure is not very reliable when the temperature field is com-

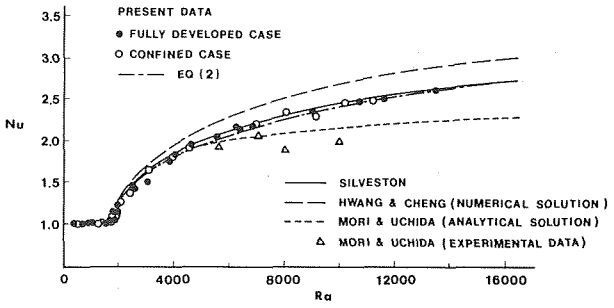

Fig. 5 Nusselt number versus Rayleigh number

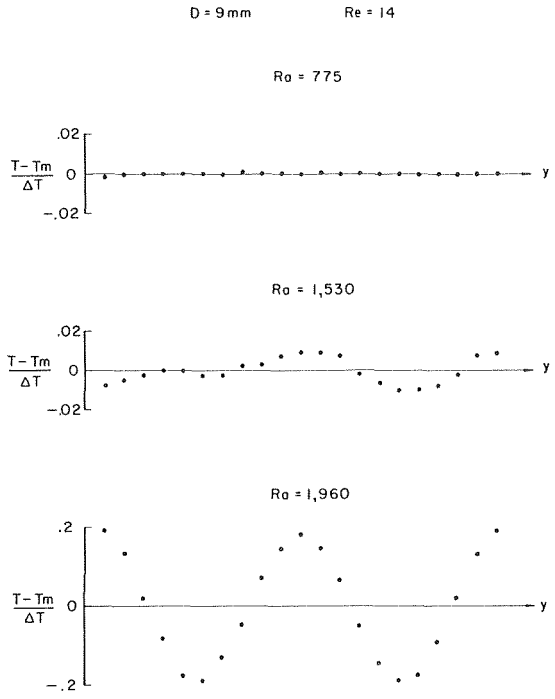

Fig. 6 *(a)* Spanwise temperature distribution

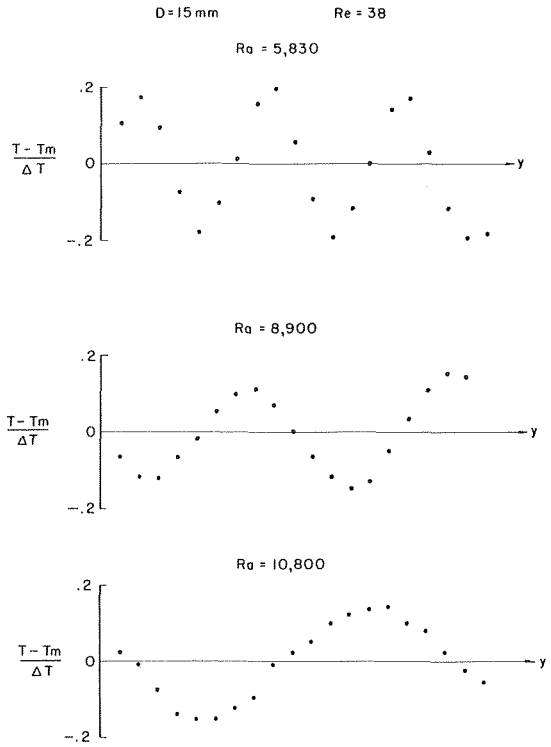

Fig. 6 *(b)* Spanwise temperature distribution

plicated as in the present problem. Moreover, as explained in the next section, for Ra > 8000 regular vortex rolls disappear, and the fluid motion becomes irregular, which makes it almost impossible to calculate with reasonable accuracy the overall heat transfer rate from temperature distributions. For those reasons, the data taken by Mori and Uchida differ from the present data by as much as 20 percent, and the difference is largest for Ra > 8000. Numerical results of Hwang and Cheng show slightly larger Nu than the present data. The difference is about 10 percent, which is within the error of the present experiments.

For large Ra (> 8000) Nu changes proportionaly to $Ra^{1/3}$. Noting the definition of Ra and Nu, this means that the heat transfer rate becomes independent of D.

The data also showed that as long as the flow in the test section was fully developed the heat transfer was independent of Reynolds number in the range of Reynolds number studied herein (Re < 100), which agrees with equation (1).

The parameter which shows the importance of buoyancy forces in a forced flow problem is called the Froude number ($\equiv Re^2/Gr$). Body forces become significant when the Froude number is of unit order of magnitude or smaller. In the present experiments the Froude number ranged from 0.04 to 10. However, if longitudinal vortex rolls are fully developed, the temperature distribution is independent of the axial distance and the axial velocity. Consequently, the heat transfer rate does not depend on Reynolds number. On the other hand, when the flow field is turbulent, a part of the main stream kinetic energy is converted into turbulent kinetic energy through the interaction of Reynolds stresses and the main shear flow. Such a process depends on the Reynolds number. Therefore, when the Rayleigh number is very large (much greater than 8000) the transfer rate is expected to depend on the Reynolds number and, thus, the Froude number becomes an important factor.

It may be useful for practical purposes to correlate the experimental data by a single equation. The method used for the correlation was developed by Churchill and Usagi [14].

Near the critical Ra, a Taylor's series expansion of equation (1) gives

$$\mathrm{Nu} \longrightarrow 1 + \frac{1.413}{\mathrm{Ra}_{cr}}(\mathrm{Ra} - \mathrm{Ra}_{cr}) \text{ as } (\mathrm{Ra} - \mathrm{Ra}_{cr}) \longrightarrow 0$$

and from the results obtained by Globe and Dropkin [6] for confined cases, we have

$$\mathrm{Nu} \longrightarrow 0.069\ (\mathrm{Ra})^{1/3} \text{ for } 1.51 \times 10^5 < \mathrm{Ra} < 6.86 \times 10^8$$

Then using the method of Churchill and Usagi, one obtains the following expression:

$$\mathrm{Nu} = 1 + \frac{8.30 \times 10^{-4}(\mathrm{Ra} - \mathrm{Ra}_{cr})}{\sqrt{1 + 1.45 \times 10^{-4}(\mathrm{Ra} - \mathrm{Ra}_{cr})^{4/3}}} \qquad (2)$$

Equation (2) is plotted in Fig. 5. It correlated the experimental data very well.

3.3 Temperature Distribution. Spanwise temperature distributions were measured for several Rayleigh numbers at z/D = 0.5. The results are shown in Fig. 6. At Ra = 1530 and Re = 14 (slightly below the critical value), the temperature distribution, which is uniform at lower Ra, is slightly disturbed (note the scale of the ordinate). The disturbance is very small, but it already shows the trace of periodicity, which indicates weak vertical fluid motion. Chandra [1] also observed the vertical motion of fluid at $\mathrm{Ra} < \mathrm{Ra}_{cr}$ in the flow visualization experiments for confined cases. At Ra = 1960 and Re = 14, the spanwise temperature distribution has very regular sinusoidal shape, which indicates the appearance of longitudinal vortex rolls. The temperature is high in the region where the fluid is moving upward and low where it is moving downward. For Ra up to about 8000, the spanwise temperature distribution in the midplane remains very similar. The similarity is shown in Fig. 7, in which the data taken under various conditions are plotted. Scaling the spanwise length by the average pitch of vortex rolls the spanwise temperature distribution in the midplane is expressed as

$$\frac{T - T_m}{\Delta T} = 0.20 \cos\left(2\pi \frac{y}{\lambda}\right) \text{ for } 1900 < \mathrm{Ra} < 8000$$

where $T_m = 1/2\ (T_1 + T_2)$

From the spanwise temperature measurements, the pitch of vortex rolls averaged over several wavelengths was calculated. In Fig. 8 the average pitch is plotted against the height of the test section. The pitch was found to be equal to $2D$, as predicted by the linearized theory [2]. Measurements showed that the pitch remains constant with Ra. As plotted in Fig. 8, the data taken by Mori and Uchida show that the pitch becomes constant for $D > 15$ mm. No such behavior was observed in the present experiment. The data by Mori and Uchida seem to contradict the smoke photographs taken by Akiyama, et al. [11] which show very regular square cells at $D = 25.4$ mm.

For Ra > 8000, the spanwise temperature distribution becomes irregular (Fig. 6), which suggests the disappearance of regular vortex rolls. At the same time fluctuations of the temperature begins to be noticeable. Fig. 9 shows the temperature fluctuation level measured by a hot wire located at the midplane. The temperature fluctuation remains nearly zero up to Ra = 8000, but for Ra > 8000 it increases sharply with increasing Ra. This behavior was observed for both the fully developed case and the confined case. The frequency of the fluctuation was rather low, mostly under 150 cycles/s. No jump of heat transfer rate was observed in this range of Ra. As mentioned in the previous section, Nu becomes proportional to $Ra^{1/3}$ from about Ra = 8000.

These fluctuations are caused by what Mori and Uchida called "second type vortex rolls." These rolls have half the size of "first type vortex rolls" (Fig. 10). They are associated with a second instability which is predicted to occur at Ra = 18,352 by the linearized theory [2] assuming the theory holds at such high Ra. However, as Mori and Uchida noted, the second type of vortex rolls can exist below the critical value deriving their energy not from

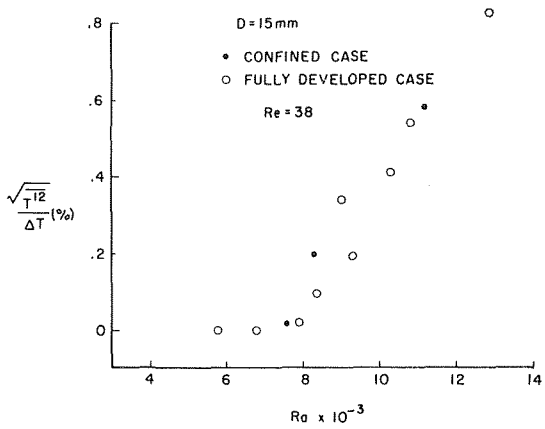

Fig. 9 Temperature fluctuation level

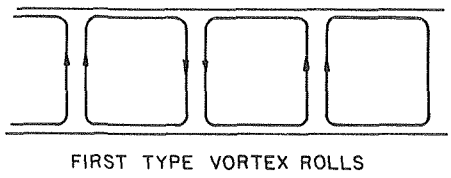

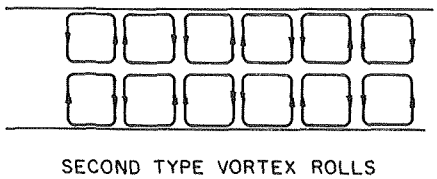

Fig. 10 First and second type vortex rolls

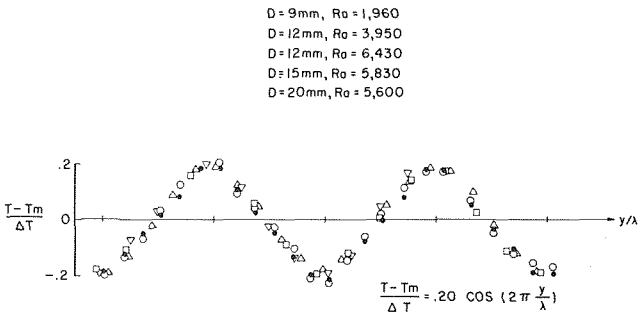

Fig. 7 Similarity of spanwise temperature distribution

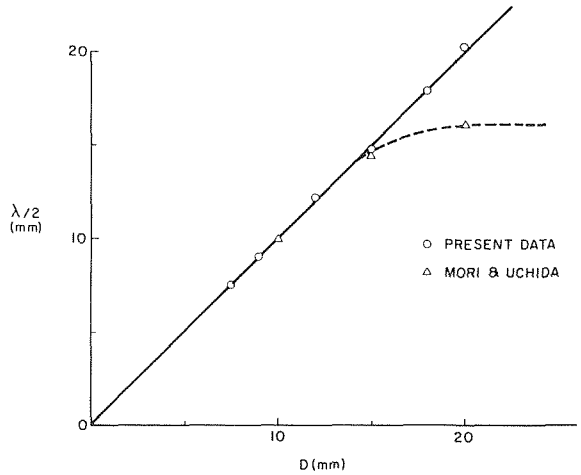

Fig. 8 Pitch of vortex rolls

buoyancy but from Reynolds stress. As the second type of vortex rolls grow stronger, they destroy the orderly vortex structure of first type vortex rolls. Whether this eventually leads to turbulent flow or to another stable state was not studied in the present experiment.

Fig. 11 shows temperature distributions in z-direction. Each point represents the average value over several wavelengths at a given z, that is

$$\bar{T}(z) = \frac{1}{L}\int_{y_0}^{y_0+L} T(y, z)\,dy$$

The vortex motion associated with the thermal instability and superposed flow induces the mixing of hot and cold fluid. Consequently, as Ra increases the temperature becomes uniform in the region near the midplane. At Ra = 7500 the temperature gradient changes sign near the midplane, as was predicted by Mori and Uchida's analysis. In such a region the direction of heat flux is opposite to that of conduction, which means that the amount of heat convected is larger than the amount of heat transferred from the lower plate to the upper one. Beyond Ra = 8000 the temperature distribution becomes uniform again near the midplane because of random mixing.

Whereas the mean temperature distribution reflects the overall mixing of cold and hot fluid, another aspect of the effect of vortex rolls on the temperature distribution can be seen from the distri-

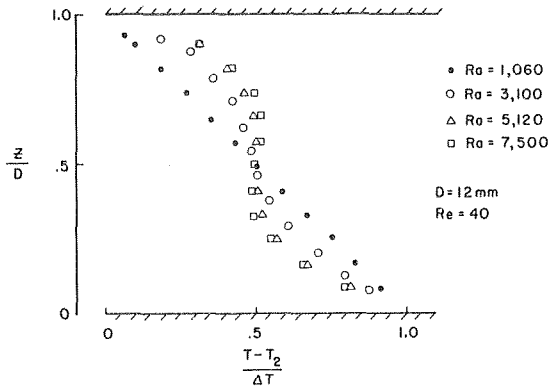

Fig. 11 Mean transverse temperature distribution

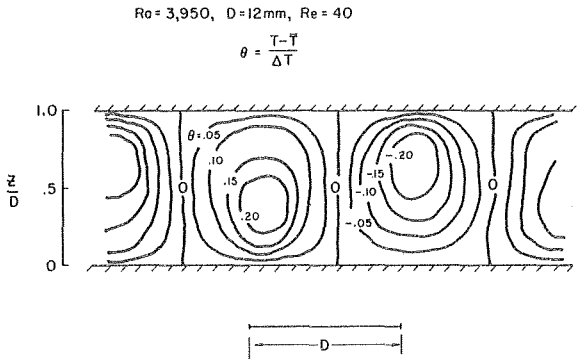

Fig. 12 Contours of constant distrubance temperature

bution of disturbance temperature which is defined as the difference between the local temperature and the mean temperature. Fig. 12 shows contours of constant dimensionless disturbance temperature θ. θ is positive in the region where the fluid is moving upward, and negative where it is moving down. As can be seen in Fig. 12, contours of θ are not symmetric with respect to the midplane ($z/D = 0.5$). The centers of contours are below the midplane in the positive θ region, and above in the negative θ region. Such asymmetry was found to become more noticeable as Ra increases. This asymmetry is due to nonsinusoidal spanwise temperature distributions off the midplane caused by second type vortex rolls. The temperature distribution is distorted by second type vortex rolls in such a way that θ decreases in the upper half of the passage ($0.5 < z/D < 1$), and increases in the lower half ($0 < z/D < 0.5$), resulting in the asymmetry of the contours.

4 Conclusions

Experiments were carried out to investigate the effects of longitudinal vortex rolls in fully developed laminar flow between two horizontal plates on the heat transfer rate and the temperature field. The following conclusions were obtained from the experiments.

1 Appreciable heat transfer augmentation (Nu greater than 2.5) is obtained by superposing a fully developed flow on the cellular flow generated by heating a horizontal fluid layer from below.

2 There is no appreciable difference between the heat transfer rate for the fully developed flow and that for the stationary horizontal layer of fluid despite the fact that forms of fluid motion are different in two cases.

3 The first type of vortex rolls create periodic spanwise temperature distributions whose wavelength is exactly equal to twice the height of the passage. However, second type of vortex rolls which are found to exist even at low Rayleigh numbers distort the temperature distribution. Such distortion increases as Ra increases, and eventually the flow becomes unstable at around Ra = 8000. For Ra > 8000 no stable vortex rolls are observed.

Acknowledgment

This research was supported by the U.S. Air Force Office of Scientific Research under Grant AFOSR NA 74-064.

References

1 Chandra, K., "Instability of Fluids Heated From Below," *Proceedings of the Royal Society (London)*, Series A, Vol. 164, 1938, pp. 231–242.

2 Mori, Y., and Uchida, Y., "Forced Convective Heat Transfer Between Horizontal Plates," *International Journal of Heat and Mass Transfer*, Vol. 9, 1966, pp. 803–817.

3 Jakob, M., *Heat Transfer*, Wiley, New York, Vol. 1, 1949.

4 Malkus, W. V. R., "Discrete Transitions in Turbulent Convection," *Proceedings of the Royal Society (London)*, Series A, Vol. 225, 1954, pp. 185–195.

5 Silveston, P. L., "Warmedurchgang in waagerechten Flussigketisschichten," *Forschung auf dem Gebiete des Ingenieurwesens*, Vol. 24, No. 2, 1958, pp. 59–69.

6 Globe, S., and Dropkin, D., "Natural-Convection Heat Transfer in Liquids Confined by Two Horizontal Plates and Heated From Below," JOURNAL OF HEAT TRANSFER, TRANS. ASME, Series C, Vol. 81, 1959, pp. 24–28.

7 Plows, W. H., "Some Numerical Results for Two-Dimensional Steady Laminar Benard Convection," *The Physics of Fluids*, Vol. 11, 1968, pp. 1593–1599.

8 Ogura, Y., and Yagihashi, A., "A Numerical Study of Convection Rolls in a Flow Between Horizontal Parallel Plates," *Journal of the Meterological Society of Japan*, Vol. 47, 1969, pp. 205–217.

9 Hwang, G. J., and Cheng, K. C., "A Boundary Vorticity Method for Finite Amplitude Convection in Plane Poiseuille Flow," *Developments in Mechanics*, Proceedings of the 12th Midwestern Mechanics Conference, Vol. 6, 1971, pp. 207–220.

10 Nakayama, W., Hwang, H. J., and Cheng, K. C., "Thermal Instability in Plane Poiseuille Flow," JOURNAL OF HEAT TRANSFER, TRANS. ASME, Series C, Vol. 92, No. 1, 1970, pp. 61–68.

11 Akiyama, M., Hwang, G. J., and Cheng, K. C., "Experiments on the Onset of Longitudinal Vortices in Laminar Forced Convection Between Horizontal Plates," JOURNAL OF HEAT TRANSFER, TRANS. ASME, Series C, Vol. 93, No. 4, 1971, pp. 335–341.

12 Schlüter, A., Lortz, D., and Busse, F., "On the Stability of Steady Finite Amplitude Convection," *Journal of Fluid Mechanics*, Vol. 23, 1965, pp. 129–144.

13 Segel, L. A., and Stuart, J. T., "On the Question of the Preferred Mode in Cellular Thermal Convection," *Journal of Fluid Mechanics*, Vol. 13, 1962, pp. 289–306.

14 Churchill, S. W., and Usagi, R., "A General Expression for the Correlation of Rates of Transfer and Other Phenomena," *AIChE Journal*, Vol. 18, No. 6, 1972, pp. 1121–1128.

V. S. Sastry

Asst. Professor, Department of Mechanical Engineering, Tennessee State University, Nashville, Tenn. Mem. ASME.

N. M. Schnurr

Assoc. Professor, Department of Mechanical Engineering, Vanderbilt University, Nashville, Tenn. Mem. ASME.

An Analytical Investigation of Forced Convection Heat Transfer to Fluids Near the Thermodynamic Critical Point[1]

A numerical solution is carried out for heat transfer to fluids near the thermodynamic critical point for turbulent flow through a circular tube with constant wall heat flux. An adaptation of the Patankar-Spalding implicit finite difference marching procedure is used. Agreement of the results with experimental data for water and carbon dioxide show the solution to be quite accurate very near the critical point provided the wall temperature at inlet is less than the pseudocritical temperature of the fluid.

Introduction

Forced convection heat transfer to supercritical and near critical fluids is of great interest because of the large number of practical applications. These include uses of supercritical water in electric generating power plants, supercritical hydrogen as a working fluid for both chemical and nuclear rockets, and near-critical helium as a coolant for the coils of superconducting magnets and superconducting electronic and power equipment. Although a significant amount of research has been carried out in this area over the past two decades [1],[2] the information necessary for practical design and even the understanding of the heat transfer mechanism is still somewhat inadequate.

Most of the studies of near critical forced convection reported to date have been experimental. The working fluids which have been used include water [2–5], carbon dioxide [6–9], hydrogen [10–12], oxygen [13], and nitrogen tetroxide [14]. In several of these studies a correlation of the type

$$\mathrm{Nu} = a\mathrm{Re}^b\mathrm{Pr}^c \tag{1}$$

was used where a, b, and c are constants. In some cases [4, 5] equation (1) was multiplied by ratios of various properties evaluated at wall and bulk conditions raised to some power. In others [6, 8], the fluid properties used in equation (1) were evaluated at a reference temperature which was a function of T_w, T_b, and the pseudocritical temperature T_m. Other investigators [11] have postulated the existence of a "boiling-like" phenomenon as the dominant heat transfer mechanism and attempted correlations based on the Martinelli two-phase parameter. No general correlation applying to a variety of fluids over a very wide range of test conditions has been achieved.

Analytical approaches to the problem have been presented by Deissler [15], Goldmann [16], and Skiralkar and Griffith [9]. All used some type of numerical integration in the cross stream direction. This eliminated the effects of upstream conditions. The axial momentum term was, therefore, implicitly assumed negligible compared to the shear stress. While this assumption is valid for fully developed constant property flow, it is questionable in regions where the fluid properties vary rapidly, i.e., near the critical point.

The analyses of Goldmann and Deissler were completed two decades ago and were based on fluid property data and eddy diffusivity formulations less accurate than those available today. Shiralkar and Griffith had to make several simplifying assumptions (such as negligible axial momentum and linear radial variation of heat flux) in order to achieve computational efficiency. Nevertheless, reasonable agreement with experimental data was obtained by these analytical methods. This indicates that a numerical solution of the governing differential equations might yield an accurate prediction of heat transfer to near critical fluids.

The purpose of the work reported here was to develop a numerical method for predicting forced convection heat transfer to supercritical and near critical fluids, to determine the ranges of conditions for which this procedure is valid, and to correlate results in a

[1] Based on a PhD dissertation submitted to the Mechanical Engineering Faculty of Vanderbilt University by V. S. Sastry, 1974.

[2] Numbers in brackets designate References at end of paper.

Contributed by the Heat Transfer Division and presented at the Winter Annual Meeting, New York, N. Y., November 17–22, 1974, of THE AMERICAN SOCIETY OF MECHANICAL ENGINEERS. Journal manuscript received by the Heat Transfer Division February 18, 1975. Paper No. 74-WA/HT-29.

form which may be used in design and analysis of heat transfer equipment.

Statement of the Problem

The problem to be analyzed is heat transfer to a near critical fluid flowing through a smooth walled circular tube having a uniform wall heat flux. The flow is assumed steady and axisymmetric. Viscous dissipation of energy, axial conduction, and free convection effects are assumed negligible.

The applicable equations for conservation of mass, momentum, and energy are

$$\frac{1}{r}\frac{\partial}{\partial r}(r\rho v_r) + \frac{\partial}{\partial x}(\rho u) = 0 \tag{2}$$

$$\rho u\frac{\partial u}{\partial x} + \rho v_r\frac{\partial u}{\partial r} + g_c\frac{dP}{dx} = \frac{1}{r}\frac{\partial}{\partial r}(r\mu_{\text{eff}}\frac{\partial u}{\partial r}) \tag{3}$$

and

$$\rho u\frac{\partial i}{\partial x} + \rho v_r\frac{\partial i}{\partial r} - \frac{1}{r}\frac{\partial}{\partial r}(k_{\text{eff}}\frac{\partial T}{\partial r}) = 0 \tag{4}$$

where

$$\mu_{\text{eff}} = \rho(\epsilon_M + \nu)$$

and

$$k_{\text{eff}} = \rho C(\epsilon_H + \alpha)$$

A crucial assumption is that of neglecting buoyancy effects. An approximate stability analysis by Shiralkar and Griffith [17] predicts that this assumption will be valid if the free convection parameter, defined as (Gr/Re^2) is much less than 0.004 for water or 0.02 for CO_2. Note that as the fluid state approaches the critical point, Gr approaches infinity and this assumption will fail. The free convection parameter was therefore computed for all runs to make sure that it did not exceed the values listed in the foregoing. The ultimate test, however, is the comparison of the numerical results to experimental data.

Numerical Method

Since equations (2), (3), and (4) are coupled and the fluid properties are tabulated functions of both pressure and temperature, a numerical method must be used. The approach used here is an adaptation of the Patankar-Spalding method [18]. Their method is an implicit marching procedure applicable to boundary layer[3] type flows. It has a number of unique features which make it an extremely rapid method without the sacrifice of accuracy. It is a two-dimensional method so that upstream conditions are accounted for and the axial momentum term is included. Since a detailed discussion and complete statement listing is available elsewhere [19] only the details directly applicable to this work will be discussed.

The effective viscosity formulation used here is the Van Driest [20] hypothesis

$$\mu_{\text{eff}} = \mu + \rho\eta^2 y\{1 - \exp(\frac{-y\sqrt{\tau\rho}}{\mu A^+})\}|\frac{\partial u}{\partial y}|$$

where $A^+ = 26$ and $\eta = 0.4$

The turbulent Prandtl number ϵ_M/ϵ_H is assumed to be unity. This is a good assumption as long as the Prandtl number is close to unity which is the case here. Property subroutines were developed which effectively stored tables of viscosity, specific heat, thermal conductivity, density, and enthalpy as functions of temperature and pressure. A double interpolation scheme was used to obtain the correct value of these properties at any given state.

The analysis is begun at a particular cross section where the enthalpy and velocity profiles, and the tube diameter and fluid pressure, are specified. The initial profiles selected here were 1/7 power law profiles. Although any thermal boundary condition at the tube wall may be handled including variable wall temperature or heat flux, the condition used here was constant wall heat flux. The solution proceeds by calculating new velocity and enthalpy profiles and values of heat transfer coefficient, wall temperature, and pressure at successive downstream locations. This is done by effectively solving equations (2), (3), and (4) simultaneously in finite difference form using a successive substitution technique. This process continues until some termination condition such as a specified fluid bulk temperature is reached. A more detailed discussion of this method and complete statement listing are available in reference [21].

Results for Supercritical Water

The first fluid investigated was water. The conditions at the critical point are $T_c = 374.1°\text{C}$ and $P_c = 22.1 \times 10^6\ \text{N/m}^2$. A series of runs was made for comparison with the experimental data of Swenson, et al. [4]. Their data were selected since they covered a fairly wide range of pressures and the test section length and heat flux were of sufficient magnitude to produce large changes in fluid bulk temperature and film coefficient. Their data showed little scatter which implies good accuracy and reproducibility.

Results of a pressure of $22.8 \times 10^6\ \text{N/m}^2$ ($P_R = 1.029$) and a heat

[3] "Boundary layer" includes any flow in which the derivatives of the dependent variables in the cross stream direction are much larger than those in the streamwise direction.

Nomenclature

A^+ = constant in van Driest's expression for effective viscosity
C = local specific heat, J/kg-K
D = diameter of tube, mm
g = acceleration of gravity, m/s²
G = mass velocity kg/m²s
Gr = Grashoff number = $\left(\frac{\rho_b - \rho_w}{\rho_w}\right)\times\left(\frac{\rho_w}{\mu_w}\right)^2 D^3 g$
h = local heat transfer coefficient, W/m²C
i = specific enthalpy, J/kg
i_b = bulk enthalpy, J/kg
k = thermal conductivity, W/m-C
k_{eff} = effective conductivity (in turbulent flows), W/m-C
Nu = Nusselt number = hD/k
P = pressure, N/m²
P_c = critical pressure, N/m²
P_R = reduced pressure = P/P_c
Pr = Prandtl number = $\mu C/k$
Q = wall heat flux, W/m²
r = local radius, m
R = radius of wall, m
Re = Reynolds number = GD/μ
T = local temperature, °C
T_b = bulk temperature, °C
T_c = critical temperature, °C
T_f = film temperature = $(T_b + T_w)/2$, °C
T_m = pseudocritical temperature (temperature at which specific heat is a maximum for that pressure), °C
T_w = wall temperature, °C
u = local velocity in the X-direction, m/s
T_z = reference temperature, °C
v_r = local velocity in the radial direction, m/s
X = distance from entrance, m
Z = $(T_z - T_b)/(T_w - T_b)$
α = thermal diffusivity = $k/\rho C$, m²/s
ϵ_H = eddy diffusivity of heat, m²/s
ϵ_M = eddy diffusivity of momentum, m²/s
λ = constant in expression for eddy diffusivity
η = constant = 0.09
μ = absolute viscosity, kg/s-m
μ_{eff} = effective viscosity for turbulent flow, kg/s-m
ν = kinematic viscosity = m²/s
θ = $(T_m - T_b)/(T_w - T_b)$
ρ = mass density, kg/m³
τ = shear stress, N/m²

Subscripts

b = denotes bulk conditions
w = denotes wall conditions
Z = properties evaluated at the reference temperature, T_z

flux of 7.88×10^5 W/m^2 are shown in Fig. 1. Note that the heat transfer coefficient peaks sharply at a bulk enthalpy of 1.78×10^6 J/kg. This occurs when the wall temperature is almost exactly equal to the pseudocritical temperature of 376°C and the bulk temperature is somewhat lower. Additional heating causes a rapid deterioration in h with a minimum occurring when $T_w > T_m$ and $T_b \approx T_m$. The heat transfer coefficient then increases, attains another peak, and then decreases in the low density region.

A comparison of these results with those of reference [4] is shown in Fig. 2. Note that h is plotted as a function of a film temperature defined by $T_f = 0.5\ (T_w + T_b)$. This is a somewhat poor choice (according to the numerical predictions) since h is a multivalued function of T_f for $400 \leq T_f \leq 500$°C. Agreement is amazingly good considering the proximity to the critical point. The only lack of agreement may occur in the region where h is predicted to be a multivalued function of T_f. No wall temperature or film temperature profiles are given in reference [5] so it is not possible to determine if the unusual behavior predicted by the analysis may actually occur and be overlooked due to the method of plotting results. This would seem to be unlikely since the data points corresponding to the curve in Fig. 2 show little scatter. The most likely conclusion is that the analysis underpredicts h when $T_b \approx T_m$. There is some speculation that the usual formulations for eddy diffusivity are inaccurate in this region due to the extremely large density differences. Shiralkar and Griffith [17] discuss this in some detail and suggest various modifications which might be used to predict an augmentation of eddy diffusivity. Since these methods are somewhat questionable and lead to inaccuracies very near the wall they were not used here. Further study is necessary to determine whether the unusual behavior predicted in this analysis may actually occur. It is possible that its occurance may depend on other conditions which effect the stability of the flow. Resolution of this problem is beyond the scope of this paper.

The next case considered was at $P = 31.0 \times 10^6$ N/m^2 ($P_R = 1.40$) and $Q = 7.88 \times 10^5$. Results are compared to those of reference [4] in Fig. 3. At this higher pressure, the variations of specific heat and density with temperature are not nearly so steep. In this case the film temperature increases monotonically with heating and the sharp minimum in h at $T_b \approx T_m$ does not occur. Again, agreement with the data of reference [4] is excellent.

Also shown in Fig. 3 are results for a case having $P = 31.0 \times 10^6$ N/m^2 and $Q = 1.73 \times 10^6$ W/m^2. In this case the analysis predicts a peak in h more than 50 percent higher than that of reference [4]. As a further check the results for both values of heat flux shown in Fig. 3 were compared to the correlation of Gunsen and Kellogg [5]. Their equation correlated over 400 data points covering the following range of conditions:

$$P = 22.7 \times 10^6 - 27.5 \times 10^6 \text{ N/m}^2$$
$$Q = 3.15 \times 10^5 - 3.46 \times 10^6 \text{ W/m}^2$$
$$G = 678 - 3661 \text{ kg/m}^2\text{s}$$

Although the pressure of 31.0×10^6 N/m^2 is above those considered in their correlation their equation might be expected to give reasonably accurate results at this slightly higher pressure. The heat transfer coefficients predicted by their correlation were within ±15 percent of the values predicted analytically.

It appears that the discrepancy for the high heat flux case may be due to the effect of inlet enthalpy on downstream values of h. This is discussed in more detail in the next section.

Finally an attempt was made to obtain a correlation of analytical results over the entire range of variables investigated. One method which showed some promise was a correlation using equation (1) and a variable reference temperature. The best correlation obtained was of the form

$$\text{Nu}_z = 0.0225\ \text{Re}_z^{0.8}\ \text{Pr}_z^{0.55} \tag{5}$$

where all fluid properties are evaluated at $T_z = T_b + Z(T_w - T_b)$. The parameter Z is a function of $\theta = (T_m - T_b)/(T_w - T_b)$. This functional relationship is shown in Fig. 4. It was possible to obtain a single correlation at a fixed pressure. For $P_R = 1.40$ for example the correlation includes heat fluxes of 7.88×10^5 to 9.45×10^6 W/m^2 and flow rates of 2150–4070 kg/m^{2}s. Different curves must be used at different pressures, however. It should also be noted that

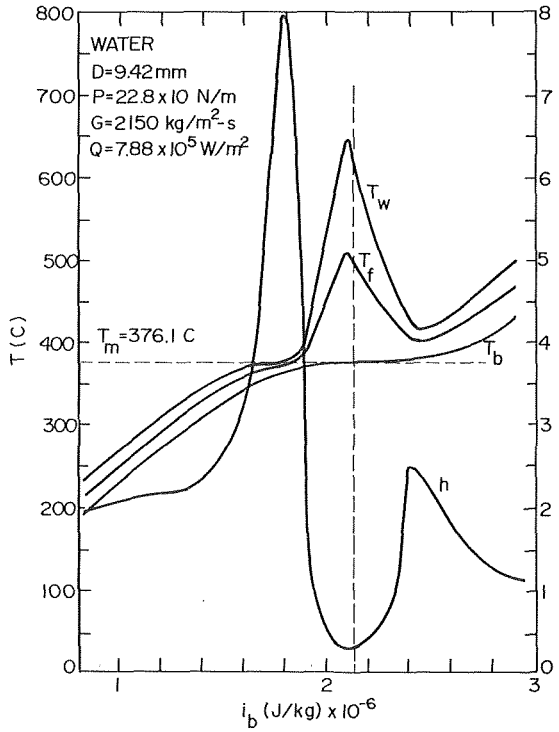

Fig. 1 Numerical results for water at $P_R = 1.029$

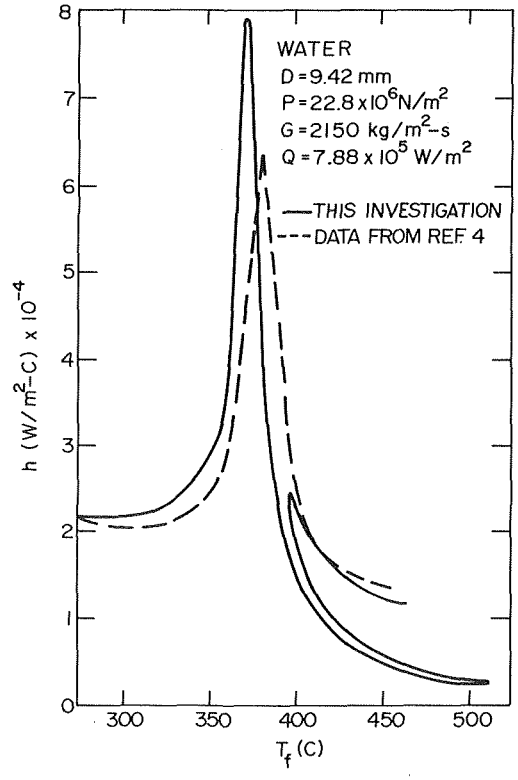

Fig. 2 Comparison of numerical results to experimental data of reference [4]—$P_R = 1.029$

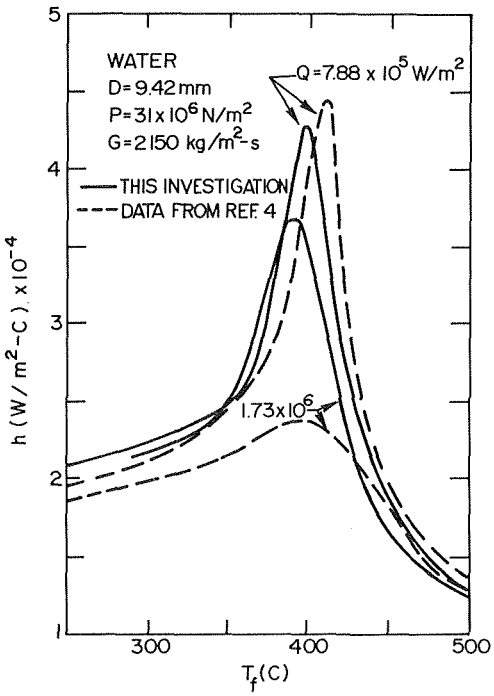

Fig. 3 Comparison of numerical results to experimental data of reference [4]—P_R = 1.40

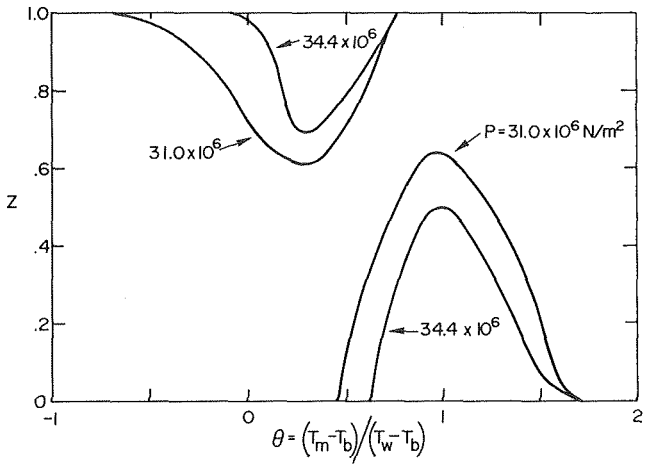

Fig. 4 Variation of Z with θ for use with equation (5); water

Table 1

$(T_m - T_b)/(T_w - T_b)$	T_z
<0	T_b
0–1.0	T_m
>1.0	T_w

this correlation could not be used at P_R = 1.028 since there were some regions for which no reference temperature between T_w and T_b gave a correlation.

Although attempts at obtaining a general correlation were not entirely successful the results showed some promise and indicated that some type of general correlation may be possible.

Results for Supercritical Carbon Dioxide

The second fluid studied was carbon dioxide. It was selected because a large amount of experimental data is available for heat transfer to near critical CO_2. The conditions at the critical point are T_c = 31.0°C and $P_c = 7.38 \times 10^6$ N/m^2.

The first series of runs was made for D = 4.57 mm and $P = 8.27 \times 10^6$ N/m^2 (P_R = 1.12). These conditions are identical to the test conditions of Bringer and Smith [6]. The ranges of heat fluxes and mass velocities considered were $Q = 3.15 \times 10^4$ to 2.36×10^5 W/m^2 and G = 378–2577 kg/m^{2}s. The data of reference [6] were correlated by using equation (1) with Nu and Re evaluated at a reference temperature, T_z, and Pr evaluated at the wall temperature. The reference temperature is defined in Table 1.

Bringer and Smith chose to retain the Re exponent, b, which Deissler had used for water. The coefficient, a, had to be increased to give a better fit. The resulting equation was

$$\mathrm{Nu}_z = 0.0375\ \mathrm{Re}_z^{0.77}\ \mathrm{Pr}_w^{0.55}$$

It was found however, that a better correlation could be achieved for their data by using a larger exponent on Reynolds number. The application of a least-squares curve fit subroutine to their data gave the equation

$$\mathrm{Nu}_z = 0.0092\ \mathrm{Re}_z^{0.885}\ \mathrm{Pr}_w^{0.55} \quad (6)$$

The best correlating equation for the analytical results calculated in this investigation is

$$\mathrm{Nu}_z = 0.0105\ \mathrm{Re}_z^{0.875}\ \mathrm{Pr}_w^{0.55} \quad (7)$$

For the range of Reynolds numbers considered, the maximum deviation between equations (6) and (7) is 2.5 percent. It is interesting to note that for both the experimental and analytical results, the scatter in the data from the best-fit correlations is approximately ±30 percent. One may conclude that the deviations of experimental data from the correlating equation is due less to experimental error than to the failure of that equation to accurately describe the physical process.

A final comparison was made to the experimental data and analytical predictions of Shiralkar and Griffith [17]. A comparison for one selected set of conditions is shown in Fig. 5 in the form of the wall temperature profile.[4] Although the trends predicted are accurate, the peaks in the curves are shifted somewhat. The predictions for h are particularly poor in the low enthalpy (i.e., upstream) region. There are several possible causes for this discrepancy. The most important is related to entrance effects. Shiralkar and Griffith point out that the downstream heat transfer coefficient and wall temperatures are strongly influenced by inlet enthalpy. Since they are primarily interested in the region past the peak in h, their inlet conditions are at wall temperatures above T_m and bulk temperatures slightly below T_m. These effects would presumably be eliminated if both T_b and T_w at inlet were below T_m. They have no data for these conditions, however.

An additional source of difficulty in the near critical region is the lack of sufficiently accurate property data. The extremely high peak in specific heat is a major source of error. There are signifcant differences in the thermal conductivity and viscosity data found in the literature. Calculations of heat transfer were made using various combinations of properties from different sources and significantly different results were found. The question of whether the analysis gives accurate results very close to the critical point is, therefore, left unanswered.

A correlation of the type used for H_2O was also obtained for CO_2. The plot of Z versus θ is given in Fig. 6. Note that these curves are quite similar to those shown in Fig. 4. This indicates that there is some hope of obtaining a single correlation which may be applicable to various fluids.

[4] The calculated curve for $Q = 1.89 \times 10^5$ W/m^2 is truncated since the wall temperature exceeded the limits of the fluid property subroutines.

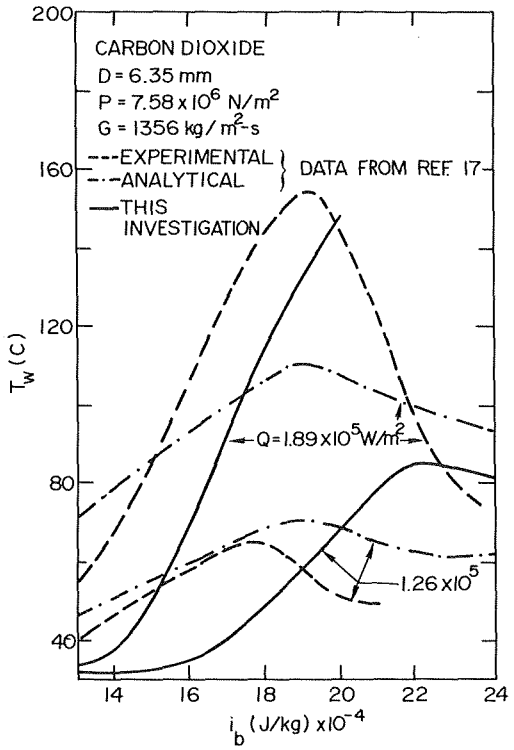

Fig. 5 Comparison of numercial results to experimental and analytical results of reference [17]

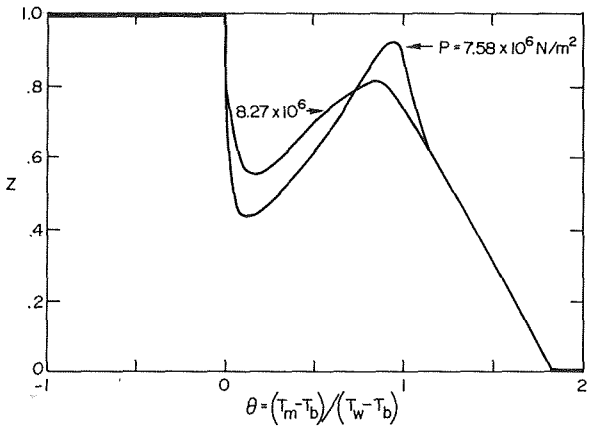

Fig. 6 Variation of Z with θ for use with equation (5); carbon dioxide

Conclusions

A numerical method has been developed for predicting heat transfer to near critical fluids in turbulent flow through circular tubes with constant wall heat flux. Agreement with experimental data is very good for water at reduced pressures down to 1.028 except for a narrow range of bulk temperatures very near the pseudocritical temperature. Agreement is also good for CO_2 at $P_R \geq 1.12$ but is in question for $P_R = 1.027$. The analysis does not give results which agree well with experimental data, however, for cases where the wall temperature at inlet is above the transposed critical temperature.

Correlations using fluid properties evaluated at a reference temperature which is a function of T_b, T_w, and T_m have been obtained. Their use should be restricted to the range of variables covered by the analysis and to cases where T_w at inlet is less than T_m.

The unusual behavior of the film coefficient in the near critical region is predicted quite well by the analysis. It is therefore concluded that free convection effects and boiling-like phenomena are not significant for the range of conditions investigated here. Inlet conditions do appear to have a significant effect on downstream heat transfer coefficients and wall temperatures. Further analytical and experimental studies should be made to study this effect.

References

1 Hendricks, R. C., Simoneau, R. J., and Smith, R. V., "Survey of Heat Transfer to Near Critical Fluids," NASA TN D-5886, Nov. 1970.

2 Dickinson, N. L., and Welch, C. P., "Heat Transfer to Supercritical Water," ASME Paper No. 57-HT-7.

3 Goldmann, K., "Heat Transfer to Supercritical Water at 5000 Psi Flowing at High Mass Flow Rates Through Round Tubes," *International Developments in Heat Transfer*, ASME 1963, pp. 561–568.

4 Swenson, H. S., Carver, J. R., and Kakarala, C. R., "Heat Transfer to Supercritical Water in Smooth-Bore Tubes," JOURNAL OF HEAT TRANSFER, TRANS. ASME, Series C, Vol. 87, No. 4, Nov. 1965, pp. 477–484.

5 Gunsen, W. E., and Kellog, H. B., "Engineering Application Technique for Supercritical-Pressure Heat-Transfer Correlations," ASME Paper No. 66-WA/HT-11.

6 Bringer, R. P., and Smith, J. M., "Heat Transfer in the Critical Region," *AIChE Journal*, Vol. 3, No. 1, Mar. 1957, pp. 49–55.

7 Wood, R. D., and Smith, J. M., "Heat Transfer in the Critical Region—Temperature and Velocity Profiles in Turbulent Flow," *AIChE Journal*, Vol. 10, 1964, p. 180.

8 Schnurr, N. M., "Heat Transfer to Carbon Dioxide in the Immediate Vicinity of the Critical Point," JOURNAL OF HEAT TRANSFER, TRANS. ASME, Series C, Vol. 91, No. 1, Feb. 1969, pp. 16–20.

9 Shiralkar, B. S., and Griffith, P., "Deterioration in Heat Transfer to Fluids at Supercritical Pressure and High Heat Fluxes," JOURNAL OF HEAT TRANSFER, TRANS. ASME, Series C, Vol. 91, No. 1, Feb. 1969, pp. 27–36.

10 Hess, H. L., and Kunz, H. R., "A Study of Forced Convection Heat Transfer to Supercritical Hydrogen," JOURNAL OF HEAT TRANSFER, TRANS. ASME, Series C, Vol. 87, No. 1, Feb. 1965, p. 41.

11 Hendricks, R. C., et al., "Correlation of Hydrogen Heat Transfer in Boiling and Supercritical Pressure States," *American Rocket Society Journal*, Vol. 32, 1962, p. 244.

12 Szetela, E. J., "Heat Transfer to Supercritical Hydrogen," *American Rocket Society Journal*, Vol. 32, No. 8, pp. 1289–1292.

13 Powell, W. B., "Heat Transfer to Fluids in the Region of the Critical Temperature," *Jet Propulsion*, Vol. 27, 1957, pp. 776–783.

14 McCarthy, J. R., Seader, J. E., and Trebes, D. M., "Heat Transfer to Supercritical Nitrogen Tetroxide at High Heat Fluxes and in Axially Curved Flow Passages," ASME Paper No. 67-HT-69.

15 Deissler, R. G., "Heat Transfer and Fluid Friction for Fully Developed Turbulent Flow of Air and Supercritical Water With Variable Fluid Properties," TRANS. ASME, Vol. 76, 1954, p. 73.

16 Goldmann, Kurt, "Heat Transfer to Supercritical Water and Other Fluids With Temperature Dependent Properties," *Chemical Engineering Progress Symposium*, Series II, Vol. 50, 1954, p. 105.

17 Shiralkar, B. S., and Griffith, P., "The Deterioration in Heat Transfer to Fluids at Supercritical Pressure and High Heat Fluxes," Report No. DSR 70332-55, Engineering Projects Laboratory, M.I.T., June 30, 1968.

18 Patankar, S. V., and Spalding, D. B., "A Finite Difference Procedure for Solving the Equations of the Two Dimensional Boundary Layer," *International Journal of Heat Mass and Transfer*, Vol. 10, 1967, pp. 1389–1411.

19 Patankar, S. V., and Spalding, D. B., Heat and Mass Transfer in Boundary Layers," Second ed., *Intertext Books*, London, 1970.

20 Van Driest, E. R., "On Turbulent Flow Near a Wall," *J. Aero. Sci.*, Vol. 23, 1956, p. 1007.

21 Sastry, V. S., "An Analytical Investigation of Forced Convection Heat Transfer in a Circular Duct at Supercritical and Near Critical Pressures," PhD thesis, Vanderbilt University, Nashville, Tenn., May 1974.

H. Ramm
Research Scientist.

K. Johannsen
Professor.
Mem. ASME

Heat Transfer Group,
Institut für Kerntechnik,
Technische Universität Berlin,
Berlin, Germany

A Phenomenological Turbulence Model and its Application to Heat Transport in Infinite Rod Arrays With Axial Turbulent Flow

The "turbulence-model" approach has been applied to solve the Reynolds equations of momentum and energy for an incompressible, steady-state, one-directional, hydrodynamically fully developed, turbulent internal flow. To close the turbulence equations, a phenomenological model of turbulent motion and energy transport has been developed which includes anisotropy effects. Predictions made for the turbulent diffusivities of heat in turbulent flow in a plain tube are found to be in good agreement with the experimental data over a wide range of Reynolds and Prandtl numbers. Corresponding results for infinite rod arrays with in-line flow also compare favorably with the few reliable data available.

Introduction

In recent years, a large volume of work on aspects of hydrodynamics and heat transfer has been devoted to noncircular ducts with axial forced convection because of their increasing technical importance in heat exchanger design. For laminar flow conditions, the momentum and heat transport processes in these channel geometries may be treated theoretically by analytical or numerical solution of the conservation equations with the appropriate boundary conditions. In principle, similar methods may also be used to investigate the turbulent flow case; however, additional information on the turbulent transport characteristics of the flow is required. At present, sufficiently complete and accurate knowledge of turbulence properties exists only for axially symmetric ducts of constant cross section (circular tube, plane duct, concentric annular duct). This unsatisfactory situation has led to the development of a considerable number of engineering approaches which make use of certain known turbulence characteristics of these simple flows, e.g., expressions for the eddy diffusivity of momentum in the radial direction of an annular flow, to predict momentum and heat transfer in noncircular channels. One of the disadvantages of all these methods is that further assumptions on turbulent momentum and heat transport have to be implied which require adjustment at almost any particular channel geometry to be investigated and/or are limited to certain ranges of the independent variables such as Reynolds and Prandtl number.

In principle, the indispensible knowledge on turbulent characteristics of noncircular channel flow and heat transfer could either be furnished by experimental investigations or supplied by theoretical studies based on statistical turbulence theory. The theoretical approach usually concentrates on a few of the statistical properties of turbulence which are supposed to obey simple laws of generation, dissipation and transport. These "models" consist of a set of differential equations and associated algebraic ones, the solutions of which simulate the real behavior of turbulent flows in important respects. Certainly, these theoretical approaches cannot get by without thorough empirical verification; however, if general enough, they may be able to significantly reduce the large efforts spent in experimental studies.

In the present paper, a phenomenological turbulence model is proposed which has been especially tailored to fluid flow and heat transfer in channels of axially constant cross section when the flow field is fully established. Its principal usefulness over a wide range of Reynolds and Prandtl numbers is first demonstrated by comparing results obtained for the eddy diffusivity for heat and temperature distributions in a circular tube with the available empirical data. Emphasis is then devoted to its application to predict momentum and heat transport in infinite rod arrays of regular arrangement. Special attention is given to the turbulent thermal transport properties at low Prandtl numbers characteristic for liquid metals where empirical information is still lacking.

Contributed by the Heat Transfer Division for publication in the Journal of Heat Transfer. Manuscript received by the Heat Transfer Division, January 15, 1974. Paper No. 75-HT-MM.

The Model

The "turbulence-model" approach has been applied to solve the Reynolds equations of momentum and energy for an incompressible, steady-state, one-directional, hydrodynamically fully developed, turbulent internal flow. With the usual assumptions of constant fluid properties and negligible axial energy transport and dissipation, the time-averaged momentum and energy equations in cylindrical coordinates become

$$\frac{1}{r}\frac{\partial}{\partial r}(r\nu\rho\frac{\partial u}{\partial r}) - \frac{1}{r}\frac{\partial}{\partial r}(r\rho\overline{u'v'}) + \frac{1}{r^2}\frac{\partial}{\partial\varphi}(\nu\rho\frac{\partial u}{\partial\varphi}) - \frac{1}{r}\frac{\partial}{\partial\varphi}(\rho\overline{u'w'}) = \frac{\partial p}{\partial z} \quad (1)$$

and

$$\frac{1}{r}\frac{\partial}{\partial r}(rk\frac{\partial T}{\partial r}) - \frac{1}{r}\frac{\partial}{\partial r}(rC_p\rho\overline{v'T'}) + \frac{1}{r^2}\frac{\partial}{\partial\varphi}(k\frac{\partial T}{\partial\varphi}) - \frac{1}{r}\frac{\partial}{\partial\varphi}(C_p\overline{\rho w'T'}) = C_p\rho u\frac{\partial T}{\partial z} \quad (2)$$

To describe the Reynolds shear stresses and turbulent heat fluxes in these equations, a phenomenological turbulence model has been formulated which is based on the principal ideas of Buleev's theoretical model of turbulent transfer in three-dimensional fluid flow [1, 2].[1]

Developing a phenomenological model rather than applying one of the more complex multiequation turbulence models [3] has been preferred in view of the greater potential for adjustment which a phenomenological model offers when restricted to the simple kind of flow under consideration.

Applying the usual suffix notation, where i, j, or k can be 1, 2, or 3, denoting components of velocity u in the r, φ, z directions, respectively, the general defining equations of the Reynolds shear stresses, $-\overline{\rho u_i'u_j'}$, and turbulent heat fluxes, $C_p\overline{\rho u_i'T'}$, may be written as

$$-\overline{\rho u_i'u_j'} = \lim_{t\to\infty}\frac{1}{t}\int_0^t(-\rho u_i'u_j')d\eta \quad (3)$$

and

$$C_p\overline{\rho u_i'T'} = \lim_{t\to\infty}\frac{1}{t}\int_0^t C_p\rho u_i'T'd\eta \quad (4)$$

[1] Numbers in brackets designate References at end of paper.

The phenomenological turbulence model is based on the assumption that the time integration in equations (3) and (4) may be replaced by a volume integration. Obviously, this assumption is valid for a steady-state, homogeneous flow only. For a shear flow, an importance function Ψ, similar to the Eulerian space correlation function, has to be introduced such that

$$\overline{\rho u_i'u_j'} = \int_{\text{Vol}} C_p\rho u_i'u_j'\Psi d\tau, \quad (5)$$

and

$$C_p\overline{\rho u_i'T'} = \int_{\text{Vol}} C_p\rho u_i'T'\Psi d\tau \quad (6)$$

To conveniently describe the momentum and heat transfer caused by random motion of fluid portions inside transient eddies it is supposed that fluid lumps depart in all directions with equal probability from the vicinity of every point M in the flow. Point M is considered in the coordinate system moving with the velocity of the average flow at point M_0. For the initial velocity V' of these fluid lumps occurring in the vicinity of point M, an assumption similar to Prandtl's mixing length hypothesis is introduced,

$$V' = \kappa L_{\min}\sqrt{\overline{(\frac{dV}{dn})^2}} \quad (7)$$

where $L_{\min}$ is the minimum macrolength. Generally, the minimum macrolength follows from

$$L_{ij,k} = \int_0^\infty R_{ij}dr_k \quad (8)$$

when evaluated for the direction of minimum wall distance. Only those fluid lumps will contribute to the statistical quantities at the considered point M_0, which arrive there and have not already lost all their momemtum and energy due to interaction with the surrounding on their path s from M to M_0. In analogy to Taylor's hypothesis, the interaction with the surrounding may mathematically be described in terms of attenuation functions, f_n. These "decay" functions are different for momentum and energy and may be found in the Appendix.

Assuming that the macroscales depend on locus and direction only, the following expressions for the Reynolds shear stresses and turbulent heat fluxes in the radial and tangential directions may be derived [4]

$$\overline{\rho u'v'} = -\kappa\rho\frac{\partial u}{\partial r}\int_\tau L_r\sqrt{\overline{(\frac{dV}{dn})^2}}f_0f_1s\Psi\cos^2(s,r)d\tau \quad (9)$$

Nomenclature

a = constant
C_p = specific heat at constant pressure
D = rod diameter, $(2R)$
d_{eq} = equivalent hydraulic diameter
d_τ = differential volume element
f_0, f_1, f_2 = attenuation functions
L = turbulent macrolength
P = pitch
Pr = Prandtl number
p = mean pressure
q'' = wall heat flux
R = rod radius
R_{ij} = Eulerian time-space correlation function
r = radial coordinate
Re = Reynolds number, $(\bar{u}d_{eq}/\nu)$
s = path of a turbulent eddy
T = fluid temperature
T^+ = dimensionless fluid temperature, $[|T - T_w|/(q''/\rho C_pu^*)]$
t = time
u = axial velocity component
u^+ = dimensionless axial velocity component, (u/u^*)
u^* = axial shear stress velocity, $(\tau_w/\rho)^{1/2}$
V' = relative velocity of a turbulent eddy
v = velocity component normal to the wall
w = velocity component tangential to the wall
y = distance from rod surface, $(r - R)$
y^+ = dimensionless wall distance (yu^*/ν)
z = axial coordinate
α = thermal diffusivity
ϵ = eddy diffusivity
η = dummy variable
κ = constant
ν = kinematic viscosity
ρ = fluid density
τ = wall shear stress
Φ = $u^*\hat{y}/\nu$
φ = angular coordinate
Ψ = importance function
ψ = angular coordinate, cf. Fig. 4

Superscripts and Subscripts

H = heat
M = momentum
max = maximum value of characteristic symmetry segment
min = minimum
r = radial direction
φ = circumferential direction
w = wall
$\bar{}$ = spatial or time average
$'$ = fluctuating component
$\hat{}$ = maximum distance (cf. Fig. 1)

$$\rho\overline{u'w'} = -\kappa\rho\frac{1}{r}\frac{\partial u}{\partial\varphi}\int_{\text{Vol}} L_\varphi\sqrt{\overline{\left(\frac{dV}{dn}\right)^2}}\, f_0 f_1 s\,\Psi\cos^2(s,\varphi)\,d\tau \quad (10)$$

$$C_p\rho\overline{v'T'} = -\kappa C_p\rho\frac{\partial T}{\partial r}\int_{\text{Vol}} L_r\sqrt{\overline{\left(\frac{dV}{dn}\right)^2}}\, f_0 f_2 s\,\Psi\cos^2(s,r)\,d\tau \quad (11)$$

$$C_p\rho\overline{w'T'} = -\kappa C_p\frac{1}{r}\frac{\partial T}{\partial\varphi}\int_{\text{Vol}} L_\varphi\sqrt{\overline{\left(\frac{dV}{dn}\right)^2}}\, f_0 f_2 s\,\Psi\cos^2(s,\varphi)\,d\tau \quad (12)$$

where

$$\frac{dV}{dn} = \sqrt{\left(\frac{\partial u}{\partial r}\right)^2 + \left(\frac{1}{r}\frac{\partial u}{\partial\varphi}\right)^2} \quad (13)$$

In equations (9)–(12), the macrolength is taken to be a function of both the space coordinates and direction. The macrolength in the radial direction is identical to L_{min} as introduced in equation (7). If the turbulence-energy equation is approximated neglecting all terms except those for production and dissipation, the macrolength may be determined from purely geometrical conditions. Buleev [1, 2] proposed the formula

$$\frac{1}{L_{min}} = \frac{1}{2a}\int_0^{2\pi}\frac{1}{l(\psi)}\,d\psi \quad (14)$$

where l is defined as the distance of the point M_0 from the surrounding wall(s) and a is constant ($a = 0.42$). In the present model, l is taken as the distance of the point M_0 from the boundaries of that surrounding flow area which is assumed to contribute to the turbulent properties prevailing at M_0 [5, 4]. Obviously, this "effective" flow area will be different for each channel geometry and, in general, limited by both channel walls and hypothetical surfaces. The construction of this effective area is merely based on intuitive grounds supported by physical considerations [4]. Only for the circular tube and the square duct, equation (14) has been applied directly, i.e., with $l(\psi)$ being the wall distance. For evaluating the macrolength in the tangential direction, a different procedure is applied which is also outlined in reference [4]. It is based on the principal assumption that, in view of equation (8), the macrolength in the tangential direction is primarily affected by the distance of point M_0 from the wall in this direction unless M_0 approaches the channel wall where the turbulent fluctuations are attenuated causing the macrolength to vanish with decreasing wall distance.

Having defined the macrolengths, the expressions (9)–(12) for the Reynolds shear stresses and turbulent heat fluxes may be introduced into the time-averaged momentum and energy equations (1) and (2), respectively. The resultant integro-differential equations of the velocity and temperature fields may then be solved numerically for a given set of boundary conditions.

In pertinent engineering approaches to evaluate heat transfer in turbulent channel flow, the Reynolds equation of energy transport is simplified by relating the turbulent energy flux terms to time-averaged temperature gradients thus defining turbulent diffusivities of heat in the various directions. In the radial and tangential direction these relations are written as

$$\overline{v'T'} = -\epsilon_{Hr}\frac{\partial T}{\partial r} \quad (15)$$

and

$$\overline{w'T'} = -\epsilon_{H\varphi}\frac{1}{r}\frac{\partial T}{\partial\varphi} \quad (16)$$

respectively. Introducing these definitions into equations (11) and (12), respectively, the following expressions for the turbulent thermal diffusivities are obtained

$$\epsilon_{Hr} = \kappa\int_{\text{Vol}} L_r\sqrt{\overline{\left(\frac{dV}{dn}\right)^2}}\, f_0 f_2 s\,\Psi\cos^2(s,r)\,d\tau \quad (17)$$

$$\epsilon_{H\varphi} = \kappa\int_{\text{Vol}} L_\varphi\sqrt{\overline{\left(\frac{dV}{dn}\right)^2}}\, f_0 f_2 s\,\Psi\cos^2(s,\varphi)\,d\tau \quad (18)$$

These relations may immediately be evaluated when the gradients of the velocity field in the various directions are known. It seems interesting to note that according to these equations the turbulent diffusivities are assumed to be independent of thermal boundary conditions but related to the space variables, macroscopic flow parameters, and molecular transport properties.

Results for Heat Transfer in Uniform Channels

For heat transfer of ordinary fluids in uniform channels, a sufficient amount of data is available for a comparison with theoretical results. Very satisfactory agreement between experimental results and predictions has already been demonstrated in previous papers [4, 6, 7, 8, 9] which places some confidence in the feasibility of the theoretical model developed. As an example, Fig. 1 compares the predicted eddy diffusivity for heat in the wall region of a circular tube with empirical data by several investigators which have been compiled by Hughmark [10, 11].

Reliable empirical knowledge on ϵ_H in liquid metals which might be used to also verify the applicability of the present prediction method at low Prandtl numbers ($Pr \ll 1$) is rather scarce. Comparison with recent data on ϵ_{Hr}/α for turbulent pipe flow of sodium, however, indicates that apparently very satisfactory agreement in both trend with Reynolds number and absolute values is obtained (Fig. 2). Note that data by Fuchs and Faesch [12] and Curve *A* of present results represent spatial averages over the entire cross section, while the experimental result by Sheriff, et al. [13] and Curve *B* results are for the pipe central region ($0 \le \tau/R \le 0.5$) only. It should be pointed out that there also was good agreement between Curve *B* and further experimental results by Sheriff, et al. [14]. At a given Reynolds number, ϵ_{Hr}/α in the center region is higher than the spatial average.

In Fig. 3, temperature distributions for various turbulent Reynolds numbers are plotted in terms of the dimensionless coordinates T^+ and y^+Pr and compared to Fuchs' [15] recent empirical data for sodium heat transfer in a pipe. Despite the fact that the data and predictions slightly differ in the quantities used for normalization—Fuchs [15] used Reichardt's data [16] while we applied our velocity field predictions—the agreement between prediction and data may be considered satisfactory. Note that T^+ is not a "universal" function of the dimensionless variable y^+Pr as assumed, for example, by Kirillov [17] and Taccoen [18] whose data are also plotted in Fig. 3.

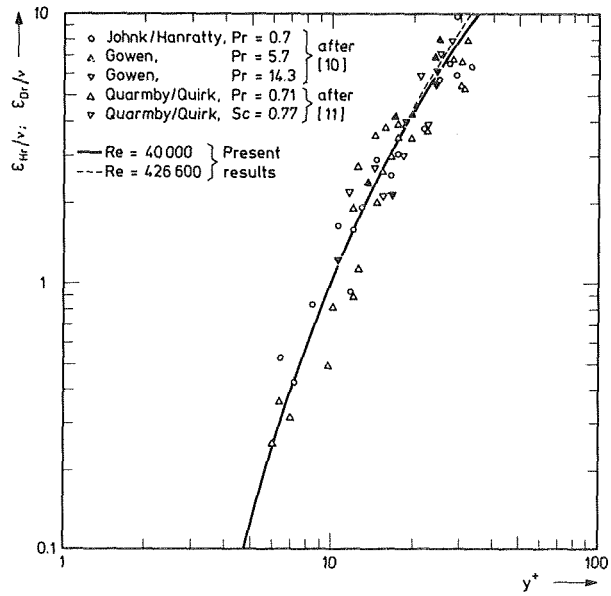

Fig. 1 Comparison of eddy diffusivities of heat and mass transfer for turbulent pipe flow

Application to Infinite, Bare Rod Arrays

Considering typical infinite rod arrays of equilateral triangular and square arrangement with in-line flow as schematically represented in Fig. 4, we may apply symmetry arguments and focus our attention to the cross-hatched characteristic areas. To apply the proposed turbulence model for predicting fluid flow and heat transfer in a channel of this nonuniform cross section, first the local behavior of macroscales in the radial and tangential directions has to be specified.

Estimation of Macrolengths. Measurements of the relevant space correlation functions R_{ij} in rod arrays that would permit evaluation of the macrolengths L_r and L_φ by use of equation (8) seem not to exist yet. Thus the present procedure to estimate the macrolengths in rod arrays is without any direct empirical justification. It rather has been derived on plausible physical considerations properly extrapolated from previous investigations of the less complex axisymmetric channel geometries where at least some useful empirical information on relevant turbulence properties is available. It is important to note, however, that the available data are still very limited and by far too inaccurate to permit any reliable conclusions with respect to the absolute magnitude of the macrolengths and their dependence on the relevant variables [4]. Thus, even in these comparatively simple cases, the principal soundness of the proposed procedure to estimate the macrolengths could be sufficiently proved only by demonstrating satisfactory agreement of model predictions and experimental results with respect to macroscopic quantities (velocities, temperatures, etc.) over a wide range of parameter values [4, 7, 8]. A similar indirect proof for the equilateral triangular and square rod arrays has also been very satisfactory. These results seem to indicate that the principal functional dependences are reasonably estimated by the procedure used. Nevertheless, the concept also requires direct empirical verification, and thus accurate measurements of turbulence properties in any type of channel geometry are highly desirable.

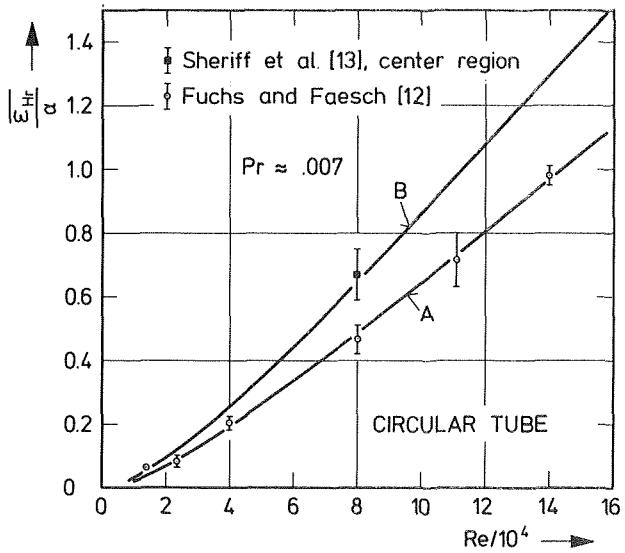

Fig. 2 Eddy diffusivity of heat in radial direction for turbulent sodium pipe flow

Macrolength in the Radial Direction. The macrolength in the radial direction, L_r, within a characteristic flow area of the infinite rod arrays (Fig. 4) is determined from equation (14). The length l is defined as the distance of M_0 from the boundaries of an effective flow area whose construction at an arbitrary angle φ is shown in Fig. 5 for each array. It may be noted that for $\varphi = 0$ the effective area reduces to that previously assumed for the plane duct [4].

Macrolength in the Tangential Direction. Estimating the macrolength L_φ, it is convenient to distinguish between the wall near region of the flow area where viscous forces prevail and the central region which is considered first. In the center of the circular tube, L_φ is equal to L_r for reason of symmetry. As measurements by Laufer [20] and Compte-Bellot [21] seem to indicate, this equality approximately exists at the center line of the plane duct as well. With regard to the rod array, one is completely left with his intuition. One might start his considerations from the fact that, in a regular square rod array, symmetry requires L_φ being equal to L_r at the subchannel centroid (point A in Fig. 4). In first approximation, this may be assumed to also hold for the triangular array. Further, considering the possible behavior of L_φ along the symmetry line $\overline{AB}$ of the characteristic flow area (Fig. 4), it seems almost equally reasonable to assume that either *(A)* the ratio L_φ/L_r = constant, or *(B)* $L_\varphi = L_r$ ($\hat{y}$, $\varphi = 30$ deg) = constant along this line. Option A presupposes that the turbulent behavior of the flow along line $\overline{AB}$ is similar to that along the center line of the plane

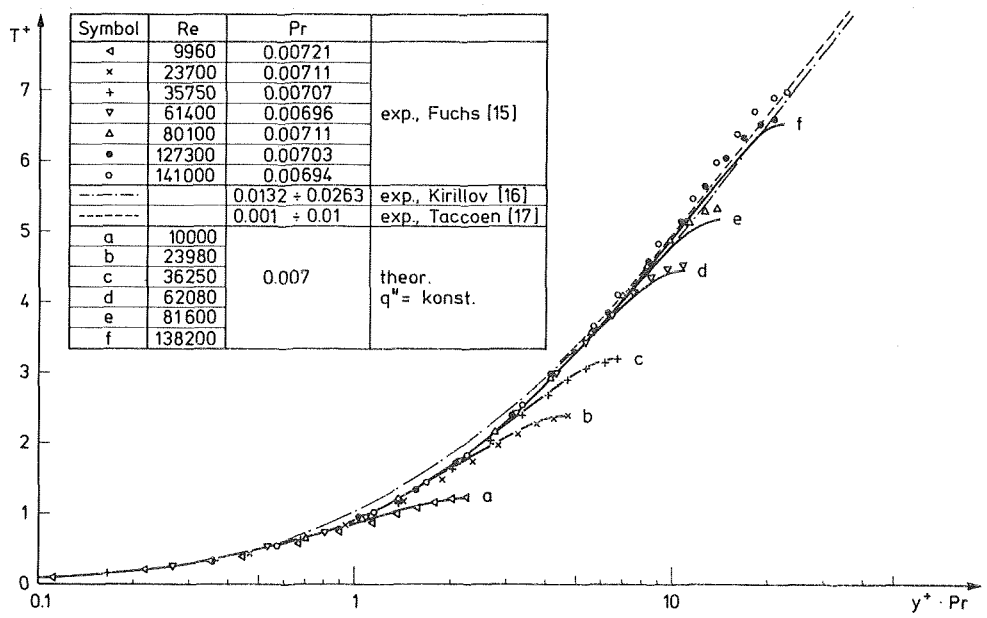

Fig. 3 Temperature profiles for turbulent sodium pipe flow in "universal" presentation

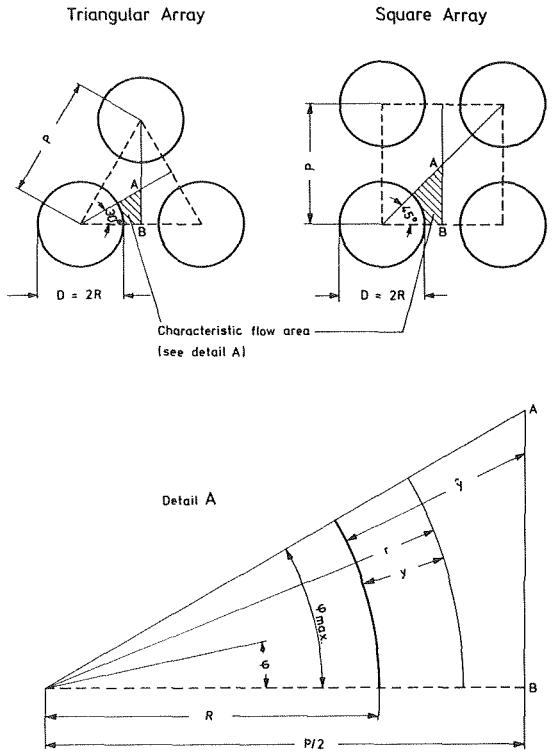

Fig. 4 Cross section of rod arrays having equilateral triangular and square arrangement

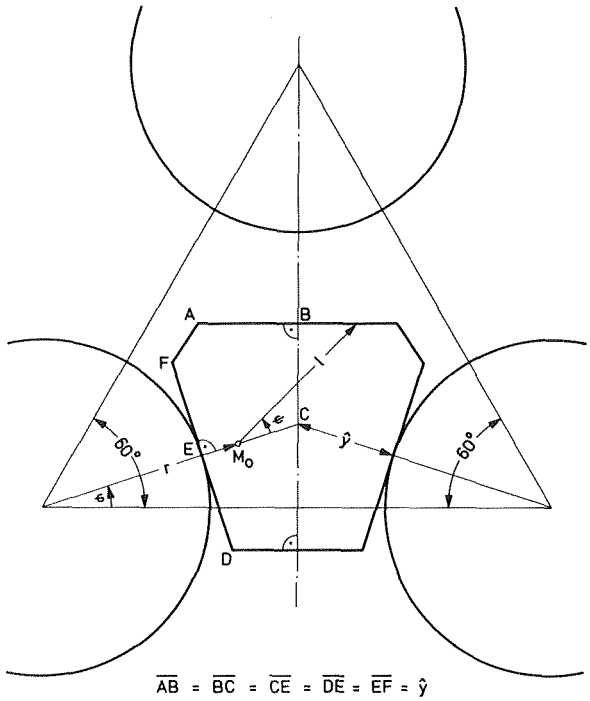

Fig. 5(a) Effective flow area of an infinite triangular rod array for estimating the macrolength in the tangential direction

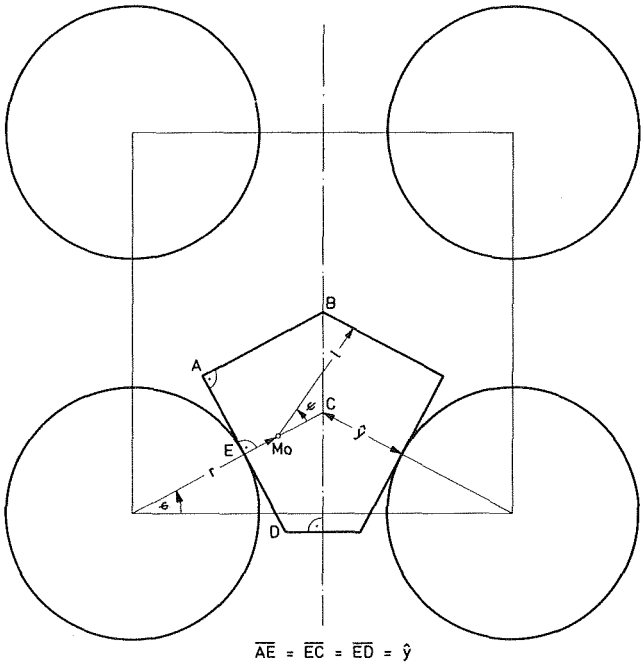

Fig. 5(b) Effective flow area of an infinite square rod array for estimating the macrolength in the tangential direction

duct. Option B may be deduced from the fact that all points along the line $\overline{AB}$ are rather far from any neighboring wall in the tangential direction and, thus, the relevant correlation function in that direction remains almost unaffected by the distance from the wall. Accordingly, the macrolength L_φ may be assumed constant along $\overline{AB}$. This assumption as well applies for the entire flow region except very close to the wall. In this region, one may postulate that the turbulent fluctuations are attenuated causing the macrolengths to vanish with decreasing wall distance. From purely theoretical considerations, it further follows that the ratio $(\epsilon_{M\varphi}/\epsilon_{M\tau})$ will approach infinity provided that $\lim_{y\to 0}(\partial u'/\partial y)$ and $\lim_{y\to 0}(\partial w'/\partial y)$ attain finite but nonzero values.[2] To estimate the limiting behavior of the macrolengths in the near wall region required to satisfy these postulates for L_φ, L_r, and $\epsilon_{M\varphi}/\epsilon_{M\tau}$ at the wall, one may apply Prandtl's mixing length hypothesis. The result is:

$$\lim_{y\to 0}(\partial L_\varphi/\partial y) = \infty.^{3}$$

These considerations have been combined in the following relations to approximately describe the tangential macrolength in an infinite rod array:

Option A:

$$L_\varphi = L_r(\hat{y}, \varphi)(y/\hat{y})^m \tag{19}$$

Option B:

$$L_\varphi = L_r(\hat{y}, \varphi_{max})(y/\hat{y})^m \tag{20}$$

where

$$m = 0.01/\ln(\Phi/25)$$

Unless indicated otherwise all results presented in this paper have been obtained using Option A for it gives conservative heat transfer results (see the following).

Results for Turbulent Transport Properties. The only published empirical data on local turbulent transport properties in rod arrays seem to be those by Kjellström [18, 19], who investigated turbulent flow of air in a triangular rod configuration of P/D = 1.22. A Reynolds number range from $1.5 \cdot 10^5$ to $3.7 \cdot 10^5$ was covered. The results obtained for the turbulent diffusivity of momen-

[2] In previous publications by the authors [6, 5, 7, 8], theoretical results for the eddy diffusivity ratios $\epsilon_{M\varphi}/\epsilon_{Mr}$ and $\epsilon_{H\varphi}/\epsilon_{Hr}$ have been presented which revealed a sharp maximum very close to the wall ($y^+ \approx 4$). This incorrect behavior was a consequence of an obviously erroneous assumption for L_φ/L_r in the near wall region. Fortunately, the present changes have virtually no effect on other results which thus are valid as previously presented (cf. also [22]).

[3] This implies that $\lim_{y\to 0}(\partial L_r/\partial y) = 0$ and $\lim_{y\to 0}(\partial^2 L_r/\partial y^2)$ = finite as suggested by van Driest's [23] mixing length formula.

tum in the radial direction are reproduced from reference [18] in Fig. 6 and compared to corresponding predictions. The distributions of ϵ_{Mr} as well as $\epsilon_{M\varphi}$, if made dimensionless by division with $u^*\hat{y}$, have been assumed by Kjellström to be independent of macroscopic turbulent flow parameters, and thus data points have been reported without identification with respect to Reynolds number of test run. Though scatter of data is considerable, the agreement of theory and experiment is satisfactory. The diffusivity first increases with distance from the wall, then passes through a maximum, and decreases as the local maximum velocity is approached. From the additional theoretical results for different P/D and Re presented in Fig. 6, it may be deduced that in fact, at highly turbulent conditions, the dimensionless ratio $\epsilon_{Mr}/u^*\hat{y}$ primarily depends on dimensionless wall distance only and is rather independent of Re number and angle φ. This behavior is not found with respect to tangential diffusivity, and hence plotting data in terms of $\epsilon_{M\varphi}/u^*\hat{y}$ versus $y/\hat{y}$ without stating the corresponding Reynolds number seems inadequate. Regarding Kjellström's data for $\epsilon_{M\varphi}/u^*\hat{y}$, however, this negligence certainly is of rather minor importance in view of their very large scatter which questions their statistical significance. Moreover, these results seem to be strongly affected by systematic errors connected with the test channel used (overall asymmetry, geometrical inaccuracies, flow disturbances and maldistribution from the inlet). Hence, no conclusions relative to the quality of model predictions can be expected from a comparison.

In Fig. 7, the eddy diffusivity for heat in both the radial and tangential direction is plotted versus relative wall distance $y/\hat{y}$ at the angles $\varphi = 0$ deg and 30 deg for a given set of the parameters P/D, Re, and Pr. The functional dependence of ϵ_H with wall distance is very similar to that experienced for ϵ_{Mr} (Fig. 6). As expected, the diffusivity is lowest in the gap region ($\varphi = 0$ deg) and increases toward the center of the subchannel. Curves A and B represent results which have been obtained using Option B to estimate the macrolength L_φ. It becomes evident that taking $L_\varphi \approx L_r(\hat{y}, 30 \text{ deg})$ almost across the entire flow area results in a substantial increase of the tangential eddy diffusivity in the gap region while the effect on the radial diffusivity is rather moderate. The differences between predictions according to Options A and B decrease with angle and are almost zero at $\varphi = 30$ deg. It further is observed that the diffusivity is strongly anisotropic. Plotting the ratio $\epsilon_{H\varphi}/\epsilon_{Hr}$ versus $y/\hat{y}$ reveals that the anisotropy continuously increases as the wall is approached. When using Option A to estimate L_φ, the ratio is almost unaffected by changes in φ and P/D, while Option B would yield a considerable increase of $\epsilon_{H\varphi}/\epsilon_{Hr}$ when φ and P/D de-

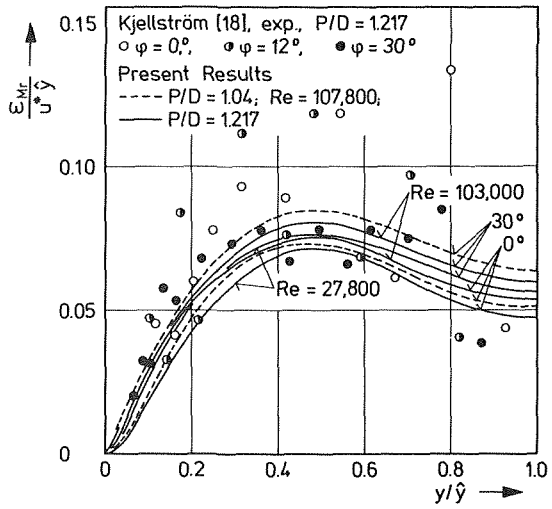

Fig. 6 Radial eddy diffusivity of momentum for in-line flow through triangular rod bundles

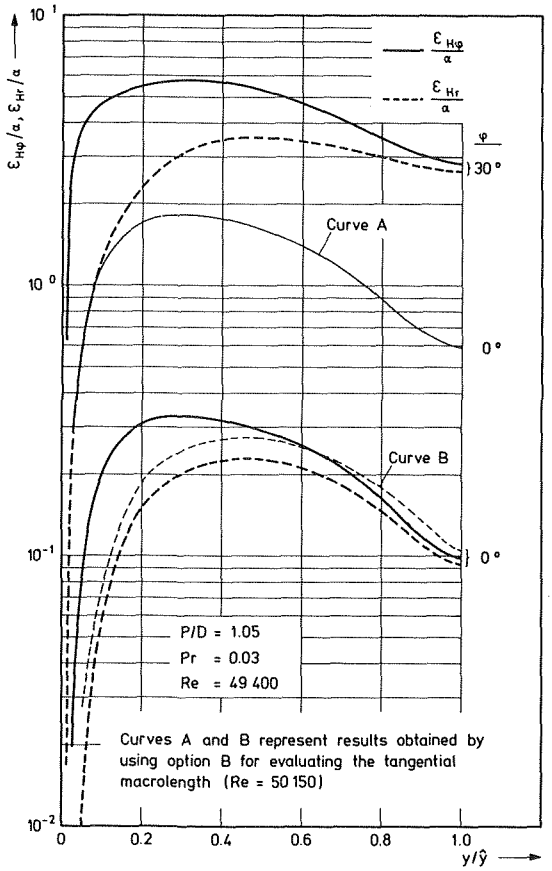

Fig. 7 Radial and tangential eddy diffusivity of heat for in-line flow through triangular rod bundles

Table 1 Predictions for average Nusselt numbers and maximum circumferential surface temperature variations for fully developed in-line flow through bare triangular rod arrays with two different thermal boundary conditions using different options to evaluate L_φ. Re = 50,410

	Pr	$\overline{Nu}$		$\frac{T_w(\varphi=0^\circ) - T_w(\varphi=30^\circ)}{\overline{T}_w - \overline{T}}$
		B.C.: T_w=const.	B.C.: q''_w=const.	
Option A	0.007	9.34	6.80	2.28
	0.7	105.4	95.85	1.075
	3.0	245.2	232.2	0.753
Option B	0.007	9.53	7.38	2.11
	0.7	108.7	105.2	0.623
	3.0	258.4	252.5	0.444

crease. The latter trend seems to be supported by current measurements; however, it cannot be excluded that, to a considerable extent, this result is due to net crossflow through the gap which has been observed in the test section.

The quantitative effect of the different options on heat transfer results is demonstrated in Table 1 for a triangular array of P/D = 1.1. In this table, calculated values are presented for the asymptotic Nusselt numbers and the maximum circumferential variation of the rod surface temperature, T_w (φ = 0 deg) − T_w (φ = 30 deg), normalized by the average temperature difference between the rod surface and the flowing fluid, $\bar{T}_w - \bar{T}$. Two sets of thermal boundary conditions, relative to the rod surface were used: *(a)* uniform temperature in the circumferential direction, with uniform heat flux in the axial direction, and *(b)* uniform wall heat flux in all directions. The Prandtl numbers studied are 0.007, 0.7, and 3, and the Reynolds number is 50,410. As expected, Nusselt numbers evaluated by use of Option B are generally significantly higher than those for Option A due to the increased circumferential transport assumed which leads to a flatter temperature field. For the same reason, Option B results for the boundary condition *(b)* come closer to those for boundary condition *(a)*. It is interesting to note that the corresponding reduction in the normalized circumferential wall temperature variation is rather pronounced for ordinary fluids, while it amounts only to about 7.5 percent for the low Prandtl number case. This is the result of the minor contribution of turbulent transport to the overall heat transfer. Since absolute values for the Nusselt numbers lie well within the range of experimental uncertainty definite conclusions relative to the validity of either option cannot be drawn. Hence, improvement of the present turbulence model as well as that of other ones heavily relies on future experimental investigations of high accuracy and rather bacic nature.

Acknowledgments

The financial support of the German Research Foundation is gratefully acknowledged. The authors would further like to express their appreciation to their colleague Horst Nagel for helpful suggestions and fruitful discussions. Thanks are also due to Mrs. M. Bauditt for preparing the graphs and Mrs. W. Jahnke for typing the manuscript.

References

1 Buleev, N. I., "Theoretical Model of the Mechanism of Turbulent Exchange in Fluid Flow," Report AERE-Trans 957, English translation from: *Teploperedacha,* USSR Academy of Science, Moscow, 1962, pp. 64–98.

2 Buleev, N. I., "Theoretical Model for Turbulent Transfer in Three-Dimensional Fluid Flow," Paper No. 329 presented at the *3rd UN Intern. Conf. on Peaceful Uses of Atomic Energy,* Geneva, 1964.

3 Spalding, D. B., "A Two-Equation Model of Turbulence," *VDI-Forsch.-Heft,* No. 549, 1972, pp. 5–16.

4 Ramm, H., "Theoretical Model for Determining Momentum and Heat Transport in Turbulent Channel Flows," TUBIK-31, Spring 1975, Institut für Kerntechnik, Technische Universität Berlin, Berlin, Germany (in German).

5 Ramm, H., and Johannsen, K., "Hydrodynamics and Heat Transfer in Regular Arrays of Circular Tubes," Paper No. I/5 presented at the *1972 International Seminar on Recent Developments in Heat Exchangers* of the Inter. Center for Heat and Mass Transfer, Trogir, Yugoslavia, 1972.

6 Ramm, H., and Johannsen, K., "Radial and Tangential Turbulent Diffusivities of Heat and Momentum Transfer in Liquid Metals," *Progress in Heat and Mass Transfer,* Vol. 7, 1973, pp. 45–58.

7 Gärtner, D., Johannsen, K., and Ramm, H., "Turbulent Heat Transfer in a Circular Tube With Circumferentially Varying Thermal Boundary Conditions," *International Journal of Heat and Mass Transfer,* Vol. 17, 1974, pp. 1003–1018.

8 Gärtner, D., "Theoretische Untersuchung des Wärmetransports bei erzwungener turbulenter Ringspaltströmung und örtlich beliebig veränderlichen Randbedingungen," Dr.-Ing. thesis, Technische Universität Berlin, Berlin, Mar. 1974.

9 Johannsen, K., and Ramm, H., "Note on Tangential Eddy Diffusivity in a Circular Tube," *International Journal of Heat and Mass Transfer,* Vol. 16, 1973, pp. 1803–1805.

10 Hughmark, G. A., "Heat and Mass Transfer in the Wall Region of Turbulent Pipe Flow," *AIChE Journal,* Vol. 17, 1971, pp. 51–56.

11 Hughmark, G. A., "Additional Note on Transfer in Turbulent Pipe Flow," *AIChE Journal,* Vol. 19, 1973, pp. 1054–1055.

12 Fuchs, H., and Faesch, S., "Measurement of Eddy Conductivity in Sodium," *Progress in Heat and Mass Transfer,* Vol. 7, 1973, pp. 39–43.

13 Sheriff, N., O'Kane, D. J., and Mather, B., "Measurement of Eddy Diffusivity of Heat in Sodium," *Heat Transfer 1970,* Proceedings of the 4th International Heat Transfer Conference, Paris-Versailles, 1970, Vol. 7, Paper No. MT 2.5.

14 Sheriff, N., et al., unpublished.

15 Fuchs, H., "Wärmeübergang an strömendes Natrium," EIR-241, Eidg. Institut für Reaktorforschung, Würenlingen, Switzerland, 1973.

16 Kirillov, P. L., "Generalization of Experimental Data on Heat Transfer in Molten Metals," *Sov. At. Energy,* Vol. 13, 1963, pp. 1103–1106.

17 Taccoen, L., "Contribution à l'Etude des Echanges Thermiques en Ecoulement Turbulent dans un Tube Lisse," *International Journal of Heat and Mass Transfer,* Vol. 10, 1967, pp. 1649–1660.

18 Kjellström, B., "Studies of Turbulent Flow Parallel to a Rod Bundle of Triangular Array," STU 68-263/U210, 1971, AB Atomenergi, Studsvik, Sweden.

19 Kjellström, B., "Studies of Turbulent Flow Parallel to a Rod Bundle of Triangular Array," AE-487, 1974, AB Atomenergi, Studsvik, Sweden.

20 Laufer, J., "Investigation of Turbulent Flow in a Two-Dimensional Channel," NACA Report 1053, 1951.

21 Comte-Bellot, G., "Ecoulement Turbulent entre Deux Parois Parallèles," Publications Scientifiques et Techniques du Ministere de l'Air No. 419, 1965.

22 Quarmby, A., "Calculations of the Effect of Tangential Eddy Diffusivity on a Non-Symmetric Turbulent Diffusion in a Plain Tube," *International Journal of Heat and Mass Transfer,* Vol. 15, 1972, pp. 866–870.

23 Van Driest, E. R., "On Turbulent Flow Near a Wall," *Journal of Aeronautical Sciences,* Vol. 23, 1956, pp. 1007–1011.

APPENDIX

Model Functions. Importance function, introduced in eqs. (5) and (6):

$$\Psi = \frac{(2/\pi)^{1/2}}{4\pi L_{\min} s^2} \exp\left(-0.5\,(s/L_{\min})^2\right) \tag{A. 1}$$

Attenuation functions, introduced in equations (9)–(12):

$$f_0 = \exp\left(-p_1 s\right) \tag{A. 2}$$

$$f_1 = \frac{1}{p_1 s}\left(1 - \exp\left(-p_1 s\right)\right) \tag{A. 3}$$

$$f_2 = f_1' \frac{1 + f_0'}{1 + f_0'^2} \tag{A. 4}$$

where

$$f_0' = \exp\left(-p_2 s\right); \qquad f_1' = \frac{1}{p_2 s}\left(1 - \exp\left(-p_2 s\right)\right);$$

$$p_1 = \frac{12\,\nu(1 + b_t)}{\kappa L_{\min}^3 (dV/dn)}; \qquad p_2 = \frac{12\,\nu(\mathrm{Pr}^{-0.75} + b_t)}{\kappa L_{\min}^3 (dV/dn)}$$

with κ = 4.48 and

$$b_t = \begin{cases} Q \cdot (y^+/5) & \text{for } y^+ \le 5 \\ Q & \text{for } 5 < y^+ \le 7 \\ Q \cdot \exp\left(-0.04\,(y^+ - 7)\right) & \text{for } y^+ > 7 \end{cases}$$

$$Q = 6.33 + 1.8\left(\log\left(u^* d_{eq}/2\nu\right) - 2.176\right).$$

H. Ramm
Research Scientist.

K. Johannsen
Professor.
Mem. ASME

Heat Transfer Group,
Institut für Kerntechnik,
Technische Universität Berlin,
Berlin, Germany

Prediction of Local and Integral Turbulent Transport Properties for Liquid-Metal Heat Transfer in Equilateral Triangular Rod Arrays

A theoretical method based on a phenomenological turbulence model has been applied to evaluate turbulent transport properties for liquid-metal heat transfer in bare equilateral triangular rod bundles. Results obtained for local distributions of thermal eddy diffusivity in the various directions are presented in terms of correlations. From a subsequent solution of the three-dimensional heat transfer problem between two characteristic interior subchannels under conditions characteristic for tracer-type mixing experiments, integral thermal mixing coefficients and thermal length scales have been evaluated. Results demonstrate that the basic concept of subchannel analysis treating molecular conduction and turbulent transport independently of each other tends to underestimate intersubchannel transport. The uncertainties which are involved in principal assumptions of the turbulence-model as well as in the available empirical results are discussed in some detail.

Introduction

Present designs for liquid-metal cooled fast breeder reactors (LMFBR) involve parallel flow past tightly packed cylindrical fuel pins arranged in symmetrical triangular arrays within hexagonal channels. The design of such fuel elements for optimum performance and safe operation under steady and transient conditions requires prediction of their thermal and hydraulic characteristics to a degree of accuracy which is far beyond what can be achieved by customary prediction methods using an equivalent diameter concept to arrive at bundle average parameters. Thus, better methods which are able to predict local flows and enthalpies (or temperatures) have been developed. Two basically different types of approaches may be distinguished: lumped parameter and distributed parameter methods.

In the lumped parameter methods, often referred to as subchannel analyses, the rod bundle is divided into a number of subchannels, whose boundaries are defined arbitrarily by appropriate fuel rod and duct surfaces and by imaginary lines drawn between rod centers. Then average subchannel parameters are evaluated solving the equations of continuity, momentum, and energy for each subchannel. The equations for each subchannel are coupled with those of its neighbors by intersubchannel transport of mass, momentum, and energy which is treated in terms of global (integral) transport coefficients ("mixing coefficients"). The main advantage of this concept is that large systems of complicated geometry can be treated, even in three dimensions and under transient conditions. However, the description of the system is rather rough due to the limited number and size of subchannels which can be included. Also, temperatures of fuel rods cannot be determined unless correlations for the "film heat transfer coefficient" are introduced as input data.

Distributed parameter methods essentially consist of solving the time-averaged Reynolds equations of momentum and energy transport for velocity and temperature distributions. Principally, these results may then be used to also evaluate integral parameters to feed into lumped parameter analyses. Application of these methods has been rather restricted, however, due to numerical and computer problems as well as lack of knowledge on local Reynolds shear stresses and turbulent heat fluxes in the various directions. These difficulties primarily arise from the complexity of general bundle geometry. Most of the effort has thus been to investigate bare rod assemblies applying different levels of sophistication with respect to input information on turbulent transport properties. Nevertheless, the geometrically simplified analyses may be considered as indispensible base technology, since significant further progress on local descriptions of rod bundles with grid-type and

Contributed by the Heat Transfer Division for publication in the JOURNAL OF HEAT TRANSFER. Manuscript received by the Heat Transfer Division January 15, 1974. Paper No. 75-HT-NN.

wire-wrap spacers can only be expected when the physical behavior of the more simple bare rod bundle is well understood and can be predicted with sufficient reliability. For instance, from special investigations of the effect of grid-spacers on fluid flow and heat transfer in otherwise bare rod bundles, one might be able to elaborate correction functions which, when applied to three-dimensional bare rod bundle predictions, will yield adequate results for bundles with grids. Considering the rather extensive number of local investigations on bare rod bundles in the last years and, especially, those by Eifler and Nijsing [1, 2],[1] it may be concluded that the mathematical procedures to locally predict turbulent flow and heat transfer in a finite bundle are in principle available. The problems are now concentrated in supplying the input information required to be fed into the mathematical procedures. In the most advanced approaches in turbulent fluid flow, this is information on turbulent transport properties for momentum and on secondary flow. The recent results of Eifler and Nijsing [1, 3], who have been successful in predicting fully developed turbulent velocity distributions, indicate that the status achieved at present can be considered satisfactory. In this context, it seems worth noting that introducing rather simple assumptions on secondary flow has proved sufficient to yield excellent results, while Rowe [4] estimated a surprisingly complex secondary flow pattern from his recent experimental investigations on turbulence structure in bare rod bundle arrangements. However, these estimates have merely been deduced from distortions of axial velocity and turbulence intensity maps measured by laser-Doppler anemometer. In view of the considerable uncertainty which presently still exists on the causes of secondary flow of second kind, this procedure seems somewhat premature. Moreover, it seems very unlikely that physical reasons could be found to explain why a fully developed, completely stabilized flow should assume such an extremely complex flow pattern.

For predicting turbulent heat transfer, knowledge of the velocity field including secondary flow as well as local turbulent diffusivities for heat is required. In liquid-metal heat transfer, secondary flow has a rather minor effect on temperature distribution compared to transport by molecular and turbulent diffusion as both our calculations and those of others [2, 3] have shown. Thus, at this time, specifying the thermal turbulent transport properties seems to be the bottleneck. Unfortunately, very little reliable information exists thus far. In view of the considerable difficulties to obtain this information from appropriate liquid-metal heat transfer experiments, we have emphasized developing a theoretical method to evaluate both local and integral thermal transport properties. This method, which has been described and discussed in a previous paper [5], consists in solving the Reynolds equations of momentum and energy for an incompressible, steady-state, one-directional, hydrodynamically fully developed, turbulent internal flow. The Reynolds equations are closed by a phenomenological turbulence model which has been especially adjusted to this rather simple kind of flow.

In this paper, results of this analysis are presented for liquid-metal in-line flow through bare equilateral triangular rod arrays of infinite extent (Fig. 1).[2] These results might particularly be useful to better understand the relevant transport processes in liquid-metal cooled rod bundles. This seems essential for achieving a physically sound description of transport in the near wall region of finite rod bundles where limiting design conditions usually occur.

Local Turbulent Transport Properties for Heat

The functional dependence of the eddy diffusivity for heat in both the radial and tangential direction with wall distance is very similar to that experienced for circular channels as demonstrated in Fig. 7 of reference [5]. Thus we may concentrate in this paper on results which typically exhibit the effect of pitch-to-diameter ratio, Reynolds number, and Prandtl number. The parameter ranges studied have been selected such that the operating conditions characteristic for liquid-metal cooled fast reactors are covered.

In heat transfer analyses, specification of turbulent thermal diffusivities is customarily being done by applying separate assumptions on ϵ_{Mr}/ν and appropriate diffusivity ratios, e. g.,

$$\frac{\epsilon_{Hr}}{\alpha} = \frac{\epsilon_{Mr}}{\nu}\left(\frac{\epsilon_{Hr}}{\epsilon_{Mr}}\right)\mathrm{Pr} \tag{1}$$

or

$$\frac{\epsilon_{H\varphi}}{\alpha} = \frac{\epsilon_{Mr}}{\nu}\left(\frac{\epsilon_{M\varphi}}{\epsilon_{Mr}}\right)\left(\frac{\epsilon_{H\varphi}}{\epsilon_{M\varphi}}\right)\mathrm{Pr} \tag{2}$$

whereby, due to lack of sufficient knowledge, the spatial variation of the latter is usually neglected and spatial averages are introduced. For two Prandtl numbers characteristic for liquid metals and different P/D ratios, Fig. 2 shows results for the average ratio of the radial turbulent diffusivities of heat and momentum as a function of Reynolds number. The ratio $(\epsilon_{Hr}/\epsilon_{Mr})$ for rod bundle configuration behaves very similarly to that experienced in tube

[1] Numbers in brackets designate References at end of paper.

[2] Unless indicated otherwise, all results presented in this paper have been obtained using Option A to describe the macrolength in the tangential direction (i.e., equation (19) of [5]) for it gives conservative results.

Nomenclature

B = correction function
C_p = specific heat at constant pressure
c = thermal conduction coefficient
D = rod diameter, $(2R)$
d_{eq} = equivalent hydraulic diameter
h = fluid enthalpy
L = mixing length scale or turbulent macrolength
m = flow rate
P = pitch
Pe = Péclet number
Pr = Prandtl number
q_i' = heat addition per unit length of rod i
R = rod radius
r = radial coordinate
Re = Reynolds number, $(\bar{u}d_{eq}/\nu)$
T = fluid temperature
u = axial velocity component
u^* = axial shear stress velocity, $(\tau_w/\rho)^{1/2}$
w = mixing flowrate or velocity component tangential to the wall
Y_{ij} = centroid distance
y = distance from rod surface, $(r - R)$
y^+ = dimensionless wall distance, (yu^*/ν)
z = axial coordinate
α = thermal diffusivity
ϵ = eddy diffusivity
μ = dynamic viscosity
ν = kinematic viscosity
ρ = density
τ_w = wall shear stress
Φ = $u^*\hat{y}/\nu$

Superscripts and Subscripts

H = heat
M = momentum
max = maximum value of characteristic symmetry segment
i, j = subchannel identification number
ij = subchannel connection i to j
r = radial direction
φ = circumferential direction
$\bar{}$ = spatial average
$'$ = turbulent transport component
$\hat{}$ = maximum distance (cf. Fig. 1)
∞ = asymptotic value
$*$ = simultaneous molecular and turbulent transport

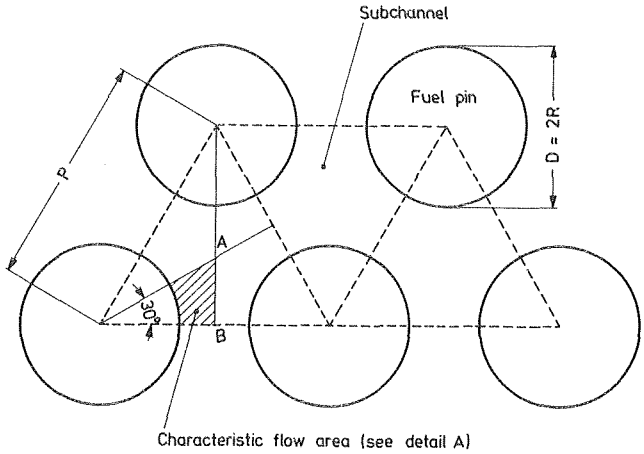

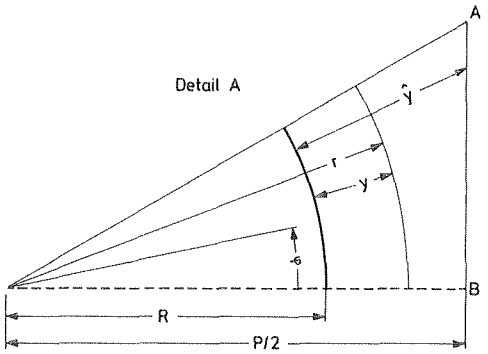

Fig. 1 Cross section of a five-rod portion of rod array having equilateral triangular arrangement

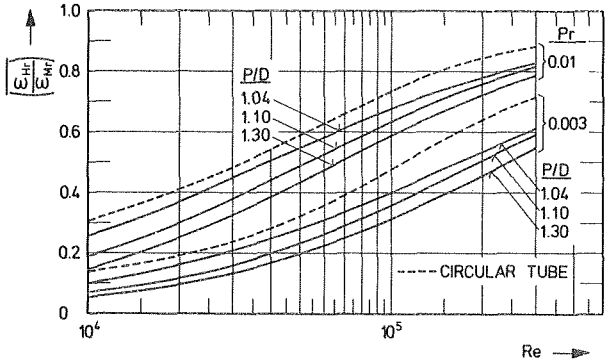

Fig. 2 Spatially averaged ratio of radial eddy diffusivity of heat to that of momentum

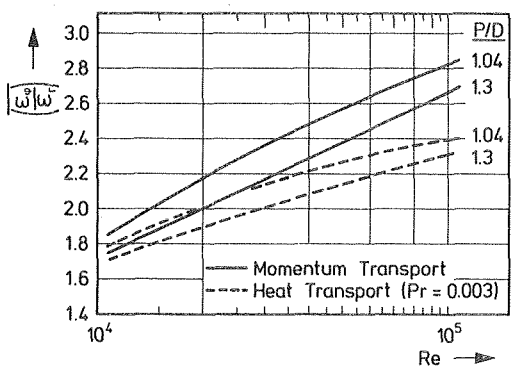

Fig. 3 Spatially averaged ratio of eddy diffusivity in tangential direction to that in radial direction

flow, absolute values being always less at given Re and Pr numbers. The differences increase with P/D ratio. Corresponding results for ϵ_H in the tangential direction are very similar in trends with relevant parameters, but less (up to about 10 percent) at a given set of P/D, Re, and Pr. The predicted effect of the same parameters on the anisotropy of momentum and heat transport in liquid metals becomes evident from Fig. 3. At constant P/D and Re, the anisotropy of turbulent momentum transport seems to be slightly greater than that of liquid-metal heat transport. The averaged ratio of $\epsilon_{H\varphi}/\epsilon_{Hr}$ increases with Reynolds and Prandtl number while changes in P/D ratio have the opposite effect.

To facilitate possible further use of the model, predictions correlations describing the behavior of ϵ_H/α in the low Prandtl number range have been developed. For fully developed turbulent longitudinal flow through infinite regular rod arrays, the eddy diffusivity for heat may be represented as a function of the following parameters:

$$\frac{\epsilon_H}{\alpha} = f(y/\hat{y}, \varphi, P/D, \mathrm{Re}, \mathrm{Pr}) \tag{3}$$

Examining the functional dependences of ϵ_H/α which briefly have been discussed in the previous paragraph, it is found that equation (3) for the various directions can be represented very satisfactorily by

$$\frac{\epsilon_{Hr}}{\alpha} = g_1(y/\hat{y}, \Phi, \Phi_{\max}) g_3{}^r(\mathrm{Re}, \mathrm{Pr}, P/D)\,\mathrm{Pr} \tag{4}$$

and

$$\frac{\epsilon_{H\varphi}}{\alpha} = g_1(y/\hat{y}, \Phi, \Phi_{\max}) g_2(y/\hat{y}, \Phi) g_3{}^{\varphi}(\mathrm{Re}, \mathrm{Pr}, P/D)\,\mathrm{Pr} \tag{5}$$

respectively. Note that the variable $\Phi = u^*\hat{y}/\nu$ is a function of Re, φ, and P/D. Φ attains its maximum value $\Phi_{\max}$ at $\varphi = 30$ deg (cf. Fig. 1). For the parameter ranges $P/D \geq 1.04$, $10^4 \leq \mathrm{Re} \leq 2 \cdot 10^5$, and $0.003 \leq \mathrm{Pr} \leq 0.03$, the following expressions for the functions g_1, g_2, and g_3 have been found to well correlate the theoretical results for infinite triangular rod arrays:

$$g_1 = (\Phi/\Phi_{\max})^n \Big(\sum_{m=1}^{8} A_{2m-1}(y/\hat{y})^{2m-1}\Phi - B\Big) \tag{6}$$

where

$$A_1 = 0.27920 \qquad A_7 = -0.26073$$
$$A_3 = -0.64217 \qquad A_9 = A_{11} = A_{13} = 0$$
$$A_5 = 0.68053 \qquad A_{15} = 0.004653$$

and

$$n = 3.29(\mathrm{Re}/1000)^{-0.86941}$$

The function $B(y^+, \mathrm{Re})$ represents a correction for the wall region which reverts, practically speaking, to zero when $y^+ \gtrsim 70$ ($\mathrm{Re} \geq 10^4$)

$$B(y^+, \mathrm{Re}) = (0.424 - 0.0118 \ln \mathrm{Re})(y^+)^{0.342+0.0704 \ln \mathrm{Re}} \times \exp\{(0.0844 - 0.01376 \ln \mathrm{Re})y^+\}$$

$$g_2 = (y/\hat{y})^q \tag{7}$$

where

$$q = -0.0923\{8.393 - \mathrm{arctg}[\exp(-\Phi/768.6 - 2.8)]180/\pi\}$$

$$g_3 = \frac{a\mathrm{Re}^b\,\mathrm{Pr}^c}{1 + a\mathrm{Re}^b\,\mathrm{Pr}^c} \tag{8}$$

where

$$a = P_1 + P_2 \exp(P_3(P/D-1))$$
$$b = R_1 + R_2 \exp(R_3(P/D-1))$$
$$c = 0.941254$$

The coefficients P and R for the r- and φ-direction to give the corresponding functions $g_3{}^r$ and $g_3{}^{\varphi}$, respectively, are

r-direction

$$R_1 = 0.0068 \qquad P_1 = 0.003988$$
$$R_2 = -0.37638 \qquad P_2 = 0.0654$$
$$R_3 = -31.01 \qquad P_3 = -34.873$$

φ-direction:

$$R_1 = 0.7444 \qquad P_1 = 0.015423$$
$$R_2 = -0.23416 \qquad P_2 = 0.170915$$
$$R_3 = -18.664 \qquad P_3 = -25.77$$

It should be pointed out that the structure of correlations (4) and (5) is similar to that of equations (1) and (2), respectively. g_2 represents the ratio $\epsilon_{M\varphi}/\epsilon_{Mr}$ while $g_3{}^r$ and $g_3{}^\varphi$ are identical to the spatially averaged ratios $\overline{(\epsilon_{Hr}/\epsilon_{Mr})}$ and $\overline{(\epsilon_{H\varphi}/\epsilon_{M\varphi})}$, respectively. Note that spatial averages of diffusitity ratios rather than ratios of averages have been correlated since, by this procedure, better representation of ϵ_H in the wall near region is obtained.

Integral Transport Properties

Results. Applying the usual assumptions of subchannel analysis to a bare rod bundle and assuming that pressure gradients between subchannels do not exist, the steady-state energy equation for subchannel i adjacent to N other subchannels may be written as [6]

$$m_i \frac{dh_i}{dz} = q_i' - \sum_{j=1}^{N} (h_i - h_j)\,\overline{w_{ij}{}'^H} - \sum_{j=1}^{N} (T_i - T_j)\,\overline{c_{ij}} \qquad (9)$$

where the quantities m, h, q', and T represent subchannel averages. The right-hand terms account for heat transfer from the fuel rod and thermal energy transfer between adjacent subchannels by turbulent diffusion and molecular conduction. Note that in equation (9) the different transport phenomena are assumed to act independently of each other. This assumption, however, is justified only if the competing effects are significantly different in magnitude which is not the case with respect to molecular and turbulent transport in liquid metals. As a result, the corresponding integral transport coefficients, $\overline{w_{ij}{}'^H}$ and $\overline{c_{ij}}$, cannot be determined separately from liquid-metal heat transfer experiments. Rather, only a combined coefficient, $\overline{w_{ij}{}^{*H}}$, can be determined. The appropriate energy equation to be used reads

$$m_i \frac{dh_i}{dz} = q_i' - \sum_{j=1}^{N} (h_i - h_j)\,\overline{w_{ij}{}^{*H}} \qquad (10)$$

All integral quantities of interest for characterization of thermal transport between subchannels as mixing flowrate and length scale may be evaluated from results of three-dimensional distributed parameter analyses [7].

Accordingly,

$$\frac{\overline{w_{ij}{}^{*H}}}{\mu} = -\frac{2}{T_i - T_j} \int_1^{P/D} \left[\frac{1}{\mathrm{Pr}} + \left(\frac{\epsilon_{H\varphi}}{\nu}\right)_{\varphi=0}\right]\left[\frac{1}{r/R}\frac{\partial T}{\partial \varphi}\right]_{\varphi=0} d(r/R) \qquad (11)$$

$$\overline{L_{ij}{}^{*H}} = \frac{\mu}{\overline{w_{ij}{}^{*H}}} \frac{4(P/D-1)\left[\frac{1}{\mathrm{Pr}} + \overline{\left(\frac{\epsilon_{H\varphi}}{\nu}\right)_{\varphi=0}}\right]}{Y_{ij}/D} \qquad (12)$$

To simulate typical tracer-type mixing experiments, calculations have been performed assuming the rods to be unheated and the flow of subchannels i and j initially at different but uniform temperatures. Under these conditions and for low Prandtl number fluids, the entrance region is rather short as demonstrated by Fig. 4. Here, characteristic results for the axial development of $\overline{w_{ij}{}^{*H}}$ are plotted. Note that the entrance length required to establish thermally fully developed flow increases with increasing Reynolds and Prandtl numbers and decreasing geometric spacing. As far as the behavior of the entrance length with variation in Reynolds and Prandtl number is concerned, the same trends have recently been found to occur when the slug flow approximation is employed for solving the problem [8]. Caution should be used in applying the present theoretical results for $\overline{w_{ij}{}^{*H}}$ to study entrance heat transfer in a liquid-metal cooled reactor fuel-rod bundle by use of a lumped-parameter analysis code. It is important to keep in mind that for practical reactor conditions, boundary conditions are quite different from those applied here. Hence the behavior of $\overline{w_{ij}{}^{*H}}$ in the entrance region will also be different from that shown in Fig. 4. In contrast to present conditions ("plane source" of heated fluid), rods i and j of an actual fuel rod bundle generate heat at different rates while initial fluid temperatures of both subchannels are identical. As a result, the thermal mixing flowrate $\overline{w_{ij}{}^{*H}}$ increases with axial distance from zero to an asymptotic value, while in the plane source case, $\overline{w_{ij}{}^{*H}}$ decreases from positive infinity to an asymptotic

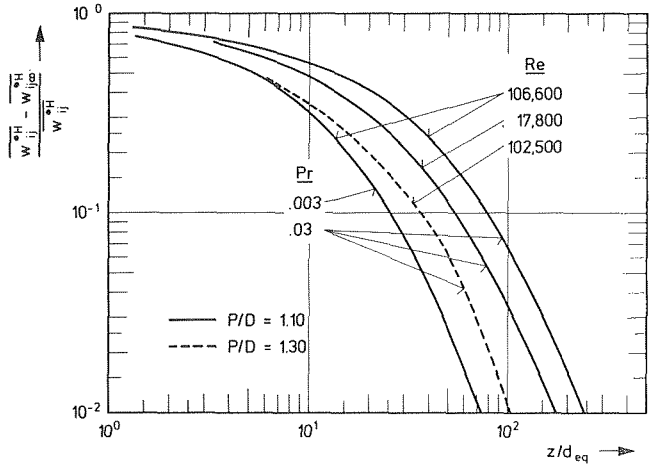

Fig. 4 Axial development of thermal mixing flowrate in infinite triangular rod array

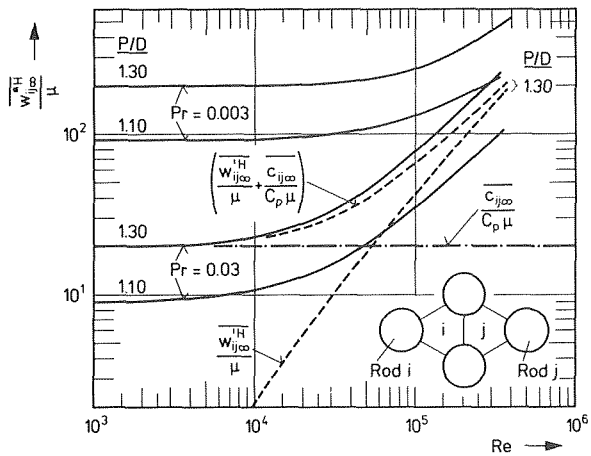

Fig. 5 Asymptotic thermal mixing flowrates for infinite triangular rod array

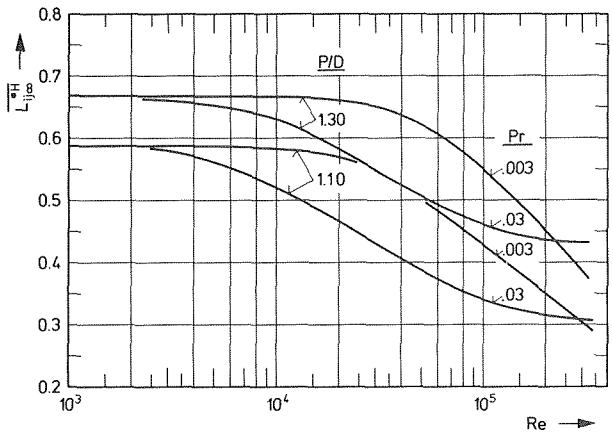

Fig. 6 Asymptotic thermal mixing length scale for infinite triangular rod array

value [2, 7, 8]. Asymptotic values, however, are not much different in magnitude [8]. Results for the asymptotic values of the thermal mixing flowrate and length scale are presented in Figs. 5 and 6. They clearly demonstrate that, for liquid metals, turbulent diffusion affects energy transfer between subchannels at medium and high Reynolds numbers only. Note the typical gradual increase of $\overline{w_{ij\infty}}^{*H}$ and decrease of $\overline{L_{ij\infty}}^{*H}$, respectively, with increasing Reynolds number.

To prove the validity of the basic assumption of subchannel analysis, namely that different modes of intersubchannel transport may be treated separately and summed up to give the overall transfer rate, special calculations at turbulent flow conditions have been performed for the cases of molecular conduction only and turbulent transport only. The procedure to follow simply is solving the Reynolds equation of turbulent energy transport (i. e., equation (2) of reference [5]) for the three dimensions of the subchannel i and substituting the result into equation (11) under the assumption that either the tubulent heat fluxes (or ϵ_H) or the molecular thermal conductivity is equal to zero. The resultant normalized transport coefficients obtained for a set of the parameters Pr, Re, and P/D are those for pure molecular conduction, $\overline{c_{ij}}/\mu C_p$, and pure turbulent transport, $\overline{w_{ij}'^H}/\mu$. A sample result for Pr = 0.03 and P/D = 1.3 is included in Fig. 5. The molecular conduction coefficient $\overline{c_{ij\infty}}/C_p$ is almost, i.e., within one percent, independent of Reynolds number and thus practically not affected by changes of the velocity field. The sum of $\overline{c_{ij\infty}}/C_p$ and $\overline{w_{ij\infty}'^H}$ is always less than the mixing flowrate evaluated for simultaneous molecular and turbulent transport ($\overline{w_{ij\infty}}^{*H}$), thus indicating that the procedure applied in subchannel analysis treating different transport processes independently of each other tends to underestimate intersubchannel transport, at least for low Prandtl number fluids.

The results of a parametrical study for the asymptotic thermal mixing flow rate $\overline{w_{ij\infty}}^{*H}$ (plane source case) have been correlated in terms of Péclet number, Prandtl number, and P/D ratio. In view of possible application to LMFBR situations, the following range of these parameters has been considered: $1.10 \leq P/D \leq 1.30$, $0.003 \leq$ PR ≤ 0.03, Re $< 350{,}000$. The approximate formula with constants which resulted from a least-square fit is given by:

$$\frac{\overline{w_{ij\infty}}^{*H}}{\mu}\,\mathrm{Pr} = \left[A_1 + A_2\frac{P}{D}\right] + \left[\left(B_1 + B_2\frac{P}{D}\right)\left(\frac{\mathrm{Pe}}{100}\right)^{C_1+C_2\,\mathrm{Pr}+C_3\,\mathrm{Pr}^2}\right] \quad (13)$$

$A_1 = -1.5$ $\quad C_1 = 1.411353$
$A_2 = 1.617$ $\quad C_2 = -40.0644$
$B_1 = -0.097879$ $\quad C_3 = 1006.44$
$B_2 = 0.106061$

It may be noted that the first right-hand term of equation (13) represents the contribution of molecular conduction to intersubchannel transport which is taken to be independent of Reynolds number. The second term, representing the effect of turbulent transport, depends on all three parameters (P/D, Pr, and Re) as expected in view of the results obtained for the local turbulent diffusivities for heat.

Discussion. The most striking feature of the results presented is probably the rather strong dependence of the mixing flowrate on the geometric spacing, P/D, as shown in Fig. 7 for Pr = 0.03 and 1.0. Changing P/D from 1.1 to 1.3 results in an increase of $\overline{w_{ij\infty}}^{*H}$ by a factor of more than two. As far as the contribution of turbulent transport is concerned, this seems to be in contradiction to previous experimental results on turbulent mixing in water and air flows where $\overline{w_{ij\infty}}^{*H}$ has been observed to be weakly dependent on P/D only. In a previous paper [7], we have attributed this divergence to both experimental errors, which tend to considerably increase the observed mixing flowrate, preferably at low values of P/D and Reynolds number, and the negligence of secondary flow in the theoretical model used for the predictions.

The accuracy of experimentally determined mixing flowrates,

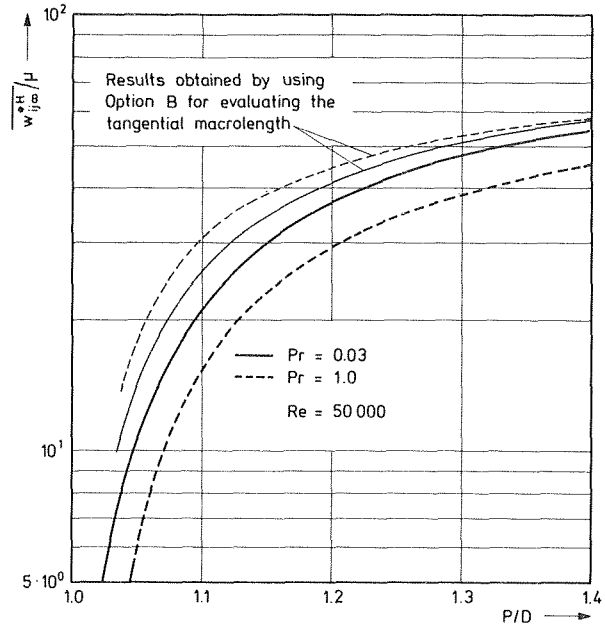

Fig. 7 Effect of geometric spacing on asymptotic thermal mixing flowrate for infinite triangular rod array

which shall be representative for infinite regular rod arrays, is probably most affected by intersubchannel cross-flow phenomena caused by flow disturbances at the entrance, undeveloped flow, or geometric asymmetry of the rod array with respect to the boundary between subchannels under consideration. Since geometric inaccuracies causing asymmetry will always be present in practice, it can be concluded that small secondary flows crossing the subchannel boundary will exist leading to a substantial increase of the intersubchannel transport observed. Kjellström [9] estimated that (for his geometry $P/D \approx 1.22$) crossflow of 0.3 percent of the axial bulk velocity would suffice to give a convective momentum transport of the same magnitude as the turbulent transport. Since crossflow velocities required to balance the turbulent transport decrease with decreasing P/D, only slightly imperfect test conditions will excessively increase the magnitude of the mixing flow rate observed at small P/D ratios. Increased incorrect convective transport thus counterbalances the actually reduced turbulent transport at low P/D and, as a result, only a weak dependence of $\overline{w_{ij}'}$ on P/D is experienced in the experiments.

On the other hand, present predictions of mixing flowrates can be expected to assume higher values in the low P/D range (P/D < 1.4, hence, to show less dependence on P/D) when secondary flows within the subchannel are included in the model and Option B is used to evaluate the tangential macrolengths, L (see reference [5]). This leads to higher predictions for ϵ_H, especially in the gap region. The effect of secondary flow within a symmetry element has been estimated by incorporating the method proposed by Nijsing and Eifler [1, 10] to predict secondary flow within the present model. For the empirical constant C_s in the relation proposed for the tangential velocity component w, a value of 0.415 rather than 0.57 has been applied. Sample calculations for a Reynolds number of $5 \cdot 10^4$ clearly revealed that, for infinite regular triangular rod arrays with P/D ratios above 1.10, the contribution of secondary flow to intersubchannel transport (plane source) is absolutely insignificant for both liquid metals and ordinary fluids. Only at P/D ratios less than 1.10 does secondary flow have some minor effect on intersubchannel transport which increases with the Prandtl number of the fluid.

On the contrary, applying Option B for estimating the tangential macrolengths in the turbulence model leads to a substantial increase of the thermal mixing flowrates calculated. According to equation (11), this is essentially due to the direct effect of increas-

ing $\epsilon_{H\varphi}$ in the gap region rather than to changes in the resultant velocity and temperature fields. In line with expectations, the mixing flow rate is most increased at low P/D ratios and high Prandtl number. Nevertheless, even at Pr = 1.0, $\overline{w_{ij\infty}{}^{*H}}$ still depends to quite an extent on the P/D ratio. Since Option B is certainly not very far from being an upper limit for L_{φ}, it seems to be very likely that, up to now, experimental errors have prevented the proper empirical verification of the dependence of $\overline{w_{ij\infty}{}^{*H}}$ on P/D.

Concluding Remarks

The main purpose of this theoretical study was to investigate the principal functional dependences of both local and integral turbulent transport properties for heat on the geometric and physical parameters which are characteristic for liquid-metal in-line flow through infinite bare rod arrays of regular triangular arrangement. It has been found [5] that the prediction of the eddy diffusivity in the lateral direction severely depends on the estimate for the tangential macrolength applied in the turbulence model. In an infinitely extended array, however, the temperature distribution is relatively invariant in the laterial direction and, thus, rather insensitive to changes of the transport properties in this direction. For practical applications, where results for infinite rod arrays are applied to study heat transport in the central region of fuel rod bundles, the present range of uncertainty in both tangential eddy diffusivity for heat as well as the thermal mixing flowrate can be tolerated.

Unfortunately, this does not hold for the periphery of finite (fuel) rod bundles where rather large lateral variations of fluid temperature may occur. Hence, it would be very desirable to reduce the margin of uncertainty (or the inherent conversatism) of the present model before extending its application to the peripheral bundle area. For this aim, however, extremely accurate measurements of the structure of turbulence in rod arrays or other noncircular ducts are indispensible.

Acknowledgments

The financial support of the German Research Foundation is gratefully acknowledged. The authors would further like to express their appreciation to R. Schönfeld for correlating the results, to Mrs. M. Bauditt for preparing the graphs and Mrs. M. Hein for typing the manuscript.

References

1 Eifler, W., and Nijsing, R., "Berechnung der turbulenten Geschwindigkeitsverteilung und Wandreibung in asymmetrischen Stabbündeln," *Atomkernenergie*, Vol. 18, 1971, pp. 189–197.

2 Nijsing, R., and Eifler, W., "Axial Development of Temperature Fields in Hexagonal Fast Reactor Fuel Rod Assemblies With Liquid Metal Cooling," *Proceedings of the International Meeting on Reactor Heat Transfer*, Karlsruhe, Germany, 1973, pp. 252–280.

3 Eifler, W., and Nijsing, R., "VELASCO-Velocity Field in Asymmetric Rod Configurations," EUR-4950 e, 1973, EURATOM, Ispra, Varese, Italy.

4 Rowe, D. S., "Measurement of Turbulent Velocity, Intensity and Scale in Rod Bundle Flow Channels," BNWL-1736, Battelle Pacific Northwest Laboratories, Richland, Wash., May 1973.

5 Ramm, H., and Johannsen, K., "A Phenomenological Turbulence Model and Its Application to Heat Transport in Infinite Rod Arrays With Axial Turbulent Flow," JOURNAL OF HEAT TRANSFER, TRANS. ASME, Series C, Vol. 97.

6 Rowe, D. S., "COBRA-III, A Digital Computer Programme for Steady State and Transient Thermal-Hydraulic Analysis of Rod Bundle Nuclear Fuel Elements," BNWL-B-82, Battelle Pacific Northwest Laboratories, Richland, Wash., 1971.

7 Ramm, H., Johannsen, K., and Todreas, N. E., "Single Phase Transport Within Bare Rod Arrays at Laminar, Transition and Turbulent Flow Conditions," *Nuclear Engineering and Design*, Vol. 30, 1974, pp. 186–204.

8 France, D. M., and Ginsberg, T., "Evaluation of Lumped-Parameter Heat Transfer Techniques for Nuclear Reactor Applications," *Nuclear Science and Engineering*, Vol. 51, 1973, pp. 41–51.

9 Kjellström, B., "Studies of Turbulent Flow Parallel to a Rod Bundle of Triangular Array," AE-487, 1974, AB Atomenergi, Studsvik, Sweden.

10 Nijsing, R., and Eifler, W., "A Rapid Analytical Approach for Determining Velocity and Temperature Distributions in Fuel Rod Bundles," in: *Reaktortagung 1970*, Dt. Atomforum, ed., pp. 9–12.

K. C. Cheng
R. C. Lin
J. W. Ou

Department of Mechanical Engineering,
University of Alberta,
Edmonton, Alberta, Canada

Graetz Problem in Curved Square Channels

Thermal entrance region heat transfer problem in curved square channels is solved by a numerical method for the two basic thermal boundary conditions of constant wall temperature and uniform wall heat flux by including the curvature ratio effect in the formulation as an independent parameter. Solutions are obtained for Pr = 0.1, 0.7, 5, 10.05 and 500 and Dean numbers ranging from 0–488. Local Nusselt number results are qualitatively similar to those reported in the literature for the case of curved circular pipes. The numerical results for the asymptotic Nusselt number agree well with the only experimental data available for the case of uniform wall heat flux. A correlation equation for the asymptotic Nusselt number is proposed.

Introduction

The problem of laminar forced convection heat transfer in the thermal entrance region of curved pipes or channels represents an extension of the classical Graetz problem and is one of the basic problems in convective heat transfer. However, it is only recently that the problem has been studied for the case of curved circular pipes [1, 2, 3, 4].[1] For the equally important case of curved rectangular channels, heat transfer results are reported so far only for the limiting conditions corresponding to the hydrodynamically and thermally fully developed flow fields [5, 6] under the thermal boundary condition of constant wall temperature gradient. Within the assumption of constant physical properties, the momentum and energy equations are uncoupled and the Navier-Stokes equations governing a steady fully developed laminar flow can be solved independently. For the fully developed laminar forced convection in curved rectangular channels, the theoretical solutions have previously been reported for the low Dean number regime [6] using numerical method and for the high Dean number regime [5] using boundary-layer approximation. Furthermore, the analyses reported so far are based on Dean's original formulation with the curvature ratio R/d $\gg$ 1. As a result, the curvature ratio does not appear as an independent parameter in the formulation.

Recently, a numerical analysis on the fully developed laminar flow in curved rectangular channels with the curvature ratio effect was reported for the aspect ratios (vertical height over horizontal width) 1,2,5 and 0.5 [7, 8]. For the case of a curved square channel, the numerical solution covers the Dean numbers ranging from 0 to about 700. It was found that an additional pair of counter-rotating vortex rolls appears near the central outer region of the channel in addition to the familiar secondary flow at a certain higher Dean number depending on the aspect ratio (see Fig. 1). This phenomenon appears to be consistent with Dean's centrifugal instability problem in a curved parallel-plate channel flow [9] where the flow is known to be unstable near the outer wall and stable near the inner wall. The numerical analysis and flow results are presented elsewhere [7].

In view of the occurrence of the two pairs of counter-rotating vortex rolls for some range of Dean numbers, it is desirable to

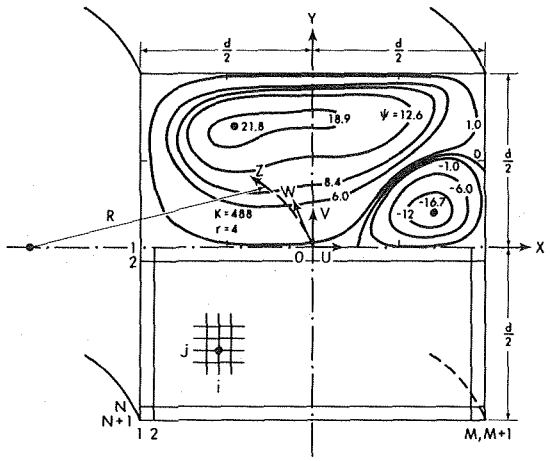

Fig. 1 Coordinate system for curved square channel and secondary flow pattern at $K = 488$ and $r = 4$

[1] Numbers in brackets designate References at end of paper.

Contributed by the Heat Transfer Division for publication in the JOURNAL OF HEAT TRANSFER. Manuscript received by the Heat Transfer Division, May 29, 1974. Paper No. 75-HT-EE.

study the Graetz problem in curved rectangular channels based on an accurate flow field obtained from the numerical solution of the full Navier-Stokes equations considering the curvature ratio effect.

The purpose of this paper is to present heat transfer results for the Graetz problem in curved square channels for the two basic thermal boundary conditions of constant wall temperature and uniform wall heat flux. An effort is made to study the heat transfer mechanism in the thermal entrance region and the results of the present analysis are compared against the available theoretical and experimental results for the limiting asymptotic case.

Analysis For Graetz Problem

Consideration is given to a steady fully developed laminar flow of viscous incompressible fluid in a curved square channel. The following assumptions are introduced to limit the scope of the analysis:

1 The physical properties are constant and free convection effect is negligible.

2 Axial conduction term is negligible compared with radial conduction term in the energy equation (Pe $\gtrsim$ 50).

3 Viscous dissipation is negligible and no other heat sources exist.

Using the toroidal coordinate system shown in Fig. 1, the governing equations for the steady fully developed laminar incompressible flow can be shown to be [7, 8]:

Continuity equation

$$\frac{\partial U}{\partial X} + \frac{\partial V}{\partial Y} + [1/(1 + \frac{X}{R})]\frac{U}{R} = 0 \tag{1}$$

Equations of motion

$$U\frac{\partial U}{\partial X} + V\frac{\partial U}{\partial Y} - \frac{W^2}{R(1 + X/R)} = -\frac{1}{\rho}\frac{\partial P}{\partial X} + \nu[\frac{\partial^2 U}{\partial X^2} + \frac{\partial^2 U}{\partial Y^2} + \frac{1}{R(1 + X/R)}\frac{\partial U}{\partial X} - \frac{U}{R^2(1 + X/R)^2}] \tag{2}$$

$$U\frac{\partial V}{\partial X} + V\frac{\partial V}{\partial Y} = -\frac{1}{\rho}\frac{\partial P}{\partial Y} + \nu[\frac{\partial^2 V}{\partial X^2} + \frac{\partial^2 V}{\partial Y^2} + \frac{1}{R(1 + X/R)}\frac{\partial V}{\partial X}] \tag{3}$$

$$U\frac{\partial W}{\partial X} + V\frac{\partial W}{\partial Y} + \frac{UW}{R(1 + X/R)} = -\frac{1}{(1 + X/R)}\frac{1}{\rho}\frac{\partial P}{\partial Z} + \nu[\frac{\partial^2 W}{\partial X^2} + \frac{\partial^2 W}{\partial Y^2} + \frac{1}{R(1 + X/R)}\frac{\partial W}{\partial X} - \frac{W}{R^2(1 + X/R)^2}] \tag{4}$$

The boundary conditions for the flow problem are

$$U = V = W = 0 \quad \text{at wall} \tag{5}$$

$$V = \partial U/\partial Y = \partial W/\partial Y = 0 \text{ along line of symmetry } Y = 0$$

The numerical solution of the foregoing set of equations for curved rectangular channels is presented elsewhere [7, 8] and the flow equations are given here for reference purpose.

The energy equation for the Graetz problem in a curved square channel is

$$U\frac{\partial T}{\partial X} + V\frac{\partial T}{\partial Y} + \frac{W}{(1 + X/R)}\frac{\partial T}{\partial Z} = \alpha[\frac{\partial^2 T}{\partial X^2} + \frac{\partial^2 T}{\partial Y^2} + \frac{1}{R(1 + X/R)}\frac{\partial T}{\partial X}] \tag{6}$$

The two wall boundary conditions to be considered are:

1 Constant wall temperature

$$T = T_0 \text{ at thermal entrance } (Z \leq 0) \text{ and } T = T_w \text{ at wall } (Z > 0) \tag{7}$$

2 Uniform wall heat flux

$$T = T_0 \text{ at thermal entrance } (Z \leq 0) \text{ and } q_w = k(\partial T/\partial N)_w \text{ for } Z > 0 \tag{8}$$

The other common boundary condition $\partial T/\partial Y = 0$ results from the symmetry about the plane of curvature ($Y = 0$).

After using the nondimensional variables as defined in Nomenclature, the energy equation and the boundary conditions become

$$\Pr(u\frac{\partial \theta}{\partial x} + v\frac{\partial \theta}{\partial y}) + \frac{w}{1 + x/r}\frac{\partial \theta}{\partial z} = \frac{\partial^2 \theta}{\partial x^2} + \frac{\partial^2 \theta}{\partial y^2} + \frac{1}{r(1 + x/r)}\frac{\partial \theta}{\partial x} \tag{9}$$

1 $\theta = 1$ at $z \leq 0$ and $\theta = 0$ at wall for $z > 0$ (10)

2 $\theta = 0$ at $z \leq 0$ and $\partial\theta/\partial n = 1$ at wall for $z > 0$

It is noted that Dean's original formulation corresponds to the case with $1/r = 0$. For the Graetz problem, the local Nusselt number variation in the thermal entrance region is of primary interest. It is useful to employ two means of evaluating the local Nusselt number $\mathrm{Nu} = \bar{h}d/k$ by considering either the local wall temperature gradient or the local axial overall energy balance. The results are given as

1 Constant wall temperature case

$$\mathrm{Nu}_1 = (\overline{\partial\theta}/\partial n)_w/\theta_b, \quad \mathrm{Nu}_2 = -\frac{1}{4\theta_b}(\overline{\frac{w}{1 + x/r}\frac{\partial \theta}{\partial z}}) \tag{11}$$

Nomenclature

d = width or height of a curved square channel
$\bar{h}$ = average heat transfer coefficient
K = Dean number, $\mathrm{Re}(d/R)^{1/2}$
k = thermal conductivity
M, N = number of divisions in X and Y-directions, or inward-drawn normal for N
Nu = local Nusselt number, $\bar{h}d/k$
n = dimensionless inward-drawn normal, N/d, or nth axial step
P = fluid pressure
Pr = Prandtl number, ν/α
q_w = uniform wall heat flux
R = radius of curvature of a curved square channel
Re = Reynolds number, $d\bar{W}/\nu$
r = dimensionless radius of curvature, R/d
T, T_w, T_0 = fluid temperature, constant wall temperature and uniform fluid temperature at thermal entrance $Z = 0$, respectively
U, V, W = velocity components in X, Y and Z-directions
u, v, w = dimensionless velocity components, $[(U, V)/(\nu/d), W/\bar{W}]$
$\bar{W}$ = average velocity
X, Y, Z = Cartesian coordinates
x, y, z = dimensionless coordinates, $[(X, Y)/d, Z/d(\mathrm{PrRe})]$
α = thermal diffusivity
θ = dimensionless temperature difference, $(T - T_w)/(T_0 - T_w)$ for constant wall temperature case and $(T - T_0)/(q_w d/k)$ for uniform wall heat flux case
θ_b, θ_w = bulk temperature, $\int\int_A \theta w dx dy / \int\int_A w dx dy$, and local wall temperature
ν = kinematic viscosity
ρ = density
ψ = dimensionless stream function [7, 8]

Subscript and Superscript

w = value at wall
$-$ = average value

2 Uniform wall heat flux case

$$\mathrm{Nu}_1 = 1/(\bar{\theta}_w - \theta_b),\ \mathrm{Nu}_2 = \frac{1}{4(\bar{\theta}_w - \theta_b)}\left(\overline{\frac{w}{1 + x/r}\frac{\partial\theta}{\partial z}}\right) \quad (12)$$

where the bar indicates an average value. For the case of uniform wall heat flux, one obtains also the following relationship by considering the energy balance over an axial length dZ.

$$\left(\overline{\frac{w}{1 + x/r}\frac{\partial\theta}{\partial z}}\right) = 4 \text{ or simply } \partial\theta_b/\partial z = 4 \text{ for } x/r << 1 \quad (13)$$

The two separate methods of calculating Nu together with equation (13) provide a means of assessing the accuracy of the numerical solution.

Numerical Solution

The velocity components, u, v, and w are available from the numerical solution of the fully developed flow problem [7, 8]. Consequently, the finite-difference grid-size $M \times N$ used for the energy equation is identical with that used in [7, 8]. With $u = v = 0$ and $1/r \approx 0$, the present Graetz problem is seen to be analogous to the unsteady state two-dimensional heat conduction problem. However, the convective terms due to secondary flow become increasingly important in equation (9) as the Dean or Prandtl number increases. The alternating direction implicit (ADI) method due to Peaceman and Rachford [10] is employed to transform equation (9) into a set of algebraic equations. By using the second order central difference approximations for all derivatives, a "tridiagonal" system of algebraic equations results at each of the half and full axial steps and can be solved by a Gaussian elimination method such as the Thomas algorithm.

The stability of the numerical solution depends on the grid-size ($M \times N$) and the axial step size (Δz). For the flow problem in curved square channel, the grid-size of 20×10 or occasionally 40×20 was found to be satisfactory from the viewpoint of the accuracy and computing time [7, 8]. For the present problem, the following scheme of axial step variation obtained by a trial and error method leads to a stable and convergent solution.

Axial step, n	Step size, Δz
$1 \sim 100$	5×10^{-5}
$101 \sim 450$	10^{-4}
$451 \sim 650$	2×10^{-4}
$651 \sim 850$	5×10^{-4}
$n > 851$	10^{-3}

The solution is terminated when the asymptotic solution is reached.

A discussion on the convergence of the numerical solution and the accuracy of the numerical result such as Nusselt number is now in order. The average quantities appearing in equations (11) to (13) are evaluated numerically using the Simpson's rule. A three-point finite-difference formula is used for $(\partial w/\partial n)_w$ and a first order backward difference approximation is employed for $\partial\theta/\partial z$. The accuracy of the numerical result can be assessed by noting the known asymptotic Nusselt numbers of 2.988 and 3.091 for the constant wall temperature and uniform wall heat flux cases, respectively, for the straight tube Graetz problem. The present calculations agree very well with the foregoing values. For the case of constant wall temperature, the difference in the values for Nu_1 and Nu_2 from equation (11) is found to be relatively large when the Prandtl or Dean number is large. For example, the asymptotic Nusselt number Nu_1 or Nu_2 deviates from the average value of Nu_1 and Nu_2 by 7 percent with $\mathrm{Pr} = 0.7$, $K = 368$ and $M \times N = 40 \times 20$. A similar observation is also noted in [2] for the case of curved circular pipes. By a further reduction in the mesh size and axial step, it is confirmed that the value from Nu_1 is a reasonably accurate one and consequently the numerical value from Nu_1 is used in presenting the result. It is suspected that the numerical evaluation for $\partial\theta/\partial z$ is a source of difficulty for Nu_2. For the case of uniform wall heat flux, Nu_1 and Nu_2 are seen to be identical if the relationship represented by equation (13) is used. It is also clear that the numerical evaluation of Nu_1 is easier and is thus expected to be more accurate than Nu_2. In contrast to the case of constant wall temperature, however, the two values from Nu_1 and Nu_2 are found to agree with each other very well. At a high Dean number $K = 488$, the deviation from the average value of Nu_1 and Nu_2 is found to be 3 percent with $\mathrm{Pr} = 0.1$ and $M \times N = 20 \times 10$. The numerical result also checks well with equation (13).

From the foregoing discussion, it is concluded that the numerical values from Nu_1 are sufficiently accurate for both thermal boundary conditions and the accuracy is considered to be within about 2 percent. The computing time required in obtaining a complete numerical result for each Dean number is approximately 3 min with $M \times N = 20 \times 10$ and 9 min with $M \times N = 40 \times 20$ on IBM360/67 system. All details of the numerical analysis are presented in [8].

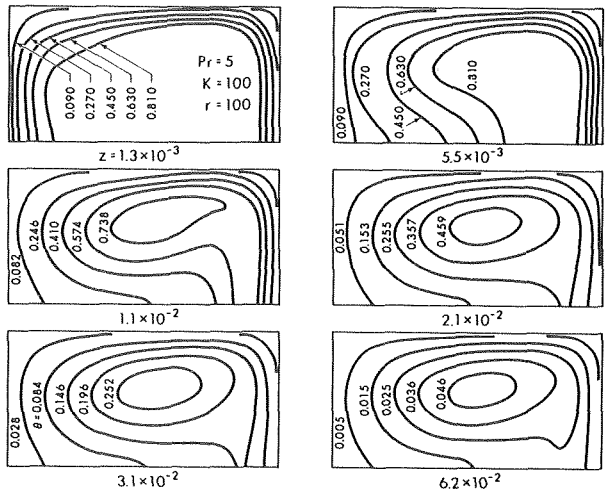

Fig. 2 Development of isothermals with Pr = 5, K = 100, r = 100 for constant wall temperature case

Results for Constant Wall Temperature Case

Temperature Field Development. In this study, the effect of the Dean number on the development of the temperature field in the thermal entrance region is of special interest in interpreting the Nusselt number behavior. The temperature profile developments along the central vertical and horizontal axes are presented in [8] for Dean numbers K = 14, 100, 368 and 488, respectively, with Pr = 0.7. It is pointed out that at K = 368 and 488 two pairs of counter-rotating vortex rolls already appear and the detailed secondary flow patterns are shown in [7, 8]. The development of

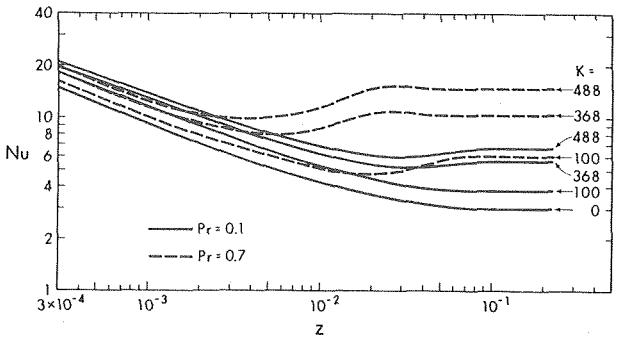

Fig. 3 Dean number effect on local Nusselt number variation with Pr = 0.1 and 0.7 for constant wall temperature case

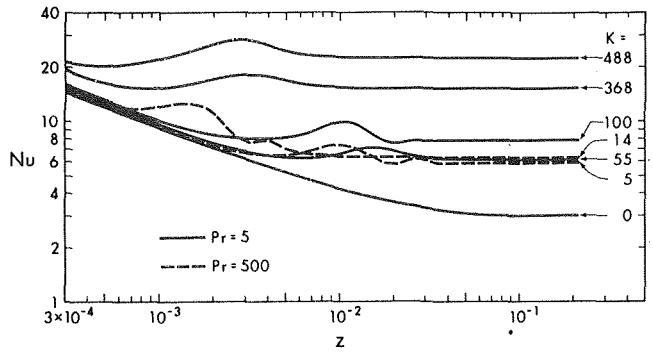

Fig. 4 Dean number effect on local Nusselt number variation with Pr = 5 and 500 for constant wall temperature case

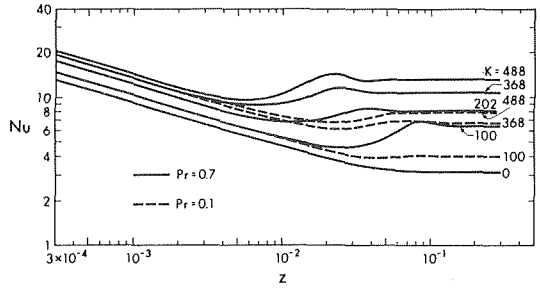

Fig. 6 Dean number effect on local Nusselt number variation with Pr = 0.1 and 0.7 for uniform wall heat flux case

isothermals at several axial locations for Pr = 5 and K = 100 is illustrated in Fig. 2. The development of the plume-like behavior in the form of warm current penetrating into the cold fluid core region and the appearance of the two eyes for the isothermals are noteworthy. The phenomenon is similar to that observed in curved circular pipes [1, 3, 4].

Heat Transfer Result. The variation of the local Nusselt number in the thermal entrance region is of practical importance and the results for Pr = 0.1, 0.7, 5, and 500 are shown in Figs. 3 and 4. At Pr = 0.1, the general feature of the local Nusselt number variation is similar to that of the classical Graetz solution (K = 0). The behavior for Nu can be explained from equation (9). At a small Prandtl number, the axial convective term dominates over the convective terms due to secondary flow. Consequently, the curves for the different Dean numbers are nearly parallel and straight in the Leveque solution region near the thermal entrance (z = 0) and the difference in Nusselt number values is caused by the different degree of the axial velocity profile distortion for w due to Dean number effect. For small Prandtl numbers, the role of the axial convective term in the energy equation is important.

At Pr = 0.7, one can clearly see the existence of a minimum Nusselt number value at some downstream location depending on Dean number. At this particular location, apparently the axial convective term and the convective terms due to secondary flow are equally important and one may conclude that the entrance effect due to the axial convective term in equation (9) and the secondary flow effect are in balance. After passing the minimum Nusselt number point, the secondary flow effect dominates over the entrance effect and the local Nusselt number continues to increase until the local maximum value is reached. Eventually, the Nusselt number value remains constant further downstream and one may conclude that the limiting asymptotic value corresponding to the fully developed temperature field is approached. It is clear that the thermal entrance length decreases with the increase of the Dean number.

A characteristically different kind of the Nusselt number behavior appears when the Prandtl number is large. For example, at Pr = 500 and a relatively low Dean number K = 14, the secondary flow is rather weak and the Nusselt number variation in the Leveque solution region is quite close to the case with K = 0. However, at some downstream position the secondary flow effect appears and the deviation begins. After reaching the local maximum value for Nu, an oscillatory phenomenon appears before a stationary value is reached further downstream. The present oscillatory Nusselt number phenomenon is similar to that reported in the earlier numerical studies [1, 2] for the case of curved circular pipes. It should be pointed out that a numerical difficulty was encountered for $K > 14$ with Pr = 500. From the foregoing discussion, one can also understand the Nusselt number behavior for Pr = 5 as shown in Fig. 4.

Results for Uniform Wall Heat Flux Case

The typical temperature profile developments are shown in [8]. The development of the isothermals and heat transfer results are shown in Figs. 5–7. For the case of uniform wall heat flux, the left-hand corner is found to be a hot spot and the wall temperature is highest there. When the temperature field becomes fully developed, the axial distributions for $\bar{\theta}_w$ and θ_b become parallel to each other [8] and correspondingly, the local Nusselt number approaches a constant value which depends on the Prandtl and Dean numbers. The thermal entrance length is of practical interest and can be determined by noting the above fact. The local Nusselt number result shows that for a given Prandtl number, the thermal entrance length decreases with the increase of the Dean number and the Prandtl number effect is also seen to be similar for a given Dean number. The roles of the Dean and Prandtl numers on heat transfer result are thus seen to be similar and this observation can also

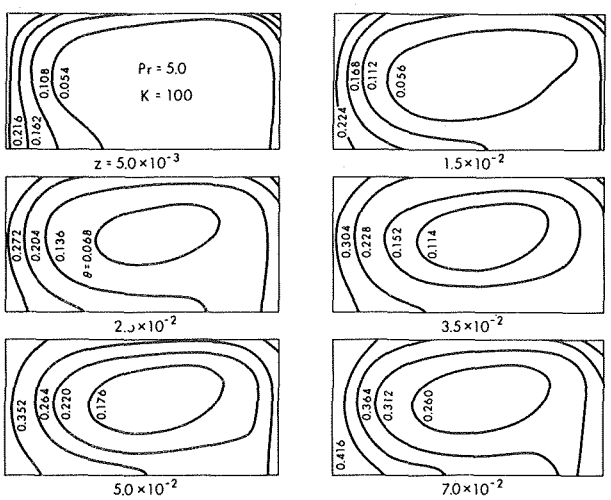

Fig. 5 Development of isothermals with Pr = 5, K = 100 for uniform wall heat flux case

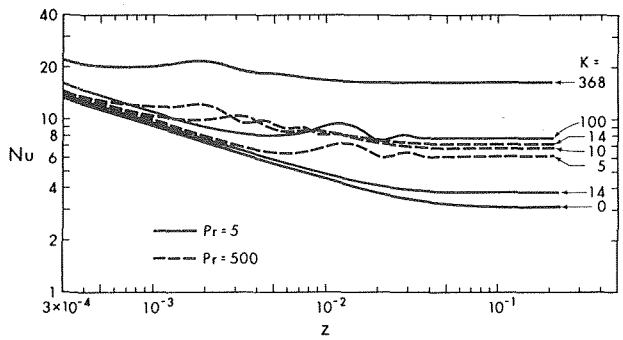

Fig. 7 Dean number effect on local Nusselt number variation with Pr = 5 and 500 for uniform wall heat flux case

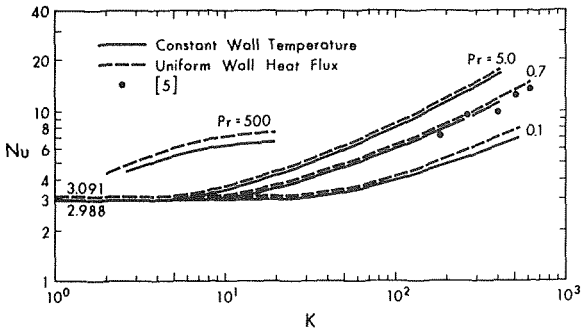

Fig. 8 Asymptotic Nusselt number results and comparison with experimental data

be seen from energy equation (9) where the relative magnitude of the convective terms due to secondary flow, $\mathrm{Pr}\cdot(u\partial\theta/\partial x + v\,\partial\theta/\partial y)$, increases with the increase of the Prandtl or Dean number.

The behavior of the local Nusselt number in the Leveque solution region and the occurrence of the minimum and local maximum Nusselt numbers can be explained. However, the oscillatory Nusselt number phenomenon before approaching an asymptotic value as shown in Fig. 7 cannot be explained readily. The reported numerical results [1, 2, 12] and the present work show qualitative agreement regarding the above mentioned oscillatory Nusselt number phenomenon. Apparently, the oscillatory phenomenon is caused by the convective terms due to secondary flow in the energy equation (9). Considering the fact that a numerical difficulty also arises when the Prandtl or Dean number is very large, one cannot rule out entirely the possibility that the phenomenon is caused by the numerical instability [3, 4]. At present it is not clear why the local Nusselt number in the case with the oscillatory phenomenon decreases faster along the axial direction than the case of a straight channel. Perhaps the question can only be answered by very precise and accurate experimental measurements. However, the oscillatory phenomenon is perhaps of theoretical interest only and in practical applications the asymptotic Nusselt number is important when Prandtl or Dean number is large.

Asymptotic Nusselt Number Results

The asymptotic Nusselt number is of practical importance and the numerical results for the two thermal boundary conditions are listed in [8] and are plotted in Fig. 8. The experimental data [5] for the case of uniform wall heat flux with Pr = 0.71 are also shown there for comparison. The agreement with the present analysis is seen to be reasonable confirming the good accuracy of the numerical analysis noted earlier. The difference between the two thermal boundary conditions is seen to be relatively small for Pr = 0.7 and 5. In view of this fact, the numerical results for the two boundary conditions were correlated by the following equation within a maximum deviation of 12 percent using the least-squares method.

$$\mathrm{Nu} = 0.152 + 0.627(K^{1/2}\mathrm{Pr}^{1/4}),\quad 0.7 \le \mathrm{Pr} \le 5,\quad 14 \le K \le 500 \qquad (14)$$

The parameter $(K\mathrm{Pr}^{1/2})$ is based on the earlier study [11] for curved circular pipes and may be justified for the present simple correlation.

Concluding Remarks

1 The present analysis includes the curvature ratio effect in the formulation. However, the recent work [13] for the fully developed laminar forced convection in curved circular tubes with the thermal boundary condition of axially uniform wall heat flux and peripherally uniform wall temperature concludes that the curvature ratio parameter has a negligible effect on the average Nusselt number in the range of R/a = 10–100. For the present problem involving curved square channels, the curvature ratio effect on Nu is also expected to be negligible for $r \gtrsim 10$.

2 The present numerical results reveal an oscillatory or cyclic Nusselt number behavior before reaching an asymptotic value when the Prandtl or Dean number is large. The phenomenon is similar to that observed in curved circular pipes [1, 2, 12]. An attempt was made to clarify the heat transfer mechanism particularly the Prandtl and Dean number effects in the thermal entrance region of curved square channels.

3 In order to limit the scope of the investigation, the aspect ratio effect on the present convective heat transfer problem in curved rectangular channels was not studied. However, the analysis can be made by using the flow fields reported in [7, 8].

Acknowledgement

This work was supported by the National Research Council of Canada through Grant NRC A1655. Thanks are also due to the editor and referees for their suggestions leading to the editorial revision of the original manuscript.

References

1 Dravid, A. N., Smith, K. A., Merrill, E. W., and Brian, P. L. T., "Effect of Secondary Fluid Motion on Laminar Flow Heat Transfer in Helically Coiled Tubes," *AIChE Journal*, Vol. 17, 1971, pp. 1114–1122.

2 Tarbell, J. M., and Samuels, M. R., "Momentum and Heat Transfer in Helical Coils," *The Chemical Engineering Journal*, Vol. 5, 1973, pp. 117–127.

3 Akiyama, M., and Cheng, K. C., "Laminar Forced Convection in the Thermal Entrance Region of Curved Pipes with Uniform Wall Temperature," *The Canadian Journal of Chemical Engineering*, Vol. 52, 1974, pp. 234–240.

4 Akiyama, M., and Cheng, K. C., "Graetz Problem in Curved Pipes With Uniform Wall Heat Flux," *Applied Scientific Research*, (in press).

5 Mori, Y., Uchida, Y., and Ukon, T., "Forced Convective Heat Transfer in a Curved Channel With a Square Cross Section," *International Journal of Heat and Mass Transfer*, Vol. 14, 1971, pp. 1787–1805.

6 Cheng, K. C., and Akiyama, M., "Laminar Forced Convection Heat Transfer in Curved Rectangular Channels," *International Journal of Heat and Mass Transfer*, Vol. 13, 1970, pp. 471–490.

7 Cheng, K. C., Lin, R. C., and Ou, J. W., "Fully Developed Laminar Flow in Curved Rectangular Channels," To be published in the *Journal of Fluids Engineering*, TRANS. ASME.

8 Lin, R. C., "Fully Developed Laminar Flow and Graetz Problem in Curved Rectangular Channels," MSc thesis, University of Alberta, Edmonton, Alberta, Canada, 1974.

9 Stuart, J. T., "Hydrodynamic Stability," Laminar Boundary Layers, L. Rosenhead, ed., Oxford University Press, 1963, p. 505.

10 Peaceman, D. W., and Rachford, H. H., "The Numerical Solution of Parabolic and Elliptic Differential Equations," *Journal of the Society of Industrial and Applied Mathematics*, Vol. 3, 1955, pp. 28–41.

11 Akiyama, M., and Cheng, K. C., "Boundary Vorticity Method for Laminar Forced Convection Heat Transfer in Curved Pipes," *International Journal of Heat and Mass Transfer*, Vol. 14, 1971, pp. 1659–1675.

12 Patankar, S. V., Pratap, V. S., and Spalding, D. B., "Prediction of Laminar Flow and Heat Transfer in Helically Coiled Pipes," *Journal of Fluid Mechanics*, Vol. 62, 1974, pp. 539–551.

13 Kalb, C. E., and Seader, J. D., "Heat and Mass Transfer Phenomena for Viscous Flow in Curved Circular Tubes," *International Journal of Heat and Mass Transfer*, Vol. 15, 1972, pp. 801–817.

M. J. Lewis
Abteilung fur die Sicherheit der Kernanlagen,
Wurenlingen, Switzerland

An Elementary Analysis for Predicting the Momentum- and Heat-Transfer Characteristics of a Hydraulically Rough Surface

A simple model is presented which approximates the turbulent shear flow over a well-defined rough surface as a series of attached and separated flow regions. An elementary analysis applied to the model provides values for the well-known momentum- and heat-transfer roughness functions $R(h^+)$ and $g(h^+, Pr)$, respectively. In order to use the calculation method the exact shape and distribution of the roughness elements are required together with a form drag coefficient and a characteristic separation length. These may be found in the literature for many roughness shapes of interest.

Introduction

The purpose of this paper is to present an analytical model for the flow over a rough surface. This model complements the work of Kays [1],[1] Kacker [2], Lavalee and Popovitch [3], and Perry, et al. [4]. It fills the gap between the wholly empirical treatment of rough surfaces [5, 6] and the extensive investigations on single elements [7]. The analysis provides a quick and simple means of evaluating or optimizing rough surfaces [8], it should help to avoid unnecessary and costly experiments [9], and it will provide a framework for more sophisticated methods.

A simple surface—equally spaced, rectangular ribs—is considered and the flow is represented by a series of attached and separated flow regions. For widely spaced roughness the flow reattaches between the elements, but for closely spaced roughness the flow does not reattach in the gaps and each element shields the one downstream. Wall shear stresses for the attached flows are determined from an assumed velocity profile, a logarithmic law-of-the-wall [10] for a smooth surface, which also provides the dynamic pressure for the form drag [11] of each element. This dynamic pressure is reduced by the shielding effect of closely spaced elements. A modified Reynolds analogy [10], which restricts the heat-transfer analysis to fluids with Pr (see Nomenclature) of order unity or greater, provides local heat transfer coefficients in the attached flow regions. Empirical information from cavities and steps [12–16] supplies coefficients in the separated flow areas.

Attention is restricted to the steady, incompressible, turbulent flow of a constant property, single-phase, Newtonian fluid in a channel of constant cross section with rough walls. Any curvature of the channel is small and a constant mean heat-flux is applied at the surfaces. Extensions of the simple model to other roughness shapes and to other flow situations, and a fuller development of the equations presented here, may be found elsewhere [17].

The Physical Nature of the Flow Over a Rough Surface and an Approximate Flow Model

We consider a fully developed channel flow and ribs with $h \ll D$. The flow may be divided into two layers; one of thickness δ, which is of order h and which envelopes the roughness elements, and the other the core between the roughness elements and the channel center line. We are concerned solely with the former layer. The basic pattern of the flow over the ribs is illustrated by Fig. 1*(a)*. The channel Reynolds number is assumed to be high enough and the ribs widely spaced such that the separated flow regions shown are formed. Separation and reattachment imply that the shear stress, wall temperature, and velocity profiles are cyclic functions of z in the vicinity of the roughness.

To simplify the problem the physical flow in Fig. 1*(a)* is replaced by the model of Fig. 1*(b)*, where four regions 1, 2, 3, and 4 are indicated. The separation "bubble" on top of each rib in region 1 is now completely ignored. Separated flow regions are specified by characteristic separation lengths c_3 and c_4. The flow is assumed to remain attached to the top of the rib giving a mean wall stress

[1] Numbers in brackets designate References at end of paper.

Contributed by the Heat Transfer Division for publication in the JOURNAL OF HEAT TRANSFER. Manuscript received by the Heat Transfer Division May 29, 1974. Paper No. 75-HT-JJ.

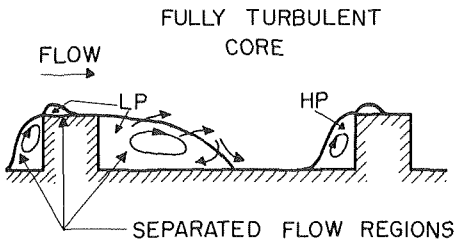

Fig. 1(a) Physical flow over roughness elements, not to scale—HP = High Pressure, LP = Low Pressure

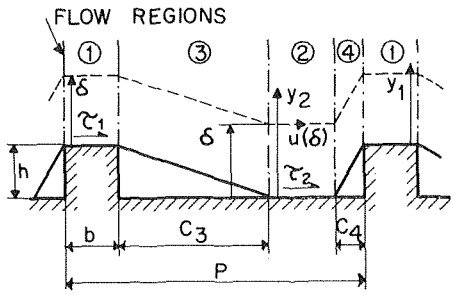

Fig. 1(b) Approximate model $p - b \geq c_3 + c_4$

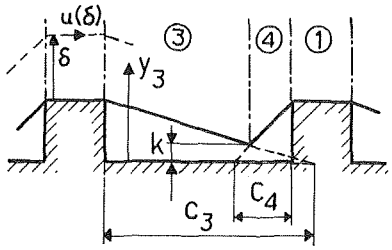

Fig. 1(c) Approximate model $p - b \leq c_3 + c_4$

τ_1, over b. Similarly τ_2 is defined for region 2. Both τ_1 and τ_2 are smaller than the total average wall shear stress τ_w which contains contributions from the form drag of each element.

As the pitch of the ribs is reduced the flow will no longer reattach between the ribs and a cavity will be formed. This occurs when $p - b \lesssim c_3 + c_4$. The dynamic pressure acting on the front-face of each element is reduced, as well as the area over which this pressure acts, by the shielding from each upstream element. Flow in the cavity is approximated by the model of Fig. 1(c) where region 2 is now lost altogether. A solution of the Navier Stokes equations for the separated flows would provide the dimensions c_3 and c_4 as well as the cavity flow. Here we specify these regions and linearly approximate the flow dipping into the cavity by the dimension k which is assumed to be directly related to c_3 and c_4 as indicated.

Basic Analysis, $p - b \geq c_3 + c_4$. A force balance over a length L of channel of unit width containing a large number of ribs gives

$$A_w \tau_w \equiv \Sigma A_1 \tau_1 + \Sigma A_2 \tau_2 + \Sigma D_f \tag{1}$$

where A_w, defined as $A_w \equiv L \times 1$, is an overall mean surface area Σ indicates a sum over L, and the drag, caused by any change in the channel flow static pressure across each element, is assumed small compared with D_f. Contributions to τ_w from the shear stresses in the separated flow regions are assumed to be incorporated in D_f.

We need to relate D_f and the shear stresses to characteristic velocities and dimensions of the flow field in each region. We define a form drag coefficient C_D through $D_f \equiv C_D \rho \bar{u}^2 A_F 1/2$. The dynamic pressure term arises naturally from momentum balance considerations over a control volume enclosing a roughness element:

Nomenclature

A = surface area, or constant (2.5) in log-laws
b = width of roughness element
B = constant in log-laws
c = $c_3 + c_4$, characteristic separation length
C = specific heat
C_D = form drag coefficient
d = $p - b$ for $p - b \leq c_3 + c_4$ and c otherwise
D = hydraulic diameter
D_f = form drag
g = heat-transfer roughness function
h = height of roughness element
h^+ = hu_{τ_w}/ν, roughness Reynolds number
k = conductivity coefficient, or length characterizing the flow dipping into the cavity
l = viscous or laminar sublayer thickness
l^+ = lu_τ/ν dimensionless sublayer thickness
L = length of channel
m = exponent
n = exponent
p = pitch of roughness elements
Pr = Prandtl number
Pr_t = turbulent Prandtl number
$\dot{q}''$ = heat flux per unit area
R = momentum transfer roughness function
T = temperature
T^+ = $(T_w - T)\rho C u_{\tau_w}/\dot{q}_w''$, dimensionless temperature
u = velocity
u_τ = $(\tau/\rho)^{1/2}$, friction velocity
u^+ = u/u_τ, dimensionless velocity
$\bar{u}$ = average velocity
U_∞ = velocity upstream of cavity
W = empirical function
X = characteristic length
y = distance from surface
y^+ = $y u_{\tau_w}/\nu$, dimensionless y
z = flow direction
α = heat transfer coefficient
δ = characteristic displacement thickness of rough surface
ν = kinematic viscosity
ρ = density
τ = mean surface shear stress
Σ = sum over L

Subscripts

1, 2, 3, 4 = regions 1, 2, 3, 4, mean quantities
a = adiabatic wall
c = cavity empirical information
e = effective
F = projected frontal area
i = 1, 2, 3, 4, R, or S
R = mean over rear of element
S = mean over effective front of element
SA = perturbed hydraulically smooth wall
SM = unperturbed hydraulically smooth wall
w = overall mean surface quantity

$$h\tilde{u}^2 = \int_{y_2=0}^{y_2=h} u_2^2 dy_2 \tag{2}$$

The definition of shear velocity $u_\tau \equiv (\tau/\rho)^{1/2}$ enables us to rewrite equation (1), for uniformly distributed elements, as

$$u^2_{\tau_w} = u^2_{\tau_1} b/p + u^2_{\tau_2}[p - b - (c_3 + c_4)]/p + C_D\rho\tilde{u}^2 h/2p \tag{3}$$

The layer adjacent to the wall, which encloses the roughness elements, is of thickness δ with a mean velocity $u(\delta)$ at its edge. It is not possible to define the origin for y and δ, Fig. 2, but we can assume that, in the physical flow over the elements, Fig. 1, $u(\delta)$ is also, to a first approximation, the velocity at $y_1 = y_2 = \delta$. This gives the coupling between the physical flow and overall surface quantities.

Defining the velocity $u^+ \equiv u/u_\tau$ and dividing equation (3) by $[u(\delta)]^2$ gives

$$[u^+(\delta)]^{-2} = [u_1^+(\delta)]^{-2} b/p + [u_2^+(\delta)]^{-2}[p - b - (c_3 + c_4)]/p + C_D\rho[\tilde{u}/u(\delta)]^2 h/2p \tag{4}$$

We see that $u^+(\delta)$ is a velocity in a dimensionless form suitable for characterizing the average properties of the whole surface, while u_1^+ and u_2^+ are velocities for the smooth wall regions 1 and 2. $u^+(\delta)$ may be related to the well-known roughness function $R(h^+)$ [18].

A heat balance over the length L may be written

$$A_w\dot{q}_w'' = \Sigma A_1\dot{q}_1'' + \Sigma A_2\dot{q}_2'' + \Sigma A_3\dot{q}_3'' + \Sigma A_4\dot{q}_4'' + \Sigma A_F\dot{q}_S'' + \Sigma A_F\dot{q}_R'' \tag{5}$$

where $\dot{q}_i''$ are mean wall heat transfer rates per unit area in regions 1, 2, 3, 4, and over the front S and rear R faces. Defining the temperature $T^+(\delta) \equiv [T_w - T(\delta)]\rho C u_{\tau_w}/\dot{q}_w''$, where $T_w - T(\delta)$ is the temperature difference at $y_1 = \delta$ and $y_2 = \delta$, and introducing $T^+(\delta)$ into equation (5) gives

$$\rho C u_{\tau_w}/T^+(\delta) = \alpha_1 b/p + \alpha_2(p - b - c_3 - c_4)/p + \alpha_3 c_3/p + \alpha_4 c_4/p + \alpha_S h/p + \alpha_R h/p \tag{6}$$

where α_i is an average heat-transfer coefficient for each region, defined by $\alpha_i \equiv \dot{q}_i''/[T_w - T(\delta)]$, and the convective transport through the ends of the control volume is neglected.

$T^+(\delta)$ is a parameter suitable for characterizing the average heat-transfer properties of the whole rough surface and may readily be related to the roughness function $g(h^+, \mathrm{Pr})$ [18]. The α_i are determined from empirical relations for cavities and steps.

Modifications for $p - b \le c_3 + c_4$

We extend the foregoing equations to this case by simply assuming that each element shields its downstream neighbor, reducing its effective frontal area. Also, because the flow outside the separated flow region 3 is a shear layer, the dynamic pressure acting on the effective area is reduced. For the flow field of Fig. 1*(c)*, the effective height h_e of each element is $h_e \equiv (h - k)$, and $\tilde{u}$ now takes the form:

$$(h - k)\tilde{u}^2 = \int_{y_3=k}^{y_3=h} u_3^2 dy_3 \tag{7}$$

where y_3 is measured from the base of the cavity and u_3 is the profile in region 3. Strictly, a separated flow profile should be employed for u_3, but we retain simplicity by assuming $u_3 = u_2$, with $u_3 = 0$ for $0 \le y_3 \le k$. Equations (4) and (6) now take the form:

$$[u^+(\delta)]^{-2} = [u_1^+(\delta)]^{-2} b/p + C_D\rho[\tilde{u}/u(\delta)]^2 h_e/2p \tag{8}$$

and

$$\rho C u_{\tau_w}/T^+(\delta) = \alpha_1 b/p + \alpha_3 c_3 h_e/hp + \alpha_4 c_4 h_e/hp + \alpha_S h_e/p + \alpha_R h/p \tag{9}$$

with $h_e \equiv (h - k) = h(p - b)/(c_3 + c_4)$. The contribution to the heat transfer of the frontal area between $0 \le y_3 \le k$ is assumed negligible.

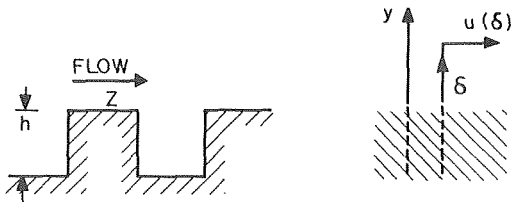

Fig. 2 A rough wall and its origin uncertainty

Velocity Profiles

To evaluate the integrals in equation (2) and (7) and to determine the surface mean parameter $u^+(\delta)$ from equations (4) or (8), velocity profiles u_1^+, u_2^+, and u_3^+ are required. An assymptotic profile, for very widely or closely spaced elements, is a smooth wall one, typically [10]

$$u_{SM}^+ = A\ln y^+ + B_{SM} \tag{10}$$

Subscript SM indicates that we are referring to a smooth wall in the presence of a turbulent shear flow in which no artificial disturbances are introduced, for example, by upstream separated flows. We assume that equation (10) remains representative for regions 1, 2, and 3 (for $y_3 > k$) except that B_{SM} is modified because of turbulence generated by the separated flows. Thus a representative velocity u_{SA}^+ is introduced as

$$u_{SA}^+ = A\ln y^+ + B_{SA} = u_1^+(y_1) = u_2^+(y_2) = u_3^+(y_3) \tag{11}$$

with the origin for u_3 taken from $y_3 = k$.

To determine B_{SA} we recall that B_{SM} is defined in terms of a laminar sublayer thickness l_{SM}^+ (≈ 11.63)

$$B_{SM} \equiv l_{SM}^+ - A\ln l_{SM}^+ \approx 5.5 \tag{12}$$

and, by analogy,

$$B_{SA} \equiv l_{SA}^+ - A\ln l_{SA}^+ \tag{13}$$

where l_{SA}^+ is representative of the laminar sublayer thickness in regions 1 and 2. We assume that any increase in local turbulence intensity, generated by the separated flows, is reflected by a decrease in l_{SA}^+ and that this decrease is given by

$$l_{SA}^+ = l_{SM}^+ u_{\tau_{SA}}/u_{\tau_w} = l_{SM}^+ u^+(\delta)/u_{SA}^+(\delta) \tag{14}$$

The Heat Transfer Coefficients α_i

Employing the modified Reynolds analogy [10] to the layer between l_{SA}^+ and δ in each region 1 and 2, we obtain

$$\alpha_1 = \alpha_2 = \rho C u_{\tau_w} u^+(\delta)/\{\mathrm{Pr}_t[u_{SA}^+(\delta)]^2 + l_{SA}^+ u_{SA}^+(\delta)[\mathrm{Pr}^{2/3} - \mathrm{Pr}_t]\} \tag{15}$$

For regions 3, 4, and for R and S, we use Seban's [12–14] experimental information for rectangular cavities, which is summarized in Fig. 3. The variation of α_c in the cavity is given by

$$\alpha_c \equiv \dot{q}_w''/(T_w - T_a) = (U_\infty X/\nu)^n (Wk/X)(\mathrm{Pr}/0.71)^m \tag{16}$$

where, following Presser [16], the Prandtl number is introduced to generalize Seban's results in air. U_∞, X, and T_a define a flat plate heat-transfer coefficient upstream of the cavity itself, and the variation of α_c is determined from the given variation of W. From Seban's information it is difficult to estimate the effect on α_c of the cavity length $d \equiv (p - b)$. We infer this effect from the results of Charwat, et al. [15], where a linear approximation gives $\alpha_c \propto (0.5 + 0.5d/c)$ until the flow reattaches in the cavity, that is, until $p - b \ge c_3 + c_4$. We have anticipated the result that α_c is a maximum when $d = c$. This, in fact, contradicts Charwat's measurements for $d > c$ and is a weakness of the present model in which region 2 is suddenly introduced. Combining Charwat's and Seban's results gives

$$\alpha_c = (U_\infty X/\nu)^n(\mathrm{Pr}/0.71)^m(Wk/X)(0.5 + 0.5d/c) \quad (17)$$

where $d = c$ for $p - b \geq c$.

We make the transformation from the single cavity experiments to the present rough surface model by assuming that the heat-transfer coefficient distribution is the same in both cases when U_∞, X, and T_a are replaced by $u(\delta)$, δ, and $T(\delta)$, respectively. Then, taking the average values for W from Fig. 3, we obtain

$$\alpha_3 = \alpha_4 = 0.025(k/\delta)[u(\delta)\delta/\nu]^n(\mathrm{Pr}/0.71)^m(0.5 + 0.5d/c) \quad (18)$$

with $\alpha_R = 0.8\alpha_3$ and $\alpha_S = 2\alpha_3$, and $d = c$ for $p - b \geq c$. Equation (18) may be written with more convenient variables as

$$\alpha_3 = \rho C u_{\tau_w} 0.025[u^+(\delta)]^n(0.5 + 0.5d/c)/[0.71^m \mathrm{Pr}^{1-m}(h^+\delta/h)^{1-n}] \quad (19)$$

again, $d = c$ for $p - b \geq c$.

Roughness Functions

The fundamental parameters controlling the momentum- and heat-transfer properties of a rough surface are $R(h^+)$ and $g(h^+, \mathrm{Pr})$, respectively [18]. We have expressions for surface average parameters $u^+(\delta)$ and $T^+(\delta)$, at some mean distance δ from an undefined mean origin for the surface. We need to relate these to the roughness functions. The mathematical representation of a rough surface in terms of $R(h^+)$ and a log-law

$$u^+ = A\ln y/h + R(h^+) \quad (20)$$

does not allow us to specify the origin for y. We avoid the origin problem by assuming that $R(h^+)$ is a mean velocity found by integrating equation (20) over the surface mean control volume of thickness δ. This gives δ the character of a displacement thickness for a rough surface. Integration gives

$$u^+(\delta) = R(h^+) + A \text{ and } A\ln\delta/h = A \quad (21)$$

It immediately follows from the modified Reynolds analogy that

$$T^+(\delta) = g(h^+, \mathrm{Pr}) + \mathrm{Pr}_t A \quad (22)$$

Our solution procedure for $p - b \geq c_3 + c_4$ is to substitute equation (11) into (2). Equation (4), after substituting for $\tilde{u}$ and multiplying by $[u_{SA}{}^+(\delta)]^2$, becomes

$$[u_{SA}{}^+(\delta)/u^+(\delta)]^2 = 1 - c/p + C_D[(u_{SA}{}^+(\delta) - 2A)^2 + A^2]h/2p \quad (23)$$

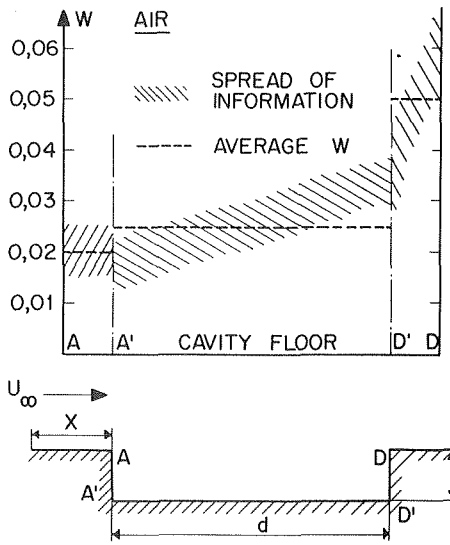

Fig. 3 Heat transfer distribution in a shallow rectangular cavity $2 < d/h < 5$, after Seban, et al. [12–14]

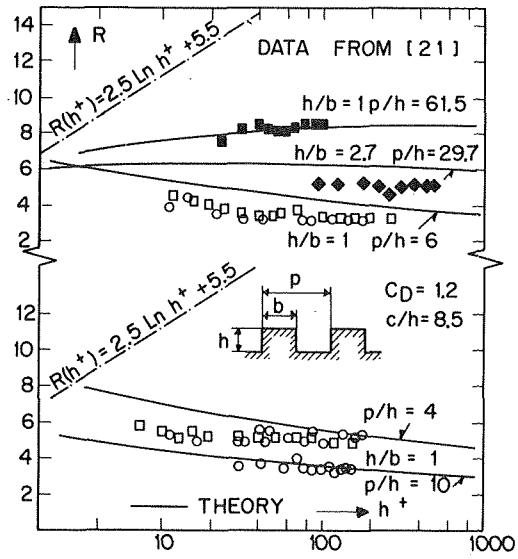

Fig. 4 Comparison with experiment, rectangular rib

From equation (11), after substituting for δ/h from (21), $u_{SA}{}^+(\delta)$ is given by

$$u_{SA}{}^+(\delta) = A\ln h^+ u^+(\delta)/u_{SA}{}^+(\delta) + A + B_{SA} \quad (24)$$

with B_{SA} evaluated from equations (13) and (14). For a given geometry, C_D and c, equations (23) and (24) may be solved for $u^+(\delta)$, then equations (15) and (19) for the α_i, giving $T^+(\delta)$ from equation (6). R and g are readily evaluated from equations (21) and (22).

When $p - b \leq c_3 + c_4$, equations (7) and (8) give, after substituting for $\tilde{u}$ from equation (11) and integrating,

$$[u_{SA}{}^+(\delta)/u^+(\delta)]^2 = b/p + C_D[\{u_{SA}{}^+(\delta) - 2A + A\ln(p-b)/c\}^2 + A^2]h(p-b)/2pc \quad (25)$$

which, together with equations (13), (14), and (24), may be solved for $u^+(\delta)$. Equation (19) is solved for α_3. The remaining α_i are determined as above and $T^+(\delta)$ is given by equation (9). R and g readily follow from equations (21) and (22).

Comparison With Experiments and Discussion

When the geometry p, h, and b of the ribs is given, values of R and g may be determined as functions of h^+, from the equations presented, provided Pr_t, m, n, c/h, and C_D are known. We follow Seban and choose $n = 0.8$. A mean value of Presser's measurements gives $m = 0.5$. An acceptable mean value for Pr_t is 0.9 [10]. Hoerner [11] gives $C_D = 1.2$ for rectangular ribs with sharp edges. From Abbott and Kline [19] we estimate $c_3/h \approx 7.5$ and from Luzhanskiy and Solntsev [20] $c_4/h \approx 1.0$. These and the cavity measurements suggest that $c/h = 8.5$ is a representative value. Both C_D and c/h are expected to be functions of some local Reynolds number and, possibly, of the rib width [10], but we assume here that they are constants. The constants A, B_{SM}, and $l_{SM}{}^+$ are chosen 2.5, 5.5, and 11.63, respectively.

Predicted values of R are compared with some representative measurements [21] from an annulus test rig in Fig. 4. This comparison is typical of the discrepancy between theory and experiment with good agreement at high values of h^+, but too high values of R at lower values of h^+. Correct trends are shown: R increasing with decreasing h^+ for closely spaced elements but decreasing with h^+ for widely spaced elements. The reason for this behavior is not clear. To give some idea of the discrepancies over a very wide range of roughness shapes a comparison is made in Fig. 5 between predicted values of R and a correlation of experimental information [22]. Considering the approximations in the theory and the wide scatter (not indicated on the correlation) in the experiments the agreement is very reasonable. The theory indicates $R \neq R(b)$ for p

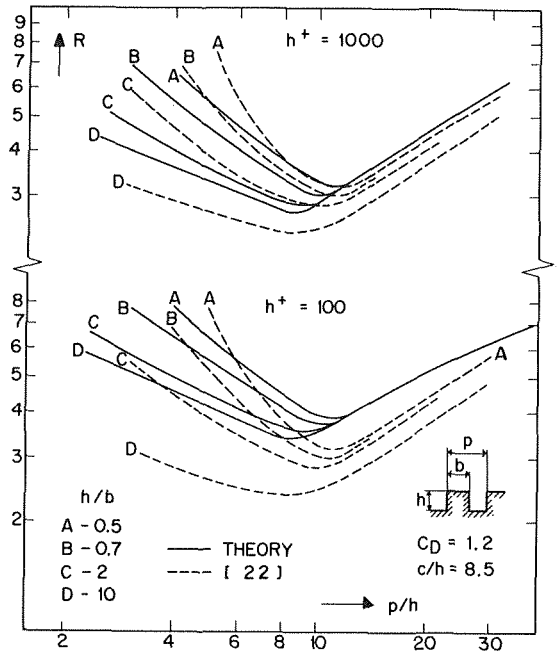

Fig. 5 Comparison with experiment, rectangular rib

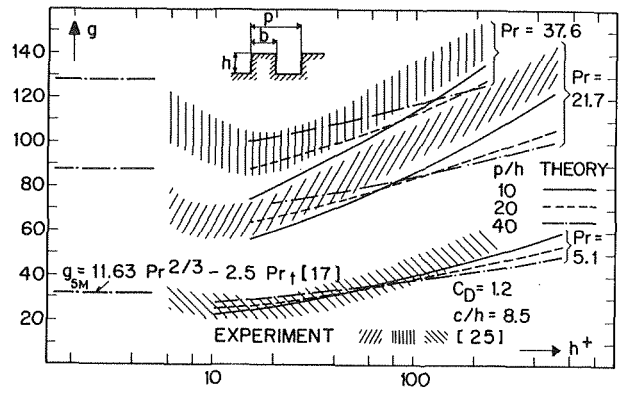

Fig. 7 Comparison with experiment, rectangular rib

$- b > c$ and this appears to be qualified by the experiments. Furthermore, both theory and experiment suggest that $R \neq R(D)$, although Baumann [23] has shown that this is true only when $h \ll D$.

Most measurements of R and g have been performed in annuli, which has introduced unknown errors when transformations are employed [18]. Consistency of results [24] has indicated that transformation errors in R are small, so that experimental results in Figs. 4 and 5 may be considered representative of both circular tube and annulus measurements. However, significant errors [24] are indicated in transformed values of g. Therefore predicted values of g are compared only with those measured in circular tubes. Representative results [25] are given in Figs. 6 and 7. The agreement is very reasonable at Prandtl numbers of order unity but discrepancies occur at higher Prandtl numbers, probably because of the very simple power law used for the Prandtl number dependency.

Some idea of why discrepancies occur may be obtained from Fig. 8, where a comparison is made between the measured [26] and predicted local heat-transfer coefficient α_i. The α distribution was recovered from the average values of W by scaling Fig. 3. There is evidence that by taking average values some discrepancies cancel. The greatest discrepancy occurs over the top of the rib DA which corresponds to region 1. The experiments indicate that a separation bubble forms near D and after this bubble reattachment occurs. Not only will such separated flows influence the separated flow regions 3 and 4, but high heat-transfer rates may be associated with the reattachment. These mechanisms are not considered in the theory.

The minimum in g that occurs for high values of Pr and at $h^+ \approx 20$, Fig. 7, is not predicted by the theory. This is because Seban's correlation is for a fully turbulent separated flow. As the local Reynolds number is reduced the separated flow probably becomes transitional then laminar and corresponding changes in the heat transfer mechanism occur. A transition from a turbulent to a laminar separated flow, with decreasing h^+, offers a possible explanation for a rough wall acting like a thermally smooth wall before it becomes hydraulically smooth. The concept of a low local Reynolds number also leads to the suggestion that a hydraulically smooth wall is one at which the flow at the surface is a Stokes flow. This is also supported by the work of Richardson [27].

Improvements to the model can be envisaged. The attached flow regions need not be treated as regions of constant shear stress, although the type of boundary layer formed in the turbulent shear flow is not clearly understood. Better velocity profiles could be employed for the attached and separated flow regions. A region 5 could be introduced to encompass the separation bubble at the front of the sharp edged elements, but all turbulent separated flows [28] are extremely difficult to analyze. The influence of upstream and downstream separated flows on the attached flow regions is not clearly understood—it was very crudely included in the analysis. Solution of the turbulence energy equation will provide useful information on these influences. Significant progress will only follow detailed local measurements of the basic phenomena.

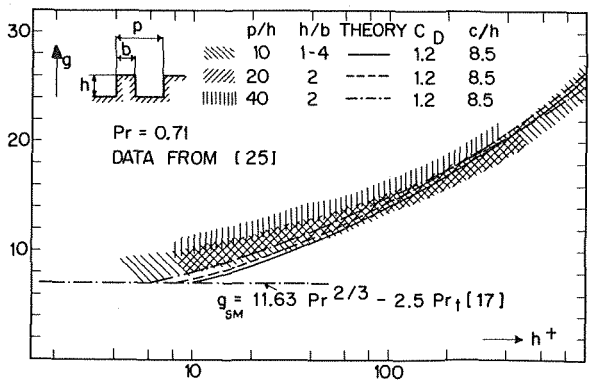

Fig. 6 Comparison with experiment, rectangular rib

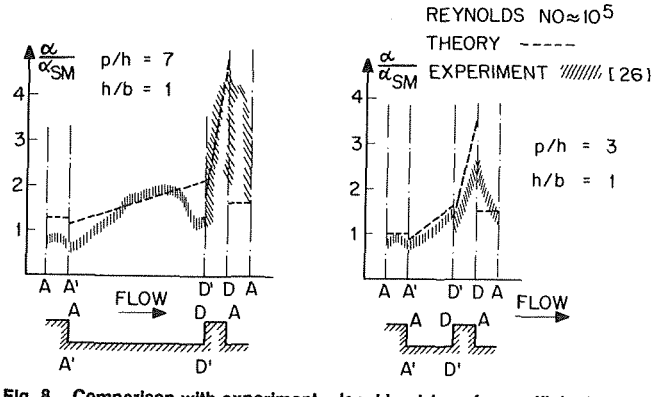

Fig. 8 Comparison with experiment—local heat-transfer coefficient ratios over rectangular ribs

Concluding Remarks

The main purpose of this paper has been to lay some foundations for analyzing the momentum- and heat-transfer characteristics of rough surfaces. Simple equations have been developed to account, in a rather crude fashion perhaps, for the separated flows and turbulence phenomena found on rough surfaces. Although the present analysis is for evenly spaced rectangular-ribs, its extension to nonrectangular ribs has been carried out [17]. Further extensions to unevenly spaced elements, to three dimensional elements, to flow situations other than fully developed pipe flows [29], and to variable property situations [30] are readily envisaged. The present model cannot be used where large adverse static pressure gradients are imposed which might cause overall flow separation without reattachment.

Acknowledgments

The author expresses his grateful thanks to the EIR for allowing him sufficient time to complete this work. Many thanks are extended to P. Buettiker, friend and colleague, for his constructive criticism and advice throughout the course of this work.

References

1 Kays, W. M., "Compact Heat Exchanger," AGARD-LS-57-72, *Heat Exchangers*, J. J. Ginoux, editor, Von Karman Inst., Belgium, Jan. 1972.

2 Kacker, S. C., "Estimation of Friction Factor of Rough Surfaces From the Pressure Distribution Around a Roughness Element," CEGB, Berkeley, RD/B/N1967, Apr. 1971.

3 Lavallee, H. C., and Popovitch, A. T., "Fluid Flow Near Roughness Elements Investigated by Photolysis Method," *Chem. Eng. Sc.*, Vol. 29, 1974, pp. 49–59.

4 Perry, A. E., Schofield, W. H., and Joubert, P. N., "Rough Wall Turbulent Boundary Layers," *Journal of Fluid Mechanics*, Vol. 37, Part 2, 1969, pp. 383–413.

5 Nikuradse, J., "Laws of Flow in Rough Pipes," VDI Forsch. 361, 1933 or NACA TM-1292, 1965.

6 Dipprey, D. F., and Sabersky, R. H., "Heat and Momentum Transfer in Smooth and Rough Tubes at Various Prandtl Numbers," *International Journal of Heat and Mass Transfer*, Vol. 6, 1963, pp. 329–353.

7 Sedney, R., "A Survey of the Effects of Small Protuberances on Boundary-Layer Flows," *AIAA Journal*, Vol. 11, No. 6, June 1973, pp. 728-792.

8 Lewis, M. J., "Optimising the Thermohydraulic Performance of Rough Surfaces," to be published in the *International Journal of Heat and Mass Transfer*, 1975.

9 Wilkie, D., "Forced Convection Heat Transfer From Surfaces Roughened by Transverse Ribs," I. Mech. E. Int. Heat Trans. Conf., Chicago, Vol. 3, 1966.

10 Schlichting, H., *Boundary Layer Theory*, McGraw Hill, New York, 1968.

11 Hoerner, S. F., "Fluid Dynamic Drag," Published by the Author, 148 Busteed Drive, Midland Pk., N. J., USA, 1958.

12 Seban, R. A., and Fox, J., "Heat Transfer to the Air Flow in a Surface Cavity," *International Devel. in Heat Transfer*, ASME, 1962, pp. 426–431.

13 Seban, R. A., "Heat Transfer to the Turbulent Separated Flow of Air Downstream of a Step in the Surface of a Plate," JOURNAL OF HEAT TRANSFER, TRANS. ASME, Series C, Vol. 86, No. 2, May 1964, pp. 259–264.

14 Seban, R. A., "Heat Transfer and Flow in a Shallow Rectangular Cavity With Subsonic Turbulent Air Flow," *International Journal of Heat and Mass Transfer*, Vol. 8, 1965, pp. 1353–1368.

15 Charwat, A. F., Dewey, C. F., Jr., Roos, J. N., and Hitz, J. A., "An Investigation of Separated Flows—Part II: Flow in the Cavity and Heat Transfer," *Journ. Aerospace Scs.*, Vol. 28, No. 7, July 1961, pp. 513–527.

16 Presser, K. H., "Empirische Gleichungen zur Berechnung der Stoffund Wärmeübertragung für den Spezialfall der abgerissenen Strömung," *International Journal of Heat and Mass Transfer*, Vol. 15, 1972, pp. 2447–2471.

17 Lewis, M. J., "An Elementary Analysis for Predicting the Momentum- and Heat-Transfer Characteristics of a Hydraulically Rough Surface," EIR Würenlingen, CH, Report TM-IN-569, 1974.

18 Lewis, M. J., "Roughness Functions, the Thermohydraulic Performance of Rough Surfaces and the Hall Transformation—an Overview," *International Journal of Heat and Mass Transfer*, Vol. 17, 1974, pp. 809–814.

19 Abbott, D. E., and Kline, S. J., "Experimental Investigation of Subsonic Turbulent Flow over Single and Double Backward Facing Steps," *Journal of Basic Eng.*, Vol. 84, Sept. 1962, pp. 317–325.

20 Luzhanskiy, B. Ye., and Solntsev, V. P., "Experimental Study of Heat Transfer in the Zone of Turbulent Boundary Layer Separation Ahead of a Step," *Heat Transfer—Soviet Research*, Vol. 3, No. 6, Nov.–Dec., 1971.

21 Dalle Donne, M., and Meerwald, E., "Heat Transfer From Rough Surfaces, Latest Results," Kernforschungszentrum Karlsruhe report, presented at the heat transfer specialist meeting, Windscale, May 1972.

22 Maubach, K., "Rough Annulus Pressure Drop—Interpretation of Experiments and Recalculation for Square Ribs," *International Journal of Heat and Mass Transfer*, Vol. 15, 1972, pp. 2489–2496.

23 Baumann, W., "Pressure Drop Performance of Artificial Roughness as a Function of Roughness Geometry," International Meeting on Reactor Heat Transfer, Karlsruhe, Oct. 1973.

24 Lewis, M. J., "Errors that Arise When Estimating the Heat-Transfer Characteristics of Rough Surfaces From 'Bulk' Measurements in Annular Channels," EIR Würenlingen, CH, TM-IN-535, May 1973.

25 Webb, R. L., Eckert, E. R. G., and Goldstein, R. J., "Heat Transfer and Friction in Tubes With Repeated Rib Roughness," *International Journal of Heat and Mass Transfer*, Vol. 14, 1971, pp. 601–617.

26 Williams, F., and Watts, J., "The Development of Rough Surfaces With Improved Heat Transfer Performance and a Study of the Mechanisms Involved," *Proc. 4th Int. Heat Transfer Conf.*, Paris, Vol. II, Paper FC 5.5, 1970.

27 Richardson, S., "On the Non-Slip Boundary Conditions," *Journal of Fluid Mechanics*, Vol. 59, Part 4, 1973, pp. 707–719.

28 Chang, P. K., *Separation of Flow*, Pergamon, 1970.

29 Dirling, R. B., Jr., "A Method for Computing Roughwall Heat Transfer Rates on Reentry Nosetips," AIAA Paper 73-763, 1973.

30 Nijsing, R., "Predictions on Momentum, Heat and Mass Transfer in Turbulent Channel Flow With the Aid of a Boundary Layer Growth—Breakdown Model," *Wärme und Stoffübertragung*, Vol. 2, 1969, pp. 65–86.

B. W. Jones
J. D. Parker

School of Mechanical and Aerospace Engineering, Oklahoma State University, Stillwater, Okla.

Frost Formation With Varying Environmental Parameters

In practical applications frost formation often takes place with varying environmental parameters (air velocity, temperature, and humidity). Most correlations that have been developed are for constant parameters. Since the frost formation process is dependent on both time and on the history of the frost layer, the correlations for constant environmental parameters will not work when the parameters vary. For this reason, a study was made to develop a method to predict frost formations with varying parameters.

A theoretical model of frost growth based on molecular diffusion of water vapor at the frost surface and using energy and mass balances was developed. The model can incorporate varying environmental parameters. The model uses functions relating heat and mass transfer coefficients at the frost surface to the environmental parameters.

The model was first tested and calibrated using data taken by previous investigators. A facility was then built to test the validity of the model for varying environmental parameters. Tests were made for changes in humidity and air velocity.

The model showed good agreement with the basic trends observed for varying parameters. The qualitative results were generally within 25 percent of the predicted values for time periods up to 3 hr.

Introduction

Frost formation is a problem often encountered in the refrigeration industry. The formation of frost on heat exchanger surfaces can be extremely detrimental to their efficient operation. The frost acts as a thermal insulator, reducing the ability of the surface to transfer heat. Also, accumulations of frost often become thick enough to restrict airflow. In extreme cases the frost will completely block the flow of air. Usually the frost is removed periodically to improve the efficiency of operation. This normally involves heating the surface to melt the frost, a costly operation since energy is required to melt the frost and the heat exchanger is out of operation during the process.

When a surface below 273°K (32°F) comes into contact with moist air having a dew point temperature greater than the temperature of the surface, frost will form. The nature of the frost formation process makes it difficult to predict such factors as rate of formation and density of the frost. The process is accumulative in nature, creating a continually changing situation. This prevents any steady-state analysis. The effect of the frost depends on its density as well as its thickness. The frost density depends on how it was formed. This causes characteristics of frost at any given time to be dependent on the history of its formation.

Model Development

Because of the history dependent nature of frost formation, the common types of correlations used in other heat and mass transfer problems do not apply. Instead, a diffusional model similar to the one developed by Brian, Reid, and Branzinsky is used to describe the process [1].[1] The model treats the frost layer as a porous substance. Water vapor is considered to be transported to the frost surface in the same manner as for any other surface. This allows correlations of mass transfer coefficients developed for nonfrosting conditions to be used. The vapor transported to the frost surface is divided into two parts. Part of it diffuses into the existing frost layer and increases the density of the frost. The rest goes to increase the thickness of the frost layer.

An important assumption is made to simplify the development of the model. There is assumed to be no spatial variation of frost density even though it varies with time. Although this assumption has not been proven valid on a theoretical basis, other studies have shown this to be the case in many instances [2].

Contributed by the Heat Transfer Division for publication in the JOURNAL OF HEAT TRANSFER. Journal manuscript received by the Heat Transfer Division July 2, 1974.

[1] Numbers in brackets designate References at end of paper.

If the diffusion of water vapor into the frost is assumed to be by molecular diffusion at the frost surface, equation (1) describes the process of densification. Derivations appear in the Appendix.

$$\frac{d\rho_f}{dt} = \frac{M_v D_s (1 - \rho_f/\rho_{ice})}{RT_s \tau_s x_s} \left(\frac{dP_v}{dT}\right)_s \left(\frac{dT}{dx}\right)_s \quad (1)$$

Using the assumption of spatially constant frost density the rate at which the thickness increases can be found.

$$\frac{dx_s}{dt} = \frac{h_M(\rho_{va} - \rho_{vs}) - \dfrac{M_v D_s (1 - \rho_f/\rho_{ice})}{RT_s \tau_s} \left(\dfrac{dP_v}{dT}\right)_s \left(\dfrac{dT}{dx}\right)_s}{\rho_f} \quad (2)$$

In order to solve equations (1) and (2) it is necessary to know T_s and $(dT/dx)_s$. In addition some of the parameters in the equations are functions of T_s. Both T_s and $(dT/dx)_s$ are found by setting up an energy balance on the frost layer as described in the Appendix. This energy balance results in a second degree polynomial for the temperature profile. This is characteristic of the temperature profiles measured by Brian, et al. [1].

The equation for T_s is implicit and is solved with a Newton-Rhapson iteration technique. $(dP_v/dT)_s$ is found by assuming the water vapor is near thermodynamic equilibrium within the frost. Steam tables and the Clapeyron equation can then be used to determine its value as a function of temperature. The density of the water vapor at the surface is found using the same assumption and steam tables. K_f is determined by the correlation used by Brian, Reid, and Shah [2]. h_H and h_M are determined using the Colburn equation. An empirical equation for D_s given by Eckert and Drake [10] is used. Tortuosity was assumed to be 1.1, a value used by Brian, et al. [1]. These were used to solve equations (1) and (2) numerically.

A problem immediately arises in trying to integrate the equations. Initial values of frost thickness and density are required to start the integration. For most practical applications it is desired to start the prediction from the time the frost starts forming so no initial values are available. Zero values cannot be used since the equations are discontinuous for both zero thickness and zero density.

A number of initial conditions were tried to see what effect they had on later predictions. It was found that the initial thickness could be made to approach zero ($\approx 2 \times 10^{-5}$ m) without causing problems in the numerical solutions. Using such an initial value for thickness, the initial frost density was varied over a wide range of values. It was found that as long as the value was significantly lower than the densities that would be expected later on there was very little difference resulting from further reductions in initial density. Under these conditions the density converged to the same value within a few minutes regardless of the starting value. This resulted in essentially identical predictions by the model as shown in Fig. 1. This indicated that the model could be used starting at zero time by using sufficiently small initial values for thickness and density.

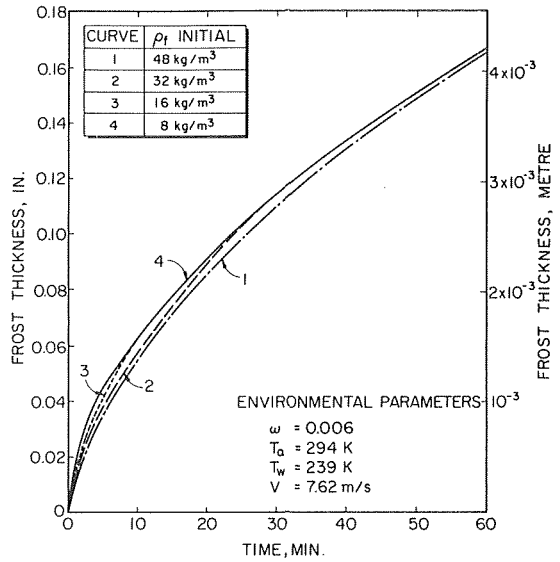

Fig. 1 Effect of initial frost density on model prediction

Results

The model does a good job of predicting the general trends in frost formation. It has been known for some time that frost tends to keep getting denser with time. For extremely long time periods it will approach the density of ice. This is commonly called aging of frost. The reason for this can be seen by looking at equation (1). All of the terms in the equation are positive at all times except for $(dT/dx)_s$. Equation (13A) shows that $(dT/dx)_s$ will be positive as long as the term $[h_H(T_a - T_s) + h_M(\rho_{va} - \rho_{vs})\Delta H]$ is positive. There are very few circumstances where this will not be positive. This explains why frost always seems to grow denser. Situations can even arise where the frost is getting denser but the thickness of the frost is decreasing.

A lot of data have been taken of frost thickness changes with time for constant environmental parameters [2–6]. The general trend is for very rapid growth at first and then the rate goes down to a much lower level, which slowly decreases with time. The growth rate is high at first since the frost is forming at a low density and a small amount of water vapor will make a large increase in the frost thickness. As the density increases it takes more and more water vapor to make the same increase in thickness so the growth rate goes down.

To check the validity of the quantitative predictions given by the model it was programmed onto the IBM 360 computer and the results compared to data taken by Yonko and Sepsy [4]. These are the only frost data that could be found, in which the correlations

Nomenclature

D = molecular diffusivity
h_H = heat transfer coefficient
h_M = mass transfer coefficient
ΔH = heat of sublimation
K = thermal conductivity
$\dot{m}$ = mass flux per unit area
M = molecular weight
P = partial pressure
q = heat flux
R = universal gas constant
t = time
T = temperature
x = distance from wall
ρ = density
$\bar{\rho}$ = avg. density
τ = tortuosity
ω = specific humidity

Subscripts

a = in the airstream
f = frost
fi = that part of the newly formed frost that goes to increase the thickness
ice = solid ice
s = frost surface
sd = at frost surface and diffusing inward
t = total to frost
v = water vapor
w = wall

used in the model would be valid. The results are fairly consistent, showing the same trends as the data, Fig. 2.

It appears the slopes of the curves do not decrease as rapidly for the model as the data do. The reason for this may be that during the first few minutes of frost formation the frost is not a continuous porous material but individual crystals. This would cause higher heat and mass transfer coefficients. The effect of increased heat and mass transfer coefficients is to increase the density of the frost. An increased density will cause a lower growth rate later on.

For a great number of practical situations the environmental parameters—air temperature, wall temperature, air velocity, and air humidity will not remain constant. There seems to be no information available in the literature to indicate how to handle varying parameters. The form of the diffusion model makes the incorporation of varying parameters a simple matter.

Since no data existed to test the model for varying parameters, a test facility was constructed to get the necessary data. A flow loop used for other work was converted for use under frosting conditions. A 0.152 m square copper plate was installed on one wall of a 0.152 m by 0.102 m rectangular duct. The plate was cooled by refrigeration coils soldered to the back side.

The method used in taking the data was to introduce large step changes in one parameter. It was felt that if the model could predict behavior for these changes it would also make good predictions for more gradual changes. Comparisons of data and predictions are shown in Figs. 4, 5, 6, and 7. Since the humidity was the most easily controlled parameter, most of the data were taken for changes in it.

Conclusions

The trends predicted by the model are in good agreement with the data. For most of the predictions there is only about 30 percent difference between the data and the model's predictions. This is not considered too bad for this type of work. These data are not complete in that all possible parameter variations were not considered. It does indicate that variable parameters are no problem for the diffusional model.

A literature review indicated there exist no other correlations or methods of prediction for frost formation that can incorporate unsteady environmental parameters.

Also, since the frost surface temperature is known, the calculations for heat transfer should be more accurate than methods which do not solve for it. However, if at any time the surface temperature reaches 273°K, melting will occur, and the model will not be valid since the assumption of molecular diffusion is obviously invalid.

References

1 Brian, P. L. T., Reid, R. C, and Branzinsky, I., "Cryogenic Frost Properties," *Cryogenic Technology*, Vol. 5, Sept-Oct. 1969, pp. 205–212.

2 Brian, P. L. T., Reid, R. C., and Shah, Y. T., "Frost Deposits on Cold Surfaces," *Ind. Eng. Chem. Fundamentals*, Vol. 9, No. 3, pp. 375–380.

3 Chung, P. M., and Algren, A. B., "Frost Formation and Heat Transfer on a Cylinder Surface in Humid Air Cross Flow," *ASHRAE Transactions*, Vol. 65, Parts I and II, 1959, pp. 213–244.

4 Yonko, J. D., and Sepsy, C. F., "An Investigation of the Thermal Conductivity of Frost While Forming on a Flat Horizontal Plate," *ASHRAE Transactions*, Vol. 73, Part I, pp. 1.1–1.11.

5 Trammell, G. J., Little, D. C., and Killgore, E. M., "A Study of Frost Formed on a Flat Plate Held at Sub-Freezing Temperatures," *ASHRAE Journal*, Vol. 10, No. 7, July 1968, p. 42–47.

6 Schneider, H. W., "Measurement and Correlation of the Growth Rate of Frost While Forming on a Cylindrical Tube in Crossflow," XIIIth International Congress of Refrigeration, Institute of Refrigeration, Preprint.

7 Reid, R. C., Brian, P. L. T., and Weber, M. E., "Heat Transfer and Frost Formation Inside a Liquid Nitrogen Cooled Tube," *AIChE Journal*, Vol. 12, Nov. 1966, pp. 1190–1195.

8 Biguria, G., and Wenzen, L. A., "Measurement and Correlation of Water Frost Thermal Conductivity and Density," *I.E. and C. Fundamentals*, Vol. 9, No. 1, Feb. 1970, pp. 129–138.

9 White, J. E., and Cremers, C. J., "Heat and Mass Transfer in Thick Frost Layers," XIIIth International Congress of Refrigeration, Institute of Refrigeration, Preprint.

10 Eckert, E. R. G., and Drake, R. M., Jr., *Analysis of Heat and Mass Transfer*, McGraw-Hill, New York, 1972, p. 787.

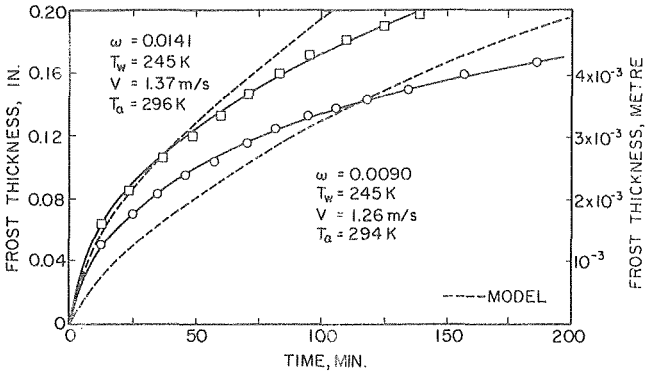

Fig. 3 Comparison of data and model for constant parameters

APPENDIX

Consider the water vapor being transported to a surface during the process of frost formation. Part of this water vapor will be diffused into the existing layer of frost before it freezes, which serves to increase the frost density. The rest of this water vapor freezes out at the frost surface, which serves to increase the frost thickness.

$$\frac{d\bar{\rho}_f}{dt} x_s = \dot{m}_{sd} \tag{1A}$$

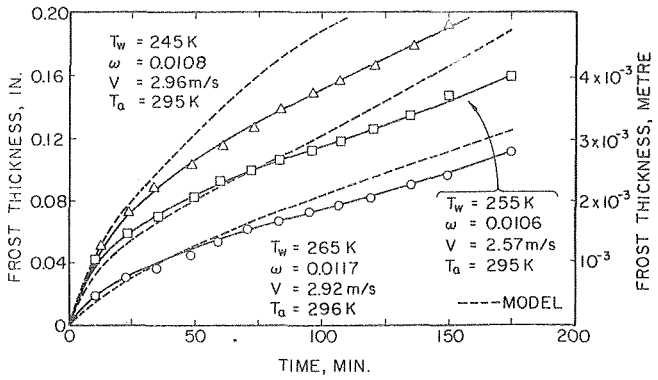

Fig. 2 Comparison of data and model for constant parameters

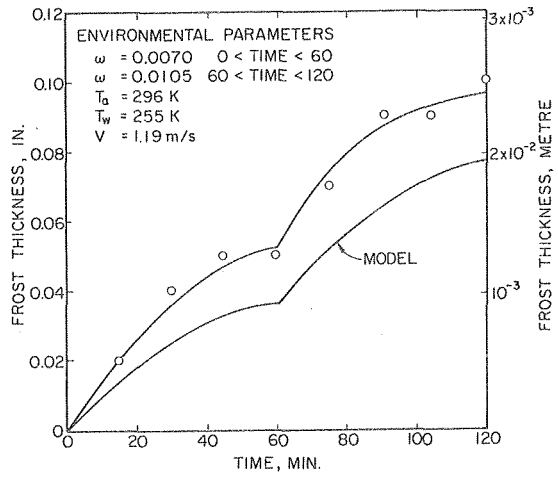

Fig. 4 Comparison of data and model for variable humidity

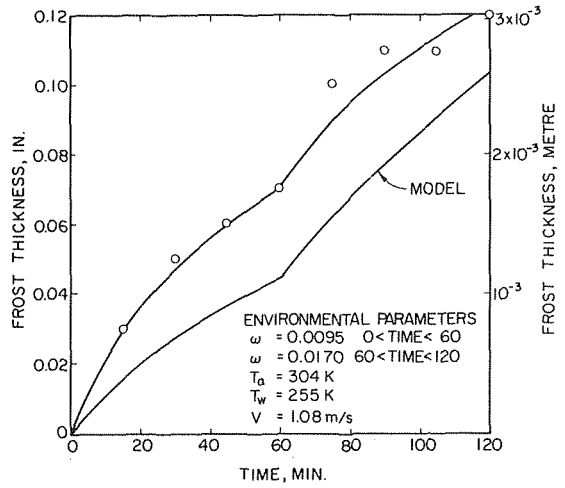

Fig. 5 Comparison of data and model for variable humidity

$$\frac{dx_s}{dt}\rho_{fi} = \dot{m}_t - \dot{m}_{sd} \tag{2A}$$

The water vapor being transported to the frost is described by:

$$\dot{m} = h_M(\rho_{va} - \rho_{vs}) \tag{3A}$$

Molecular diffusion is assumed to be the primary process by which the water vapor is carried into the frost layer at the surface. It is also assumed that the variation in density of the water vapor is much greater perpendicular to the wall than parallel to the wall.

For this case molecular diffusion is described by:

$$\dot{m}_v = -D\frac{d\rho_v}{dx} + \left(\frac{\omega}{1+\omega}\right)(\dot{m}_v + \dot{m}_a)$$

$\dot{m}_a = 0$ for frost formation so this reduces to:

$$\dot{m}_v = \frac{-D\frac{d\rho_v}{dx}}{1 - \left(\frac{\omega}{1+\omega}\right)}$$

However, in the air-water vapor systems considered in frost formation the term $\omega/(1+\omega)$ is usually much smaller than one. This allows the equation to be reduced to:

$$\dot{m}_v = -D\frac{d\rho_v}{dx}$$

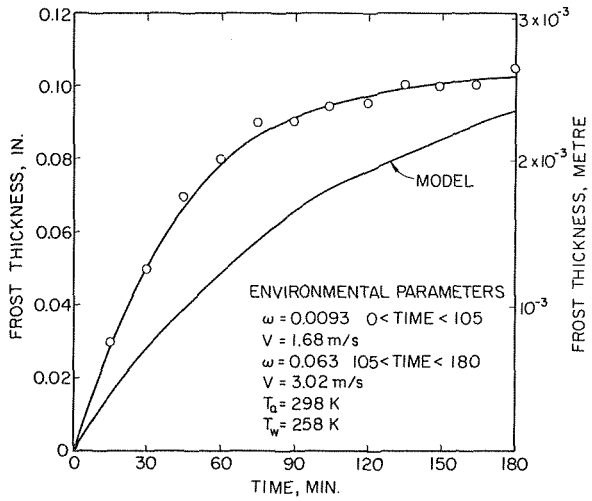

Fig. 6 Comparison of data and model for variable humidity

Diffusion in frost must also allow for the decreased effective cross-sectional area for diffusion and the increased path length the molecules must travel (tortuosity). This can be accounted for by multiplying the above equation by $(1 - \rho_f/\rho_{ice})/\tau$.

The transport of water vapor into the frost layer is then given by:

$$\dot{m}_{sd} = D_s\frac{(1 - \rho_{fs}/\rho_{ice})}{\tau_s}\left(\frac{d\rho_v}{dx}\right)_s$$

Using ideal gas relationships this can be put in terms of the water vapor partial pressure.

$$\dot{m}_{sd} = D_s\frac{(1 - \rho_{fs}/\rho_{ice})}{\tau_s}\frac{M_v}{RT_s}\left(\frac{dP_v}{dx}\right)_s \tag{4A}$$

$(dP_v/dx)_s$ can be expanded by the chain rule.

$$\left(\frac{dP_v}{dx}\right)_s = \left(\frac{dP_v}{dT}\right)_s\left(\frac{dT}{dx}\right)_s$$

This allows equation (4A) to be rewritten.

$$\dot{m}_{sd} = D_s\frac{(1 - \rho_{fs}/\rho_{ice})}{\tau_s}\frac{M_v}{RT_s}\left(\frac{dP_v}{dT}\right)_s\left(\frac{dT}{dx}\right)_s$$

If one final assumption is made then the growth rate and densification rates can be computed. This assumption requires that the density of the frost not vary with x, however it may still vary with time. Dropping the average notation on the density,

$$\frac{d\rho_f}{dt} = \frac{M_v D_s(1 - \rho_f/\rho_{ice})}{RT_s\tau_s x_s}\left(\frac{dP_v}{dT}\right)_s\left(\frac{dT}{dx}\right)_s \tag{5A}$$

$$\frac{dx_s}{dt} = \frac{h_M(\rho_{va} - \rho_{vs}) - \frac{M_v D_s(1 - \rho_f/\rho_{ice})}{RT_s\tau_s}\left(\frac{dP_v}{dT}\right)_s\left(\frac{dT}{dx}\right)_s}{\rho_f} \tag{6A}$$

Since the frost temperature is involved in these equations and since some of the parameters are functions of the frost surface temperature an energy balance must be set up to determine this temperature. Fig. A1 shows both a heat and mass balance on the frost. For a layer inside the front, ignoring sensible energy storage, the energy balance gives:

$$K_f\left[\left(\frac{dT}{dx}\right)_{x+dx} - \left(\frac{dT}{dx}\right)_x\right] = -\Delta H(\dot{m}_{x+dx} - \dot{m}_x) \tag{7A}$$

This can be rewritten as:

$$K_f\left(\frac{d^2T}{dx^2}\right)_x = -\Delta H\left(\frac{d\dot{m}}{dx}\right)_x \tag{8A}$$

Since it has been assumed that the frost density does not vary with x, then the amount of water vapor being frozen must be the same at all locations in the frost layer. This results in:

$$\frac{d\dot{m}}{dx} = \frac{\dot{m}_{sd}}{x_s} \tag{9A}$$

Combining equations (8A) and (9A) gives a simple second order differential equation for the frost temperature profile. If we assume that thermal conductivity does not change significantly over the temperature range within a given frost layer, then:

$$\frac{d^2T}{dx^2} = \frac{-\dot{m}_{sd}\Delta H}{K_f x_s} \tag{10A}$$

Equation (10A) can be integrated, using the boundary conditions $T = T_w$ at $x = 0$ and the fact that the heat transfer is equal to the heat convected to the frost surface plus the heat from the freezing of water vapor. The second boundary condition can be written in terms of the temperature gradient.

At $x = 0$;

$$\frac{dT}{dx} = \frac{h_H(T_a - T_s) + \dot{m}_t\Delta H}{K_f}$$

Integrating once and applying the second boundary condition

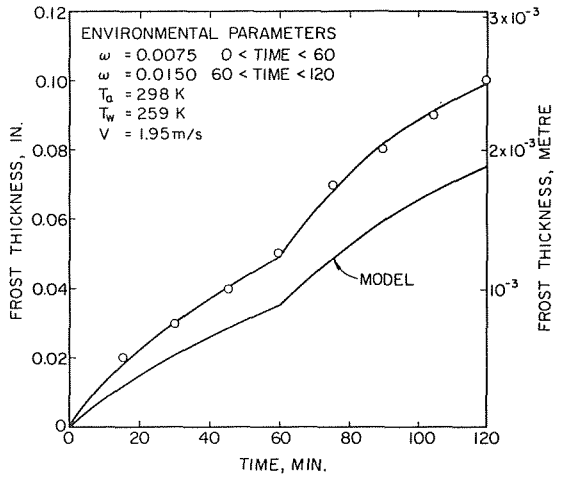

Fig. 7 Comparison of data and model for variable humidity and velocity

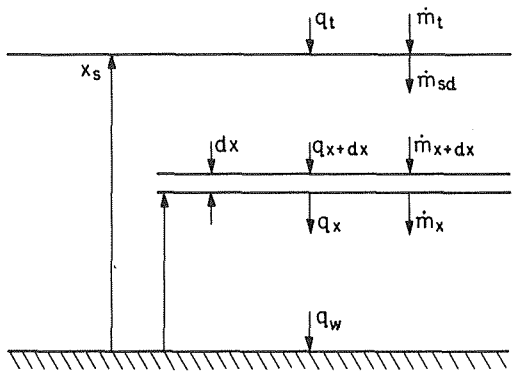

Fig. A1 Energy and mass balance for frost layer

gives:

$$\frac{dT}{dx} = \frac{-\dot{m}_{sd}\Delta H}{K_f x_s} x + \frac{h_H(T_a - T_s) + \dot{m}_t \Delta H}{K_f} \tag{11A}$$

Integrating a second time and applying the first boundary condition gives:

$$T = \frac{-\dot{m}_{sd}\Delta H}{K_f x_s} x^2 + \frac{h_H(T_a - T_s) + \dot{m}_t \Delta H}{K_f} x + T_w \tag{12A}$$

In order to solve equations (5A) and (6A) both $(dT/dx)_s$ and T_s must be found. $(dT/dx)_s$ can be found by substituting $x = x_s$ into equation (11A). $\dot{m}_{sd}$ is a function of $(dT/dx)_s$, but since it is a simple function, $(dT/dx)_s$ can be solved for explicitly.

$$\left(\frac{dT}{dx}\right)_s = \frac{h_H(T_a - T_s) + h_M(\rho_{va} - \rho_{vs})\Delta H}{K_f + \dfrac{M_v D_s(1 - \rho_f/\rho_{ice})}{RT_s\tau_s}\left(\dfrac{dP_v}{dT}\right)_s \Delta H} \tag{13A}$$

T_s can be found by substituting $x = x_s$ into equation (12A). However, a very complicated implicit equation results.

$$T_s = -\left[\frac{M_{vs}D_s(1 - \rho_f/\rho_{ice})}{RT_s\tau_s}\left(\frac{dP_v}{dT}\right)_s \cdot \frac{h_H(T_a - T_s) + h_M(\rho_{va} - \rho_{vs})\Delta H}{K_f + \dfrac{M_v D_s(1 - \rho_f/\rho_{ice})}{RT_s\tau_s}\left(\dfrac{dP_v}{dT}\right)_s \Delta H}\right]\frac{\Delta H}{2K_f} x_s + \frac{h_H(T_a - T_s) + h_M(\rho_{va} - \rho_{vs})\Delta H}{K_f} \cdot x_s + T_w \tag{14A}$$

It would be impossible to solve (14A) explicitly for T_s since in addition to the use of T_s on the right-hand side of the equation many of the parameters are also functions of T_s. It can be solved by trial and error, however.

R. C. Foster
Technical Training Coordinator,
Vought Systems Division,
L.T.V. Aerospace Corp.,
Dallas, Texas

A. Haji-Sheikh
Professor,
Mechanical Engineering Department,
University of Texas at Arlington,
Arlington, Texas

An Experimental Investigation of Boundary Layer and Heat Transfer in the Region of Separated Flow Downstream of Normal Injection Slots

An experimental investigation was conducted to determine the flow characteristics, heat transfer coefficients, and film cooling effectiveness in the region immediately downstream of flush, normal injection slots. Air was injected through these slots into a turbulent primary flow produced by a small wind tunnel. Velocity measurements and tuft studies indicated that there was a significant region of separated flow immediately downstream of the slot. The heat transfer coefficients were appreciably increased as a result of this flow separation, and the film cooling effectiveness was decreased in comparison to previous studies involving no flow separation.

Introduction

Film cooling describes a situation in which a cool secondary fluid is injected into the boundary layer of a hot primary fluid flowing along a surface. The secondary flow is injected into the primary flow through a variety of configurations, such as tangential slots, angled slots, multiple louvers, porous materials and, more recently, rows of holes. An extensive review of the subject of film cooling is provided by Goldstein [1].[1]

Some of the earliest work in this field is that of Wieghardt [2], who measured surface temperatures on an adiabatic plate (adiabatic wall temperature) resulting from injection through a near tangential slot. Later, various investigators, including Scesa [3], Hartnett, et al. [4], Samuel and Joubert [5], and Goldstein, et al. [6], sought to define surface heat transfer rates downstream of the injection location from measurement of adiabatic wall temperature distributions and primary stream heat transfer coefficients.

Heat transfer rates, however, cannot be predicted in the region immediately downstream of the injection location from primary stream heat transfer coefficients and adiabatic wall temperatures. Therefore, measurement of heat transfer coefficients and the description of flow patterns in this region are very important. Metzger, et al. [7] and Metzger and Fletcher [8] investigated heat transfer coefficients in this region resulting from injection through inclined slots, and an inclined row of holes, respectively. Metzger, et al. [9] measured velocity and temperature profiles upstream and downstream of flush angled slots, together with heat transfer rates on the downstream surface.

This paper presents an experimental investigation of the extent of the separated flow region resulting from injection through flush, normal slots. Slot widths of 1.58 mm, 3.17 mm, and 6.35 mm were employed, and three different blowing rates were investigated for each slot. The effect of pressure gradient was also examined for the 1.58-mm slot. Further, the influence of this separated region on heat transfer coefficients and effectiveness in the region immediately downstream of the slot was determined.

Apparatus and Procedure

The primary flow is provided by a variable speed wind tunnel with an inlet section measuring 0.914 m × 0.914 m. This inlet is followed by a converging section containing multiple rows of honeycomb screening for straightening the flow. The test section is shown schematically in Fig. 1. A diffuser section is located immediately downstream of the test section and the fan is located near the end of this diffuser section. Tunnel pressure gradient is provided by varying the geometry of the test section through the use of a flexible plexiglas sheet. Additional information concerning the primary flow system is given by Welty [10].

The secondary flow is supplied by a compressor. The air passes from the compressor through a pressure regulator, a venturi, and a distribution plenum, and finally exits in the tunnel through a flush slot oriented perpendicular to the tunnel floor. The secondary flow system is shown in Fig. 1. The flow is measured by the venturi,

[1] Numbers in brackets designate References at end of paper.

Contributed by the Heat Transfer Division for publication in the JOURNAL OF HEAT TRANSFER. Journal manuscript received by the Heat Transfer Division August 8, 1974.

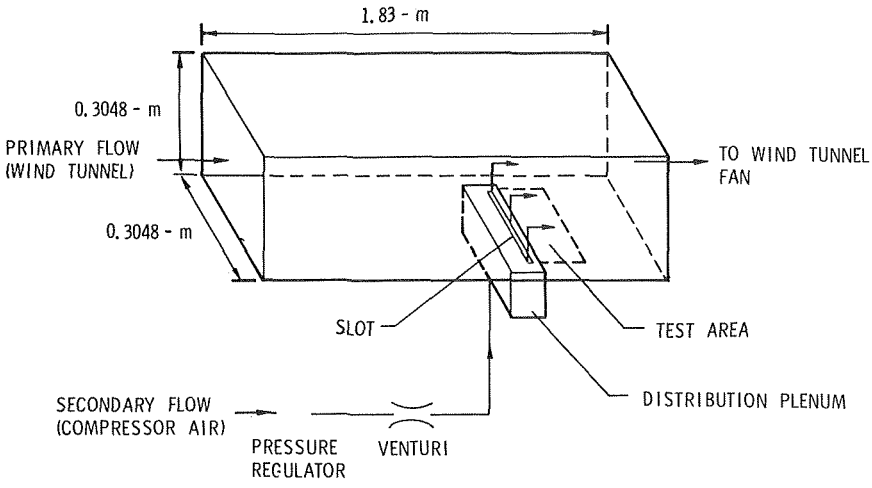

Fig. 1 Primary and secondary flow system schematic

which has an inlet diameter of 2.144 cm and a throat diameter of 1.072 cm. The venturi is calibrated by placing it downstream of a critical flow nozzle with an accurately known throat area. The distribution plenum serves as a point of attachment for the slot plates and as a housing for flow baffles. Flow baffles are necessary to provide a uniform flow velocity in the slot. These baffles are made by constructing a labyrinth-type construction of small wood strips followed by approximately 2.54 cm of air-conditioning filter material. The uniformity of the slot velocity is checked by measuring the velocity along the length of the slot. These measurements indicate that the maximum nonuniformity in velocity is ±2 percent along the length of the slot. The floor of the tunnel immediately above the plenum is recessed 3.17 mm to provide for various slot plates. These plates are made from plexiglas and each has dimensions of 2.54 cm × 3.94 cm × 0.317 cm. Three such plates are used to provide for slot widths of 1.58 mm, 3.17 mm, and 6.35 mm, with each plate having an individual slot. The secondary air was heated for the film cooling effectiveness tests by a belt type resistance heating element which provides for secondary air outlet temperatures ranging from approximately 54.4°C for the lowest mass flow rate, to 40.5°C for the highest mass flow rate.

A row of 1.19-mm dia holes is drilled along the center line of the tunnel floor at distances from the slot equal to 1.14, 2.41, 3.68, 4.95, 6.22, 13.84, and 18.79 cm. These holes serve both as static pressure ports and as access ports for the velocity probe. Velocity profiles are obtained using a pitot tube velocity probe. The velocity probe is made from 0.889 mm OD stainless steel tubing having a wall thickness of 0.1587 mm. The tip of the probe is flattened to a height of 0.584 mm and the bottom of a length of tube near the tip is polished to provide a flat surface. The probe is traversed into the boundary layer with a precision micrometer which provides for increments of travel equal to 0.0254 mm. Velocity profiles and static pressure distributions are measured downstream of the slot for various combinations of slot width and blowing parameter. These velocity measurements and static pressure distributions are conducted for a maximum and a zero pressure gradient condition (defined in Fig. 3). The probe is connected to one side of a Meriam inclined tube manometer, the other side of which is connected to the static pressure ports located in the floor of the wind tunnel. The point of zero velocity is identified as the point at which the manometer deflection is observed to be zero. Some error may be inherent in the velocity measurement system due to the variation of static pressure normal to the wall, but no satisfactory method of accounting for this variation could be found. It should also be noted that the probe measures only the component of velocity parallel to the tunnel floor (x-component), and that no attempt is made to orient the probe with the velocity vector. Corrections are applied to the velocity data obtained at the locations nearest to the wall [11]. Repeatability of velocity measurements is established through reruns of data at several locations.

A 20.7 cm × 15.2 cm heater section is installed (Fig. 2) immediately downstream of the injection location after completion of the velocity profile measurements. The heating element is made from 18-gauge nichrome wire having a resistance of 0.42 ohms per ft. This wire is set in 1.58-mm grooves, on 6.35-mm centers, which were milled in the 9.52-mm textolite plate to yield a continuous circuit with a resistance of 7.5 ohms. The actual heater surface is a 4.76-mm thick aluminum plate which is placed on top of the textolite plate containing the heating element. The aluminum plate has 1.58-mm slots, milled on 2.54-cm centers, which divide the surface into six equal parts with each part covering four strands of the nichrome heating element. These slots in the aluminum plate are filled with balsa wood to insulate each section. Copper-constantan thermocouples are made from 30B and S-gauge wire and are in-

Nomenclature

A_{strip} = surface area of heater
H_{12} = boundary layer shape factor, $\frac{\delta_1}{\delta_2}$
$\bar{h}$ = average heat transfer coefficient over element of heater surface
M = blowing parameter, $\frac{\rho_2 U_2}{\rho_\infty U_\infty}$
T_p = surface temperature of plate
T = temperature
P_{atm} = ambient pressure
P_s = tunnel static pressure
Re_s = slot Reynolds number, $\frac{U_2 s}{\nu_2}$
s = slot width
U = velocity
u = boundary layer velocity
x = distance from slot
X^* = distance from slot to end of reversed flow region
y = distance perpendicular to wall
δ = boundary layer thickness
δ_1 = displacement thickness, $\int_0^\delta (1 - \frac{u}{U_\infty})\, dy$
δ_2 = momentum thickness, $\int_0^\delta [\frac{u}{U_\infty}(1 - \frac{u}{U_\infty})]\, dy$
η = effectiveness, $\frac{T_{aw} - T_\infty}{T_2 - T_\infty}$

Subscripts

2 = secondary flow
∞ = primary flow
aw = adiabatic wall

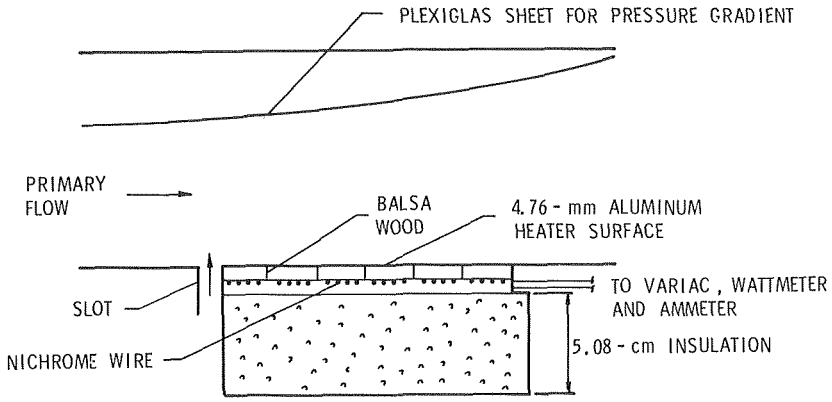

Fig. 2 Heater assembly schematic

stalled in the aluminum plate to record surface temperatures. A total of twelve thermocouples are installed in the plate, each section having one thermocouple at its center and the three sections nearest the slot having two additional thermocouples. The additional thermocouples are placed 2.54 cm from the plate center line, with one thermocouple on each side. One thermocouple is located between the inner surface of the insulation and the textolite plate for the purpose of computing the heat loss through the insulation. The tunnel air temperature is monitored by a thermocouple located directly over the heater section. The thermocouple leads are connected to a multi-position selector switch which incorporates a single ice bath reference junction into the circuit, and the voltage output of the thermocouples is measured by a Dana Model 5403 Digital Voltmeter having a readability of 0.001 mV. The thermocouples are calibrated using a Rosemont Model 910 a-c variable temperature bath, a Leeds and Northrup Model 8167-25-B platinum resistance thermometer, and a Leeds and Northrup 7556-A-12 type K-6 guarded potentiometer facility. Test temperatures are then determined from recorded voltage outputs and calibration data showing temperatures versus voltage output. Electrical power is supplied to the heater section by an auto-transformer and the power input is determined by a Westinghouse Wattmeter (a-c) with a readability of one W.

Heat transfer measurements are conducted for various combinations of slot width and blowing parameter. Each combination is tested using 100, 125, and 150 W power inputs. These measurements are made with a zero and a maximum pressure gradient (pressure gradient conditions are defined in Fig. 3). The primary flow velocity is adjusted to a value of 31.7 m/s and the desired power input delivered to the heater. The heater surface is allowed to reach an equilibrium temperature and the thermocouple outputs are recorded after equilibrium is established. The plate reaches this equilibrium temperature in approximately one and one-half hr. Secondary air, at ambient temperature, is then introduced through the slot. The plate is again allowed to approach equilibrium—usually requiring a time period of some 40 min—and the thermocouple output is recorded. The energy lost by convection from the heater surface to the primary air flow is

$$Q_{\text{convection}} = \text{Power Input} - Q_{\text{losses}} \tag{1}$$

where the losses are composed of radiation losses from the surface of the plate and conduction losses (approximately 1 percent of power input) through the insulation. Since each strip receives an equal amount of energy from the nichrome heating element, the energy lost by convection for each strip is

$$Q_{\text{strip}} = Q_{\text{convection}}/6 \tag{2}$$

and the average heat transfer coefficient, $\bar{h}$, over the one-in. strip is defined by,

$$\bar{h} = \frac{Q_{\text{convection}}/6}{A_{\text{strip}} \cdot (T_p - T_\infty)} \tag{3}$$

The heat transfer coefficient, $\bar{h}$, is calculated from surface temperature data at various distances downstream of the slot.

Film cooling effectiveness, η, measurements are conducted for various combinations of slot width and blowing parameter. These measurements are made with a zero and a maximum pressure gradient (pressure gradient conditions are shown in Fig. 3). An adiabatic surface is obtained for these tests by disconnecting the transformer and wattmeter from the heater section. The secondary injection air is heated for these measurements and the air temperature monitored by a thermocouple located just upstream of the slot exit in the distribution plenum. The primary flow velocity is set at

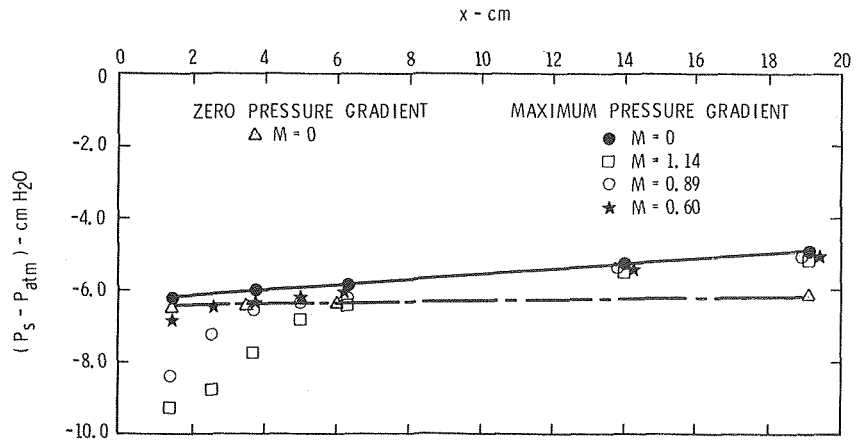

Fig. 3 Pressure distribution, $s = 1.58$ mm

31.7 m/s and the desired secondary flow rate obtained. Both the secondary air and the plate temperature are allowed to reach an equilibrium temperature. Initially, a time period of approximately one hour is required to reach equilibrium, but tests following immediately require a time period of 30 min to reach equilibrium. The heater plate temperature, as well as the primary and secondary air temperatures, are recorded after equilibrium is established. These temperatures are then used to find the effectiveness as defined by

$$\eta = \frac{T_{aw} - T_\infty}{T_2 - T_\infty} \tag{4}$$

Values of effectiveness are determined in this manner at selected distances from the slot.

Tunnel flow conditions are studied by utilizing the calculation of a boundary layer shape factor, H_{12}, to determine the nature, laminar or turbulent, of the primary flow. The velocity data is plotted and values for the momentum thickness, δ_2, and displacement thickness, δ_1, are determined by graphical integration. These data, in turn, are used to calculate the boundary layer shape factor, H_{12}, which has a very nearly constant value of 1.47 over the length of the plate. This is in agreement with a value of 1.40 recommended by Schlichting [12] and establishes that the primary flow downstream of the slot is turbulent for the value 31.7 m/s of the primary flow free stream velocity utilized in all tests.

Results and Discussion

Static Pressure Distributions. The static pressure distributions for the 1.58-mm slot, under the influence of the maximum pressure gradient, are shown in Fig. 3. These distributions indicate that the static pressure is appreciably lowered in the region immediately downstream of the injection location for a blowing parameter, M, equal to 1.14. They also indicate a decrease in static pressure, though not as large, for the lower values of blowing parameter. The extent of this region of decreased pressure in the downstream direction is approximately 6.35 cm for the maximum blow-

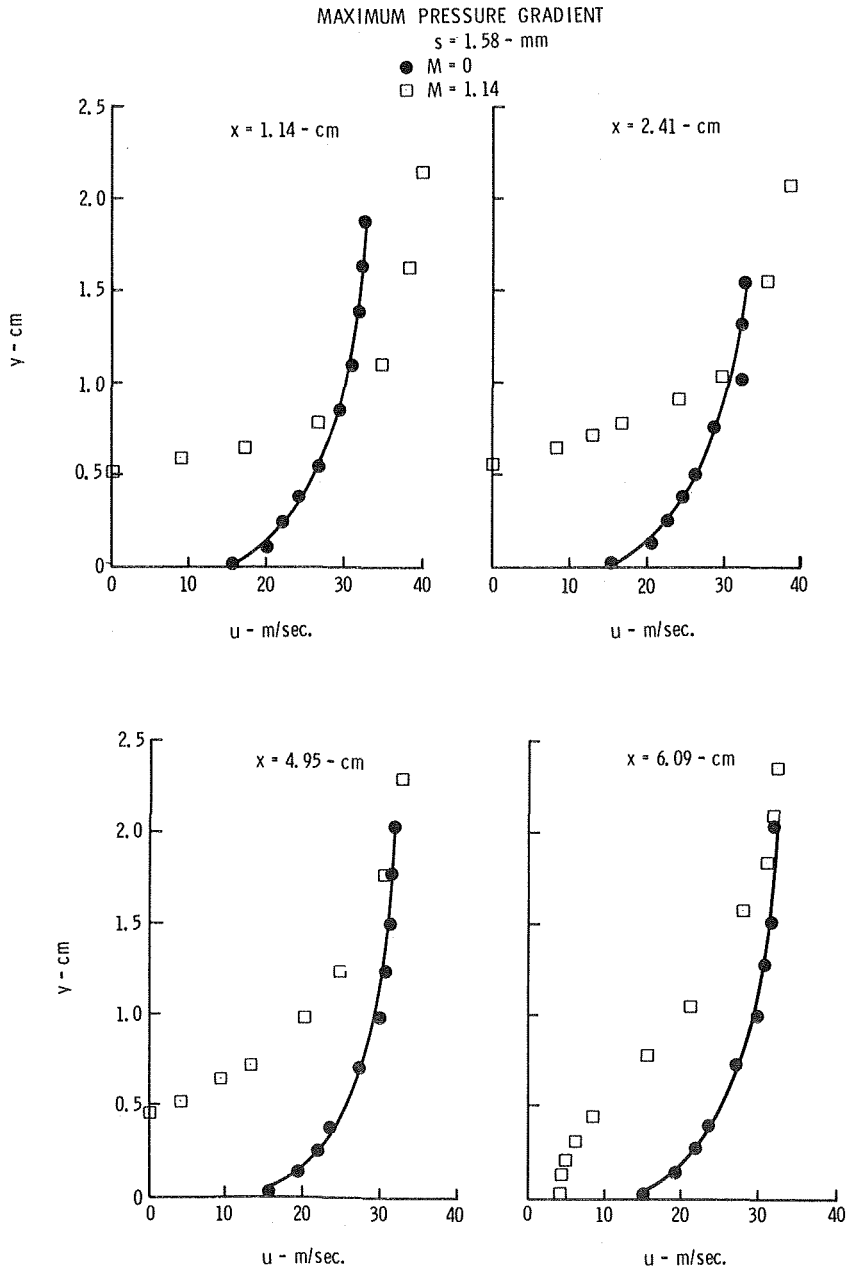

Fig. 4 Velocity profiles, $s = 1.58$ mm

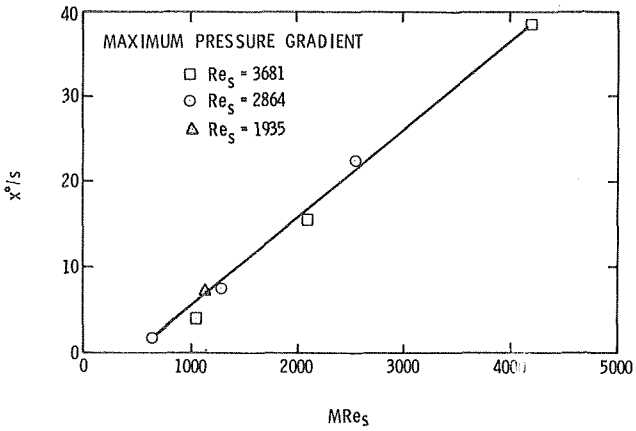

Fig. 5 Extent of reversed flow region downstream of slot

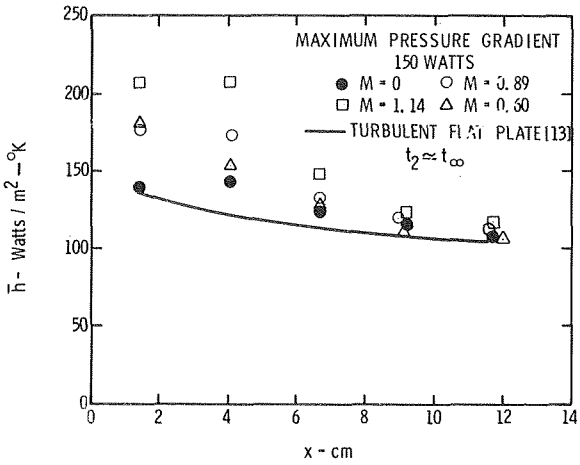

Fig. 6 Variation of heat transfer coefficient, s = 1.58 mm

ing parameter, M = 1.14. The distributions obtained for the 3.17-mm and 6.35-mm slots indicate a similar trend, with a reduction in magnitude in each case.

Velocity Profiles. Velocity profiles are shown in Fig. 4 for the 1.58-mm slot, M = 1.14, under the influence of maximum pressure gradient at distances from the slot equal to 1.14, 2.41, 4.95, and 6.09 cm. The velocity profile at the location x = 1.14 cm indicates a velocity equal to zero at a distance from the wall equal to 5.08 mm, and therefore defines the outer edge of the reversed flow region at this location. The velocity then increases quite rapidly and attains a value somewhat greater than the free stream value obtained without secondary injection. This increase may be attributed to the presence of the secondary injection jet in the region very near the slot. The outer edge of the reversed flow region, or the point at which the velocity is equal to zero, is observed to decrease in height to 4.57 mm at a distance equal to 4.95 cm from the slot. The existence of a near-zero velocity gradient at a distance of 6.09 cm indicates that flow reversal may be ending at this location. Additional velocity data for the 3.17-mm and 6.35-mm slots may be obtained from reference [11].

Tuft studies were also conducted for the 1.58-mm slot, M = 1.14, under the influence of maximum pressure gradient. Photographs [11] of the tufts, under this condition, confirm the existence of a region of reversed flow immediately downstream of the injection location, but do not conclusively verify the length of the reversed flow region as indicated by the velocity probe.

Extent of Reversed Flow Region. A nondimensional representation of the extent of the reversed flow region is obtained by plotting X^*/s versus $M\mathrm{Re}_s$ as shown in Fig. 5. The parameter X^*/s is observed to increase in a linear fashion for increasing values of the parameter $M\mathrm{Re}_s$. This correlation also suggests that the extent X^* would approach zero (no reversed flow) for small, but finite, values of the blowing parameter, M.

Heat Transfer. Local values of convective heat transfer coefficient, as determined from equation (3), are presented as a function of distance from the slot in Fig. 6. The experimental values of heat transfer coefficient without secondary injection and the results from an analytical expression [13] for turbulent flow over a flat plate (unheated for some distance from the leading edge) are observed to be in satisfactory agreement. The heat transfer coefficient, for M = 1.14, is appreciably increased (power input maintained at the same value used in tests without injection) in the region immediately downstream of the slot and decays to the value obtained with primary flow and no secondary injection at approximately 8.89 cm from the slot. The reversed flow region for these same conditions was observed to extend approximately 6.09 cm downstream of the slot, and therefore this increase in heat transfer coefficients may be attributed to flow separation in this region.

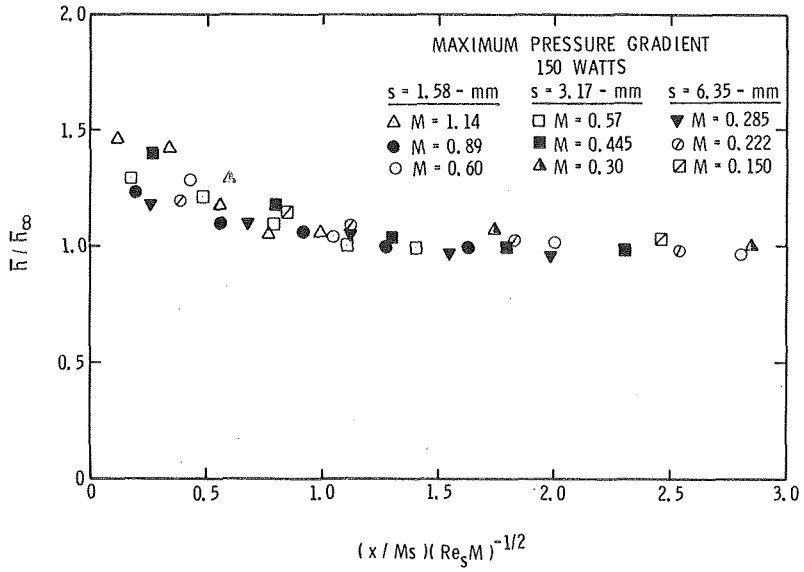

Fig. 7 Correlation of heat transfer coefficients

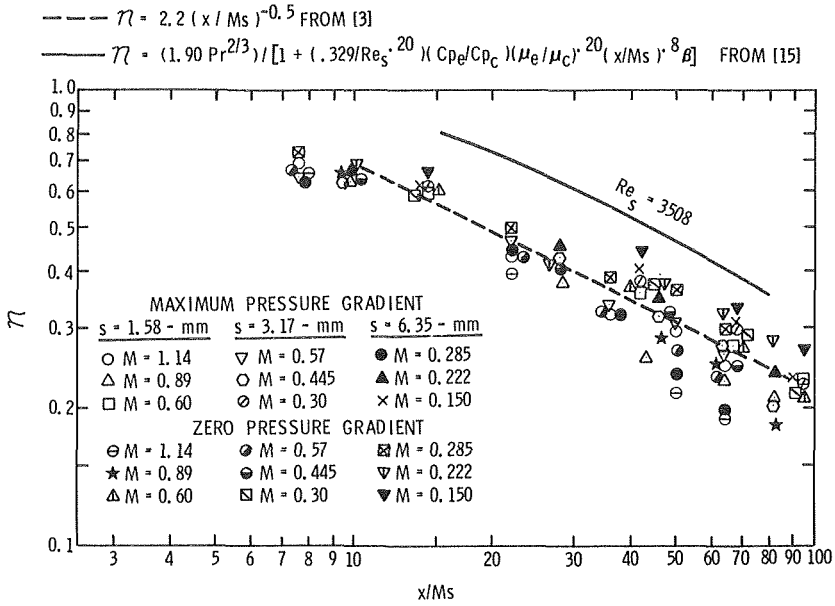

Fig. 8 Comparison of effectiveness results

The same trend is noted for the cases of $M = 0.89$ and 0.60, but the separation in the downstream direction is somewhat diminished in each case. The tests conducted with the 3.17-mm and 6.35-mm slots also exhibited similar behavior, with the heat transfer coefficient and separation in the downstream direction being less in each case. Experimental uncertainties were estimated using the method of Kline and McClintock [14], and an uncertainty of ±3 percent in the determination of the heat flux leads to an estimated uncertainty of ±4 percent in the value of the heat transfer coefficient, $\bar{h} = 209$ W/m² °K. The value of heat transfer coefficient was not influenced by a variation in the wall heating rate or by the small pressure gradient employed. A reasonable dimensionless correlation of heat transfer results is achieved by plotting the ratio, $(\bar{h}/\bar{h}_\infty)$, versus $(x/Ms)\,(Re_s M)^{-1/2}$ as shown in Fig. 7. The data are well correlated in this manner with the greatest deviation occurring immediately downstream of the slot, i.e., near $x = 1.72$ cm. The heat transfer coefficient obtained with secondary injection is observed to approach the value of the heat transfer coefficient obtained without secondary injection for a value of the parameter $(x/Ms)\,(Re_s M)^{-1/2}$ equal to 1.10.

Film Cooling Effectiveness. The film cooling effectiveness is presented in terms of a dimensionless parameter, x/Ms, in Fig. 8. A comparison between the experimental data obtained in the present investigation and an effectiveness correlation from reference [3] is also shown in Fig. 8. The agreement between the two is satisfactory except for distances very near the end of the plate where the inaccuracy of the experimental data is thought to be high. The experimental uncertainty, using the method of Kline and McClintock, is estimated to be ±1 percent for a value of effectiveness $\eta = 0.63$ and ±3 percent for a value of effectiveness $\eta = 0.23$. A comparison between the experimental data obtained in the present investigation and an effectiveness correlation from reference [15] is also presented in Fig. 8. This correlation was derived from experimental data for normal injection through porous materials, and the range of blowing parameter, M, utilized to obtain this correlation was not large enough to produce any separated flow. The experimental values for the effectiveness obtained in the present investigation are significantly lower than those expressed by this correlation in all cases. This difference may be attributed to the greater mixing efficiency achieved between the secondary and primary flow resulting from flow separation downstream of the slot.

Conclusions

A region of separated flow exists immediately downstream of the slot for normal secondary injection into a primary flow. The reversed flow associated with this flow separation was observed with velocity measurements and confirmed by tuft studies. This region, for the 1.58-mm slot, was quite extensive for a blowing rate, M, of 1.14. This reversed flow region was diminished for a blowing rate of 0.89 and was not observed for $M = 0.60$. This region, for the 3.17-mm slot, was observed to exist for blowing rates of 0.57 and 0.45.

The effect of an increase in pressure in the direction of the primary flow is to increase the extent of the separated region downstream of the slot.

The heat transfer coefficients in the region immediately downstream of the slot are increased as a result of this flow separation. No appreciable change in coefficients was indicated by variation of the wall heating rate or the pressure gradient.

The ratio of the heat transfer coefficient with secondary injection to the heat transfer coefficient with only primary flow, $\bar{h}/\bar{h}_\infty$, is well correlated in terms of a parameter defined by $(x/Ms)\,(Re_s M)^{-1/2}$.

The effectiveness values obtained for the blowing parameters, M, sufficient to produce flow separation downstream of the slot are significantly lower than the effectiveness values previously reported for flows without separation.

References

1 Irvine, T. F., and Hartnett, J. P., *Advances in Heat Transfer,* Academic Press, New York, 1971, pp. 321–379.

2 Wieghardt, K., "Hot-Air Discharge for De-Icing," AAF Translation Report No. F-TS-919-Re, Wright Field, 1946.

3 Scesa, S., "Effect of Normal Blowing on Flat Plate Heat Transfer," PhD thesis, University of California, Berkeley, Calif., 1954.

4 Hartnett, J. P., Birkebak, R. C., and Eckert, E. R. G., "Velocity Distributions, Temperature Distributions, Effectiveness and Heat Transfer for Air Injected Through a Tangential Slot Into a Turbulent Boundary Layer," JOURNAL OF HEAT TRANSFER, TRANS. ASME, Series C, Vol. 83, No. 3, Aug. 1961, pp. 293–306.

5 Samuel, A. E., and Joubert, P. N., "Film Cooling of an Adiabatic Flat Plate in Zero Pressure Gradient in Presence of Hot Mainstream and Cold Tangential Secondary Injection," JOURNAL OF HEAT TRANSFER, TRANS. ASME, Series C, Vol. 87, 1965, pp. 409–418.

6 Goldstein, R. J., Eckert, E. R. G., Tsou, F. K., and Haji-Sheikh, A., "Film Cooling With Air and Helium Injection Through Rearward Facing Slot Into a Supersonic Air Flow," *AIAA Journal,* Vol. 4, No. 6, June, 1966, pp. 981–985.

7 Metzger, D.E., Carper, H. J., and Swank, L. R., "Heat Transfer With Film Cooling Near Nontangential Injection Slots," *Journal of Engineering for Power,* Apr. 1968, pp. 157–163.

8 Metzger, D. E., and Fletcher, D. D., "Evaluation of Heat Transfer for Film-Cooled Turbine Components," *Journal of Aircraft*, Vol. 8, No. 1, Jan. 1971, pp. 33–38.

9 Metzger, D. E., Carper, J. H., and Warren, J. M., "Predicted Film Cooling Near Flush Slots—Comparison With Experiment," *Journal of Aircraft*, Vol. 9, No. 12, Dec. 1972, pp. 857–863.

10 Welty, D. E., "A Comparative Study of Separation Criteria by Analytical and Experimental Methods," MS thesis, The University of Texas at Arlington, 1971.

11 Foster, R. C., "Experimental Study of Boundary Layer and Heat Transfer in the Region of Separated Flow Downstream of Normal Injection Slots," PhD thesis, The University of Texas at Arlington, 1973.

12 Schlichting, H., *Boundary-Layer Theory*, McGraw-Hill New York, 1968, p. 436.

13 Eckert, E. R. G., and Drake, R. M., *Heat and Mass Transfer*, McGraw-Hill, New York 1959, p. 217.

14 Kline, S. J., and McClintock, F. A., "Describing Uncertainties in Single-Sample Experiments," *Mechanical Engineering*, Vol. 75, Jan. 1953, p. 3.

15 Eckert, E. R. G., and Drake, R. M., *Analysis of Heat and Mass Transfer*, McGraw-Hill, New York, 1972, p. 460.

F. W. Ahrens[1]
Graduate Student,
Department of Mechanical Engineering,
University of Wisconsin,
Madison, Wisc.
Mem. ASME

H. N. Powell
Professor,
University of Wisconsin,
Madison, Wisc.

Effects of a Transverse Magnetic Field on a Constricted Electric Arc

The interaction of a constricted electric arc (argon at 1 atm) with an applied perpendicular magnetic field has been investigated analytically. The resulting (two-dimensional) flow and temperature fields, conductive and radiative wall heat transfer, and voltage-current characteristics of the arc are predicted. Three characteristic parameters are isolated: (I/a = current/tube radius), (Re = Lorentz and viscous force parameter), (R_T = radiation parameter). When radiation is negligible, the first two are sufficient to scale the effects of any combination of current, tube radius, and applied magnetic field strength. A twin vortex flow pattern is predicted, with the displacement of the vortex "eyes" greatest for high applied magnetic fields and low currents. Comparisons with experimental results from the literature are good to satisfactory.

Introduction

The purpose of this study is to analytically investigate the steady-state effects of a transverse magnetic field on an electric arc which is constricted by a cooled tube. In addition to its scientific significance, this subject is expected to be pertinent to technically important constricted arc applications such as plasma torch design and plasma transport property measurement, to magnetically propelled arc situations in circuit breakers, arc heaters, and new welding techniques, and to potential applications in centrifugal separation of gas mixtures, magnetically variable electrical resistors and possibly rock boring. The specific objectives are to:

1 Develop a realistic physical and analytical model which predicts the arc behavior and identifies the important parameters.

2 Obtain information on the power requirement of the arc as a function of the applied magnetic field and arc current.

3 Obtain information about the heat flux variation around the periphery of the arc at the tube wall.

4 Determine details of the flow field and temperature distribution in the arc.

Numerical results relating to items 2–4 are restricted to argon arcs at atmospheric pressure. For simplicity, only arcs of large length-to-diameter ratio (L/D) are considered, and the applied magnetic field is taken to be uniform. As a consequence of $L/D \gg 1$, it is assumed that variation of conditions with axial position is negligible over the major portion of the arc column. It is this two-dimensional region that is studied here. In the work by Sauter [1][2] on argon arcs, an arc L/D of 12 was sufficient to establish such conditions experimentally.

The experimental results which are available [1, 2] indicate that:

1 A double vortex flow pattern exists in the arc cross section.

2 The peak temperature is deflected in the Lorentz force direction.

3 The magnetic field effects are relatively less pronounced for high current arcs than for low current ones.

These characteristics have also been shown by previous analytical investigations [3–6], but their limitations make it unlikely that they can give adequate quantitative predictions over a range of arc operation. Furthermore, information on arc phenomena such as the wall heat flux distribution, the effects of tube radius, of radiative energy loss, etc., have not been adequately studied previously, and simultaneous inclusion of all effects expected to be influential has not been attempted heretofore.

Analysis

The physical model for the constricted arc is characterized as follows. A direct current arc is operating with current, I, in a tube of radius, a. The wall is assumed to have a uniform temperature, T_W. The tube wall is electrically nonconducting in the axial direction. Since positions near the electrodes are not considered, the applied electric field (axial voltage gradient) has a uniform value $\vec{E}$, over the arc cross section. It is taken to act in the negative z-direction (see Fig. 1 for coordinate systems employed). The uniform magnetic field, $\vec{B}$, is transverse to the tube axis, in the y-direction.

The following assumptions are made:

1 Local thermodynamic equilibrium (LTE) prevails over the entire arc cross section.

2 The induced electric field caused by motion of the plasma across magnetic field lines is negligible compared to the applied electric field.

3 Effects of the self-induced magnetic field are negligible rela-

[1] Presently: Research Engineer, Whirlpool Corp., Research Center, Benton Harbor, Mich.

[2] Numbers in brackets designate References at end of paper.

Contributed by the Heat Transfer Division for publication in the JOURNAL OF HEAT TRANSFER. Manuscript received by the Heat Transfer Division Sept. 19, 1974.

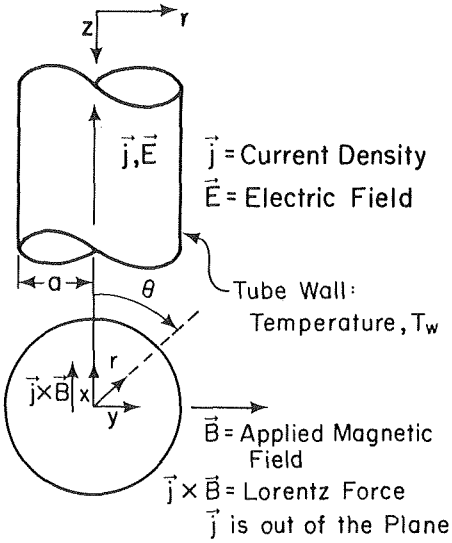

Fig. 1 Coordinate systems and system configuration

tive to those of the applied field.

4 Hall effects and dependence of plasma properties on the magnetic field are negligible.

5 For the purpose of considering energy losses by thermal radiation, the arc plasma may be regarded as emission-dominated [7] and the tube wall may be considered black.

6 Buoyancy forces are negligible relative to the Lorentz forces.

7 The flow is laminar.

8 Viscous dissipation is negligible.

The LTE assumption is not uniformly valid [8], but Sauter [1], who studied this same arc problem experimentally, found that his measurements were internally consistent when tested with equilibrium properties. Considering arc conditions typical of Sauter's experiments, assumptions 2 and 4 are readily supported by estimates using results from the present analysis. Typically, the induced electric field is less than one percent of the applied field and the Hall parameter is less than 0.05, when the magnetic field is below 500 gauss. With regard to assumption 3, it may be shown for the arc model considered here that the self-induced part of the Lorentz force distribution is irrotational and consequently does not influence the flow field. All the assumptions are discussed in more detail elsewhere [8]. Since the pressure variations are expected to be a small fraction of the nominal operating pressure, it is sufficient to consider the plasma thermophysical properties to be dependent on temperature only.

With the foregoing assumptions the total current is given by Ohm's law:

$$I = E\int_0^{2\pi}\int_0^a \sigma r dr d\theta \tag{1}$$

The motivating force of all flow effects is the Lorentz force; for the $\vec{j}$ and $\vec{B}$-direction shown in Fig. 1, the local Lorentz force density is: $\vec{j} \times \vec{B} = \sigma EB\vec{x}$, where $\vec{x}$ is the x-direction unit vector. The momentum equation representing the balance of forces on a fluid element is thus:

$$\rho\vec{v}\cdot\nabla\vec{v} = -\nabla p - \nabla(\frac{2}{3}\mu\nabla\cdot\vec{v}) + \nabla\cdot\mu(\mathrm{def}\ \vec{v}) + \sigma EB\vec{x} \tag{2}$$

The deformation tensor, def $\vec{v}$, is defined by $\mathrm{def}\,\vec{v} \equiv (\nabla\vec{v}) + (\nabla\vec{v})^T$.

Any fluid motion must also satisfy the familiar continuity equation:

$$\nabla\cdot\rho\vec{v} = 0 \tag{3}$$

The thermal energy equation, including Joule heating and radiation terms, but neglecting the work term $\vec{v}\cdot\nabla p$, is

$$\rho\vec{v}\cdot\nabla h = \nabla\cdot k\nabla T + \sigma E^2 - U \tag{4}$$

where, h is the enthalpy, k the equilibrium thermal conductivity, and U the volumetric radiative power loss. The work term, $\vec{v}\cdot\nabla p$, may be shown to be negligible compared to the Joule heating term if the induced electric field is negligible, as assumed.

Since the problem as defined requires a numerical solution technique, it is convenient to replace the continuity and momentum equations by the following more readily solved stream function and vorticity equations [8]:

$$\nabla^2\psi = -\rho\omega - \frac{\nabla\rho}{\rho}\times[\nabla\times(\psi\hat{\vec{z}})]\cdot\hat{\vec{z}} \tag{5}$$

$$[\nabla\times(\psi\hat{\vec{z}})]\cdot\nabla\omega + \nabla\rho\times\nabla e_K\cdot\hat{\vec{z}} = \mu\nabla^2\omega + EB[\nabla\times(\sigma\hat{\vec{x}})]\cdot\hat{\vec{z}} \tag{6}$$

where $e_K = |\nabla\times(\psi\vec{z})|^2/2\rho^2$ = local fluid kinetic energy and $\vec{z}$ is a unit vector in the axial direction. Equations (5) and (6) may be considered as elliptic partial differential equations for ψ and ω. For the simpler case of incompressible, constant property flow without

Nomenclature

a = tube radius
$\vec{B}$ = applied magnetic field strength
c_p = specific heat at constant pressure
e_K = kinetic energy per unit mass
$\vec{E}$ = applied electric field
h = specific enthalpy
H = a heat flux potential (equation (7))
I = arc current
$\vec{j}$ = current density
k = thermal conductivity
p = pressure
Pr = Prandtl number
$\vec{q}$ = conduction heat flux
$\vec{q}_R$ = radiation heat flux
q_{wc} = conduction heat flux at wall
q_{w0} = reference heat flux
q_{wR} = radiation heat flux at wall
r = radial coordinate
R_T = thermal radiation parameter (equation (15))
Re = Reynolds number
T = temperature
U = volumetric radiative power
$\vec{v}$ = velocity in x-y plane
x = Lorentz force direction coordinate
y = coordinate normal to both the Lorentz force direction and the tube axis
z = coordinate in direction of tube axis
θ = azimuthal angular coordinate
μ = viscosity
ρ = mass density
σ = electrical conductivity
τ = viscous stress tensor
ϕ_R = radiation heat-flux potential
ψ = compressible stream function
ω = vorticity ($= \nabla\times\vec{v}$)

Subscripts

c = conduction
r = radial
R = radiation; reference value
w = wall
θ = azimuthal
0 = reference value

Superscripts

$(^-)$ = dimensionless quantity

Operators

def = deformation
∇ = gradient
$(\nabla\vec{v})^T$ = transpose of velocity gradient tensor
∇^2 = Laplacian

coupling to the energy equation, numerical methods for solving stream function and vorticity equations are well-established [9]. Also, for computational convenience, temperature and enthalpy are replaced as variables in the energy equation by the introduction of a "modified heat flux potential" defined as:

$$H \equiv \left(\frac{c_p}{k}\right)_w \int_{h_w}^{h} \frac{k}{c_p}\,(h')\,dh' \tag{7}$$

where $(c_p/k)_w$ and h_w are evaluated at the wall temperature. This simplifies the heat conduction term, establishing an elliptic form for the energy equation:

$$\left(\frac{k}{c_p}\right)_w \frac{c_p}{k}\left[\nabla \times (\hat{\psi z})\right] \cdot \nabla H = \left(\frac{k}{c_p}\right)_w \nabla^2 H + \sigma E^2 - U \tag{8}$$

For a given p and T_w, H is a function of T only. Therefore, the fluid properties used in solving the governing equations may alternatively be expressed as functions of H, tending to cause smoother variations than with T.

The source term for the radiative heat transfer to the wall is the distribution of volumetric radiation rate, U. It has been noticed previously [8, 10, 11] that, for emission-dominated radiation, the heat flux is proportional to the gradient of a scalar potential, ϕ_R,

$$\vec{q}_R = -\Delta \phi_R \tag{9}$$

so that an energy balance for the radiation gives

$$\nabla^2 \phi_R = -\,U \tag{10}$$

The correct boundary condition on ϕ_R is that it becomes independent of azimuthal position, θ, as the distance from the source becomes infinite. However, as an approximation in this study, ϕ_R is assumed to be uniform (at an arbitrary value of zero) at the tube radius.

Equations (1) and (5–10) together with the property relations $k(T)$, $\sigma(T)$, $\mu(T)$, $h(T)$, $\rho(T)$, and $U(T)$, and the conditions at the wall ($T = T_w$, $\phi_R = 0$, and $\vec{v} = 0$), embody a mathematical description of a constricted arc interacting with a transverse magnetic field as a function of the following parameters: tube radius, kind of gas, pressure, arc current, applied magnetic field strength, and tube wall temperature. It should be noted that with the absence of axial temperature gradients the analysis would not be altered by the possible existence of a fully developed axial flow component.

Noting that a symmetry of flow and thermal patterns about the plane $y = 0$ exists, the boundary conditions may be stated as

$$0 \le r \le a: \qquad \psi(r, 0) = \psi(r, \pi) = 0 \tag{11a}$$

$$0 \le \theta \le \pi: \qquad \psi(a, \theta) = 0 \tag{11b}$$

$$0 \le r \le a: \qquad \omega(r, 0) = \omega(r, \pi) = 0 \tag{11c}$$

$$0 \le \theta \le \pi: \qquad \omega(a, \theta) = \frac{\partial}{\partial r}\left(\frac{1}{\rho}\frac{\partial \psi}{\partial r}\right)(a, \theta) \tag{11d}$$

$$\left(\text{with } v_\theta(a, \theta) = -\frac{1}{\rho}\frac{\partial \psi}{\partial r}(a, \theta) = 0\right)$$

$$0 \le r \le a: \qquad \frac{\partial H}{\partial \theta}(r, 0) = \frac{\partial H}{\partial \theta}(r, \pi) = 0;\ \frac{\partial H}{\partial r}\left(0, \frac{\pi}{2}\right) = 0 \tag{11e}$$

$$0 \le \theta \le \pi: \qquad H(a, \theta) = 0 \tag{11f}$$

$$0 \le r \le a: \qquad \frac{\partial \phi_R}{\partial \theta}(r, 0) = \frac{\partial \phi_R}{\partial \theta}(r, \pi) = 0;\ \frac{\partial \phi_R}{\partial r}\left(0, \frac{\pi}{2}\right) = 0 \tag{11g}$$

It is desirable to nondimensionalize the basic equations in order to ascertain what groupings of parameters are influential in determining the arc behavior. The dimensionless variables are designated with an overbar, e.g., $\bar{\sigma} = \sigma/\sigma_R$ in which the reference value is designated with the subscript R. The characteristic length is taken to be the tube radius, a. Thus, $\bar{\nabla} = a\nabla$. To avoid the occurrence of trivial dimensionless groups in the basic equations, the following relationships among reference parameters are specified. (The reference wall heat flux is given the subscript "0" to avoid confusion with the designation for radiation heat flux.)

$$\psi_R = \rho_R a v_R, \quad E_R = \frac{I}{2\pi a^2 \sigma_R}, \quad \text{and } q_{w_0} = \frac{k_w}{c_{p_w}}\frac{H_R}{a}$$

When the dimensionless variables and foregoing definitions are used in the governing equations, five dimensionless groups appear. The first and second parameters are the familiar Reynolds and Prandtl numbers, evaluated with reference state values:

$$\mathrm{Re} = \frac{\rho_R v_R a}{\mu_R};\quad \mathrm{Pr} = \frac{c_{p_R}\mu_R}{k_R}$$

The third, rearranged as

$$\frac{IB}{2\pi \mu_R v_R} = \frac{(\rho_R I B a)/(2\pi \mu_R{}^2)}{(\rho_R v_R a/\mu_R)} = \frac{\mathrm{Gr}}{\mathrm{Re}} \tag{12}$$

is the ratio of a Grashof number (Gr) based on Lorentz force to the Reynolds number: Gr/Re. To define the reference velocity, v_R, let the body forces and viscous forces be in balance (i.e., take Gr/Re $\equiv$ 1) giving

$$v_R = IB/2\pi\mu_R \tag{13}$$

The fourth parameter represents a ratio of heat production by Joule heating to heat transfer to the tube wall by conduction: $c_{p_w} I^2/4\pi^2 k_w H_R \sigma_R a^2$. On physical grounds, this ratio should be of magnitude unity provided the reference values of σ_R and H_R are realistically chosen. Making this definition gives

$$\sigma_R H_R = (c_{p_w}/4\pi^2 k_w) \cdot (I/a)^2 \tag{14}$$

because $\sigma(T)$ is a monotonic function of T and $H = H(T)$, equation (14) effectively specifies a reference T_R value in relation to the wall temperature and the ratio of arc current to tube radius, I/a. It is consistent to use this T_R (or H_R) in evaluating the other fluid reference properties, σ_R, ρ_R, μ_R, k_R, c_{pR}, and of course, Re and Pr. As a practical matter, it is inconvenient to evaluate U_R at T_R because at typical values of T_R (often below 10^4 °K) the radiant energy emission rate is exceedingly small, so a constant (arbitrary) value of 1000 W/cm^3 is used.

The fifth dimensionless group is basically a thermal radiation parameter, termed R_T:

$$R_T \equiv (c_{p_w} a^2 U_R)/(k_w H_R) \tag{15}$$

It is seen that R_T represents a ratio of radiative to conductive heat loss. It is interesting to note from the form of R_T that the importance of radiation changes rapidly with a, for a given I/a.

Having specified all the reference quantities and dimensionless groups, the governing equations become:

$$\bar{\nabla}^2 \bar{\psi} = -\bar{\rho}\bar{\omega} - \frac{\bar{\nabla}\bar{\rho}}{\bar{\rho}} \times \left[\bar{\nabla} \times (\bar{\psi}\hat{\bar{z}})\right] \cdot \hat{\bar{z}} \tag{16}$$

$$\mathrm{Re} \cdot \left[\left[\bar{\nabla} \times (\bar{\psi}\hat{\bar{z}})\right] \cdot \bar{\nabla}\bar{\omega} + \bar{\nabla}\bar{\rho} \times \bar{\nabla}\frac{\left|\bar{\nabla} \times (\bar{\psi}\hat{\bar{z}})\right|^2}{2\bar{\rho}^2} \cdot \hat{\bar{z}}\right] = \bar{\mu}\bar{\nabla}^2\bar{\omega} + \bar{E}\bar{\nabla} \times (\bar{\sigma}\hat{\bar{x}}) \cdot \hat{\bar{z}} \tag{17}$$

$$\mathrm{Pr}\ \mathrm{Re}\frac{\bar{c}_p}{\bar{k}}\left[\bar{\nabla} \times (\bar{\psi}\hat{\bar{z}})\right] \cdot \bar{\nabla}\bar{H} = \bar{\nabla}^2\bar{H} + \bar{\sigma}\bar{E}^2 - R_T\bar{U} \tag{18}$$

$$\bar{E}\int_0^{\pi}\int_0^{1}\bar{\sigma}\bar{r}\,d\bar{r}\,d\bar{\theta} = \pi \tag{19}$$

$$\bar{\nabla}^2\phi_R = -\,R_T\bar{U} \tag{20}$$

The boundary conditions on these equations are simply the dimensionless analogs of equations (11a)–(11g).

Based on the foregoing formulation, a solution of the governing equations for a given gas and wall temperature depends, in effect, on the values of the three parameters: I/a, Re, and R_T, noting that

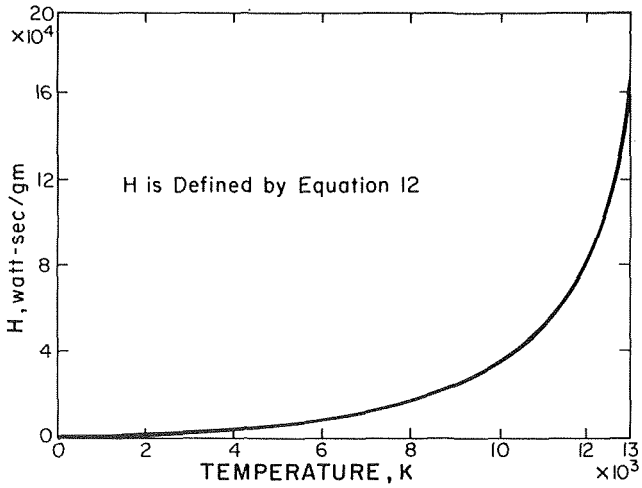

Fig. 2 The modified heat flux potential *(H)* as a function of *T* for atmospheric pressure argon with a T_w = 1000°K

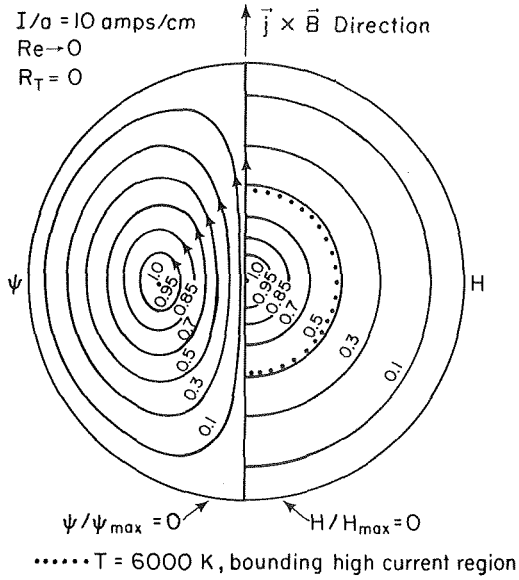

Fig. 3 Example streamlines (constant ψ) and isotherms (constant *H*), with $\psi_{max} \rightarrow 1.25 \times 10^{-4}$ Re (gm/cm-s) and T_{max} = 8000°K

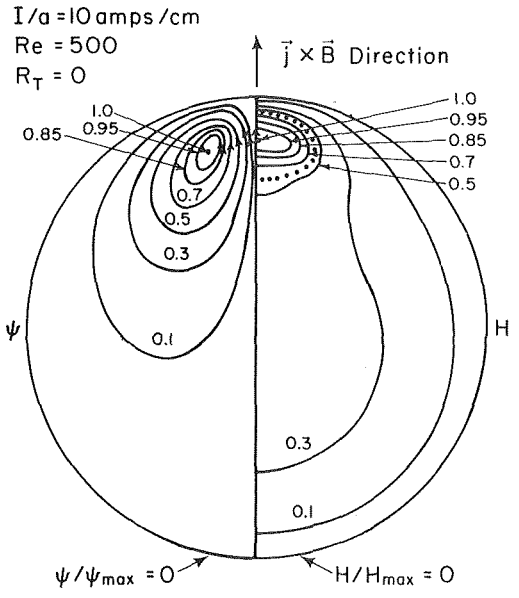

Fig. 4 Example streamlines and isotherms with ψ_{max} = 8.6 × 10^{-3} gm/cm-s and T_{max} = 7650°K

I/a is dimensional. Furthermore, from their definitions, it may be seen that Re is a function of I/a and Ba^2 and that R_T is a function of I/a and a^2. Thus, one must specify I, B, and a to achieve a solution, and no general dimensionless solutions exist. However, it should be noted that some degree of generality of solutions does appear if the radiative energy loss can be neglected ($R_T \rightarrow 0$). This is a good approximation for either small diameter arcs or low maximum temperature arcs (i.e., low I/a values). For a given arc gas, wall temperature, nominal pressure and for $R_T \rightarrow 0$, the same dimensionless solution applies for any combinations of I, B, and a for which both Ba^2 and I/a remain constant; this limiting behavior justifies the retention of the dimensionless equations in obtaining and presenting numerical results.

Numerical Solution Procedure

The numerical solution of the dimensionless governing equations may be achieved by an iterative method for solving the corresponding finite difference equations in cylindrical coordinates. In this study, the angular and radial grid point spacings were uniform. As a compromise between cost and accuracy, a 21 by 21 grid point array was used. A detailed description of the finite difference equations, the iterative numerical solution method, the fluid property functions, and the computer program is available elsewhere [8].

Results and Discussion

The numerical results summarized here are for constricted argon arcs operating at atmospheric pressure with a wall temperature of 1000°K and for three values of I/a (10, 80, and 200 amps/cm). A much more extensive compilation of results at these I/a values is available in [8].

Space does not allow a detailed discussion of the plasma property values used in this study. Approximate curve fits of functions synthesized from published data [1, 12–18] were employed; the interested reader is referred to [8]. Fig. 2 gives the basic $H(T)$ relation to 13,000°K at 1 atm. The steep rise in H at high T reflects the rapidly increasing degree of ionization. Table 1 gives various reference parameters, for use in converting dimensionless results into physical quantities, for the three I/a values considered.

Table 1 Reference parameters

I/a (amp/cm)	T_R (K)	a^2B/Re (cm^2 – gauss)	R_T/a^2 (cm^{-2})	aE_R (V)	aq_{w0} (W/cm)
10	6100	0.30	175	3.54	5.7
80	8250	0.095	85.2	0.94	11.5
200	10800	0.063	34.7	0.90	28.7

Examples of the detailed streamline patterns (constant $\bar{\psi}$ lines) and isotherms (constant $\bar{H}$ lines) are shown in Figs. 3–6. A dotted isotherm is included along which the temperature is 6000°K. Because the electrical conductivity is extremely low below this isotherm, it may be considered as the approximate boundary of the current-carrying region (arc core). There is much contrast in the results: The arc core is confined to a small region when I/a = 10 amps/cm, while at higher I/a the core nearly fills the tube. Because of the small size of the arc core at I/a = 10 amps/cm, it is easily deflected by the magnetic field, which causes the temperature distribution to become very distorted and the core size to shrink due to more intense cooling (Figs. 3 and 4). Because of the strong coupling between the fluid vortex motion and the electrical conductiv-

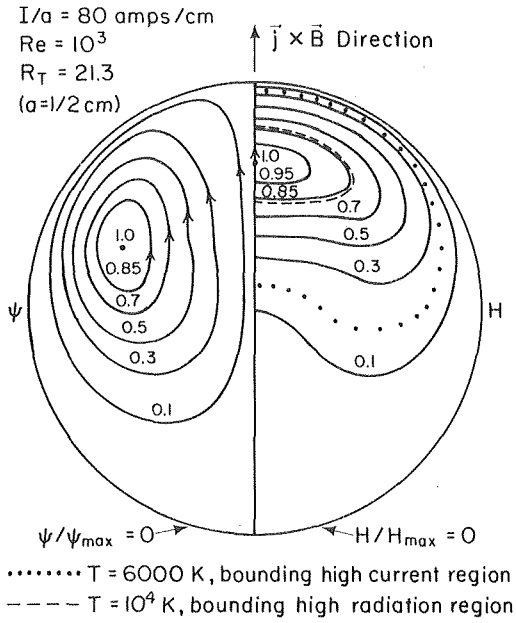

Fig. 5 Example streamlines and isotherms with $\psi_{max} = 1.56 \times 10^{-2}$ gm/cm-s and $T_{max} = 10{,}500°K$

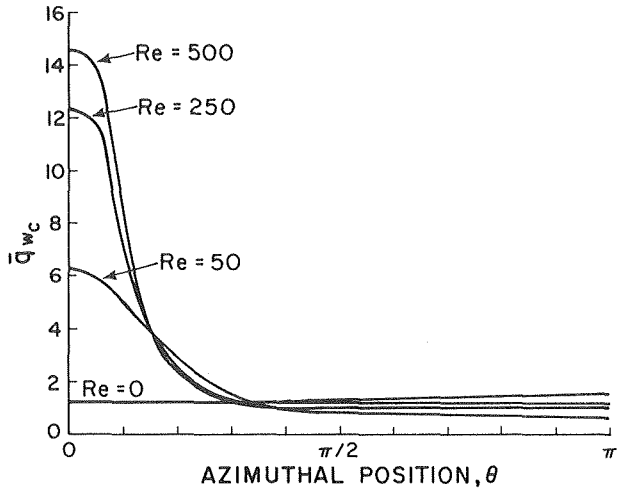

Fig. 7 Dimensionless wall heat flux by conduction ($\bar{q}_{w_c}$) for I/a = 10 amps/cm and $R_T = 0$

ity (and, hence, temperature) distribution, there is a tendency for the vortex centers to move in the direction of the deflected arc core for low and moderate I/a (Figs. 4 and 5). At higher I/a, however, this does not occur (Fig. 6), probably due to the counteracting influence of expansion effects and the smaller deflection of the larger arc core.

The high power dissipation typically occurring in a constricted arc causes the heat transfer rate to the tube to be large. For example, with zero magnetic field, and a tube radius of ½ cm, the power dissipation per unit tube length (EI) is calculated to be 190 W/cm for I = 40 amps and 540 W/cm for I = 100 amps, giving uniform wall heat fluxes of 60 and 172 W/cm, respectively. The isotherm patterns presented in the foregoing have indicated that when a magnetic field is applied (Re ≠ 0) there will be an appreciable asymmetry in the distribution of heat flux to the tube wall. This fact, combined with an increased power dissipation caused by the magnetic field (described in the following), implies that the maximum wall heat fluxes will be very large. A knowledge of the heat flux to be expected is, therefore, of importance in the thermal design of a constricted arc device. Predicted dimensionless wall heat flux distributions are shown in Figs. 7 and 8. It is clear that the effect of an applied magnetic field is very strong at low I/a: for I/a = 10 amps/cm and Re = 500, the maximum heat flux is 12 times the heat flux for Re → 0. Since radiation energy losses are negligible at this I/a value, only the heat transfer by conduction is given. Heat transfer results for a case in which radiation losses are considered (a = ½ cm, I = 100 amps) are shown in Fig. 8. The contribution of radiation is nearly half that of conduction at zero magnetic field (Re = 0), but becomes relatively unimportant at high Re, where convective effects are large.

The electric field is an important arc parameter, since it determines the power required in operating at a given current and arc

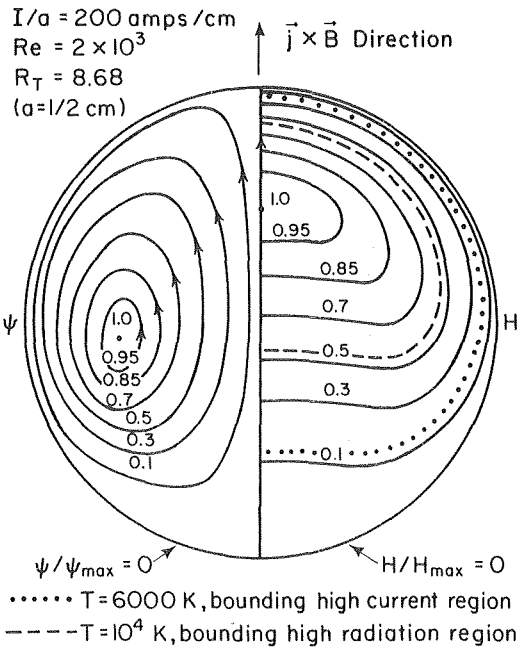

Fig. 6 Example streamlines and isotherms with $\psi_{max} = 1.94 \times 10^{-2}$ gm/cm-s and $T_{max} = 11{,}500°K$

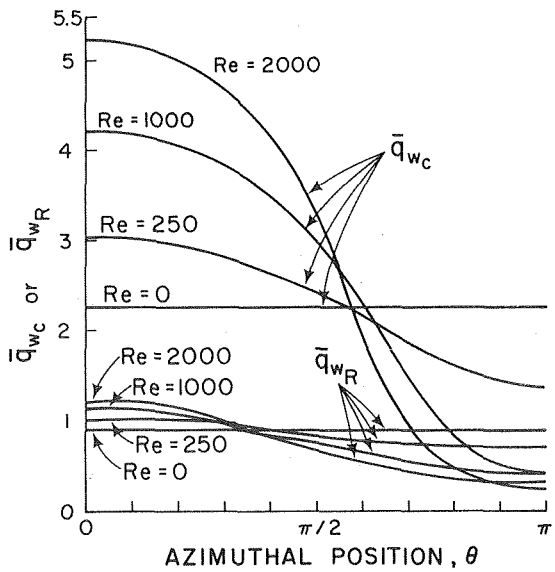

Fig. 8 Dimensionless wall heat fluxes by conduction ($\bar{q}_{w_c}$) and radiation ($\bar{q}_{w_R}$) for I = 100 amps and a = ½ cm ($R_T = 8.68$)

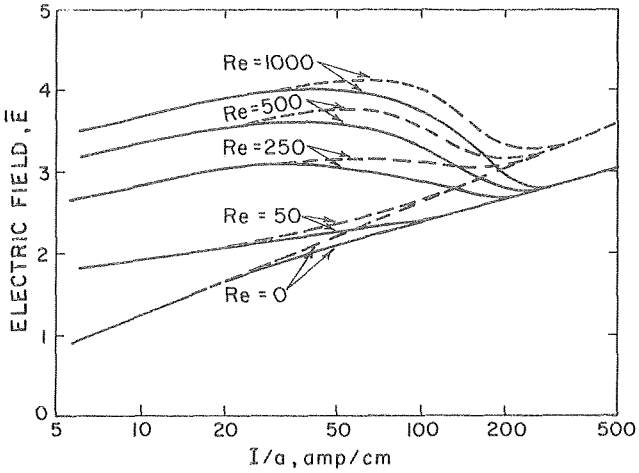

Fig. 9 Dimensionless electric field—solid curves: negligible radiation (R_T or $a \to 0$); dashed curves: $a = \frac{1}{2}$ cm, radiation considered

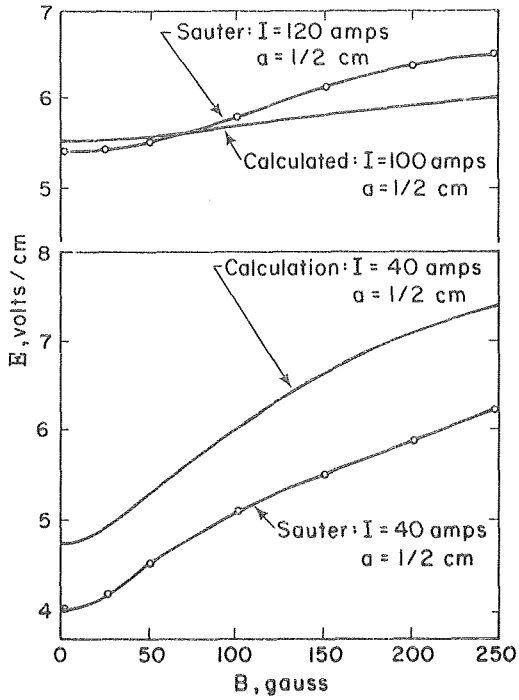

Fig. 10 Comparison of measured and calculated electric field variation with applied magnetic field

column length. Furthermore, the shape of the $E - I$ characteristic, in relation to that of the power supply, has a direct bearing on whether operation at a given condition is stable. The applied magnetic field can affect both the magnitude and the shape of the arc characteristic (see Fig. 9). These results are crossplotted from plots of $\bar{E}$ versus Re at the three I/a values considered in the numerical solutions. It is seen that the effect of Re is profound for $I/a = 10$ amps/cm. The value of $\bar{E}$ nearly triples as Re is increased from zero to 500. For a 10 amp arc in a tube of 1 cm radius, the actual B field causing this increase in only 150 gauss. When $I/a = 200$ amps/cm there is little variation of $\bar{E}$ with Re. In this case, the radiation effects (dependent on tube radius) cause the dominant variation. This representation is particularly enlightening with regard to the $\bar{E}$ field behavior in the high and low I/a regions. It is seen that at low I/a (<25) the $\bar{E}$ field becomes independent of R_T, while at high I/a (>300) it becomes nearly independent of Re.

Self-absorption of the ultraviolet component of the emitted radiation has been found to become increasingly important as argon arc axis temperatures exceed 12,000°K [19] (i.e., for high I/a). Due to the flattening of the temperature profile which results, the Re (magnetic field) effects would be somewhat further diminished at high I/a, while the reduced heat loss would cause some reduction in the $\bar{E}$ field. These changes should be minor for the arc conditions discussed in this paper.

The major test of the validity of the analytical model which can be made at this time is to determine how it compares with the experimental results obtained by Sauter [1]. One significant area of comparison is in regard to the thermal field. The only qualitatively noticeable difference is that Sauter's isotherms appear to be more deflected by a given B field than the calculated ones are. The measured values of peak temperature are within 100°K of the theoretical values [8].

Another primary area for comparing theoretical predictions with measured data is the effect of an applied magnetic field on the electric field. The predicted variation, as well as Sauter's measured values, are shown in Fig. 10 for a 40 amp arc in a tube of ½ cm radius. It is seen that in this case the agreement is quite good, the theoretical predictions being about 20 percent above the measured values at all magnetic field strengths. A similar comparison is shown for a calculated 100 amp arc and a measured 120 amp arc. The calculations correctly predict that the electric field is rather insensitive to B in this current range. However, the relative variation of the experimental data with B is greater than is theoretically predicted. This difference may be due to the greater deflection of the hot arc core toward the wall exhibited by the actual arcs, causing greater heat losses.

It has been suggested by Maecker [20] that better agreement between Sauter's results [1] and those predicted by the present analytical model would be likely if more accurate property values are employed. This could resolve minor discrepancies which exist in flow pattern and core deflection effects, but would not significantly alter the major results or conclusions of this study.

Conclusions

The analytical model developed here gives reasonable quantitative agreement with the findings of the previous principal experimental study by Sauter. This gives confidence in the new information presented on the nonuniform heat flux to the wall, the magnitude and nature of the effects of radiation and the effect of a B field on the E field. The study also provides a rational basis for selection of reference properties.

The most significant features of the constricted arc–magnetic field interaction are

(a) The applied B-field influences the arc performance by inducing a dual-vortex flow, which displaces the hot core toward the wall, giving rise to a very nonuniform distribution of heat transfer to the wall and also increasing the E field necessary for steady operation.

(b) The above effects are most pronounced when the arc core is small in relation to the tube size (low I/a).

(c) At high I/a, the electric field is influenced more by the radiation parameter, reflecting tube size effects, than by the Reynolds number, reflecting the B field effects; at low I/a, all radiation effects are negligible.

(d) When radiation is negligible the dimensionless arc behavior is specified by only two parameters.

Acknowledgments

The support of this work by the National Science Foundation, under Grant GK-629 and by the provision of an NSF Traineeship, at the University of Wisconsin-Madison, is gratefully acknowledged.

References

1 Sauter, K., "Das Temperatur-und Strömungsfeld in einem wandstabilisierten, magnetisch abgelenkten Bogen," *Zeitschrift für Naturforschung*, Vol. 24A, 1969, pp. 1694–1706.

2 Rosenbauer, H., "Messung der durch ein Quermagnetfeld erzeugten Gasströmung in einem wandstabiliserten Niederstrombogen," *Zeitschrift für Physik*, Vol. 245, 1971, pp. 295–307.

3 Fischer, E., and Uhlenbusch, J., "D.C. Arcs in Transverse Force Fields," *Proceedings VII. International Conference on Phenomena in Ionized Gases*, Vol. 1, 1966, pp. 725–728.

4 Raeder, J., Seeger, G., and Gorenflo, H. H., "Treatment of the Magnetically Deflected, Wall-Stabilized Arc by Means of Green's Functions," *Physics of Fluids*, Vol. 17, No. 1, Jan. 1974, pp. 137–141.

5 Harvey, R. L., "An Experimental and Theoretical Investigation of Magnetically Balanced Arcs," dissertation, University of Michigan, Ann Arbor, 1968.

6 Nicolai, L. M., and Kuethe, A. M., "Properties of Magnetically Balanced Arcs," *Physics of Fluids*, Vol. 12, Oct. 1969, pp. 2072–2082.

7 Vincenti, W. G., and Kruger, C. H., *Introduction to Physical Gas Dynamics*, Wiley, New York, 1965.

8 Ahrens, F. W., "An Investigation of the Effects of a Transverse Magnetic Field on a Confined Electric Arc," PhD thesis, University of Wisconsin, Madison, 1971.

9 Roache, P. J., *Computational Fluid Dynamics*, Hermosa Publishers, Albuquerque, 1972.

10 Cohen, I. M., "Radiative Heat-Flux Potential," *AIAA Journal*, Vol. 3, No. 5, May 1965, pp. 981–982.

11 Traugott, S. C., "Radiative Heat-Flux Potential for a Nongrey Gas," *AIAA Journal*, Vol. 4, No. 3, Mar. 1966, pp. 541–542.

12 Emmons, H. W., "Arc Measurement of High-Temperature Gas Transport Properties," *Physics of Fluids*, Vol. 10, June 1967, pp. 1125–1136.

13 Drellishak, K. S., Knopp, C. F., and Cambel, A. B., "Partition Functions and Thermodynamic Properties of Argon Plasma," Gas Dynamics Laboratory, Northwestern University, Report A-3-62, Mar. 1962.

14 Knopp, C. F., and Cambel, A. B., "Experimental Determination of the Thermal Conductivity of Atmospheric Argon Plasma," *Physics of Fluids*, Vol. 9, 1966, pp. 989–996.

15 deVoto, R. S., "Transport Coefficients of Partially Ionized Argon," *Physics of Fluids*, Vol. 10, Feb. 1967, pp. 354–364.

16 Olsen, H. N., "Thermal and Electrical Properties of an Argon Plasma," *Physics of Fluids* Vol. 2, 1959, pp. 614–623.

17 Kanzawa, A., and Kimura, I., "Measurement of Viscosity and Thermal Conductivity of Partially Ionized Argon Plasmas," *AIAA Journal*, Vol. 5, 1967, pp. 1315–1319.

18 Evans, D. L., and Tankin, R. S., "Measurement of Emission and Absorption of Radiation by an Argon Plasma," *Physics of Fluids*, Vol. 10, June 1967, pp. 1137–1144.

19 Hermann, W., "Strahlungsenergietransport mit Absorption in zylindrischen Bögen," *Zeitschrift für Physik*, Vol. 216, 1968, pp. 33–51.

20 Private communication from H. Maecker, Electrophysikalisches Institut der Technischen Hochschule München, Aug. 3, 1971.

ERRATA

An errata on C. C. Lin and S. H. Chan, "An Analytical Solution for a Planar Nongray Medium in Radiative Equilibrium," published in the Feb. 1975 issue of the JOURNAL OF HEAT TRANSFER, pp. 29-34.

C. C. Lin is the Graduate Student
S. H. Chan is the Assoc. Professor
Page 30, right-hand column, line three should read:

where $\bar{A}' = d\bar{A}/d\,\tau$, $\tau_0 = C_1 L/C_3$, $\phi(\tau) = e_{\omega 0}(\tau)/e_{\omega 0}(T_1)$, $M = e_{\omega 0}(T_2)/e_{\omega 0}(T_1)$,

Equation (33) should read:

$$\phi(0) = [\pi a_0\sqrt{\tau_0} - 4a_0\sqrt{a_1} - (M + 1)]/(\pi a_0\sqrt{\tau_0} - 4a_0\sqrt{a_1} - 2) \tag{33}$$

R. J. Pryputniewicz
Research Assistant.

W. W. Bowley
Professor.

Mechanical Engineering Department,
University of Connecticut,
Storrs, Conn.

An Experimental Study of Vertical Buoyant Jets Discharged Into Water of Finite Depth

This paper presents an experimental study of turbulent buoyant jets discharged vertically through a single circular submerged pipe into a large body of stagnant nonstratified water of finite depth. The experiments were carried out in laboratory facilities consisting of a closed system capable of maintaining steady-state conditions. The temperature characteristics of a hot rising plume were obtained, for numerous flows, as a function of discharge Froude number and discharge depth. The governing equations to predict jet characteristics are also presented, using an integral approach. A computer was used for reduction of experimental data and the numerical solution to the governing equations. The experimental and theoretical results compared favorably.

Introduction

The enormous quantities of waste heat discharged into seas and lakes by existing and planned thermal power plants of coastal cities, throughout the world, create serious environmental problems. Although the primary concern of this so-called "thermal pollution" is its ecological impact, it is necessary, as a first step, to assess the resultant receiving water temperature alterations.

At present, there exist several prediction methods, depending on the center-line trajectory, to analyze buoyant jet thermal and velocity fields. Very general analytical formulations based on the integral conservation equations were presented by Hirst [1, 2][1] and Fan [3]. The methods of Rouse, Yih, and, Humphreys [4] and Schmidt [5], based on integral equations, predict the development of vertically discharged buoyant jets. Abraham [6], in his analysis, also considered the effect of buoyancy in the zone of flow establishment.

A very important parameter used in analysis of buoyant jets is the so-called entrainment rate, which is the rate of influx of mass, momentum, and energy from outside of the plume. This ingestion of free stream fluid is primarily determined by the turbulent structure within the jet, particularly near the edge of the plume. The expression for the entrainment function was developed by combined effort of many researchers [7], and is presented here in the form given by Hirst [1, 2]:

$$E = \left[a_1 + \frac{a_2}{2(\mathrm{F}_L)^2}\sin\theta_2\right]\left[b\left|u_c - u_a\sin\theta_1\cos\theta_2\right|\right] + \left[a_3 + \frac{a_4}{2(\mathrm{F}_L)^2}\sin\theta_2\right]u_a b\sqrt{1-(\sin\theta_1\cos\theta_2)^2} \quad (1)^2$$

Of the large number of articles treating the interaction of a buoyant jet with a free surface only those few of dominant influence will be discussed.[3] Robideau [8] used an integral approach to analyze a submerged, turbulent, buoyant jet discharging into water of finite depth. He predicted the maximum surface temperature for such a discharge as a function of discharge angle, Froude number, and water depth. Shirazi and Davis [9] compared experiments and theory for vertical discharge, from numerous sources, and developed (nomographical) computational procedures for predictions of physical properties of thermal waste discharge into large bodies of water. Trent [10] used a finite difference method in analyzing the dispersion of thermal effluents issuing from large single-port vertical outfalls in shallow coastal receiving water.

Bains and Turner [11], Frankel and Cumming [12], and Hart [13] conducted experimental studies with buoyant jets discharging into a nonoverflowing tank which resulted in transient conditions. Mahajan and John [14] achieved steady-state conditions in their experiments with buoyant jets, but the effect of discharge Froude number on flow characteristics was not specifically investigated. Jirka and Harleman [15] in their recent study have investigated the general case of a diffuser in arbitrary depth of water with un-

[1] Numbers in brackets designate References at end of paper.

Contributed by the Heat Transfer Division for publication in the JOURNAL OF HEAT TRANSFER. Manuscript received by the Heat Transfer Division Sept. 16, 1974. Paper No. 75-HT-RR.

[2] Definitions of all of the symbols appear in the Nomenclature.

[3] More detailed literature survey can be found in [7].

specified buoyancy. The particular emphasis, however, was put on a diffuser in shallow receiving water with low buoyancy.

Vertical Plume Theory

The buoyant jet issuing from a submerged port can be divided into several flow regimes, see Fig. 1, each of them possessing its own characteristics, namely:

1 the zone of flow establishment, ZFE;
2 the zone of established flow, ZEF;
3 the zone of transition from established to drift flow; and
4 the zone of drift flow.

The results of analysis of the ZFE are used as the initial conditions for analysis of the ZEF. At present, there are two theories for obtaining these conditions: one, neglecting buoyancy effects within the ZFE, and the other, taking these effects into account. Although neither of these theories has been fully investigated experimentally, an analytical study has been carried out by several investigators. The initial conditions obtained using the first theory state that the length of the ZFE is the same for all flows, regardless of discharge Fourde number, and equal to 6.2 discharge diameters, ($Z_e^* = 6.2$); the jet half-width at the beginning of the ZEF is equal to $1/\sqrt{2}$ discharge diameters, ($b_e^* = 1\sqrt{2}$); and finally the centerline velocity, u_c, and local Froude number, F_L, within the potential core, see Fig. 1, are constant and equal to u_0 and F_0, respectively. The analytical solutions of the governing equations (equations (8)–(10)) using these initial conditions did not compare favorably with the experimental results obtained in this study. The second theory was presented in a very general form by Hist [2], whose analysis of the ZFE was primarily directed toward the effect of the current; these results also did not supply all the required initial conditions for this study. Robideau [8] modified Hirst's formulations and determined at what point buoyancy effects must be considered in specifying these initial conditions. According to [8] the ratio of the Froude number at the beginning of the ZEF and the discharge Froude number, i.e., F_L/F_0, is highly dependent on F_0 and varies from 1.47 for $F_0 = 1.0$ to 1.08 for $F_0 \gg 30.0$. Robideau also determined the length of the ZFE, Z_e^*, and the half width, b_e^*, of the plume at the beginning of the ZEF, both as functions of F_0. These initial conditions, given by Robideau [8], were used to initialize solutions of the governing equations.

An excellent analytical method for prediction of jet characteristics has recently been developed by Hirst [1]. Hirst's method was closely followed, [7], to develop a degenerate form of this solution—a form suitable for the analysis of vertical jets.

According to [7] the basic equations for conservation of mass,

VERTICAL JET
DISCHARGED FROM A SUBMERGED DIFFUSER

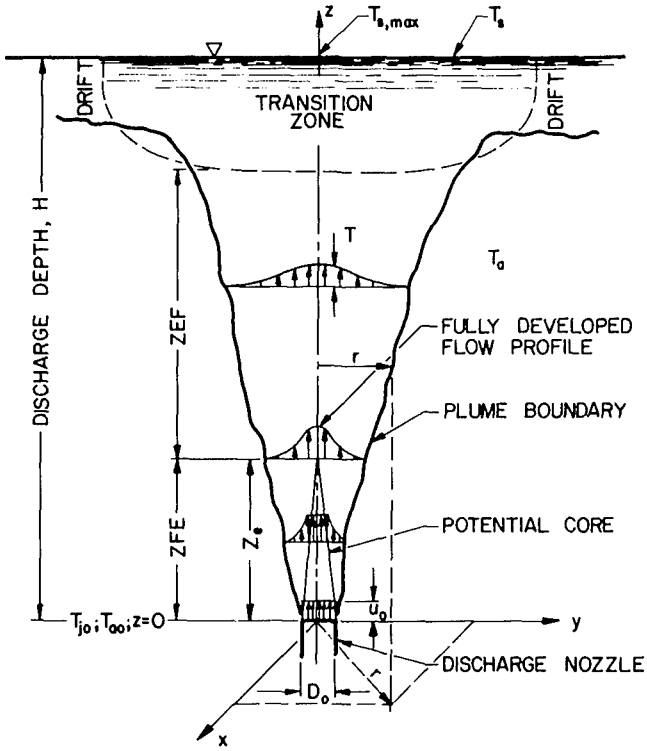

Fig. 1 Vertical jet discharged from a submerged diffuser

Nomenclature

$a_1 = 0.057$ = shear similarity parameter
$a_2 = 2\lambda^2 - (3\lambda^2/(\lambda^2 + 1))$ = similarity parameter
a_3, a_4 = parameters, equation (1)
b = local jet half-width
b_e = jet half-width at the beginning of the zone of established flow
D_0 = discharge nozzle diameter
E = entrainment rate
$F_0 = \left[\frac{u_0}{\sqrt{D_0 g \frac{\rho_{a0} - \rho_{j0}}{\rho_{a0}}}}\right]$ = discharge Froude number
$F_L = \left[\frac{u_{cL}}{\sqrt{2bg \frac{\rho_a - \rho_{cL}}{\rho_{a0}}}}\right]$ = local Froude number
g = gravitational acceleration
r = radial coordinate, Fig. 1
H = discharge depth, below free surface, Fig. 1
$\mathrm{Re} = \frac{\rho_{j0} u_0 D_0}{\mu_{j0}}$ = nozzle Reynold's number
T = temperature
u = axial velocity component within plume
z = vertical coordinate, Fig. 1
Z_e = length of the zone of flow establishment, Fig. 1
$\Delta( ) = ( ) - ( )_a$
θ_1 = angle between projection of jet center line onto x-y plane and x-axis, equation (1); $\theta_1 = 0$ deg for vertical jet
θ_2 = angle between jet center line and x-y plane, equation (1); $\theta_2 = 90$ deg for vertical jet
λ = spreading ratio between temperature (density) and velocity profiles
ρ = density
μ = water viscosity
$( )$ = dimensional quantities
$( )^*$ = dimensionless quantities, with respect to discharge conditions
$(\bar{\ })$ = average with respect to time
$( )_a$ = ambient (free stream) value
$( )_{a0}$ = ambient characteristics at the discharge depth, $z = 0$
$( )_c$ = value at the jet center line, $r = 0$
$( )_{cL}$ = local value at the jet center line, $r = 0$, $z > 0$
$( )_{j0}$ = jet characteristics at the discharge depth, $z = 0$
$( )_0$ = discharge characteristics
$( )_s$ = measured at the free surface
∇ = free surface of water

energy, and momentum can be written as

$$\frac{d}{dz}\left[\int_0^\infty \bar{u}^2\, r\, dr\right] = E \tag{2}$$

$$\frac{d}{dz}\left[\int_0^\infty \bar{u}(\bar{T} - T_a) r\, dr\right] = 0 \tag{3}$$

$$\frac{d}{dz}\left[\int_0^\infty \bar{u}^2\, r\, dr\right] = \int_0^\infty g\frac{\rho_a - \bar{\rho}}{\rho_{a0}}\, r\, dr \tag{4}$$

In order to solve equations (2)–(4), the velocity, temperature, and density profiles normal to the plume axis must be assumed. Rouse, Yih, and Humphreys [4] in their work with round and slot plumes have verified the similarity assumptions. Their measurements were closely approximated by Gaussian profiles such that

$$\bar{u} = u_c \exp[-(\frac{r}{b})^2] \tag{5}$$

$$\Delta\bar{T} = \Delta T_c \exp[-(\frac{r}{\lambda b})^2] \tag{6}$$

$$\Delta\bar{\rho} = \Delta\rho_c \exp[-(\frac{r}{\lambda b})^2] \tag{7}$$

where the spreading ratio, λ, is related to the turbulent Schmidt number, Sc, by $Sc = 1/\lambda^2$. Forstal and Gaylord [16], among others, have shown experimentally that the turbulent Schmidt number lies in the range $0.75 < Sc < 0.85$, for which $1.08 < \lambda < 1.16$. The higher value, $\lambda = 1.16$, is commonly used in analyzing round buoyant jets. Using the value of $\lambda > 1$ implies that the temperature (density) profiles are slightly "flatter" than the velocity profiles. From equation (5) it is seen that for a Gaussian profile, b is the radial distance at which $\bar{u}$ falls off to $1/e$ of its center-line value.

Substituting the similarity assumptions into equations (2)–(4), combining with equation (1), and performing indicated integrations, the equations can be written in the dimensionless form as

$$\frac{d}{dz^*}\left[(b^*)^2 u_c^*\right] = 2\left[a_1 + \frac{a_2}{2(\mathrm{F}_L)^2}\right] b^* u_c^* \tag{8}$$

$$\frac{d}{dz^*}\left[(b^*)^2 u_c^* \Delta T_c^*\right] = 0 \tag{9}$$

$$\frac{d}{dz^*}\left[(b^*)^2 (u_c^*)^2\right] = 2\frac{\lambda^2}{(\mathrm{F}_0)^2}(b^*)^2 \Delta T_c^* \tag{10}$$

Equations (8)–(10) are the governing equations for the buoyant jet flow through a stagnant, nonstratified ambient and together with Robideau's initial conditions, discussed previously, were used for prediction of temperature along the jet axis. Solutions to the governing equations were obtained on the IBM 360 using standard numerical techniques [7].

Experimental Apparatus and Procedure

The experiments were performed in laboratory facilities shown schematically in Fig. 2; all symbols used in this section will be with reference to this figure.

The test tank[4] of total capacity of about 2200 gal and dimensions shown in Fig. 2 consisted of an outer tank and of an inner cylinder, and was filled with ordinary water taken from city supply, SW, after it passed through the filter, F. The upper edge of the outer tank was reinforced and made as smooth as possible to allow free sliding of an I-beam instrument support carrying platforms with thermistor rake and nozzle holder. The inner cylinder was provided with an adjustable sluice gate to control the amount and rate of overflow of warm water coming from the hot jet discharged into the test tank. This water was collected in an overflow reservoir and then was removed, from there, by means of ten equally spaced siphons equipped with inserts. The siphon inserts were used to decrease the nonuniformity of head losses within siphons, caused by their different lengths. Siphoned water was cooled to a preset temperature of 70°F in a cooling reservoir, CR, and then some of it was pumped, P, to the constant-head-overflow-tank, COT. In order to satisfy the original assumption of steady-state condition, the remaining water was returned back to the tank by means of six tubes, also equipped with inserts, equally spaced within the return reservoir—space between inner cylinder and outer tank. The water from COT was heated to a temperature of about 170°F in the heaters, MH and AH. Flow rate of hot water discharging through a nozzle was measured by means of a Fisher Flowmeter. The nozzle was an exchangeable piece of straight, thin-walled stainless steel tubing of various diameters so that different flow conditions could be obtained [7]. The nozzle could easily be positioned anywhere within the tank. The deaerator tubes, DAT, and the constant-head-overflow-bubble-separator, BS, were provided to facilitate removal of air that was separating from heated water.

The thermal characteristics of the rising plume were determined by measuring temperatures, within the area of interest, by means of thermistors [7] manufactured by Fenwal Electronics of Framingham, Massachusetts. There were 16 thermistors used for measurements. A multichannel switch allowed the placement of the thermistors, one at a time, into the arm of a Wheatstone bridge. As a result of temperature variations within the vicinity of the thermistor, its resistance changed causing an unbalance of bridge which, in turn, resulted in a signal that was averaged in the integrator and then read on Hewlett-Packard digital voltmeter.

The length of time over which the reading was averaged in the integrator was precisely measured with a stop watch. Three consecutive readings were taken at a point. Then the point arithmetic average for these readings was corrected using error curves [7]. These were obtained during calibration of the test facilities to give true temperature in the immediate environment of the thermistor. The temperatures were nondimensionalized with respect to the jet temperature at the discharge depth and the ambient water temperatures using the following formula:

$$\Delta T^* = \frac{T - T_a}{T_{j0} - T_{a0}} \tag{11}$$

The location of the particular point under consideration was also nondimensionalized with respect to the discharge nozzle diameter, D_0. The data are presented in nondimensional form.

Discussion of Experimental Results

The prime purpose of this research was to obtain the center-line and surface excess temperatures as functions of discharge Froude number, F_0, ranging from 1 to 50, and discharge depth, H/D_0, with the range of 10–80 discharge diameters. Discharge parameters were chosen in such a way that a nozzle flow Reynold's number, Re, was over 2500, i.e., the flow was turbulent. In addition to the foregoing, it was also attempted to investigate experimentally the influence of the discharge nozzle size and discharge temperature on the flow characteristics developed at the same discharge Froude number. Certain assumptions (similarity of flow profiles, axisymmetricity of flow, etc.) used in derivation of the governing equations were also investigated experimentally.

Numerous experiments have shown that the temperature distribution profiles within the ZEF are truly similar and are closely approximated by Gaussian function, equation (6), regardless of discharge nozzle diameter. Examining these experimental data for shallow discharges, $H/D_0 = 10$, it was found that for the $Z/D_0 \leq 8.0$ the agreement with theoretical predictions was excellent. The experiments also showed that for $Z/D_0 > 8.0$ the temperature measured at $R/D_0 > 1.0$ was slightly higher than that obtained theoretically, as for example shown in Fig. 3. This discrepancy increased with the increasing discharge Froude number. Nevertheless, the experimental and theoretical results showed better and better agreement as the discharge depth increased. Furthermore, it was shown experimentally that: *(a)* vertical plume boundary is straight-edged; *(b)* plume half-width decreases—at a given axial location—as the discharge Froude number, F_0, increases; *(c)* the potential core length, Z_e, is constant for a given F_0, regardless of

[4] For more detailed description of the test facilities see [7].

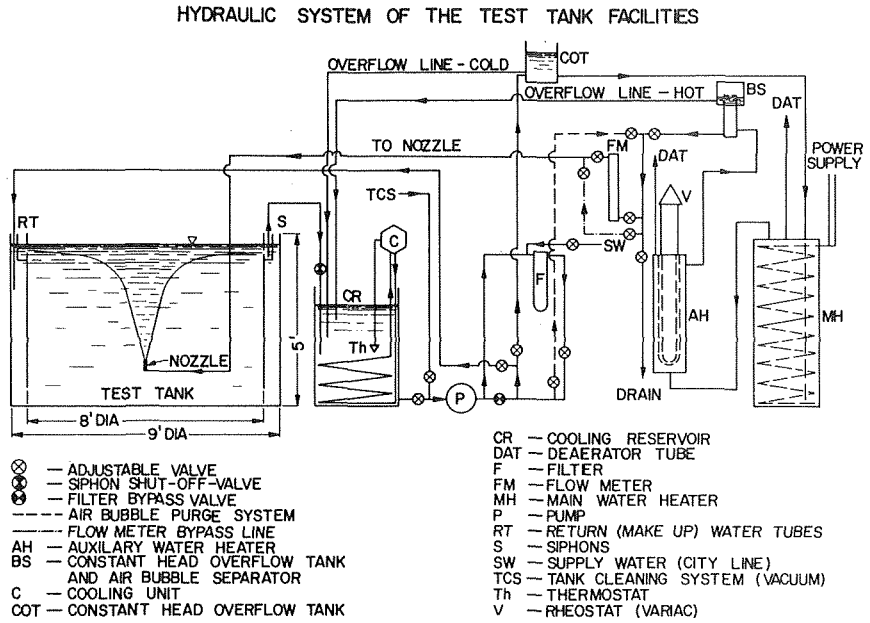

Fig. 2 Hydraulic system of the test tank facilities

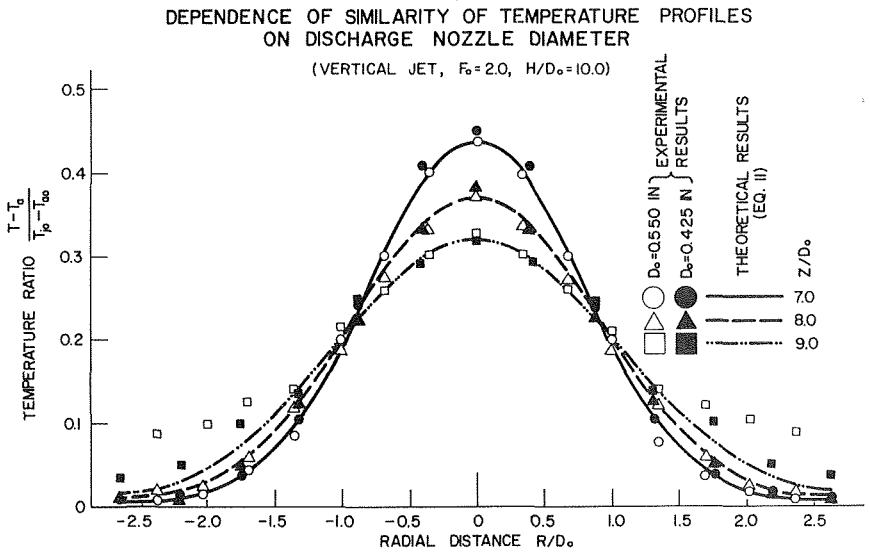

Fig. 3 Dependence of similarity of temperature profiles on discharge nozzle diameter (vertical jet, $F_0 = 2.0$, $H/D_0 = 10.0$)

H/D_0; and *(d)* the Z_e increases, for a given H/D_0, as the F_0 increases. All of the foregoing statements agree with the theoretical assumptions. Another series of experiments proved that the center-line and surface excess temperatures are independent of the jet discharge temperature, providing the same F_0 was obtained.

The second phase of experiments was designed to obtain information on the center-line and surface excess temperatures as functions of discharge Froude number and discharge depth. Figs. 4 and 5[5] show that for a given H/D_0 there is a significant decrease in center-line excess temperature for decreasing F_0. It can be easily shown that the rate of change of center-line excess temperature is relatively independent of the discharge depth, except at higher Froude numbers, $F_0 > 16$, and also, the discrepancy between the experimental and theoretical results, Fig. 3, can be explained. Clearly, for shallow discharge at high Froude number the jet impinges on a surface with a force much greater than if it were discharged at large H/D_0. Because of this proximity of the free surface of water, acting as a constant pressure boundary, the jet "turned back" and there was an extremely active turbulent mixing reaching down to 5–10 dia as measured from the free surface. Because of this phenomenon, the jet was discharging into ambient water of much higher temperature. This was not taken into account in the theoretical assumptions and, therefore, resulted in serious disagreement.

Figs. 6 and 7 present the experimental results on surface excess temperature for a given H/D_0 as a function of F_0. Obviously, the final temperature, measured at any radial position, lowers for the decreasing F_0. Again, it can be shown that for $H/D_0 > 40$ the surface excess temperature remained nearly uniform in the radial direction. Results displayed in Fig. 8 show, as expected, that the greatest influence of discharge Froude number on maximum sur-

[5] A more detailed presentation of experimental results is given in [7].

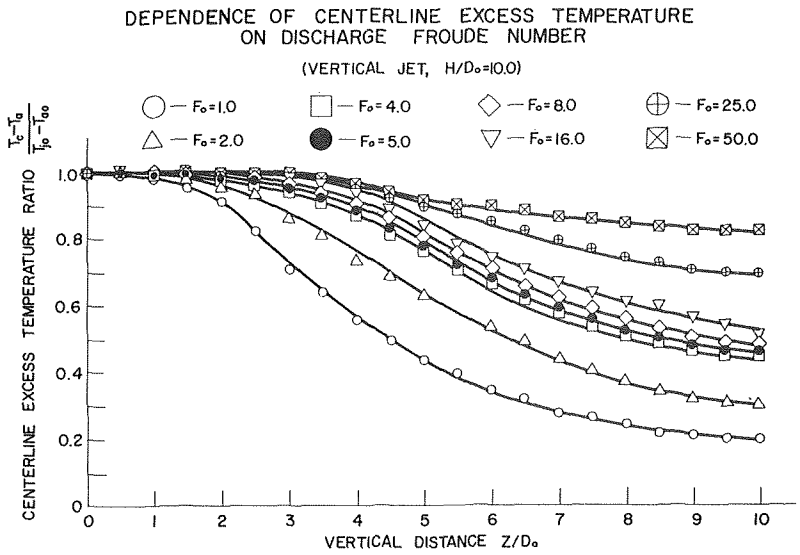

Fig. 4 Dependence of center-line excess temperature on discharge Froude number (vertical jet, $H/D_0 = 10.0$)

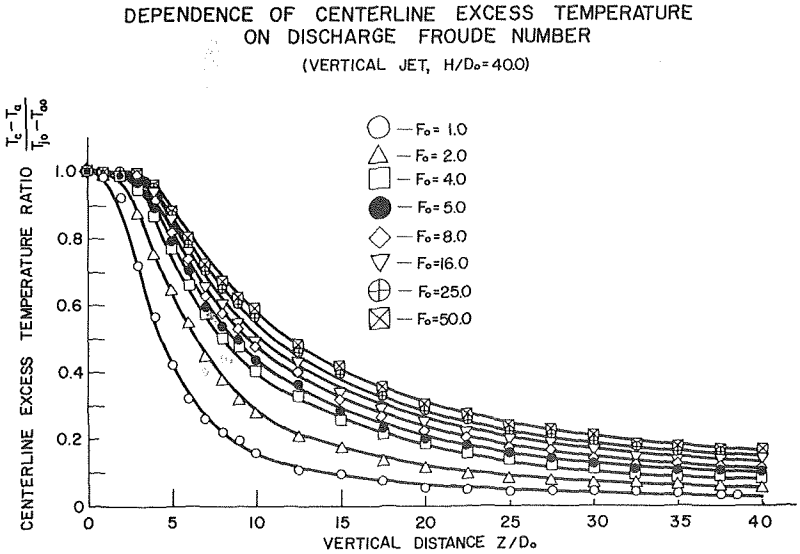

Fig. 5 Dependence of center-line excess temperature on discharge Froude number (vertical jet, $H/D_0 = 40.0$)

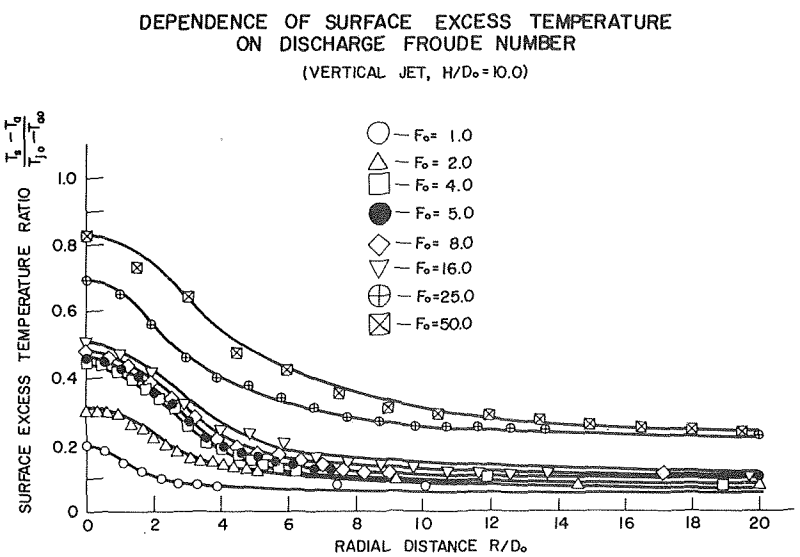

Fig. 6 Dependence of surface excess temperature on discharge Froude number (vertical jet, $H/D_0 = 10.0$)

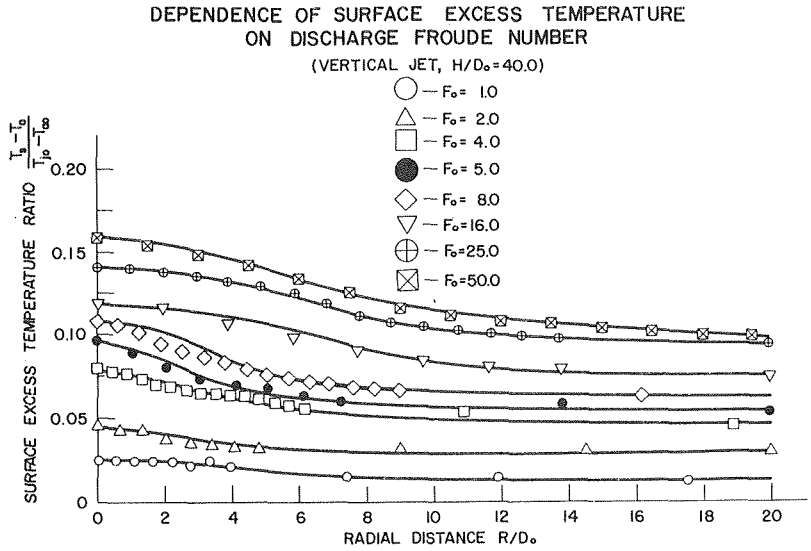

Fig. 7 Dependence of surface excess temperature on discharge Froude number (vertical jet, $H/D_0 = 40.0$)

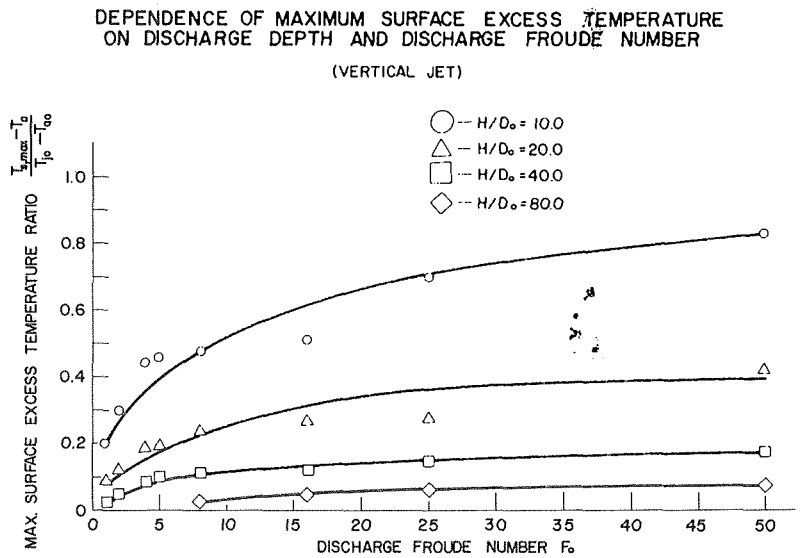

Fig. 8 Dependence of maximum surface excess temperature on discharge depth and discharge Froude number (vertical jet)

face temperature is for $H/D_0 = 10$ and that this influence is decreasing with increasing discharge depth and is practically vanishing at $H/D_0 = 80$.

To complete this study the experimental results were compared with two theoretical methods for prediction of plume development—one, developed by Trent [10], and the other, presented in this paper, equation (8)–(10), and based on Hirst's method [1]. Figs. 9 and 10 show comparison of the theoretical and experimental results for the center-line excess temperature as a function of discharge Froude number for various discharge depths. In general, solutions to equations (8)–(10) agree more favorably with the experimental results than Trent's solutions.

The computer model of thermal discharge was tested for various initial conditions at the beginning of the established flow regime. Comparison of these results showed that the model is very sensitive to the initial conditions imposed upon it. The best agreement with experiments was obtained with the initial conditions which included the buoyancy effects in the ZFE.

Figs. 9 and 10 show that the agreement of theoretical and experimental results is satisfactory, except within a short distance from the discharge nozzle, where the initial conditions used in the analytical solutions have the greatest effect on flow development. Fig. 11 shows the comparison of the experimental and theoretical results for the maximum surface excess temperature as a function of F_0. The experimentally measured temperature at large F_0 is higher than that predicted theoretically, which again can be explained by proximity of the free surface acting as a constant pressure boundary.

Another source of the discrepancies between the experimental and theoretical results, presented in Figs. 9–11, may have its origin in the entrainment function itself. Even the most advanced one postulated by Hirst [1] and including the effects of local conditions within the jet, buoyancy, jet orientation, and free stream velocity has certain coefficients that have to be determined experimentally, and various investigators give different values for them. The results obtained using this entrainment function depend greatly on the values assigned to these coefficients. It should be stressed that the entrainment coefficients have been kept constant and

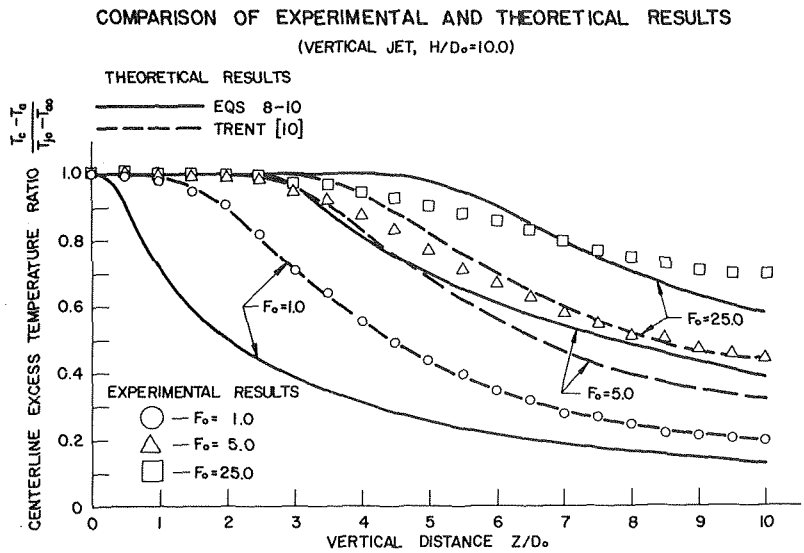

Fig. 9 Comparison of experimental and theoretical results (vertical jet, $H/D_0 = 10.0$)

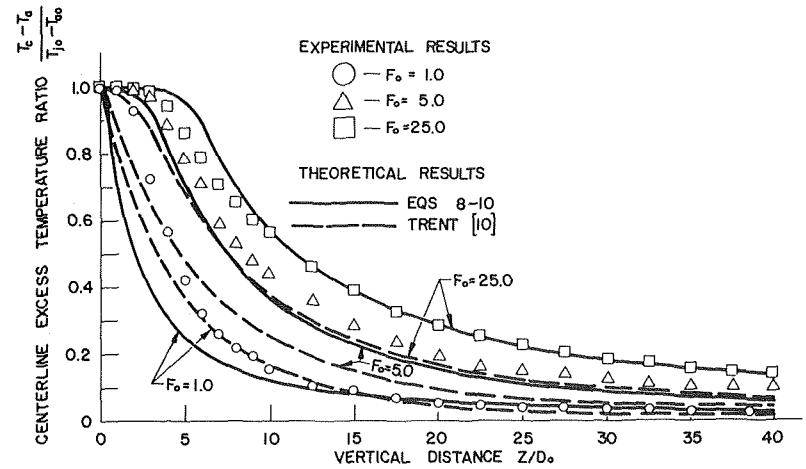

Fig. 10 Comparison of experimental and theoretical results (vertical jet, $H/D_0 = 40.0$)

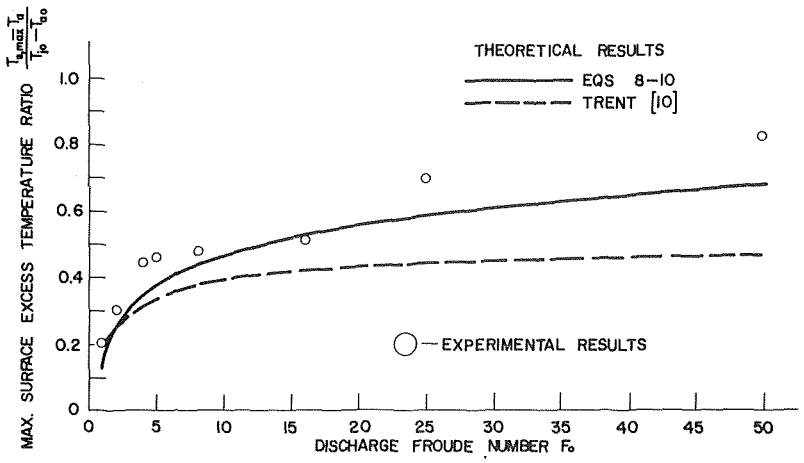

Fig. 11 Comparison of experimental and theoretical results (vertical jet, $H/D_0 = 10.0$)

equal to the most generally used values, for all the flows studied here analytically.

It should also be pointed out that this experimental study has been carried out in the laboratory facilities consisting of a closed system capable of maintaining steady-state conditions continuously throughout all of the experiments, whereas other studies, to the present knowledge of the authors, were not carried out in facilities with such capabilities.

Acknowledgments

The computer analyses were made possible through a grant from the University of Connecticut Research Computer Center.

The Construction of the test facilities was financed by a grant from the United States Department of the Interior through General Dynamics Corporation, Electric Boat Division, Groton, Connecticut.

This research is a special case of a more general study presently being conducted by Mr. L. Hafetz at the same institution.

References

1 Hirst, E. A., "Analysis of Round Turbulent Buoyant Jets Discharged to Flowing, Stratified Ambients," ORNL Report No. 4685, Oak Ridge National Laboratory, Oak Ridge, Tenn., 1971.

2 Hirst, E. A., "Analysis of Buoyant Jets Within the Zone of Flow Establishment," ORNL Report No. TM-3470, Oak Ridge National Laboratory, Oak Ridge, Tenn., Aug. 1971.

3 Fan, L. N., "Turbulent Buoyant Jets Into Stratified or Flowing Ambient Fluids," Report No. KH-R-15, California Institute of Technology, Pasadena, Calif., June 1967.

4 Rouse, H., Yih, C. S., and Humphreys, H. W., "Gravitational Convection From a Boundary Source," *Tellus,* Vol. 4, 1952, pp. 201–210.

5 Schmidt, F. H., "On the Diffusion of Heated Jets," *Tellus IX,* Vol. 3, 1957, pp. 378–383.

6 Abraham, G., "Horizontal Jets in Stagnant Fluid of Other Density," *Journal of the Hydraulics Division,* Proc. ASCE, Vol. 91, No. HY7, July 1965, pp. 139–154.

7 Pryputniewicz, R. J., "An Experimental Study of the Free Surface Effects on a Submerged Vertical Buoyant Jet," MS thesis, Mechanical Engineering Department, University of Connecticut, Storrs, Conn., Apr. 1974.

8 Robideau, R. F., "The Discharge of Submerged Buoyant Jets Into Water of Finite Depth," General Dynamics Corporation, Electric Boat Division, Groton, Conn. 1972.

9 Shirazi, M. A., and Davis, L. R., "Workbook of Thermal Plume Prediction, Vol. I, Submerged Discharge," Pacific Northwest Water Laboratory, National Env. Res. Center, Corvallis, Ore., Aug. 1972.

10 Trent, D. S., "A Numerical Model for Predicting Energy Dispersion in Thermal Plume Issuing From Large Vertical Outfalls in Shallow Coastal Water," PhD thesis, Mechanical Engineering Department, Oregon State University, 1973.

11 Bains, W. B., and Turner, J. S., "Turbulent Buoyant Convection From a Source in a Confined Region," *Journal of Fluid Mechanics,* Part 1, 1969, pp. 51–80.

12 Frankel, R. J., and Cumming, J. D., "Turbulant Mixing Phenomena of Ocean Outfalls," *Journal of the Sanitary Division,* Proc. ASCE, Vol. 91, No. SA2, Apr. 1965, pp. 33–59.

13 Hart, W. E., "Jet Discharge Into a Fluid With a Density Gradient," *Journal of the Hydraulics Division,* Proc. ASCE, Vol. 87, No. HY6, Nov. 1961, pp. 171–201.

14 Mahajan, B. M., and John, J. E. A., "Mixing of a Shallow Submerged Heated Water Jet With an Ambient Reservoir," *AIAA Journal,* Vol. 9, No. 11, Nov. 1971, pp. 2135–2140.

15 Jirka, G., and Harleman, D. R. F., "The Mechanics of Submerged Multiport Diffusers for Buoyant Discharges in Shallow Water," M.I.T., R. M. Parsons Laboratory for Water Resources and Hydrodynamics, Report No. 169, Mar. 1973.

16 Forstal, W., and Gaylord, E. W., "Momentum and Mass Transfer in a Submerged Water Jet," *Journal of Applied Mechanics,* June 1955, pp. 161–164.

ERRATA

An errata on H. Q. Oliviera and R. P. Forslund, "The Effect of Thermal Constriction Resistance in the Design of Channel-Plate Heat Exchangers," published in the Aug. 1974 issue of the JOURNAL OF HEAT TRANSFER, pp. 292–295.

The word Construction in the title should be Constriction.

Equation (17) should read:

$$D_0 = -Qt/bk \tag{17}$$

Equation (22) should read:

$$D_i = \alpha_i\{[-\Delta T + D_0(-1 - 1/\phi_0 t)][(\sin \lambda_i a)/\lambda_i a] + \sum_{\substack{j=1 \\ j\neq i}}^{\infty} \Psi_0(j) B_{ij} D_j\} \tag{22}$$

J. D. Means[1]
Lone Star Steel Co.,
Lone Star, Texas

R. D. Ulrich[2]
Professor,
Brigham Young University,
Provo, Utah.
Mem. ASME

Transient Convective Heat Transfer During and After Gas Injection Into Containers

This paper presents experimental data correlations for the spatially averaged convective heat transfer coefficient for thin-walled closed containers during and after gas injection. The different modes of heat transfer are identified, and correlations are presented for each. Correlations are presented for the injection period, post-top injection, post-bottom injection, post-tangential injection, post-radial injection, and post-ejection heat transfer for various tank geometries. Of special significance are the very high heat transfer rates that are shown to be present in some cases immediately after injection. Heat transfer rates are shown to be, for a short period, up to almost two orders of magnitude higher than natural convection predictions would indicate.

Introduction

Background Information. Many physical systems involve gas injection into or ejection from otherwise closed containers. Important examples of these two processes are injection to monopropellant gas generators, blow-down from high-pressure air storage tanks into wind tunnels, and inside closed piston-cylinders, like those used in a Stirling cycle engine. These processes result in an upset of the state of the gas in the closed container, which in turn results in transfer of heat either to or from the container until thermodynamic equilibrium occurs between the container and its surroundings. This heat loss or gain is sometimes of considerable importance, necessitating a good means of prediction. This paper is concerned with providing a method for predicting heat transfer from, or to, closed containers during and after gas injection or ejection.

Survey of Literature. A survey of literature revealed several papers which were useful in the evaluation and guidance of this work. Ring [1][3] suggested that the heat transfer in closed containers is best predicted by turbulent natural convection.

Reynolds [2, 3] noted the increase in heat transfer coefficient immediately after injection is probably due to the stirring effect of the inlet jet during injection, but states that the decreased effectiveness of the natural convection on the top and bottom of the tank should offset the stirring effect. He therefore suggested McAdam's [4] natural convection correlation for vertical flat plates as a reasonable analysis of the heat transfer during injection.

The most pertinent work related to this paper was by Ulrich, et al. [5, 6], wherein a procedure was outlined for determining a spatially averaged heat transfer coefficient after mass injection into a closed container.

These were the only references found which contained information about the transient state between the end of the injection period and the start of free convection. Limited data agreed with data presented herein as they identified two very distinct modes of heat transfer after gas was injected into a tank. Immediately following injection there existed a rapidly decaying period characterized by very high heat transfer rates which changed after a few seconds, rather abruptly, into another mode which agreed very well with vertical flat plate natural convection predictions.

An analytical work of significance to this effort was made by Lighthill [7], who conducted a study of heat transfer in cylindrical tubes closed on one end and open to an infinite reservoir on the other end. One of the significant contributions of this work was the prediction of the growth of a stagnation region, starting at the bottom of the tube and working upward with time.

Steiger [8] and Lyons [9] obtained experimental data for heat transfer during injection through small inlets into containers. Their data indicated that, following an initial transient, the heat transfer coefficient was essentially constant when the mass addition rate was constant.

Based on this survey there appear to be at least five different periods of heat transfer in a closed container during and after injection: (1) injection period, during which heat is transferred by forced convection; (2) transient period, between the end of injection and the beginning of natural convection; (3) turbulent natural convection period; (4) laminar natural convection period; and (5)

[1] Formerly a graduate student at Brigham Young University.
[2] Presently on leave to U. S. Naval Weapons Center, China Lake, Calif.
[3] Numbers in brackets designate References at end of paper.

Contributed by the Heat Transfer Division for publication in the JOURNAL OF HEAT TRANSFER. Manuscript received by the Heat Transfer Division May 10, 1974. Paper No. 75-HT-KK.

Table 1 Receiver tank geometry

Tank no.	Dia in.	Length in.	Volume ft³	Surface area ft²	Remarks
1	12	12	0.524	3.142	Spherical tank
2	12	24	1.236	5.991	Type G-1 Spec 94-40321 oxygen tank
3	12	43	2.550	11.26	Type G-1 Spec 94-40321 with added length
4	6	24	0.445	3.590	SCUBA oxygen tank
5	6	43	0.790	6.600	SCUBA tank with added length

the tailoff period, during which the internal flow begins to stagnate from the bottom upward.

Objectives. The objectives are to: (1) present a system from which representative experimental data were obtained for the heat transferred from, or to, a closed container during and after gas injection, or ejection; (2) identify the various modes of heat transfer present in the system; and (3) show correlations of the heat transfer data obtained during the various modes by which heat transfer coefficients may be predicted.

Description of Equipment

To obtain experimental data relative to this problem the apparatus illustrated in Fig. 1 was assembled. A thin-wall cylindrical tank with hemispherical ends was suspended vertically inside an ice water-filled tank, equipped with a circulation pump. The suspended tank was connected to a much larger air storage tank so that high-pressure air (300 psig) could be injected into the receiver tank. Several receiver tanks were used for geometry variations as listed in Table 1. Provision was made for evacuation of the receiver tank and injection control was provided by a quick-operating hand valve. All pressurized systems, including this valve, were made leak proof, so that any change in tank pressure was due solely to changes in the thermodynamic state and/or controlled mass addition.

Air was injected sonically into the tank by using choked nozzles at the tank entrance. The throat diameters used were 0.045, 0.100, 0.150, 0.250, and 0.450 in.

Instrumentation. Low thermal-mass iron-constantan thermocouples were installed inside the receiver tank to measure air temperature, in the inlet line to measure the stagnation temperature of the air entering the tank, and in the ice water bath. The thermocouple outputs were recorded on a Speedmax-H strip chart recorder of sensitivity 1°F. Digital temperature measurements were also recorded on the system used to record pressure. Pressure transducers were installed to measure receiver tank pressure and injection stagnation pressure. The pressure transducers were strain-gage type with excitation and output signal provided and conditioned by a Martin signal-conditioning system. Amplification was by Electro-Incorporated solid state amplifiers. Sensitivity of this system was 1 mV of a 10 V range. The output signals from the amplifiers were digitized by a Dynamec Model 2401C digital voltmeter and recorded on a Hewlett-Packard Model 5245L counter set at one ms intervals, and printed simultaneously with the DVM output.

Time zero, the starting point of each run was obtained by means of a pressure switch installed downstream of the inlet valve, and set to operate at less than 1 psi differential. This switch triggered the counter so that zero time on the counter was the same as the starting time of injection. Further details of the test hardware and instrumentation are given in [10].

Test Procedure. As each configuration was assembled, checks were made to assure a leak-proof condition. Initially, and periodically during the tests, the transducers were calibrated using a dead weight standard. Prior to each series of tests, electrical calibrations were made to assure accurate data. On a typical data run, the following sequence of events occurred:

1 The test tank was evacuated.

2 The digital printer and strip chart recorder were started.

3 The ball valve was quickly opened while observing the tank pressure on a bourdon-tube gage.

4 The ball valve was closed when the desired pressure was reached.

5 The subsequent data printout was monitored, and when steady state was reached, the data acquisition system was stopped.

6 Steady-state air temperature and pressure in the tank, and barometric pressure were recorded.

Nomenclature

A_n = nozzle throat area, ft²
A = inside surface of tank, ft²
c_p = gas specific heat at constant pressure, B/lbm-°F
c_V = gas specific heat at constant volume, B/lbm-°F
d = diameter of inlet flow nozzle throat, ft
D = diameter of tank, ft
Fo = Fourier number, $\alpha t/D^2$
Gr = Grashof number, $gD^3(T - T_W)/T\nu^2$
h = instantaneous spatial-average convective heat transfer coefficient, B/ft²-hr-°F
k = thermal conductivity, B/ft-hr-°F
L = tank length, ft
m = gas mass in the test tank at any particular time, lbm
$\dot{m}$ = gas flow rate, lbm/s
Nu = Nusselt number, hD/k
P = instantaneous gas pressure, psia
$\dot{P}$ = pressure-time derivative, psf/s
P_f = final gas pressure, psia
P_n = injection nozzle throat pressure, psia
P_0 = stagnation pressure upstream of inlet flow nozzle, psia
ΔP = pressure rise in tank during injection, psi
Pr = Prandtl number, $c_p\mu/k$
Ra = Rayleigh number, Gr·Pr
Re = Reynolds number, $\rho D v_n/\mu$
T = instantaneous gas temperature, °R
T_f = final gas temperature, °R
T_0 = upstream stagnation temperature, °R
T_w = wall temperature, °R
t = time, s
v_n = gas velocity at injection nozzle throat, ft/s
V = tank volume, ft³
α = thermal diffusivity, ft²/s
γ = ratio of specific heats, c_p/c_v
μ = dynamic viscosity, lbm/ft-s
ν = kinematic viscosity, ft²/s
ρ = gas density, lbm/ft³

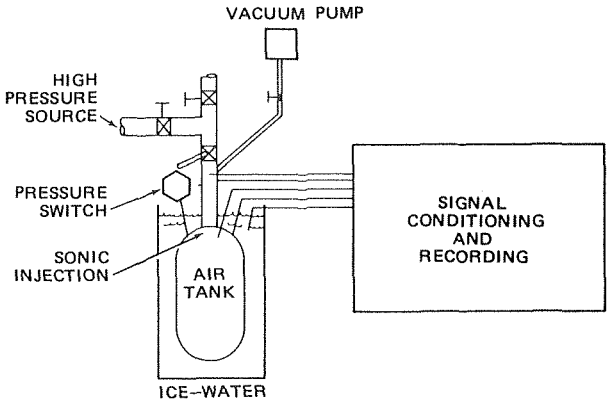

Fig. 1 Schematic sketch of experimental equipment

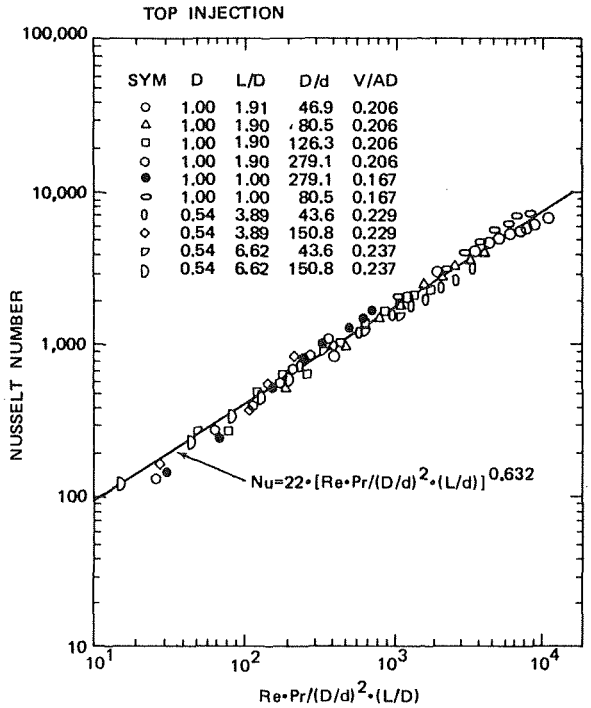

Fig. 2 Top injection period data correlation

Analysis

Heat Transfer Coefficients. The heat transfer coefficient during injection may be determined from measured physical parameters by considering an energy balance on the system. Consider the energy equation during injection into a system with not outlet.

$$\frac{d(mc_vT)}{dt} = \dot{m}c_pT_0 - hA(T - T_w) \tag{1}$$

Equation (1) is sufficient to determine the heat transfer coefficient from experimental measurements of the parameters involved, provided that reliable experimental data can be obtained. Because of the difficulties involved in obtaining reliable gas temperature data and its time derivative, one can obtain better results by applying the Equation-of-State, $PV = mRT$, to convert temperature variables to pressure variables. Therefore, one may rearrange equation (1) as follows:

$$h = \frac{\dot{m}c_pT_0 - \dfrac{\dot{P}V}{\gamma - 1}}{A\left\{\dfrac{PV}{mR} - T_w\right\}} \tag{2}$$

The reason for changing from temperature to pressure parameters is that instantaneous pressure and pressure derivatives are easier to measure accurately than instantaneous temperature and temperature derivatives. Furthermore, pressure is uniform over the tank, while temperature may vary locally. Pressure integrates and averages all the local temperature effects. Heat transfer coefficients for the post-injection period may be calculated in a similar manner to the injection period calculations, but leaving out the mass flow term and using the final mass. The resulting equation is

$$h = \left(\frac{V}{A}\right)\left(\frac{1}{1-\gamma}\right)\frac{\dot{P}}{P\dfrac{T_f}{P_f} - T_w} \tag{3}$$

Data Correlation and Discussion

Injection Period. Nondimensionalizing equation (2) using the dimensionless variables: $\tau = \alpha t/D^2$, $p = P/P_c$, $\Phi = T/T_c$, assuming $P_n = P_c$, and substituting $A/An = 4(L/D)\ (D/d)^2$ yields

$$\mathrm{Nu} = \frac{\dfrac{V}{\gamma AD}\dfrac{dp}{d\tau} - \dfrac{\mathrm{RePr}(P_n/P_0)^{\frac{\gamma-1}{\gamma}}}{4(L/D)(D/d)^2}}{\Phi - \Phi_w} \tag{4}$$

This equation suggests a correlation of Nusselt number with the dimensionless ratio $\mathrm{RePr}/(L/D)\ (D/d)^2$ with $V/AD\gamma$ as a parameter. In these tests P_n/P_0 was constant. Data were correlated during injection by plotting Nu versus $\mathrm{RePr}/(D/d)^2\ (L/D)$. Typical data for top injection are presented in Fig. 2. The results for radial and tangential injection were similar. Equation (4) indicates possible significant parameters V/AD and P_n/P_0. These data, however, indicate that V/AD is insignificant within the range tested. Since these data are for sonic injection velocities, the parameter P_n/P_0 was not experimentally explored. Means [10] describes a method whereby they may be adjusted for subsonic inlet velocity.

Note that in determining Nusselt number the value of γ was evaluated at the gas average temperature. All other gas properties were evaluated at a gas film temperature, assumed to be the average of the average gas temperature and wall temperature. The wall temperature was assumed to be the same as the temperature of the ice water bath. The characteristic length used was the tank diameter. The correlation of injection data taken from all configurations fit the equation

$$\mathrm{Nu} = 22[\mathrm{RePr}/(L/D)(D/d)^2]^{0.635} \tag{5}$$

The mean error was 10 percent with standard deviation of 8 percent. These data show excellent correlation, considering that L/D varied from 1 to 6.62, D/d varied from 43 to 279 and V/AD varied from 0.167 to 0.237, where the entire range for hemisphere-cylinders is $\frac{1}{6} \le V/AD \le \frac{1}{4}$.

Post Top or Bottom Injection Period. Correlation of heat transfer data after top injection required two different types of data plots. The transient period immediately following injection may be correlated on a Fourier number–Nusselt number plot. A typical plot is presented in Fig. 3. The natural convection portion may be correlated by Rayleigh number–Nusselt number and a typical plot is shown in Fig. 4. The break point between the two types of regions is rather abrupt, and the breakaway point for the Fourier correlation corresponds to the attachment point of the Rayleigh correlation.

In Fig. 4 the solid symbols represent the last point of the injection portion of each run, thus beginning the post-injection period. They were computed from Fig. 2, based on the final gas density. When the Rayleigh number was about 10^8, the slope changed from about $\frac{1}{3}$ to about $\frac{1}{4}$, indicating that turbulent to laminar transition occurs and may be noted in Fig. 4.

Summary plots of data correlations following top injection are presented in Figs. 5 and 6. Fig. 5 correlates the data immediately following injection, while Fig. 6 correlates the data during the nat-

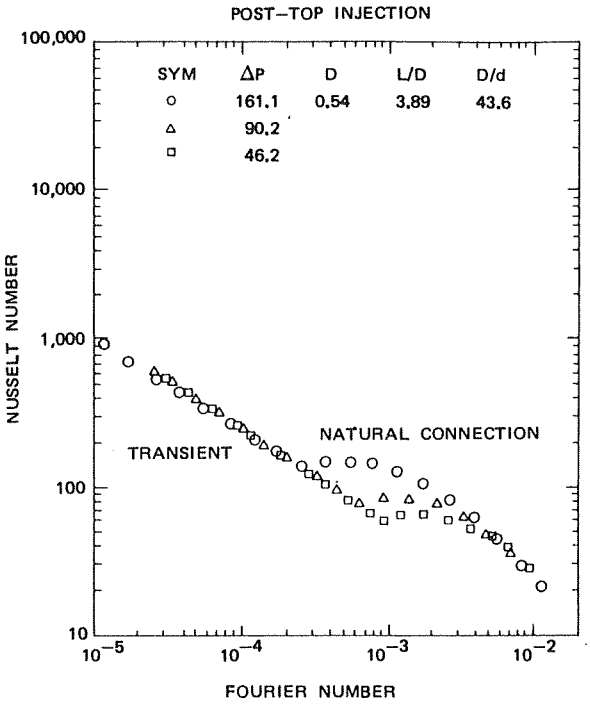

Fig. 3 Fourier number (time) correlation following top injection

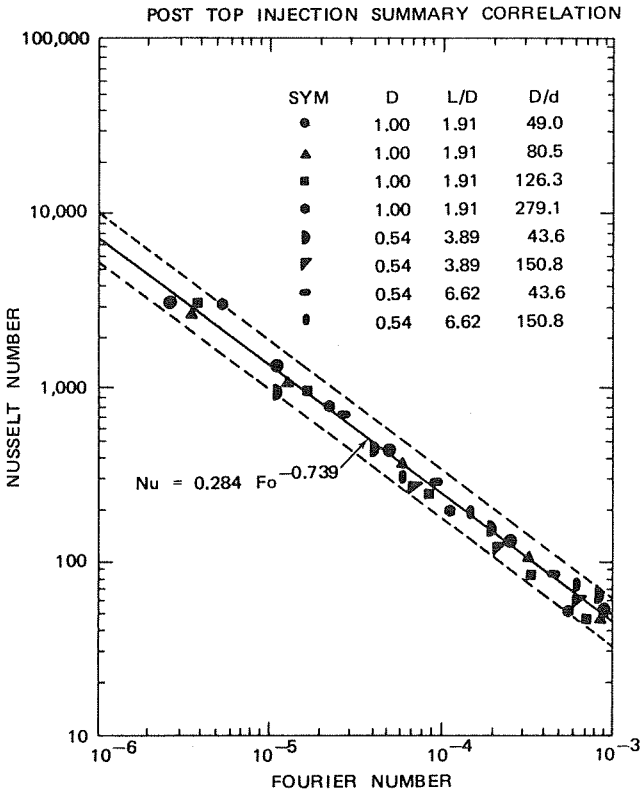

Fig. 5 Summary correlation following top injection—transient period

ural convection period which follows the initial transient condition. Data from Fig. 5 may be fitted within 25 percent by the equation

$$\mathrm{Nu} = 0.284\ \mathrm{Fo}^{-0.739} \tag{6}$$

Data from Fig. 6 may be fitted within 10 percent by the equation for turbulent flow

$$\mathrm{Nu} = 0.12\ \mathrm{Ra}^{0.333} \quad (\mathrm{Ra} > 10^8) \tag{7}$$

or by the equation for laminar flow

$$\mathrm{Nu} = 0.53\ \mathrm{Ra}^{0.25} \quad (\mathrm{Ra} < 10^8) \tag{8}$$

One should use equation (6) until the Nusselt number calculated by equation (6) is as low as the Nusselt number calculated by equation (7) or (8), from which time the latter Nusselt number should be used in estimating the heat transfer coefficient.

Equations (6), (7), and (8) may also be used for post-bottom injection, as there appeared to be no significant difference in data from the two configurations.

Post-Tangential Injection Period. Heat transfer after tangential injection may be correlated on Nu-Fo plots. Fig. 7 shows typical data recorded after tangential injection. The natural convection forces were not sufficient to overpower the vortex established by the tangential injection, as was the case in top injection. However, the Lighthill "tailoff" could be noted after sufficient time. Fig. 8 is a summary data correlation for post-tangential injection heat transfer. These data may be fitted within 30 percent by the equation

$$\mathrm{Nu} = 0.89\ \mathrm{Fo}^{-0.71} \tag{9}$$

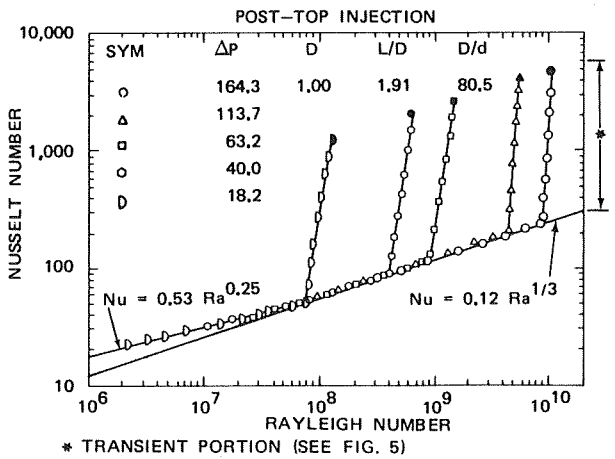

Fig. 4 Rayleigh number correlation following top injection

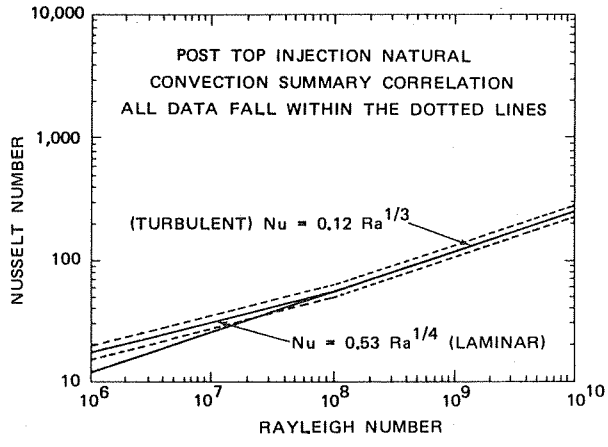

Fig. 6 Summary correlation following top injection—natural convection period

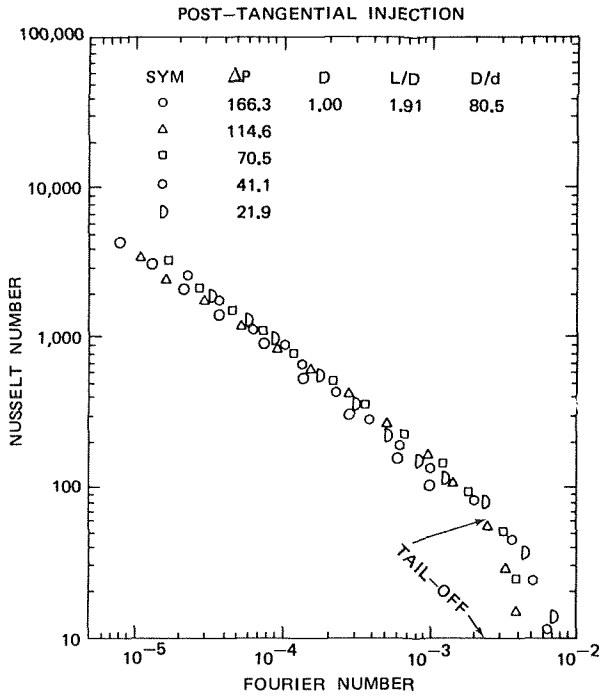

Fig. 7 Data correlation following tangential injection—including tailoff

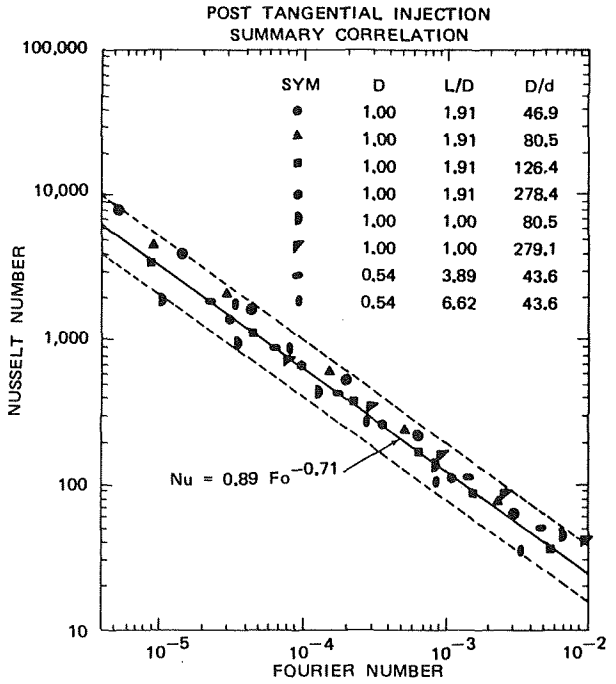

Fig. 8 Fourier number summary correlation for post-tangential injection—transient period

Unlike post-top injection data, only one correlation was needed for post-tangential injection data. Again, these data correlated well enough that within the geometric parameters tested there was no particular effect of geometry.

Post-Radial Injection Period. Post-radial injection data are very similar in character to post-tangential injection data, though the values are slightly different as shown in Fig. 9.

Smoke flow pattern studies by Kilpack [11] indicated that radial injection (on a two-dimensional model) induced two vortices while tangential injection induced one large vortex. One would expect three-dimensional models to be somewhat similar. Also, since both types of injection develop large vortices which persist for a considerable time, one would expect similar heat transfer patterns. And, since radial injection has two vortices (or its three-dimensional equivalent) and tangential injection only one vortex, the values of the heat transfer coefficients are somewhat different.

Fig. 9 is a summary data correlation for post-radial injection heat transfer. These data may be fitted within 25 percent by the equation

$$\mathrm{Nu} = 1.49\ \mathrm{Fo}^{-0.644} \tag{10}$$

This equation is similar to equation (9) but it has slightly lower sensitivity to time, i.e., the vortex pattern seems to decay a little more slowly.

Post-Ejection. Equations (7) and (8) may be used for post-ejection calculations for any ejection geometry, as the heat transfer data always correlated with the natural convection after an ejection. Apparently this was due to the absence of a jet stirring the internal gas. No ejection data were taken, but a reasonable conclusion is that natural convection existed during ejection, since post-ejection always started in this mode.

Conclusions

The following conclusions may be drawn from this work:

1 Post-ejection heat transfer may always be predicted by a natural convective correlation, with no discernible differences due to ejection geometry.

2 Heat transfer from a closed container after gas injection may or may not be predictable by natural convection correlations, as suggested by Ring [1], depending on injection geometry and time.

3 Post-injection heat transfer always has a forced convection transient immediately after injection, which is correlatable with Fourier number. This time correlatable transient mode may or may not transist to a natural convection mode, depending upon injection geometry. For example, post-top or -bottom injection transists to natural convection, while post-radial or post-tangential injection does not.

4 There was no discernible difference between data from top and bottom injection runs.

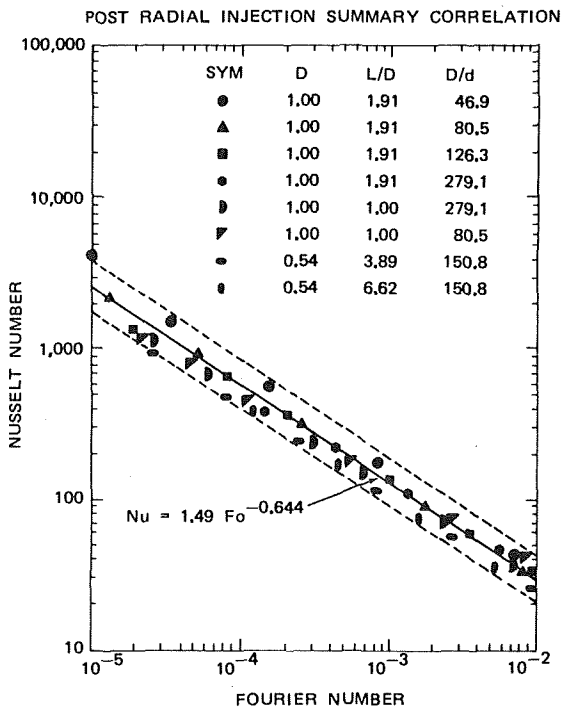

Fig. 9 Fourier number summary correlation for post-radial injection

5 Heat transfer during injection (for sonic injection velocities) was not a function of the geometric variables tested.

6 The Lighthill [7] stagnation tailoff appears to occur as equilibrium conditions are approached.

References

1 Ring, Elliot, *Rocket Propellant and Pressurizing Systems,* Prentice-Hall, Inc., Englewood Cliffs, N.J., 1964.

2 Reynolds, W. C., Millard, J. W., and Kays, W. M., "An Experimental Investigation of the Blowdown Process in a Single Receiver, Including the Effects of Heat Transfer," Stanford Technical Report T-R, Stanford University, Stanford, Calif.

3 Reynolds, W. C., "An Analytical Investigation of the Blowdown and Charging Process in a Single Gas Receiver, Including the Effect of Heat Transfer," Technical Report T-1, Contract N6-)NR-25, Task Order 6 (NR-065-104) for the Office of Naval Research, Department of Mechanical Engineering, Stanford University, Stanford, Calif.

4 McAdams, W. H., *Heat Transmission,* Third ed., McGraw-Hill, New York, 1954.

5 Ulrich, R. D., Wirtz, D. P., and Nunn, R. H., "Thermal Analysis of Gas Pressurized Expulsion Systems, Heat Transfer in Closed Containers With Gas Injection," NWC TP 4569, Part I, Naval Weapons Center, China Lake, Calif., July 1968.

6 Ulrich, R. D., Wirtz, D. P., and Nunn, R. H., "Transient Heat Transfer in Closed Containers After Gas Injection, Transactions of the American Society of Mechanical Engineers," JOURNAL OF HEAT TRANSFER, TRANS. ASME, Series C, Vol. 91, Aug. 1969.

7 Lighthill, M. J., "Theoretical Considerations on Free Convection in Tubes," *Quarterly Journal of Mechanics and Applied Mathematics,* Vol. 6, 1953, p. 400.

8 Steiger, J, E., "A Transient Convective Heat Transfer Coefficient for Injection into a Rigid Vessel," MS thesis, Brigham Young University, Provo, Utah, May 1971.

9 Lyons, J. T., "Heat Transfer Considerations in a Pressure Vessel Being Charged," MS thesis, Naval Postgraduate School, Monterey, Calif., Mar. 1969.

10 Means, J. D., "Transient Convective Heat Transfer in Closed Containers During and After Gas Injection," PhD dissertation, Brigham Young University, Provo, Utah, Apr. 1973.

11 Kilpack, R. K., "Flow Visualization in Compressed Gas Heat Transfer," Masters Project Report, Mechanical Engineering Science Department, Brigham Young University, 1970.

K. M. Atesmen
Senior Scientist,
Koc Holding Research and Development Center,
Medidiyekoy, Istanbul, Turkey.
Assoc. Mem. ASME

Heat Transfer in Rotary Combustion Engines

In the first part of this study, a one-dimensional quasi-steady-state heat transfer model is developed for an axial forced flow system in rotary combustion engines. This computer model is useful in optimizing the cooling system in accordance with the heat input from the combustion chambers. In the second part of this study, a two-dimensional quasi-steady-state heat transfer model is developed for an axial forced flow cooling system in a rotor housing in an effort to minimize the thermal stresses and the thermal distortions of the trochoidal surfaces. In the third part of this study, a two-dimensional transient heat transfer model is developed for an axial forced flow cooling system in a critical portion of the rotor housing in order to determine the critical thermal loads that occur in the through-bolts during the sudden acceleration of a cold rotating combustion engine.

Introduction

This paper deals with the heat transfer problems of rotary combustion engines which have successfully demonstrated a high level of durability, performance, environmental emission standards, and a wider application range than any other engine in use today. The automotive industry around the world has been developing the rotary combustion engine with intense concentration in the last decade.

There are three parts of this work. In the first part, a general one-dimensional quasi-steady-state heat transfer computer model is developed for a multi-pass, axial, forced flow cooling system where the coolant flows axially, namely parallel to the mainshaft axis, through the rotor housings from one end cover to the other, and back again. The distribution of the flow rates are directed by internal ribbings of the end covers. The computer model follows the coolant and calculates iteratively the wall and the coolant temperatures and the heat that is transferred to the coolant throughout the entire engine at every 5 deg increment. The local and instantaneous fuel-side heat transfer coefficients are obtained from the modified empirical equation proposed by Annand [1][1] for reciprocating internal combustion engines. The empirical constants of Annand's empirical equation are adjusted to give the local and instantaneous fuel-side heat transfer coefficients by the help of classified experimental data taken from marketed rotary combustion engines. The water-side heat transfer coefficients are obtained from the empirical Colburn j-factor equation in which all the physical properties are evaluated at the average fluid bulk temperature and the variations in physical properties caused by the temperature differences are accounted for by a viscosity correction factor. Also the entrance effects on the heat transfer coefficients in turbulent flows are accounted for. At every incremented location in the engine, the wall temperatures and the coolant bulk temperatures are not directly available, and an iteration solution becomes necessary. The one-dimensional heat transfer computer model helps to optimize the cooling system while the fluid mechanics properties, namely the passage flow rates, passage hydraulic diameters, are inputs to the program. Several different cooling systems are tested to minimize the temperature differences throughout the engine in order to avoid excessive thermal stress concentration spots and to avoid excessive thermal distortions which cause deterioration in the gas, oil, and water seals. A multipass axial cooling system with five spark-plug-side inlet and nine inlet and exhaust ports side outlet passages permits the best cooling with a desirable circumferential heat balance in a two-rotor rotary combustion engine.

In the second part of this paper, a two-dimensional quasi-steady-state heat transfer computer model is developed for the rotor housing. This model gives the steady-state temperatures at 1366 nodal points on the rotor housing and calculates the amount of heat that is transferred to and from each coolant passage. The same expression of the previous model along with the appropriate empirical equation for the laminar forced convection heat transfer to lubricating oil are used for evaluating the necessary heat transfer coefficients. This computer model is particularly useful in determining high thermal stress concentration locations and thermal distortions in the rotor housing, especially around the spark plug and the exhaust port, which are taken into consideration in determining the rotor housing materials, cooling requirements, and also in determining the cold rotor housing dimensions versus the hot

[1] Numbers in brackets designate References at end of paper.

Contributed by the Heat Transfer Division for publication in the JOURNAL OF HEAT TRANSFER. Manuscript received by the Heat Transfer Division June 18, 1974. Paper No. 75-HT-FF.

rotor housing dimensions.

In the third part of this paper, a two-dimensional transient heat transfer model is developed for a segment of the rotor housing at the expansion phase including a through-bolt. Same expressions of the previous models for the heat transfer coefficients are used in evaluating the temperature rise during a sudden acceleration of a cold engine. The rotor housing walls and the through-bolts are exposed to critical thermal and distortion loads, respectively, because of excessive temperature differences in the entire engine.

These heat transfer models contribute significantly to the design and development of rotary combustion engines. The present calculations are used for the design of a two-rotor, 70 hp axially-cooled rotary combustion engine with a 9.2:1 compression ratio, namely TRM-102.

The work reported here is a part of the research and development program for rotary combustion engines that has been undertaken at KOC HOLDING Research and Development Center in Istanbul, Turkey. The computer models are written in FORTRAN IV and run on IBM-360.

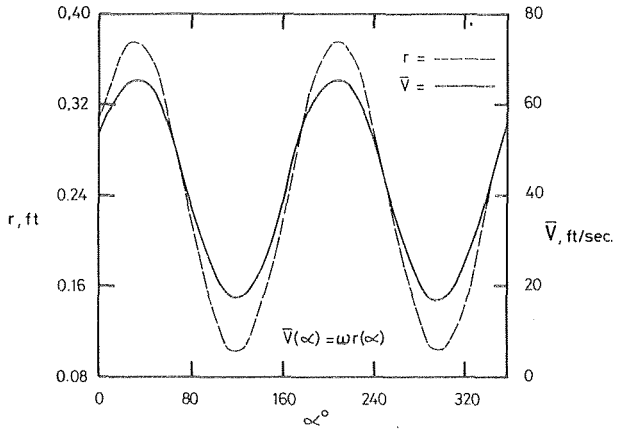

Fig. 1 Mean fuel-air mixture velocity and local characteristic length of the combustion chamber versus angular position α at 5000 rpm for TRM-102

Theory

In all the computer models, local and instantaneous fuel-side heat transfer coefficients are necessary for the incremental heat transfer analysis of a rotary combustion engine. The procedure starts with finding the indicator diagram of the design in question with a known compression ratio. The indicator diagram follows the theoretical Otto-cycle except that during the combustion process the heat release versus time diagram is assumed to be triangular. The instantaneous fuel-air mixture temperatures are obtained with the help of the indicator diagram and the thermodynamic property charts for unburned and for burned mixture of fuel and air at a ratio of 0.0782 for reciprocating combustion engines. The instantaneous fuel-air mixture properties are evaluated at the instantaneous fuel-air mixture temperatures, which are assumed to be uniform throughout the chamber, by using known polynomial approximations. Working fluid compositions after combustion in a typical reciprocation combustion engine are used because of the lack of published information in rotary combustion engines. The combustion process in a rotary engine can also be investigated in detail by solving the appropriate conservation equations, i.e., see Bracco and Sirignano [2].

The instantaneous fuel-side heat transfer coefficient is due to the turbulent motion of the fuel-air mixture relative to the walls. Accordingly the characteristic velocity is the local and instantaneous fuel-air mixture velocity relative to the housing, and the characteristic length is the local and instantaneous hydraulic diameter. The local and the instantaneous fuel-air mixture velocity relative to the housing is made up of three components. The first component is due to the motion of the chamber relative to the housing. The second one is the squishing velocity due to the changing chamber geometry. The third one is the velocity induced by the expanding combustion products in between the two flame fronts. The relative magnitudes of the three components change with time and position, but the first two can be of the same order while the third one can be considerably larger than the other two.

By knowing the local and instantaneous working fluid properties, velocities, and the chamber characteristic lengths, one can obtain the local and instantaneous fuel-side heat transfer coefficients by using the McAdams correlation,

$$h_f = \frac{0.023\, k_f}{D_h} \mathrm{Re}_{D_h}^{0.8} \mathrm{Pr}^{0.4} \tag{1}$$

because intuitively, in a rotary engine, the motion of the working fluid with respect to the housing is like the motion of a parcel of gas in a pipe. However, the squishing and the flame front velocities have to be estimated in order to find the effective fuel-air mixture velocities. Equation (1) gives as expected low fuel-side heat transfer coefficients, shown in Fig. 2, using only the known component

Nomenclature

A = heat transfer area (L^2)
a, b, c = Annand's [1] empirical constants in equation (1)
D = hydraulic diameter of flow passage (L)
D_H = local and instantaneous hydraulic diameter of the combustion chamber (L)
h = heat transfer coefficient (LF/tL^2T)
k = thermal conductivity (LF/tLT)
L = hydraulic length of flow passage (L)
q = heat transfer (LF/t)
Q = mass flow rate (L^3/t)
T = temperature (T)
V = tangential rotor velocity (L/t)
V_{EFF} = local and instantaneous gas velocity (L/t)
α = angular position on the epitrochoid surface where $\alpha = 0$ is the major axis
ϵ = iteration convergence criteria on q/A (LF/tL^2)
θ = time (t)
μ = absolute viscosity (M/Lt)
σ = stress (F/L^2)
ω = angular velocity

Subscripts

b = refers to bulk temperature
c = refers to convective heat transfer coefficient for an infinitely long tube
cl = refers to convective heat transfer coefficient for a finite length tube
D = refers to the characteristic length used in dimensionless groups
f = refers to fuel side
s = refers to surface or wall
w = refers to wall

Superscripts

$-$ = refers to a time-averaged value

Dimensionless Groups

Gr = Grashof number, $\rho^2 g\beta\, \bar{V} TD^3/\mu^2$, a natural convection heat transfer parameter that represents the ratio of buoyant to viscous forces
Nu = Nusselt number, hr/k, a heat transfer parameter
Pr = molecular Prandtl number, $\mu c/k$, fluid property group
Re = Reynolds number, $\bar{V}r/\nu$, the fluid dynamical parameter
St = Stanton number, Nu/RePr, a heat transfer parameter

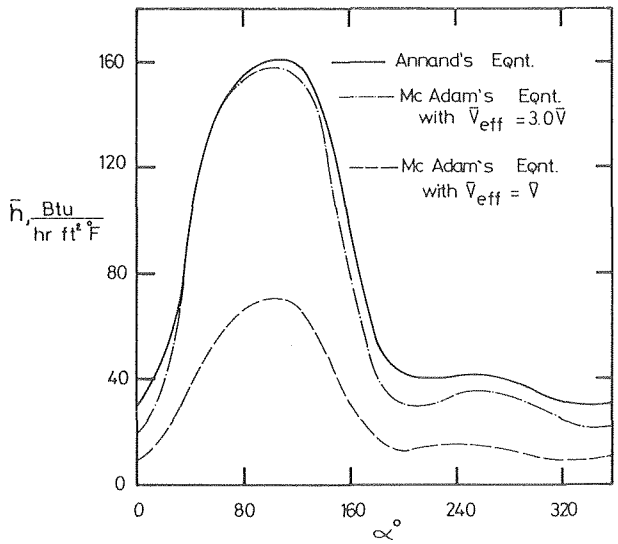

Fig. 2 Local and time-averaged fuel-side heat transfer coefficients versus angular position α at 5000 rpm for TRM-102

of the fuel-air mixture velocity, namely the motion of the chamber relative to the housing for a fixed engine geometry and rotor rotation.

Rather than going into a detailed analysis of the unknown fuel-air mixture velocity components, it is decided to evaluate the local and instantaneous fuel-side heat transfer coefficients by making improvements on the Annand's [1] empirical formula for reciprocating combustion engines.

$$h_f = \frac{ak_f}{r} \mathrm{Re}_r^{\,b} + c\,\frac{(T_f^4 - T_w^4)}{(T_f - T_w)} \tag{2}$$

where $b = 0.7$ is assumed, namely the slope of Nu versus Re functional relationship is assumed to be the same for the local and instantaneous fuel-side heat transfer coefficients and for the averaged ones over the heat transfer surface. Annand [1] suggests the value for the empirical constant a to be between $0.35 < a < 0.8$ for the reciprocating combustion engines. Later, Millar, and Hutchinson [4] suggest the value for the empirical constant a to be between 0.5 a 0.7 for the rotary combustion engines. These values of the empirical constant a are high for the local and instantaneous fuel-side heat transfer coefficients. The localized value of the empirical constant a is determined by the help of classified experimental local heat transfer data taken from a marketed two-rotor rotary combustion engine. The value of a is found to be 0.25 for the local and instantaneous fuel-side heat transfer coefficient of a two-rotor rotary combustion engine. During the combustion and the expansion phases the radiative heat transfer constant $c = 1.30 \times 10^{-10}$ Btu/hr ft^2 R^4 and otherwise $c = 0$.

The average local fuel-air mixture velocity in the combustion chamber at a rotor position is taken as the average surface tangential velocity of the rotor at that particular position which is known for a fixed engine geometry and rotor rotation. The local characteristic length of the rotating combustion chamber for a rotor position is taken as the radius at which the chamber is rotating with a constant angular velocity, ω, and has the average surface tangential velocity of the rotor surface, namely $\bar{V}(\alpha) = \omega r(\alpha)$.

The local characteristic lengths and the local fuel-air mixture velocities are shown in Fig. 1 for the TRM-102 rotary combustion engine at 5000 rpm. The local and time-averaged fuel-side heat transfer coefficients that are obtained from equation (2) are shown in Fig. 2 for the TRM-102 two-rotor rotary combustion engine at 5000 rpm. Fig. 2 also shows that the effective fuel-air mixture velocity to be used in the McAdams correlation is three times the velocity of the chamber relative to the housing which should give an idea about the magnitudes of the squishing plus the flame front

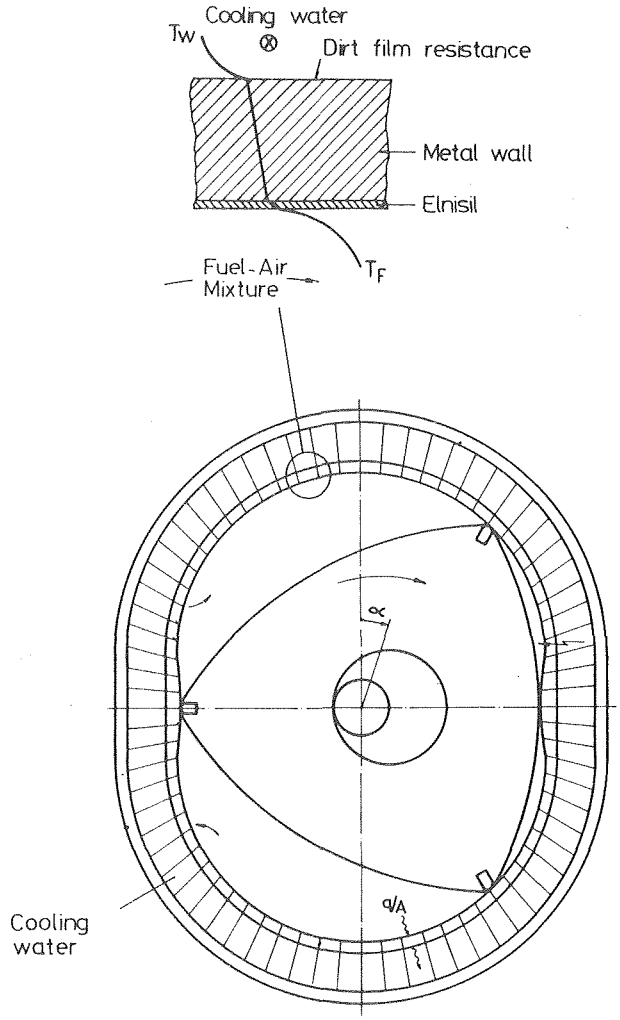

Fig. 3 One-dimensional quasi-steady-state heat transfer model for the rotor housing

velocities.

For the water-side heat transfer coefficients the following Colburn j-factor equation, reference [3], is used.

$$\mathrm{StPr}^{2/3} = 0.023\ \mathrm{Re}^{-0.2} \tag{3}$$

The physical properties in equation (3) are evaluated at the average film temperature of water. The variations in physical properties caused by the temperature gradients are accounted for by a viscosity correction factor namely $(\mu_s/\mu_b)^{0.36}$. The entrance effects on the heat transfer coefficients are represented approximately by the equation,

$$\bar{h}_{c1} = \bar{h}_c[1 + (D/L)^{0.7}] \tag{4}$$

Also a dirt film resistance of 0.0001 hr ft^2/Btu is taken into consideration on the water side.

In the one-dimensional heat transfer model, each housing is divided into seventy-two epitrochoidal increments where heat is transferred only in the normal direction to the incremented surface between the fuel and the water as shown in Fig. 3. The water jacket is assumed to enclose completely the housing inner walls. The inputs to the program are the water inlet temperature, the housing wall and the epitrochoid coating thickness, the thermal conductivities of metals that are in use; the fuel-air mixture temperatures, densities, velocities, and the combustion chamber characteristic lengths at each five degree increment; the heat transfer surface areas, water flow mean velocities, water passage hydraulic diameters and hydraulic lengths at each five degree increment of every housing.

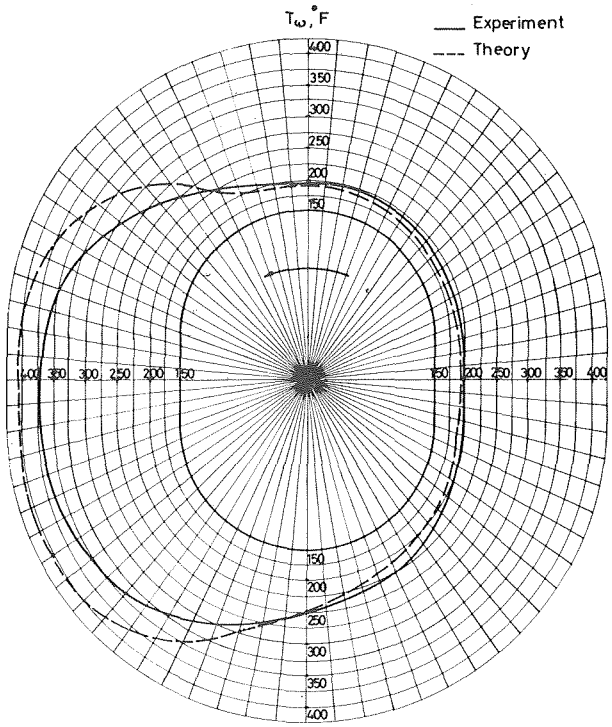

Fig. 4 Comparison of experimental and theoretical wall temperature distributions

The housing wall temperatures and the heat that is transferred to water at each increment are calculated iteratively in order to include the radiation heat transfer effects and the property variations. It takes four or five iterations for the convergence of the calculated temperature and the heat flux values with a convergence criteria of $\epsilon_{q/A} < 100$. It takes thirty minutes to run this program on an IBM-360 digital computer.

Fig. 3 also shows the one-dimensional heat transfer simulation model for a rotor housing. Fig. 4 shows the comparison of the wall temperature distribution data taken from a marketed two-rotor rotary combustion engine and the present theoretical model. In the experimental marketed rotary engine the cool side of the engine is heated by bleeding exhaust gases in order to minimize the circumferential temperature differences. In the theoretical wall temperature calculations that are shown in Fig. 4, the exhaust gas bleeding process is not accounted for. Fig. 5 shows an optimized inlet and outlet passage combination for an axial cooling system of a two-rotor rotary combustion engine. The temperature and the heat flux distributions of the designed engine, namely TRM-102, are shown, respectively, in Figs. 6 and 7. The TRM-102 engine loses 17 percent heat to cooling water and the difference of the inlet and outlet water temperature is 10 deg F at 5000 rpm.

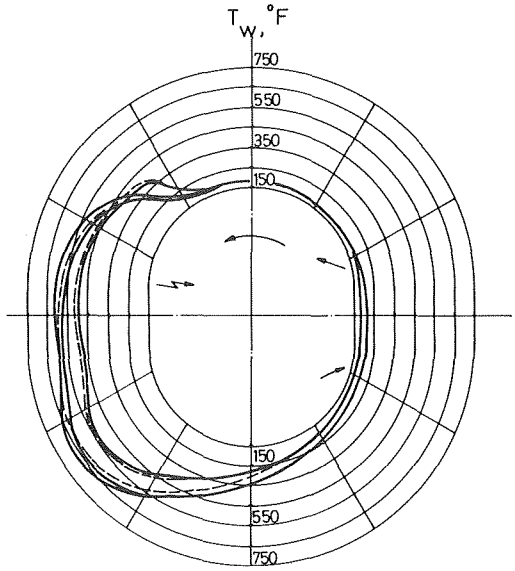

Fig. 6 Front, first rotor, intermediate, second rotor, and rear housing wall temperatures of TRM-102 at 5000 rpm

In the second part of this study, the two-dimensional quasi-steady-state heat transfer problem is solved for a rotor housing on a digital computer by using the numerical network shown in Fig. 8. The temperatures at 1366 nodal points are evaluated by solving the appropriate partial-differential equation by the relaxation method. The heat transfer coefficients mentioned previously and the equation

$$\overline{\mathrm{Nu}}_D = 0.53\ (\mathrm{Gr}_D \mathrm{Pr})^{1/4} \tag{5}$$

for the average heat transfer coefficient from a sphere in free convection are used in the numerical solutions. Also the empirical relationship suggested by Sieder and Tate [3] has been used for laminar oil flow in the lubrication passages.

$$\mathrm{Nu}_D = 1.86\ (\mathrm{Re}_D \mathrm{Pr} D/L)^{0.33} (\mu_b/\mu_s)^{0.14} \tag{6}$$

The computer program inputs are the same as the previous ones in the one-dimensional heat transfer model except that they correspond only to the rotor housing. It takes 26 min to run this pro-

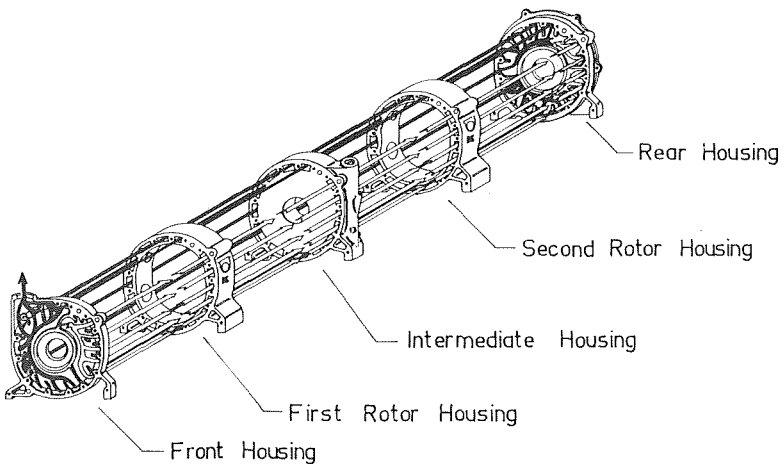

Fig. 5 An optimized inlet and outlet passage combination for an axial cooling system of a two-rotor rotary combustion engine

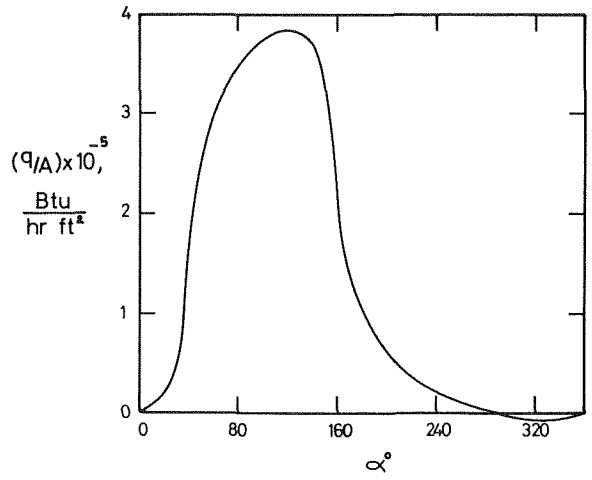

Fig. 7 Heat flux distribution in the rotor housing of TRM-102 at 5000 rpm

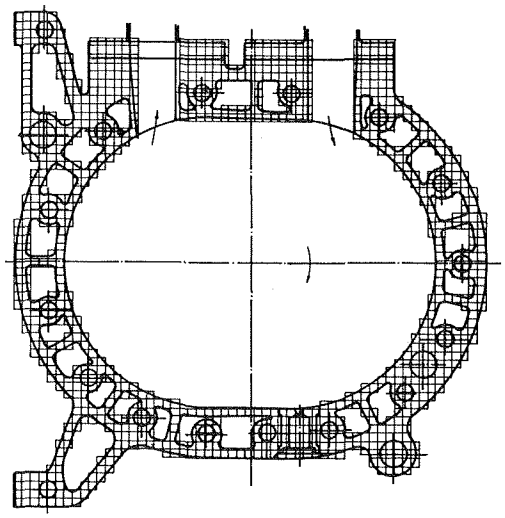

Fig. 8 Two-dimensional quasi-steady-state heat transfer model network for the rotor housing

gram on an IBM-360 digital computer for 300 iterations in order to reduce all the residues to less than 0.1.

The isotherms on a rotor housing are shown in Fig. 9 which is

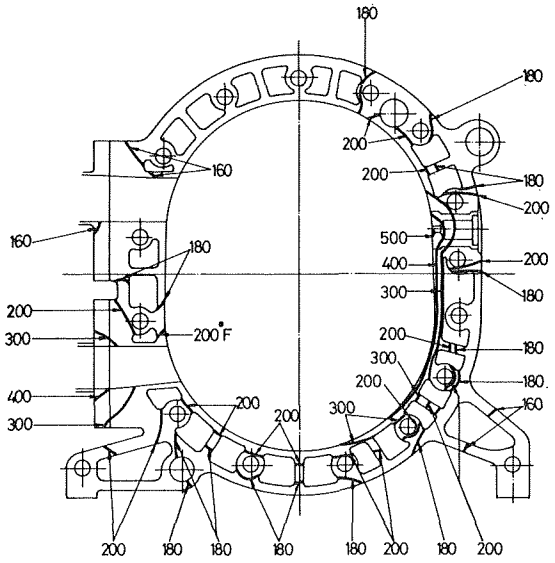

Fig. 9 The isotherms on the rotor housing of TRM-102 at 5000 rpm

very useful in seeing the thermal loads at the critical regions around the spark plugs and the exhaust port. Also the epitrochoid wall temperature distributions of the TRM-102 rotor housing which are evaluated by the one-dimensional and by the two-dimentional heat transfer models, are compared in Fig. 10. The total heat loss to water in a rotor housing as calculated from the two-dimensional heat transfer model is 10.5 percent larger than the value calculated from the one-dimensional heat transfer model. This increase in heat transfer is caused by taking into account the entire surface area of each water passage in the two-dimensional heat transfer model. From the rotor housing fuel-side and water-side surface temperature distributions, Fig. 9, the steady-state thermal stresses on both surfaces are obtained by assuming two different thermal stress models. The time variation of the wall temperatures are neglected because as time changes, the local fuel-air mixture temperature changes considerably while the corresponding wall temperature changes negligibly and this is due to the gas relaxation time being considerably shorter than the solid one. In the first thermal stress model, a thin-walled cylinder with a concentric circular hole and a radial variation of temperature are assumed [5]. In the second thermal stress model, a thin-walled cyl-

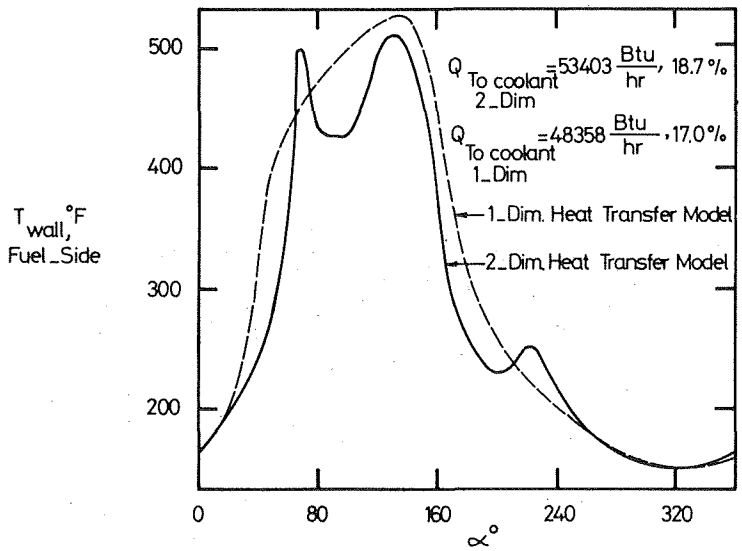

Fig. 10 Fuel-side wall temperature distribution in the first rotor housing of TRM-102 at 5000 rpm

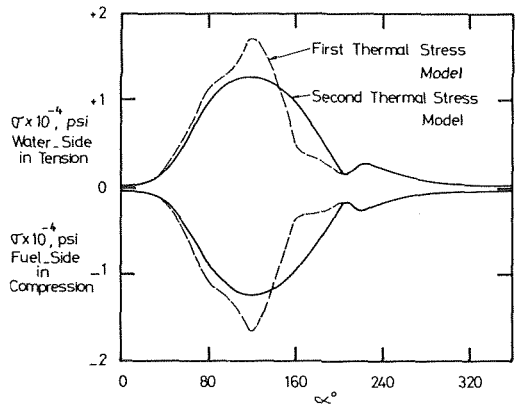

Fig. 11 Thermal stresses at the fuel-side and at the water-side of the rotor housing for TRM-102 at 5000 rpm

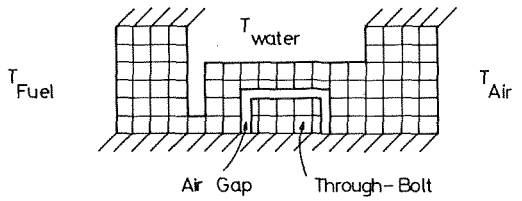

Fig. 12 Two-dimensional transient heat transfer model numerical network

inder with a concentric hole is assumed, and the fuel-side and the water-side temperatures which vary circumferentially, are represented by the Fourier series to account for both radial and tangential temperature variations [5]. The compressive thermal stresses for the fuel-side and the tensile thermal stresses for the water-side that are obtained from the previously cited models are shown in Fig. 11.

In the third section of this study a two-dimensional transient heat transfer model is developed for a section in expansion sector of the rotor housing. The rotor housing section is divided into 115 nodal points and the symmetry conditions are considered as shown in Fig. 12. The appropriate partial differential equations are replaced by the finite-difference equations. All the 115 time-dependent central difference approximation equations are tested for stability conditions, and the time increment is chosen to be 0.01 s. for the calculations. The computer program inputs are the same as the previous ones as in the other models except that they correspond only to the above mentioned expansion sector of the rotor housing. It takes 167 min to run this program on an IBM-360 digital computer. The calculations start initially from the cold engine conditions and go up to 235 s of actual engine running time.

The temperature rise in a cold rotary engine acceleration is seen in Fig. 13 as a function of time for two different housing materials. There is a large temperature difference between the through-bolt and the housing materials. This temperature difference adds extra stress on the through-bolts as shown also in Fig. 13. The transient heat transfer section simulation that is presented here can be applied appropriately to any critical part or parts in a rotary combustion engine.

The three heat transfer digital computer models that are described in this paper, can be, obtained from the author with a complete description of program variables.

Conclusions

1 The local and instantaneous fuel-side heat transfer coefficients for the rotary combustion engines are obtained from the modified empirical equation (2) of Annand for the reciprocating combustion engines. The local fuel-side heat transfer coefficients are calculated by using the appropriate local characteristic lengths

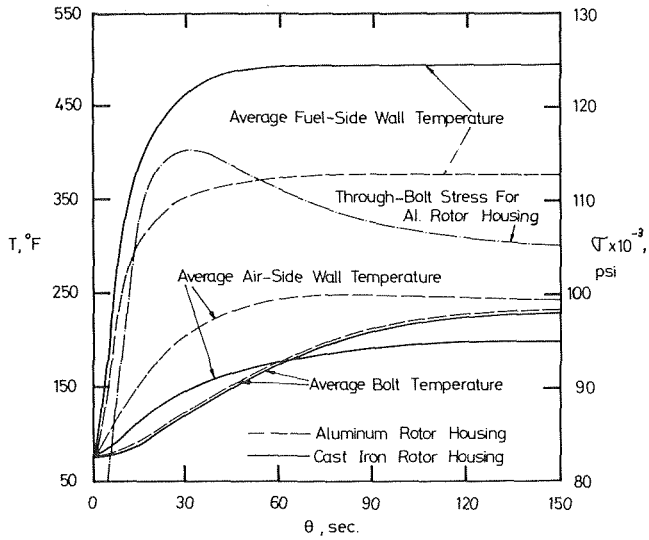

Fig. 13 Transient temperature distribution and through-bolt stress at the expansion section of rotor housing

and the local fuel-air mixture mean velocities. The plausible values for the empirical constants of the modified equation (2) are:

$a = 0.25$

$b = 0.7$

$c = 1.30 \times 10^{-10} \frac{\text{Btu}}{\text{hr ft}^2 R^4}$ during combustion and expansion phases.

2 The one-dimensional quasi-steady-state heat transfer simulation helps to design optimumly the complete cooling system of a rotary combustion engine as shown in Fig. 5 for a two-rotor TRM-102 engine.

3 The two-dimensional quasi-steady-state heat transfer simulation helps to determine the range of local thermal stresses and distortions in the critical sections of a rotary combustion engine.

4 The two-dimensional transient heat transfer simulation helps to determine the critical thermal stresses and distortions in the through-bolts in the expansion sector of the rotor housing during a sudden acceleration with a cold engine.

5 A similar local heat transfer analysis can be made by using McAdams correlation, equation (1), for the local and instantaneous fuel-side heat transfer coefficients after determining the effective fuel-air mixture velocities.

6 The local and instantaneous gas properties can be obtained from the solutions of appropriate conservation equations [2] and be inputed to the present heat transfer simulations.

Acknowledgment

The author would like to thank his co-workers Mr. Claude Nahum, Mr. Mithat Kuleli, Mr. Erol Perksoy, and Mr., Attila, Salepcioglu, who helped with constructive criticism in every phase of this study.

References

1 Annand, W. J. D., "Heat Transfer in the Cylinders of Reciprocating Internal Combustion Engines," *Prod. Inst. Mech. Engrs.*, Vol. 177, No. 36, 1963.

2 Bracco, F. V., and W. A. Sirignano, "Theoretical Analysis of Wankel Engine Combustion," *Combustion Science and Technology*, Vol. 7, 1973, pp. 109–123

3 Kreith, F., "Principles of heat transfer," *International Textbook Co.*, 2nd ed., 1965.

4 Millar, D. H., Hutchinson, D. P., and B. Lawton, "Digital Simulation of Rotary Piston Engines," Royal Military College of Science Research Paper, 1973.

5 Timoshenko, S., and J. N. Goodier, "Theory of Elasticity," McGraw-Hill, New York, 2nd ed., 1951.

journal of heat transfer

technical briefs

This section consists of contributions of 1500 words or less (about 5 double-spaced typewritten pages, including figures). Technical briefs will be reviewed and approved by the specific division's reviewing committee prior to publication. After approval such contributions will be published as soon as possible, normally in the next issue of the journal.

Local Similarity Solutions for Free Convection Boundary Layer Flows

B. T. Chao[1] and F. N. Lin[2]

Nomenclature

a = positive constant having the dimension of acceleration
Gr = Grashof number, $a\beta|T_w - T_\infty|L^3/\nu^2$
k = thermal conductivity
L = reference length
Nu = Nusselt number, $q_w L/(T_w - T_\infty)k$
Pr = Prandtl number
q_w = wall heat flux
$\bar{r}$ = radial distance from axis of symmetry to a surface element; $r = \bar{r}/L$
T = temperature; T_w and T_∞ refer to surface and undisturbed ambient temperature, respectively
$\bar{x}$ = streamwise coordinate; $x = \bar{x}/L$
$\bar{y}$ = coordinate normal to $\bar{x}$; $y = \mathrm{Gr}^{1/4}\bar{y}/L$
β = thermal expansion coefficient
ν = kinematic viscosity
ϕ = dimensionless function of x, $a\phi$ is the x-component of body force per unit mass (in gravitational field, ϕ = sine of the angle between gravitational acceleration vector and the outdrawn normal to body surface)
ψ = stream function in (x,y) coordinates

Introduction

In a recent paper by the authors [1],[3] a fairly general computational scheme was described for the prediction of heat transfer in laminar free convection over isothermal objects submerged in a quiescent fluid of large extent. The body shape is arbitrary, the essential restriction being that the flow is of the boundary layer character, either two-dimensional or axisymmetrical, and does not separate. The analysis employs a suitable coordinate transformation and the solutions of the governing momentum and energy equations are expressed in terms of a sequence of universal functions which depend on the Prandtl number and a configuration function Λ. In general, the latter depends on the streamwise coordinate. It was there noted that the first terms of the series solutions, f_0 and θ_0, are, respectively, the local similarity solution for the stream function and for the temperature. If the body contour is such that the free convection flow is similar, then Λ is a constant and only the first term is retained in the series. When the special case of a vertical flat plate is examined, the governing equations differ in appearance from those earlier given by Schmidt and Beckmann [2] and by Ostrach [3]. However, if the dimensionless coordinate η and the stream function $f(\xi,\eta)$ defined in [1] were rewritten, respectively, as $(2/9)^{1/4}\ \eta$ and $(1/3)(9/2)^{1/4}\ f$, then these equations become identical to those reported in [2, 3].[4]

It is the purpose of this note to demonstrate that by using a different coordinate transformation, one is led to a set of momentum and energy boundary layer equations which, if specialized for a vertical plate, reduce naturally to those given in [2, 3]. In addition, their solutions can likewise be expressed in terms of a sequence of universal functions and the first terms are again the local similarity solutions. However, these local similarity solutions are associated with a different configuration function λ. In similar flows, λ is also a constant as it must be. For nonsimilar flows, the ratio λ/Λ varies with streamwise location and the local similarity solutions associated with the two coordinate systems differ. Hence, it is only meaningful to speak of local similarity solutions with respect to a specified coordinate system.

Analysis, Results, and Discussion

The governing conservation equations for the problem under consideration were presented and discussed in [1]. For convenient reference, the essential steps are reiterated as follows.

Upon introducing a hypothetical outer stream velocity function:

$$U = (2\int_0^x \phi\ dx)^{1/2} \tag{1}$$

the Görtler-Meksyn coordinates:

$$\xi = \int_0^x r^2 U\, dx, \quad \eta = rU(2\xi)^{-1/2}\, y \tag{2a, b}$$[5]

[1] University of Illinois at Urbana-Champaign, Urbana, Ill. Fellow ASME.
[2] Northrop Services, Inc., Huntsville, Ala.
Contributed by the Heat Transfer Division of THE AMERICAN SOCIETY OF MECHANICAL ENGINEER. Manuscript received by the Heat Transfer Division December 6, 1974.
[3] Numbers in brackets designate references at end of technical brief.

[4] The authors are indebted to the reviewer for pointing out the existence of this simple affine transformation.
[5] Here and in other expressions which follow, set $r = 1$ for two-dimensional flows.

Table 1 Variation of Λ and λ in streamwise direction

	Cylinder		Sphere	
ϑ, deg[a]	Λ	λ	Λ	λ
0	1	3	1/2	3/2
30	0.98267	2.9153	0.50593	1.5312
60	0.92820	2.6282	0.52672	1.6517
90	0.82843	2	0.57516	2
120	2/3	0.53918	0.69630	3.2979
150	0.41121	−4.6116	1.1343	13.868

[a] ϑ is measured from the forward stagnation point.

a stream function $f(\xi,\eta) = (2\xi)^{-1/2}\psi(x,y)$ and a temperature function $\theta(\xi,\eta) = (T - T_\infty)/(T_w - T_\infty)$, the momentum and energy boundary layer equation become, respectively,

$$f''' + ff'' + \Lambda[\theta - (f')^2] = 2\xi\frac{\partial(f',f)}{\partial(\xi,\eta)} \tag{3}$$

and

$$\mathrm{Pr}^{-1}\theta'' + f\theta' = 2\xi\frac{\partial(\theta,f)}{\partial(\xi,\eta)} \tag{4}$$

with boundary conditions:

$$f(\xi,0) = f'(\xi,0) = 0, \qquad \theta(\xi,0) = 1 \tag{5a,b,c}$$

$$f'(\xi,\infty) \longrightarrow 0, \qquad \theta(\xi,\infty) \longrightarrow 0 \tag{6a,b}$$

In the foregoing expressions, the prime denotes $\partial/\partial\eta$ and $\partial(\ ,\ )/\partial(\xi,\eta)$ is the Jacobian. The configuration function Λ is given by

$$\Lambda = 2\frac{\xi}{U}\frac{dU}{d\xi} = 2\frac{\phi\xi}{r^2U^3} \tag{7}$$

$$f(\xi,\eta) = f_0(\Lambda,\eta) + \xi\frac{d\Lambda}{d\xi}f_1(\Lambda,\eta) + \xi^2\frac{d^2\Lambda}{d\xi^2}f_2(\Lambda,\eta) + (\xi\frac{d\Lambda}{d\xi})^2 f_3(\Lambda,\eta) + \ldots \tag{8}$$

Series solutions for (3) and (4) have been reported in [1]. They are:

$$\theta(\xi,\eta) = \theta_0(\Lambda,\eta) + \xi\frac{d\Lambda}{d\xi}\theta_1(\Lambda,\eta) + \xi^2\frac{d^2\Lambda}{d\xi^2}\theta_2(\Lambda,\eta) + (\xi\frac{d\Lambda}{d\xi})^2\theta_3(\Lambda,\eta) + \ldots \tag{9}$$

wherein the functions $f_i(\Lambda,\eta)$ and $\theta_i(\Lambda,\eta)$, $i = 0, 1, 2$, etc., are universal and have been tabulated for wide ranges of Λ and Prandtl number.

An alternative series solution follows from the use of a different coordinate transformation:

$$\tilde{\xi} = 4\int_0^x r^{4/3}\phi^{1/3}\,dx, \qquad \tilde{\eta} = (r\phi)^{1/3}\tilde{\xi}^{-1/4}y \tag{10a,b}$$

Upon introducing a stream function $\tilde{f}(\tilde{\xi},\tilde{\eta}) = \tilde{\xi}^{-3/4}\psi(x,y)$ and a temperature function $\tilde{\theta}(\tilde{\xi},\tilde{\eta})$, identically defined as $\theta(\xi,\eta)$, the resulting conservation equations read:

$$\tilde{f}''' + 3\tilde{f}\tilde{f}'' - \lambda(\tilde{f}')^2 + \tilde{\theta} = 4\tilde{\xi}\frac{\partial(\tilde{f}',\tilde{f})}{\partial(\tilde{\xi},\tilde{\eta})} \tag{11}$$

and

$$\mathrm{Pr}^{-1}\tilde{\theta}'' + 3\tilde{f}\tilde{\theta}' = 4\tilde{\xi}\frac{\partial(\tilde{\theta},\tilde{f})}{\partial(\tilde{\xi},\tilde{\eta})} \tag{12}$$

where the prime denotes $\partial/\partial\tilde{\eta}$ and the configuration function λ is given by

$$\lambda = 2 + \frac{1}{3}\frac{\tilde{\xi}}{r^{4/3}\phi^{1/3}}\left(\frac{1}{\phi}\frac{d\phi}{dx} - \frac{2}{r}\frac{dr}{dx}\right) \tag{13}$$

The boundary conditions are the same as those prescribed by (5) and (6). Series solutions analogous to (8) and (9) have been constructed for (11) and (12) and the two zeroth order functions $\tilde{f}_0(\lambda,\tilde{\eta})$ and $\tilde{\theta}_0(\lambda,\tilde{\eta})$ are found to satisfy the following coupled equations.

$$\tilde{f}_0''' + 3\tilde{f}_0\tilde{f}_0'' - \lambda(\tilde{f}_0')^2 + \tilde{\theta}_0 = 0 \tag{14}$$

$$\mathrm{Pr}^{-1}\tilde{\theta}_0'' + 3\tilde{f}_0\tilde{\theta}_0' = 0 \tag{15}$$

For similar flows, λ is a constant and hence, $\tilde{f} = \tilde{f}_0$ and $\tilde{\theta} = \tilde{\theta}_0$. In particular, $\lambda = 2$ for a vertical flat plate and, in this instance, the equation pair (14) and (15) becomes precisely that given in [2, 3].

The functions $\tilde{f}_0$ and $\tilde{\theta}_0$ are related to f_0 and θ_0 as follows:

$$\tilde{f}_0(\lambda,\tilde{\eta}) = 3^{-3/4}\Lambda^{-1/4}f_0(\Lambda,\eta), \quad \tilde{\theta}_0(\lambda,\tilde{\eta}) = \theta_0(\Lambda,\eta) \tag{16a,b}$$

with $\lambda = 3\Lambda$ and $\tilde{\eta} = (\Lambda/3)^{1/4}\eta$. As noted earlier, both Λ and λ are constants in similar flows and, hence, the ratio λ/Λ equals 3 *everywhere* in the flow field. When expressed in physical variables, the two methods of solution yield identical results. In the more general case of nonsimilar flows, λ at a given streamwise location is *not* three times the value of Λ at the same location except at the forward stagnation point where the flow is truly locally similar. This fact is illustrated in Table 1 for a horizontal circular cylinder and for a sphere. Since the local similarity solutions are not the same for the two solution methods, a selection needs to be made. The one which more closely approximates the true solution is obviously desired. In the absence of a true solution, an assessment of the error involved in the local similarity solution can be made by com-

Table 2 Local heat transfer parameter, $\mathrm{Nu}\cdot\mathrm{Gr}^{-1/4}$, for isothermal horizontal circular cylinder—a comparison of predictive methods ($\mathrm{Pr} = 0.70$)

	Series Solution in (ξ,η) Coordinates Configuration Function Λ [1]				Series Solution in $(\tilde{\xi},\tilde{\eta})$ Coordinates Configuration Function λ				2-Term Blasius Series [4]	2-Term Görtler Series [5]
ϑ deg.	1st Term	2nd Term	3rd Term	Sum	1st Term	2nd Term	3rd Term	Sum		
0	0.4402	0.0000	0.0000	0.4402	0.4402	0.0000	0.0000	0.4402	0.4402	0.4402
10	0.4393	0.0000	0.0000	0.4393	0.4393	0.0000	0.0000	0.4393	0.4396	0.4396
20	0.4376	-0.0001	0.0000	0.4375	0.4376	0.0000	0.0000	0.4376	0.4379	0.4375
30	0.4347	-0.0001	0.0000	0.4346	0.4348	0.0000	0.0000	0.4348	0.4350	0.4340
40	0.4306	-0.0002	0.0000	0.4304	0.4307	-0.0001	-0.0001	0.4305	0.4309	0.4290
50	0.4255	-0.0003	0.0000	0.4252	0.4255	-0.0001	-0.0001	0.4253	0.4256	0.4227
60	0.4191	-0.0005	0.0001	0.4187	0.4191	-0.0002	-0.0002	0.4187	0.4192	0.4148
70	0.4116	-0.0007	0.0001	0.4110	0.4117	-0.0003	-0.0004	0.4110	0.4116	0.4055
80	0.4027	-0.0009	0.0002	0.4020	0.4031	-0.0006	-0.0008	0.4017	0.4029	0.3946
90	0.3925	-0.0012	0.0004	0.3917	0.3934	-0.0010	-0.0014	0.3910	0.3930	0.3822
100	0.3808	-0.0014	0.0006	0.3800	0.3828	-0.0020	-0.0021	0.3787	0.3819	0.3680
110	0.3676	-0.0017	0.0010	0.3669	0.3714	-0.0043	-0.0038	0.3633	0.3697	0.3520
120	0.3527	-0.0019	0.0015	0.3523	0.3599	-0.0101	-0.0053	0.3445	0.3563	0.3338
130	0.3358	-0.0020	0.0024	0.3338	0.3497	-0.0283	0.0094	0.3308	0.3417	0.3132
140	0.3161	-0.0016	0.0038	0.3145	0.3496	-0.1571	0.3484	---	0.3260	0.2896
150	0.2924	-0.0001	0.0060	0.2923	0.4147	-3.543	21.13	---	0.3091	0.2617
159	0.2661	0.0039	0.0092	0.2700	---	---	---	---	0.2928	

ϑ is measured from the forward stagnation point; the reference length in Nu and Gr is cylinder diameter.

puting additional terms in the series and examining their convergence behavior. Accordingly, a comparison study was made for both the cylinder and the sphere. Table 2 summarizes the local heat transfer results around the cylinder. The reader may recall that the first term of the series represents the local similarity solution. Data fenced in rectangular boundaries are evaluated from the convergent part of the series, i.e., from the first two terms only. An alternative is to use Euler's method for ascertaining the sum. However, in view of the small number of terms available, it is uncertain that a definite improvement would result. Included in the table are data computed from the Blasius type series due to Chiang and Kaye [4] and from the Görtler type series due to Saville and Churchill [5], both based on two terms. For $0 \leq \vartheta \leq 90$ deg, all discrepancies are small. When ϑ reaches 140 deg and beyond, the series associated with $(\tilde{\xi},\tilde{\eta})$ coordinates entails unacceptable error while the series associated with (ξ,η) remains useful. These results and others on the details of velocity and temperature profiles which we obtained in this study attest to the relative superiority of the latter series and its associated local similarity solution. They also imply that the configuration function Λ provides a better characterization of local similarity for the category of free convection flows considered in [1].

References

1 Lin, F. N., and Chao, B. T., "Laminar Free Convection Over Two-Dimensional and Axisymmetric Bodies of Arbitrary Contour," JOURNAL OF HEAT TRANSFER, TRANS. ASME, Series C, Vol. 96, 1974, pp. 435–442.

2 Schmidt, E., and Beckmann, W., "Das Temperatur- und Geschwindigheitsfeld von einer Wärme abgebenden Senkrechten Platte bei Natürlicher Konvection," *Technische Mechanik und Thermodynamik*, Oct. 1930, pp. 341–349, Nov. 1930, pp. 391–406.

3 Ostrach, S., "An Analysis of Laminar Free-Convection Flow and Heat Transfer About a Flat Plate Parallel to the Direction of the Generating Body Force," NACA Report No. 1111, 1953.

4 Chiang, T., and Kaye, J., "On Laminar Free Convection From a Horizontal Cylinder," *Proceedings of the Fourth National Congress of Applied Mechanics*, 1962, pp. 1213–1219.

5 Saville, D. A., and Churchill, S. W., "Laminar Free Convection in Boundary Layers Near Horizontal Cylinders and Vertical Axisymmetric Bodies," *Journal of Fluid Mechanics*, Vol. 29, 1967, pp. 391–399.

Free Convection Flow Patterns Between a Body and Its Spherical Enclosure

R. E. Powe,[1] R. C. Baughman,[2] J. A. Scanlan,[3] and J. T. Teng[4]

Introduction

The purpose of this note is to present flow visualization results for natural convection in somewhat more complicated geometries than have been studied in the past. These geometries include heated vertically eccentric spheres and concentric vertical cylinders with hemispherical end caps, all located within a cooled spherical enclosure. Air (Pr $\simeq$ 0.7), water (Pr $\simeq$ 3–10), 20 cs silicone oil (Pr $\simeq$ 150–300), and 350 cs silicone oil (Pr $\simeq$ 2000–5000) were used as the working fluid. With air as the test fluid, cigar smoke was used to make the flow visible, and a detergent technique [1][5] was used to provide tracer particles in water. For the oils, tracer particles were obtained by spraying fluorescent paint over a free surface of the oil. This paint would separate into small particles which would diffuse throughout the fluid and remain in suspension indefinitely.

Eccentric Sphere Results

Air and 350 fluid were tested for diameter ratios, D, of 1.40 and 2.17 for Rayleigh numbers ranging from 6.4×10^3 to 3.2×10^6. Eccentricity ratios (ratio of eccentricity to difference between radii of outer and inner spheres, e/L) of from -0.75 to $+0.75$ were utilized. The previously observed steady crescent eddy pattern [2, 3] was the basic flow obtained for all diameter ratios and all eccentricities at low Rayleigh numbers with air as the working fluid. For D = 2.17, a second steady pattern, the kidney shaped eddy pattern, occurred for moderate Rayleigh numbers for all except the largest positive and negative eccentricities when the inner and outer spheres are in close proximity. When the Rayleigh number exceeded some transition value, shown in Fig. 1, the flow was observed to become unsteady.

For D = 1.40, the unsteady flow was of the three-dimensional spiral type [2] for all eccentricities. No effect on the transition Rayleigh number was noted for negative eccentricities, while positive eccentricities resulted in slightly increased values, in agreement with temperature field results [4]. In contrast, the unsteady flow pattern observed for D = 2.17 was distinctly dependent on eccentricity. The spiral flow existed only for the largest positive eccentricity, and for all other cases the unsteadiness was limited to the central low speed flow region resulting in a constant, and much larger, transition Rayleigh number. This is in accordance with concentric cylinder results [3] where it was found that the transition Rayleigh number for the onset of the spiral flow pattern is much lower than for other unsteady patterns.

With the 350 fluid the crescent eddy pattern was also observed at low Rayleigh numbers, and an unsteady pattern was observed at high Rayleigh numbers (see Fig. 1). In all cases the unsteadiness was comprised basically of multiple vortices in the upper portion of the gap as illustrated in Fig. 2. Increasing the eccentricity led to an increase in the transition Rayleigh number, and this tends to confirm the results of temperature field studies [4] where it was concluded that positive eccentricities tend to stabilize the flow field while negative eccentricities enhance the convective activity.

Cylinder-Sphere Results

Air, water, 20 fluid, and 350 fluid were all tested for diameter ratios of 1.29 and 2.17 for Rayleigh numbers ranging from 2.0×10^4 to 7.0×10^8. Aspect ratios, α, (ratio of difference between cylinder height and inner sphere diameter to difference between outer sphere and inner sphere diameters) ranging from 0 to 0.8 were utilized.

The crescent eddy pattern was the basic steady pattern observed for the 350 fluid. This pattern was observed at low Rayleigh numbers for aspect ratios of 0.380 and 0.759 for D = 2.17. With α = 0.380, this pattern persisted until a Rayleigh number of about 1.3×10^6 was attained, at which point secondary vortices were formed immediately adjacent to the chimney. When the Rayleigh number exceeded 2.6×10^6, these secondary vortices became very unsteady and were periodically dissipated. For α = 0.759, the flow became unsteady at a smaller Rayleigh number, 1.0×10^6, due to the fact that the high speed flow layer adjacent to the inner body separated from the surface near the intersection of the cylindrical section and the hemispherical end. This resulted in numerous small eddies which were formed and dissipated in a rather random fashion in the upper portion of the gap. D = 1.29 and α = 0.8 yielded a small spacing between the cylinder and the sphere in the

[1] Assoc. Professor, Mississippi State University, Miss. Mem. ASME.
[2] Mechanical Engineer, Eastman Kodak, Rochester, N. Y.
[3] Professor, Montana State University, Mem. ASME.
[4] Graduate Research Assistant, University of California, Berkeley, Calif.

[5] Numbers in brackets designate References at end of technical brief.

Contributed by the Heat Transfer Division of THE AMERICAN SOCIETY OF MECHANICAL ENGINEERS. Manuscript received by the Heat Transfer Division August 12, 1974.

puting additional terms in the series and examining their convergence behavior. Accordingly, a comparison study was made for both the cylinder and the sphere. Table 2 summarizes the local heat transfer results around the cylinder. The reader may recall that the first term of the series represents the local similarity solution. Data fenced in rectangular boundaries are evaluated from the convergent part of the series, i.e., from the first two terms only. An alternative is to use Euler's method for ascertaining the sum. However, in view of the small number of terms available, it is uncertain that a definite improvement would result. Included in the table are data computed from the Blasius type series due to Chiang and Kaye [4] and from the Görtler type series due to Saville and Churchill [5], both based on two terms. For $0 \leq \vartheta \leq 90$ deg, all discrepancies are small. When ϑ reaches 140 deg and beyond, the series associated with $(\tilde{\xi},\tilde{\eta})$ coordinates entails unacceptable error while the series associated with (ξ,η) remains useful. These results and others on the details of velocity and temperature profiles which we obtained in this study attest to the relative superiority of the latter series and its associated local similarity solution. They also imply that the configuration function Λ provides a better characterization of local similarity for the category of free convection flows considered in [1].

References

1 Lin, F. N., and Chao, B. T., "Laminar Free Convection Over Two-Dimensional and Axisymmetric Bodies of Arbitrary Contour," JOURNAL OF HEAT TRANSFER, TRANS. ASME, Series C, Vol. 96, 1974, pp. 435–442.

2 Schmidt, E., and Beckmann, W., "Das Temperatur- und Geschwindigheitsfeld von einer Wärme abgebenden Senkrechten Platte bei Natürlicher Konvection," *Technische Mechanik und Thermodynamik*, Oct. 1930, pp. 341–349, Nov. 1930, pp. 391–406.

3 Ostrach, S., "An Analysis of Laminar Free-Convection Flow and Heat Transfer About a Flat Plate Parallel to the Direction of the Generating Body Force," NACA Report No. 1111, 1953.

4 Chiang, T., and Kaye, J., "On Laminar Free Convection From a Horizontal Cylinder," *Proceedings of the Fourth National Congress of Applied Mechanics*, 1962, pp. 1213–1219.

5 Saville, D. A., and Churchill, S. W., "Laminar Free Convection in Boundary Layers Near Horizontal Cylinders and Vertical Axisymmetric Bodies," *Journal of Fluid Mechanics*, Vol. 29, 1967, pp. 391–399.

Free Convection Flow Patterns Between a Body and Its Spherical Enclosure

R. E. Powe,[1] R. C. Baughman,[2] J. A. Scanlan,[3] and J. T. Teng[4]

Introduction

The purpose of this note is to present flow visualization results for natural convection in somewhat more complicated geometries than have been studied in the past. These geometries include heated vertically eccentric spheres and concentric vertical cylinders with hemispherical end caps, all located within a cooled spherical enclosure. Air (Pr $\simeq$ 0.7), water (Pr $\simeq$ 3–10), 20 cs silicone oil (Pr $\simeq$ 150–300), and 350 cs silicone oil (Pr $\simeq$ 2000–5000) were used as the working fluid. With air as the test fluid, cigar smoke was used to make the flow visible, and a detergent technique [1][5] was used to provide tracer particles in water. For the oils, tracer particles were obtained by spraying fluorescent paint over a free surface of the oil. This paint would separate into small particles which would diffuse throughout the fluid and remain in suspension indefinitely.

Eccentric Sphere Results

Air and 350 fluid were tested for diameter ratios, D, of 1.40 and 2.17 for Rayleigh numbers ranging from 6.4×10^3 to 3.2×10^6. Eccentricity ratios (ratio of eccentricity to difference between radii of outer and inner spheres, e/L) of from -0.75 to $+0.75$ were utilized. The previously observed steady crescent eddy pattern [2, 3] was the basic flow obtained for all diameter ratios and all eccentricities at low Rayleigh numbers with air as the working fluid. For D = 2.17, a second steady pattern, the kidney shaped eddy pattern, occurred for moderate Rayleigh numbers for all except the largest positive and negative eccentricities when the inner and outer spheres are in close proximity. When the Rayleigh number exceeded some transition value, shown in Fig. 1, the flow was observed to become unsteady.

For D = 1.40, the unsteady flow was of the three-dimensional spiral type [2] for all eccentricities. No effect on the transition Rayleigh number was noted for negative eccentricities, while positive eccentricities resulted in slightly increased values, in agreement with temperature field results [4]. In contrast, the unsteady flow pattern observed for D = 2.17 was distinctly dependent on eccentricity. The spiral flow existed only for the largest positive eccentricity, and for all other cases the unsteadiness was limited to the central low speed flow region resulting in a constant, and much larger, transition Rayleigh number. This is in accordance with concentric cylinder results [3] where it was found that the transition Rayleigh number for the onset of the spiral flow pattern is much lower than for other unsteady patterns.

With the 350 fluid the crescent eddy pattern was also observed at low Rayleigh numbers, and an unsteady pattern was observed at high Rayleigh numbers (see Fig. 1). In all cases the unsteadiness was comprised basically of multiple vortices in the upper portion of the gap as illustrated in Fig. 2. Increasing the eccentricity led to an increase in the transition Rayleigh number, and this tends to confirm the results of temperature field studies [4] where it was concluded that positive eccentricities tend to stabilize the flow field while negative eccentricities enhance the convective activity.

Cylinder-Sphere Results

Air, water, 20 fluid, and 350 fluid were all tested for diameter ratios of 1.29 and 2.17 for Rayleigh numbers ranging from 2.0×10^4 to 7.0×10^8. Aspect ratios, α, (ratio of difference between cylinder height and inner sphere diameter to difference between outer sphere and inner sphere diameters) ranging from 0 to 0.8 were utilized.

The crescent eddy pattern was the basic steady pattern observed for the 350 fluid. This pattern was observed at low Rayleigh numbers for aspect ratios of 0.380 and 0.759 for D = 2.17. With α = 0.380, this pattern persisted until a Rayleigh number of about 1.3×10^6 was attained, at which point secondary vortices were formed immediately adjacent to the chimney. When the Rayleigh number exceeded 2.6×10^6, these secondary vortices became very unsteady and were periodically dissipated. For α = 0.759, the flow became unsteady at a smaller Rayleigh number, 1.0×10^6, due to the fact that the high speed flow layer adjacent to the inner body separated from the surface near the intersection of the cylindrical section and the hemispherical end. This resulted in numerous small eddies which were formed and dissipated in a rather random fashion in the upper portion of the gap. D = 1.29 and α = 0.8 yielded a small spacing between the cylinder and the sphere in the

[1] Assoc. Professor, Mississippi State University, Miss. Mem. ASME.
[2] Mechanical Engineer, Eastman Kodak, Rochester, N. Y.
[3] Professor, Montana State University, Mem. ASME.
[4] Graduate Research Assistant, University of California, Berkeley, Calif.

[5] Numbers in brackets designate References at end of technical brief.

Contributed by the Heat Transfer Division of THE AMERICAN SOCIETY OF MECHANICAL ENGINEERS. Manuscript received by the Heat Transfer Division August 12, 1974.

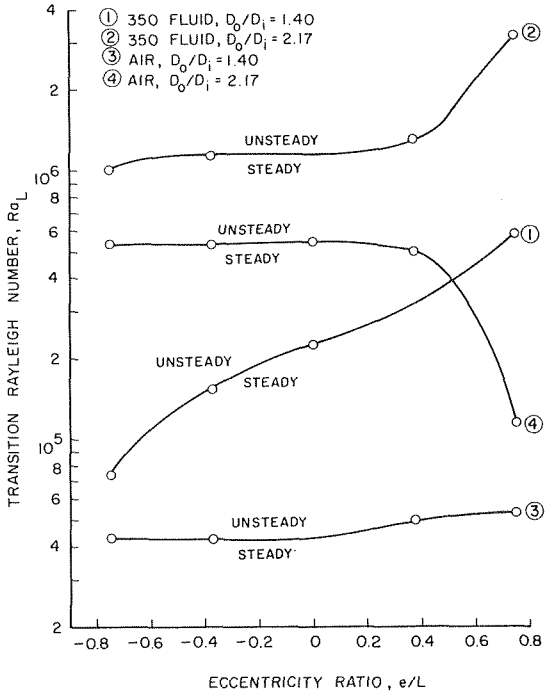

Fig. 1 Effect of eccentricity on transition Rayleigh number

Fig. 2 Multiple vortex flow pattern for 350 fluid, $D = 1.40$, $e/L = -0.375$

Fig. 3 Flow pattern for 20 fluid, $D = 1.29$, $\alpha = 0.8$, $Ra_L = 1.5 \times 10^7$, Pr = 140

upper region of the flow field. As a result, for all Rayleigh numbers above the minimum observed value of 2.6×10^4, separation occurred near the top of the inner body, and the flow did not penetrate the upper gap region.

For the 20 fluid a crescent eddy pattern was again observed for the larger diameter ratio for Rayleigh numbers below about 2.6×10^7. For larger values, secondary vortices were formed, and these vortices became increasingly unsteady as the Rayleigh number was increased. For $D = 1.29$ a completely different flow pattern was observed for all Rayleigh numbers considered (7.3×10^5 to 1.5×10^7). This pattern, shown in Fig. 3, consisted of multiple vortices throughout the entire flow field. As the Rayleigh number was increased these vortices generally tended to become smaller in size and larger in number. For Rayleigh numbers below about 1.3×10^6 the main flow extended completely into the upper portion of the gap, but for larger Rayleigh numbers flow separation occurred leaving the typical three-dimensional vortices in the upper region of the flow field. Although this pattern is very unusual, a certain degree of similarity with results for natural convection in a vertical slot [5] is noted.

Using water as the test fluid, the typical steady flow pattern previously reported [2] was observed for aspect ratios of 0.380 and 0.759 at low Rayleigh numbers for $D = 2.17$. For $\alpha = 0.380$ the unsteady pattern was characterized by the periodic disappearance of the upper secondary cell in the flow field. A periodic falling vortices pattern, reflecting the smaller gap width near the upper vertical axis, was observed as the unsteady pattern for $\alpha = 0.759$. For $D = 1.29$ the high speed flow layer separated from the inner body leaving the three-dimensional vortices in the upper gap region throughout the range of observed Rayleigh numbers.

For air as the gap fluid, the crescent eddy pattern occurred at low Rayleigh numbers for diameter ratios of 2.17 and 1.29, and the kidney shaped eddy pattern also occurred for moderate Rayleigh numbers for $D = 2.17$. For this diameter ratio an unsteady pattern consisting of irregular expansion and contraction of the interior flow region was observed for Rayleigh numbers above 4.6×10^5. For D = 1.29, the unsteady pattern consisted of numerous small vortices in the upper portion of the gap. This pattern occurred for Rayleigh numbers in excess of 3.8×10^4.

It should be noted that the foregoing flow visualization results are in excellent agreement with available temperature field results for natural convection from a vertical cylinder to its spherical enclosure [6]. In that paper, the temperature profile results for the upper gap region were explained by hypothesizing that, in most instances, the high speed flow layer near the inner body does not extend completely into the upper portion of the gap but separates from the inner surface near the junction of the cylinder and its hemispherical end. From the current results this is observed to be the case. Also, for small diameter ratios the existence of a multicellular flow pattern was postulated to explain the temperature field, and this was also confirmed by the current results.

References

1 Powe, R. E., Yin, S. H., Scanlan, J. A., and Bishop, E. H., "A Technique for Visualization of the Very Slow Motion of Water in Enclosed Spaces," JOURNAL OF HEAT TRANSFER, TRANS. ASME, Series C, Vol. 95, No. 3, 1973.

2 Yin, S. H., Powe, R. E., Scanlan, J. A., and Bishop, E. H., "Natural Convection Flow Patterns in Spherical Annuli," *International Journal of Heat and Mass Transfer*, Vol. 16, 1973, pp. 1785–1795.

3 Powe, R. E., Carley, C. T., and Bishop, E. H., "Free Convective Flow Patterns in Cylindrical Annuli," JOURNAL OF HEAT TRANSFER, TRANS. ASME, Series C, Vol. 91, No. 3, 1969, pp. 310–314.

4 Weber, N., Powe, R. E., Bishop, E. H., and Scanlan, J. A., "Heat Transfer by Natural Convection Between Vertically Eccentric Spheres," JOURNAL OF HEAT TRANSFER, TRANS. ASME, Series C, Vol. 95, No. 1, 1973, pp. 47–52.

5 Elder, J. W., "Laminar Free Convection in a Vertical Slot," *Journal of Fluid Mechanics*, Vol. 23, 1, 1965, pp. 77–98.

6 McCoy, C. T., Powe, R. E., Bishop, E. H., Weber, N., and Scanlan, J. A., "Free Convection Between a Vertical Cylinder and a Spherical Enclosure," *Proceedings of the 5th International Heat Transfer Conference*, Tokyo, 1974.

Effect of Uniform Rotation on Streamlines in Benard Convection Cells Induced by Surface Tension and Buoyancy

C. V. Gopalakrishnan Nair[1]

The work of Nield [1][2] is extended to include the effect of uniform rotation about a vertical axis. As the rate of rotation increases the velocity perturbation vector becomes more and more symmetrical with the midlayer for buoyancy driven convection, and asymmetrical for surface tension driven convection. The result which shows that the rotation weakens the coupling of the buoyancy and surface tension forces is confirmed.

Introduction

The coupling of buoyancy and surface tension forces in Benard convection cells formed in a horizontal layer of fluid heated from below when it is uniformly rotated, has been discussed by Namikawa, Takashima, and Matsushita [2]. They found that the degree of coupling between the two agencies depends on the magnitude of the Taylor number T and the Biot number L. In other words, as T becomes large the coupling becomes less tight and this tendency is more pronounced as the Biot number becomes larger. The streamline pattern in the vertical plane of symmetry within a cell has not been discussed. Nield [1] has considered this problem when the rotational effect is absent. In the present brief the problem is discussed for the case when the effect of the rotation is included. The analysis of the problem is done by the method described in [1].

Analysis

The eigen function $W(z)$, giving the z dependence of the vertical component of the perturbation velocity is given by (cf. p. 1343. equation (4.15) in [2])

$$W(z) = \sum_{n=1}^{\infty}[A_n + \frac{2}{n^3\pi^3}(-1)^n D^2W(1) - \frac{2}{n^3\pi^3}D^2W(0)]\sin n\pi z \quad (1)$$

where

$$n\pi A_n = [-2E_n + \frac{2}{n^2\pi^2}]D^2W(0) + (-1)^n[2E_n - \frac{2}{n^2\pi^2}]D^2W \quad (1)'$$

$$-2a^2\mathrm{R}(-1)^n F_n \mathrm{H}(1) + 2\mathrm{T}^{1/2}F_n DZ(0) \quad (2)$$

$D^2W(0)$, $D^2W(1)$, H (1), $D\,Z(0)$ are given by the homogeneous equations:

$$\begin{bmatrix} 0 & 1 & a^2\mathrm{M} & 0 \\ -\Sigma E_n & \Sigma(-1)^n E_n & -a^2\mathrm{R}\Sigma(-1)^n F_n & \mathrm{T}^{1/2}\Sigma F_n \\ -\Sigma(-1)^n F_n & \Sigma F_n & -a^2\mathrm{R}\Sigma G_n + L/2 + a^2 H & \mathrm{T}^{1/2}\Sigma(-1)^n G_n \\ -\Sigma F_n & \Sigma(-1)^n F_n & -a^2\mathrm{R}\Sigma(-1)^n G_n & \mathrm{T}^{1/2}\Sigma G_n - \frac{H}{\mathrm{T}^{1/2}} \end{bmatrix} \begin{bmatrix} D^2W(0) \\ D^2W(1) \\ H(1) \\ DZ(0) \end{bmatrix} = 0 \quad (3)$$

where

$$E_n = \frac{n^2\pi^2(n^2\pi^2 + a^2)}{(n^2\pi^2 + a^2)^3 + n^2\pi^2\mathrm{T} - a^2\mathrm{R}}, \quad F_n = \frac{n^2\pi^2}{(n^2\pi^2 + a^2)^3 + n^2\pi^2\mathrm{T} - a^2\mathrm{R}}$$

$$G_n = \frac{n^2\pi^2}{(n^2\pi^2 + a^2)[(n^2\pi^2 + a^2)^3 + n^2\pi^2\mathrm{T} - a^2\mathrm{R}]}, \quad H = \frac{1}{2a}\,\mathrm{Cotha}$$

R = the Rayleigh number, T = the Taylor number, M = the Marangoni number, L = the Biot number, a = the wavenumber. The temperature perturbation H (z) may be obtained in a similar fashion.

Results and Discussion

The vertical velocity perturbation eigen function $W(z)$ has been calculated for several cases. In Figs. 1*(a)* and 1*(b)* the values of W, normalised by its maximum value are plotted for different values of T for two chosen cases, when the convection is induced by buoyancy alone and when the convection is induced by surface tension forces alone. It is found that all the curves are similar in shape except for a variable skewness which signifies the difference in the values of z at which W reaches a maximum value. As it was pointed out in [1] after drawing the streamline patterns for one particular physical case we can get a qualitative picture of any other case from the knowledge of the horizontal wavenumber a and the eigen function $W(z)$. So the main factor of interest is the value of z, say z_w at which $W(z)$ has the maximum value.

In Tables 1, 2, and 3 z_w values are given for different cases. In the buoyancy driven convection, as the rate of rotation is increased the eigenfunction $W(z)$ becomes more symmetrical about the middle of the layer, $z = \frac{1}{2}$. Nield [3] has observed a similar behavior of

[1] Department of Mathematics, Indian Institute of Technology, Bombay, India.

[2] Numbers in brackets designate References at end of technical brief.

Contributed by the Heat Transfer Division of THE AMERICAN SOCIETY OF MECHANICAL ENGINEERS. Manuscript received by the Heat Transfer Division August 23, 1974.

References

1 Powe, R. E., Yin, S. H., Scanlan, J. A., and Bishop, E. H., "A Technique for Visualization of the Very Slow Motion of Water in Enclosed Spaces," JOURNAL OF HEAT TRANSFER, TRANS. ASME, Series C, Vol. 95, No. 3, 1973.

2 Yin, S. H., Powe, R. E., Scanlan, J. A., and Bishop, E. H., "Natural Convection Flow Patterns in Spherical Annuli," *International Journal of Heat and Mass Transfer*, Vol. 16, 1973, pp. 1785–1795.

3 Powe, R. E., Carley, C. T., and Bishop, E. H., "Free Convective Flow Patterns in Cylindrical Annuli," JOURNAL OF HEAT TRANSFER, TRANS. ASME, Series C, Vol. 91, No. 3, 1969, pp. 310–314.

4 Weber, N., Powe, R. E., Bishop, E. H., and Scanlan, J. A., "Heat Transfer by Natural Convection Between Vertically Eccentric Spheres," JOURNAL OF HEAT TRANSFER, TRANS. ASME, Series C, Vol. 95, No. 1, 1973, pp. 47–52.

5 Elder, J. W., "Laminar Free Convection in a Vertical Slot," *Journal of Fluid Mechanics*, Vol. 23, 1, 1965, pp. 77–98.

6 McCoy, C. T., Powe, R. E., Bishop, E. H., Weber, N., and Scanlan, J. A., "Free Convection Between a Vertical Cylinder and a Spherical Enclosure," *Proceedings of the 5th International Heat Transfer Conference*, Tokyo, 1974.

Effect of Uniform Rotation on Streamlines in Benard Convection Cells Induced by Surface Tension and Buoyancy

C. V. Gopalakrishnan Nair[1]

The work of Nield [1][2] is extended to include the effect of uniform rotation about a vertical axis. As the rate of rotation increases the velocity perturbation vector becomes more and more symmetrical with the midlayer for buoyancy driven convection, and asymmetrical for surface tension driven convection. The result which shows that the rotation weakens the coupling of the buoyancy and surface tension forces is confirmed.

Introduction

The coupling of buoyancy and surface tension forces in Benard convection cells formed in a horizontal layer of fluid heated from below when it is uniformly rotated, has been discussed by Namikawa, Takashima, and Matsushita [2]. They found that the degree of coupling between the two agencies depends on the magnitude of the Taylor number T and the Biot number L. In other words, as T becomes large the coupling becomes less tight and this tendency is more pronounced as the Biot number becomes larger. The streamline pattern in the vertical plane of symmetry within a cell has not been discussed. Nield [1] has considered this problem when the rotational effect is absent. In the present brief the problem is discussed for the case when the effect of the rotation is included. The analysis of the problem is done by the method described in [1].

Analysis

The eigen function $W(z)$, giving the z dependence of the vertical component of the perturbation velocity is given by (cf. p. 1343. equation (4.15) in [2])

$$W(z) = \sum_{n=1}^{\infty}[A_n + \frac{2}{n^3\pi^3}(-1)^n D^2W(1) - \frac{2}{n^3\pi^3}D^2W(0)]\sin n\pi z \quad (1)$$

where

$$n\pi A_n = [-2E_n + \frac{2}{n^2\pi^2}]D^2W(0) + (-1)^n[2E_n - \frac{2}{n^2\pi^2}]D^2W \quad (1)'$$

$$-2a^2\mathrm{R}(-1)^n F_n \mathrm{H}(1) + 2\mathrm{T}^{1/2}F_n DZ(0) \quad (2)$$

$D^2W(0)$, $D^2W(1)$, H (1), $D\ Z(0)$ are given by the homogeneous equations:

$$\begin{bmatrix} 0 & 1 & a^2\mathrm{M} & 0 \\ -\Sigma E_n & \Sigma(-1)^n E_n & -a^2\mathrm{R}\Sigma(-1)^n F_n & \mathrm{T}^{1/2}\Sigma F_n \\ -\Sigma(-1)^n F_n & \Sigma F_n & -a^2\mathrm{R}\Sigma G_n + L/2 + a^2 H & \mathrm{T}^{1/2}\Sigma(-1)^n G_n \\ -\Sigma F_n & \Sigma(-1)^n F_n & -a^2\mathrm{R}\Sigma(-1)^n G_n & \mathrm{T}^{1/2}\Sigma G_n - \dfrac{H}{\mathrm{T}^{1/2}} \end{bmatrix} \begin{bmatrix} D^2W(0) \\ D^2W(1) \\ H(1) \\ DZ(0) \end{bmatrix} = 0 \quad (3)$$

where

$$E_n = \frac{n^2\pi^2(n^2\pi^2 + a^2)}{(n^2\pi^2 + a^2)^3 + n^2\pi^2\mathrm{T} - a^2\mathrm{R}}, \quad F_n = \frac{n^2\pi^2}{(n^2\pi^2 + a^2)^3 + n^2\pi^2\mathrm{T} - a^2\mathrm{R}}$$

$$G_n = \frac{n^2\pi^2}{(n^2\pi^2 + a^2)[(n^2\pi^2 + a^2)^3 + n^2\pi^2\mathrm{T} - a^2\mathrm{R}]}, \quad H = \frac{1}{2a}\,\mathrm{Cotha}$$

R = the Rayleigh number, T = the Taylor number, M = the Marangoni number, L = the Biot number, a = the wavenumber. The temperature perturbation H (z) may be obtained in a similar fashion.

Results and Discussion

The vertical velocity perturbation eigen function $W(z)$ has been calculated for several cases. In Figs. 1*(a)* and 1*(b)* the values of W, normalised by its maximum value are plotted for different values of T for two chosen cases, when the convection is induced by buoyancy alone and when the convection is induced by surface tension forces alone. It is found that all the curves are similar in shape except for a variable skewness which signifies the difference in the values of z at which W reaches a maximum value. As it was pointed out in [1] after drawing the streamline patterns for one particular physical case we can get a qualitative picture of any other case from the knowledge of the horizontal wavenumber a and the eigen function $W(z)$. So the main factor of interest is the value of z, say z_w at which $W(z)$ has the maximum value.

In Tables 1, 2, and 3 z_w values are given for different cases. In the buoyancy driven convection, as the rate of rotation is increased the eigenfunction $W(z)$ becomes more symmetrical about the middle of the layer, $z = \frac{1}{2}$. Nield [3] has observed a similar behavior of

[1] Department of Mathematics, Indian Institute of Technology, Bombay, India.

[2] Numbers in brackets designate References at end of technical brief.

Contributed by the Heat Transfer Division of THE AMERICAN SOCIETY OF MECHANICAL ENGINEERS. Manuscript received by the Heat Transfer Division August 23, 1974.

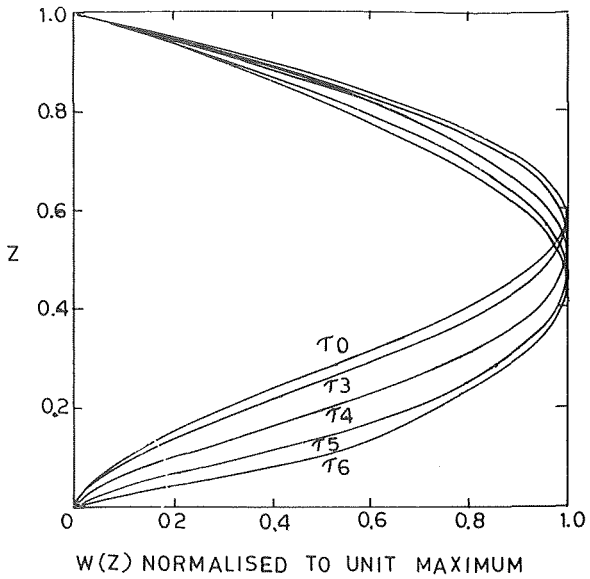

Fig. 1*(a)* **The dependence of the vertical component of the velocity on the height above the lower boundary surface is expressed for purely buoyancy driven convection, upper boundary insulated—T0, T3, T4, T5, T6 denote curves corresponding to T = 1, 10^3, 10^4, 10^5, 10^6, respectively**

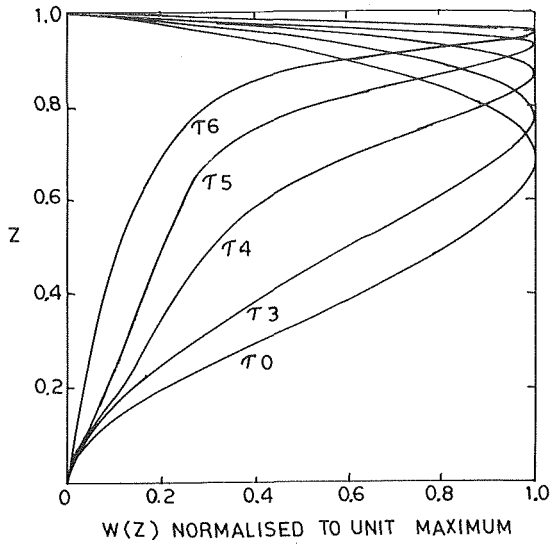

Fig. 1*(b)* **The same as Fig. (1*a*) but for purely surface tension driven convection**

the eigenfunction $W(z)$ with increase in Q (the nondimensional number which relates to the magnetic effect). However, the value of z_w was found to be always greater than ½ in his case. In the present case, $W(z)$ becomes maximum at $z = ½$ for a certain value of T; as T is increased further, z_w reaches a steady value, slightly less than ½ (cf. Table 1). It is expected that in the magneto-hydrodynamic case, the same tendency should be observed for Q greater than 2500, which is the maximum value given for Q in [3]. However, for surface tension driven convection, $W(z)$ become more asymmetrical about the middle of the layer as T is increased. Hence the streamlines are buckled nearer to the upper surface for larger values of T provided the surface is free and the surface tension effect is considered.

Thus our numerical calculations are in conformity with the experimental observations of Vidal and Acrivos [4]; "Convective sublayer becomes smaller as the speed of rotation was increased." Also from Tables 1 and 2 it can be noted that when R = 0, and for all values of $T > 10^3$, $1 - z_2 \simeq 1.3\ T^{-1/4}$. This result is found to be valid for all finite L. Hence in the absence of buoyancy forces, the thickness of the surface boundary layer is proportional to $T^{-1/4}$ when T is large. This result is in qualitative agreement with the results of Vidal and Acrivos [4]. They have shown that the temperature and velocity fluctuations are confined to an Ekman layer, whose thickness is proportional to $T^{-1/4}$, as T approaches infinity.

As mentioned in [1], for R = R_c (R_c – critical Rayleigh number when M = 0), z_w becomes greater as the value of L increases, and for R = 0, z_w is smaller for larger values of L. The same tendency is observed for all considered values of T (cf. Table 2), but for very large values of T, there is no appreciable change in z_w with a change in L. For $T = 10^7$, z_w remains almost constant as L is increased.

Table 1 The numerical values of z_w for various values of T when the upper boundary is insulated

T =	0	10	10^2	10^3	10^4	10^5	10^6	10^7
z_w for R = R_c	0.585	0.585	0.584	0.569	0.512	0.469	0.458	0.456
z_w for R = 0	0.689	0.691	0.707	0.782	0.873	0.928	0.959	0.977

Table 2 The numerical values of z_w for various values of L, when the rotational effect is included

	R = R_c				R = 0			
	L = 0	L = 1	L = 10	L = 100	L = 0	L = 1	L = 10	L = 100
T = 0	0.585	0.581	0.570	0.565	0.689	0.696	0.712	0.720
10^3	0.569	0.563	0.548	0.541	0.782	0.784	0.792	0.799
10^5	0.469	0.468	0.465	0.462	0.928	0.928	0.929	0.931
10^7	0.456	0.456	0.456	0.456	0.977	0.977	0.977	0.978

Table 3 Values of z_w for various combinations of the critical Rayleigh number and critical Marangeni number

		R = 0 z_w	R = 1/4R_c z_w	R = 1/2R_c z_w	R = 3/4R_c z_w	R = R_c z_w
T = 0	L = 0	0.689	0.664	0.637	0.610	0.585
	L = 100	0.720	0.678	0.642	0.601	0.565
$T = 10^7$	L = 0	0.977	0.977	0.977	0.977	0.456
	L = 100	0.978	0.978	0.977	0.977	0.456

Finally we discuss the coupling between buoyancy and surface tension forces. It is found that as the rate of rotation increases the coupling becomes weaker (cf. [2]). In Table 3, z_w is given for different combinations of the critical Rayleigh number and critical Marangoni number. When T = 0, the value of z_w decreases monotonically as R/R_c increases from 0 to 1. When T is large ($T = 10^7$), z_w remains almost constant for increasing value of R/R_c until R/R_c is approximately one; at the later stage z_w suddenly falls to a very low value. In other words, for large T, the depth of the convective sublayer remains almost the same for increasing Rayleigh number. This phenomenon changes abruptly when $R \simeq R_c$ at which stage the depth of the sublayer increases suddenly. However, the result discussed in [2], that the coupling is weakened with increase in T is confirmed with the present analysis. Also the coupling between surface tension and buoyancy forces decreases monotonically as T increases.

Acknowledgment

The author wishes to thank Prof. P. C. Jain for his help.

References

1 Nield, D. A., "Streamlines in Benard Convection Cells Induced by Surface Tension and Buoyancy," *Z.A.M.P.*, Vol. 17, 1966, pp. 226–232.

2 Namikawa, T., Takashima, M., and Matsushita, S., "The Effect of Rotation on Convective Instability Induced by Surface Tension and Buoyancy," *Journal of the Physical Society of Japan*, Vol. 28, 1970, pp. 1340–1349.

3 Nield, D. A., "Effect of a Magnetic field on Streamlines in Benard Convection Cells Induced by Surface Tension and Buoyancy," *Z.A.M.P.*, Vol. 17, 1966, pp. 340–342.

4 Vidal, A., and Acrivos, Andreas, "The Influence of Coriolis Force on Surface Tension Driven Convection," *Journal of Mech Vol. 26, 1966, pp. 807–818.*

Perturbation Solution for Convecting Fin With Variable Thermal Conductivity

A. Aziz[1] and S. M. Enamul Huq[2]

Nomenclature

h = heat transfer coefficient
k = thermal conductivity
L = fin length
N = nondimensional fin parameter = $[2hL^2/k_a w]^{1/2}$
q = heat transfer rate per unit depth
T = temperature
w = fin thicknes
X = nondimensional coordinate = x/L
x = axial distance measured from fin tip
β = slope of the thermal conductivity-temperature curve divided by the intercept k_a
ϵ = thermal conductivity parameter = $(k_b - k_o)/k_a$
η = fin efficiency
θ = nondimensional temperature = $(T - T_a)/(T_b - T_a)$

Subscripts

a = ambient
b = fin base

Introduction

The effect of variable thermal properties on the performance of fins (convecting, radiating, or both) has been studied by several workers and shown to be quite significant particularly when large temperature differences exist. Stockman and Kramer [1][3] discuss the effects of linearly varying thermal conductivity and surface emissivity on heat transfer in purely radiating fins. Hung and Appl [2] analyze fins with simultaneous surface convection and radiation and present the temperature distributions for variable thermal properties and internal heat generation. More recently, Kosarev and Nevrovskii [3] have considered purely convecting fin with temperature dependent thermal conductivity and given the method of predicting the tip temperature and heat transfer rate. Because of the nonlinear nature of these problems, most approaches inevitably involve numerical procedures.

This note, however, presents a regular perturbation solution for a straight convecting fin with temperature dependent thermal conductivity and demonstrates that for usual fin materials and operating variables, the perturbation solution provides a rapid and accurate means of predicting the performance of the fin. To check the accuracy of the perturbation solution, the problem has also been solved numerically. The closed form of the perturbation solution has enabled the dependence of optimum fin parameter on thermal conductivity-temperature variation to be established.

Analysis

The analysis considers a straight fin of length L and thickness w exposed on both faces to a convective environment at temperature T_a and with heat transfer coefficient h. A sketch of the fin geometry is shown as insert in Fig. 2, the axial distance x being measured from fin tip. The usual boundary conditions of constant base temperature T_b and adiabatic tip are assumed. The thermal conductivity of the fin material, k, is assumed to vary linearly with temperature according to

$$k = k_a[1 + \beta(T - T_a)] \tag{1}$$

where k_a is the thermal conductivity at temperature T_a and β is the slope of the thermal conductivity-temperature curve divided by the intercept k_a. Assuming one-dimensional conduction, the energy equation with the aforesaid boundary conditions is

$$(1 + \epsilon\theta)\frac{d^2\theta}{dX^2} + \epsilon\left(\frac{d\theta}{dX}\right)^2 - N^2\theta = 0 \tag{2}$$

$$X = 0, \frac{d\theta}{dX} = 0; X = 1, \theta = 1 \tag{3}$$

where

$$\theta = \frac{T - T_a}{T_b - T_a}, X = \frac{x}{L}, N^2 = \frac{2hL^2}{k_a w} \tag{4}$$

$$\epsilon = \frac{k_b - k_a}{k_a} = \beta(T_b - T_a)$$

For $\epsilon \ll 1$, a first order asymptotic expansion for θ in the perturbation parameter ϵ may be assumed which gives

$$\theta = \theta_0 + \epsilon\theta_1 \tag{5}$$

Substituting (5) into (2) and equating the coefficients of zero and unit powers of ϵ to zero, equations for θ_0 and θ_1 with the appropriate boundary conditions are obtained as

[1] Assist. Professor, Faculty of Engineering, University of Riyadh, Riyadh, Saudi Arabia.

[2] Assist. Professor, Faculty of Engineering, University of Riyadh, Riyadh, Saudi Arabia.

Contributed by the Heat Transfer Division of THE AMERICAN SOCIETY OF MECHANICAL ENGINEERS. Manuscript received by the Heat Transfer Division April 29, 1974.

[3] Numbers in brackets designate References at end of technical brief.

Finally we discuss the coupling between buoyancy and surface tension forces. It is found that as the rate of rotation increases the coupling becomes weaker (cf. [2]). In Table 3, z_w is given for different combinations of the critical Rayleigh number and critical Marangoni number. When T = 0, the value of z_w decreases monotonically as R/R_c increases from 0 to 1. When T is large ($T = 10^7$), z_w remains almost constant for increasing value of R/R_c until R/R_c is approximately one; at the later stage z_w suddenly falls to a very low value. In other words, for large T, the depth of the convective sublayer remains almost the same for increasing Rayleigh number. This phenomenon changes abruptly when $R \simeq R_c$ at which stage the depth of the sublayer increases suddenly. However, the result discussed in [2], that the coupling is weakened with increase in T is confirmed with the present analysis. Also the coupling between surface tension and buoyancy forces decreases monotonically as T increases.

Acknowledgment

The author wishes to thank Prof. P. C. Jain for his help.

References

1 Nield, D. A., "Streamlines in Benard Convection Cells Induced by Surface Tension and Buoyancy," *Z.A.M.P.*, Vol. 17, 1966, pp. 226–232.

2 Namikawa, T., Takashima, M., and Matsushita, S., "The Effect of Rotation on Convective Instability Induced by Surface Tension and Buoyancy," *Journal of the Physical Society of Japan*, Vol. 28, 1970, pp. 1340–1349.

3 Nield, D. A., "Effect of a Magnetic field on Streamlines in Benard Convection Cells Induced by Surface Tension and Buoyancy," *Z.A.M.P.*, Vol. 17, 1966, pp. 340–342.

4 Vidal, A., and Acrivos, Andreas, "The Influence of Coriolis Force on Surface Tension Driven Convection," *Journal of Mech Vol. 26, 1966, pp. 807–818.*

Perturbation Solution for Convecting Fin With Variable Thermal Conductivity

A. Aziz[1] and S. M. Enamul Huq[2]

Nomenclature

h = heat transfer coefficient
k = thermal conductivity
L = fin length
N = nondimensional fin parameter = $[2hL^2/k_a w]^{1/2}$
q = heat transfer rate per unit depth
T = temperature
w = fin thicknes
X = nondimensional coordinate = x/L
x = axial distance measured from fin tip
β = slope of the thermal conductivity-temperature curve divided by the intercept k_a
ϵ = thermal conductivity parameter = $(k_b - k_o)/k_a$
η = fin efficiency
θ = nondimensional temperature = $(T - T_a)/(T_b - T_a)$

Subscripts

a = ambient
b = fin base

Introduction

The effect of variable thermal properties on the performance of fins (convecting, radiating, or both) has been studied by several workers and shown to be quite significant particularly when large temperature differences exist. Stockman and Kramer [1][3] discuss the effects of linearly varying thermal conductivity and surface emissivity on heat transfer in purely radiating fins. Hung and Appl [2] analyze fins with simultaneous surface convection and radiation and present the temperature distributions for variable thermal properties and internal heat generation. More recently, Kosarev and Nevrovskii [3] have considered purely convecting fin with temperature dependent thermal conductivity and given the method of predicting the tip temperature and heat transfer rate. Because of the nonlinear nature of these problems, most approaches inevitably involve numerical procedures.

This note, however, presents a regular perturbation solution for a straight convecting fin with temperature dependent thermal conductivity and demonstrates that for usual fin materials and operating variables, the perturbation solution provides a rapid and accurate means of predicting the performance of the fin. To check the accuracy of the perturbation solution, the problem has also been solved numerically. The closed form of the perturbation solution has enabled the dependence of optimum fin parameter on thermal conductivity-temperature variation to be established.

Analysis

The analysis considers a straight fin of length L and thickness w exposed on both faces to a convective environment at temperature T_a and with heat transfer coefficient h. A sketch of the fin geometry is shown as insert in Fig. 2, the axial distance x being measured from fin tip. The usual boundary conditions of constant base temperature T_b and adiabatic tip are assumed. The thermal conductivity of the fin material, k, is assumed to vary linearly with temperature according to

$$k = k_a[1 + \beta(T - T_a)] \tag{1}$$

where k_a is the thermal conductivity at temperature T_a and β is the slope of the thermal conductivity-temperature curve divided by the intercept k_a. Assuming one-dimensional conduction, the energy equation with the aforesaid boundary conditions is

$$(1 + \epsilon\theta)\frac{d^2\theta}{dX^2} + \epsilon\left(\frac{d\theta}{dX}\right)^2 - N^2\theta = 0 \tag{2}$$

$$X = 0, \frac{d\theta}{dX} = 0; X = 1, \theta = 1 \tag{3}$$

where

$$\theta = \frac{T - T_a}{T_b - T_a}, X = \frac{x}{L}, N^2 = \frac{2hL^2}{k_a w} \tag{4}$$

$$\epsilon = \frac{k_b - k_a}{k_a} = \beta(T_b - T_a)$$

For $\epsilon \ll 1$, a first order asymptotic expansion for θ in the perturbation parameter ϵ may be assumed which gives

$$\theta = \theta_0 + \epsilon\theta_1 \tag{5}$$

Substituting (5) into (2) and equating the coefficients of zero and unit powers of ϵ to zero, equations for θ_0 and θ_1 with the appropriate boundary conditions are obtained as

[1] Assist. Professor, Faculty of Engineering, University of Riyadh, Riyadh, Saudi Arabia.

[2] Assist. Professor, Faculty of Engineering, University of Riyadh, Riyadh, Saudi Arabia.

Contributed by the Heat Transfer Division of THE AMERICAN SOCIETY OF MECHANICAL ENGINEERS. Manuscript received by the Heat Transfer Division April 29, 1974.

[3] Numbers in brackets designate References at end of technical brief.

$$\frac{d^2\theta_0}{dX^2} - N^2\theta_0 = 0 \quad (6)$$

$$X = 0, \frac{d\theta_0}{dX} = 0; X = 1, \theta_0 = 1 \quad (7)$$

and

$$\frac{d^2\theta_1}{dX^2} - N^2\theta_1 = -\left(\frac{d\theta_0}{dX}\right)^2 - \theta_0\frac{d^2\theta_0}{dX^2} \quad (8)$$

$$X = 0, \frac{d\theta_1}{dX} = 0; X = 1, \theta_1 = 0 \quad (9)$$

The zero-order problem, equations (6) and (7) corresponds to a fin of constant thermal conductivity and its solution is

$$\theta_0 = sh\ N \cosh\ N\ X \quad (10)$$

The first-order problem, equations (8) and (9) has the solution

$$\theta_1 = \frac{1}{3} sh\ N\ [(1 + \tanh^2 N) \cosh\ N\ X - sh\ N \cosh\ 2\ N\ X] \quad (11)$$

The complete solution is

$$\theta = sh\ N \cosh\ N\ X + \frac{1}{3}\epsilon sh\ N\ [(1 + \tanh^2 N) \cosh\ N\ X - sh\ N \cosh\ 2\ N\ X] \quad (12)$$

The heat transfer rate q per unit depth is readily obtained from (12) as

$$\frac{qL}{k_a w(T_b - T_a)} = N \tanh\ N\ [(1 - \epsilon^2) + \frac{1}{3}\epsilon(1 + \epsilon) \tanh^2 N] \quad (13)$$

The efficiency of the fin η defined as the ratio of actual heat transfer to the ideal heat transfer for a fin of infinite thermal conductivity thus becomes

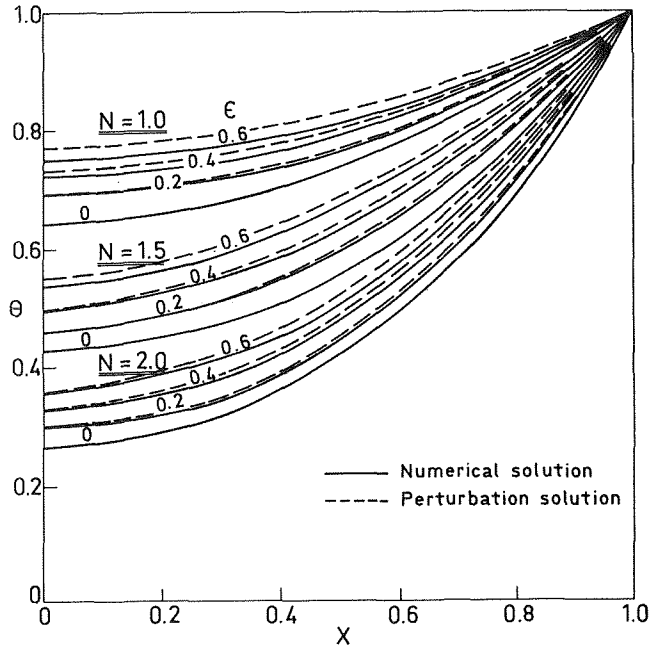

Fig. 1 Temperature distribution in a convecting fin with variable thermal conductivity

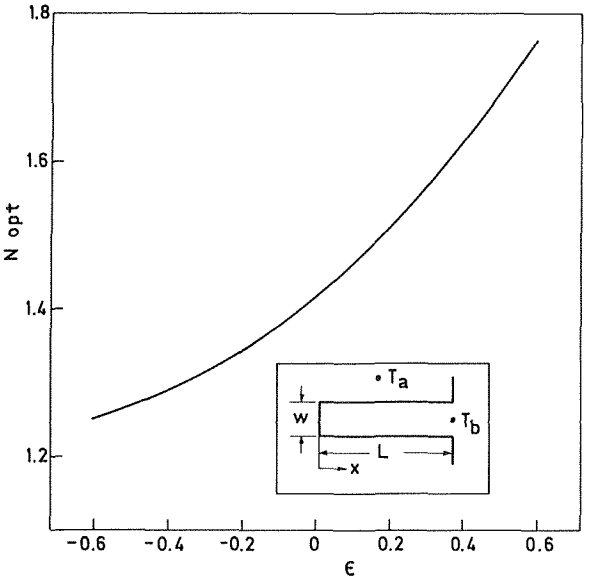

Fig. 2 Relationship between optimum N and ϵ

$$\eta = \frac{\tanh N}{N}[(1 - \epsilon^2) + \frac{1}{3}\epsilon(1 + \epsilon) \tanh^2 N] \quad (14)$$

Equations (2) and (3) were also solved numerically to check the accuracy of the perturbation solution. Fig. 1 compares the perturbation solution with the numerical solution for $\epsilon = 0.2$, 0.4, and 0.6 for three values of N namely, $N = 1.0$, 1.5, and 2.0. The perturbation solution matches almost exactly with the numerical solution for ϵ up to 0.4 for all values of N. The accuracy of the solution, however, decreases as ϵ increases particularly at low values of N where the temperature distribution is relatively more sensitive to thermal conductivity variation. For the sake of clarity, results are shown for positive values of ϵ only but the same accuracy is applicable for negative values of ϵ. Since for the usual fin materials and operating temperatures ϵ lies in the range of -0.5 to $+0.5$, the perturbation solution can predict quite accurately the performance of the fin with variable thermal conductivity.

The optimum fin dimensions are usually based on the criterion of maximum heat transfer per unit volume for a fixed profile area, $w\,L$. From equation (13) the condition $d\,q/d\,w = 0$ gives

$$6N[(1 - \epsilon^2) + \epsilon(1 + \epsilon) \tanh^2 N] = (1 - \epsilon^2) \sinh 2N + \frac{2}{3}\epsilon(1 + \epsilon) \tanh N \sinh^2 N \quad (15)$$

The optimum values of N obtained by solving equation (15) for a range of values of ϵ for which the perturbation solution is valid are shown plotted in Fig. 2. The use of Fig. 2 permits the optimum dimensions of a convecting fin to be established with allowance for thermal conductivity variation.

References

1 Stockman, N. O., and Kramer, J. L., "Effect of Variable Thermal Properties on One-Dimensional Heat Transfer in Radiating Fins," NASA, TN D-1878, Oct. 1963.

2 Hung, H. M., and Appl, F. C., "Heat Transfer of Thin Fins With Temperature Dependent Thermal Properties and Internal Heat Generation," JOURNAL OF HEAT TRANSFER, TRANS. ASME, Series C, Vol 89, May 1967, pp. 155–162.

3 Kosarev, D. A., and Nevrovskii, V. A., "Calculating Heat Transfer Through Finned Surfaces With Variable Coefficient of Thermal Conductivity of the Material," *Thermal Engineering*, No. 2, 1972, pp. 140–141.

Periodic Heat Transfer In Annular Fins

A. Aziz[1]

Introduction

In a recent paper, Yang[2] presented an analysis of heat transfer in a straight rectangular fin with periodic variation of base temperature and discussed the effect of amplitude and frequency of base temperature oscillation on the performance of the fin. This note extends the analysis to an annular fin and provides representative results for temperature distribution, heat flux, and time-average fin efficiency. The results are discussed and compared with those for a rectangular fin.

Analysis

The insert in Fig. 3 shows the geometry of an annular fin of base radius r_b, tip radius r_t, and thickness b, exposed on both sides to convective environment at temperature T_a with heat transfer coefficient h. The fin material has thermal conductivity k and thermal diffusivity α. The tip is assumed to be adiabatic while the base temperature T_b is assumed to vary periodically around the mean temperature T_m with frequency ω. Assuming one-dimensional conduction and constant thermal properties the energy equation and the boundary conditions can be written in nondimensional form as

$$\frac{\partial^2\theta}{\partial R^2} + \frac{1}{R}\frac{\partial\theta}{\partial R} - N^2\theta = \frac{\partial\theta}{\partial\tau} \tag{1}$$

$$R = R_t,\ \frac{\partial\theta}{\partial R} = 0 \tag{2}$$

$$R = R_b,\ \theta = 1 + A\cos B\tau \tag{3}$$

where $\theta = (T - T_a)/(T_m - T_a)$; $R = r/(r_t - r_b)$; $R_b = r_b/(r_t - r_b)$; $R_t = r_t/(r_t - r_b)$; $\tau = \alpha t/(r_t - r_b)^2$; $N^2 = 2h(r_t - r_b)^2/bk$; $B = \omega(r_t - r_b)^2/\alpha$; $A = (T_{bm} - T_m)/(T_m - T_a)$; t denotes time and T_{bm} denotes the maximum temperature of the fin base.

The temperature θ is assumed to be the sum of steady component $\theta_1(R)$ and an oscillatory component $\theta_2(R, \tau)$, the latter being of the form

$$\theta_2 = \mathrm{Re}[Ae^{iB\tau}\phi(R)] \tag{4}$$

Equations (1)–(3) thus become equivalent to the following system of equations

$$\frac{d^2\theta_1}{dR^2} + \frac{1}{R}\frac{d\theta_1}{dR} - N^2\theta_1 = 0 \tag{5}$$

$$\frac{d^2\phi}{dR^2} + \frac{1}{R}\frac{d\phi}{dR} - (N^2 + iB)\phi = 0 \tag{6}$$

$$R = R_t,\ \frac{d\theta_1}{dR} = \frac{d\phi}{dR} = 0 \tag{7}$$

$$R = R_b,\ \theta_1 = \phi = 1 \tag{8}$$

The solutions for θ_1 and ϕ are readily obtained as

$$\theta_1 = \frac{I_0(NR)K_1(NR_t) + K_0(NR)I_1(NR_t)}{I_0(NR_b)K_1(NR_t) + K_0(NR_b)I_1(NR_t)} \tag{9}$$

$$\phi = \frac{I_0(uR + ivR)K_1(uR_t + ivR_t) + K_0(uR + ivR)I_1(uR_t + ivR_t)}{I_0(uR_b + ivR_b)K_1(uR_t + ivR_t) + K_0(uR_b + ivR_b)I_1(uR_t + ivR_t)} \tag{10}$$

where I_0, I_1, and K_0, K_1 are the modified Bessel functions of the first and second kind, respectively, and

$$u = \left[\frac{N^2 + (N^4 + B^2)^{1/2}}{2}\right]^{1/2},\quad v = \left[\frac{-N^2 + (N^4 + B^2)^{1/2}}{2}\right]^{1/2} \tag{11}$$

Equations (4), (9), and (10) were programmed to give direct numerical results for the temperature distribution.

The rate of heat transfer from the fin surface can be evaluated in terms of temperature gradient at the base. In nondimensional form it becomes

$$\frac{q}{2\pi R_b bk(T_m - T_a)} = N\frac{I_1(NR_t)K_1(NR_b) - I_1(NR_b)K_1(NR_t)}{I_0(NR_b)K_1(NR_t) + K_0(NR_b)I_1(NR_t)} + \frac{\partial\theta_2}{\partial R}\Big|_{R = R_b} \tag{12}$$

The efficiency of the fin defined as the ratio of actual heat transfer to ideal heat transfer for a fin of infinite thermal conductivity can be obtained as

$$\eta = \frac{2R_b}{N_1(1 + A\cos B\tau)}\left[N\frac{I_1(NR_t)K_1(NR_b) - I_1(NR_b)K_1(NR_t)}{I_0(NR_b)K_1(NR_t) + I_1(NR_t)K_0(NR_b)} + \frac{\partial\theta_2}{\partial R}\Big|_{R = R_b}\right] \tag{13}$$

where $N_1 = 2h(r_t^2 - r_b^2)/bk$. Finally, the time average efficiency over a cycle may be obtained from

$$\bar{\eta} = \frac{1}{2\pi}\int_0^{2\pi}\eta\, d(B\tau) \tag{14}$$

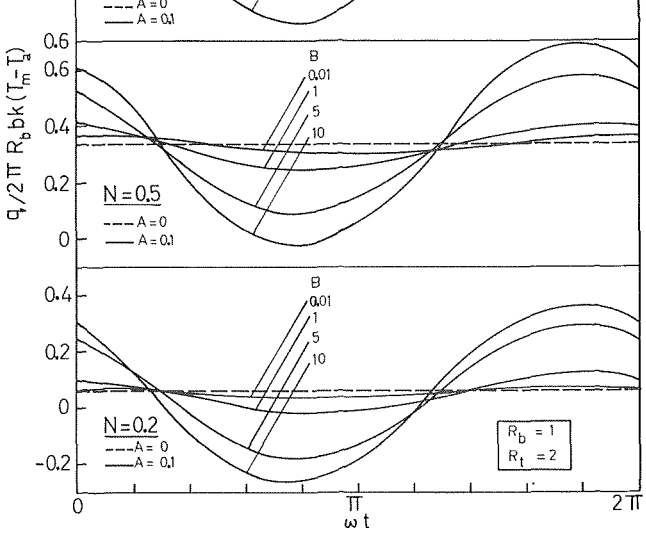

Fig. 1 Effect of parameters *N* and *B* on temperature-time variation in an annular fin

[1] Assist. Professor, Faculty of Engineering, University of Riyadh, Riyadh, Saudi Arabia.

Contributed by the Heat Transfer Division of THE AMERICAN SOCIETY OF MECHANICAL ENGINEERS. Manuscript received by the Heat Transfer Division February 8, 1974.

[2] Yang, J. W., "Periodic Heat Transfer in Straight Fins," JOURNAL OF HEAT TRANSFER, TRANS. ASME, Series C, Vol. 94, No. 3, Aug. 1972, pp. 310–314.

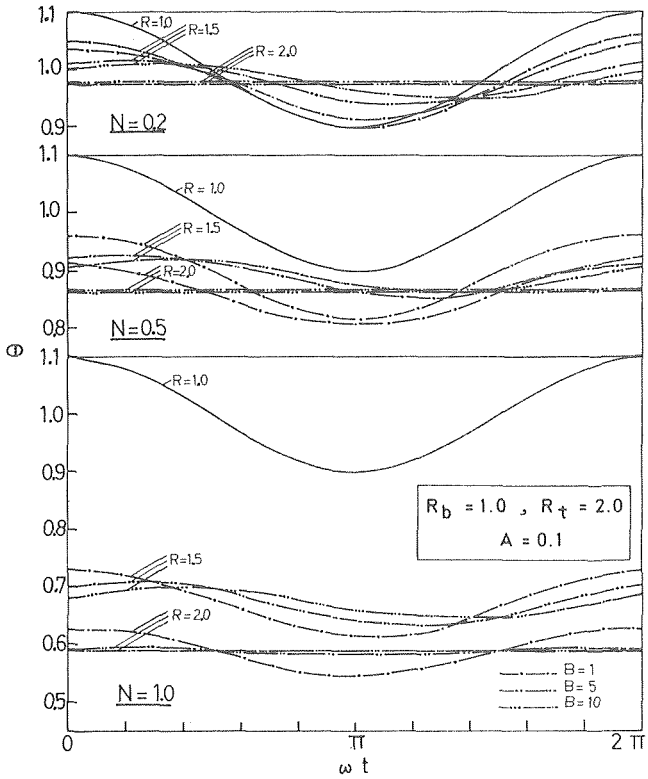

Fig. 2 Effect of parameters N and B on heat flux variation in an annular fin

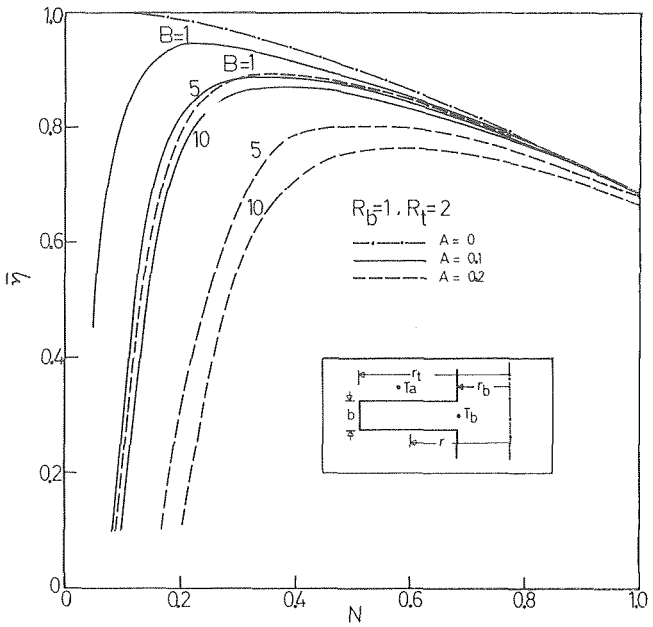

Fig. 3 Effect of parameters B and A on time-average efficiency of an annular fin

Equations (12), (13), and (14) were also programmed to give numerical results for the heat flux and time-average fin efficiency.

Results and Discussion

The foregoing analysis shows that the performance of the fin depends on the amplitude parameter A, frequency parameter B, steady-state fin parameter N, and the geometrical parameters R_b and R_t. Because of space limitations, the presentation of numerical results is restricted to few representative cases. The effect of amplitude parameter A on time-wise temperature distribution is evident from equation (4) which shows that the oscillatory component θ_2 is directly proportional to A. Fig. 1 shows the effect of parameters N and B on time-wise temperature patterns in a typical fin with $R_b = 1$, $R_t = 2$ and with $A = 0.1$. Temperature variations at midpoint ($R = 1.5$) and tip ($R = 2.0$) are shown together with the imposed temperature at base ($R = 1.0$). At any radial position, the temperature oscillates periodically around the corresponding steady-state temperature. To avoid congestion, the steady-state temperature has not been indicated. At low values of B the temperature at every radial position is almost in phase with the base temperature for all three values of N considered but the amplitude of oscillation decreases with increase of N. As the value of B increases, the effect of N on amplitude of oscillation becomes less pronounced and at $B = 5$ and 10, it is negligibly small.

For a given N, the variation of frequency parameter B affects both the amplitude and phase of temperature variation at every radial position. As B increases, the amplitude decreases but the phase difference increases. Also, at high values of B, the fin tip ($R = 2.0$) ceases to respond to base temperature variation and its temperature remains practically at steady-state value. This is in contrast to the behavior of a straight rectangular fin for which significant oscillations of tip temperature have been reported by Yang. Indeed, for a location situated at a fixed distance from the base, the amplitude of oscillation in an annular fin is smaller than that in a straight rectangular fin. This appears to be due to the fact that in a straight fin the heat capacity is constant whereas for an annular fin it increases as one proceeds from base to the tip.

The heat flux patterns corresponding to Fig. 1 are shown in Fig. 2. The heat flux oscillates periodically around the steady-state value which increases with N in accordance with known steady-state behavior. At low values of B (say 0.01), which imply low frequency of base temperature variation or high thermal diffusivity of fin material, the amplitude is primarily governed by N and increases with N. Also, the heat flux remains in phase with base temperature. As the value of B increases, the amplitude increases and becomes relatively insensitive to changes in N. For $N = 0.5$ and 0.2 the heat flux becomes negative as B increases and the effect is more pronounced at $N = 0.2$. This as noted previously by Yang is due to thermal inertia of the fin causing back heat flow from the fin to the base. For the fin geometry under consideration and for $A = 0.1$, the limiting value of N below which back heat flow occurs are 0.2, 0.47, and 0.52 for $B = 1$, 5, 10, respectively. For higher values of B, the limiting value of N was found to increase but only slightly. The increase in A may, however, lead to significant increase in the limiting value of N. It is also worth noting that as B increases the heat flux leads the base temperature variation. For example, for $B = 5$, the heat flux leads the base temperature by time interval of about $\pi/5$ for all three values of N.

In Fig. 3, the time-average efficiency is plotted against N for parameteric values of B. In so far as the temperature and heat flux are concerned, equations (4) and (12) show that their oscillatory components are directly proportional to amplitude parameter A. The effect of A on the time-average efficiency (equations (13) and (14)) however is not so obvious. To display the effect of A, two sets of curves are shown in Fig. 3, one for $A = 0.1$ and the other for $A = 0.2$. The effect of B is to reduce the efficiency. The reduction in efficiency compared to steady-state efficiency ($A = 0$) is noticeable for $N < 1$ and becomes quite significant at low values of N. Further reduction occurs as the parameter A is increased. These findings are consistent with the results of Yang for a straight fin of rectangular profile.

Application of Integral Method to Heat Conduction in Nonhomogeneous Media

S. Hameed[1] and S. A. Lebedeff[2]

Introduction

The integral method has proved useful in the study of heat transfer in composite regions consisting of several layers (see, e.g., Goodman [1],[3] Ozisik [2], and Yang [3]). Here we apply this method to heat conduction in a medium in which the thermal conductivity k and specific heat c vary continuously with distance. Consider the semi-infinite region extending over positive x with a uniform and constant heat flux at the surface $x = 0$:

$$k(x)\frac{\partial T}{\partial x} = -q;\ x = 0 \tag{1}$$

The initial condition is $T(x,t) = 0$ and it is assumed that T as well as the heat flux are zero at $x = \infty$. The problem is to find the temperature T at the surface $x = 0$.

The approach of the integral method is to assume that x dependence of the solution can be described by a simple form, such as a polynomial. The problem considered here indicates how one may anticipate conditions under which this assumption fails to work. It turns out that, since we are interested in the value of the solution at the surface $x = 0$ it is important to have a profile with the correct behavior in the immediate neighborhood of the surface, and that the correct profile is very sensitive to the analytic behavior of $k(x)$ and $c(x)$ in this neighborhood. To study the applicability of the integral method we, therefore, expand c and k at $x = 0$ and represent them near the surface by

$$c(x) = c_0 x^{\alpha},\ k(x) = k_0 x^{\beta} \tag{2}$$

Analysis and Solutions

Integration of the heat conduction equation gives the Heat Balance Integral (HBI):

$$\frac{d\theta}{dt} = k_0 x^{\beta}\frac{\partial T}{\partial x}\Big|_0^{\delta} = q \tag{3}$$

where

$$\theta = \int_0^{\delta} \rho c(x) T(x,t)\,dx$$

and it is assumed, as usual, that heat is not transferred beyond $x = \delta(t)$. ρ is the density of the medium. The HBI involves the value of $k(x)$ only at the two boundaries and the solution obtained is therefore insensitive to the variation of k between the boundaries. This difficulty may be avoided by transforming to a new space variable ω in terms of which the conductivity becomes constant:

$$\omega = \int \frac{dx}{k(x)} \tag{4}$$

The boundary condition (1) now becomes

$$\frac{\partial T}{\partial \omega} = -q;\ \omega = 0$$

and the initial condition is $T(\omega,t) = 0$. When $k(x)$ is given by the power law of equation (2), the transformation variable is $\omega = x^{1-\beta}/k_0(1-\beta)$ and the HBI becomes

$$\frac{d\theta}{dt} = \frac{\partial T}{\partial \omega}\Big|_0^{\delta} = q \tag{5}$$

$$\theta = a\int_0^{\delta} \omega^{\mu} T(\omega,t)\,d\omega \tag{6}$$

where

$$a = k_0^{(1+\mu)}\rho c_0(1-\beta)^{\mu} \text{ and } \mu = (\alpha+\beta)/(1-\beta)$$

If one follows the conventional procedure of the integral method, a quadratic profile for T may be chosen:

$$T_A = T_A^0\left(1 - \frac{\omega}{\delta}\right)^2 \tag{7}$$

where T_A^0 is the required temperature at the surface $\omega = 0$. Application of the boundary condition (1) gives $T_A^0 = q\,\delta/2$. Substitution of the T_A profile into equation (6) and the further substitution of (6) into the HBI, equation (5), gives

$$T_A^0 = \frac{q}{2}\left[\frac{2}{aB(1+\mu,3)}t\right]^{\nu} \tag{8}$$

where $\nu = (1-\beta)/(2+\alpha-\beta)$ and B is the beta function. The exact solution of the problem, when specialized to $x = 0$, yields

$$T_E^0 = \frac{q}{k_0}\frac{(2+\alpha-\beta)^{2\nu-1}}{\nu\Gamma(1-\nu)}\left(\frac{k_0 t}{\rho c_0}\right)^{\nu} \tag{9}$$

The comparison between the exact solution and equation (8) is shown in Fig. 1, where we plot the precent error in T_A^0 against μ (curve A). As μ increases from zero the error at first decreases, becoming nearly zero near $\mu = 0.51$. It then becomes negative, being -6.1 percent at $\mu = 1$. For larger μ the error increases rapidly in magnitude so that the quadratic profile cannot be regarded as a good assumption for $\mu \gg 1$.

One reason for the difficulty with this profile for large μ can be seen by considering equation (1), the flux condition, at $x = 0$,

$$k(x)\frac{\partial T}{\partial x} = T_A^0\left(-\frac{2}{\delta} + \frac{(2-2\beta)}{k_0(1-\beta)^2\delta^2}x^{1-\beta}\right) \tag{10}$$

The right-hand side of equation (10) is infinite at $x = 0$ when $\beta \geq 1$

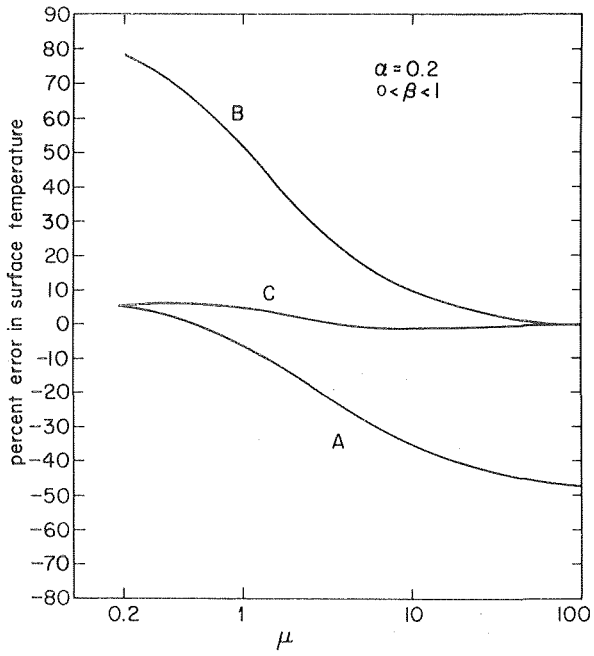

Fig. 1 Percent error $= [(T^0 - T_E^0)/T_E^0] \times 100$ in the predicted surface temperature T^0 for the three profiles T_A, equation (7), T_B, equation (12), and T_C, equation (14)—T_A gives small errors for small values of $\mu(\beta \ll 1)$ and errors in T_B are small for large $\mu(\beta \approx 1)$

[1] Institute for Space Studies, NASA, New York, N. Y.

[2] G.T.E., Programming Methods Inc., New York, N. Y.

[3] Numbers in brackets designate References at end of technical brief.

Contributed by the Heat Transfer Division of THE AMERICAN SOCIETY OF MECHANICAL ENGINEERS. Manuscript received by the Heat Transfer Division September 3, 1974.

and the flux condition cannot be satisfied. Because of this one may expect this profile to become a poor approximation as β approaches 1, i.e., as μ becomes infinite. It may also be observed that for large μ the weighting function ω^μ in equation (6) becomes very small for $\omega < 1$. This makes the value of the integral θ insensitive to the behavior of the profile $T_A(\omega)$ near the surface.

The question therefore arises as to what kind of profile would be appropriate in the case of large μ. An indication may be obtained from the work of Lardner and Pohle [5] who considered heat conduction in cylindrical geometry, that is, with $\alpha = \beta = 1$. They noted that a profile parabolic in x is inadequate and showed that a good solution is obtained if the profile is taken to be of the form

$$(1 - \frac{x}{\delta})^2 \ln (\frac{x}{\delta}) \tag{11}$$

The logarithmic multiplier of the usual quadratic profile is necessary to satisfy the flux boundary condition, equation (1). In the general case discussed here, the same is accomplished by the transformation $\omega = \int dx/k(x)$. In terms of ω, which is proportional to $x^{1-\beta}$, the profile (11) may be written as

$$T_B = T_B{}^0(1 - (\frac{\omega}{\delta})^{\frac{1}{1-\beta}})^2(1 - \frac{\omega}{\delta}) \tag{12}$$

The usual procedure of the integral method then gives

$$T_B{}^0 = q[\frac{1}{a(1-\beta)[B(1+\alpha, 3) - B(2+\alpha-\beta, 3)]} t]^\nu \tag{13}$$

The error in this solution is shown as curve B in Fig. 1. We find that the solution gives good results for large values of μ, the error being less than 10 percent for $\mu > 10$. For small μ the errors are very large, however, being more than 50 percent for $\mu < 1$. This profile is constructed to represent the singular behavior of the equation at $\beta = 1$. Its inadequacy for $\beta \ll 1$ may be seen also by noting that its derivative $(\partial T/\partial\omega)_{\omega=0}$, is discontinuous at $\beta = 0$.

Thus, we find that near $\beta = 0$ the quadratic profile satisfies the flux boundary condition, has the correct asymptotic form, and therefore gives accurate solutions. The same is true of the Lardner and Pohle profile at $\beta = 1$. We may therefore expect that a profile which incorporates the correct behavior in the two limits would give small errors for all values of β and μ. One such profile, which reduces to equation (7) for $\beta = 0$ and to equation (12) for $\beta = 1$, is

$$T_c = T_c{}^0[1 - \frac{\omega}{\delta}][1 - (1-\beta)\frac{\omega}{\delta} - \beta(\frac{\omega}{\delta})^{\frac{1}{1-\beta}}] \tag{14}$$

It gives, for the surface temperature

$$T_c{}^0 = \frac{q}{(2-\beta)}[\frac{1}{a(1-\beta)B} t]^\nu$$

where

$$B = \frac{1}{(1+\alpha)} - \frac{1}{(2+\alpha-\beta)} - \frac{\beta}{(2+\alpha)} + \frac{\beta}{(3+\alpha-\beta)} - \frac{(1-\beta)}{(2+\alpha-\beta)} + \frac{(1-\beta)}{(3+\alpha-2\beta)}$$

As may be seen in curve C of Fig. 1, this solution gives a good approximation to the exact solution for all values of β and μ. The profile (14) would therefore give accurate results if the conductivity $k(x)$ and the specific heat $c(x)$ are represented by functions which can be approximated near the surface by the power laws of equation (2).

Acknowledgment

S. Hameed holds a Senior Resident Research Associateship of the National Academy of Sciences of the National Research Council, Washington, D. C.

References

1 Goodman, T. R., "Application of Integral Methods to Transient Non-Linear Heat Transfer," *Advances in Heat Transfer*, Vol I, T. F. Irvine, Jr., and J. P. Hartnett, eds., Academic Press, New York, 1964, pp. 51–122.

2 Ozisik, M. N., *Boundary Value Problems of Heat Conduction*, International Textbook Company, Scranton, Pa., 1968, pp. 301–343.

3 Yang, K. T., "Calculation of Unsteady Heat Conduction In Single-Layer and Composite Finite Slabs With And Without Property Variations By An Improved Integral Procedure," *International Developments in Heat Transfer*, ASME, Paper 3, 1961, pp. 18–27.

4 Carslaw, H. S., and Jaeger, J. C., *Conduction of Heat in Solids*, Oxford University Press, London, 1959, 2nd ed., p. 412.

5 Lardner, T. J., and Pohle, F. V., "Application of the Heat Balance Integral to Problems of Cylindrical Geometry," TRANS. ASME, Vol. 28, 1961, p. 310.

Extrapolation Errors in Thermal Contact Resistance Measurements

T. R. Thomas[1]

In the classic split-bar determination of thermal contact resistance the temperature drop across the interface is estimated by extrapolating a temperature gradient measured remotely. It is shown that this can give rise to substantial errors which cannot greatly be reduced by increasing the number of measurements. It is suggested that due to extrapolation errors few interface temperature drops have ever been determined to better than $^1/_2$ °K, and that this may account for some of the discrepancies between published contact resistances, particularly those measured at high loads.

Nomenclature

a = thermocouple separation
n = number of thermocouples in a bar
R = bar radius
ΔT = extrapolated interface temperature drop
x = distance along bar from arbitrary origin
ξ = distance of interface from origin
σ = standard deviation

Professor Rohsenow has drawn my attention to a paper by Wilcox and himself [1][2] which points out a source of error inherent in wall-temperature measurements in condensation experiments, arising from the fact that the wall temperature is not measured directly but is inferred by linear extrapolation from a set of temperatures measured by thermocouples buried in the condensing block. According to Wilcox and Rohsenow the principal uncertainty in a given temperature measurement is due to uncertainty in the position of the thermocouple, and the effect of the combined uncertainties is magnified by extrapolation.

If this source of error is serious in condensation experiments it is still more so in determinations of thermal contact resistance, where two extrapolations are involved. In the classic split-bar arrangement (Fig. 1) the desired parameter, the temperature drop across the interface, is deduced from extrapolation of temperature distributions in each bar measured remotely from the interface. If there are n thermocouples in a bar at distances x from some arbitrary origin, then the variance of the error due to extrapolation at a point ξ is [2]

[1] Principal Lecturer, Teesside Polytechnic, Middlesbrough, Cleveland TS1 3BA, United Kingdom.

[2] Numbers in brackets designate References at end of technical brief.

Contributed by the Heat Transfer Division of THE AMERICAN SOCIETY OF MECHANICAL ENGINEERS. Manuscript received by the Heat Transfer Division October 22, 1974.

and the flux condition cannot be satisfied. Because of this one may expect this profile to become a poor approximation as β approaches 1, i.e., as μ becomes infinite. It may also be observed that for large μ the weighting function ω^μ in equation (6) becomes very small for $\omega < 1$. This makes the value of the integral θ insensitive to the behavior of the profile $T_A(\omega)$ near the surface.

The question therefore arises as to what kind of profile would be appropriate in the case of large μ. An indication may be obtained from the work of Lardner and Pohle [5] who considered heat conduction in cylindrical geometry, that is, with $\alpha = \beta = 1$. They noted that a profile parabolic in x is inadequate and showed that a good solution is obtained if the profile is taken to be of the form

$$(1 - \frac{x}{\delta})^2 \ln (\frac{x}{\delta}) \tag{11}$$

The logarithmic multiplier of the usual quadratic profile is necessary to satisfy the flux boundary condition, equation (1). In the general case discussed here, the same is accomplished by the transformation $\omega = \int dx/k(x)$. In terms of ω, which is proportional to $x^{1-\beta}$, the profile (11) may be written as

$$T_B = T_B{}^0(1 - (\frac{\omega}{\delta})^{\frac{1}{1-\beta}})^2(1 - \frac{\omega}{\delta}) \tag{12}$$

The usual procedure of the integral method then gives

$$T_B{}^0 = q[\frac{1}{a(1-\beta)[B(1+\alpha, 3) - B(2+\alpha-\beta, 3)]} t]^\nu \tag{13}$$

The error in this solution is shown as curve B in Fig. 1. We find that the solution gives good results for large values of μ, the error being less than 10 percent for $\mu > 10$. For small μ the errors are very large, however, being more than 50 percent for $\mu < 1$. This profile is constructed to represent the singular behavior of the equation at $\beta = 1$. Its inadequacy for $\beta \ll 1$ may be seen also by noting that its derivative $(\partial T/\partial\omega)_{\omega=0}$, is discontinuous at $\beta = 0$.

Thus, we find that near $\beta = 0$ the quadratic profile satisfies the flux boundary condition, has the correct asymptotic form, and therefore gives accurate solutions. The same is true of the Lardner and Pohle profile at $\beta = 1$. We may therefore expect that a profile which incorporates the correct behavior in the two limits would give small errors for all values of β and μ. One such profile, which reduces to equation (7) for $\beta = 0$ and to equation (12) for $\beta = 1$, is

$$T_c = T_c{}^0[1 - \frac{\omega}{\delta}][1 - (1-\beta)\frac{\omega}{\delta} - \beta(\frac{\omega}{\delta})^{\frac{1}{1-\beta}}] \tag{14}$$

It gives, for the surface temperature

$$T_c{}^0 = \frac{q}{(2-\beta)}[\frac{1}{a(1-\beta)B} t]^\nu$$

where

$$B = \frac{1}{(1+\alpha)} - \frac{1}{(2+\alpha-\beta)} - \frac{\beta}{(2+\alpha)} + \frac{\beta}{(3+\alpha-\beta)} - \frac{(1-\beta)}{(2+\alpha-\beta)} + \frac{(1-\beta)}{(3+\alpha-2\beta)}$$

As may be seen in curve C of Fig. 1, this solution gives a good approximation to the exact solution for all values of β and μ. The profile (14) would therefore give accurate results if the conductivity $k(x)$ and the specific heat $c(x)$ are represented by functions which can be approximated near the surface by the power laws of equation (2).

Acknowledgment

S. Hameed holds a Senior Resident Research Associateship of the National Academy of Sciences of the National Research Council, Washington, D. C.

References

1 Goodman, T. R., "Application of Integral Methods to Transient Non-Linear Heat Transfer," *Advances in Heat Transfer*, Vol I, T. F. Irvine, Jr., and J. P. Hartnett, eds., Academic Press, New York, 1964, pp. 51–122.

2 Ozisik, M. N., *Boundary Value Problems of Heat Conduction*, International Textbook Company, Scranton, Pa., 1968, pp. 301–343.

3 Yang, K. T., "Calculation of Unsteady Heat Conduction In Single-Layer and Composite Finite Slabs With And Without Property Variations By An Improved Integral Procedure," *International Developments in Heat Transfer*, ASME, Paper 3, 1961, pp. 18–27.

4 Carslaw, H. S., and Jaeger, J. C., *Conduction of Heat in Solids*, Oxford University Press, London, 1959, 2nd ed., p. 412.

5 Lardner, T. J., and Pohle, F. V., "Application of the Heat Balance Integral to Problems of Cylindrical Geometry," TRANS. ASME, Vol. 28, 1961, p. 310.

Extrapolation Errors in Thermal Contact Resistance Measurements

T. R. Thomas[1]

In the classic split-bar determination of thermal contact resistance the temperature drop across the interface is estimated by extrapolating a temperature gradient measured remotely. It is shown that this can give rise to substantial errors which cannot greatly be reduced by increasing the number of measurements. It is suggested that due to extrapolation errors few interface temperature drops have ever been determined to better than $\frac{1}{2}$ °K, and that this may account for some of the discrepancies between published contact resistances, particularly those measured at high loads.

Nomenclature

a = thermocouple separation
n = number of thermocouples in a bar
R = bar radius
ΔT = extrapolated interface temperature drop
x = distance along bar from arbitrary origin
ξ = distance of interface from origin
σ = standard deviation

Professor Rohsenow has drawn my attention to a paper by Wilcox and himself [1][2] which points out a source of error inherent in wall-temperature measurements in condensation experiments, arising from the fact that the wall temperature is not measured directly but is inferred by linear extrapolation from a set of temperatures measured by thermocouples buried in the condensing block. According to Wilcox and Rohsenow the principal uncertainty in a given temperature measurement is due to uncertainty in the position of the thermocouple, and the effect of the combined uncertainties is magnified by extrapolation.

If this source of error is serious in condensation experiments it is still more so in determinations of thermal contact resistance, where two extrapolations are involved. In the classic split-bar arrangement (Fig. 1) the desired parameter, the temperature drop across the interface, is deduced from extrapolation of temperature distributions in each bar measured remotely from the interface. If there are n thermocouples in a bar at distances x from some arbitrary origin, then the variance of the error due to extrapolation at a point ξ is [2]

[1] Principal Lecturer, Teesside Polytechnic, Middlesbrough, Cleveland TS1 3BA, United Kingdom.

[2] Numbers in brackets designate References at end of technical brief.

Contributed by the Heat Transfer Division of THE AMERICAN SOCIETY OF MECHANICAL ENGINEERS. Manuscript received by the Heat Transfer Division October 22, 1974.

$$\sigma_\xi^2 = \sigma_T^2 \frac{\Sigma(x-\xi)^2}{n\Sigma x^2 - (\Sigma x)^2} \quad (1)$$

where σ_T is related to the standard deviation σ_r of the temperature residuals i.e., the differences between the observed temperatures and the corresponding temperatures predicted from a least-mean-squares straight line through the observations.

σ_ξ^2 is a minimum at the centroid $\Sigma x/n$ of the observations and increases nearly linearly at points remote from the centroid. Suppose for simplicity that there are an odd number of thermocouples in a bar, spaced at equal intervals a. If ξ is measured from the centroid a little manipulation of equation (1) will yield

$$\left(\frac{\sigma_\xi}{\sigma_T}\right)^2 = \frac{1}{n} + \frac{12(\xi/a)^2}{n(n^2-1)} \quad (2)$$

σ_T is itself dependent on the number of thermocouples:

$$(\sigma_T/\sigma_r)^2 = n/(n-2)$$

where σ_r is the standard deviation of the residuals. Hence

$$\frac{\sigma_\xi}{\sigma_r} = \sqrt{\frac{1}{n-2} + \frac{12(\xi/a)^2}{(n-2)(n^2-1)}} \quad (3)$$

Clearly the magnification of error due to extrapolation can be large (Fig. 2). Increasing the number of thermocouples is not quite as helpful in reducing the extrapolation error as it appears at first sight, for the absolute separation of the interface from the nearest thermocouple is fixed by the constraint that the isotherms still be parallel at this point. This condition depends on a number of factors, including the geometry of the bar; in practice few experimenters care to set their nearest thermocouple less than one bar radius R from the interface. For example, in the arrangement shown in Fig. 1, $n = 3$, $a = R$ and $\sigma_\xi = 2.65\ \sigma_r$. If the number of thermocouples were increased to 5 in the same overall length, then $a = R/2$, $\xi = 4a$ and $\sigma_\xi = 1.72\ \sigma_r$; similarly for $n = 7$, $\sigma_\xi = 1.40\ \sigma_r$. Increasing the number of thermocouples from 3 to 7 thus does not even halve the extrapolation error, while increasing the complexity of the instrumentation and introducing the danger of systematic error from the extra heat leak.

In the split-bar experiment, the effective temperature drop across the interface is the difference of two extrapolated temperatures, and its error in turn is the root mean square of the two extrapolation errors. If the bars are of the same material the standard deviations of the residuals will be of the same order, and

$$\sigma_{\Delta T} = \sqrt{2}\,\sigma_T$$

$= 3.75\ \sigma_r$ for the example of Fig. 1. In practice σ_r is unlikely to be

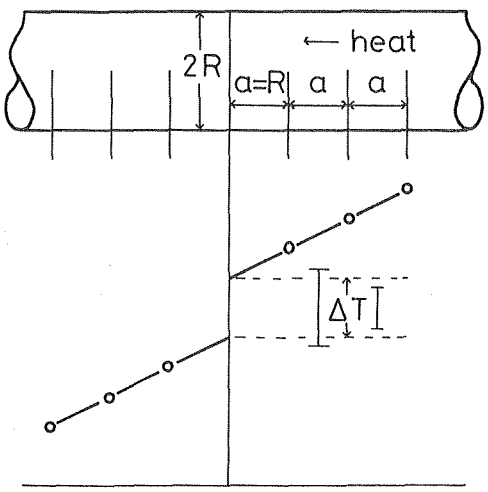

Fig. 1 Split-bar experiment for determination of thermal contact resistance, showing 95 percent confidence limits of extrapolated temperature drop across interface

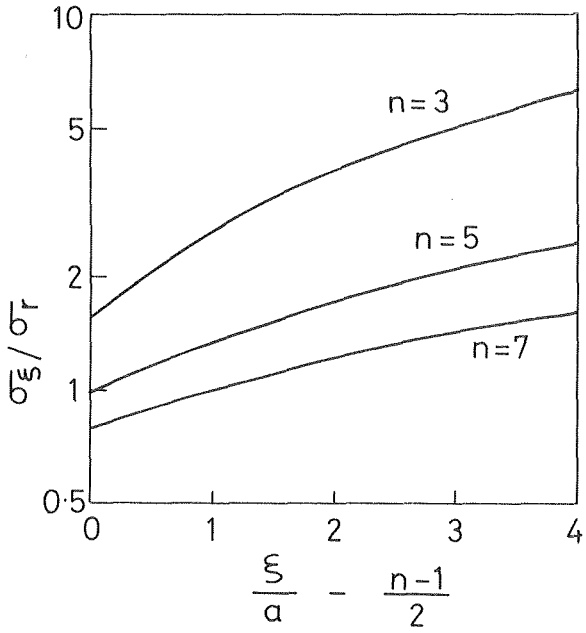

Fig. 2 Ratio of extrapolation error to S.D. of residuals, as a function of extrapolation distance, for 3, 5, and 7 thermocouples—extrapolation distance is measured from nearest thermocouple to interface, in units of thermocouple separation

significantly less than 0.1 °K. For the example of Fig. 1 this would give $\Delta T = 2.00 \pm 0.38$ °K, a 19 percent error.

Most of the measurements reported in the literature have been made with either 3 or 4 thermocouples in each bar. On the basis of this analysis it seems unlikely that many of these temperature drops have been measured to much better than ½ °K. Wilcox and Rohsenow's analysis of positional uncertainties would probably give even more pessimistic results. At high interfacial stresses the temperature drop across the interface is often only a degree or two, suggesting that many published determinations contain very large errors indeed. Wilcox and Rohsenow also point out that extrapolation errors, although correctly treated as mathematically random, would appear systematic to the experimenter; that is to say, their magnitude might change slowly with experimental conditions but they would remain unchanged in sign throughout an experimental run and would thus be extremely difficult to detect except by repeating the experiment with a new set of thermocouples, something which few experimenters have had the time or patience to do. These considerations may explain at least some of the discrepancies noticed between the measurements of different workers on apparently similar interfaces [3].

Wilcox and Rohsenow discuss the possibility of obtaining apparent negative temperature drops in this way and imply that when this happens it goes unreported: "Who could get such data published?" they ask rhetorically. Here Professor Rohsenow does himself less than justice, as a report from his own laboratory some years ago described a negative temperature drop observed during a determination of thermal contact resistance [4]. I have myself published details of a negative temperature drop which persistent and determined experimentation failed to exorcize [5], but would now attribute this to gross distortion of the isotherms due to an uneven radial distribution of thermal strains at the interface.

References

1 Wilcox, S. J., and Rohsenow, W. M., "Film Condensation of Potassium Using Copper Condensing Block for Precise Wall-Temperature Measurement," JOURNAL OF HEAT TRANSFER, TRANS. ASME, Series C, Vol. 92, 1970, pp. 359–371.

2 Birge, R. T., "The Calculation of Errors by the Method of Least Squares," *Phys. Rev.*, Vol. 40, 1932, pp. 207–227.

3 Thomas, T. R., and Probert, S. D., "Correlations for Thermal Contact

Conductance in Vacuo," JOURNAL OF HEAT TRANSFER, TRANS. ASME, Series C, Vol. 94, 1972, pp. 276–280.
4 Adamantiades, A., "Experimental Determination of Contact Conductance for Some Stainless Steel Contacts," USAEC Report NYO-9458, 1962.
5 Thomas, T. R., and Probert, S. D., "Thermal Contact Resistance: the Directional Effect and Other Problems," *International Journal of Heat and Mass Transfer*, Vol. 13, 1970, pp. 789–807.

Results of the Numerical Solution for Outward Solidification With Flux Boundary Conditions

J. S. Goodling[1] and M. S. Khader[2]

Nomenclature

N = coordinate system designator (0-Cartesian; 1-cylindrical; 2-spherical)
S* = modified Stephan number, $q''c_p/hL(N = 0)$ or $q''c_p r_0/Lk(N = 1, 2)$
y = spatial coordinate, $hr/k(N = 0)$ or $r/r_0(N = 1, 2)$
β = flux parameter, $h(T_f - T_\infty)/q''(N = 0)$ or $h_0(T_f - T_\infty)/q''r_0{}^a(N = 1, 2)$
$\bar{\epsilon}$ = thickness of solid phase, $h\epsilon/k(N = 0)$ or $\epsilon/r_0(N = 1, 2)$
τ = time, $(q''h/\rho Lk)t(N = 0)$ or $(q''/\rho Lr_0)t(N = 1, 2)$
θ = temperature, $(T - T_f)h/q''(N = 0)$ or $(T - T_f)k/q''r_0(N = 1, 2)$

Introduction

The prediction of solidification rates on the outside of a cold wall is of practical interest in refrigeration, metallurgy, and plastics. While the only known exact solution is that by Neumann [1][3] for the planar problem, several good approximate methods of solution are found in the literature. London and Seban [2] showed that for the class of solidification problems where the sensible heat is negligible in comparison to the latent heat (Stephan number $\simeq 0$), analytical solutions can be obtained for the interface movement by solving the energy equation at the solid-liquid boundary only. The solutions are valid when S* < 1. Goodman [3] presented solutions to several problems using a "heat balance integral" technique similar to the momentum integral method in fluid flow problems. His results compared favorably with the exact solution of Neumann for small values of the Stephan number. Goodman also works the freezing problem in Cartesian space with a flux boundary condition at the fixed wall, the result of which is an explicit expression for the solidification time as a function of the interface position. By expanding this function in a Taylor series and reverting it, the result is a series expression for the interface position as a function of time. A comparison is made with series solution for the same problem by Evans, Issacson, and MacDonald [4] and the two series differ by a 4 percent factor in the coefficient of the fifth ordered term.

While Goodman restricts the approximation of the temperature distribution inside the solid phase to a cubic polynomial, Megerlin [5] extends the method to any ordered polynomial and suggests that as the order of the polynomial approximation is increased, the solution asymptotically approaches the exact solution. However, the Megerlin method does not follow a pattern such that one can define the order of the polynomial necessary for convergence for any Stephan number.

This paper shows the results of solutions to outward solidification problems with constant heat flux at the inner wall, obtained by numerical solution of the governing equations.

Formulation

The analysis deals with one-dimensional outward growth of a region of solid resulting from a step change of heat flux at the inner boundary. The surrounding fluid is at a temperature above the fusion temperature, resulting in convective heat transfer to the interface. The problem is displayed schematically for the three coordinate systems in Fig. 1.

The dimensionless diffusion equation, interface energy equation and associated boundary and initial conditions are:

$$\frac{\partial^2\theta}{\partial y^2} + \frac{N}{y}\frac{\partial\theta}{\partial y} = S^*\frac{\partial\theta}{\partial\tau};\quad \theta(\bar{\epsilon},\tau) = 0$$

$$\left.\begin{aligned} \frac{\partial\theta}{\partial y}(0,\tau) &= -1 \\ \bar{\epsilon}(0) &= 0 \\ \frac{d\bar{\epsilon}}{d\tau} &= -\frac{\partial\theta}{\partial y}(\bar{\epsilon},\tau) - \beta \end{aligned}\right\} N = 0$$

$$\left.\begin{aligned} \frac{\partial\theta}{\partial y}(1,\tau) &= -1 \\ \bar{\epsilon}(0) &= 1 \\ \frac{d\bar{\epsilon}}{d\tau} &= -\frac{\partial\theta}{\partial y}(\bar{\epsilon},\tau) - \beta\bar{\epsilon}^a \end{aligned}\right\} N = 1,2$$

The dependency of the interface radius on the heat transfer coefficient has been accounted for in the cylindrical and spherical systems. The position of the interface in time is dependent upon the coordinate system *(N)*, the modified Stephan number (S*), a flux parameter (β) and the exponent a (for $N = 1,2$ only).

Solution and Results

Since no exact analytical solutions are known for the present problem, results were obtained by a numerical method. The spatial derivatives were approximated by central difference quotients and the time derivatives by backward implicit quotients. The method of solution was to advance the interface position in regularly spaced intervals, Δy, and to solve the resulting nonlinear algebraic equations for the time required for that incremental movement. A trial and error technique was used for solving the equations, the details of which are found in a previous work by the authors [6].

By the method of London and Seban [2], the results are for S* = 0

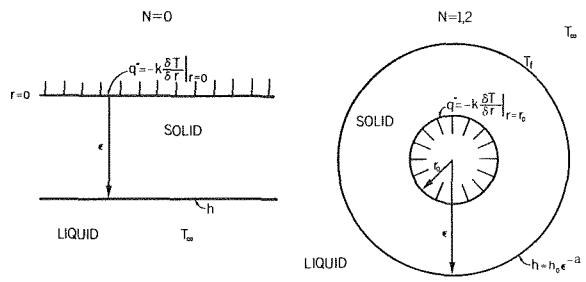

Fig. 1 One-dimensional Cartesian, cylindrical and spherical systems for outward solidification

[1] Assoc. Professor, Department of Mechanical Engineering, Auburn University, Auburn, Ala. Mem. ASME.
[2] Lecturer, Faculty of Engineering, Cairo University, Giza, Egypt. Assoc. Mem. ASME.
[3] Numbers in brackets designate References at end of technical brief.

Contributed by the Heat Transfer Division of THE AMERICAN SOCIETY OF MECHANICAL ENGINEERS. Transcript received by the Heat Transfer Division February 1, 1974.

Conductance in Vacuo," JOURNAL OF HEAT TRANSFER, TRANS. ASME, Series C, Vol. 94, 1972, pp. 276–280.
4 Adamantiades, A., "Experimental Determination of Contact Conductance for Some Stainless Steel Contacts," USAEC Report NYO-9458, 1962.
5 Thomas, T. R., and Probert, S. D., "Thermal Contact Resistance: the Directional Effect and Other Problems," *International Journal of Heat and Mass Transfer*, Vol. 13, 1970, pp. 789–807.

Results of the Numerical Solution for Outward Solidification With Flux Boundary Conditions

J. S. Goodling[1] and M. S. Khader[2]

Nomenclature

N = coordinate system designator (0-Cartesian; 1-cylindrical; 2-spherical)
S* = modified Stephan number, $q''c_p/hL(N = 0)$ or $q''c_p r_0/Lk(N = 1, 2)$
y = spatial coordinate, $hr/k(N = 0)$ or $r/r_0(N = 1, 2)$
β = flux parameter, $h(T_f - T_\infty)/q''(N = 0)$ or $h_0(T_f - T_\infty)/q''r_0{}^a(N = 1, 2)$
$\bar{\epsilon}$ = thickness of solid phase, $h\epsilon/k(N = 0)$ or $\epsilon/r_0(N = 1, 2)$
τ = time, $(q''h/\rho Lk)t(N = 0)$ or $(q''/\rho Lr_0)t(N = 1, 2)$
θ = temperature, $(T - T_f)h/q''(N = 0)$ or $(T - T_f)k/q''r_0(N = 1, 2)$

Introduction

The prediction of solidification rates on the outside of a cold wall is of practical interest in refrigeration, metallurgy, and plastics. While the only known exact solution is that by Neumann [1][3] for the planar problem, several good approximate methods of solution are found in the literature. London and Seban [2] showed that for the class of solidification problems where the sensible heat is negligible in comparison to the latent heat (Stephan number $\simeq 0$), analytical solutions can be obtained for the interface movement by solving the energy equation at the solid-liquid boundary only. The solutions are valid when S* < 1. Goodman [3] presented solutions to several problems using a "heat balance integral" technique similar to the momentum integral method in fluid flow problems. His results compared favorably with the exact solution of Neumann for small values of the Stephan number. Goodman also works the freezing problem in Cartesian space with a flux boundary condition at the fixed wall, the result of which is an explicit expression for the solidification time as a function of the interface position. By expanding this function in a Taylor series and reverting it, the result is a series expression for the interface position as a function of time. A comparison is made with series solution for the same problem by Evans, Issacson, and MacDonald [4] and the two series differ by a 4 percent factor in the coefficient of the fifth ordered term.

While Goodman restricts the approximation of the temperature distribution inside the solid phase to a cubic polynomial, Megerlin [5] extends the method to any ordered polynomial and suggests that as the order of the polynomial approximation is increased, the solution asymptotically approaches the exact solution. However, the Megerlin method does not follow a pattern such that one can define the order of the polynomial necessary for convergence for any Stephan number.

This paper shows the results of solutions to outward solidification problems with constant heat flux at the inner wall, obtained by numerical solution of the governing equations.

Formulation

The analysis deals with one-dimensional outward growth of a region of solid resulting from a step change of heat flux at the inner boundary. The surrounding fluid is at a temperature above the fusion temperature, resulting in convective heat transfer to the interface. The problem is displayed schematically for the three coordinate systems in Fig. 1.

The dimensionless diffusion equation, interface energy equation and associated boundary and initial conditions are:

$$\frac{\partial^2\theta}{\partial y^2} + \frac{N}{y}\frac{\partial\theta}{\partial y} = S^*\frac{\partial\theta}{\partial\tau};\quad \theta(\bar{\epsilon},\tau) = 0$$

$$\left.\begin{aligned} \frac{\partial\theta}{\partial y}(0,\tau) &= -1 \\ \bar{\epsilon}(0) &= 0 \\ \frac{d\bar{\epsilon}}{d\tau} &= -\frac{\partial\theta}{\partial y}(\bar{\epsilon},\tau) - \beta \end{aligned}\right\} N = 0$$

$$\left.\begin{aligned} \frac{\partial\theta}{\partial y}(1,\tau) &= -1 \\ \bar{\epsilon}(0) &= 1 \\ \frac{d\bar{\epsilon}}{d\tau} &= -\frac{\partial\theta}{\partial y}(\bar{\epsilon},\tau) - \beta\bar{\epsilon}^{-a} \end{aligned}\right\} N = 1,2$$

The dependency of the interface radius on the heat transfer coefficient has been accounted for in the cylindrical and spherical systems. The position of the interface in time is dependent upon the coordinate system (N), the modified Stephan number (S*), a flux parameter (β) and the exponent a (for $N = 1,2$ only).

Solution and Results

Since no exact analytical solutions are known for the present problem, results were obtained by a numerical method. The spatial derivatives were approximated by central difference quotients and the time derivatives by backward implicit quotients. The method of solution was to advance the interface position in regularly spaced intervals, Δy, and to solve the resulting nonlinear algebraic equations for the time required for that incremental movement. A trial and error technique was used for solving the equations, the details of which are found in a previous work by the authors [6].

By the method of London and Seban [2], the results are for S* = 0

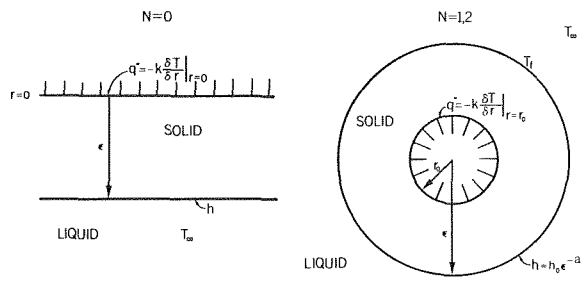

Fig. 1 One-dimensional Cartesian, cylindrical and spherical systems for outward solidification

[1] Assoc. Professor, Department of Mechanical Engineering, Auburn University, Auburn, Ala. Mem. ASME.
[2] Lecturer, Faculty of Engineering, Cairo University, Giza, Egypt. Assoc. Mem. ASME.
[3] Numbers in brackets designate References at end of technical brief.

Contributed by the Heat Transfer Division of THE AMERICAN SOCIETY OF MECHANICAL ENGINEERS. Transcript received by the Heat Transfer Division February 1, 1974.

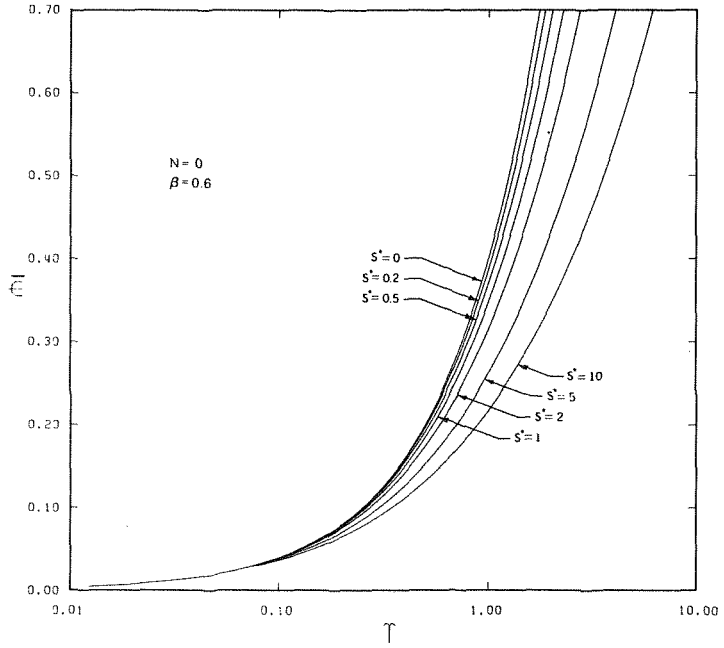

Fig. 2 Solidification front position with time for Cartesian system with $\beta = 0.6$

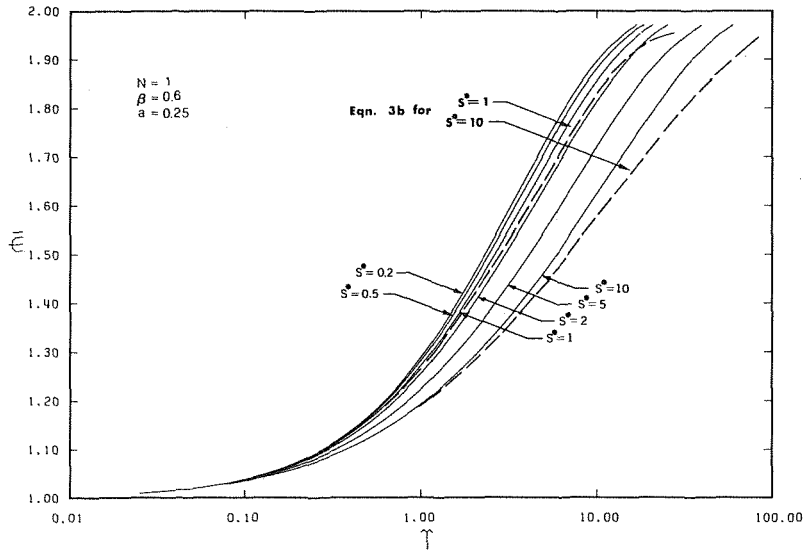

Fig. 3 Solidification front position with time for cylindrical system with $\beta = 0.6$, $a = 0.25$

$$\left.\begin{aligned} \tau &= \bar{\epsilon}/(1-\beta) && N = 0 \\ \tau &= \int_1^{\bar{\epsilon}} \frac{\bar{\epsilon}\,d\bar{\epsilon}}{[1-\beta\bar{\epsilon}^{(1-a)}]} && N = 1 \\ \tau &= \int_1^{\bar{\epsilon}} \frac{\bar{\epsilon}^2\,d\bar{\epsilon}}{[1-\beta\bar{\epsilon}^{(2-a)}]} && N = 2 \end{aligned}\right\} \quad (1)$$

For the case where the fluid is at the fusion temperature at the beginning of the solidification process ($\beta = 0$) Goodman obtained a solution for the Cartesian problem by approximating the temperature distribution inside the solid phase by a second ordered polynomial. Although the dimensionless parameters chosen by Goodman are not the same as in this paper, his results can be put in terms of dimensionless time and space, and the modified Stephan number used here.

$$\tau = \frac{\bar{\epsilon}}{6}[\bar{\epsilon}S^* + 5 + (1 + 4\bar{\epsilon}S^*)^{1/2}] \quad (2)$$

This yields results which compare favorably with results obtained here by numerical analysis for $N = 0$ and $\beta = 0$ for all realistic values of S* (<10).

Using Megerlin's method and approximating the temperature distribution by a second ordered polynomial in $(\epsilon - y)$, $\ln(\epsilon/y)$ and $(\epsilon - y)/\epsilon$ for the three coordinate systems, respectively, gives the following integrals for the solidification time as a function of interface position[4]

$$\tau = \int_0^{\bar{\epsilon}} 2/[\sqrt{\{(\frac{1}{S^*\bar{\epsilon}} - \beta)^2 + \frac{4}{S^*\bar{\epsilon}}\}} - (\frac{1}{S^*\bar{\epsilon}} + \beta)]d\bar{\epsilon} \quad (N = 0) \quad (3a)$$

$$\tau = \int_1^{\bar{\epsilon}} 2/[\sqrt{\{(\frac{1}{S^*\bar{\epsilon}\ln\bar{\epsilon}} - \beta\bar{\epsilon}^{-a})^2 + \frac{4}{S^*\bar{\epsilon}^2\ln\bar{\epsilon}}\}}$$

[4] These equations were derived by a journal referee and verified by the authors.

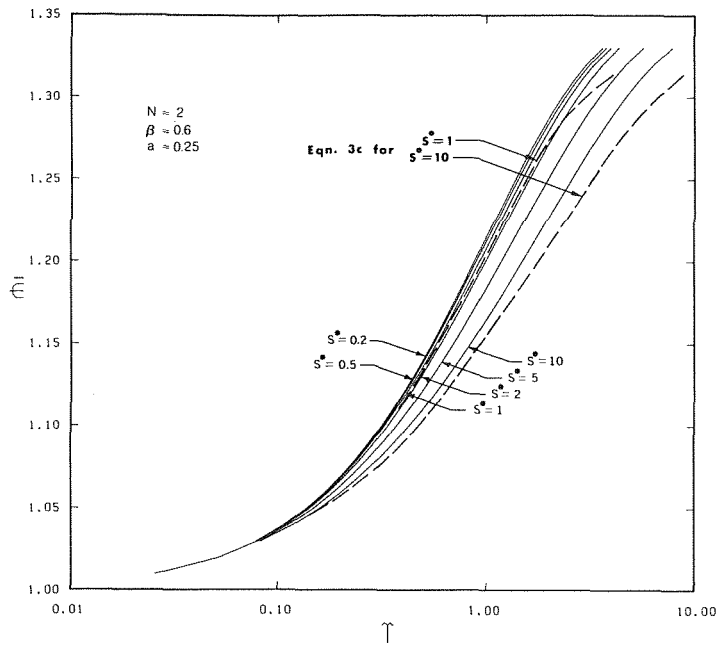

Fig. 4 Solidification front position with time for spherical system with β = 0.6, a = 0.25

$$- \left(\frac{1}{S^*\bar{\epsilon}\ln\bar{\epsilon}} + \beta\bar{\epsilon}^{-a}\right)\Big]\, d\bar{\epsilon} \quad (N = 1) \quad (3b)$$

$$\tau = \int_1^{\bar{\epsilon}} 2/\left[\sqrt{\left\{\left(\frac{1}{S^*\bar{\epsilon}(\bar{\epsilon}-1)} - \beta\bar{\epsilon}^{-a}\right)^2 + \frac{4}{S^*\bar{\epsilon}^3(\bar{\epsilon}-1)}\right\}}\right.$$

$$\left. - \left(\frac{1}{S^*(\bar{\epsilon}-1)\bar{\epsilon}} + \beta\bar{\epsilon}^{-a}\right)\right] d\bar{\epsilon} \quad (N = 2) \quad (3c)$$

Results of the numerical solutions for the governing equations are shown in Figs. 2, 3, and 4. The exponent a was taken as 0.25 (for N = 1,2) and the flux parameter as 0.6. As a means of verifying the method of solution, the same numerical procedure was used to solve the Neumann problem and the results compared with the exact solution. Deviations from Neumann's exact solution were of order 1 percent. As a second check, for the problems analyzed here, the size of the space increment was diminished by an order of magnitude and it was noted that the results were not significantly altered.

Equation (3a) is in good agreement with Fig. 2 (N = 0) for all values of S* investigated. For the cylindrical and spherical cases however, the times for the solidification front to reach particular points as predicted by Megerlin's method are about 10–30 percent greater than those formed by the numerical technique for S* $\sim$ 10. This is probably because for S* > 1 the second ordered approximation is insufficient for the two coordinate systems where the area of the interface is increasing with time.

References

1 Carslaw, H. S., and Jaeger, J. C., *Conduction of Heat in Solids*, Second ed., Oxford University Press, London and New York, 1959.

2 London, A. L., and Seban, R. A., "Rate of Ice Formation," Trans. ASME, Vol. 65, 1943, p. 771.

3 Goodman, T. R., "The Heat-Balance Integral and Its Application to Problems Involving a Change of Phase," Trans. ASME, Vol. 80, 2, 1958, p. 335.

4 Evans, G. W., Issacson, E., and MacDonald, J. K. L., "Stefan-Like Problems," *Q. App. Math.*, Vol. 8, 1950, p. 312.

5 Megerlin, F., "Geometrisch Eindimensionale Warmeleitung beim Schmeltzen und Erstarren," *Forsch. Ing.-Wes.*, Vol. 34, 1968, p. 40.

6 Goodling, J. S., and Khader, M. S., "A Numerical Solution for Outward Solidification With Flux Boundary Conditions," ASME Paper No. 73-WA/HT-17.

Enhancement of Cooling Effectiveness by Porous Materials in Coolant Passage

J. C. Y. Koh[1] and R. L. Stevens[1]

Nomenclature

L = length of coolant passage (ft)
$\dot{m}$ = coolant flux (lb/ft^2-s)
p = pressure (lb/ft^2)
Δp = pressure drop along coolant passage (lb/ft^2)
q = wall heat flux (Btu/ft^2-s)
$\bar{\rho}$ = mean density of coolant (lb/ft^3)

Introduction

In reference [1],[2] it was shown analytically that the cooling effectiveness of a regenerative cooling scheme can be increased significantly by packing the coolant passage with porous materials. The purpose of this brief is to show experimentally that the cooling effectiveness can indeed be increased several times by the use of porous materials.

Test Facility and Model

A 275 KW plasma arc heater was used as an energy source for this test. The model was a stainless steel cylindrical annulus having a 1.5 in. ID and a total length of 8 in. Thermocouples were spot welded to both the inner and outer tubes. The annulus was filled

[1] The Boeing Co., Seattle, Wash.

[2] Numbers in brackets designate References at end of technical brief.

Contributed by the Heat Transfer Division of THE AMERICAN SOCIETY OF MECHANICAL ENGINEERS. Manuscript received by the Heat Transfer Division September 16, 1974.

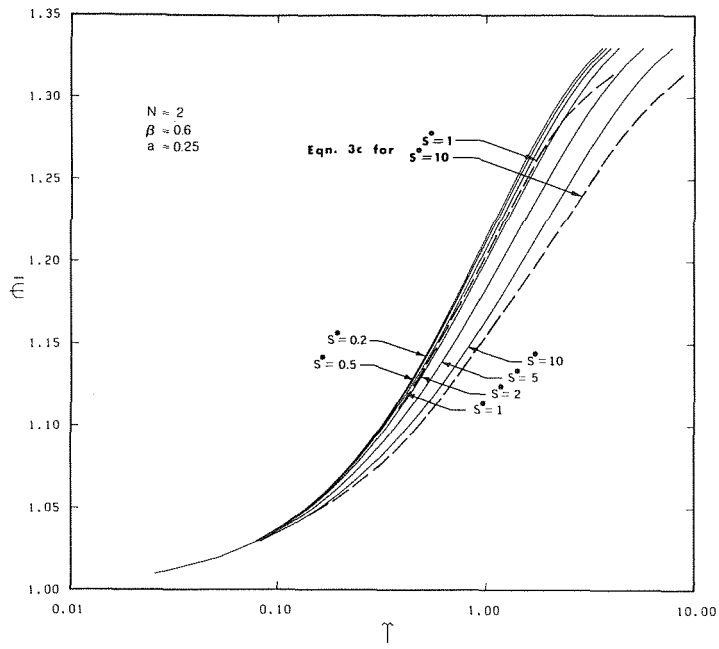

Fig. 4 Solidification front position with time for spherical system with β = 0.6, a = 0.25

$$- \left(\frac{1}{S^*\bar{\epsilon}\ln\bar{\epsilon}} + \beta\bar{\epsilon}^{-a}\right)\Big]\, d\bar{\epsilon} \quad (N = 1) \quad (3b)$$

$$\tau = \int_1^{\bar{\epsilon}} 2/\left[\sqrt{\left\{\left(\frac{1}{S^*\bar{\epsilon}(\bar{\epsilon}-1)} - \beta\bar{\epsilon}^{-a}\right)^2 + \frac{4}{S^*\bar{\epsilon}^3(\bar{\epsilon}-1)}\right\}}\right.$$

$$\left. - \left(\frac{1}{S^*(\bar{\epsilon}-1)\bar{\epsilon}} + \beta\bar{\epsilon}^{-a}\right)\right] d\bar{\epsilon} \quad (N = 2) \quad (3c)$$

Results of the numerical solutions for the governing equations are shown in Figs. 2, 3, and 4. The exponent a was taken as 0.25 (for N = 1,2) and the flux parameter as 0.6. As a means of verifying the method of solution, the same numerical procedure was used to solve the Neumann problem and the results compared with the exact solution. Deviations from Neumann's exact solution were of order 1 percent. As a second check, for the problems analyzed here, the size of the space increment was diminished by an order of magnitude and it was noted that the results were not significantly altered.

Equation (3a) is in good agreement with Fig. 2 (N = 0) for all values of S* investigated. For the cylindrical and spherical cases however, the times for the solidification front to reach particular points as predicted by Megerlin's method are about 10–30 percent greater than those formed by the numerical technique for S* $\sim$ 10. This is probably because for S* > 1 the second ordered approximation is insufficient for the two coordinate systems where the area of the interface is increasing with time.

References

1 Carslaw, H. S., and Jaeger, J. C., *Conduction of Heat in Solids*, Second ed., Oxford University Press, London and New York, 1959.

2 London, A. L., and Seban, R. A., "Rate of Ice Formation," Trans. ASME, Vol. 65, 1943, p. 771.

3 Goodman, T. R., "The Heat-Balance Integral and Its Application to Problems Involving a Change of Phase," Trans. ASME, Vol. 80, 2, 1958, p. 335.

4 Evans, G. W., Issacson, E., and MacDonald, J. K. L., "Stefan-Like Problems," *Q. App. Math.*, Vol. 8, 1950, p. 312.

5 Megerlin, F., "Geometrisch Eindimensionale Warmeleitung beim Schmeltzen und Erstarren," *Forsch. Ing.-Wes.*, Vol. 34, 1968, p. 40.

6 Goodling, J. S., and Khader, M. S., "A Numerical Solution for Outward Solidification With Flux Boundary Conditions," ASME Paper No. 73-WA/HT-17.

Enhancement of Cooling Effectiveness by Porous Materials in Coolant Passage

J. C. Y. Koh[1] and R. L. Stevens[1]

Nomenclature

L = length of coolant passage (ft)
$\dot{m}$ = coolant flux (lb/ft^2-s)
p = pressure (lb/ft^2)
Δp = pressure drop along coolant passage (lb/ft^2)
q = wall heat flux (Btu/ft^2-s)
$\bar{\rho}$ = mean density of coolant (lb/ft^3)

Introduction

In reference [1],[2] it was shown analytically that the cooling effectiveness of a regenerative cooling scheme can be increased significantly by packing the coolant passage with porous materials. The purpose of this brief is to show experimentally that the cooling effectiveness can indeed be increased several times by the use of porous materials.

Test Facility and Model

A 275 KW plasma arc heater was used as an energy source for this test. The model was a stainless steel cylindrical annulus having a 1.5 in. ID and a total length of 8 in. Thermocouples were spot welded to both the inner and outer tubes. The annulus was filled

[1] The Boeing Co., Seattle, Wash.

[2] Numbers in brackets designate References at end of technical brief.

Contributed by the Heat Transfer Division of THE AMERICAN SOCIETY OF MECHANICAL ENGINEERS. Manuscript received by the Heat Transfer Division September 16, 1974.

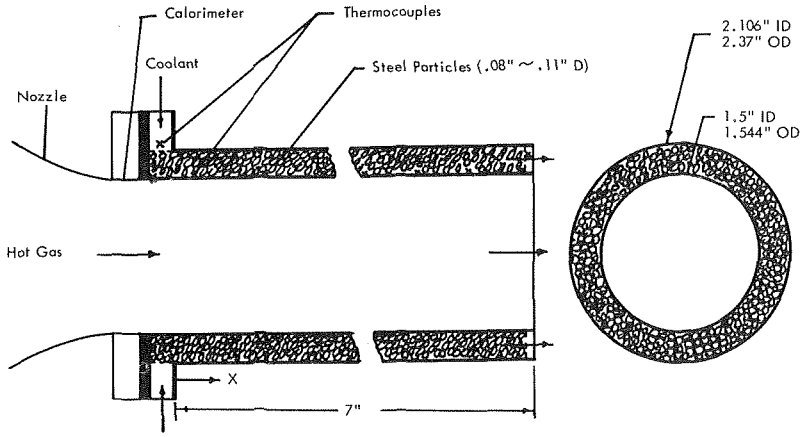

Fig. 1 Test model

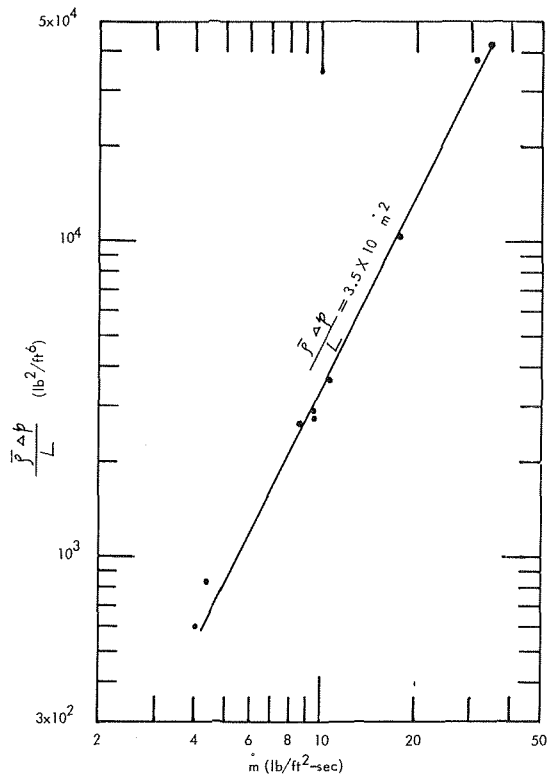

Fig. 2 Pressure drop in coolant passage packed with 0.08–0.11 particles

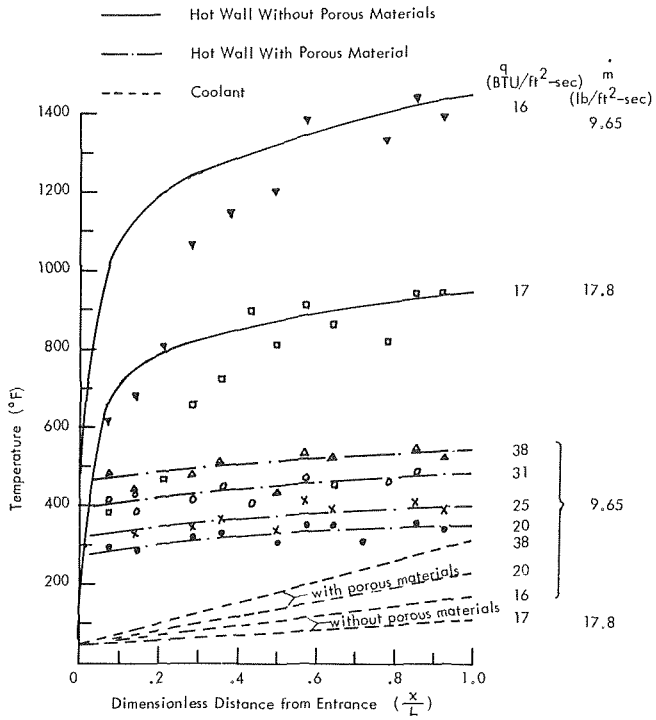

Fig. 3 Effects of porous materials in coolant passage on temperature

with peen shot (steel particles) having a diameter of from 0.08 in. to 0.11 in. The porosity of the packed passage was 0.5. Nitrogen gas was used as coolant. The coolant temperature at both the inlet and outlet locations were measured by use of thermocouples. A schematic diagram of the model is shown in Fig. 1.

Pressure Drop

The pressure drop in the coolant passage was measured for a range of coolant flux from 4 to 35 lb/ft^2-s. Results are shown in Fig. 2.

Temperature Distributions and Cooling Effectiveness

The cold wall heat flux at the test section was measured by use of four HyCal asymptotic calorimeters for a wide range of plasma operation conditions. It was found that the heat flux along the test section was approximately uniform. Using this information together with a wall temperature correction, the actual heat flux to the test model was determined. During the test, the heat flux upstream of the model but downstream of the nozzle was measured by a calorimeter (Fig. 1). This provided a double check on the heat flux determined from the calibration tests.

The temperature distribution of the hot wall and the coolant at different heat flux and coolant flux are shown in Figs. 3 and 4. The set of dashed lines in the lower part of Figs. 3 and 4 for coolant temperatures were drawn by connecting the measured temperature at the inlet ($x = 0$) and the outlet ($x = L$) locations. The solid lines for the hot wall temperature without porous materials were found by use of Hausen's equation, given in reference [2], for channel flow taking the entrance length into consideration.

The top two lines in Figs. 3 and 4 show that without porous materials, the maximum wall temperature increases as the coolant flow decreases, holding the heat flux constant.

The increase in cooling effectiveness due to the presence of the porous materials in the coolant passage can be seen by examining two separate cases.

(a) For fixed coolant flux $\dot{m}$: the wall heat flux is increased and the hot wall temperature is reduced due to the presence of porous material.

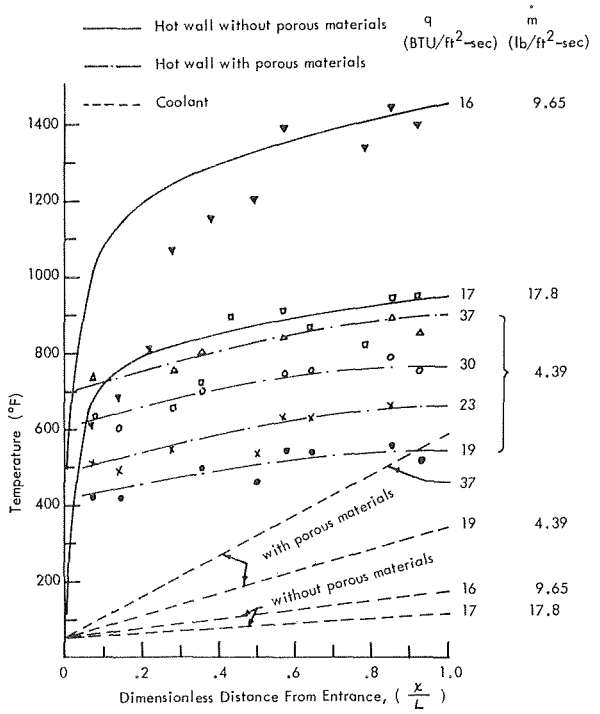

Fig. 4 Effects of porous materials in coolant passage on temperature

(b) For approximately fixed maximum hot wall temperature: the wall heat flux is again increased and a decrease of coolant flux is obtained due to the porous material.

These two comparisons can be found in Figs. 3 and 4. Fig. 3 shows that, for a fixed coolant flux of 9.65 lb/ft²-s, the wall heat flux was increased from 16 to 20 Btu/ft²-s while the maximum wall temperature was reduced from 1450°F to 350°F due to the packing of porous material in the coolant passage. On the other hand, Fig. 4 shows that, for a fixed maximum wall temperature from 900°F to 950°F, the wall heat flux was increased from 17 to 37 Btu/ft²-s while the coolant flux was reduced from 17.8 to 4.39 lb/ft²-s. Thus, the cooling effectiveness was indeed increased by several times by the packing of porous materials in the coolant passage.

Further Enhancement of Cooling Effectiveness

The cooling effectiveness can further be enhanced by the elimination of interface resistance between the wall and the porous material and by use of high conductivity porous material and high conductivity wall material.

Application of the Cooling Scheme

Clearly, the use of porous materials in the coolant passage of a regenerative cooled nozzle such as the space shuttle engines and nuclear rocket engines would increase the heat flux capability of the engine, reduce the maximum wall temperature, and thereby reduce the possibility of engine failure due to thermal stresses.

References

1 Koh, J. C. Y., and Colony, R., "Analysis of Cooling Effectiveness for Porous Materials in a Coolant Passage," JOURNAL OF HEAT TRANSFER, TRANS. ASME, Series C, Vol. 96, No. 3, Aug. 1974, pp. 324–330.

2 Eckert, E. R. G., and Drake, R. M., Jr., *Heat and Mass Transfer*, McGraw-Hill, New York, 1959.

The Effects of Scattering of Radiation Upon Compressible Boundary Layer Flow Over an Adiabatic Flat Plate

M. A. Boles[1] and M. N. Özişik[2]

Most investigations of radiating boundary layer flows have been restricted to absorbing and emitting fluids and the effects of scattering have been neglected because of the difficulty arising from the computation of the radiative heat flux term in the energy equation. Many investigators have considered approximate expressions for the radiative heat flux vector. Novotny and Yang [1][3] considered the optically thick limit approximation for boundary layer flow over a flat plate. The optically thin limit approximation has been used in the radiating boundary layer flow by such investigators as Cess [2], Smith and Hassan [3], and Tabaczynski and Kenney [4].

Oliver and McFadden [5] and Taitel and Hartnett [6] used iterative approaches to solve the problem of radiative interactions with boundary layer flows of absorbing and emitting fluids over flat plates. The former investigators were concerned with an isothermal flat plate, while the latter ones considered an adiabatic flat plate. Recently, Cheng and Özişik [7] included the effects of scattering in the problem of interaction of radiation with free convection boundary layer flow. In the present study the effects of scattering of radiation upon an absorbing, emitting, isotropically scattering, compressible laminar boundary layer flow over an adiabatic flat plate is investigated by treating the radiation part of the problem exactly with the normal-mode-expansion technique.

Consider the steady laminar boundary layer flow of an absorbing, emitting, isotropically scattering, compressible fluid over a flat plate as illustrated in Fig. 1. The wall is impervious to flow, and adiabatic, the temperature T_0, and the velocity u_∞ of the external flow are uniform. The continuity, momentum, and energy equations are transformed into [8]

$$\frac{d^3f}{d\eta^3} + \frac{1}{2} f \frac{d^2f}{d\eta^2} = 0 \tag{1}$$

$$\frac{1}{\Pr} \frac{\partial^2\theta}{\partial\eta^2} + \frac{1}{2} f \frac{\partial\theta}{\partial\eta} = \frac{df}{d\eta} \xi \frac{\partial\theta}{\partial\xi} + \sqrt{\frac{\xi}{N\Pr}} \frac{\partial Q^r}{\partial\eta} - E_\infty \left(\frac{d^2f}{d\eta^2}\right)^2 \tag{2}$$

subject to the boundary conditions

$$f = \frac{df}{d\eta} = 0 \text{ at } \eta = 0, \tag{3a}$$

$$\frac{df}{d\eta} = 1 \text{ at } \eta \longrightarrow \infty, \tag{3b}$$

$$\frac{q_w}{4n_0^2\sigma T_0^4} = -\sqrt{\frac{N}{\xi \Pr}} \frac{\partial\theta}{\partial\eta} + Q^r = 0 \quad \text{at } \eta = 0, \tag{3c}$$

$$\theta = 1 \quad \text{at } \eta \longrightarrow \infty, \tag{3d}$$

$$\theta = \theta^*(\eta) \quad \text{at } \xi = 0. \tag{3e}$$

where $\theta^*(\eta)$ is the solution of the foregoing problem for nonradiating flow. The foregoing formulation implies that the thermal conductivity k and the viscosity μ vary linearly with the temperature. Other variables are defined as

[1] Assist. Professor, Department of Aerospace and Mechanical Engineering, Indiana Institute of Technology, Fort Wayne, Ind.

[2] Professor, Department of Mechanical and Aerospace Engineering, North Carolina State University, Raleigh, N. C.

[3] Numbers in brackets designate References at end of technical brief.

Contributed by the Heat Transfer Division of THE AMERICAN SOCIETY OF MECHANICAL ENGINEERS. Manuscript received by the Heat Transfer Division November 27, 1974.

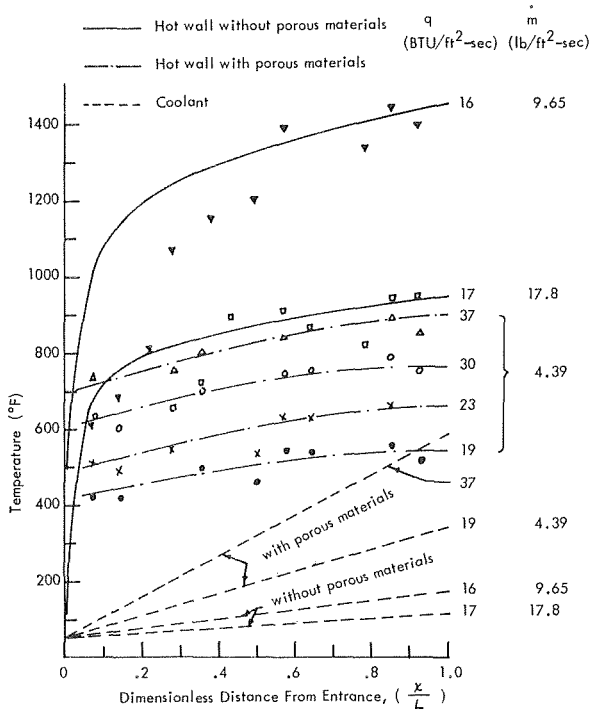

Fig. 4 Effects of porous materials in coolant passage on temperature

(b) For approximately fixed maximum hot wall temperature: the wall heat flux is again increased and a decrease of coolant flux is obtained due to the porous material.

These two comparisons can be found in Figs. 3 and 4. Fig. 3 shows that, for a fixed coolant flux of 9.65 lb/ft²-s, the wall heat flux was increased from 16 to 20 Btu/ft²-s while the maximum wall temperature was reduced from 1450°F to 350°F due to the packing of porous material in the coolant passage. On the other hand, Fig. 4 shows that, for a fixed maximum wall temperature from 900°F to 950°F, the wall heat flux was increased from 17 to 37 Btu/ft²-s while the coolant flux was reduced from 17.8 to 4.39 lb/ft²-s. Thus, the cooling effectiveness was indeed increased by several times by the packing of porous materials in the coolant passage.

Further Enhancement of Cooling Effectiveness

The cooling effectiveness can further be enhanced by the elimination of interface resistance between the wall and the porous material and by use of high conductivity porous material and high conductivity wall material.

Application of the Cooling Scheme

Clearly, the use of porous materials in the coolant passage of a regenerative cooled nozzle such as the space shuttle engines and nuclear rocket engines would increase the heat flux capability of the engine, reduce the maximum wall temperature, and thereby reduce the possibility of engine failure due to thermal stresses.

References

1 Koh, J. C. Y., and Colony, R., "Analysis of Cooling Effectiveness for Porous Materials in a Coolant Passage," JOURNAL OF HEAT TRANSFER, TRANS. ASME, Series C, Vol. 96, No. 3, Aug. 1974, pp. 324–330.

2 Eckert, E. R. G., and Drake, R. M., Jr., *Heat and Mass Transfer*, McGraw-Hill, New York, 1959.

The Effects of Scattering of Radiation Upon Compressible Boundary Layer Flow Over an Adiabatic Flat Plate

M. A. Boles[1] and M. N. Özişik[2]

Most investigations of radiating boundary layer flows have been restricted to absorbing and emitting fluids and the effects of scattering have been neglected because of the difficulty arising from the computation of the radiative heat flux term in the energy equation. Many investigators have considered approximate expressions for the radiative heat flux vector. Novotny and Yang [1][3] considered the optically thick limit approximation for boundary layer flow over a flat plate. The optically thin limit approximation has been used in the radiating boundary layer flow by such investigators as Cess [2], Smith and Hassan [3], and Tabaczynski and Kenney [4].

Oliver and McFadden [5] and Taitel and Hartnett [6] used iterative approaches to solve the problem of radiative interactions with boundary layer flows of absorbing and emitting fluids over flat plates. The former investigators were concerned with an isothermal flat plate, while the latter ones considered an adiabatic flat plate. Recently, Cheng and Özişik [7] included the effects of scattering in the problem of interaction of radiation with free convection boundary layer flow. In the present study the effects of scattering of radiation upon an absorbing, emitting, isotropically scattering, compressible laminar boundary layer flow over an adiabatic flat plate is investigated by treating the radiation part of the problem exactly with the normal-mode-expansion technique.

Consider the steady laminar boundary layer flow of an absorbing, emitting, isotropically scattering, compressible fluid over a flat plate as illustrated in Fig. 1. The wall is impervious to flow, and adiabatic, the temperature T_0, and the velocity u_∞ of the external flow are uniform. The continuity, momentum, and energy equations are transformed into [8]

$$\frac{d^3f}{d\eta^3} + \frac{1}{2} f \frac{d^2f}{d\eta^2} = 0 \tag{1}$$

$$\frac{1}{\Pr} \frac{\partial^2\theta}{\partial\eta^2} + \frac{1}{2} f \frac{\partial\theta}{\partial\eta} = \frac{df}{d\eta} \xi \frac{\partial\theta}{\partial\xi} + \sqrt{\frac{\xi}{N\Pr}} \frac{\partial Q^r}{\partial\eta} - E_\infty \left(\frac{d^2f}{d\eta^2}\right)^2 \tag{2}$$

subject to the boundary conditions

$$f = \frac{df}{d\eta} = 0 \text{ at } \eta = 0, \tag{3a}$$

$$\frac{df}{d\eta} = 1 \text{ at } \eta \longrightarrow \infty, \tag{3b}$$

$$\frac{q_w}{4n_0^2\sigma T_0^4} = -\sqrt{\frac{N}{\xi \Pr}} \frac{\partial\theta}{\partial\eta} + Q^r = 0 \quad \text{at } \eta = 0, \tag{3c}$$

$$\theta = 1 \quad \text{at } \eta \longrightarrow \infty, \tag{3d}$$

$$\theta = \theta^*(\eta) \quad \text{at } \xi = 0. \tag{3e}$$

where $\theta^*(\eta)$ is the solution of the foregoing problem for nonradiating flow. The foregoing formulation implies that the thermal conductivity k and the viscosity μ vary linearly with the temperature. Other variables are defined as

[1] Assist. Professor, Department of Aerospace and Mechanical Engineering, Indiana Institute of Technology, Fort Wayne, Ind.

[2] Professor, Department of Mechanical and Aerospace Engineering, North Carolina State University, Raleigh, N. C.

[3] Numbers in brackets designate References at end of technical brief.

Contributed by the Heat Transfer Division of THE AMERICAN SOCIETY OF MECHANICAL ENGINEERS. Manuscript received by the Heat Transfer Division November 27, 1974.

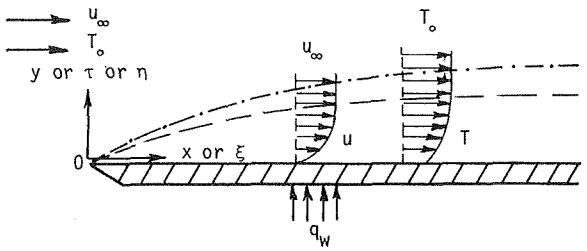

Fig. 1 Boundary layer flow of a radiating gas over a flat plate

$$N = \frac{k_0\beta_0}{4n_0^2\sigma T_0^3}, \quad \tau = \sqrt{\xi N \Pr \eta}, \quad \xi = \frac{4n_0^2\sigma T_0^3\beta_0 x}{\rho_0 c_p u_\infty} \tag{4}$$

where n_0 is the refractive index and β_0 is the extinction coefficient.

Clearly, a relation defining the dimensionless radiative heat flux term Q^r is needed to solve the energy equation; Q^r is obtained from the solution of the equation of radiative transfer in plane parallel medium for an absorbing, emitting, and isotropically scattering medium. The radiation part of the problem is solved with the normal-mode expansion technique [9, 10] by following a procedure described in references [11, 12].

The energy equation was reduced from a partial differential equation to an ordinary differential equation in the η-direction by replacing the partial derivative of the temperature with respect to ξ by two- and three-point finite difference formulas, where the three-point formula allowed for variable ξ step size.

The momentum equation and the resulting energy equation were integrated in the η-direction by a Runge-Kutta method. The integration scheme is started by setting $\xi = 0$ and solving the resulting energy equation for the nonradiating temperature distribution by setting $\partial\theta/\partial\eta|_{\eta=0} = 0$ and guessing the values of $\theta|_{\eta=0}$.

Results

The effects of scattering on the temperature profile in the boundary layer for the adiabatic wall condition are presented in Fig. 2. The temperature profile is plotted as a function of η for several values of the parameter ξ for Pr = 1.0, E = 2.0, ϵ_w = 1, and N = 0.5. The temperature profile for ξ = 0 characterizes the case without radiation. The highest wall temperature occurs with the nonradiative case; radiation reduces temperature in the boundary layer due to viscous energy dissipation. As the value of ξ is increased, the temperature is reduced and a positive temperature gradient with respect to η is established at the wall; the temperature gradient at the wall is controlled by a balance between the conductive heat flux and the radiative heat flux at the wall. The scattering reduces the effects of radiation; that is, the temperature profiles with scattering are shifted toward the temperature profile for nonradiating flow. The nonscattering temperature profiles agree with those presented by Taitel and Hartnett [6] for an absorbing and emitting fluid. Included on this figure is the solution of this problem using the optically thick limit approximation. Clearly, significant error is introduced in the temperature distribution especially for small values of η and ξ with this approximation. In the curve for $\xi = 0$ the maximum occurs at the wall because it corresponds to nonradiative case. The maximum also occurs at the wall for the optically thick limit approximation, because this approximation does not take into account the radiation from the boundary surface, hence the solution is governed by the boundary condition for the energy equation which specifies an adiabatic wall. For the cases $\xi \neq 0$, the maximum does not occur at the wall because the net heat flux at the wall is equal to the sum of radiative and conductive heat fluxes; that is, since the boundary condition for the radiation problem includes the emission of radiation from the wall into the fluid, there must be a conductive heat flux into the wall if the adiabatic wall condition is to be satisfied.

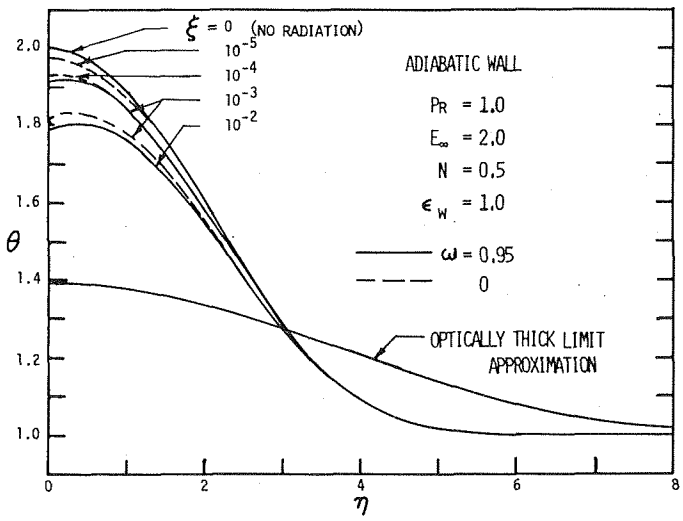

Fig. 2 Effect of scattering on temperature distribution in boundary layer flow over an adiabatic flat plate

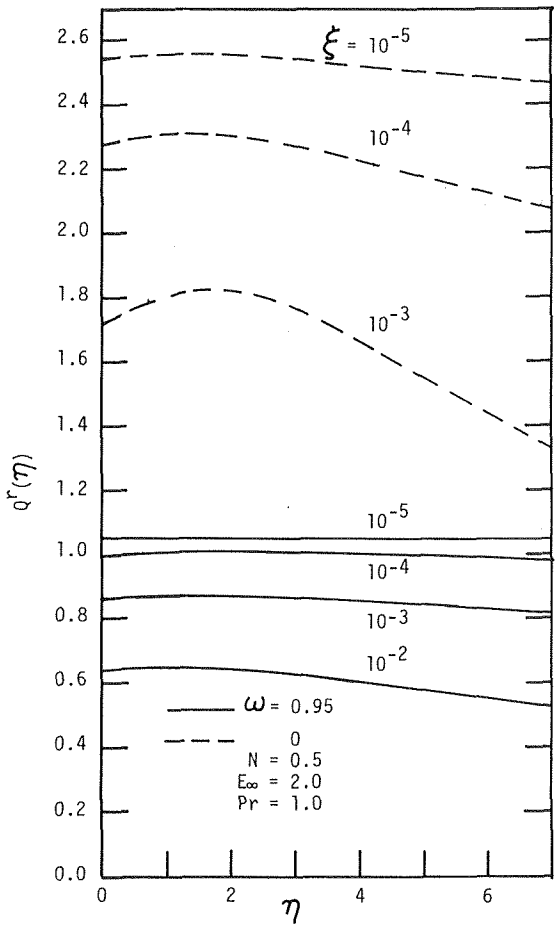

Fig. 3 Effect of scattering on net radiative heat flux in boundary layer flow over an adiabatic flat plate

Fig. 3 shows the distribution of the dimensionless radiative heat flux in the medium at various axial positions ξ along the plate with and without scattering. The nonscattering value of the dimensionless radiative heat flux is almost twice as large as that of the scattering case with ω = 0.95.

Table 1 The effects of scattering on temperature gradient and dimensionless net radiative heat flux at wall for laminar flow over an adiabatic flat plate for $N = 0.5$, $Pr = 1.0$, $E_\infty = 2.0$, $\epsilon_w = 1.0$

ξ	Scattering $\omega = 0.95$		Non-scattering $\omega = 0$	
	$\left.\frac{\partial\theta}{\partial\eta}\right\|_{\eta=0}$	$Q^r\|_{\eta=0}$	$\left.\frac{\partial\theta}{\partial\eta}\right\|_{\eta=0}$	$Q^r\|_{\eta=0}$
10^{-5}	0.0047	1.057	0.0114	2.546
10^{-4}	0.0142	1.006	0.0322	2.278
10^{-3}	0.0518	0.8200	0.0772	1.726
10^{-2}	0.0910	0.6439		

Table 1 lists the values of the derivative of temperature and the net radiative heat flux at the wall at different positions along the plate for the nonscattering ($\omega = 0$) and scattering ($\omega = 0.95$) cases.

Acknowledgment

This work was supported in part by the National Science Foundation through Grant GK-41605

References

1 Novotny, J. L., and Yang, K. T., "The Interaction of Thermal Radiation in Optically Thick Boundary Layers," ASME Paper No. 67-HT-9.

2 Cess, R. D., "Radiation Effects Upon Boundary-Layer Flow of an Absorbing Gas," JOURNAL OF HEAT TRANSFER, TRANS. ASME, Series C, Vol. 86, 1964, pp. 469–475.

3 Smith, A. M., and Hassan, H. A., "Non-Gray Radiation Effects on the Boundary Layer at Low Eckert Numbers," ASME Paper No. 66-WA/HT-35.

4 Tabaczynski, R. J., and Kennedy, L. A., "Thermal Radiation Effects in Laminar Boundary-Layer Flow," *AIAA Journal*, Vol. 5, 1967, pp. 1893–1894.

5 Oliver, C. C., and McFadden, P. W., "The Interaction of Radiation and Convection in the Laminar Boundary Layer," JOURNAL OF HEAT TRANSFER, TRANS. ASME, Series C, Vol. 88, 1966, pp. 205–213.

6 Taitel, Y., and Hartnett, J. P., "Equilibrium Temperatures in a Boundary Layer Flow Over a Flat Plate of Absorbing-Emitting Gas," ASME Paper No. 66-WA/HT-48.

7 Cheng, E. H., and Özişik, M. N., "Radiation With Free Convection in an Absorbing, Emitting and Scattering Medium," *International Journal of Heat and Mass Transfer*, Vol. 15, 1972, pp. 1243–1252.

8 Özişik, M. N., *Radiative Transfer*, Wiley, New York, 1973.

9 Case, K. M., "Elementary Solutions of the Transport Equation and Their Applications," *Ann. Phys.*, Vol. 9, 1960, pp. 1–23.

10 Case, K. M., and Zeifel, P. F., *Linear Transport Theory*, Addison-Wesley, Reading, Mass., 1967.

11 Özişik, M. N., and Siewert, C. E., "On the Normal-Mode-Expansion Technique for Radiative Transfer in a Scattering, Absorbing and Emitting Slab With Reflecting Boundaries," *International Journal of Heat and Mass Transfer*, Vol. 12, 1969, pp. 611–620.

12 Beach, H. L., Özişik, M. N., and Siewert, C. E., "Radiative Transfer in Linearly Anisotropic-Scattering, Conservative and Non-Conservative Slabs With Reflective Boundaries," *International Journal of Heat and Mass Transfer*, Vol. 14, 1971, pp. 1551–1565.

Design and Construction of a Low-Velocity Boundary-Layer Temperature Probe[1]

B. F. Blackwell[2] and R. J. Moffat[3]

Introduction

When a temperature-sensing instrument such as a thermocouple is immersed in a fluid, the indicated temperature will usually differ from the true temperature of the undisturbed fluid, even if the presence of the sensor does not alter the flow field. Heat conduction along the thermoelectric wires, which is a common source of thermocouple error, can be particularly severe in the small probes used in turbulent boundary-layer measurements because the sensing element must operate in regions of very steep temperature gradients. This technical brief shows that conduction errors can be kept within acceptable limits by the proper choice of thermoelectric pair and/or probe geometry and that turbulent boundary-layer temperature profiles can be measured accurately.

Analysis

Blackwell, Kays, and Moffat sought, in an experimental turbulent boundary-layer study [1],[4] to measure mean temperature profiles inside the logarithmic portion of the boundary layer to determine the turbulent Prandtl number in this region. Because the extent of this region may be only a few thousandths of an inch, the probe for performing the measurements had to be extremely small in design. The basic probe configuration chosen was a thermocouple with two wires of equal diameter and with the junction formed by butt welding. A schematic of the probe is shown in Fig. 1, along with a completed probe assembly.

The geometrical characteristics (L_1, L_2, D) and thermal conductivity (k_1, k_2) of the thermoelectric elements were chosen with the intent that heat-conduction errors would be kept below an acceptable level. This was accomplished by analyzing the probe as a one-dimensional fin with convection from the surface and a specified (and equal) temperature at the two ends. From the analysis of Davis [2] or Blackwell, et al. [1], it can be shown that the nondimensional junction temperature can be expressed as

$$\theta_j = \frac{T_j - T_f}{T_0 - T_f} = \frac{\kappa \sinh(\kappa p_2) + \sinh(p_2)}{\kappa \sinh(\kappa p_2)\cosh(p_2) + \sinh(p_2)\cosh(\kappa p_2)} \tag{1}$$

where the fin parameters are defined by

$$p_{1,2} = 2\sqrt{\frac{hD}{k_{1,2}}}\,\frac{L_{1,2}}{D} \tag{2}$$

and

$$\kappa = \frac{p_1}{p_2} = \sqrt{\frac{k_2}{k_1}}\,\frac{L_1}{L_2} \tag{3}$$

Here, h is the convective heat transfer coefficient. All temperatures in equation (1) are defined with the aid of Fig. 1.

Up to this point in the analysis, it has been assumed that κ can take on a continuous range of values. Because only certain materials (k_1, k_2) are functional as a thermocouple, the continuous property of κ depends on whether the length ratio L_2/L_1 can assume a continuous range of values (see equation (3)). In some applications, it might be desirable to specify L_2/L_1 on some basis other than the elimination of conduction errors. For example, to eliminate interference problems, the thermocouple junction should be

[1] This work was supported by NASA Grant NGL-05-020-134 and, in part, by ERDA.

[2] Member of Technical Staff, Aerodynamics Projects Department, Sandia Laboratories, Albuquerque, N. M.

[3] Director of Thermosciences Division, Mechanical Engineering Department, Stanford University, Stanford, Calif.

[4] Numbers in brackets designate References at end of technical brief.

Contributed by the Heat Transfer Division of THE AMERICAN SOCIETY OF MECHANICAL ENGINEERS. Manuscript received by the Heat Transfer Division August 5, 1974.

Table 1 The effects of scattering on temperature gradient and dimensionless net radiative heat flux at wall for laminar flow over an adiabatic flat plate for $N = 0.5$, $Pr = 1.0$, $E_\infty = 2.0$, $\epsilon_w = 1.0$

ξ	Scattering $\omega = 0.95$		Non-scattering $\omega = 0$	
	$\left.\frac{\partial\theta}{\partial\eta}\right\|_{\eta=0}$	$Q^r\|_{\eta=0}$	$\left.\frac{\partial\theta}{\partial\eta}\right\|_{\eta=0}$	$Q^r\|_{\eta=0}$
10^{-5}	0.0047	1.057	0.0114	2.546
10^{-4}	0.0142	1.006	0.0322	2.278
10^{-3}	0.0518	0.8200	0.0772	1.726
10^{-2}	0.0910	0.6439		

Table 1 lists the values of the derivative of temperature and the net radiative heat flux at the wall at different positions along the plate for the nonscattering ($\omega = 0$) and scattering ($\omega = 0.95$) cases.

Acknowledgment

This work was supported in part by the National Science Foundation through Grant GK-41605

References

1 Novotny, J. L., and Yang, K. T., "The Interaction of Thermal Radiation in Optically Thick Boundary Layers," ASME Paper No. 67-HT-9.

2 Cess, R. D., "Radiation Effects Upon Boundary-Layer Flow of an Absorbing Gas," JOURNAL OF HEAT TRANSFER, TRANS. ASME, Series C, Vol. 86, 1964, pp. 469–475.

3 Smith, A. M., and Hassan, H. A., "Non-Gray Radiation Effects on the Boundary Layer at Low Eckert Numbers," ASME Paper No. 66-WA/HT-35.

4 Tabaczynski, R. J., and Kennedy, L. A., "Thermal Radiation Effects in Laminar Boundary-Layer Flow," *AIAA Journal*, Vol. 5, 1967, pp. 1893–1894.

5 Oliver, C. C., and McFadden, P. W., "The Interaction of Radiation and Convection in the Laminar Boundary Layer," JOURNAL OF HEAT TRANSFER, TRANS. ASME, Series C, Vol. 88, 1966, pp. 205–213.

6 Taitel, Y., and Hartnett, J. P., "Equilibrium Temperatures in a Boundary Layer Flow Over a Flat Plate of Absorbing-Emitting Gas," ASME Paper No. 66-WA/HT-48.

7 Cheng, E. H., and Özişik, M. N., "Radiation With Free Convection in an Absorbing, Emitting and Scattering Medium," *International Journal of Heat and Mass Transfer*, Vol. 15, 1972, pp. 1243–1252.

8 Özişik, M. N., *Radiative Transfer*, Wiley, New York, 1973.

9 Case, K. M., "Elementary Solutions of the Transport Equation and Their Applications," *Ann. Phys.*, Vol. 9, 1960, pp. 1–23.

10 Case, K. M., and Zeifel, P. F., *Linear Transport Theory*, Addison-Wesley, Reading, Mass., 1967.

11 Özişik, M. N., and Siewert, C. E., "On the Normal-Mode-Expansion Technique for Radiative Transfer in a Scattering, Absorbing and Emitting Slab With Reflecting Boundaries," *International Journal of Heat and Mass Transfer*, Vol. 12, 1969, pp. 611–620.

12 Beach, H. L., Özişik, M. N., and Siewert, C. E., "Radiative Transfer in Linearly Anisotropic-Scattering, Conservative and Non-Conservative Slabs With Reflective Boundaries," *International Journal of Heat and Mass Transfer*, Vol. 14, 1971, pp. 1551–1565.

Design and Construction of a Low-Velocity Boundary-Layer Temperature Probe[1]

B. F. Blackwell[2] and R. J. Moffat[3]

Introduction

When a temperature-sensing instrument such as a thermocouple is immersed in a fluid, the indicated temperature will usually differ from the true temperature of the undisturbed fluid, even if the presence of the sensor does not alter the flow field. Heat conduction along the thermoelectric wires, which is a common source of thermocouple error, can be particularly severe in the small probes used in turbulent boundary-layer measurements because the sensing element must operate in regions of very steep temperature gradients. This technical brief shows that conduction errors can be kept within acceptable limits by the proper choice of thermoelectric pair and/or probe geometry and that turbulent boundary-layer temperature profiles can be measured accurately.

Analysis

Blackwell, Kays, and Moffat sought, in an experimental turbulent boundary-layer study [1],[4] to measure mean temperature profiles inside the logarithmic portion of the boundary layer to determine the turbulent Prandtl number in this region. Because the extent of this region may be only a few thousandths of an inch, the probe for performing the measurements had to be extremely small in design. The basic probe configuration chosen was a thermocouple with two wires of equal diameter and with the junction formed by butt welding. A schematic of the probe is shown in Fig. 1, along with a completed probe assembly.

The geometrical characteristics (L_1, L_2, D) and thermal conductivity (k_1, k_2) of the thermoelectric elements were chosen with the intent that heat-conduction errors would be kept below an acceptable level. This was accomplished by analyzing the probe as a one-dimensional fin with convection from the surface and a specified (and equal) temperature at the two ends. From the analysis of Davis [2] or Blackwell, et al. [1], it can be shown that the nondimensional junction temperature can be expressed as

$$\theta_j = \frac{T_j - T_f}{T_0 - T_f} = \frac{\kappa \sinh(\kappa p_2) + \sinh(p_2)}{\kappa \sinh(\kappa p_2)\cosh(p_2) + \sinh(p_2)\cosh(\kappa p_2)} \tag{1}$$

where the fin parameters are defined by

$$p_{1,2} = 2\sqrt{\frac{hD}{k_{1,2}}}\,\frac{L_{1,2}}{D} \tag{2}$$

and

$$\kappa = \frac{p_1}{p_2} = \sqrt{\frac{k_2}{k_1}}\,\frac{L_1}{L_2} \tag{3}$$

Here, h is the convective heat transfer coefficient. All temperatures in equation (1) are defined with the aid of Fig. 1.

Up to this point in the analysis, it has been assumed that κ can take on a continuous range of values. Because only certain materials (k_1, k_2) are functional as a thermocouple, the continuous property of κ depends on whether the length ratio L_2/L_1 can assume a continuous range of values (see equation (3)). In some applications, it might be desirable to specify L_2/L_1 on some basis other than the elimination of conduction errors. For example, to eliminate interference problems, the thermocouple junction should be

[1] This work was supported by NASA Grant NGL-05-020-134 and, in part, by ERDA.

[2] Member of Technical Staff, Aerodynamics Projects Department, Sandia Laboratories, Albuquerque, N. M.

[3] Director of Thermosciences Division, Mechanical Engineering Department, Stanford University, Stanford, Calif.

[4] Numbers in brackets designate References at end of technical brief.

Contributed by the Heat Transfer Division of THE AMERICAN SOCIETY OF MECHANICAL ENGINEERS. Manuscript received by the Heat Transfer Division August 5, 1974.

Fig. 1 Boundary-layer probe, schematic and assembly

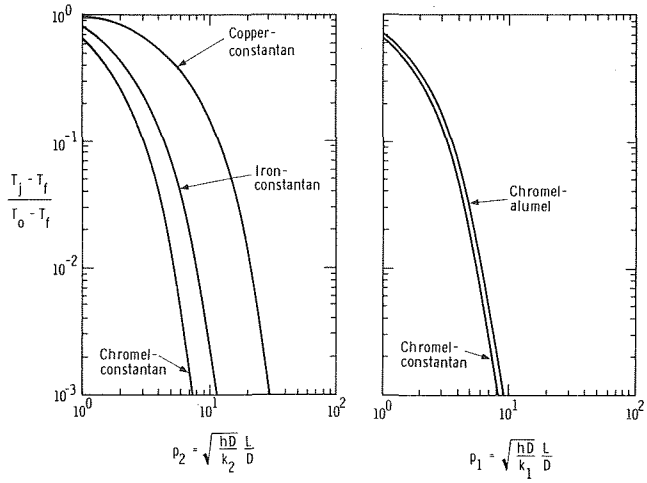

Fig. 2 Dimensionless junction temperature for various thermocouple pairs

located as far as possible from either probe support. For this situation, one might choose L_2/L_1, approximately unity. In this case, κ becomes a discrete parameter that depends only on the thermal conductivity of the two thermoelectric materials.

By restricting the analysis to some of the more common thermocouple materials, a useful design curve can be obtained. Fig. 2*(a)* presents the thermocouple junction temperature as a function of the fin parameter p_2 for three thermocouples, each with constantan as the negative element. The thermal conductivity values used are presented in Table 1. The subscripts 1 and 2 refer to the first- and second-named elements of the thermocouple, respectively. Of the three thermocouples in Fig. 2*(a)*, chromel-constantan is the best from the standpoint of conduction losses. In fact, copper-constantan will require an aspect ratio *(L/D)* approximately 4 times that of chromel-constantan if the same value of nondimensional junction temperature θ_j is to be maintained.

In Fig. 2*(b)*, a chromel-alumel probe is compared with a chromel-constantan probe. Because chromel (k_1) is common to both, θ_j is presented as a function of p_1 to allow a more direct comparison of the two thermocouple pairs. Based on these data, the analysis shows that the chromel-constantan probe will require a smaller aspect ratio *(L/D)* if a given value of junction temperature is to be maintained.

Table 1 Thermal conductivity data (from Benedict [3])

Thermoelectric element	k, Btu/ft s °F
Copper	0.0616
Iron	0.0096
Alumel	0.0048
Constantan	0.0038
Chromel	0.0031

On the basis of the information given in the foregoing discussion, the thermocouple material selected was chromel-constantan.[5] Commercially available 0.003-in.- (0.076-mm-) dia thermocouple wire with a Teflon insulator was butt welded to form the thermocouple junction. The electric discharge welding technique has been described by Stover [4]. After welding, the thermocouple was rolled between two pieces of flat steel to remove kinks. The sensing element was supported between two 22-gage stainless-steel hypodermic needles, and the Teflon was used to provide electrical insulation between the thermocouple wire and the stainless steel. The Teflon insulator was burned off the part of the thermocouple exposed to the gas stream. Contact between the bare thermocouple wire and the hypodermic needle occurred only at the end of the needle. Because the two needles were electrically isolated from each other, this contact did not form a closed loop, which would have introduced an additional emf. The hypodermic needles were shaped to give some spring to the probe assembly when it contacted the wall. A completed probe assembly is shown in Fig. 1.

The probe span *(L)* was chosen with the aid of the design curves in Fig. 2. It was estimated that the minimum velocity to be encountered in the laminar sublayer (in air) would be approximately 2 ft/s (0.6 m/s), and the experimenters wanted to keep the dimensionless junction temperature θ_j below 0.005. The data in Fig. 2 indicate that a span of 0.5 in. (1.27 cm) is adequate to satisfy the foregoing condition on θ_j for a chromel-constantan probe.

[5] Of the four thermocouples considered in this paper, the chromel-constantan combination has the steepest emf-versus-temperature relationship.

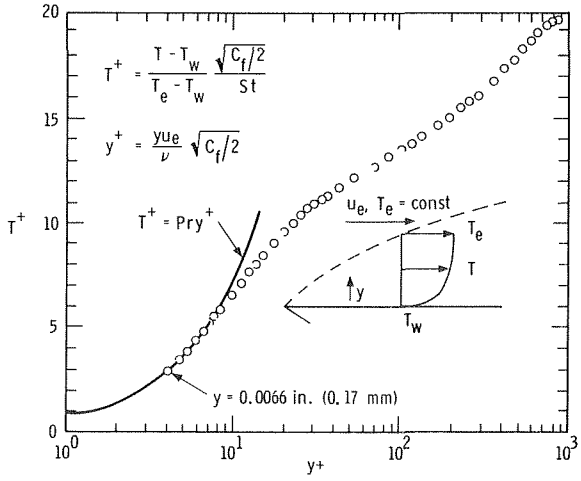

Fig. 3 Comparison of experimental turbulent boundary-layer temperature data with laminar sublayer equation

Experimental Versus Theoretical Results

Fig. 3 presents a typical turbulent boundary-layer temperature profile (in wall coordinates) taken from the study of Blackwell, et al. [1]. The Stanton number for this data set was obtained from an energy balance technique [1], and the skin friction was obtained by a hot wire anemometer technique [5]. Also shown is the theoretical laminar sublayer equation $T^+ = \Pr\, y^+$. The laminar sublayer equation and experimental results are in close agreement. It is more difficult to make accurate temperature measurements in the laminar sublayer than in any other region of the boundary layer. The fact that experimental data and theory agree in this region indicates that the probe is essentially free of conduction errors.

Conclusions

From the standpoint of conduction losses, chromel-constantan is the best of the four thermocouples considered for the configuration in which the junction is located in the center of the span.

References

1 Blackwell, B. F., Kays, W. M., and Moffat, R. J., "The Turbulent Boundary Layer on a Porous Plate: An Experimental Study of the Heat Transfer Behavior With Adverse Pressure Gradients," HMT-16, Thermosciences Division, Mechanical Engineering Department, Stanford University, Stanford, Calif., Aug. 1972.

2 Davis, M. R., "General Response of Resistance Thermometers and Thermocouples in Gases at Low Pressure," *AIAA Journal*, Vol. 10, No. 4, Apr. 1972, pp. 546–547.

3 Benedict, R. P., *Fundamentals of Temperature, Pressure, and Flow Measurements*, Wiley, New York, 1969, p. 151.

4 Stover, C. M., "Method of Butt Welding Small Thermocouples 0.001 to 0.010 Inch in Diameter," *The Review of Scientific Instruments*, Vol. 31, No. 6, June 1960, pp. 605–608.

5 Andersen, P. S., Kays, W. M., and Moffat, R. J., "The Turbulent Boundary Layer on a Porous Plate: An Experimental Study of the Fluid Mechanics for Adverse Free-Stream Pressure Gradients," HMT-15, Thermosciences Division, Mechanical Engineering Department, Stanford University, Stanford, Calif., May 1972.

A Note on Viscous Fluids in a Rectangular Duct

T. Govindarajulu[1]

Recently Butler and McKee[2] considered the flow of temperature-dependent viscous fluids in heated rectangular ducts. They treated the case when the thermal conductivity and viscosity of the fluid vary, respectively, as T^{-1} and T^{-n}, T being the fluid temperature. In this note, it is shown that the problem admits a wide class of property variations with temperature, the governing equation remaining the same in form.

The equations of energy and flow of an incompressible fluid in a rectangular duct bounded by the planes $x = 0$, $x = a$ and $y = 0$, $y = b$ may be written in the form

$$\frac{d}{d\eta}\left(k\frac{d\theta}{d\eta}\right) = 0 \tag{1}$$

and

$$E^2\frac{\partial}{\partial\zeta}\left(\bar{\mu}\frac{\partial u}{\partial\zeta}\right) + \frac{\partial}{\partial\eta}\left(\bar{\mu}\frac{\partial u}{\partial\eta}\right) + 1 = 0 \tag{2}$$

The new variables are related to the old ones by

$$\zeta = x/a, \quad \eta = y/b, \quad \bar{\mu} = \mu/\mu_1, \quad \bar{k} = k/k_1, \quad \theta = T/T_1$$
$$u = \mu_1 v/(-b^2\frac{\partial p}{\partial z}) \tag{3}$$

Here E is the aspect ratio b/a and the reference state indicated by the suffix 1 is taken at the lower wall. The nondimensional variables (3), except for u, are the same as in the footnote.[2] The side walls $x = 0$ and $x = a$ are insulated thus resulting in one-dimensional heat equation (1).

Set

$$h = n\int_0^\theta \bar{k}(\lambda)d\lambda, \quad \bar{\mu} = e^{-h} \tag{4}$$

The case treated in the footnote[2] is obtained by putting $\bar{K} = \theta^{-1}$ in equation (4). Another case of interest is given by $\bar{K} = 1$ and $\bar{\mu} = e^{-n(\theta-1)}$. On using the transformations (4), equation (1) reduces to

$$\frac{d^2h}{d\eta^2} = 0 \tag{5}$$

This gives $h = A\eta$, where

$$A = n\int_1^{T_2/T_1} \bar{k}(\lambda)d\lambda \tag{6}$$

T_2 being the temperature of the upper wall. The temperature profile is then obtained as

$$A\eta = n\int_1^\theta \bar{k}(\lambda)d\lambda \tag{7}$$

The parameter A appearing in the temperature solution is more general than the corresponding parameter α of the footnote.[2]

The momentum equation (2) is transformed into

$$E^2\frac{\partial^2 u}{\partial\zeta^2} + \frac{\partial^2 u}{\partial\eta^2} - A\frac{\partial u}{\partial\eta} + e^{A\eta} = 0 \tag{8}$$

which is similar to equation (6) of the footnote.[2] The solution of equation (8) subject to no-slip condition at the walls can be obtained directly using the Fourier sine transform. This solution turns out to be much simpler than the one given in the footnote,[2] which was obtained by separation of the variables after effecting a transformation on the dependent variable. The solution is

$$u(\zeta,\eta) = \frac{4}{E^2\pi^3}\exp(A\eta/2)\sum_{r=1}^{\infty}\frac{1}{(2r-1)^3}\left[\exp(A\eta/2) - \frac{\exp(A/2)\sin h\omega\eta + \sin h\omega(1-\eta)}{\sin h\omega}\right]\sin(2r-1)\pi\zeta \tag{9}$$

where

$$\omega^2 = (A/2)^2 + (2r-1)^2\pi^2E^2$$

Acknowledgment

The author wishes to thank Prof. P. S. Mani Sundaram for his interest in this research.

[1] Assist. Professor of Mathematics, Regional Engineering College, Tiruchirapalli. 620015. India.

[2] Butler, H. W., and McKee, D. E., "An Exact Solution for the Flow of Temperature-Dependent Viscous Fluids in Heated Rectangular Ducts," JOURNAL OF HEAT TRANSFER, TRANS. ASME, Series C, Vol. 95, 1973, p. 555.

Contributed by the Heat Transfer Division of the American Society of Mechanical Engineers. Manuscript received by the Heat Transfer Division December 16, 1974.

Experimental Versus Theoretical Results

Fig. 3 presents a typical turbulent boundary-layer temperature profile (in wall coordinates) taken from the study of Blackwell, et al. [1]. The Stanton number for this data set was obtained from an energy balance technique [1], and the skin friction was obtained by a hot wire anemometer technique [5]. Also shown is the theoretical laminar sublayer equation $T^+ = \Pr\, y^+$. The laminar sublayer equation and experimental results are in close agreement. It is more difficult to make accurate temperature measurements in the laminar sublayer than in any other region of the boundary layer. The fact that experimental data and theory agree in this region indicates that the probe is essentially free of conduction errors.

Conclusions

From the standpoint of conduction losses, chromel-constantan is the best of the four thermocouples considered for the configuration in which the junction is located in the center of the span.

References

1 Blackwell, B. F., Kays, W. M., and Moffat, R. J., "The Turbulent Boundary Layer on a Porous Plate: An Experimental Study of the Heat Transfer Behavior With Adverse Pressure Gradients," HMT-16, Thermosciences Division, Mechanical Engineering Department, Stanford University, Stanford, Calif., Aug. 1972.

2 Davis, M. R., "General Response of Resistance Thermometers and Thermocouples in Gases at Low Pressure," *AIAA Journal*, Vol. 10, No. 4, Apr. 1972, pp. 546–547.

3 Benedict, R. P., *Fundamentals of Temperature, Pressure, and Flow Measurements*, Wiley, New York, 1969, p. 151.

4 Stover, C. M., "Method of Butt Welding Small Thermocouples 0.001 to 0.010 Inch in Diameter," *The Review of Scientific Instruments*, Vol. 31, No. 6, June 1960, pp. 605–608.

5 Andersen, P. S., Kays, W. M., and Moffat, R. J., "The Turbulent Boundary Layer on a Porous Plate: An Experimental Study of the Fluid Mechanics for Adverse Free-Stream Pressure Gradients," HMT-15, Thermosciences Division, Mechanical Engineering Department, Stanford University, Stanford, Calif., May 1972.

A Note on Viscous Fluids in a Rectangular Duct

T. Govindarajulu[1]

Recently Butler and McKee[2] considered the flow of temperature-dependent viscous fluids in heated rectangular ducts. They treated the case when the thermal conductivity and viscosity of the fluid vary, respectively, as T^{-1} and T^{-n}, T being the fluid temperature. In this note, it is shown that the problem admits a wide class of property variations with temperature, the governing equation remaining the same in form.

The equations of energy and flow of an incompressible fluid in a rectangular duct bounded by the planes $x = 0$, $x = a$ and $y = 0$, $y = b$ may be written in the form

$$\frac{d}{d\eta}\left(k\frac{d\theta}{d\eta}\right) = 0 \tag{1}$$

and

$$E^2\frac{\partial}{\partial\zeta}\left(\bar{\mu}\frac{\partial u}{\partial\zeta}\right) + \frac{\partial}{\partial\eta}\left(\bar{\mu}\frac{\partial u}{\partial\eta}\right) + 1 = 0 \tag{2}$$

The new variables are related to the old ones by

$$\zeta = x/a, \quad \eta = y/b, \quad \bar{\mu} = \mu/\mu_1, \quad \bar{k} = k/k_1, \quad \theta = T/T_1$$
$$u = \mu_1 v/(-b^2\frac{\partial p}{\partial z}) \tag{3}$$

Here E is the aspect ratio b/a and the reference state indicated by the suffix 1 is taken at the lower wall. The nondimensional variables (3), except for u, are the same as in the footnote.[2] The side walls $x = 0$ and $x = a$ are insulated thus resulting in one-dimensional heat equation (1).

Set

$$h = n\int_0^\theta \bar{k}(\lambda)d\lambda, \quad \bar{\mu} = e^{-h} \tag{4}$$

The case treated in the footnote[2] is obtained by putting $\bar{K} = \theta^{-1}$ in equation (4). Another case of interest is given by $\bar{K} = 1$ and $\bar{\mu} = e^{-n(\theta-1)}$. On using the transformations (4), equation (1) reduces to

$$\frac{d^2h}{d\eta^2} = 0 \tag{5}$$

This gives $h = A\eta$, where

$$A = n\int_1^{T_2/T_1} \bar{k}(\lambda)d\lambda \tag{6}$$

T_2 being the temperature of the upper wall. The temperature profile is then obtained as

$$A\eta = n\int_1^\theta \bar{k}(\lambda)d\lambda \tag{7}$$

The parameter A appearing in the temperature solution is more general than the corresponding parameter α of the footnote.[2]

The momentum equation (2) is transformed into

$$E^2\frac{\partial^2 u}{\partial\zeta^2} + \frac{\partial^2 u}{\partial\eta^2} - A\frac{\partial u}{\partial\eta} + e^{A\eta} = 0 \tag{8}$$

which is similar to equation (6) of the footnote.[2] The solution of equation (8) subject to no-slip condition at the walls can be obtained directly using the Fourier sine transform. This solution turns out to be much simpler than the one given in the footnote,[2] which was obtained by separation of the variables after effecting a transformation on the dependent variable. The solution is

$$u(\zeta,\eta) = \frac{4}{E^2\pi^3}\exp(A\eta/2)\sum_{r=1}^{\infty}\frac{1}{(2r-1)^3}\left[\exp(A\eta/2) - \frac{\exp(A/2)\sin h\omega\eta + \sin h\omega(1-\eta)}{\sin h\omega}\right]\sin(2r-1)\pi\zeta \tag{9}$$

where

$$\omega^2 = (A/2)^2 + (2r-1)^2\pi^2E^2$$

Acknowledgment

The author wishes to thank Prof. P. S. Mani Sundaram for his interest in this research.

[1] Assist. Professor of Mathematics, Regional Engineering College, Tiruchirapalli. 620015. India.

[2] Butler, H. W., and McKee, D. E., "An Exact Solution for the Flow of Temperature-Dependent Viscous Fluids in Heated Rectangular Ducts," JOURNAL OF HEAT TRANSFER, TRANS. ASME, Series C, Vol. 95, 1973, p. 555.

Contributed by the Heat Transfer Division of the American Society of Mechanical Engineers. Manuscript received by the Heat Transfer Division December 16, 1974.

Optimal Design of the Ranque-Hilsch Vortex Tube

Y. Soni[1] and W. J. Thomson[1]

Introduction

The Ranque-Hilsch vortex tube has been an academic novelty ever since Rudolf Hilsch [1][2] revived interest in the device at the end of the Second World War. The operation of a vortex tube can best be described by referring to Fig. 1. Pressurized inlet air is introduced to a supply manifold where it enters the tube through one or more tangential nozzles (two were used in this study). This imparts a swirling or vortex motion to the inlet gas which subsequently spirals down the tube to the right (the "hot" tube) of the inlet nozzles. A conical valve at the end of this hot tube confines the exiting fluid to regions near the outer wall and restricts the gas in the central portion of the hot tube from making a direct exit. An orifice plate with a suitable sized hole in its center is placed immediately to the left of the inlet nozzles and allows a certain portion of the fluid near the longitudinal axis to escape through the "cold" tube. With the proper conditions cold gas escapes through the cold tube (temperatures as low as −48°C have been reported [1]) and hot gas exits through the hot tube.

Through the years there have been many attempts, both theoretical [2–5] and experimental [6–8], to determine the mechanism behind its operation. Although there is some agreement on the basic phenomena [9], the level of understanding is nowhere near the point where a vortex tube can be designed without experimental trial and error procedures. Earlier attempts to characterize the vortex tube [1, 7, 8] were all based on such procedures and do not provide a basis for design.

Given the lack of theoretical knowledge on the operation of the vortex tube and the absence of systematic experimental data from previous investigators, we set out to determine the dependency of the optimum performance of a vortex tube as a function of the pertinent design parameters. Admittedly this is a pragmatic (i.e., empirical) approach but appears to be the only recourse until theory is able to provide more than a qualitative description of the governing phenomena. Because the number of variables is large and their mutual dependence was not known, we decided to employ a systematic method of experimental design. Specifically the individual experiments were stipulated according to the simplex modification [10] of the method of Evolutionary Operations, "EVOP" [11]. As is so often the case in this type of investigations, once the experimental procedure was completed, it was then possible to synthesize a methodology which can be used to design a vortex tube for a given application.

Results

The design variables which affect the performance of the vortex tube include the diameter *(D)* and length *(L)* of the hot tube, the cross-sectional areas of the inlet nozzles and the orifice, the inlet pressure *(P_I)*, and the fraction of inlet air exiting the cold end (the "cold fraction," *CF*). Two dependent variables were evaluated, the maximum difference between the inlet and cold temperature, ΔT_C, and the maximum thermodynamic efficiency, defined by

$$\eta = \frac{(\Delta T_C)C_F}{\Delta T_{IS}} \tag{1}$$

where ΔT_{IS} is the isentropic temperature drop between the inlet and ambient pressure. The optimum values of the dependent variables were arrived at by changing the design parameters according to the EVOP procedure at fixed values of the inlet pressure. The cold fraction was not included in the EVOP but was adjusted to the optimum for each experimental run. The experimental equipment had to be designed with a high degree of flexibility in order to accommodate the large number of experimental runs (over 300) and the details are given by Soni [12].

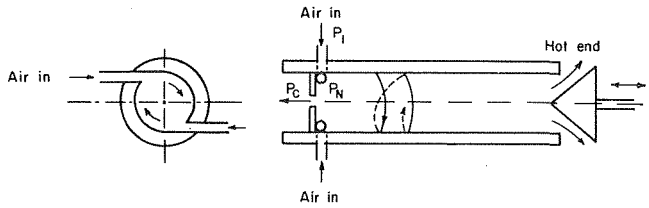

Fig. 1 Schematic of the Ranque-Hilsch vortex tube

The EVOP procedure, for inlet pressures up to 3 atm, gave ΔT_C and η values which exceeded those reported by previous investigators at the same pressures. Although this lends confidence to the success of the EVOP in arriving at optimum values, it was also found that there were a number of combinations of the design parameters which gave near optimum performance. The results indicated the following optimum design parameters for maximum ΔT_C and maximum η (given in parentheses):

A_N (nozzle area/tube area) = 0.11 ± 0.01 (0.084 ± 0.001)
A_ϕ (orifice area/tube area) = 0.08 ± 0.01 (0.145 ± 0.035)
$L/D > 45$ (>45); $D = 26$ mm (18 mm)

Design Procedure

Because of the large number of runs, an empirical regression analysis was conducted in an effort to derive a functionality between maximum ΔT_C and the independent design variables and it has been given by Soni [12]. However, in formulating the regression analysis it was discovered that one term was consistently more significant than all others. This term, β, the ratio of the actual temperature drop between the inlet and the cold end to the isentropic temperature drop through the inlet nozzle ($\Delta T_N'$) was then used to form the basis for a vortex tube design procedure. The design procedure itself is based on a trade-off between the pressure drop across the orifice and the available expansion potential of the gas through the nozzle. This then involves the selection of an optimum value of P_N for a fixed value of P_I.

To illustrate how this procedure can be utilized, let us formulate the step-by-step procedure to design a vortex tube to deliver a specified quantity of cold air at a specified temperature and pressure. We assume that the inlet pressure and temperature are known and that the inlet gas supply system is capable of delivering a quantity of air which is compatible with both the restriction that the cold fraction be between 0.1 and 0.2 and with the specified quantity of cold air. The restriction on the values of the cold fraction is based on the experimental observation that optimum ΔT_C always occurred in this range of the cold fraction. The procedure consists of:

(i) Starting with the given values of P_I, T_I, ΔT_C, and γ, we can use the empirical parameter β and the isentropic expansion equation to determine P_N

Table 1 $P_I = 7$ atm, $\Delta T_C = 81$°F

	D (mm)	D_ϕ (mm)	D_N (mm)	L/D
Predicted	19.8	5.6	4.6	45
Hilsch [1]	19.2	4.3	2.3[a]	33[b]

[a] Hilsch used only one nozzle; [b] estimated.

[1] Department of Chemical Engineering, University of Idaho, Moscow, Idaho.

[2] Numbers in brackets designate References at end of technical brief.

Contributed by the Heat Transfer Division of THE AMERICAN SOCIETY OF MECHANICAL ENGINEERS. Manuscript received by the Heat Transfer Division September 25, 1974.

$$P_N = P_I[1 - \Delta T_C/\beta T_I]^{\gamma/\gamma-1} \quad (2)$$

Soni [12] found that optimum performance was associated with a particular value of β equal to 0.43.

(ii) Given that the pressure in the cold tube, P_C, is stipulated, the pressure drop across the orifice, ΔP_ϕ, is now fixed. Using the standard equation for a sharp edged orifice [13] together with Cotton's [14] relationship for pressure recovery, the orifice diameter can be calculated from the following equations:

$$K = \frac{[2\Delta P_\phi + P_C]^2 - P_C{}^2}{4} \quad (3)$$

$$D_\phi{}^4 = \frac{1.62 W_\phi{}^2 R T_C (0.976 - 0.934 A_\phi)}{K C_V{}^2 M_W} \quad (4)$$

In these equations W_ϕ is the mass flow rate (stipulated), T_C is the cold temperature, C_V is the orifice coefficient (0.61), M_W is the molecular weight, R is the gas law constant, and A_ϕ is equal to its optimum value of 0.08.

(iii) Knowing D_ϕ, the diameter of the hot tube can be calculated using the optimum value of $A_\phi = 0.08$ and then the total cross-sectional area of the nozzles can be calculated with the optimum value of $A_N = 0.11$. The minimum length of the hot tube is set according to the criteria that $L/D > 45$.

The test of this empirically determined design procedure is to apply it to conditions beyond those investigated in this work (we were limited to a maximum P_I of 3 atm). Unfortunately only Hilsch [1] has published sufficient data at higher pressures so that we might compare our predictions with his results. This is done in Table 1 and as can be seen, the predictions are certainly reasonable with the possible exception of the nozzle diameter, D_N. It is interesting to note, however, that a calculation of the nozzle velocity used by Hilsch yields a value greater than the acoustical velocity. Thus it may be that he was limited by choke flow and perhaps could have obtained the same results using a larger nozzle diameter.

References

1 Hilsch, R., "The Use of the Expansion of Gases in a Centrifugal Field as Cooling Process," *Rev. Sci. Instr.*, Vol. 18, 1947, pp. 108–113.

2 Van Deemter, J. J., "On the Theory of the Ranque-Hilsch Cooling Effect," *Appl. Sci. Res.*, Series A, Vol. 3, 1952, pp. 174–196.

3 Lay, J. E., "An Experimental and Analytical Study of Vortex-Flow Temperature Separation by Superposition of Spiral and Axial Flow," JOURNAL OF HEAT TRANSFER, Part 2, Vol. 81, 1959, pp. 213–222.

4 Deissler, R. G., and Perlmutter, M., "Analysis of the Flow and Energy Separation in a Turbulent Vortex," *International Journal of Heat and Mass Transfer*, Vol. 1, 1960, pp. 173–191.

5 Kassner, R., and Knoernschild, E., "Pt. 1, The Laws of Shear Stress in Circular Flow," "Pt. 2, Energy Transfer in Circular Flow and Possible Applications," Wright Patterson AFB, Technical Report No. F-TR-2198-ND, 1948.

6 Hartnett, J. P., and Eckert, K. R. G., "Experimental Study of the Velocity and Temperature Distribution in a High Velocity Vortex Type Flow," *Heat Transfer & Fl. Mech. Inst.*, Stanford University Press, 1956, pp. 135–150.

7 Martynovski, V. S., and Alekseev, V. P., "Investigations of the Vortex Thermal Separation Effect for Gases and Vapors," *Soviet Phys-Tech. Phys.*, 1956, pp. 2233–2243.

8 Takahama, H., and Kawashina, K. I., "An Experimental Study of Vortex Tubes," *Memoirs of Faculty of Engineering*, Nagoya University, Vol. 12, 1960, pp. 227–245.

9 Reynolds, A. J., "Energy Flows in a Vortex Tube," *Zeitschrift Fuer Angewandte Mathematik*, Vol. 12, 1961, pp. 343–357.

10 Spendley, W., Hext, G. R., and Himsworth, F. R., "Sequential Application of Simplex Designs in Optimisation and Evolutionary Operation," *Technometrics*, Vol. 4, 1962, pp. 441–461.

11 Box, G. E. P., "Evolutionary Operation: A Method for Increasing Industrial Productivity," *Applied Statistics*, Vol. 6, 1957, pp. 3–22.

12 Soni, Y., "A Parametric Study of the Ranque-Hilsch Tube," PhD thesis.

13 McCabe, W. S., and Smith, J. C., *Unit Operations of Chemical Engineering*, McGraw-Hill, New York, 1967, pp. 225–230.

14 *Flow Measurement Symposium*, K. C. Cotton, ed., ASME, New York, 1966.

A Gas Diffusion Technique for Determining Pool Boiling Nucleation Sites

J. J. Lorenz,[1] B. B. Mikic,[2] and W. M. Rohsenow[2]

Introduction

Due to the prohibitive cost of performing boiling heat transfer tests over a wide range of fluid-surface combinations, significant motivation exists for developing simpler and more economic means to study boiling behavior. Using gas diffusion techniques to study nucleate boiling phenomena is not an entirely new idea. Westwater and Buel [1][3] studied growth of CO_2 bubbles in supersaturated water in an attempt to ascertain the influence of contact angle. By the analogy between heat and mass transfer certain generalizations were advanced regarding boiling systems. They concluded, among other things, that the effect of contact angle on bubble growth is insignificant, a fact that was merely assumed by previous investigators. One of the most novel uses of a gas diffusion experiment was devised by Brown [2] who claimed it was possible to measure the cumulative nucleation site density for a fluid surface combination with a device called the "Bubble Meter." Besides providing gross information on the nucleation site density, the gas diffusion experiment could be used as a tool for studying nucleation from individual cavities. The technique presented herein is essentially an improvement of Brown's technique.

Equilibrium Radius and Nucleation

By writing the thermodynamic equilibrium relationships for an air-water system across a spherical interface the following expression can be derived for the equilibrium interfacial radius of curvature:

$$\rho = \frac{2\sigma}{(P_a + P_v) - P_l} \quad (1)$$

where P_a and P_v are the partial pressures of air and water vapor, respectively, in the gas phase, P_l is the liquid pressure, σ is the surface tension, and ρ is the equilibrium radius of curvature.

It is a straightforward exercise to show that if dynamic effects are negligible and the thermal layer thickness is large compared to the cavity radius, the effective radius of nucleation for bubble growth by gas diffusion is precisely that for bubble growth by evaporation in nucleate boiling [3]. The superheat, ΔT, required to nucleate a bubble from a cavity of effective radius ρ is given by the following well-known expression:

$$\Delta T = \frac{2\sigma T_s V_{fg}}{h_{fg}\rho} \quad (2)$$

Apparatus and Procedure

In order to obtain effective radii for various cavity sizes it is nec-

[1] Argonne National Laboratory, Argonne, Ill.

[2] Massachusetts Institute of Technology, Cambridge, Mass.

[3] Numbers in brackets designate References at end of technical brief.

Contributed by the Heat Transfer Division of THE AMERICAN SOCIETY OF MECHANICAL ENGINEERS. Manuscript received by the Heat Transfer Division October 3, 1974.

$$P_N = P_I[1 - \Delta T_C/\beta T_I]^{\gamma/\gamma-1} \quad (2)$$

Soni [12] found that optimum performance was associated with a particular value of β equal to 0.43.

(ii) Given that the pressure in the cold tube, P_C, is stipulated, the pressure drop across the orifice, ΔP_ϕ, is now fixed. Using the standard equation for a sharp edged orifice [13] together with Cotton's [14] relationship for pressure recovery, the orifice diameter can be calculated from the following equations:

$$K = \frac{[2\Delta P_\phi + P_C]^2 - P_C{}^2}{4} \quad (3)$$

$$D_\phi{}^4 = \frac{1.62 W_\phi{}^2 R T_C (0.976 - 0.934 A_\phi)}{K C_V{}^2 M_W} \quad (4)$$

In these equations W_ϕ is the mass flow rate (stipulated), T_C is the cold temperature, C_V is the orifice coefficient (0.61), M_W is the molecular weight, R is the gas law constant, and A_ϕ is equal to its optimum value of 0.08.

(iii) Knowing D_ϕ, the diameter of the hot tube can be calculated using the optimum value of $A_\phi = 0.08$ and then the total cross-sectional area of the nozzles can be calculated with the optimum value of $A_N = 0.11$. The minimum length of the hot tube is set according to the criteria that $L/D > 45$.

The test of this empirically determined design procedure is to apply it to conditions beyond those investigated in this work (we were limited to a maximum P_I of 3 atm). Unfortunately only Hilsch [1] has published sufficient data at higher pressures so that we might compare our predictions with his results. This is done in Table 1 and as can be seen, the predictions are certainly reasonable with the possible exception of the nozzle diameter, D_N. It is interesting to note, however, that a calculation of the nozzle velocity used by Hilsch yields a value greater than the acoustical velocity. Thus it may be that he was limited by choke flow and perhaps could have obtained the same results using a larger nozzle diameter.

References

1 Hilsch, R., "The Use of the Expansion of Gases in a Centrifugal Field as Cooling Process," *Rev. Sci. Instr.*, Vol. 18, 1947, pp. 108–113.

2 Van Deemter, J. J., "On the Theory of the Ranque-Hilsch Cooling Effect," *Appl. Sci. Res.*, Series A, Vol. 3, 1952, pp. 174–196.

3 Lay, J. E., "An Experimental and Analytical Study of Vortex-Flow Temperature Separation by Superposition of Spiral and Axial Flow," JOURNAL OF HEAT TRANSFER, Part 2, Vol. 81, 1959, pp. 213–222.

4 Deissler, R. G., and Perlmutter, M., "Analysis of the Flow and Energy Separation in a Turbulent Vortex," *International Journal of Heat and Mass Transfer*, Vol. 1, 1960, pp. 173–191.

5 Kassner, R., and Knoernschild, E., "Pt. 1, The Laws of Shear Stress in Circular Flow," "Pt. 2, Energy Transfer in Circular Flow and Possible Applications," Wright Patterson AFB, Technical Report No. F-TR-2198-ND, 1948.

6 Hartnett, J. P., and Eckert, K. R. G., "Experimental Study of the Velocity and Temperature Distribution in a High Velocity Vortex Type Flow," *Heat Transfer & Fl. Mech. Inst.*, Stanford University Press, 1956, pp. 135–150.

7 Martynovski, V. S., and Alekseev, V. P., "Investigations of the Vortex Thermal Separation Effect for Gases and Vapors," *Soviet Phys-Tech. Phys.*, 1956, pp. 2233–2243.

8 Takahama, H., and Kawashina, K. I., "An Experimental Study of Vortex Tubes," *Memoirs of Faculty of Engineering*, Nagoya University, Vol. 12, 1960, pp. 227–245.

9 Reynolds, A. J., "Energy Flows in a Vortex Tube," *Zeitschrift Fuer Angewandte Mathematik*, Vol. 12, 1961, pp. 343–357.

10 Spendley, W., Hext, G. R., and Himsworth, F. R., "Sequential Application of Simplex Designs in Optimisation and Evolutionary Operation," *Technometrics*, Vol. 4, 1962, pp. 441–461.

11 Box, G. E. P., "Evolutionary Operation: A Method for Increasing Industrial Productivity," *Applied Statistics*, Vol. 6, 1957, pp. 3–22.

12 Soni, Y., "A Parametric Study of the Ranque-Hilsch Tube," PhD thesis.

13 McCabe, W. S., and Smith, J. C., *Unit Operations of Chemical Engineering*, McGraw-Hill, New York, 1967, pp. 225–230.

14 *Flow Measurement Symposium*, K. C. Cotton, ed., ASME, New York, 1966.

A Gas Diffusion Technique for Determining Pool Boiling Nucleation Sites

J. J. Lorenz,[1] B. B. Mikic,[2] and W. M. Rohsenow[2]

Introduction

Due to the prohibitive cost of performing boiling heat transfer tests over a wide range of fluid-surface combinations, significant motivation exists for developing simpler and more economic means to study boiling behavior. Using gas diffusion techniques to study nucleate boiling phenomena is not an entirely new idea. Westwater and Buel [1][3] studied growth of CO_2 bubbles in supersaturated water in an attempt to ascertain the influence of contact angle. By the analogy between heat and mass transfer certain generalizations were advanced regarding boiling systems. They concluded, among other things, that the effect of contact angle on bubble growth is insignificant, a fact that was merely assumed by previous investigators. One of the most novel uses of a gas diffusion experiment was devised by Brown [2] who claimed it was possible to measure the cumulative nucleation site density for a fluid surface combination with a device called the "Bubble Meter." Besides providing gross information on the nucleation site density, the gas diffusion experiment could be used as a tool for studying nucleation from individual cavities. The technique presented herein is essentially an improvement of Brown's technique.

Equilibrium Radius and Nucleation

By writing the thermodynamic equilibrium relationships for an air-water system across a spherical interface the following expression can be derived for the equilibrium interfacial radius of curvature:

$$\rho = \frac{2\sigma}{(P_a + P_v) - P_l} \quad (1)$$

where P_a and P_v are the partial pressures of air and water vapor, respectively, in the gas phase, P_l is the liquid pressure, σ is the surface tension, and ρ is the equilibrium radius of curvature.

It is a straightforward exercise to show that if dynamic effects are negligible and the thermal layer thickness is large compared to the cavity radius, the effective radius of nucleation for bubble growth by gas diffusion is precisely that for bubble growth by evaporation in nucleate boiling [3]. The superheat, ΔT, required to nucleate a bubble from a cavity of effective radius ρ is given by the following well-known expression:

$$\Delta T = \frac{2\sigma T_s V_{fg}}{h_{fg}\rho} \quad (2)$$

Apparatus and Procedure

In order to obtain effective radii for various cavity sizes it is nec-

[1] Argonne National Laboratory, Argonne, Ill.

[2] Massachusetts Institute of Technology, Cambridge, Mass.

[3] Numbers in brackets designate References at end of technical brief.

Contributed by the Heat Transfer Division of THE AMERICAN SOCIETY OF MECHANICAL ENGINEERS. Manuscript received by the Heat Transfer Division October 3, 1974.

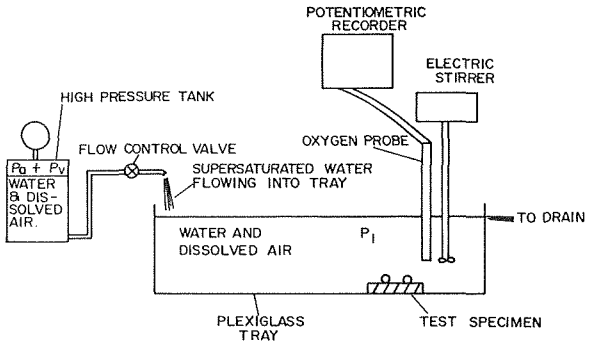

Fig. 1 Sketch of gas diffusion apparatus

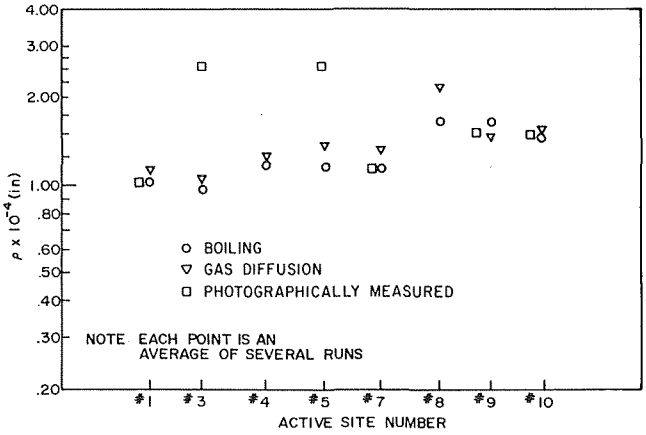

Fig. 3 Results of gas diffusion and boiling nucleation experiments for individual cavities

essary to develop a means of maintaining, controlling, and measuring different supersaturation levels. Accordingly, the apparatus shown in Fig. 1 was designed, consisting of a 15 gal glass-lined high pressure tank, 10 × 8 × 4 in. plexiglass tray, a stirring device, and an oxygen probe.

Air is vigorously bubbled at about 50 psig for 5 hr up through the bottom of the tank containing 10 gal of filtered deionized water. This operation increases the dissolved air concentration in the water to nearly that corresponding to the tank pressure. Subsequently the water is admitted into the opened plexiglass tray containing the test surface. With respect to this new condition the liquid is supersaturated and bubble growth is possible. A stirring device placed near the test surface insures that no significant concentration gradients develop. An equilibrium bulk concentration will be established between the amount of dissolved gas being supplied at the inlet, and that being lost at the drain, free surface, and consumed in bubble growth within the system. By varying the inlet flow rate the concentration can be regulated.

Various techniques for measuring the equilibrium air partial pressure were considered. Brown [2] asserted that the Bubble Meter could provide a direct measurement of the air partial pressure but later it was conclusively shown [3] that the Bubble Meter does not attain thermodynamic equilibrium due to its large diffusional resistance. In the present investigation, an alternative technique was developed employing an oxygen probe positioned near the test surface which measures the equilibrium oxygen partial pressure, P_{0_2}. In using the oxygen partial pressure to deduce the equilibrium air partial pressure, P_a, it was assumed (and verified) that nitrogen and oxygen are present in the same ratio as in common air, i.e., 3.73/1.

If the dissolved air concentration and hence P_a is sufficiently high, a large population of bubbles will nucleate and emerge from cavities on the test surface. All bubbles that appear must have initiated from cavities with effective radii greater than or equal to the equilibrium radius as specified by equation (1). At a given system condition the equilibrium partial pressure, P_a, is recorded, a ρ value is calculated from equation (1), and a photograph is taken from which the number of bubble nucleation sites per unit area, n/A, are counted. A given partial pressure level is maintained for about 5 min during which time the bubbles grow to a size which is clearly visible. Subsequently, the concentration and hence P_a is lowered stepwise by reducing the flow rate. When a steady concentration prevails the old bubbles are wiped from the surface with a teflon strip and soon a new population appears consisting of fewer bubbles. If physical wiping of the bubbles were not employed, the overall test duration would have been excessively long since the "natural" departure frequency was only about 1 per 15 min. The n/A versus ρ distribution is obtained by repeating the foregoing procedure at progressively lower concentrations until no bubbles reappear. If so desired, individual cavities can be singled out for study.

Since contact angle plays an important role in determining the effective radius, [3,4] a gas diffusion experiment must be performed with the same fluid that will be eventually boiled from the surface.

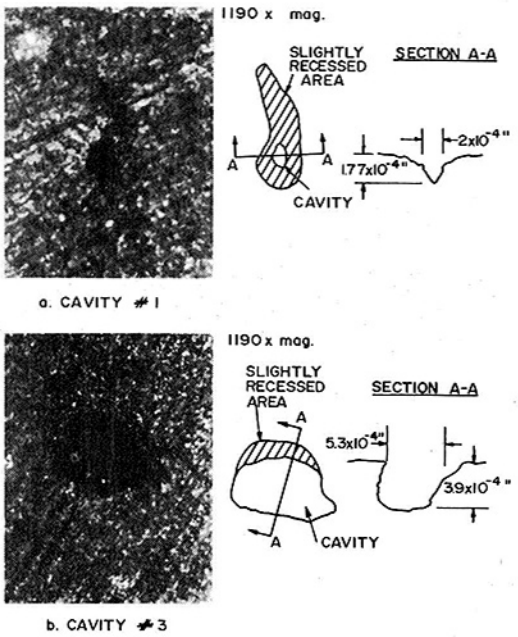

Fig. 2 Photomicrographs of typical surface cavities

Experimental Results and Discussion

Boiling and gas diffusion nucleation experiments were performed with eight individual sites on a copper surface, see Fig. 2. Initially, the surface was placed in a pool boiling apparatus, the ΔT recorded at the point where ebulition ceased for each cavity upon decreasing heat flux, and ρ values calculated from equation (2). The cavity locations were identified by small circular scale spots formed around each site during the boiling process. Analysis revealed that the scale was a negligibly thin deposit of silica derived from the water. Subsequently, the surface was placed in the gas diffusion apparatus, the value of P_a measured at the point where nucleation and bubble growth ceased (for the same eight cavities), and ρ values calculated from equation (1). The experimental results plotted in Fig. 3 reveal excellent agreement between the gas diffusion and boiling nucleation results. It is interesting to note that the effective radius of nucleation for some cavities is not nec-

essarily equal to the photographically measured cavity mouth radius. Reproducibility of the data was enhanced if prior to the gas diffusion experiment the test surface was promoted by gently washing it with Ivory Soap solution which increased the fluid-surface angle and thereby improved cavity stability. Even without the promoter, reasonably consistent results were obtained as the silica deposits surrounding the cavities appeared to act as stabilizing agents by locally reducing site wetability. No promoter was used in the boiling tests.

While gas diffusion technique was valid for studying individual sites that were known to be stable from a previous boiling experiment, the technique failed to predict ρ values for arbitrary cavities in advance. In nucleate boiling of water about 50 departures/s. occur throughout the course of boiling. Only cavities which are excellent vapor traps can survive so many departure cycles without being deactivated. If the vapor in a cavity is totally displaced by liquid in any one cycle the cavity is permanently lost, unless, of course, it is reactivated by a neighbor or homogeneous nucleation occurs. However in the gas diffusion experiment a cavity is not given the same rigorous test of stability which is associated with nucleate boiling. Even marginally stable cavities may remain active at the slow departure frequencies, i.e., 1 per 5 min (produced by physical wiping). In general, the n/A versus ρ obtained from the gas diffusion experiment will overestimate the number of cavities active in nucleate boiling. Gas diffusion experiments by other investigators [5] have also met with only limited success, but it is hoped that in a modified form gas diffusion techniques can indeed provide the cumulative distribution of surface cavities.

References

1 Buel, W. M., and Westwater, V. W., "Bubble Growth by Dissolution: Influence of Contact Angle," *AIChE Journal,* Vol. 12, No. 3, 1966, pp. 571–576.

2 Brown, W. T., Jr., "Study of Flow Surface Boiling," PhD. thesis, Department of Mechanical Engineering, MIT, 1967.

3 Lorenz, J. J., "The Effects of Surface Conditions on Boiling Characteristics," PhD thesis, Department of Mechanical Engineering, MIT, Dec. 1971.

4 Lorenz, J. J., Mikic, B. B., and Rohsenow, W. M., "The Effects of Surface Conditions on Boiling Characteristics," *Heat Transfer 1974,* Vol. IV, Proceedings of the 5th International Heat Transfer Conference, Tokyo, Japan.

5 Kenning, D. B., Oxford University, personal communication, Sept. 1974.

journal of heat transfer

discussion

Stability and Oscillation Characteristics of Finite-Element, Finite-Difference, and Weighted-Residuals Methods for Transient Two-Dimensional Heat Conduction in Solids[1]

G. E. Myers[2] The authors have restricted their discussion of the finite-element problem by considering only rectangular elements with an assumed temperature profile given by equation (5). The use of triangles (rather than rectangles) is also very common because of the versatility of the triangle in the analysis of unusually-shaped regions. Can the authors shed any light on the stability characteristics for their example, boundary conditions (25), but using triangular elements with linear elemental temperature distributions?

The authors have listed several approximations for the Laplacian term, equations (16) through (19), but seem to have selected only equation (18) for their stability analysis. Would the results be the same if another approximation had been used?

---

[1] By R. V. S. Yalamanchilli and S.-C. Chu, published in the May 1973 issue of JOURNAL OF HEAT TRANSFER, TRANS. ASME, Series C, Vol. 95, No. 2, pp. 235-239.

[2] Professor, University of Wisconsin-Madison, Madison, Wisc.